Photophysical studies of new heterocyclic molecular materials exhibiting TADF and solid-state luminescence

Antonio Maggiore

Thèse de doctorat

NNT : 2020UPASF007

Photophysical studies of new heterocyclic molecular materials exhibiting TADF and solid-state luminescence.

Thèse de doctorat de l'université Paris-Saclay

École doctorale n°571, Science Chimiques: Molécules, Matériaux, Instrumentation et Biosystèmes (2MIB)
Spécialité de doctorat: Chimie
Unité de recherche: Université Paris-Saclay, ENS Paris-Saclay, CNRS, PPSM, 91190, Gif-sur-Yvette, France.
Référent : ENS Paris-Saclay

Antonio MAGGIORE

Composition du Jury

Céline FROCHOT Directeur de recherche CNRS, Université de Lorraine (laboratoire LRGP)	Rapporteur & Examinatrice
Luca PRODI Professeur, Università di Bologna (Dipartimento di Chimica "Giacomo Ciamician")	Rapporteur & Examinateur
Rachel MEALLET-RENAULT Professeur, Université Paris-Saclay (laboratoire ISMO)	Président
Fernando DIAS Professeur, Durham University (Department of Physics)	Examinateur
Philippe HAPIOT Directeur de Recherche CNRS, Institut de Science Chimiques des Rennes	Examinateur
Fabien MIOMANDRE Professeur, École Normale Supérieure Paris-Saclay (laboratoire PPSM)	Directeur de thèse
Gilles CLAVIER Directeur de Recherche CNRS, École Normale Supérieure Paris-Saclay (laboratoire PPSM)	Co-Directeur de thèse

Acknowledgements

In the first place, I would like to express my sincere gratitude to my supervisor Fabien Miomandre for the continuous support of my Ph.D., for his patience and motivation. His support and his understanding helped me to carry on the work even in the dark moments that unfortunately occurred during this period. My thanks also go to my co-supervisor Gilles Clavier for his supervision and help. Many thanks goes also to Pierre Audebert which was always very helpful and happy to devote his time. I consider Pierre my second co-supervisor. My sincere gratitude goes to my colleague Yangyang Qu with whom I spent most of my time in the PPSM laboratory and who provided me with the majority of materials studied in this thesis. I would like to extend my sincere thanks to all the members of PPSM, but especially to Arnaud Brosseau who was always very helpful and kind to me and extremely important in the realization of my experimental part. Many thanks to Rémi Métivier for devoting his time to help me, for his important advice in photophysics. Thanks a lot to Andrée Husson for her continuous availability and help regarding all the administrative and bureaucratic parts, but especially thanks for being always kind to me giving me a great support. Thanks to Christian Jean-Baptiste, to Jacky Fromont, Laurent Galmiche, Isabelle Leray, and Luca Polacchi. Finally, I want to thank so much Cristina Verrecchia from ENS doctoral Departement, for her great kindness and availability.

Great thanks to Fernando Dias and Andy Monkmen for giving me the possibility to do part of my work in the OEM group within the Centre for Materials Physics at Durham University. Without this period I would have never been able to obtain the results achieved in this thesis. I would also like to acknowledge the other members of the OEM group, and especially Marco Colella, Andrew Danos, Piotr Pander, and Daniel Pereira. Many thanks to Miguel Ribeiro for allowing me to spend part of the period of my Ph.D. in Porto at the Centre for Nanotechnology and Smart Materials (CeNTI).

Special thanks to my colleagues, collaborators, and friends from EXCILIGHT Marie Curie ITN European project. Firstly, many thanks to Marco Colella for his availability and being a good adviser. I spent with Marco both my secondments: in Portugal and in Durham. He was always very helpful with OLED fabrication. Many thanks to Piotr Pander who became my very good friend, especially after spending time together during my secondment in Durham. I am thankful for stimulating discussions about photophysics and good advice. Moreover, special thanks to Xiaofeng Tan with whom we had good time together and fruitful conversations during his secondment in Paris and during all EXCILIGHT meetings and who provided me with some of the materials studied in the thesis. I want to also thank Przemyslaw Data who coordinated the EXCILIGHT project, thanks for his availability, advice, and great moments during all EXCILIGHT meetings. Finally, I would like to express all my sincere gratitude to all the other participants and colleagues of the EXCILIGHT project.

Great thanks go to Philippe Hapiot, who has kindly been my external supervisor and will be one of the examiners of this thesis. I am really grateful for his helpful discussions and suggestions over the meeting that we had during my thesis. I would also like to express my special gratitude to all the other members of the jury: my rapporteurs Céline Frochot and Luca Prodi and my external examiners Rachel Meallet-Renault and Fernando Dias

But my best and my deepest gratitude goes to my parents Giovanni and Donatina for their immense love. They never told me, but I believe they would prefer to have me closer to them, in Italy. They have always supported me, and they supported all my decisions. It brought to me a great sadness when my great dad Giovanni passed away in the middle of my PhD. He has always been my greatest adviser, my anchor in the most difficult moments in my life, my best motivator, and my greatest teacher ever. And he will be forever and for the rest of all my whole life.

TABLE OF CONTENTS

ABBREVIATIONS

A	Electron accepting unit/molecule
ACQ	Aggregation-caused quenching
AIE	Aggregation induced enhancement emission
AIEE	Aggregation induced emission
a.u.	Arbitrary unite
BzN	Benzonitrile
CIE	Crystallization Aggregation induced emission
CIEE	Crystallization Aggregation induced enhancement emission
CT	Charge transfer
CV	Cyclic voltammetry
Cz	Carbazole
D	Electron donating unit/molecule
D-A	Donor acceptor
DF	Delay fluorescence
DCM	Dichloromethane
HFC	Hyperfine coupling
HOMO	Highest occupied molecular orbital
IC	Internal conversion
ICT	Internal charge transfer
ISC	Inter system crossing
LE	Locally excited

LT	Low temperature (77K)
LUMO	Lowest unoccupied molecular orbital
NIR	Near Infra-red
OLED	Organic light emitting diode
PF	Prompt fluorescence
Phx	Phenoxazine
Pht	Phenotiazine
PL	Photoluminescence
PLQY	Photoluminescence quantum yield
QY	Quantum yield
RIC	Reverse internal conversion
RT	Room Temperature
RTP	Room temperature phosphorescence
SOC	Spin orbit coupling
TTA	Triplet-triplet annihilation
XRD	X-ray diffraction
UV	Ultra violet

ABSTRACT

Artificial lighting is a crucial part of human activity which consumes almost 19% of the planet's energy. Promoting lighting energy reduction plays an important role in alleviating global warming thanks to the reduction of the gases released in the atmosphere, the by-product of the combustion of oil derivatives, considered as the main responsible of the greenhouse effect. This work studies the photophysical properties of several new metal-free organic emitters showing thermally activated delay fluorescence (TADF) and room temperature phosphorescence (RTP). TADF is a triplet harvesting mechanism used in the last generation of OLED devices. These are considered to date as the best technology available to dramatically reduce the amount of energy required for lighting worldwide. TADF based OLEDs allow us to obtain internal quantum efficiency (IQE) close to 100% without using any highly expensive, rare, and toxic heavy-atom complexes. However, although especially in the last years much progress has been done on organic TADF, different aspects remain unclear especially regarding the materials design and the photophysical properties in crystalline forms. In this thesis are presented the photophysical properties of new Donor-Acceptor (D-A) emitters composed of a benzonitrile core as the acceptor moiety and various sets of carbazole and phenoxazine substituents, as donors. Interestingly these materials show either the possibility to tune the color emission with the number of substituents, and they also present a double TADF emission. Then the study of the supramolecular properties of the most efficient compounds is explored. In particular, the selected materials present mechanochromic luminescence (change of the emission color when an external stress is applied), polymorphism, and aggregation-induced emission with the possibility to change the TADF properties. It will be demonstrated how it is possible to trigger the TADF inducing a change of the molecular conformation through crystallization. Finally, a series of new A-triazine core-based Donor-Acceptor (D-A) molecules are also studied. Beyond the TADF properties, they show room temperature phosphorescence (RTP) in the crystalline neat films. In particular, it is demonstrated how the molecular design and rigidity of the medium, are crucial to determine whether the molecule emits through TADF or RTP.

GENERAL INTRODUCTION.

Among the most ambitious goals of the European Union in the coming years, there is a reduction of the energy consumption by at least 20%, the reduction of global warming through the implementations of new politics, and a drastic reduction in the use of toxic materials. Achieving these results will require a dramatic change in the current economy based mainly on the use of fossil fuels and its derivatives. In this context, many efforts are demanded from Science, especially regarding the study and the development of new technologies, new materials, and a new concept of non-toxic chemistry, so-called green chemistry. Within this context, an important area deeply studied is that of artificial lighting, which is an essential part of our lives, and consumes 19% of the planet's electricity usage. On that basis, the scientific community is mainly focused on the development of efficient devices that use less electricity, reduce energy costs, and greatly cut CO2 production. Ultra-efficient lighting will play an important role in achieving this. In particular, white organic light-emitting diodes (WOLEDs) could become an integral part of the new lighting technologies because of their ability to convert up to 99% of electric energy in lighting energy. Two types of excited states are created when charges recombine in an OLED - singlet and triplet excitons- but only the singlets directly give light, which fundamentally limits external OLED efficiency to 25%. Currently, phosphorescent heavy metal complexes are used to "harvest" both singlet and triplet states and thus to generate light. Unfortunately, these emitters suffer from toxicity but also from the scarcity and high cost of iridium and platinum which restricts their use in commercial applications. Moreover, pushing the metal-to-ligand charge-transfer excited state of these complexes into the blue, opens a non-radiative pathway via the metal d-orbitals, which limits efficiency, makes the complexes thermally and photochemically unstable and thus limits their operational lifetime. An alternative way to convert triplets to singlets in OLEDs has recently been reported by Adachi et al. using thermally activated delayed fluorescence (TADF). In this case, the use of completely low-cost and metal-free purely organic emitters allows to replace efficiently the metal complexes thanks to a suitable molecular design that allows to achieve in the devices a nearly unitary internal quantum efficiency (IQE). Moreover thanks to the formation of stable CT states it is possible to obtain a broadened emission that is highly desirable in lighting devices. On the other hand, an opportune choice of the donors and acceptors allows achieving a wide energy gap between the frontier orbitals, as well as the high lowest-excited singlet (S_1) and triplet (T_1) energies (≥2.8 eV). These characteristic makes the TADF materials a key solution for deep blue OLEDs. The work of this thesis is focused on the study of new organic molecules (Donor-Acceptor and Donor-Acceptor-Donor type) presenting Thermally Activated Delayed Fluorescence (TADF) phenomenon as materials for Easy-to-Tailor Ultra-efficient OLED Lighting, and the investigation of their photophysical properties both in solution and aggregate forms.

The work of this thesis is part of the framework of the European ITN project “EXCILIGHT”, therefore I made part of my research work collaboratively with EXCILIGHT partners: firstly in CeNTI-Centre of Nanotechnology and Smart Materials (Vila Nova de Famalicão, Portugal) where I fabricated the OLEDs. Moreover, I did the time-resolved photophysical characterizations in the organic electroactive materials OEM group (Physic Department, Durham University), which has a range of unique optical spectroscopy techniques more suitable for studying the TADF molecules. In particular in the following chapters are presented the photophysical properties of a series of new Donor-Acceptor (D-A) molecules composed by a benzonitrile attractor, as acceptor moiety and various sets of carbazole and phenoxazine substituents, as donor moieties. The photophysical characterization of the isolated molecule in different solvents and a rigid matrix of PMMA are studied together with the investigation of the supramolecular properties, e.g. mechanochromic luminescence, polymorphism, and aggregation-induced emission effects. Moreover is also obtained an interesting advancement beyond the existing TADF photophysics literature demonstrating how it is possible to switch on TADF thanks to the molecular conformation distortion induced by crystallization. Finally is reported a series of new triazine Donor-Acceptor (D-A) molecules. The photophysical study is reported for all compounds in solution, in a rigid matrix of PMMA and neat crystalline films.

The TADF molecules studied in this thesis were designed in the PPSM laboratory - ENS Paris-Saclay in the group of Prof. Pierre Audebert, Dr. Gilles Clavier and Prof Fabien Miomandre and were synthesized by Yangyang Qu (in the same group) and Xiaofeng Tan (from the Kaunas University of Technology - Department of Organic Technology) during their Ph.D. In Durham I collaborated with Marco Colella, Andrew Danos and Piotr Pander from the group of Prof. Andy Monkman and Prof. Fernando Dias.

1.1 CONTENT OF THE VARIOUS CHAPTERS.

Chapter 1: **Thermally activated delay fluorescence phenomena. State of art, photophysical characterization methods and challenges.**

This chapter introduces the thermally activated delayed fluorescence (TADF) phenomena and the strategies to design efficient TADF emitters. A brief overview of the state of the art is presented, showing the significant progress that has been made in recent years with a particular emphasis on the different class of Donor-Acceptor organic systems firstly reported by Adachi et al. This chapter will then describe and discuss the photophysics of TADF molecules and the spectroscopic methods used to investigate them. Both steady-state and time-resolved methods are presented. The effect of oxygen in delayed fluorescence is described.

Chapter 2: **Novel benzonitrile compounds with mixed carbazoles and phenoxazines substituents exhibiting dual emission and TADF properties.**

This chapter presents three series of new Donor-Acceptor (D-A) and $Donor_1$-Acceptor-$Donor_2$ (D_1-A-D_2) systems molecules featuring a benzonitrile attractor and various sets of carbazole and phenoxazine substituents. The photophysical characterization of the isolated molecule in solvents with different polarities and in a rigid matrix of PMMA is reported for all compounds. To better understand the photophysics, the effect of the temperature is also reported for time-resolved measurements. The influence of the number and the class of the donors on the photophysical properties and on the TADF are also examined and discussed. All compounds exhibit absorption in the visible range where ligands can no longer absorb. The CT band observed in absorption gives origins because of the strong intramolecular charge transfer (ICT) ability of these materials, and is formed through a direct transition from the highest occupied molecular orbital (HOMO) localized on the donor part to the lowest unoccupied molecular orbital (LUMO) localized on the benzonitrile acceptor. Thus, a small overlap between HOMO and LUMO leads to a small ΔE_{ST}, allowing to observe TADF. However, due to efficient non-radiative deactivation poor TADF properties are observed although the photophysical of these systems result new and interesting. Interestingly all compound containing different donors exhibits more than one CT absorption band and especially in the first subseries a double intense emission is observed especially in solution.

Chapter 3: **Stimulus responsive benzonitrile derivative exibithing TADF, Polymorphism, and Mechanocromic Luminescence.**

This chapter reports the investigation of the supramolecular properties of the most interesting and efficient compounds presented in the previous chapter. It will be shown how the presence of the CT state is crucial to make these molecules very sensitive to a change in photophysical properties upon changing of molecular packing. Different methods of sample preparation are used to obtain the different molecular packing using the same material which results in changes of colour emission, PL efficiency, and TADF characteristics. Mechanochromic luminescence properties were also found when external stress (like mechanical stimuli or the effect of solvent) changed their colour and photophysical properties in response to a change in their environment and packing. This effect is induced by the transition between different amorphous states or from crystalline to amorphous states and vice versa. Finally, those compounds also exhibited aggregation-induced emission-delayed fluorescence (AIE-DF); in fact, they showed weaker emission in a dilute solution that became strong in an aggregate form, due to the restriction of intramolecular rotation.

Chapter 4: Switching on the TADF trough the distortion of the molecular configuration in the crystal, and sonocrystallization induced TADF.

This chapter can be considered the most interesting, due to its advancement beyond the existing TADF photophysics literature. There are several examples of TADF molecules in the literature that also present the AIE phenomenon. However, to the best of our knowledge, the following chapter presents the first time that a TADF molecule is shown to be activated when arranged in a crystal lattice. Distortion of the molecular conformation lies at the base of this phenomenon, rather than the restriction of intramolecular motion as generally happens for common AIE materials. When the molecule is free to move in solution, upon excitation, the Donor-Acceptor plans becomes perfectly perpendicular to each other, inducing an integral overlap between HOMO and LUMO equal to zero. This leads to an extreme decrease in the oscillator strength with a very low probability of radiative decay. Alternatively, when the molecule is packed into the crystal lattice, the perfect orthogonality is broken, thus ensuring a very low ΔE_{ST}, which is a fundamental requirement for a good TADF effect. This chapter will also demonstrate how the ultrasound application to a system of non-solvent/AIE-TADF nanoparticles, can significantly affect the self-organization of the nanoparticle and dramatically change its properties. The sonication provides energy to dispersed nanoparticles which change their morphology; from a disordered amorphous form to a crystalline one.

Chapter 5: Novel chromophores with condensed 1,2,4-triazine system simultaneously achieve thermally activated delay fluorescence and crystallization-induced phosphorescence.

This chapter presents a series of seven A-triazine new Donor-Acceptor (D-A) molecules. The photophysical characterization is reported for molecules of all compounds in solvent form, in a rigid matrix of PMMA, and for aggregated molecules in neat films. The effect of the temperature is also reported for steady-state and time-resolved measurements. It is interesting to underline how most of these compounds present TADF only in solid-state (0.1wt% in PMMA) and only a weak fluorescence is detected in solution, but the most interesting thing to emphasize is the presence of room temperature phosphorescence (RTP) in the neat films in air. In fact, in neat films, it is easy to observe how the compounds are spontaneously organized in a crystalline form. The slow oxygen diffusion and the rigidity of the crystals are considered very important parameters that favour the RTP because the phosphorescence quenching of the oxygen and the non-radiative channels are suppressed by the strong rigidity of the crystal.

CHAPTER 1.

THERMALLY ACTIVATED DELAYED FLUORESCENCE PHENOMENA. STATE OF ART, PHOTOPHYSICAL CHARACTERIZATION METHODS AND CHALLENGES.

1. INTRODUCTION.

Thermally activated delayed fluorescence (TADF) phenomena, also known as E-type delayed fluorescence (DF), was discovered by Perrin in 1929[1]. Later, in 1941, Lewis reported DF in fluorescein solutions[2]. However, the first important work concerning the study of DF in organic molecules dates back to 1961, when Parker and Hatchard also reported E-type DF in eosin and benzyl[3-4]. The acronym TADF was chosen for the first time in 1968 by Wilkinson and Horrocks[5], but it was Adachi that made this mechanism famous. In fact, Adachi proposed TADF fluorescent materials as a solution to harvest non-emissive excited states triplets in organic light emitting diodes (OLEDs)[6]. Completely organic TADF materials have been developed in recent years as valid alternatives to the more expensive and toxic Pt(II) and Ir (III) complexes. However although TADF emitters allow to obtain an external quantum efficiency (EQE) in the OLEDs device as the phosphorescence third row metalorganic complexes, the photophysics of the former is much more complex than the latter. In fact, in Pt(II) and Ir(III) metalorganic compounds all the excitation energy goes directly in the triplet state and in general only a monoexponential triplet decay is observed with relatively short phosphorescence lifetime and high PLQY. These systems are characterized by the presence of a metal-ligand charge transfer (MLCT) state originated from a mix between the d-orbitals of a heavy metal with ligand-centred orbitals. The presence of a heavy metal, leads to a strong spin orbit coupling (SOC) which leads to an efficient intersystem crossing (ISC). On the other hand, in TADF materials no phosphorescence occurs at room temperature and in general no metals are involved. The SOC is obtained thanks to the presence of charge transfer (CT) state or in some cases n-π* state. However, contrarily to the phosphoresce, characteristic of metalorganic complexes, in TADF emitters the $T_1 \rightarrow S_1$ transition (reverse ISC) is highly desired, and being endoenergetic, needs thermal energy to be activated. It results that TADF materials are sensitive to temperature, polarity environment, molecular conformation and many other factors. Furthermore, several electronic states are involved in their photophysical process which leads to observe biexponential or multiexponential decays and an emission that evolves at different delay time. All this factors make the photophysics of TADF materials very complex to study and to interpret.

2. ELECTRONIC TRANSITIONS IN TADF MATERIALS.

Before discussing the electronic transitions occurring in TADF materials, it is worth mentioning that the most common organic materials used in TADF emitters are characterized by the presence of π-conjugated molecules. These molecules are characterized by the presence of one or more conjugated systems formed thanks to the overlap of p-orbitals hybridized sp^2 that are present on neighbouring atoms which are in general carbon or nitrogen. These aromatic systems are characterized by a good stability but above all, they are characterized especially by their ability to emit photoluminescence from UV to NIR.

In this context, it is important to consider how the excited states are formed in organic molecules. After the electron is excited to a higher energy level, it is possible to form a molecular excited state with distinct spin arrangement, arising from the different molecular orbitals occupation by the electrons, compared to the ground state, e.g. LUMOs. This results also in a new distribution of the electronic cloud on the molecule, which can lead to a different molecular configuration. As stated by the Pauli Exclusion principle, two electrons cannot have the same four quantum numbers (n, l, m_l, m_s) and the only two electrons that can occupy each orbital must have opposite spin states. These opposite spin states are called spin pairing. In the excited singlet state, the electron is promoted in the same spin orientation (**Figure 1.1**) as the ground state (paired). In a triplet excited state, the electron is flipped to obtain the same spin orientation (parallel) to the other unpaired electron (**Figure 1.1**). Hole and electron have spin 1/2 and they can be spin up (s = +1/2) or spin down (s = -1/2), therefore the total spin angular momentum, S (sum of all the electron spins) is S=0 for a singlet exited state and S=1 for the triplet state. From the value of the multiplicity, (2S+1) it is possible to obtain 1 for a singlet excited state and 3 for the triplet state. The multiplicity of spin represents the number of degenerate states. This difference in the electron spin arrangement of excited molecules is the base of a large amount of different properties. The singlet state is the origin of the fluorescence emission and it is in general short-lived (few nanoseconds) and strongly emissive. In contrast, the transition from triplet states to the singlet ground state is spin-forbidden and therefore is mostly non-emissive. It results that the decay of triplet states occurs mostly via non-radiative processes, except in phosphorescence materials where the transition to ground state is only partially allowed with a microsecond to second lifetime. Therefore, it results that the differences between singlet and triplet states are very important in OLEDs.

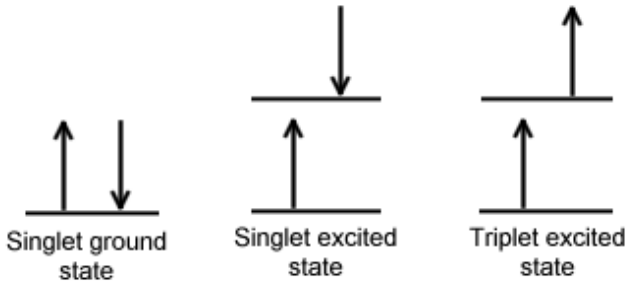

Figure 1.1*: spin in the ground and excited states*

In photophysics, a schematic representation of radiative and non-radiative processes in organic molecules is obtained through a Perrin-Jablonski diagram. The one reported in **Figure 1.2** allows to illustrate all the processes (radiative and non-radiative) that are relevant in the TADF mechanism. The transitions between states are represented by vertical lines. The thicker horizontal lines represent the electronic states and the thinner lines the vibrational states. When a TADF Donor-Acceptor molecule is excited by a light beam two different situations can occur. 1) The CT state can be directly populated through a weak $S_0 \rightarrow {}^1CT$ electronic transition, which can be described as $D(\pi) \rightarrow A(\pi^*)$. This is a transition that, if completely pure, is forbidden by geometry, and therefore in general when D-A angle is near orthogonal as in TADF molecules, it corresponds to a low oscillator strength, and thus it appears weak. This weak CT band is observed in absorption spectra in the region where the donor and acceptor moieties cannot longer absorb. 2) Secondly, the donor or the acceptor moiety is excited directly through a π-π^* transition and a locally excited singlet state (^{1}LE) is formed. Then, the singlet ^{1}CT state is populated trough an Energy Transfer (ET) process from the ^{1}LE, which is often accompanied by structural relaxations to form a new stabilized dipolar CT state. It is important to underline that the excitation is transferred to ^{1}CT state by a ET process. The ET rate depends mostly on the decoupling between the D and A units, which is caused by near orthogonality between them, both in the excited and ground states. After the formation of the CT state, the excitation can radiatively decay to the ground state trough prompt fluorescence (PF), or move to the local triplet state (^{3}LE) through an intersystem crossing process (ISC) or even deactivate by internal conversion (IC) non-radiative processes. A second path that excitation may follow is through a n-π^* or mixed n-π^*/π-π^* transition that forms directly a Charge Transfer state (^{1}CT).[7]

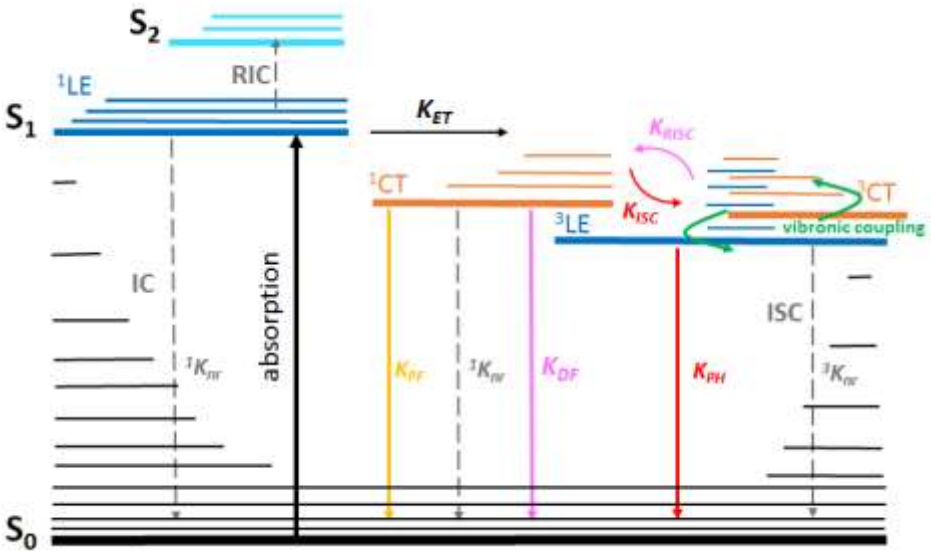

Figure 1.2: *simplified energy diagram showing of the electronic energy levels involved in TADF according to the vibronic coupling model.*

As already mentioned above, after the CT state is formed there might be three different processes: 1) PF from the CT state to the ground state, with a decay in the pico-nanosecond range and expressed by the rate constant k_{PF},; 2) non radiative deactivation, defined by the rate constant k_{nr}, and 3) ISC to the triplet state, defined by the rate constant k_{isc}. After populating the triplet state, the excitation can deactivate directly to the ground state by radiative phosphorescence emission (k_{PH}) or deactivate non-radiatively through IC ($^3k_{nr}$). In TADF materials the triplet state formed by ISC comes back to the singlet state through a spin flip (k_{RISC}). This is an adiabatic process and it can take place thanks to thermal energy that allows the triplet state to reach a vibronic sub-level, isoenergetic with the emissive singlet states thus enabling the electron to flip back into the emissive singlet through the RISC process. In fact, to have an efficient TADF process, it is fundamental that the energy splitting between the triplet and the singlet states is very small (ideally $\Delta E_{ST} < 150$ meV). Such a condition allows that most of the triplet states can be up-converted back to the singlet state, thus resulting in $k_{RISC} >> k_{PH} + {}^3k_{nr}$. When the ^{1}CT is again populated, it gives rise to the delayed fluorescence (DF) emission with a lifetime in the microsecond to millisecond regime. This long lifetime is due to the involvement of the longer-lived triplet states (DF), k_{DF}. From the above considerations, it is clear that the TADF process depends on both RISC and temperature. Therefore, this is a process that is very sensitive to cooling and oxygen quenching of the triplet state.

3. OLEDS: FROM 2ND GENERATION PHOSPHORESCENCE TO 3RD GENERATION TADF.

It is important to underline that OLEDs constitute the main application of TADF materials and the reason why many efforts have been made in recent years by the scientific community. Therefore, OLEDs are also here briefly introduced.

One of the most critical issues in OLED technology is its high power consumption, which pertains to two main parameters: quantum efficiency (QE) and driving voltage, predominantly to the former rather than the latter. QE in OLED is directly correlated with the states involved in the deactivation processes i.e. fluorescence, phosphorescence, non-radiative channels.

The first OLED generation was based on fluorescent materials, but they are limited because only 25% of injected charges can be converted into photons[8-10]. When electrons and holes are injected into the device through electrodes, an exciton is generated for every pair of hole and electron. Under electrical injection, the ratio of singlet to triplet excitons is 1:3 due to statistical recombination reasons[11]. In the case of fluorescent emitting materials, only singlet excitons can be transformed into photons, and so only 25% internal QE is theoretically possible. Such low internal QE of the fluorescent materials has pushed researchers to develop the second generation OLED [1, 11-13].

This second generation of OLEDs, employing high-efficiency phosphorescent emitting materials, can convert both singlet and triplet excitons into photons by a radiative transition process. However, although theoretically a 100% internal QE can be reached with the phosphorescent materials, statistical recombination problems still remain. The most used phosphorescent materials in OLED are complexes containing heavy metals, which mix the singlet and triplet states through SOC, to make the radiative decay of the triplet state possible[14]. Nevertheless, metalorganic complexes when used in OLEDs present some limits: firstly, they are not stable especially in the blue emission region[15]; secondly, they are expensive, and lastly, they might be toxic. Therefore, in order of replacing rare metals, Copper complexes have been introduced. In fact, it was demonstrated that they can maintain the ability of heavy metal to harvest both singlet and triplet states in OLEDs. Furthermore, some of these complexes show also a significant TADF contribution[16-17]. Another way to harvest triplet states in OLEDs is triplet harvesting through triplet fusion, via triplet–triplet annihilation (TTA)[18-19]. By TTA two triplet states produce one singlet excited state (**Figure 1.4**), which can decay radiatively and with a DF. But TTA is in general considered to be a side effect and therefore it is desirable to avoid it in OLED technology. In fact in the best possible matching of the energy levels, the maximum internal QE possible is around 62.5% [18-19].

The third generation of OLEDs takes advantage of the TADF mechanism to overcome the issues of phosphorescent metal-organic OLEDs. In fact, TADF molecules are fluorescent molecules designed to have a very low energy difference between the singlet (S_1) and triplet (T_1) excited states, so that RISC occurs between the lower singlet and triplet excited states. For TADF molecules, the theoretical triplet harvesting efficiency is 100%. Nowadays, it is possible to obtain such high efficiency levels in many molecules that emit in the blue[20-21] and green regions[7, 22]. However, in the red region, TADF materials still have numerous problems mainly because the non-radiative decay paths, that especially at RT, efficiently compete with RISC.

To ensure good TADF properties, when a molecule is designed several important aspects must be taken into account. First of all, it is very important to ensure a small energy separation between the lowest singlet and triplet excited states (ΔE_{ST}) while simultaneously minimizing internal conversion (IC) and maintaining strong photoluminescence quantum yield (PLQY). It is well known that in order to reduce singlet-triplet energy splitting, a key factor is to use CT excited states which also induce SOC. This allow that the non-radiative spin-forbidden ISC transition, between singlet and triplet states, becomes relatively fast. The most common TADF emitters are formed by a twisted donor-acceptor structure, where D and A units are covalently linked and spatially separated through the use of molecular bridges. Thus it results a strong CT character, if D and A moieties are not conjugated (geometrically decoupled), as a consequence of the small overlap between the HOMO and LUMO. Thus, a small overlap between HOMO and LUMO leads to a decrease in the electronic exchange energy, and therefore to a small ΔE_{ST}[23]. However, it is much more difficult to achieve a high fluorescent QY with a good TADF effect, and when a molecule is designed, it is important to take into consideration many other factors, such as the molecular geometry and the presence of a localised triplet (^{3}LE) on the D or A units[22, 24].

3.1 Triplet excitons harvesting in phosphorescent OLEDs

When an electrical field is applied to the OLED, an electron is injected through the cathode and a hole through the anode. These charges attract each other by Columbian interaction and form a new quasi-particle called exciton. This phenomenon is known as electroluminescence. Since both hole and electron have spins, four different spin combinations are possible: one of antiparallel spins producing a Singlet state, and three of parallel spins, giving a Triplet state (**Figure 1.3**). As electroluminescence follows a statistical recombination law, after the exciton is formed there is a 25% probability of forming a singlet state and 75% probability of forming a triplet state.

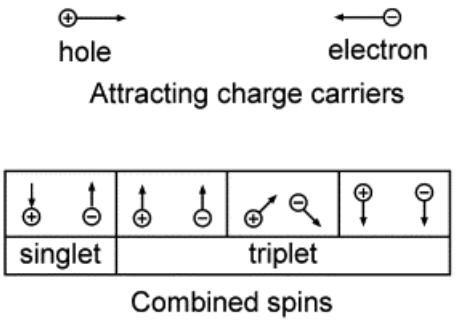

Figure 1.3: *Schematic description of (a) electron–hole recombination, (b) spin combinations, giving one singlet state and three triplet states.*

For improving the efficiency of OLEDs it is necessary to consider the **equation 1.1** which describes the total external quantum efficiency (EQE) of an OLED

$$EQE = \eta_{out} \times \eta_{fl} \times \gamma \times \eta_{fr} \qquad \textit{equation 1.1}$$

Where:

- η_{out}, represents the light out coupling efficiency and in general it is equal to 0.2. This factor considers mainly the fact that when light is emitted inside the device, there is the total internal reflection which causes light wave guiding, in addition to scattering and absorption phenomena. All these side phenomena limit the amount of light emitted by the device.

- η_{fl}, represents the PLQY of the emitting layer. It depends of several factors like non-radiative decay, aggregation quenching or self-quenching. In principle it can vary from 0 to 1.

- γ, represents the charge balance factor, which can be assumed to be 1 if the device is suitably designed, so that the fraction of injected holes and electrons that recombine to form excitons is close to 100%.

- η_{fr}, represents the fraction of emissive excited states, in particular taking into account the fraction of total excitons obtained through charge recombination that can deactivate radiatively.

In OLED using conventional organic fluorescent materials only the singlets can be converted into photons. The remaining 75% excitons cannot be converted into light and this part of the energy will only produce heat. This depends on quantum mechanical symmetry reasons since the transition from the excited triplet state T_1 to the ground state S_0 is forbidden for the selection rules.

In phosphorescent organometallic compounds containing heavy metals (e.g. iridium and platinum), the heavy atom effect breaks the selection rules through SOC and creates a

perturbation of the orbitals wave functions. This perturbation mixes the triplet and singlet states in the molecule and therefore the transition T_1 -> S_0 becomes possible. Furthermore the forbidden character of the deactivation process from T_1 to S_0 is at the origin of the longer lifetime (microsecond) of phosphorescent materials with respect to the fluorescent one, where the excitation decay directly from the singlet state, and the emission lifetime occurs in the nanosecond timescale. Thanks to the strong SOC, an electrical quantum yield of almost 100% can occur in OLED devices containing organometallic phosphorescent materials.

3.2 Triplet excitons harvesting in fluorescent OLEDs (TTA vs TADF)

As already mentioned there are two main strategies to harvest triplet exciton in OLED device using fluorescent materials. The first attempt to not lose triplet excitons consists in the use of the bimolecular triplet–triplet annihilation (TTA) process[25]. The TTA is a particular case of exchange energy transfer. Two triplet chemical groups, A (T_1*) and B (T_1*), react to produce two singlet states, one of which in the excited state and the other in the ground state (**Figure 1.4 up**). Through this process, it is possible to convert two triplet excitons into a singlet one. This can only occur when the energy gap between S_0 and T_1 is bigger than the energy separation (ΔE_{ST}) between the lowest excited singlet state (S_1) and the triplet state (T_1), thus the relation $2T_1$->S_1 is respected (**Figure 1.4 down**). It results that, if two triplet excited-state molecules approach each other, after the annihilation process, the energy level that the electron occupies will be twice of the lowest triplet energy gap. Hence, the process might have enough energy to excite one of the two molecules, to the higher singlet states. It thus finally results that the fluorescence can happen in this system. It is possible also to imagine that the TTA process will produce firstly an intermediate triplet pair complex (T_m= [T_1-T_1]*), which having energy ($2T_1$), lower than the second triplet state (T_2), will can only transfer its energy on a singlet state one (S_n) from which trough IC will be populated the lower singlet excited state (S_1) (**Figure 1.4 down**). This process is also called P-type delayed fluorescence. Through the TTA process, it is possible to convert the 75% triplet exciton produced by electrical injection up to 37.5% singlet states. Thus, an internal QE of 65.5% can be obtained for a TTA OLED device. However, in addition to a remaining energy loss of 27.5%, there are other factors that do not recommend this kind of materials in OLED like high driving voltages and concentrated sensitizers, accompanied by an increase of device efficiency roll-off that results in the OLED efficiency that typically decreases at high brightness levels.

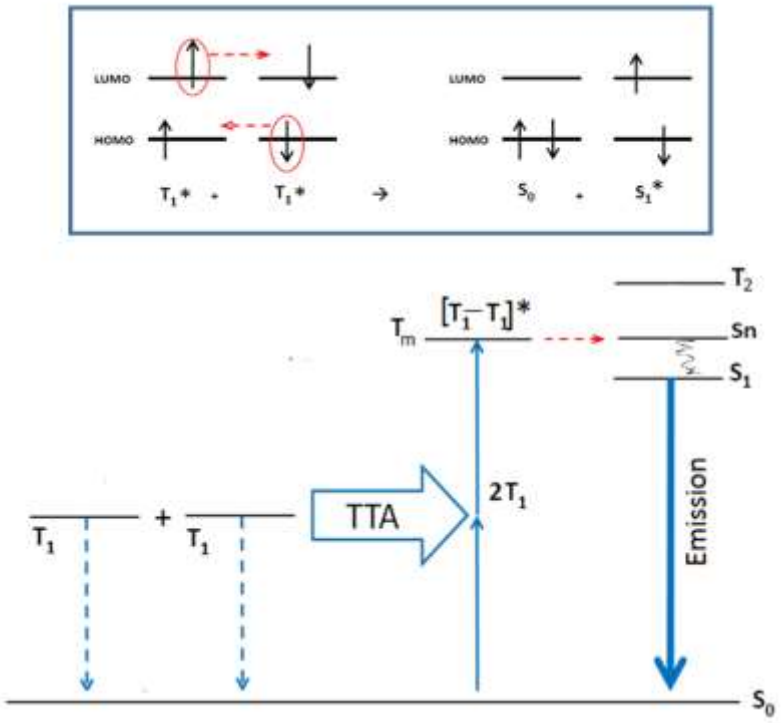

***Figure 1.4**: **up**) Schematic diagram for triplet-triplet annihilation, **down**) A generalized Jablonski diagram showing Triplet-triplet annihilation (TTA) resulting from the triplet states of two molecules which can annihilate to produce a higher energy singlet state.*

Nowadays, the TADF process is recognized as the most efficient way to harvest triplet excitons. In fact through TADF both singlet and triplet excited states of the molecule can be used in OLED devices to produce fluorescence light. It is well known that the key of the TADF process is the efficient reverse intersystem crossing (RISC) between the first excited states T_1 to S_1. This can be obtained thanks to a low singlet-triplet energy barrier (ΔE_{ST}) of the same order of magnitude as the thermal energy. In fact as T_1 has a lower energy than S_1, heat needs to be provided by the environment to the triplet to make the RISC process possible. From this comes the "Thermal Activated" term in the TADF acronym. In fact it is crucial to underline that to up-convert the triplet state to the singlet one, it is fundamental that the energy splitting between them is actually very small (ideally $\Delta E_{ST} < 150$ meV).

Initially, scientists thought that only the charge transfer states (CT) played a role in the ISC/RISC process. Presently there are several studies that have shown how the vibronic spin-orbit coupling model (VSOC) is the most reasonable one to explain how RISC works in TADF materials. This model involves mixing between the CT states with triplet localized states (^{3}LE), which also increases the ISC and RISC rates.[7, 26] However, if the energy difference between the singlet CT state and the triplet CT states is very small ($\Delta E_{ST} = {}^1CT - {}^3CT \approx 10^{-5}$ to 10^{-6} eV), hyperfine coupling (HFC) interactions

may also be involved in the ISC/RISC mechanism.[27] This mechanism arises from interactions between an electron spin and nucleus spin in the same molecule or in bimolecular systems. It results that HFC interactions become predominant to promote ISC/RISC, when it is not possible to mix the LE and CT states because they are energetically too far away.

4. MILESTONES IN THE DEVELOPMENT OF TADF MATERIALS.

This paragraph provides illustrative accounts on the progress made since Eosin was reported in 1961 phenomena (**Figure 1.5a**). In particular, TADF materials are divided into three main systems according to their molecular structures.

1) Metal-containing TADF materials: Among metalorganic complexes, those containing $\mathbf{d^{10}}$ metals are the best performing. TADF in metal complex was observed for the first time in a Cu(I)-complex (**Figure 1.5b**) and successively the most widely studied $\mathbf{d^{10}}$ TADF metal complexes remain based on Cu(I), especially because of low cost and toxicity. Other TADF metalorganic compounds reported are based on Au(I), Ag(I) and Sn (IV) complexes. Contrarily to the $\mathbf{d^6}$ and $\mathbf{d^8}$ phosphorescent metalorganic complex of the third (Ir, Pt, Os, Re) and second row (Ru), the first row $\mathbf{d^{10}}$ metalorganic complexes suffer of a much weaker SOC which makes the $T_1 \rightarrow S_0$ transition forbidden. However, they generally present a small ΔE_{ST}, which is a key factor for efficient TADF phenomenon. Furthermore, $\mathbf{d^{10}}$ metalorganic complexes also present ligands with a large steric hindrance (**Figure 1.5b**) which gives rigidity to the complex. This is another key factor for TADF phenomenon because it stabilizes the T_1 state thanks to the suppression of non-radiative deactivation process. On the other hand, the actual research is focused on increasing the complex rigidity as the distortion of excited state increases dramatically the non-radiative deactivation paths. However the $\mathbf{d^{10}}$ metal possesses another important key factor which is the electrons full d-orbitals, which suppress the possibility of having internal quenching in the excited states from d–d*.

2) Fullerenes (C_{60}, C_{70}, and higher fullerenes): in 1997 Berberan-Santos *et al.* reported the ability of fullerene (**Figure 1.5c**) to generate efficient TADF and it was used for the first time in the detection of oxygen and temperature. The unique photochemical and photophysical properties of fullerene arise from the high number of delocalized π electrons, the high symmetry and the curvature of the structure. However despite a high reverse intersystem crossing (rISC) ratio close to 100%, a relative small ΔE_{ST} (0.30 eV for C_{70}) and a long phosphorescence lifetime (28 ms for C_{70}) which make fullerenes good candidates for TADF materials, they suffer of low PLQY and moderately low solubility. These features limit the fullerenes applications only to temperature and oxygen sensors when dispersed in a polymer matrix.

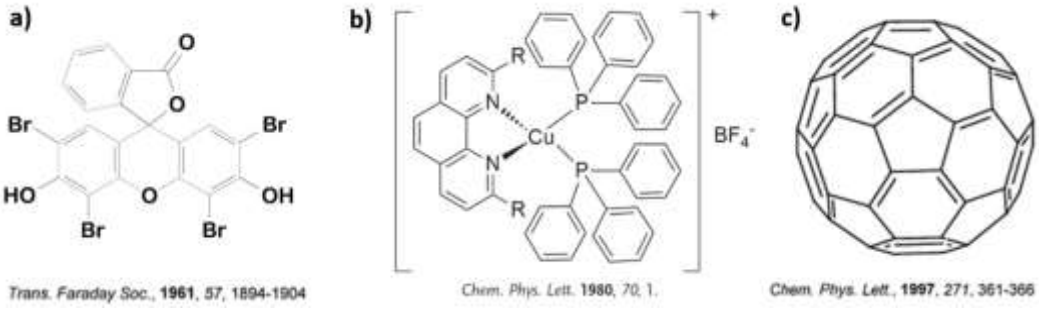

Figure 1.5: *molecular structures of:* ***a)*** *eosin,* ***b)*** *Cu-complex* ***c)*** *fullerene.*

3) Donor-Acceptor organic systems: as already mentioned above the real breakthrough in the development of TADF molecules was achieved in 2011 when pure organic donor acceptor (D-A) molecules where used by Adachi et al. for OLED applications. To date, the reported organic D-A TADF materials can be divided into two categories: (1) pure organic **intramolecular D–A** molecules and (2) **intermolecular exciplex** obtained through the use of individual donor and acceptor molecules. In this section is given a short overview of the first important D-A systems reported by Adachi et al. which constitute the most important class of TADF materials studied in literature. In **Figure 1.6** are depicted the general intramolecular D-A structure where the donor and the acceptor moieties are connected by a suitable bridge.

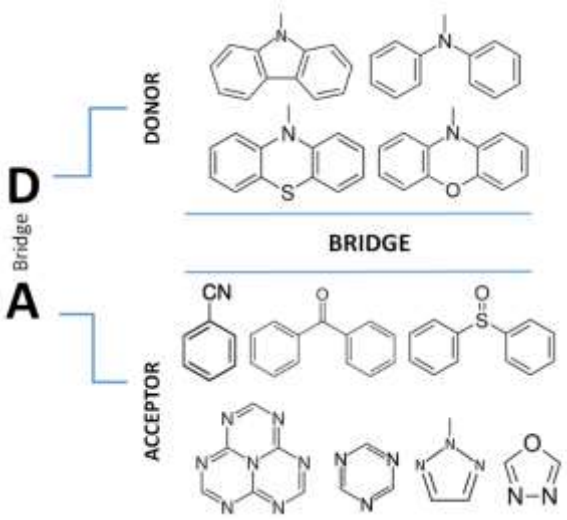

Figure 1.6: *schematic presentation of intramolecular D-A type TADF molecules.*

Although there is the possibility to employ several organic donors, *N*-containing aromatics such as carbazole, diphenylamine, phenoxazine or phenothiazine (**Figure 1.6**) and their derivatives are the most used in TADF D-A materials, mainly because of their strong electron donating ability and their stable and high energy triplet states. However, various classes of acceptors and their derivatives were used in the D-A molecules to tune the TADF emission strength, colour, and device performance. Here are reported some example of the first TADF molecules presented by Adachi and co-workers containing the most common acceptors.

- **Nitrile based acceptors**: the strong electron-withdrawing ability of the cyano group produces a significant increase in the electron affinity of the resulting compound and therefore the cyano group has wide applications in D-A type TADF molecules. The compound in **Figure 1.7a** presents two cyano units as electron acceptors and two di *p*-tolylamino electron donor moieties orthogonally connected through a spiro bridge. It was reported by Adachi in 2012 and exhibits yellow emission with a PLQY of 27%, ΔE_{ST} of 0.057 eV and an EQE in the device of 4.4%. Subsequently, the same group reported a modified **spiro-acridine** derivative (**Figure 1.7b**) giving a PLQY= 67.3%, a ΔE_{ST} = 0.028 eV and EQE of 10.1%. Further improvement of the TADF device efficiency (EQE=19.3%) was also realized in 2012 by employing a series of emitters based on **carbazolyl dicyanobenzene**. Adachi showed also how by changing the number of carbazolyl groups or introducing substituents it was possible to modulate the colour of the emission from sky blue to orange.

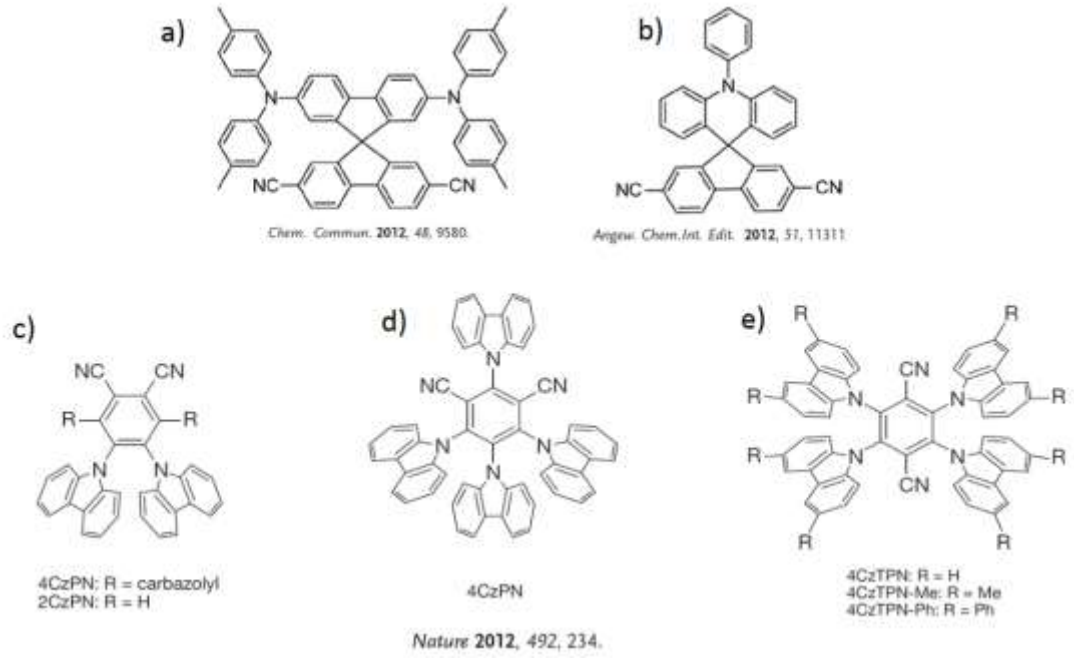

Figure 1.7: *molecular structures of some carbo-nitrile based TADF compounds reported by Adachi et al.*

- **Nitrogen heterocycle-based acceptors**: the electron-deficient nature of aromatic systems containing one or more electronegative nitrogen (N) atoms strongly increases the electron affinities of the aromatic molecule. Thus, *N*-containing arenes are typically adopted as electron-accepting moieties in high performance TADF materials. Adachi first reported TADF emitter in 2011 was based on a **triazine** compound (**Figure 1.8a**) showing a PLQY of 39%, ΔE_{ST}= 0.11 eV and an EQE=5.3%. Later in 2015 the molecule was optimized by the same group (**Figure 1.8b**) and a PLQY of ~100% and EQE=20.6% were obtained. A series of **oxadiazole and triazole derivatives** (**Figure 1.8c**) were also developed by Adachi et al. as D-A or D-A-D efficient TADF materials achieving a PLQY of 87% and a EQE=14.9%. Another interesting TADF system is based on the **heptazine** which thanks to a planar and rigid heterocyclic system of six C=N bonds surrounding a central *sp*2-hybridised N-atom, was selected by Adachi as a strong electron acceptor to realize molecular architectures for TADF emission (**Figure 1.8d**) obtaining a PLQY of 91% and a EQE= 17.5%

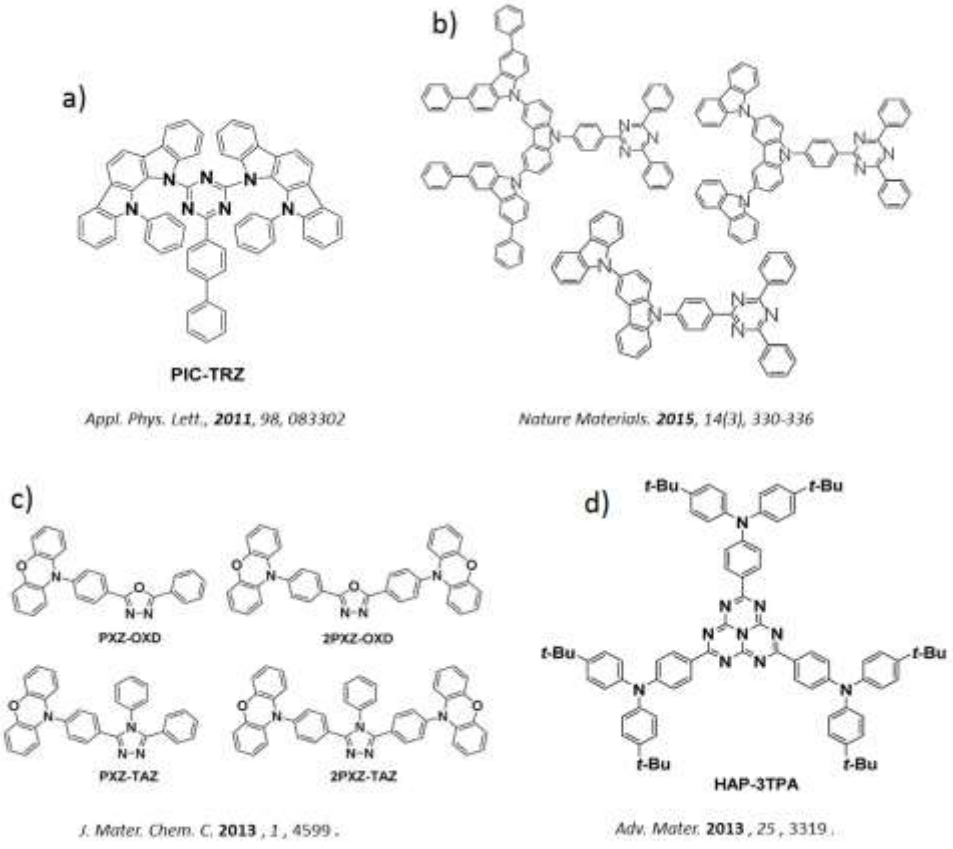

Figure 1.8: *molecular structures of some nitrogen heterocycle-based TADF compounds reported by Adachi et al.:* ***a)*** *and* ***b)*** *triazine derivatives;* ***c)*** *oxadiazole and triazole derivatives;* ***d)*** *heptazine derivative.*

- Diphenyl sulfone-based acceptors: the capability to act as a powerful electron-withdrawing group with a twist angle in the center makes diphenyl sulfone an interesting scaffold in TADF D-A acceptor materials. Adachi reported in 2012 a series of blue TADF compounds (**Figure 1.9**) achieving ΔE_{ST}= 0.32 eV, a PLQY of 80% and EQE= 9.9%. Subsequently, replacing the *tert* -butyl substituents on the carbazole donors by the more electron-rich methoxy groups, the ΔE_{ST} was reduced down to 0.21 eV, obtaining a PLQY of 80% and an EQE= 14.5%.

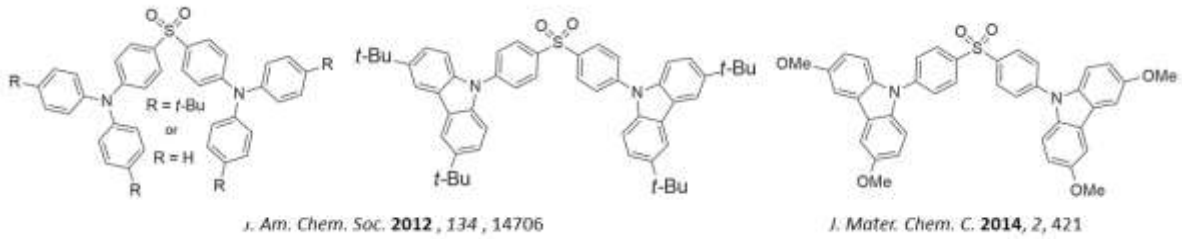

J. Am. Chem. Soc. **2012**, *134*, 14706 — *J. Mater. Chem. C.* **2014**, *2*, 421

Figure 1.9: *molecular structures of some diphenyl sulfone-based TADF compounds reported by Adachi.*

- Diphenyl ketone-based acceptors: known as a purely organic phosphor with efficient intersystem crossing, diphenyl ketone is used in TADF because of its highly electron withdrawing C=O group, which forms a twist angle with the donor moieties. Adachi et al. reported a series of butterfly-shaped D-A-D type molecules (**Figure 1.10**) achieving highly efficient TADF emissions with a PLQY of 71%, ΔE_{ST} (0.03–0.21 eV) and EQE=10.7%.

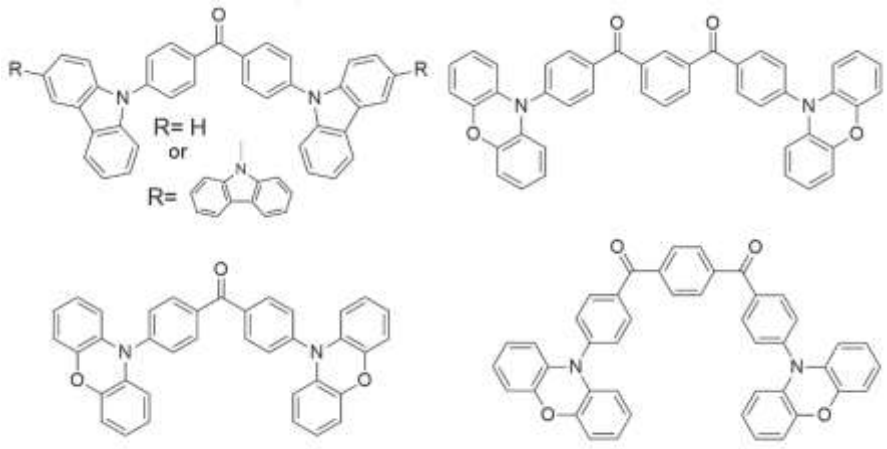

Angew. Chem. Int. Edit. **2014**, *53*, 6402

Figure 1.10: *molecular structures of some diphenyl ketone-based TADF compounds reported by Adachi et al.*

5. REVERSE INTERSYSTEM CROSSING: SPIN ORBIT COUPLING, HYPERFINE COUPLING AND VIBRONIC COUPLING.

Reverse intersystem crossing is a crucial parameter, which must be optimized to have an efficient TADF. To do this it is important to understand which states are involved during the rISC process. Firstly on this purpose, it is important to underline again that efficient TADF materials are in general donor-acceptor (D-A) charge transfer molecules linked via an aromatic bridge[28] or a N-C bridge[29] that forces the D and A units in a near-orthogonal orientation. This allows minimizing the electron interaction between D and A in the excited state, giving near zero exchange energy (equation 1.5) and thus small ΔE_{ST}.

However, it is important to consider that as already mentioned above, there are two mechanisms for the interconversion between singlet and triplet states: spin orbit coupling (SOC) and hyperfine coupling (HFC). In the D-A and D-A-D systems that are near orthogonal, the electron coupling is weak and the CT character is strong. However, in this configuration the SOC between ^{1}CT and ^{3}CT is forbidden because the orbitals involved are the same and the exchange energy approaches zero, i.e. $\langle {}^1CT|H_{SOC}|\,{}^3CT\rangle = 0$. In fact the spin flip between singlet and triplet states requires a change in the orbital angular momentum that cannot occur when the HOMO is perpendicular to the LUMO, because there is no change in spatial orbitals between these two states[30]. Consequently, any change in spin cannot be compensated by a corresponding change in angular momentum and therefore the total angular momentum cannot be conserved. This also implies that RISC is forbidden for the same reason[7].

Ogiwara et al.[27] demonstrated that RISC/ISC interconversion of the singlet and triplet emissive states can also occur through HFC which is caused by the interaction between two electronic spins or between the spins of an electron and a nucleus[31-32]. Thus is obtained a hyperfine coupling induced ISC which drives the RISC from ^{3}CT to ^{1}CT. However HFC between ^{1}CT and ^{3}CT becomes active only if the energy gap between ^{1}CT and ^{3}CT is very small (typically 1 to 20 µeV). Both HFC and SOC do not explain the fact that different D–A–D molecules with very similar energy gaps (ΔE_{ST}) exhibit large variations in k_{rISC}[33]. Furthermore, it was found that sterically hindering the D and A motion enables switching the emission from TADF to phosphorescence,[33] thus indicating a mechanism that depends on molecular vibrations.

The different studies[22, 33-34] that have been done to understand the key excited state properties to get efficient TADF properties allowed also to demonstrate that the two excited states involved in the RISC process can be tuned by changing the local environment. In addition, as the selection rules impose that the involved excited states must be of different character, ^{1}CT and ^{3}LE states have been proposed. Recently it has been demonstrated that an efficient RISC occurs via a second order vibronic coupling mechanism[26, 35-36] that involves in addition to the initial ^{3}LE and the final

^{1}CT states, the intermediate ^{3}CT state. Through this non-adiabatic vibronic coupling between ^{3}CT and ^{3}LE[26] an equilibrium between the two triplet states is reached by reverse internal conversion (RIC). In fact, the orbitals involved in the ^{3}LE state have a different electronic state with respect to the ones concerning the ^{1}CT state. This results into a different spatial orbital occupation between singlet and triplet states and consequently the coupling between them can occur because the total angular momentum is conserved. This satisfies the quantum mechanical theory which imposes that the excited states involved in the RISC must be of different character, which can finally occur between the mixed triplet states (^{3}CT and ^{3}LE) and the ^{1}CT state. The vibronic coupling mechanism is therefore responsible of ISC from ^{1}CT to ^{3}LE. It was demonstrated by Gibson at al[26] that without vibronic coupling between ^{3}LE and ^{3}CT of D-A systems, both ISC and RISC rates would be at least six orders of magnitude slower. A schematic representation of the mix between the two triplet states (^{3}CT and ^{3}LE) in terms of the energy surfaces of the states is shown in **Figure 1.11**. As already explained above, the orbital involved in the ^{3}LE electronic state mediates the spin flip mechanism via vibronic coupling to the ^{1}CT state. The vibronic (non-adiabatic) coupling between the lowest local excitation triplet (^{3}LE) and lowest charge transfer triplet (^{3}CT) can be described by a linear combination of the vibrational density states using the second-order perturbation theory. This way it has been demonstrated that a spin flip can occur between the ^{3}CT and ^{1}CT states, mediated by the ^{3}LE one[26]. Gibson and Penfold[37] in their theoretical study showed how the non-adiabatic spin-vibronic coupling significantly enhances k_{RISC}. In fact the non-adiabatic coupling mixes the ^{3}LE and ^{3}CT states allowing a significant population transfer even without temperature activation energy[37]. This allows reducing the activation barrier in TADF materials.

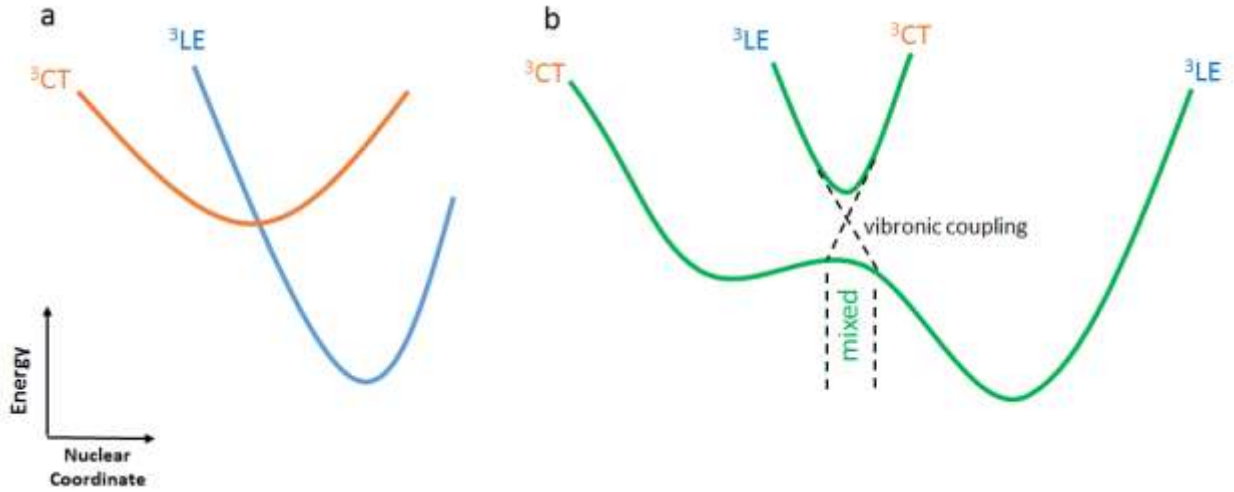

***Figure 1.11** : Vibronic coupling model for TADF. a) RISC is suppressed if there is no interaction between ^{3}LE and ^{3}CT triplet states; b) RISC is enhanced when vibronic coupling occurs between ^{3}LE and ^{3}CT, mixing the states.*

It results that the RISC mechanism is a process that occurs via 2-step mechanism:

Firstly, the vibronic coupling promotes a mixing between the ^{3}LE and ^{3}CT states through the rIC.

$$k_{RIC} = \frac{2\pi}{\hbar Z} \left| \left\langle {}^3\psi_{CT} \middle| \hat{H}_{SOC} \middle| {}^3\psi_{LE} \right\rangle \right|^2 \times \delta\left({}^3E_{LE} - {}^3E_{CT} \right) \qquad \textit{equation 1.2}$$

Secondly the ^{3}CT state is coupled to the ^{1}CT one *via* coupling elements derived from the second order perturbation theory, mediated by the ^{3}LE state:

$$k_{RISC} = \frac{2\pi}{\hbar Z} \left| \frac{\langle {}^1\psi_{CT} | \hat{H}_{SOC} | {}^3\psi_{LE} \rangle \langle {}^3\psi_{LE} | \hat{H}_{vib} | {}^3\psi_{CT} \rangle}{\delta\left({}^3E_{LE} - {}^3E_{CT} \right)} \right|^2 \times \delta\left({}^3E_{CT} - {}^1E_{CT} \right) \qquad \textit{equation 1.3}$$

The above equation (1.3) includes the non-adiabatic and spin-orbit coupling terms and takes into account the locally excited triplet state as a mediator of the RISC and TADF process. Such mechanism is very efficient because it allows a good vibrational overlap between the initial and final states, ^{3}CT and ^{1}CT respectively.

6. EFFICIENT TADF EMITTERS.

Efficient TADF molecules have to possess, first a small energy gap between the singlet and triplet excited states (ΔE_{ST}) and second, a low triplet state non-radiative decay rate ($^3k_{nr}$), to allow the triplet excited state to live long enough to maximize the possibility of RISC back to the singlet state. Therefore, to get an efficient TADF material, the key process is the RISC, which is temperature sensitive. The dependence of the RISC rate constant (k_{RISC}) on temperature can be expressed by a Boltzmann distribution which connects ΔE_{ST} to k_{RISC} by the **equation 1.4**:

$$k_{RISC} = A \times exp\left(-\frac{\Delta E_{ST}}{kT}\right) \qquad \textit{Equation 1.4}$$

Where k is the Boltzmann constant and T the temperature.
The singlet-triplet energy gap (ΔE_{ST}) is the difference between the energy of the singlet (E_S) and triplet (E_T) states defined by the equations:

$$\begin{aligned} E_S &= E + K + J \\ E_T &= E + K - J \\ \Delta E_{ST} &= E_{S1} - E_{T1} = 2J \end{aligned} \qquad \textit{Equation 1.5}$$

Where E is the energy difference between the ground state and excited state, K is the electron columbic repulsion energy and J is the exchange energy relative to the overlap of the spatial wave function of the HOMO and LUMO in organic molecules. J is derived from the first order quantum-

mechanical correction involving electron-electron repulsion of two unpaired electrons in the excited state, one in the HOMO and the other in the LUMO[38]. This repulsion is due to the Pauli principle. After some simplifications the energy J is given by the equation:

$$J = \iint \Phi(1)\Psi(2)\left(\frac{e^2}{r_1 - r_2}\right)\Phi(r_2)\Psi(r_1)dr_1dr_2 \qquad \textit{Equation 1.6}$$

Where Φ and Ψ represent the HOMO and LUMO wave functions respectively and e is the electron charge.

From **equation 1.6** it is possible to understand that the electron exchange energy (J) can be minimised by decreasing the overlap between HOMO and LUMO orbitals (**Figure 1.13**). This represents the most common strategy to obtain a small ΔE_{ST} in the design of TADF emitters. Decreasing the overlap between the HOMO and LUMO frontier orbitals can be achieved through their spatial separation. It therefore results that the best strategy so far to design TADF materials with a small ΔE_{ST} is to use molecules containing electron donor (D) and electron acceptor (A) moieties, which favour the D to A electron transfer in the excited state. The D and A units are in general linked via an aromatic bridge and an excited state with a strong CT character is formed. Another strategy to further reduce the singlet-triplet energy splitting is to twist the D and A units around the D-A axis to obtain a near-orthogonality orientation. This minimizes the interaction between the electron on the D and electron on the A in the excited state, giving near zero exchange energy and thus small ΔE_{ST}.

An alternative method to obtain efficient TADF is also contained in **equation 1.6** and consists in the formation of an exciplex state. In particular, the exchange energy J can be also minimized if the two electrons in the excited state are separated by a large distance. This situation can be achieved if the CT state is formed between two different molecules, in particular by the interaction of an electron donor (D) molecule and an electron acceptor (A) one. In this particular case an intermolecular excited state complex is obtained, also known as an exciplex. Excited states of exciplex are formed through a linear combination of the possible excited states of the D-A system, i.e. CT $|D{+}A{-}\rangle_{CT}$ and locally excited states, $|D^*A\rangle_{Loc}$ and $|DA^*\rangle_{Loc}$. The emission maximum of the exciplex is related to the ionization potential of the donor and electron affinity of the acceptor and it is stabilized by the coulomb interaction energy between the electron and the hole. As demonstrated by Adachi et al in 2012[39], such an exciplex CT state has photophysical TADF properties very similar to intramolecular CT states discussed above in this chapter.

6.1 Presence of CT state: Experimental evidence

Before discussing CT states, it is important to introduce the Frank-Condon principle (**Figure 1.12**). Such a principle, used to explain the intensity of vibronic transitions, states that during an electronic transition, a change from one vibrational energy level to another will be more likely to happen if the overlap between the two vibrational wave functions is large. Furthermore, the principle considers that electronic transitions are essentially instantaneous compared with the time scale of nuclear motions. Indeed, the absorption process only involves the rearrangement of electrons, which are much more free to move compared with the relatively heavy nuclei. It results that during the photon absorption (femtosecond time scale), electrons can move but nuclei cannot. Therefore, nuclei have no time to readjust during absorption but they move only once the absorption transition is over. This readjustment brings them into loss of energy by vibrational motion. For a system with almost identical equilibrium geometry in the ground and excited states, the same transitions are more favourable for both absorption and emission. This leads the emission spectrum to be the mirror image of the absorption spectrum, but shifted towards longer wavelengths (Stokes shift). The Stokes shift is much more pronounced in the case of CT states. The absorption spectrum presents either a broadened band at low energy, associated to the CT absorption ($S_0 \rightarrow {}^1CT$), but also more intense peaks, with vibronic structure, due to the transitions from the ground state to the electronic and vibronic levels of the locally excited states ($S_0 \rightarrow {}^1D$, $S_0 \rightarrow {}^1A$). For the CT state, the shift in the equilibrium geometry of the excited states is due to the reorganization of the dipoles of the surrounding molecules and therefore it strongly depends on the polarity of the solvent in which the emitter is dispersed.

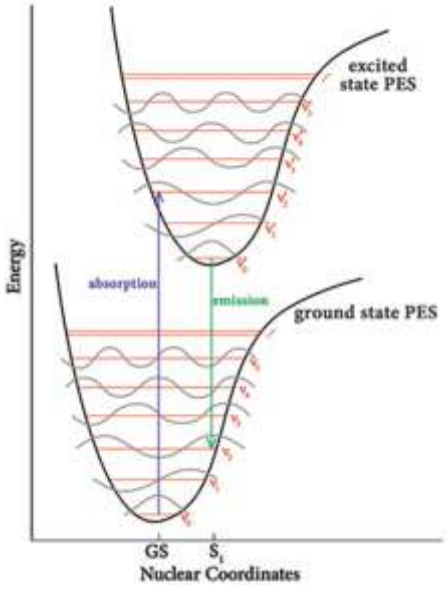

Figure 1.12 *Frank-Condon principle energy diagram[40]. Since electronic transitions are very fast compared with nuclear motions, vibrational levels are favoured when they correspond to a minimal change in the nuclear coordinates.*

It results that the most important characteristic of CT states is their very strong sensitivity to their local environment. This is due to their large dipole moment caused by the different electron density on the D and A moieties of the molecule. The pronounced spectral shift with increasing solvent polarity is mainly due to the redistribution of the electronic density associated with the CT state. The CT state emission is also broad and featureless, due to the fact that there is a distribution of different CT molecular configurations which could also arise from different solvated complexes. This leads to different overlapped spectral contributions resulting in a nearly Gaussian shape. Also the distribution of different solvent reorganization energies could lead to the emission spectra broadening.

From the experimental point of view, the general technique used to identify CT states is to measure the solvatochromic shift of their emission spectra using solvents of different polarities. Indeed the CT excited state has a large dipole moment that is stabilized by the polar solvent molecules. Interactions between the dipole moment of solvent molecules and the excited state dipole moment of the TADF molecule causes the rearrangement of the solvent shell around the molecule shielding the excited state dipole of the TADF molecules. This reduces the coulombic interaction energy of the CT state, resulting in a structural change that causes broad, featureless and red-shifted emission. In non- or moderately polar solvents, the fluorescence spectrum remains resolved because the weak interaction between the excited state dipole moment of the TADF compound and the small dipole moment of the solvent molecules causes only a slight structural change of the molecule in the excited state. Therefore, for donor–acceptor (D–A) molecules the low-lying excited state (S_1) can be formed in three different ways: a delocalized charge-transfer (^{1}CT) state, a π–π* localized electronic state (^{1}LE) and a hybrid local and charge transfer state (HLCT) CT + π–π* or so-called weak CT state[41-42]. It results that the energy of a LE state is not sensitive to the change in the environmental polarity[34, 42]. To calculate ΔE_{ST} in TADF CT-materials, one uses the ^{1}CT emission onset and the ^{3}LE emission onset, both expressed in eV.

6.2 Design of TADF molecules

The design of TADF materials starts from the selection of the donor and the acceptor moieties, which play the most important role in the final photophysical properties. However, it is necessary to find a trade-off between the strength of the donors and acceptors inside the TADF molecules. In fact, on one hand, the use of strong donors and acceptors leads to a strong localisation of the HOMO and LUMO orbitals with negligible overlap. This promotes a small ΔE_{ST} but it also decreases the radiative rate and therefore reduces the fluorescence quantum yield (Φ_f)[41]. On the other hand if weak donors and acceptors are used, the delocalization of the HOMO and LUMO might be significantly extended, leading to an increased singlet-triplet energy gap and then the resulting TADF contribution is strongly reduced. It is therefore important to find structures with a good

balance between a small ΔE_{ST} and the suppression of IC, which leads to a strong fluorescence yield Φ_f. As already stressed before a further reduction in ΔE_{ST} is also achievable by twisting the molecular geometry around the D-A linker. This way it is possible to obtain D-A molecules with a relative orientation of the donor and acceptor near orthogonality[7, 24]. In **Figure 1.13** is reported an example of such situation. Another strategy to obtain high TADF performances is to increase the D-A distance with the use of a phenyl linker[43].

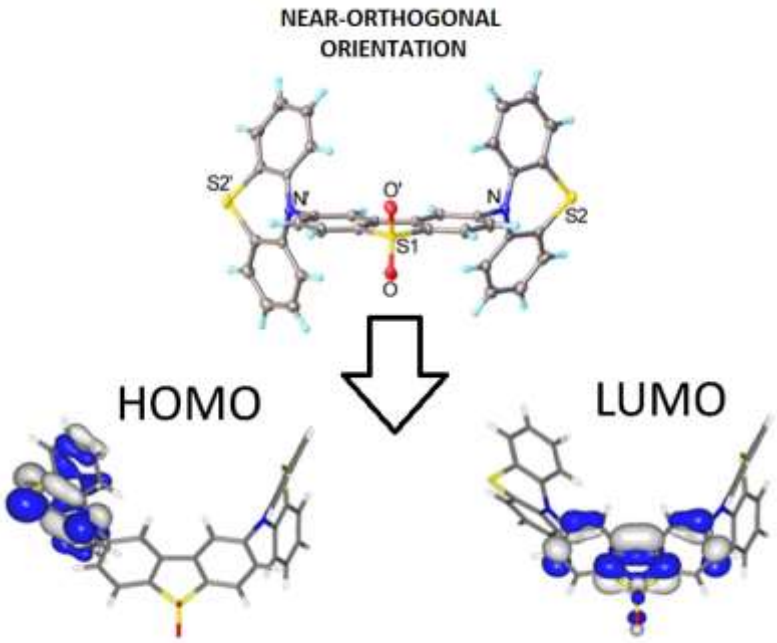

***Figure 1.13**. X-ray molecular structure and HOMO and LUMO of DPTZ-DBTO2[7, 22].*

Recently Nobuyasu et al[44] demonstrated how it is possible to switch from weak to strong TADF thanks to the presence of bulky substituents which restricts the molecular geometry due to steric repulsion effects. In particular, if the bulky substituents are on donor units, the molecules adopt an axial geometry which shifts the ^{1}CT state to higher energy; the oscillator strength and the luminescence efficiency decrease, thus resulting in a very weak TADF. Contrarily if the bulky substituents are on the acceptor unit, molecules adopt an equatorial geometry with the donor and acceptor units assuming a relative near-orthogonal geometry resulting in excellent TADF. Finally, thanks to the study of different isomers, it has been also demonstrated that even the connectivity position between the D and A units plays an important role on the singlet-triplet energy gap and intersystem crossing rate[22]. As an example in **Figure 1.14** is reported the study of Dias et al[22] on different isomers: if the carbazole or the diphenylamine electron donor (D) units

are linked in the C-2,8 positions of the dibenzothiophene-S,S-dioxide electron acceptor unit (A) the material has TADF properties whereas with substitution at the C-3,7 positions TADF is switched off.

Other important parameters to control in TADF materials design are the tuning of the colour emission and the chemical stability. The majority of TADF molecules emit in the green region and this is the region where TADF materials work the best compared to the others. On the other hand, even if some blue emitters are reported[21, 45-48] their design is difficult. In fact, to have both a small ΔE_{ST} and blue emission it is necessary to use weak donors and acceptors, in order to avoid strong shift to lower energies of the CT emission. Regarding red TADF emitters, there are not many examples to date[43, 49-51]. In fact for such low energy gap, the excited states are strongly affected by non-radiative internal conversion decay, k_{ic} governed by the energy gap law[52]. This decay competes with RISC and quenches the excited state population decreasing dramatically the QY.

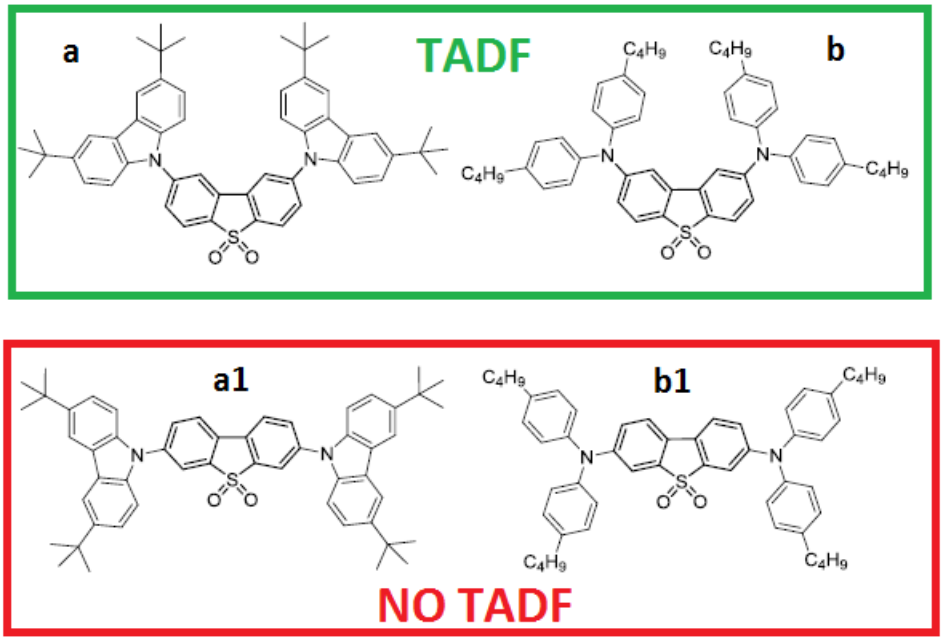

***Figure 1.14**. Effect of isomers on the TADF properties. In isomers **a** and **a1** the electron donor (D) units is carbazole while in isomers **b** and **b1** the donor is diphenylamine. Dibenzothiophene-S, S-dioxide is the electron acceptor (A). Compounds **a** and **b** have strong TADF while **a1** and **b1** show no TADF emission[22].*

7. PHOTOPHYSICAL CHARACTERIZATION AND MEASUREMENTS OF TADF MATERIALS.

The photophysics of TADF emitters is considered quite complex since it involves several energy states with different symmetries and quantum mechanical rules and properties. In addition, the

energy of such states is very sensitive to the temperature and solvent polarity. The most important method used to follow the evolution of the excited state after its formation is fluorescence time resolved measurements. After a laser pulse, the excited state of the TADF molecule is formed and it decays with two different components: one fast, the prompt fluorescence (PF) that arises from the direct deactivation of the singlet state ^{1}CT and one long that is the delayed fluorescence (DF) that happens thanks to the thermally activated reversed intersystem crossing from the mixed ^{3}CT-^{3}LE (T) to ^{1}CT (**Figure 2**). The short decay occurs in the range of a few nanoseconds while the long one is in the range of microsecond/millisecond. Therefore it is clear that the key factor to have TADF effect is the equilibrium between ^{1}CT and ^{3}CT-^{3}LE, which is governed by the intersystem crossing (k_{ISC}) and reverse intersystem crossing (k_{RISC}) rates. It results that the necessary conditions for TADF is both to have a very high yield of triplet formation (ϕ_{ISC}) as well as an efficient reverse intersystem crossing (ϕ_{RISC}) to allow the ^{1}CT repopulation.

Reverse intersystem crossing efficiency is defined by:

$$\Phi_{RISC} = \frac{k_{\mathrm{RISC}}}{k_{\mathrm{RISC}} + k_{\mathrm{IC}}^{T} + k_{\mathrm{PH}}} \qquad \textit{Equation 1.7}$$

It is equal to one for a very small energy gap between ^{1}CT and ^{3}CT-^{3}LE (less than 0.1 eV) and when the vibrational deactivation of ^{3}CT-^{3}LE is suppressed, i.e. $k_{\mathrm{RISC}} \gg k_{\mathrm{IC}}^{T} + k_{\mathrm{PH}}$.

The total fluorescence quantum yield of a TADF emitter (Φ_F) is described by the following equation that takes into account the recycling of the singlet and triplet states:

$$\Phi_F = \Phi_{PF} + \Phi_{DF} = \sum_{i=0}^{n} \Phi_{PF} (\Phi_{ISC} \Phi_{RISC})^i = \Phi_{PF} \frac{1}{(1 - \Phi_{ISC} \Phi_{RISC})} \qquad \textit{Equation 1.8}$$

Solving the equation 1.7 allows one to obtain:

$$\Phi_{ISC} \Phi_{RISC} = \frac{\Phi_{DF}/\Phi_{PF}}{1 + \Phi_{DF}/\Phi_{PF}} = \frac{\Phi_{PF}}{\Phi_{DF} + \Phi_{PF}} \qquad \textit{Equation 1.9}$$

This equation shows that it is possible to obtain a reverse intersystem crossing yield close to 100% if the ratio between the DF and PF (Φ_{DF}/Φ_{PF}) is around or above four[7] . This is valid for most emitters where the ΔE_{ST} is less than 150 meV. In fact it results that if, in ***equation 1.9***, Φ_{DF}/Φ_{PF} is equal to 4 the $\Phi_{ISC}\Phi_{RISC}$ is equal to 0.8, so that $\Phi_{RISC} = 0.8/\Phi_{ISC}$. However, the triplet yield is limited by the prompt fluorescence: $\Phi_{ISC}^{max} = 1 - \Phi_{PF}$. It results that to have $\Phi_{DF}/\Phi_{PF} \approx 4$ the Φ_{RISC} has to be close to 1.

From the above, for TADF materials where $\Phi_{DF}/\Phi_{PF} \geq 4$, it is possible to simplify the triplet yield to:

$$\Phi_{ISC} = \frac{\Phi_{DF}/\Phi_{PF}}{(1 + \Phi_{DF}\Phi_{PF})} = \frac{\Phi_{DF}}{\Phi_{DF} + \Phi_{PF}} \qquad \textit{Equation 1.10}$$

7.1 Prompt Fluorescence (PF) Quantum Yield (Φ_{PF}) and lifetime (τ_{PF})

Considering that the TADF mechanism can only work thanks to RISC from a triplet to a singlet state, it is possible to use oxygen quenching of the triplet T_1 to deactivate it. This allows determining both the PF quantum yield and lifetime. In fact these two parameters are measured using non-degassed solutions or films. Once the Φ_{PF} and τ_{PF} have been determined from, respectively, the fluorescence spectra and decay recorded in the presence of oxygen, it is possible to calculate the radiative rate constant (k_F) from the equation:

$$k_F = \frac{\Phi_{PF}}{\tau_{PF}} \qquad \textit{Equation 1.11}$$

In general, efficient TADF emitters have a low total fluorescence quantum yield Φ_F in the presence of oxygen that is strongly increased upon degassing the sample. This is due to the activation of the DF contribution as expressed in **equation 1.8**

7.2 Ratio between delayed (DF) and prompt (PF) fluorescence

The determination of the fluorescence quantum yield ratio between PF and DF (Φ_{DF}/Φ_{PF}) is of fundamental importance to characterize the TADF properties. Two main methods exist to determine it.

Method 1 consists in measuring the decay time of a degassed sample. In this way, it is possible to determine the prompt and delayed contributions. In general, the fluorescence decay is fitted by the sum of two exponentials, one typical of PF and the other one typical of DF like in the equation:

$$I_{fl}(t) = A_{PF} exp\left(-\frac{t}{\tau_{PF}}\right) + A_{DF} exp\left(-\frac{t}{\tau_{DF}}\right) \qquad \textit{Equation 1.12}$$

The Φ_{DF}/Φ_{PF} ratio is then calculated from the integral of the PF and DF components in the decay, as expressed by the equation:

$$\frac{\Phi_{DF}}{\Phi_{PF}} = \frac{\int I_{DF}(t)dt}{\int I_{PF}(t)dt} = \frac{A_{DF}\tau_{DF}}{A_{PF}\tau_{PF}} \qquad \textit{Equation 1.13}$$

Method 2 consists in measuring the steady-state emission of a solution with and without oxygen. Since the triplet excited state is strongly quenched by oxygen, the DF component is totally suppressed in non-degassed solution. Consequently, the integral of the steady-state fluorescence spectrum in air is proportional to Φ_{PF}. On the other hand, in degassed conditions the steady-state spectra contains both DF and PF and therefore the integral is proportional to the sum $\Phi_{DF} + \Phi_{PF}$ (**equation 1.8**). It results the equation:

$$\frac{\int I_{DF}^{deg}(\lambda)d\lambda}{\int I_{PF}^{O2}(\lambda)d\lambda} = \frac{\Phi_{PF}+\Phi_{DF}}{\Phi_{PF}} = 1 + \frac{\Phi_{DF}}{\Phi_{PF}} \qquad \textit{Equation 1.14}$$

7.3 Determination of reverse intersystem Crossing (RISC) rate constant

Another important parameter to consider in the photophysical characterization of the TADF molecules is the rate of reverse intersystem crossing, k_{RISC}. From the fitting of the TADF decay curve with 1.11 it is possible to obtain A_{DF}, A_{PF}, τ_{PF} and τ_{DF}. It results that:

$$\tau_{DF}^{-1} = \frac{k_{PH}+k_{IC}^{T}+k_{RISC}(1-\Phi_{ISC})}{1+ k_{RISC}\tau_{PF}} \qquad \textit{Equation 1.15}$$

Since $k_{rISC}\tau_{PF} \ll 1$, it is thus possible to derive k_{RISC}:

$$k_{RISC} = \frac{1}{\tau_{DF}}\frac{\Phi_{RISC}}{(1-\Phi_{ISC}\Phi_{RISC})} = \frac{\Phi_{RISC}}{\tau_{DF}}\left(\frac{\Phi_{PF}+\Phi_{DF}}{\Phi_{PF}}\right) \qquad \textit{Equation 1.16}$$

And if $\Phi_{RISC} = 1$

$$k_{RISC} = \frac{1}{\tau_{DF}}\frac{\Phi_{RISC}}{(1-\Phi_{ISC})} = \frac{1}{\tau_{DF}}\left(\frac{\Phi_{PF}+\Phi_{DF}}{\Phi_{PF}}\right) \qquad \textit{Equation 1.17}$$

Another practical method used to estimate the RISC consists in the use of the equation:

$$k_{RISC} = \frac{1}{\tau_{DF}}\left(1 + \frac{\int I_{DF}^{deg}(t)dt}{\int I_{PF}^{O2}(t)dt}\right) \qquad \textit{Equation 1.18}$$

Where the integrals correspond to the DF and PF regions in the decay time and τ_{DF} is the lifetime of the DF component.

7.4 Temperature dependence of TADF

As already mentioned above, the DF is temperature dependent through a Boltzmann distribution relation that connects the ΔE_{ST} to RISC (**equation 1.3**). Therefore, it results that the temperature dependence of the DF is important to demonstrate that the DF arises from a TADF mechanism. In fact, it is possible to verify that for TADF materials, in the decay time, the integral of the DF increases with the temperature. On the other hand, the PF decay is not affected by the change of temperature.

7.5 Excitation power dependence of TADF

Another experimental method used to unravel the origin of the DF is the measurement of the fluorescence intensity dependence with the excitation power. This way it is possible to determine

if the emission is a single (i.e. TADF) or two (i.e. TTA) photon per molecule process. In the TTA regime, the DF intensity varies as a quadratic function of the power. Plotting in log scale would yield a slope of +2. On the other hand, in pure TADF emitters, the DF mechanism is totally intramolecular and the DF intensity varies linearly with the excitation power over the entire regime. In this case, the logarithmic plot would yield a slope of +1. In **figure 1.15b** is given a published example[22]. Finally, there are situations where there is a mixture of TTA and TADF. It depends in general on the fact that the RISC rate is not fast enough to completely recycle the triplet level to the singlet one and then it deactivates in part through TTA. In this case, the slope is between 1 and 2.

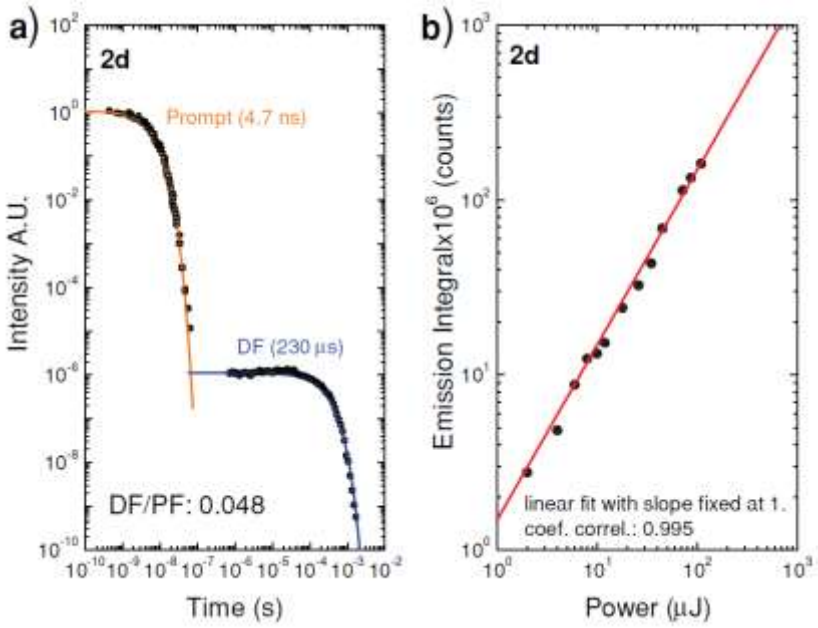

***Figure 1.15**. **a)** Prompt (PF) and delayed (DF) fluorescence exponential decay of molecule **a** in figure 14; **b)** variation of DF intensity with excitation dose showing a linear dependence in the entire TADF range, thus demonstrating the pure thermally assisted nature of the TADF mechanism in molecule **a** (adapted from ref [22]).*

8. CONCLUSION.

In this chapter is reported an overview of the most common class of TADF materials with a particular accent on the D-A intramolecular CT materials reported by Adachi and collaborators. The main differences between the second OLED generation employing pure phosphorescent metalorganic materials and the third generation containing TADF emitters are also reported in

the chapter. More in detail is reported the TADF photophysical background theory that will be used in the context of the work of this thesis. In particular, the experimental spectroscopic methods used to investigate the TADF molecular systems studied in the subsequent chapter are introduced. Both steady-state and time-resolved methods are presented. The effect of oxygen in delayed fluorescence is described. For a better understanding of the TADF mechanism, different molecular systems are compared to evaluate the effect of different electron-donating groups on their spectroscopic properties. Furthermore, are reported the recent progress on understanding the complexities involved in the TADF mechanism along with the design strategies used to have efficient TADF molecules.

This thesis is focused on pure organic D-A and D1x-A-D2y ($1 \leq x \leq 3$; $0 \leq y \leq 4$) molecular systems presenting intramolecular CT state and on the study of their photophysical properties. Two different sets of compounds are presented. The first one consists of several new benzonitrile derivatives containing various sets of carbazole, phenoxazine and phenothiazine substituents, as donor moieties. The second one consists of seven new asymmetric triazine derivatives containing the same three donors as the first set. The major contribution compared to literature was either a furtherly understanding into the design strategy to obtain a single molecule with a double TADF emission, however, the study of this thesis was mainly focused on the solid-state photophysical properties of the materials. In particular, we were able to introduce new ways of controlling the TADF properties. Firstly through polymorphism and mechanochromism we demonstrate how it is possible to control the colour emission as well as the TADF properties of the materials. Secondly, the use of the crystalline packing allows us to demonstrate how, in some cases, it is possible to switch on the TADF emission or, in others, to activate the RTP. Moreover thanks to DFT calculations it was possible to introduce an important and further contribute to the literature, concerning the understanding of the TADF phenomenon. A new method to synthesize nanoscale crystals was also presented, and we think that it could be considered as a new strategy in the use of crystalline states in nano-devices.

During my Ph.D., I also studied some exciplexes and prepared OLEDs with some of the compounds but these studies are only preliminary (or to partial) and will not be presented in the manuscript. This is the reason why the phenomenon is only briefly mentioned here.

CHAPTER 2.

NOVEL BENZONITRILE COMPOUNDS WITH MIXED CARBAZOLES AND PHENOXAZINES SUBSTITUENTS EXHIBITING DUAL EMISSION AND TADF PROPERTIES.

1. INTRODUCTION.

Efficient TADF emitters with donor−acceptor (D−A) properties[53-57] are considered to date among the most promising materials in lighting applications. In fact, the formation of intramolecular charge transfer (ICT) excited states, beside a broadened emission, allows satisfying the most important TADF requirement: having a very small singlet-triplet (^{1}CT-^{3}LE) energy gap (ΔE_{ST}).[58-60] It ensures an efficient triplet to singlet reverse intersystem crossing (RISC) interconversion that is fundamental to achieve a highly efficient TADF process[22-23, 26]. Based on this design principle, various purely organic TADF emitters have been developed to date. Furthermore, by changing the position and the number of substituents[22, 61], it is possible to tune the emission spectra of the TADF materials. This is in line with the fact that the CT state of these molecules has a crucial impact on their Band gap and luminescence. Another characteristic of the CT states is their broadened and futureless emission, which is advantageous especially for lighting applications. To date, the most promising strategy to achieve an emission broadened enough to cover the entire visible range by using TADF materials is to take advantage of the intermolecular CT state typical of exciplexes emission. Nevertheless, even if exciplexes are considered good candidates for lighting application the number of available exciplex emitters showing a true TADF mechanism is still limited. In fact, in many cases, they still present some issues such as TTA[56]. It results that despite TADF molecules are considered the next-generation luminescent materials, the research for single-component white-light TADF materials remains a challenge.

In this work, we designed and studied the photophysical properties of a new class of TADF materials that present a double CT emission, and therefore, they constitute an alternate strategy to obtain single TADF molecules whose emission can efficiently cover the entire visible range and thus emit white light. This property was obtained by employing Donor$_1$-Acceptor-Donor$_2$ (D_1-A-D_2) systems containing two different electron-donating units conveniently selected. In the literature, only a few examples of TADF D^1-A-D^2 compounds have already been reported [62-68] and these kinds of systems have not been studied much. Therefore we consider very interesting to further explore the characteristics of new systems containing two different donors on the same

central acceptor core. Three series of molecules (**Figure 2.1**) were obtained, and all the molecules are based on the central pentafluorobenzonitrile core with one to five fluorine atoms being substituted with a variable number of phenoxazine (Phx) and carbazole (Cz) donor units. Benzonitrile derivatives are of particular interest because of their electron-deficient core, and are one of the most popular electron-acceptors for constructing TADF molecules since their introduction of this field[20, 69-75]. In fact, beyond their excellent photophysical properties, the use of benzonitrile as acceptor core is motivated by the simple synthetic protocols employed to prepare D-A benzonitrile derivatives starting from fluorobenzonitriles. Based on previously reported studies were chosen phenoxazine and carbazole as donors, as they have shown to achieve red/yellow and blue emission respectively. Carbazole is one of the most commonly used donors in blue emitting D-A TADF molecules. This is due to its weak donor properties that allow obtaining a relatively low-lying energy HOMO level, which is a necessary prerequisite for the design of deep-blue TADF emitters[76]. Contrarily, phenoxazine was chosen because of its strong electron donor character, due to the presence of two heteroatoms (N and O) that are electron-rich and participate in the conjugation through their non-bonding electrons. This results in a low ionization potential that allows obtaining a more red-shifted emission. Therefore, the use of the benzonitrile core as acceptor and the mixing of two donor groups in different proportions in the same molecule results in an original molecular design for novel donor-acceptor benzonitrile derivatives. This design yields materials that apart from their TADF characteristics also exhibit aggregation-induced emission (AIE) and mechanochromic properties. These properties will be discussed in chapters 4 and 5.

In this chapter the molecules are studied in solvents of various polarity (10^{-5} M) and diluted in PMMA matrix (0.1wt %). The measurements in solution allow studying the photophysical properties of the molecules in an environment where they are free to move. Moreover, they also give a chance to investigate the interaction between the dipoles of solvent and solute. On the other hand, the rigid PMMA environment strongly suppress non-radiative decay due to rotation and vibration of the molecules as opposed to the solution. Finally, it is important to specify that we will focus on a detailed discussion of the first series of molecules (**Figure 2.1**) although a section will also be dedicated to the discussion of the other two series, reporting the main differences with respect to the first series.

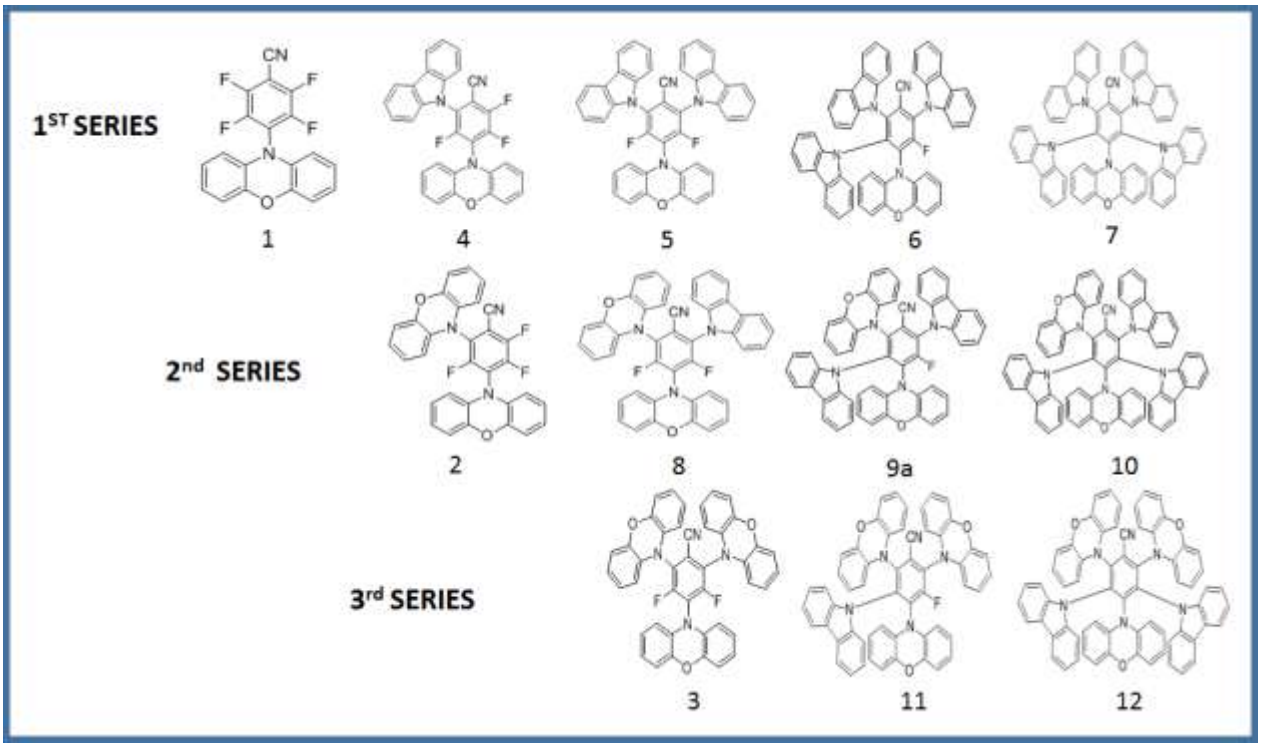

***Figure 2.1**: Structure of the molecules studied in this chapter.*

2. CRYSTALLOGRAPHIC STRUCTURES (XRD ANALYSIS).

Selected benzonitrile derivatives were studied by single-crystal X-ray diffraction (XRD). Notably, the crystal structures of **1** and **4-7** series of compounds were obtained and are presented here (**Table 1**). All the molecules possess large twisting angles between the donor and acceptor moieties, which facilitate the spatial separation of the HOMO and LUMO, leading to a small ΔE_{ST} and TADF properties. The D-A dihedral angles decrease with the increasing number of donor moieties on the molecules. Moreover, the dihedral angles between the phenoxazine moiety and the acceptor are in general larger than those between the carbazole moiety and the acceptor.

Table 1: X-ray crystallographic structures of **1** and **4-7**, and the dihedral angles between the donor (Phx= phenoxazine, Cz= carbazole) and acceptor (BzN = benzonitrile)

	XRD structure	D-A (dihedral angle)	
1		BzN-Phx 83.31° (4)	
4		BzN-Phx 69.37° (4) BzN-Cz 82.33° (2)	
5		**Mol 1** BzN-Phx 77.09° (4) BzN-Cz 72.36° (2) 70.29° (6)	**Mol 2** BzN-Phx 89.36° (4) BzN-Cz 73.82° (2) 58.43° (6)
6 **+** **Solv**		BzN-Phx 74.98° (4) BzN-Cz 75.43° (2) 72.98° (3) 66.50° (6)	
6		BzN-Phx 70.55° (4) BzN-Cz 76.46° (2) 71.65° (3) 76.20° (6)	
7	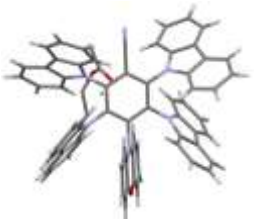	BzN-Phx 65.24° (4) BzN-Cz 68.54° (2) 70.21° (3) 70.21° (5) 68.54° (6)	

3. QUANTUMECHANICAL CALCULATIONS.

Compounds **1**-**12** have been studied by (TD)DFT calculations at the ground state and, for the smallest derivatives (up to three donors), at the first singlet and triplet excited states.

3.1 DFT calculations of the first series.

3.1.1 XRD vs Calculated Structures.

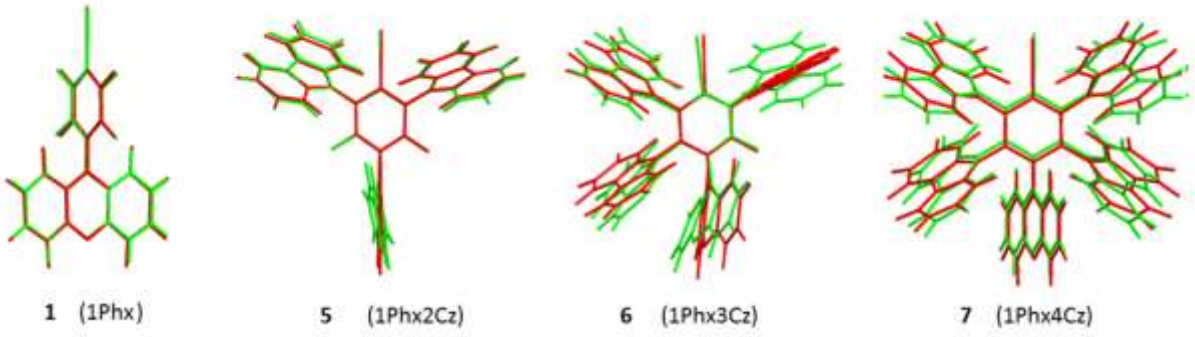

Figure 2.2: *Overlap between ground state calculated (red) and XRD structures (green).*

Figure 2.2 shows overlapped crystal structures and calculated ground state geometry. The angles between the main plans of phenoxazine and carbazole obtained from XRD structures match quite well with the calculated structures in the ground state (**Table 2**). The calculations reproduce quite well the real system.

Table 2: Angles between the main (central) plane of benzonitrile and the donors.

Comp.	D-A (mean plane angle)			
	X-Ray		DFT calculations	
1	78.17° (4)		73.61° (4)	
4	74.31°(2) 70.25° (4)		70.14° (2) 78.47° (4)	
5	**Mol. 1** 57.28° (2) 80.23° (4) 63.83° (6)	**Mol. 2** 69.11° (2) 76.12° (4) 70.50° (6)	**Mol. 1** 73.01° (2) 76.04° (4) 72.95° (6)	**Mol. 2** 70.86° (2) 88.57° (4) 76.53° (6)
6	65.54° (2) 68.93° (3) 67.37° (4) 58.79° (6)		67.65° (2) 67.52° (3) 71.54° (4) 79.32° (6)	
7	62.74° (2) 65.92° (3) 66.69° (4) 65.92° (5) 62.74° (6)		68.32° (2) 65.97° (3) 66.29° (4) 65.98° (5) 68.31° (6)	

(*The number in parenthesis refers to the position of the substituent on the benzonitrile ring, e.g. for 2 is the carbazole in ortho and 4 the phenoxazine in para*)

3.1.2 TDDFT at the ground state (S_0) geometry.

The simulated absorption spectra obtained from DFT calculations (**Figure 2.3**) show that **1** presents two different bands, the one at lower energy is less intense than that at higher energy which corresponds to several transitions underneath. On the other hand, molecules **4**-**7** clearly present three different bands. The new intermediate one (at λ≈350nm) increases with the number of carbazoles.

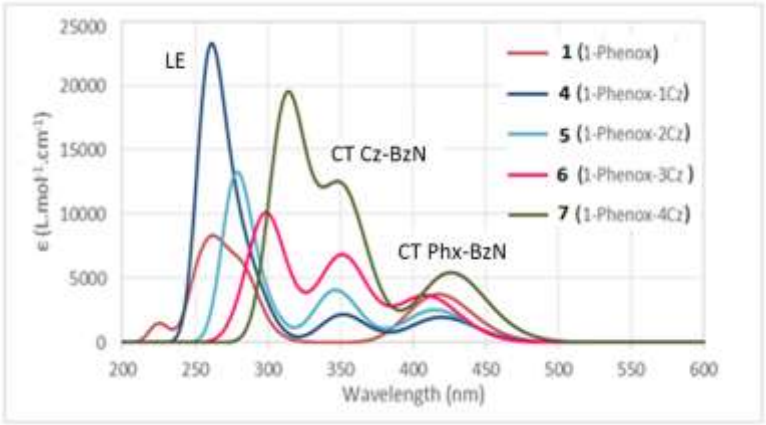

Figure 2.3: *Calculated spectra in vacuo for the compounds of the 1st series.*

For all molecules, the first 12 excited states were calculated. With the increasing number of Cz units (donor) there is an increasing number of low energy CT states (most of them with a very small oscillator strength) and the LE states progressively fall out of the first 12 states. In fact, for molecule **1** in addition to the LE for PhX was also possible to locate the LE BzN. For **4** were obtained both the LE for both Phx and Cz, then for molecule **5** was obtained only the LE PhX, and finally none for compounds **6** and **7**. The lowest calculated transitions and their corresponding electronic configurations for the first series of molecules (**1** and **4**-**7**) are shown in **Table 3**. The lowest energy transition is assigned to the CT absorption between phenoxazine and benzonitrile in all cases. The position of the calculated transition is not very sensitive to the number of added carbazoles which is not in agreement with experimental data (**Table 4**). The origin of the discrepancy could be related to the fact that there are other CT transitions contributing to the absorption band. In the case of **1**, higher energy transitions are LE states localized on Phx (300nm) and BzN (251nm). When carbazole moieties are added, additional CT transitions appear in between (λ≈300-350nm) as well as additional LE transitions (π-π*) involving the second donor.

The calculated energy of the molecular frontier orbitals of **1** and **4**-**7** molecules are reported in **Figure 2.4**, and it is possible to see that the HOMO-LUMO gaps gradually decreases as the number of Cz donor units increases. In **Figure 2.5** is shown the contour plots in molecular orbital energy relative to the HOMO-1, HOMO, LUMO and LUMO+1, and it is possible to see that the two highest energy HOMO are centered on phenoxazine and carbazole, contrarily the two lowest energy LUMOs are centred on the benzonitrile.

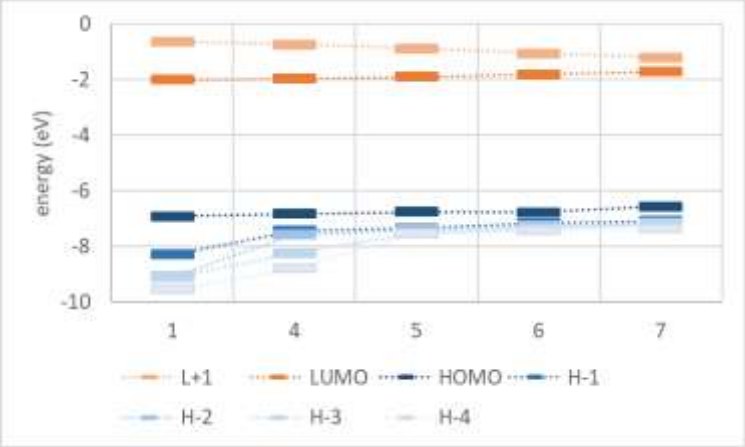

Figure 2.4: *Representation of the energy levels of the molecular frontier orbitals of **1** and **4**-**7** molecules.*

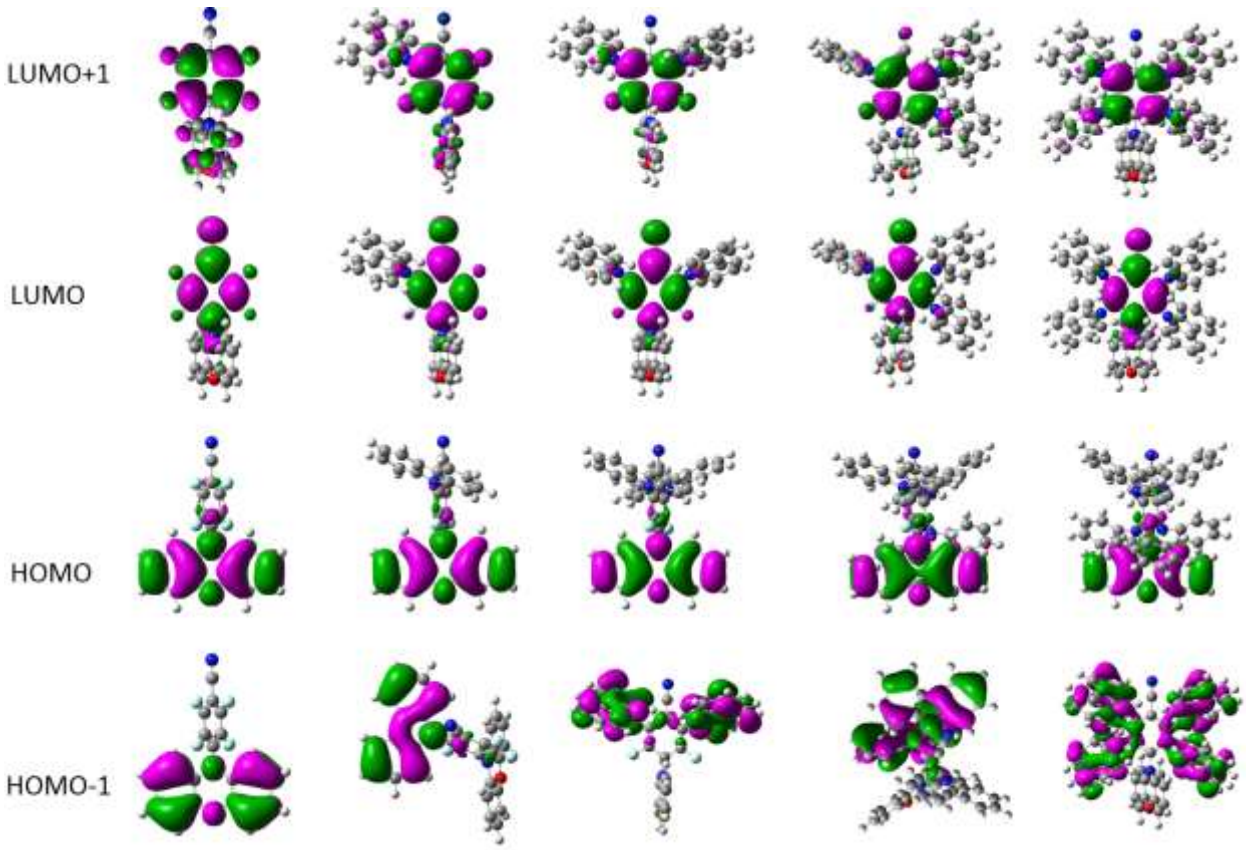

Figure 2.5: *Molecular orbital contour plots of HOMO-1, HOMO, LUMO and LUMO+1, of the* ***1*** *and* ***4****-****7*** *(left to right) molecules.*

Table 3: Calculated transitions, associated oscillator strength and electronic configuration for the compounds of the 1st series (**1** and **4-7**)

	λ_{calc} (nm)	State	Osc. Strength	Major contribution (H=HOMO, L=LUMO)
1	417	CT (Phx-BzN)	0.052	H→L
	300	LE (Phx)	0.0064	H→L+3
	251	LE(BzN)	0.0604	H-4->L
4	419	CT (Phx-BzN)	0.0247	H→L
	351	CT (Cz-BzN)	0.0303	H-1→L
	291	LE (Phx)	0.0444	H→L+4
	278	LE (Cz)	0.0612	H-1->L+2
5	415	CT (Phx-BzN)	0.0351	H→L
	351	CT (Cz-BzN)	0.0006	H-1→L
	346	CT (Cz-BzN)	0.0559	H-2→L
	315	CT (Phx-BzN)	0.0005	H→L+1
	305	CT (Cz-BzN)	0.0023	H-4→L
	297	LE (Phx)	0.0318	H→L+6
6	409	CT (Phx-BzN)	0.05	H→L
	354	CT (Cz-BzN)	0.0304	H-1→L
	352	CT (Cz-BzN)	0.0569	H-2→L
	337	CT (Cz-BzN)	0.0082	H-3→L
	322	CT (Phx-BzN)	0.00159	H→L+1
	306	CT (Cz-BzN)	0.0132	H-4→L
7	426	CT (Phx-BzN)	0.0753	H→L
	358	CT (Cz-BzN)	0.0456	H-1→L
	353	CT (Cz-BzN)	0.0078	H-2→L
	348	CT (Phx-BzN)	0.1149	H→L+1
	334	CT (Cz-BzN)	0.0033	H-3→L
	327	CT (Cz-BzN)	0.0005	H-4→L

Table 4: Calculated Vs experimental absorption maxima (nm).

Compound	TDDFT	Cyclohexane	DCM	PMMA
1	417	421	414	407
4	419/351	426/385	426/375	416 (s)/369
5	415/351	432 (s)/391	440 (s)/390	440 (s)/387
6	409/354	440 (s)/403	455 (s)/409	453 (s)/406
7	426/358	467 411	476/414	471/411

3.1.3 Ground state (S_0), singlet excited state (S_1) and triplet excited state (T_1) structures.

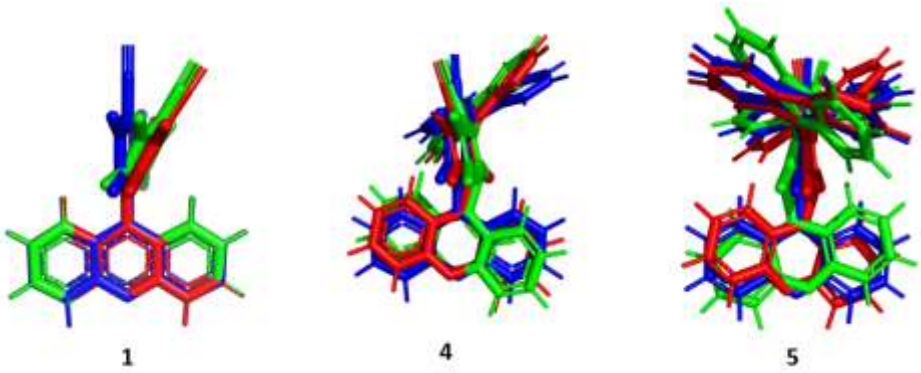

***Figure 2.6**: Overlap of the calculated structures of molecules **1**, **4** and **5** in their ground (blue), **S_1** (green) and **T_1** (red) states.*

In order to evaluate the extent of the molecular relaxation occurring upon excitation, excited state geometries were calculated. The obtained geometries for the ground state (S0) and first singlet (S_1) and triplet (T_1) excited state of compounds **1**, **4,** and **5** are reported in **Figure 2.6**. The calculations show that for molecule **1** there is a large reorganization from S0 to both S1 and T1 excited states, mainly through the twisting of the benzonitrile relative to the phenoxazine. This relaxation certainly results in a quenching of the radiative emission and we expect that compound **1** will not be emissive in solution. In contrary, small changes from S_0 to S_1 are predicted for **4** and **5**, thus we expect these molecules to be emissive in solution.

TDDFT calculations were also performed on compounds **1**, **4,** and **5** at their S_1 and T_1 geometries to locate the energy of the different possible excited state configurations. The energy of the various LE and CT transitions obtained with the three geometries are reported in **Figure 2.7**. We can see that moving from S_0 to S_1 and T_1 geometries, the energy of both CT and LE states decreases, and this is in line with the molecular relaxation that occurs after the initial population of the excited state. Moreover, we can notice that in **1** the phenoxazine centered ^{3}LE is at higher energy respect to the ^{1}CT regardless of the geometry. This is also the case in **4** at S_0 and T_1 geometries. This is in agreement with the values of ^{1}CT and ^{3}LE obtained in the time-resolved study from the onset of DF at RT (^{1}CT) and from the onset of the phosphorescence at 77K (^{3}LE). However, we don't have information about the triplet energy of the phenoxazine for molecule **5** and for S_1 configuration of molecule **4**.

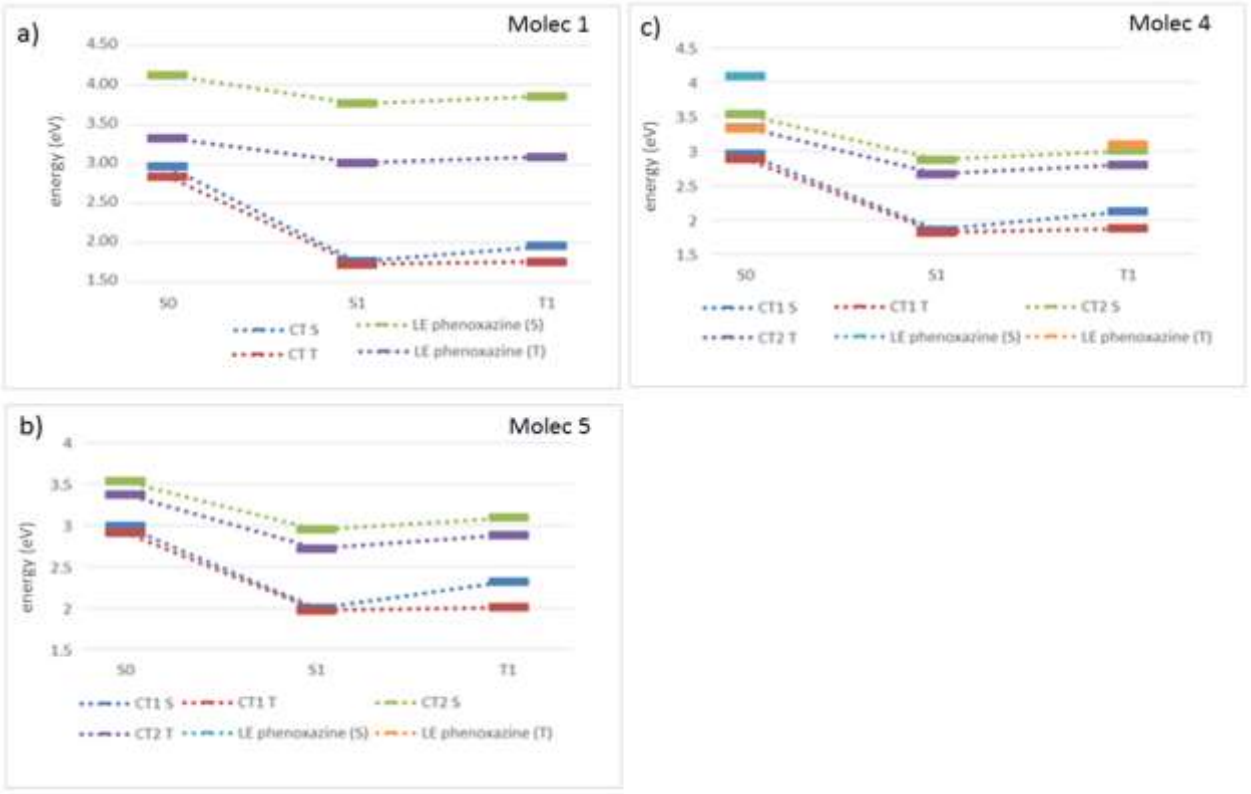

Figure 2.7: *Energy diagram of the triplet and singlet LE and CT states, for molecules **1**(a), **4** (b) and **5** (c) in the S_0, S_1 and T_1 geometry configuration, obtained with TDDFT calculations.*

Finally, in **Table 5** are reported the calculated absorption and emission maxima along with the energy of the calculated singlet and triplet in S_1 geometry. From the latter, it is possible to calculate the $\Delta E_{S\text{-}T}$. Beyond the $\Delta E_{S\text{-}T}$ in S_1, in **Table 5** are also reported the $\Delta E_{S\text{-}T}$ for **1** and **4**-**7** molecules in the S_0 and T_1 configurations. In particular, we can see that $\Delta E_{S\text{-}T}$ tends to be larger when the compounds are in the T_1 geometry than in S_1 geometry. This could indicates a large k_{ISC} but a low k_{RISC}. If the ISC is much higher than RISC we expect to observe poor TADF properties. For **6** and **7** the $\Delta E_{S\text{-}T}$ data are not available for S_1 and T_1 configurations.

Table 5: Calculated photophysical data

Compound	Abs (nm)	Fluo (nm)	S_1 (eV)*	T_1 (eV)*	Δ(S-T) eV S_0 geom	Δ(S-T) eV S_1 geom	Δ(S-T) eV T_1 geom
1	417	717	1.76	1.73	0.13	0.03	0.20
4	419	668	1.86	1.82	0.07	0.03	0.25
5	415	619	2.00	1.97	0.08	0.03	0.31
6	409	n.c.	n.c.	n.c.	0.15	n.c.	n.c.
7	426	n.c.	n.c.	n.c.	0.21	n.c.	n.c.

*n.c.=not calculated, * Calculated at the optimized S_1 geometry.*

3.1.4 DFT calculations of the 2nd and 3rd series.

The results obtained for the 2nd and 3rd series are similar to the ones in the 1st series. The simulated absorptions for the 2nd and 3rd series (**Figure A2.1**) show that **2** and **3** present two different bands, while molecules **8**-**10** and **11**-**12** have three. For all molecules, in all cases, the lowest energy transitions (λ>400nm) are assigned to the CT absorption between phenoxazine and benzonitrile, the transitions at intermediate energies (300<λ<400nm) to the CT absorption between benzonitrile and carbazole, and finally that at higher energy (λ<300nm) are associated to LE (Phx) and LE (Cz) [**Table A2.1** (**2** and **8**-**10**) and **Table A2.2** (**3** and **11**-**12**)]. The calculations of the optimized geometries show that **2**, **8**, and **3** present only small changes in S_0 to S_1 geometries, thus we expect to observe fluorescence emission in solution. Also in this case we can notice that in **2** the phenoxazine-centered ^{3}LE is at higher energy respect to the ^{1}CT regardless of the geometry (**Figure A2.4**). This is in agreement with the values of ^{1}CT and ^{3}LE obtained in the time-resolved study, calculated from the onsets of DF at RT (^{1}CT), and from the onset of the phosphorescence at 77K (^{3}LE). Finally, in **Table A3** are reported the calculated ΔE_{S-T} for molecules **2**, **8**, and **3** in the S_0, S_1, and T_1 configurations. We can see that ΔE_{S-T} tends to be larger when the compounds are in the T_1 geometry than in S_1 geometry. This could indicates a large k_{ISC} but a low k_{RISC}. If the ISC is much higher than RISC we expect to observe poor TADF properties.

4. ELECTROCHEMISTRY (CYCLIC VOLTAMMETRY).

Cyclic voltammetry (CV) experiments have been performed on all the donor-acceptor benzonitrile derivatives. In particular, they feature a reduction peak which can be assigned to the benzonitrile core reduction and one or more oxidation peaks which can be assigned to the peripheral donor moieties (carbazole or phenoxazine). It is important to note that the phenoxazine is reversibly oxidized, while the oxidation of the carbazole moieties is irreversible[77]. Therefore, only compounds **1-3** show reversible oxidation (**Figure 2.8a, 2.9a, 2.10a)**. In other cases for the hetero-substituted benzonitrile compounds, only the first oxidation waves are reversible, because the more electron-rich phenoxazines are always oxidized before the carbazoles. However, all compounds featuring carbazoles present further oxidation processes that are irreversible due to polymerization reactions (**Figure A2.5**).

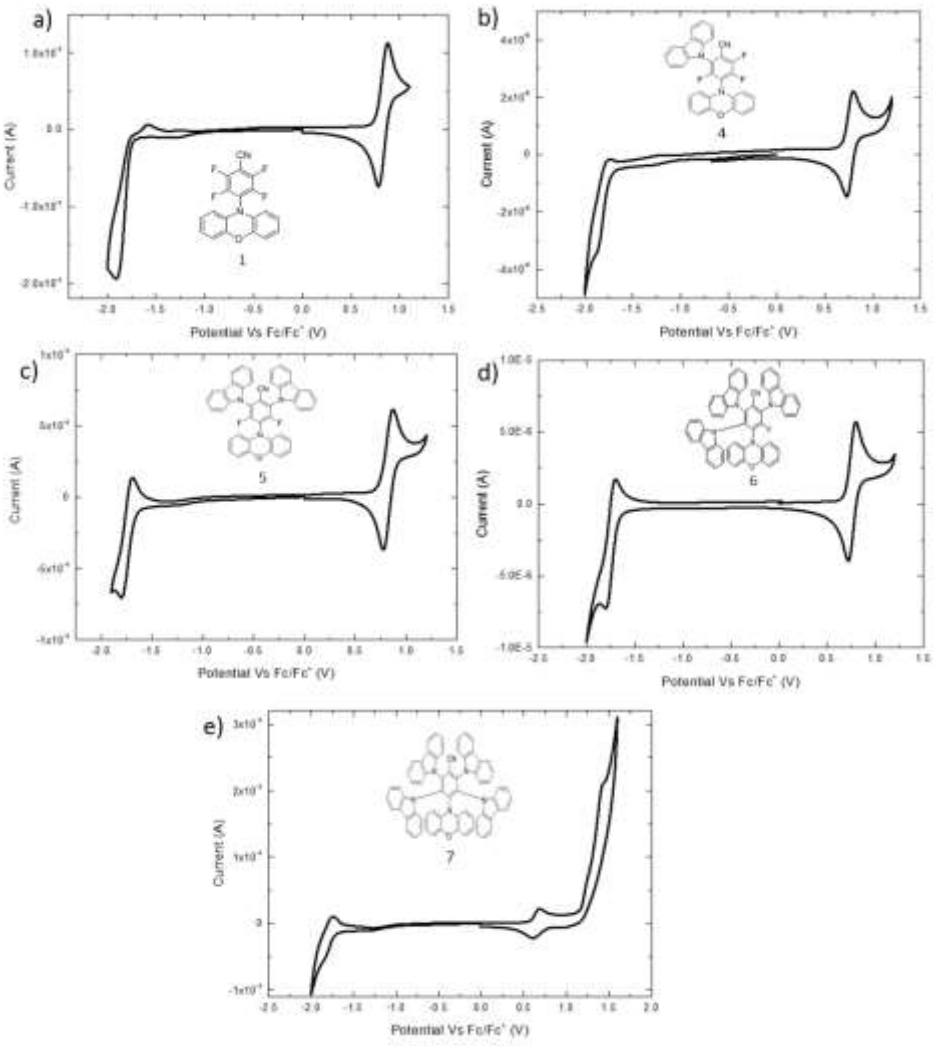

Figure 2.8**: CV traces of compounds **1, 4-7.

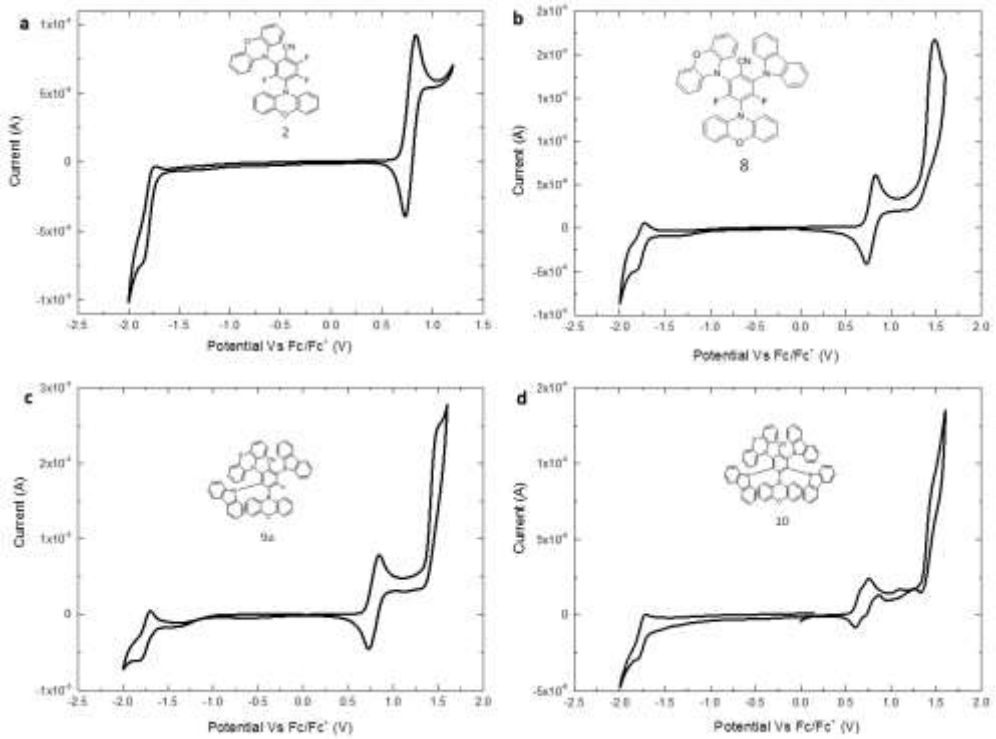

Figure 2.9**: CV traces of compounds **2, 8, 9a, 10.

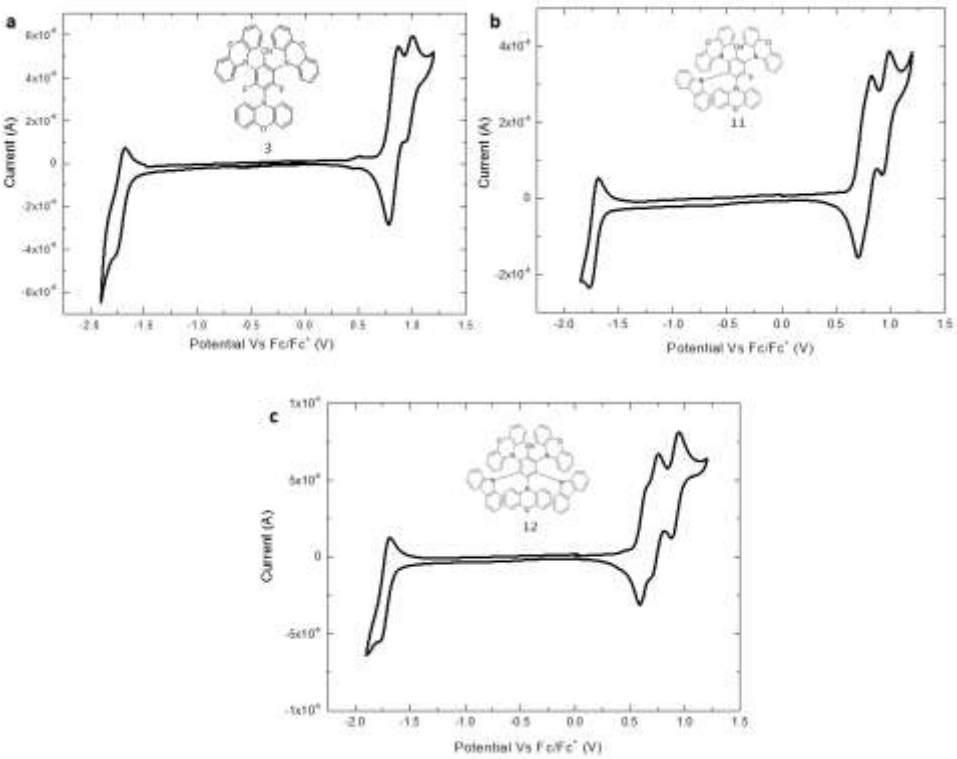

Figure 2.10**: CV traces of compounds **3, 1-12.

The reduction of the benzonitrile core gives an irreversible peak for some derivatives and a reversible one in others. This is related to the presence of a chemical reaction associated with the electron uptake in the first case. When the number of fluorine substituents decreases, the reversibility increases showing that fluorine plays the role of a leaving group, expelled upon benzonitrile reduction. The peak ratio between the first oxidation and first reduction varies from about 0.5 for **1-4** to 1 for **6**. As the first corresponds to the one-electron oxidation of phenoxazine, one can deduce that the reduction of benzonitrile involves two electrons for **1-4** and only one for **6**. Therefore, when fluorine substituents are present, the mechanism should lead to the substitution of fluorine by hydrogen through an ECEC mechanism. In the absence of fluorine, no leaving group can be removed upon the first monoelectronic reduction and the reduction stops at the anion radical level. A confirmation of this assumption is observed in **Figure 2.9** for compound **2**, where the peak ratio is close to 1 despite the presence of fluorine, but because the first oxidation involves this time two electrons (one per phenoxazine, which behaves independently). Therefore the reduction of benzonitrile is bielectronic again. One can also notice that the reduction potential shifts slightly when substituting fluorine by carbazole, the more positive potential being obtained for **6**. This is not in agreement with the electron donor effect of carbazole, but one must be careful with the reduction potentials of the other compounds involving fluorine substituents since these are influenced not only by the withdrawing effect of fluorine but also by the chemical reaction coupled, this latter facilitating the reduction and thus tending to shift the potential towards more positive values. This might globally explain why the reduction potential varies very little within the series despite the variety of substituents with different electronic effects (see **Table 6**).

When the compounds involve more than two phenoxazine moieties, the oxidation wave splits into two or three peaks, due to coulombic repulsion between the positive charges injected. The presence of electron-rich carbazoles nearby tends to slightly diminish the oxidation potential of phenoxazine (see compounds **7, 10, 12** compared to **1, 2**). However one may consider that the first oxidation potential varies little with the substituents, which is understandable since each phenoxazine moiety is not conjugated with the rest of the molecule, and therefore behaves as a more or less independent redox unit, this being also emphasized by the generation of a very stable cation-radical related to the anti-aromatic character of the neutral molecule for this family of compounds.

Table 6: electrochemical data of all compounds.

	E_{ox} vs Fc/Fc+ (V)[(a)]	E_{red} vs Fc/Fc+ (V)[(a)]	Oxid Vs Red peak current ratio	Number of electrons	HOMO (eV)[(b)]	LUMO (eV)[(c)]	HOMO-LUMO gap (eV)
1	0.56	-1.95	0.93	1	5.66	3.16	2.50
2	0.56	-1.85	1.71	2	5.66	3.25	2.41
3	0.57	-1.80	1.66	2	5.67	3.30	2.37
4	0.56	-1.87	1.05	1	5.66	3.23	2.43
5	0.57	-1.83	1.15	1	5.67	3.27	2.40
6	0.52	-1.78	1.06	1	5.62	3.32	2.30
7	0.40	-1.89	0.66	1	5.50	3.21	2.29
8	0.58	-1.81	1.40	1	5.68	3.29	2.39
9a	0.51	-1.84	2.00	2	5.61	3.26	3.35
10	0.42	-1.87	1.11	1	5.52	3.23	2.29
11	0.49	-1.81	1.62	2	5.59	3.29	2.36
12	0.39	-1.83	1.17	1	5.49	3.27	2.29

(a)Measured in DCM at room temperature by cyclic voltammetry,
(b)Estimated from the oxidation potential in DCM, HOMO = Eox + 5.1,
(c)Estimated from the reduction potential in DCM, LUMO = Ered + 5.1.

5. STEADY-STATE PHOTOPHYSICAL CHARACTERIZATION OF THE 1ST SERIES.

5.1 Absorption.

In **Figure 2.11** are reported the normalized absorption spectra of the molecules **1** and **4**-**7** in cyclohexane (left, c=10^{-5} M) and PMMA (0.05%wt, right). In **Table 7** are reported the maxima of absorption and emission in cyclohexane, for the molecules of the first series.

The less intense peaks at lower energy, for molecule **1** (421 nm) and **4**-**7** (370-470 nm), neither appear in the donors (phenoxazine[78] and Carbazole[79]) nor acceptor (benzonitrile[80]) absorption spectra, and thus they are assigned to the ^{1}CT state absorption of the D-A molecules. The CT band at 421 nm, observed in **1,** is assigned to the charge transfer between phenoxazine and benzonitrile. Interestingly, according to DFT calculations, more than one CT absorption band is visible for the molecules substituted with two different donors (carbazole and phenoxazine). In particular for compound **4** that contains one phenoxazine and one carbazole, it is possible to clearly distinguish two different absorption bands over 350 nm. Therefore we attribute the band at 385 nm (in cyclohexane) to the CT involving the carbazole (BzN-Cz) and the other at 426 nm to the CT involving the phenoxazine (BzN-Phx). In compounds **5**, **6**, and **7**, progressively substituted with additional carbazoles, beyond the two CT states involving the Cz and Phx, it is possible to spot an additional shoulder (λ_{max} in **Table 7**). This can be assigned to different CT states resulting from different carbazole donors substituted at different positions. This is in agreement with what observed in the literature about the influence of molecular isomerization on TADF. For example, Dias et al[22] showed that there are enormous differences in the TADF properties between D-A-D isomers that differ only in their linkage position of the carbazole to the electron acceptor unit. At higher energy (up to 360 nm), the absorption is almost entirely formed by the superposition of the absorption of the donors and acceptors. In particular, the absorption band at 287-289 nm, present only in compound **4**-**7**, is assigned to the π-π* localized absorption, of carbazole[79] ($S_0 \rightarrow S_1$). The one between 324 and 330nm is also associated with the localized absorption of the Carbazole[79] but it corresponds to the electronic transition: $^1S_0 \leftarrow {}^1S_2$[79]. On the other hand, the other absorption bands are assigned to the localized absorption of phenoxazine [78] (**Table 7**). In particular, the ones at lower energy show maxima between 312 and 317nm (**1**: λ_{max} = 312 nm; **4**: λ_{max} 311 nm; **5**: λ_{max} =312 nm; **6**: λ_{max} = 316 nm; **7**: λ_{max} = 317 nm). The others at higher energy, show maxima between 280 and 304 nm [**1**: λ_{max} =280(s) nm, 297 nm; **4**: λ_{max} =277(s) nm, 301(s) nm; **5**: λ_{max} =278(s) nm, 302 nm; **6**: λ_{max} = 304(s) nm].

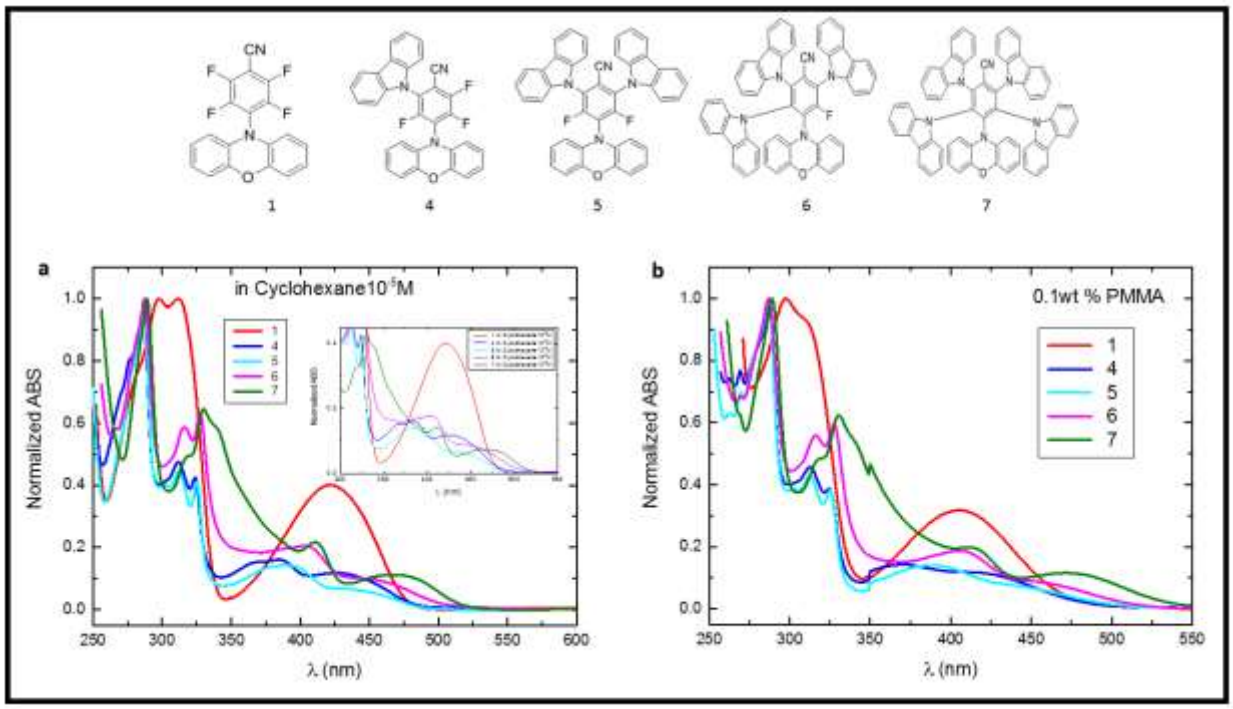

***Figure 2.11**: Normalized absorption spectra of molecules **1** and **4-7** in **a)** cyclohexane (c=10^{-5} M) and **b)** PMMA (0.1%wt) (structures of the molecules shown in the top).*

5.2 Emission.

The emission spectra of the first series (molecules **1** and **4**-**7**) in cyclohexane (left) and PMMA (right) are shown in **Figure 2.12**. We can see that a dual emission is particularly evident in cyclohexane. The double emission in D-A systems is in general attributed to the locally excited state (LE) mainly emitting in non-polar solvents (higher energy), and to the intramolecular charge-transfer state (ICT) which emits better in polar solvents[29, 81-83](lower energy). Nevertheless, in literature are also reported few cases[62-64] where the double emission is attributed to the presence of a second CT emission arising from two different CT states involving two different donors.

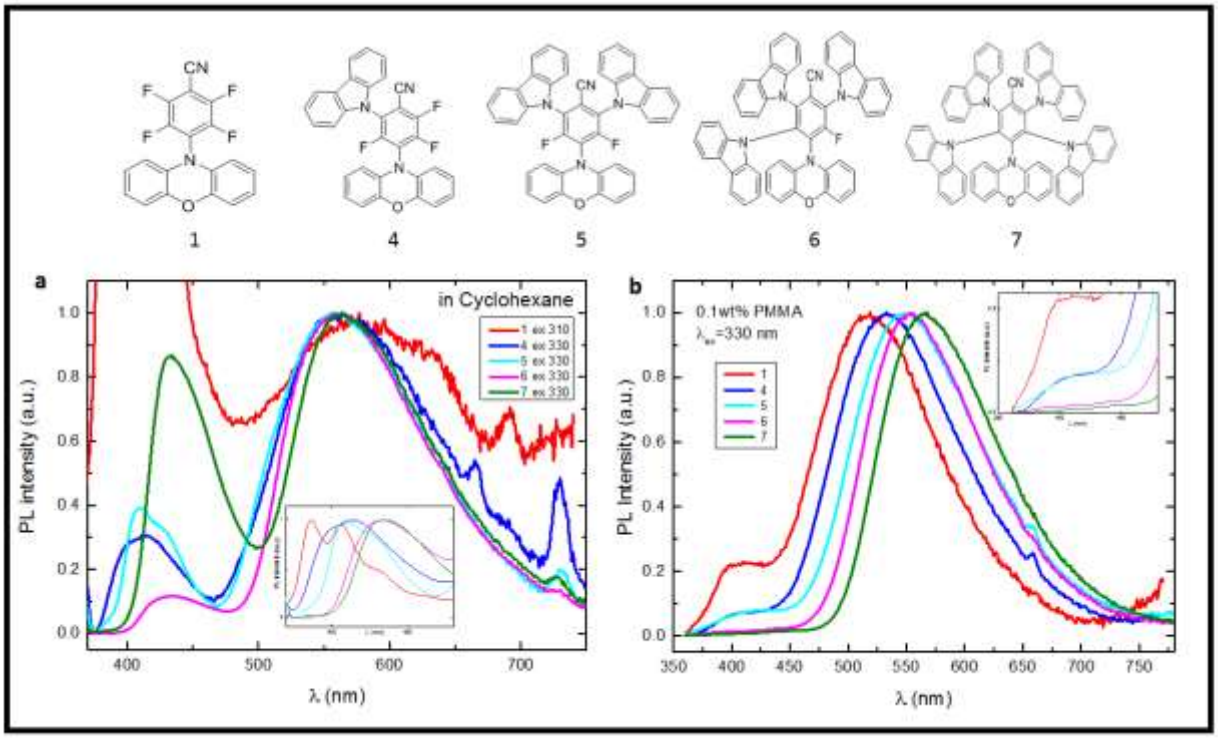

***Figure 2.12**: **a)** Normalized (to the maxima of the CT band involving the Phenoxazine) photoluminescence spectra of molecules **1** and **4**-**7** in cyclohexane (c=10^{-5} M), **inset**: normalized emission of the high energy band. **b)** normalized photoluminescence spectra of molecules **1** and **4**-**7** in PMMA (0.1%wt), **inset**: close-up of the high energy band. (λ_{ex} in legends; structures of the molecules given at the top).*

In particular, in cyclohexane, molecule **1** with only one phenoxazine donor, emits in the blue region mainly from the LE emission of the phenoxazine[84] (**Figure 2.12a**). As typical for a local state, this LE emission appears well resolved. On the other hand, in the red region, molecule **1** presents a very weak emission in cyclohexane that becomes strong in PMMA (**Figure 2.12b**). This emission at low energy is assigned to the CT state involving the phenoxazine. The quenching of the CT

emission in solution, according to what was observed in DFT calculations (in vacuum), could depends on the fact that upon excitation the molecule undergoes a large reorganization of the geometry, through the twisting of the benzonitrile relative to the phenoxazine. On the other hand, the short-lived LE state involving the phenoxazine is less sensitive to this effect. However, in the rigid PMMA environment, the rate of molecular relaxation is strongly limited and the ground state geometry is conserved in the excited state. As the emission is observed only in the rigid media (PMMA) this molecule can be considered AIE active[85]. For molecules **4**-**7** in cyclohexane, the emission band at low energy is also assigned to the CT state involving the Phenoxazine[84] (CT-Phx) (**Figure A2.10**). On the other hand, at higher energy also compounds **4** and **5** present a partially resolved emission in cyclohexane that we assign, partially to the localized contribution of phenoxazine (LE), and partially to the CT emission involving the carbazole (CT-Cz). In molecules **6** and **7** the emission at higher energy becomes structureless and resembles a Gaussian shape (**Figure 2.12a**). We assign the origin of this emission to the CT state involving carbazole (CT-Cz) that matches very well with the emission of **Cz-BzN**[1] molecule in cyclohexane (**Figure A2.10**), where the only possible CT state is the one between carbazole and benzonitrile (CT-Cz). The **inset** in **Figure 2.12a** shows that with the increasing number of carbazoles, the contribution of ^{1}LE phenoxazine (resolved emission) progressively disappears, and the dual Gaussian emission bands, observed in **6** and **7** can be exclusively associated to CT-Cz (BzN-Cz moiety) and to CT-Phx (BzN-Phx moiety). Contrarily, in PMMA (**Figure 2.12b**) we can observe that the band at higher energy drastically decreases with the increasing number of carbazoles (**inset** in **Figure 2.12b**). This indicates that most of the excitation goes directly to form the CT-Phx. The reason could depends on the energy transfer from the Cz-BzN CT state to the Phx-BzN CT state. In fact, as we can notice in **Fig 2.11** and **Fig 2.13** there is a very good overlap between the emission of Cz-BzN CT and the absorption of Phx-BzN CT. Moreover, the concentration of 0.1-0.5wt % is not enough to completely prevent the aggregation and thus make enough distant the molecules.

Table 7: photophysical data of compounds **1** and **4**-**7** in cyclohexane (c=10^{-5} M).

	Abs λ_{max} (CT),nm (λ_{ex} = 300-330 nm)	**Abs, λ_{max} (LE), nm (λ_{ex} = 300-330 nm)**	**PL, λ_{max} (CT-Cz or LE), nm (λ_{ex} = 300-330 nm)**	**PL, λ_{max} (CT-Phx),nm (λ_{ex} = 300-330 nm)**	**PL, λ_{max} (CT-Phx),nm (λ_{ex} = 390-440 nm)**
1	421	312, 297, 280(s)	387, 407, 425 (s)	577	578
4	426, 385	368(s), 324, 311, 301(s) 287, 277(s)	404 (s), 412	563	565
5	432, 391, 378(s)	325, 302, 312, 287, 278(s)	410, 423 (s)	556	559
6	440, 404, 388(s)	327, 316, 304 (s), 287	432	565	565
7	467, 411, 373(s)	339, 330, 320, 289	432	564	564

[1] The photophysical study of Cz-BzN is presented in the Chapter 4

5.3 Solvatochromism.

In order to confirm that the emission of **4**-**7** in cyclohexane originates from two different CT states, the effect of solvent polarity was investigated. In fact, especially the excited state dipole of D-A compounds is affected by solvent polarity. This depends on the redistribution of electronic density in the CT state induced by the dipole of the solvent. Therefore in addition to the photophysical properties in cyclohexane (low polarity (ε=2.0, μ=~0.0D)[2], were also tested the photophysical properties in toluene as a solvent with intermediate polarity (ε=2.4, μ=0.36D), and in dichloromethane (DCM) as a solvent with high polarity (ε=8.9, μ=1.6D).

The normalized photoluminescence (PL) spectra of molecules **4**- **7** collected in the three different solvents (**Figure 2.13**) show positive solvatochromism in both of the two emission bands. This effect gives a strong indication that the excited states producing the two different emission bands present a CT character in all the four molecules. In all cases where the CT state involves phenoxazine, the lowest emission band weakens with solvent polarity. This is due to the polar solvents stabilizing the CT and reducing the radiative decay constant, so the emission is outcompeted by non-radiative decay[26, 60, 84, 86]. On the other hand, with carbazole being a less weaker donor than phenoxazine, the polarity of the solvent could play a positive effect to stabilize the CT emission of the Cz-BzN moiety. For molecule **4**, the initial ^{1}LE contribution observed in cyclohexane in the band at high energy completely disappears in both toluene and DCM, and only a very weak CT emission remains. This indicates that in molecule **4** the carbazole is able to form only a very weak CT state with the benzophenyl ring. For molecule **5** the initial ^{1}LE contribution in cyclohexane also disappears with increasing solvent polarity, but in this case, a higher contribution of the CT state involving the carbazole is observed. For molecules **6** and **7** with increasing solvent polarity the intensity of the CT band relatively to the BzN-Cz moieties increases, thus confirming that the increased polarity could play a positive effect to enhance the emission of the Cz-BzN CT. Overall, the strongest CT emission is observed in the solvent of lowest polarity, cyclohexane. This is also confirmed by the decrease in the PLQY (especially in **6** and **7**) passing from cyclohexane to toluene (**Table 8**).

[2] ε = dielectric constant, μ = dipole moment

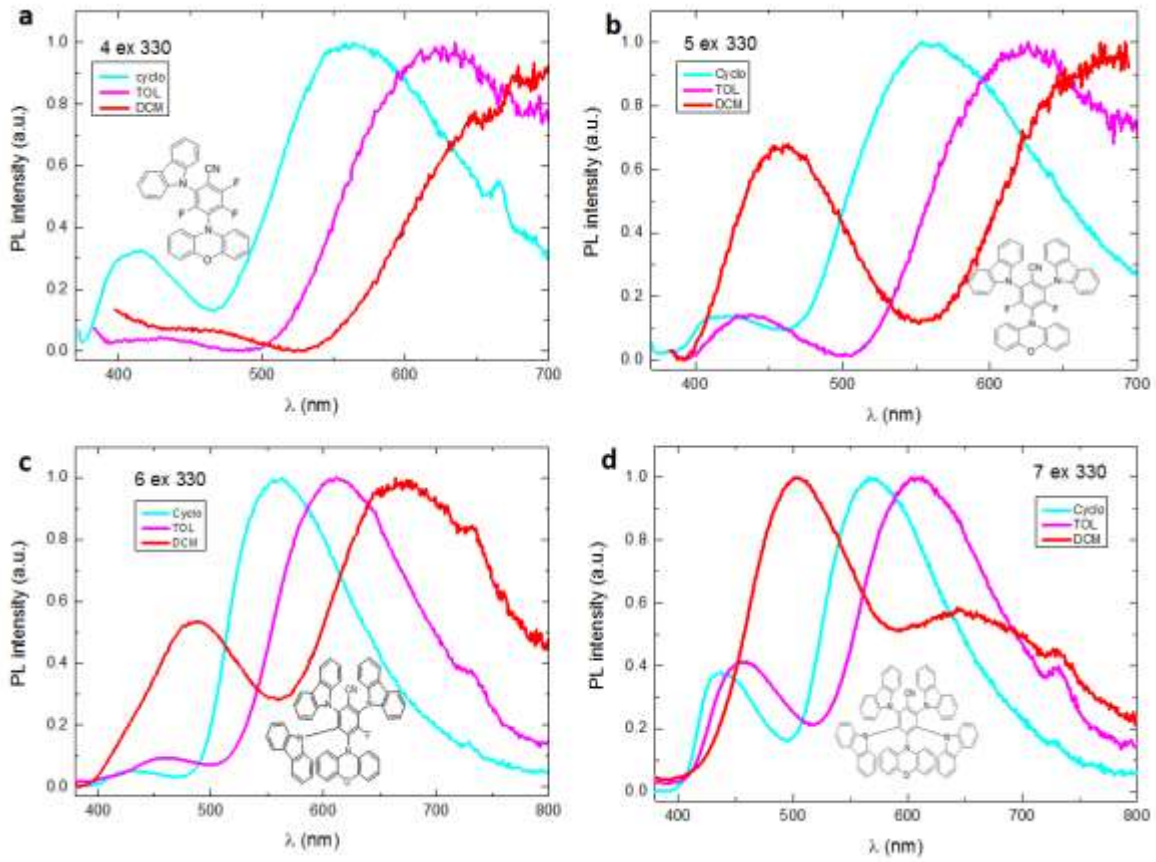

***Figure 2.13**: Normalized photoluminescence (PL) spectra in cyclohexane (c=10^{-5} M), toluene (c=10^{-5} M), and DCM (c=10^{-5} M) of **a) 4**, **b) 5**, **c) 6** and **d) 7.** (excitation wavelengths given in legends).*

5.4 Effect of the oxygen on fluorescence intensity.

In order to identify the TADF properties of the **4**-**7** molecules (**1** not emissive in solution), we measured the PL in a deoxygenated and in an air-equilibrated solution (by bubbling nitrogen for 10-15 min) (**Figure2.14**). Comparing the emission intensity in aerated solution with that obtained after deoxygenated the solutions allow also to obtain the DF contribution to the overall emission. In fact, the integral of the steady-state fluorescence spectrum in air is proportional to Φ_{PF}. On the other hand, the steady-state spectra in degassed conditions contain both DF and PF contributions, and therefore the integral is proportional to the sum $\Phi_{DF} + \Phi_{PF}$. The contribution of triplet excited states to the overall emission was determined accordingly to the method reported in Chapter 1 (**§7.2**, ***Equation 1.14***) and the DF/PF values are reported in **Table 15.**

The compounds **4** and **5** show an increase in both CT-Phx and CT-Cz emission after degassing, which indicates that both CT states present TADF properties. However, as already explained above, the blue band contains both contributions of the LE emission of phenoxazine and the CT-

Cz emission involving the carbazole. The DF is also confirmed by the increased quantum yield after degassing the systems (**4** from 0.7 % to 1%; **5** from 1.3% to 2.0%) (**Table 8**). In molecules **6** and **7** we demonstrated that the dual emission arises from both CT-Phx and CT-Cz states. Their DF contribution is also confirmed by the increase in quantum yield after degassing (**6** from 2.4% to 3.0%; **7** from 1.6% to 2.5 %), (**Table 8**). However, once the oxygen is removed from the solution, we can notice that for molecule **6** the relative intensity between the two CT bands remains the same, thus indicating that the contribution of the CT state involving the phenoxazine is predominant even for the DF process. On the other hand, molecule **7** presents a clear peak intensity inversion between the CT-Phx and CT-Cz emissions, when the solution is degassed. This could be a sign of a more efficient triplet harvesting mechanism in the BzN−Cz arm, compared to the BzN−Phx one. The DF/PF values obtained from this study show that these materials present poor TADF properties in solution (**Table 15**). As regarding the samples in PMMA, only a small difference was found after degassing the sample (**Figure 2.15**). The reason for this behaviour has to be attributed to the low oxygen permeability in PMMA.

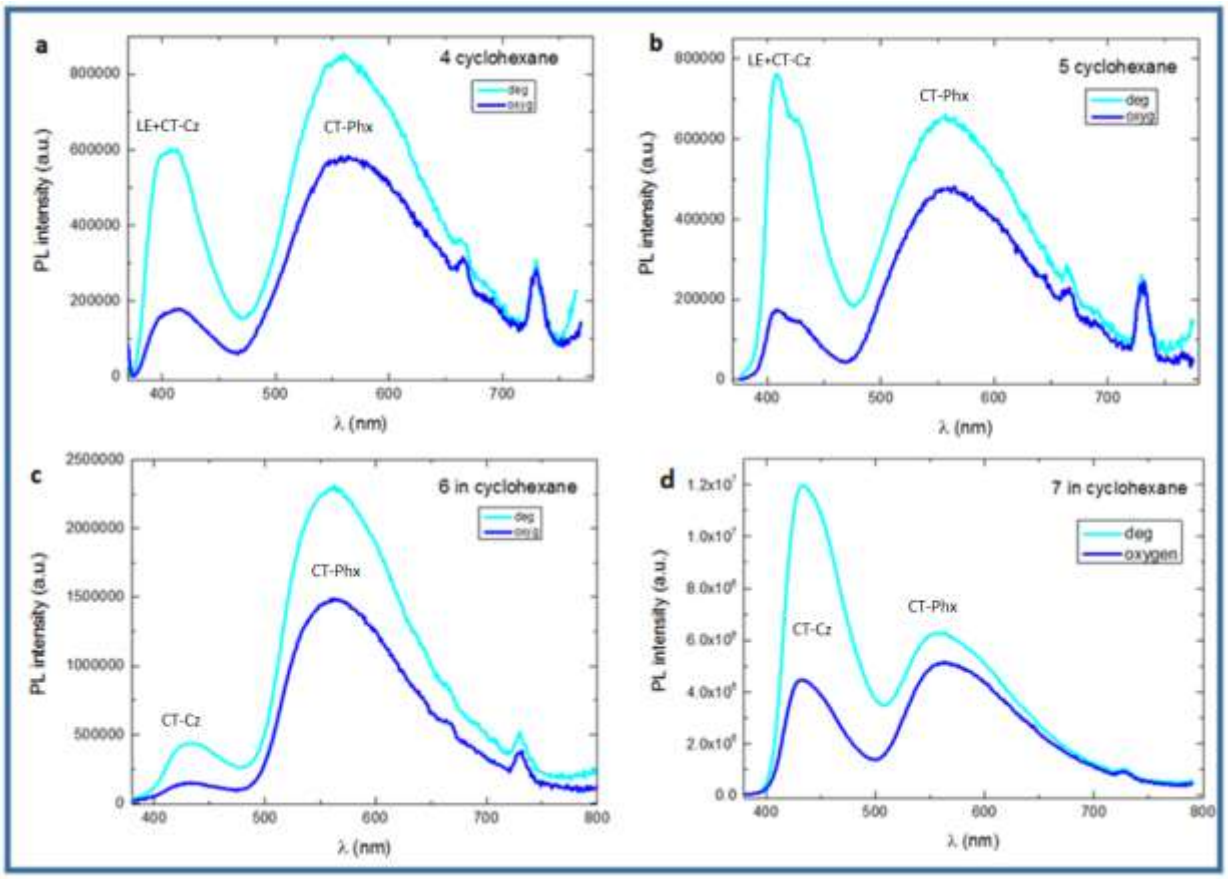

***Figure 2.14**: PL in aerated cyclohexane (c=10^{-5} M) and after degassing the solution of molecules a) **4** ,b) **5** c) **6** and d) **7**. λ_{exc}=330 nm.*

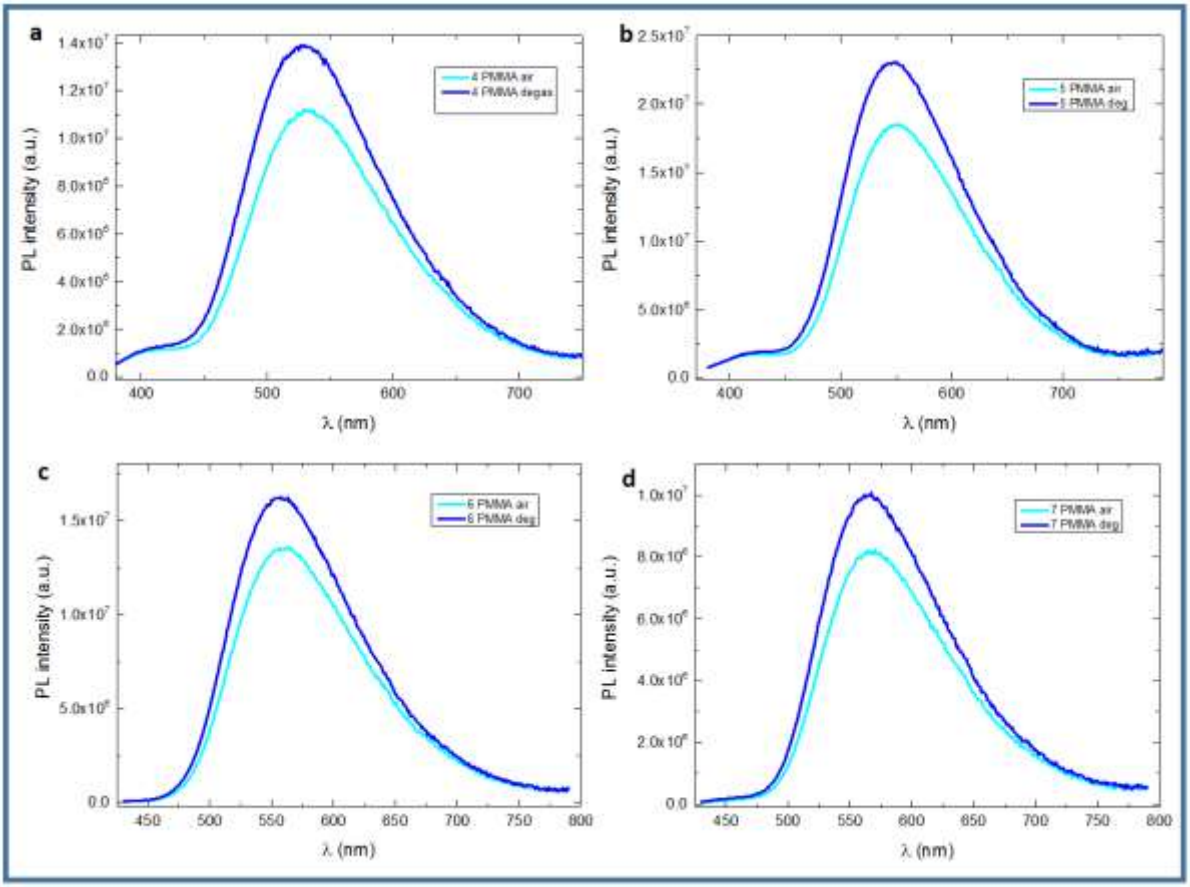

***Figure 2.15**: Steady-state emission spectra of **a) 4**, **b) 5**, **c) 6**, and **d) 7** in PMMA, both in aerated and degassed conditions at room-temperature. λ_{exc}=330 nm.*

5.5 Photoluminescence Quantum Yield.

In **Table 8** are reported the PLQYs for the molecules of the 1st series in cyclohexane, toluene and PMMA. Two different excitation wavelengths were selected, one between 300 and 330 nm, relative to the absorption region of the donors and acceptors moieties, and the other between 390 and 430nm, relative to the CT absorption. In cyclohexane, for **1** was possible to calculate the PLQY of the ^{1}LE emission of phenoxazine, by using the excitation wavelength at 330nm. In molecule **4** the same PLQY was obtained with excitation 330 nm and 400 nm. This is in line with the fact that the CT state involving the Cz is very weak. On the other hand, in molecules **5**-**7**, the QY obtained exciting at 330 nm is higher respect to that obtained for the excitation at 400nm. This is in line with the fact that the CT state involving the Cz becomes more important with the increasing number of Cz. The PLQY in PMMA is 3-9 fold higher respect to that in solution, and this is due to the rigidity of the solid matrix that strongly reduces the non-radiative paths. Overall, for

all compounds, the oxygen quenching of the emission is small and this is due to the poor TADF properties of this series of materials.

Table 8: PLQY (%) of **1** and **4-7** in cyclohexane, toluene and PMMA, with oxygen and after degassing (the experimental error is ±20% of the value)

	C_6H_{12}, λ_{ex}=300-330 nm	C_6H_{12},deg, λ_{ex}=300-330 nm	C_6H_{12}, λ_{ex}=390-430 nm	C_6H_{12},deg, λ_{ex}=390-430 nm	TOL λ_{ex}=300-330nm	TOL,deg. λ_{ex}=300-330nm	PMMA λ_{ex}=400nm	PMMA,deg λ_{ex}=400nm
1	0.2	0.2	nd	nd	-	-	4.5	5.0
4	0.7	1.0	0.7	1.0	-	-	4.3	5.2
5	1.3	2.0	1.5	1.7	0.1	0.1	4.0	4.9
6	2.4	3.0	1.9	2.1	0.3	0.3	13.6	15.9
7	1.6	2.5	1.3	1.7	0.2	0.2	15.1	18.1

[nd]not detected (too weak)

5.6 Effect of the number of substituents.

In order to study the effect of the increasing number of Cz, in this section, the steady-state photophysical properties for **1** and **4**-**5** molecules are compared in terms of λ_{Abs}^{max} and λ_{PL}^{max} and PLQY.

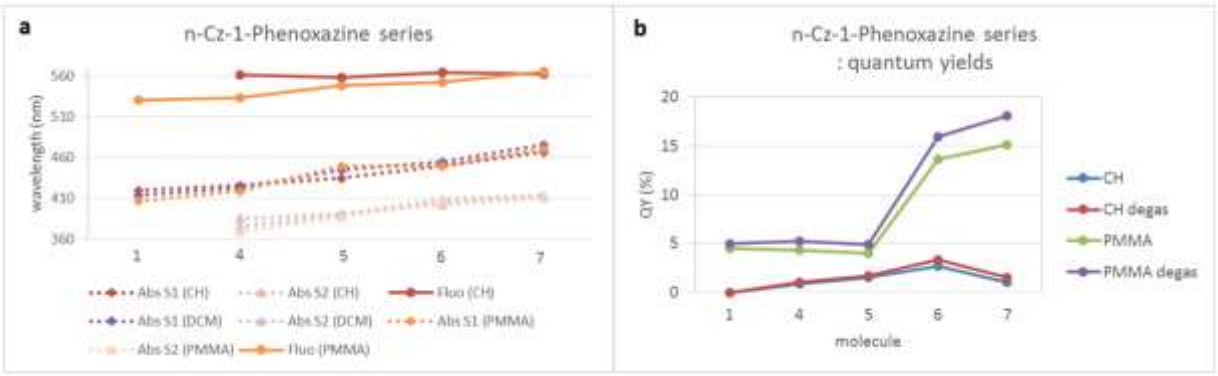

Figure 2.16: a) *Absorption and emission maximum as a function of the number of carbazoles substituents for the 1st series;* ***b)*** *quantum yield as a function of the number of substituents, in aerated and degassed conditions, for the 1st series.*

In **Figure 2.16a** we can notice that the emission maximum (λ) in PMMA progressively redshifts with the increasing number of carbazoles (λ_{1PMMA}= 519 nm, λ_{4PMMA}= 535nm, λ_{5PMMA}= 548nm, λ_{6PMMA}= 560nm, λ_{7PMMA}= 567nm). The Stokes shift decreases when increasing the number of carbazoles (**Table A2.4**). Contrary to that, in solution, no such shift occurs. In absorption, there is a gradual shift of the CT absorption maximum, approx 16 nm per additional donor (**Table A2.4**). The bathochromic shift with the increasing number of Cz substituents was already observed in

literature[57, 87], it was found to be related with the delocalization of the ICT state due to the increased number of donors. Furthermore, in **Figure 2.16b** it is shown the quantum yield increases with rising number of carbazole units, in both aerated and degassed conditions, in cyclohexane and PMMA. In cyclohexane the QYs increase with the number of substituents except for **7** (4-Cz). In PMMA the fluorescence QYs are stable until **5** (2-Cz) and increase almost 3-fold for **6** and **7**.

6. STEADY-STATE PHOTOPHYSICAL CHARACTERIZATION OF THE 2ND AND 3RD SERIES.

6.1 Absorption.

The normalized absorption spectra in cyclohexane (left, $c=10^{-5}$ M) and PMMA (0.05-0.1%wt, right) of the molecules of the 2nd and 3rd series are reported in **Figure 2.17** (**2**,**8**, **9a**[3] and **10**) and **Figure 2.18** (**3** and **11**,**12**). All molecules present a similar absorption behavior to that of the molecules **1** and **4**-**7**.

At low energy, between 350 and 550 nm, the less intense peaks do not appear either in the donors (phenoxazine[78] and Carbazole[79]) nor acceptor (benzonitrile[80]) absorption spectra, and thus are assigned to the ^{1}CT state absorptions of the D-A molecule. In particular, one band is assigned to the CT absorption involving the phenoxazine (BzN-Phx), and the other one to the CT involving the carbazole (BzN-Cz). Also in this case it is possible to observe a third peak that is assigned to different CT states associated with different positions of the donors. At higher energy (over 360 nm) the absorption corresponds to the localized absorption of the donors. In particular, the two absorption bands around 287nm and around 327nm are assigned to the localized absorption of carbazole[79], and the other peaks are assigned to the localized absorption of phenoxazine [78].

[3] It is important to underline that molecule **9a** is one of the two possible isomers.

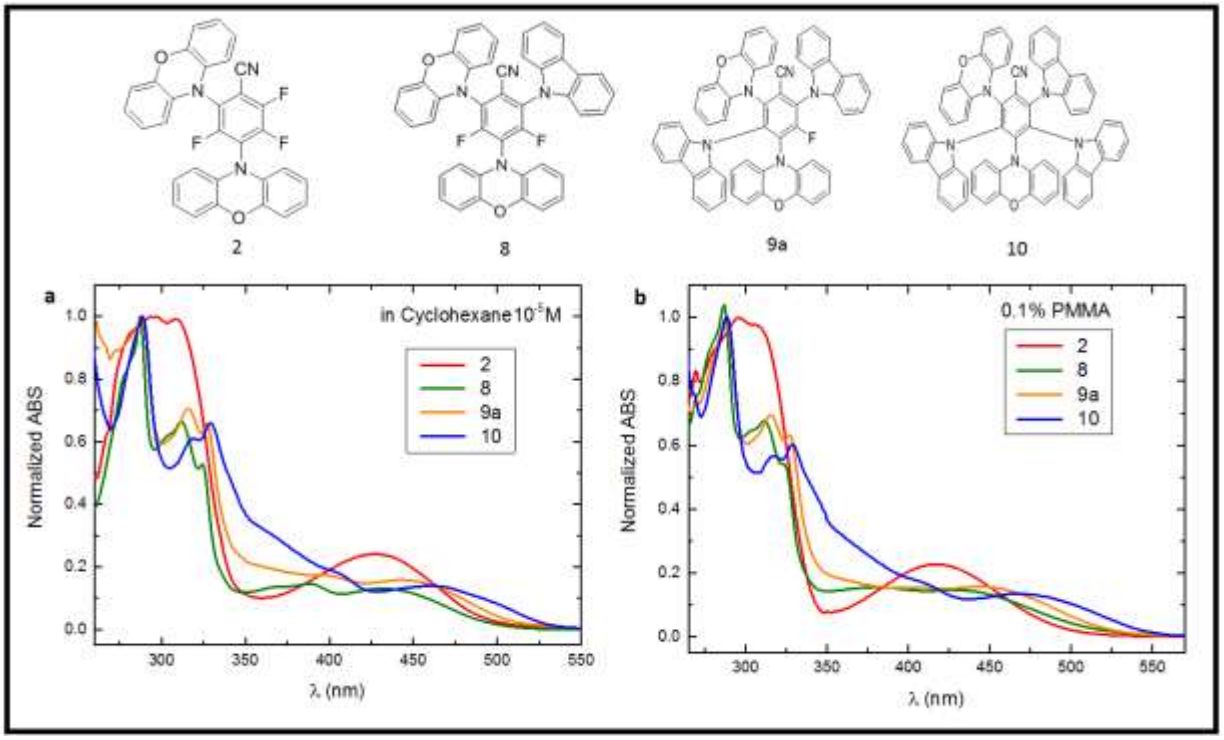

***Figure 2.17**: Normalized absorption spectra of molecules **2** and **8**-**10** in **a)** cyclohexane (c=10^{-5} M) and **b)** PMMA (0.1%wt) (structures of the molecules given on top).*

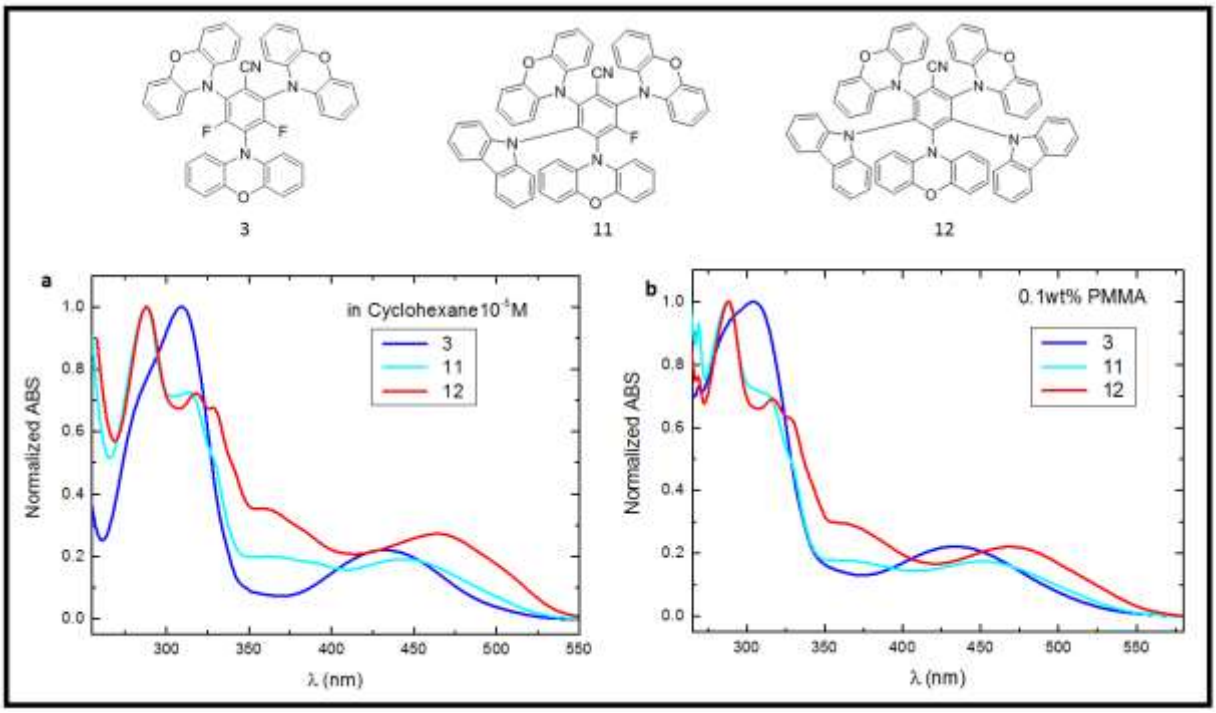

***Figure 2.18**: Normalized absorption spectra of molecules **3** and **11**-**12** in **a)** cyclohexane (c=10^{-5} M) and **b)** PMMA (0.1%wt) (structures of the molecules given on top).*

6.2 Fluorescence of 2nd and 3rd series.

The emission of the molecules in the 2nd and 3rd series in cyclohexane is reported in **Figure 2.19a** and **Figure 2.19c** respectively. All molecules present a strong emission at lower energy, arising from the CT excited state involving the phenoxazine. At higher energy, the emission is poorly visible in most cases. In particular, a weak emission centered around 390 nm is visible in molecule **2** (2Phx)(**Figure 2.19a**, **inset**) which becomes stronger in for molecule **3** (3Phx) (**Figure 2.19c**). We assign this emission exclusively to the LE emission of phenoxazine. A very weak emission at higher energy is also visible for molecules **8**, **9a** and **10** in cyclohexane (**Figure 2.19a inset**) and **11** (**Figure 2.19c inset**). The emission becomes more intense for **12** (**Figure 2.19c**). All these emissions at higher energy, present bathochromic shift in respect to the LE emission of phenoxazine. This can be seen both in the 2nd series [**8** (λ_{max} =425 nm), **9a** (λ_{max} =432nm), and **10** (λ_{max} =437 nm) *vs*. **2** (λ_{max} =390 nm)], and in the 3rd series [**11** (λ_{max} =409 nm), **12** (λ_{max} =394 nm, 417(s) nm) *vs.* **3** (λ_{max} =385 nm)]. These observations indicate that also in this case, a weak contribution of the CT emission involving the carbazole, is visible in the molecules with two different donors. However, except for **12** the CT state involving the carbazole, is very weak and only barely visible. In our opinion this depends on the higher number of phenoxazines present in the second (2Phx) and third series (3Phx). It does results that once the excited state is formed all the energy is transferred to CT state involving the phenoxazine, as this present a CT state at lower energy with respect to the one involving the carbazole. The emission of carbazole-related CT is not visible in PMMA films (**Figure 2.19b** and **2.19d**).

We also tested the solvatochromism effect (cyclohexane, toluene, and DCM). The emission of **3** in the three different solvents is reported in **Figure 2.20**. Results for other molecules are shown in **Figure A2.13** (2nd series) and **Figure A2.23** (**11** and **12**). At higher energy, the emission of **3** in the blue region doesn't shift with solvent polarity (**Figure 2.20a**) thus confirming the LE origin of this emission. In other molecules the solvatochromism was only studied for the low energy emission band. Positive solvatochromism was observed for all compounds, thus confirming that the lower energy band is a CT state involving phenoxazine. Moreover, the comparison between the emission in aerated and degassed conditions shown in **Figure A2.16** (2nd series) and **Figure A2.26** (3rd series) shows that in all cases, after degassing the solution, an increase of the CT-Phx band is observed, confirming the presence of TADF related to this transition. On the other hand, any clear increase of the emission relative to CT involving the carbazole is observed. Finally, in **Figure 2.20d** it is possible to see that the band at 385 nm in molecule **3** does not change intensity upon de-oxygenation, thus confirming the local character of the band (presumably ^{1}LE of phenoxazine), and the TADF arises only from the BzN-Phx moiety.

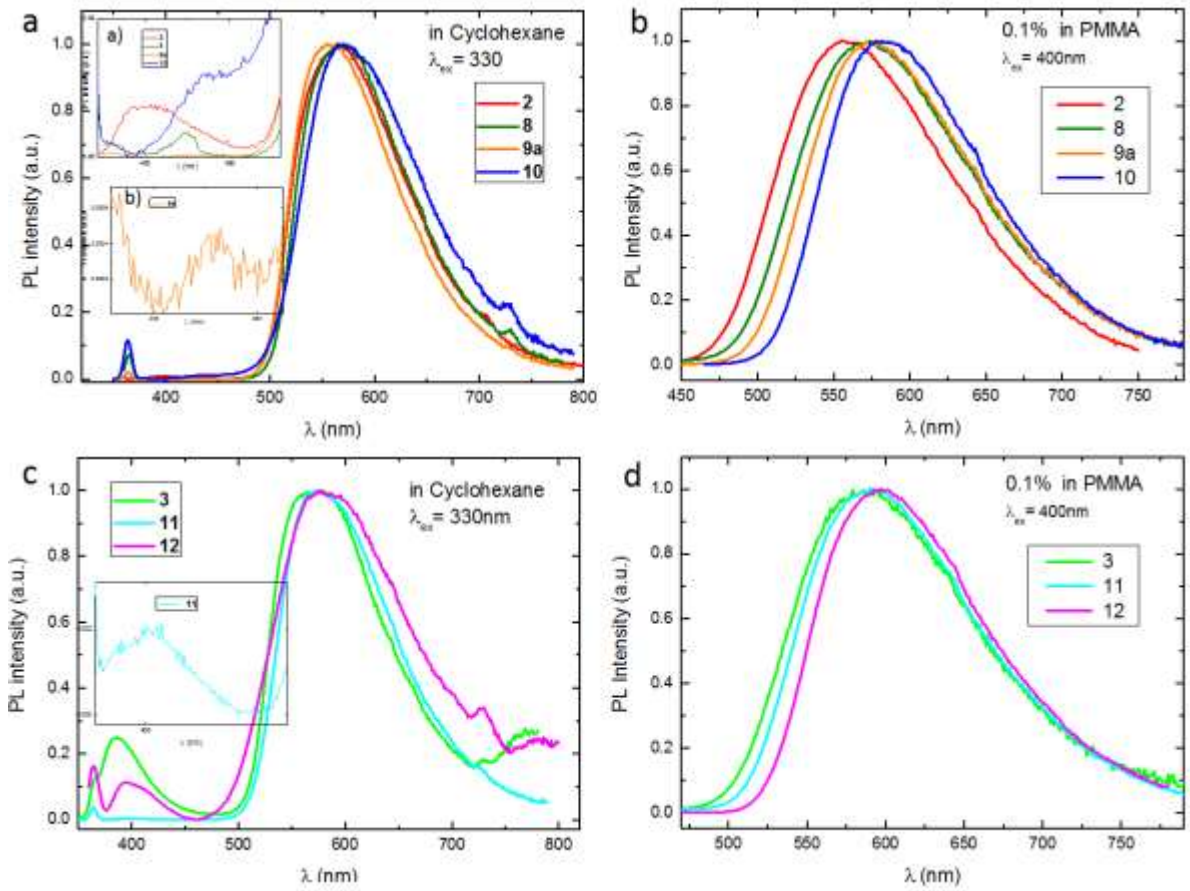

Figure 2.19: *Normalized photoluminescence (PL) spectra of molecules:* ***a) 2****,* ***8****,* ***9a*** *and* ***10*** *in cyclohexane [****inset****: close up of the high energy maxima for: a)* ***2****,* ***8****,* ***9a*** *and b)* ***10****]; **b) 2**, **8**, **9a** and **10** in PMMA; **c) 3**, **11** and **12** in cyclohexane (**inset**: close up of the peak at high energy for **11**), **d) 3**, **11** and **12** in PMMA.*

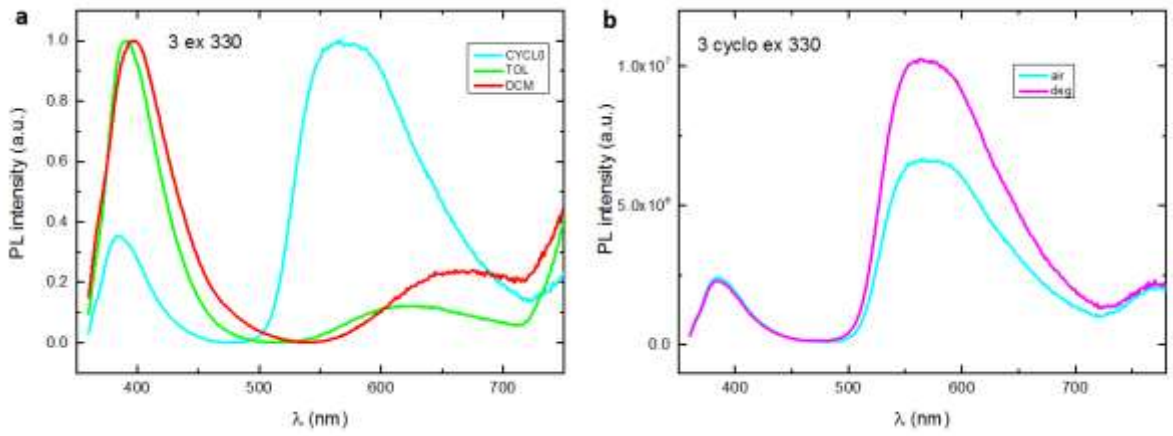

Figure 2.20: a) *Normalized photoluminescence spectra of molecule* ***3*** *in cyclohexane, toluene, and dichloromethane* ***b)*** *Normalized photoluminescence of molecule* ***3*** *in aerated cyclohexane and after degassing the solution.*

The PLQYs obtained for the molecules of the 2nd (**Table 9**) and 3rd (**Table 10**) series in cyclohexane, with the excitation at 330nm (LE) is mostly the same as that obtained for the excitation at 400nm (CT), except in the full substituted **10** and **12**. This is in line with the fact that in the second and third series the contribution of the CT-Cz on the total emission is very weak. Similarly to the first series, the PLQYs in PMMA increase for all the molecules except for molecule **3** whose PLQY decreases four times in PMMA compared to cyclohexane solution. Compared to cyclohexane, in PMMA, the QY is only slightly higher for molecules **8** and **11** but becomes 11 times higher for molecule **10** and 16 times higher for molecule **12**. Contrarily to the first series, in the second and third series, there is a pronounced oxygen quenching effect on fluorescence QYs which is more or less the double for all compounds except for the molecules **12** (totally substituted). This shows that these materials present better TADF properties, and the larger number of phenoxazine units helps to improve the TADF effect. This is in line with the stronger donor effect of the phenoxazine, which is in general used to improve the TADF properties of D-A compounds. The increase of QY upon degassing the PMMA samples is small but this is due to the low oxygen permeability of PMMA. Finally, it is worth noting that molecules **10** and **12** are almost not fluorescent in solution but in PMMA they become the most fluorescent of the 2nd and 3rd series, respectively. This behavior indicates that in solution these molecules lose most of their excitation energy trough non-radiative channels, e.g. rotation and vibration, which results efficiently suppressed once dispersed in a more rigid matrix.

Table 9: PLQY of **2** and **8-10** in cyclohexane, toluene and PMMA, with oxygen and after degassing (the experimental error is ±20% of the value).

	C_6H_{12}, λ_{ex}=300-330 nm	C_6H_{12},deg, λ_{ex}=300-330 nm	C_6H_{12}, λ_{ex}=390-430 nm	C_6H_{12},deg, λ_{ex}=390-430 nm	TOL λ_{ex}= 300-330nm	TOL,deg. λ_{ex}= 300-330nm	PMMA λ_{ex}=400nm	PMMA,deg λ_{ex}=400nm
2	2.2	3.6	2.1	3.4	-	-	3.3	4.3
8	2.8	4.5	2.3	3.5	-	-	3.7	4.9
9a	3.6	6.1	3.4	6.1	0.25	0.3	6.5	7.7
10	1.0	1.9	0.7	1.0	-	-	8.5	11.4

Table 10: PLQY of **3** and **11**-**12** in cyclohexane, toluene and PMMA, in air and after degassing (the experimental error is ±20% of the value).

	C_6H_{12}, λ_{ex}=300-330 nm	C_6H_{12},deg, λ_{ex}=300-330 nm	C_6H_{12}, λ_{ex}=390-430 nm	C_6H_{12},deg, λ_{ex}=390-430 nm	TOL λ_{ex}=300-330nm	TOL,deg. λ_{ex}=300-330nm	PMMA λ_{ex}=400nm	PMMA,deg λ_{ex}=400nm
3	3.5	7.7	3.3	7.6	0.6	1.3	1.5	1.8
11	2.5	4.2	1.5	3.5	-	-	3.8	4.3
12	0.5	0.6	0.2	0.3	-	-	6.4	7.9

6.3 Effect of the number of substituents.

Similarly to the first series, the effect of the number of Cz is also studied in 2nd and 3rd series. The steady-state photophysical properties are compared in terms of PLQY, λ_{Abs}^{max}, and λ_{PL}^{max}.

Figure 2.21a and **Figure 2.21c** show the variation of the absorption and emission maxima with increasing number of carbazoles. Also in the 2nd and 3rd series, we can observe that the emission maximum in PMMA progressively redshifts with increasing number of carbazoles. The Stokes shift reduces when the number of carbazole unit increases. The redshift is very small both for the 2nd series (e.g. +8 nm/substituent in PMMA) and for the 3rd series (≈5nm/substituent in PMMA). Furthermore, also in absorption, we can see a redshift of the maxima with the increasing number of substituents, both for the 2nd series (≈18nm/substituent in PMMA) and for the 3rd series (≈19nm/substituent in PMMA).

The variation of quantum yield with the increasing number of substituents is reported in **Figure 2.21b** (2nd series) and **Figure 2.21d** (3rd Series), in both aerated and degassed conditions. In solution, for the 2nd series, the fluorescence QYs increase with the number of substituents except for **10** (3-Cz). In contrary in the 3rd series is observed that in solution the QY decreases with the increasing number of the substituents. In PMMA the fluorescence QYs increase with the increasing number of substituents in both 2nd and 3rd series. This behaviour indicates that in solution the molecules release most of their excitation energy trough non-radiative channels, e.g. rotation and vibration. The non-radiative deactivation paths are efficiently suppressed once dispersed in a more rigid matrix.

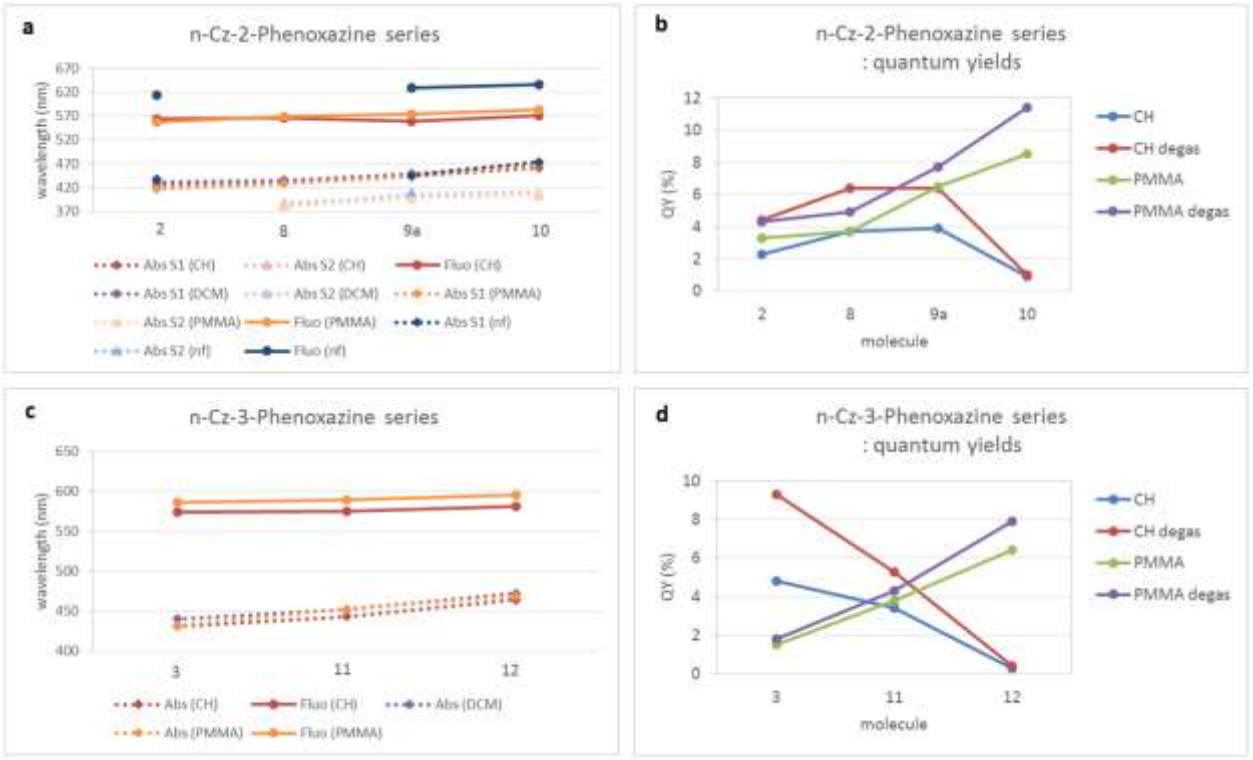

Figure 2.21**: Absorption and emission maxima as a function of the number of carbazoles substituents for:* ***a) *2nd series,* ***c)*** *3rd series. Quantum yield as a function of the number of substituents, in aerated and degassed conditions for:* ***b)*** *2nd series,* ***d)*** *3rd series.*

7. TIME-RESOLVED PHOTOPHYSICAL ANALYSIS.

The photoluminescence decay of **1-12** molecules in solution and the time-resolved photophysical properties of **1-12** dispersed in a PMMA matrix (0.1%in weight) are discussed in this section. They allow for a better understanding of the nature of the emission introduced in the previous paragraph. The photoluminescence decay in solution was only recorded at room temperature. The time-resolved investigations of **1-12** dispersed in a PMMA matrix were performed at room temperature (RT) and 77K (LT) after degassing the sample with a high vacuum pump. The RT measurements allow investigating the TADF properties of the samples. The 77K measurements allow to investigate the phosphorescence of the material and determine the triplet state energy. It is generally obtained from the onset of the most delayed time-resolved emission spectrum and is calculated using the equation:

$$E = \frac{\hbar c}{\lambda} = \frac{1240}{\lambda} \qquad \textit{Equation 2.1}$$

Where E represents the energy of the photon and $\hbar c$ is equal to 1240 eV·nm.

7.1 Decay time of 2-12 molecules in solution.

In **Table 11** are shown the decay lifetime constants of the compounds **2**-**12** measured in degassed cyclohexane. Two typical decay times were found, one in the ns domain assigned to PF and the others in the microsecond domain assigned to DF, thus confirming the presence of TADF in solution. Nanosecond components are shown in table as average lifetimes, comprising the different PF contributions, such as LE or CT-Phx and CT-Cz emissions. Surprisingly, a double exponential decay in the DF region was obtained only for those compounds where the emission relative to the CT state involving the carbazole was more intense. While in other cases only one long decay time was obtained. Therefore one of them was assigned to the CT-Phx (present in all decays) and the other one to that involving Cz. These results, further demonstrate that both double CT emissions observed in solution present TADF properties.

Table 11: Photophysical properties of all the molecules **1**-**12** in cyclohexane at RT.

in C_6H_{12}	$\tau 1_{av}$ (ns)	τ2(ns)	τ3(ns)	τ_{av} (us)	DF/PF
1	-			-	-
4	14.7	383.6	2162.3	1.9	0.62
5	8.9	1200	8828	8.6	0.68
6	8.2	1599	14403	11.4	0.59
7	17.8	2081	24291	23.7	0.67
2	17.2	715	-	0.7	1.14
8	19.8	824	-	0.8	0.93
9a	17.3	585.4	-	0.6	1.17
10	13.74	343	2330	2.3	1.18
3	18.8	651	-	0.7	1.21
11	11.7	673	-	0.7	0.54
12	3.2	574	1092	1.0	0.91

7.2 Time-resolved study in PMMA of the first series.

The Photophysical properties of molecules **1**-**12** dispersed in a PMMA matrix (0.05% in weight) were further studied by time-resolved experiments to gain insight into the nature of the emission. All the experiments were realized using an iCCD camera equipment that allows to measure individual spectra at a specific time delay (TD) with a given integration time (IT) after pulsed laser excitation. Moreover, this technique allows to build decay curves by collecting several spectra with logarithmically increasing TD and IT. The data were collected at RT and 77K. In these type of experiments, two main situations are encountered. When the emission spectra do not change upon increasing observation times, it means that the luminescence arises from the same singlet state and the long decay time is due to the population of the triplet state that up-convert back to

the singlet one through RISC (TADF) or TTA process. However, if different spectra are recorded over time, it means that the total luminescence comes from different states (*e.g.* triplet states, LE of different donors, or CT states with different energy). Furthermore, it is important to compare the time-resolved emission spectra with the decay time profile. This allows a better understanding of the states involved in each process thanks to their characteristic times. It is important to underline that only the more intense regions of the DF components are fitted (>10^1/10^2 Integrated Intensity). This part presents in general the typical form of the TADF decay. The analysis of all the spectra acquired after different delay times are shown in **Figure 2.22-2.26**.

The time-resolved analysis of **1** (only one phenoxazine as a donor) (**Figure 2.22**) shows that for both measurements at RT (**Figure 2.22b**) and 77K (**Figure 2.22a**), the early emission (2.3-10 ns) is bluer than the emission at longer delay time. This depends on the initial contribution of the localized emission (^{1}LE) of the phenoxazine. At RT, when increasing the delay time, the emission progressively redshifts and after 100 ns the ^{1}CT state involving the phenoxazine remains the dominant emissive state, which lives up to 35 microseconds. We attribute this emission to the DF arising from the population of the triplet state that is up-converted back to the singlet state through RISC (TADF). From the decay reported in **Figure 2.22d**, two decay times are obtained for PF and only one for DF (**Table 12**). The two PF decay times are associated to the ^{1}LE emission of phenoxazine and to the ^{1}CT emission involving the phenoxazine. On the other hand, the decay in the microsecond regime is attributed to the DF arising from the ^{1}CT involving the phenoxazine. At 77K, is also present an initial contribution of the LE emission that disappears with the increase of the delay time. As we can see from the decay (**Figure 2.22d**) in this case the DF contribution is very low. Therefore we think that it could arise from a TTA process since at low temperatures the thermal energy could be not enough to obtain an efficient RISC. However, given the very low $E_{S\text{-}T}$ very low[4] (0.02 eV) a weak TADF contribution cannot be totally excluded. At late times (70.8 ms), the emission at 77K is attributed to the localized phosphorescence of phenoxazine (^{3}LE), in fact, it presents the same onset of the phosphorescence of phenoxazine (**Figure 2.22c, Table12**). The intensity dependence of the DF emission as a function of the laser excitation dose is shown (**Figure A2.31**). Integrating emission from 100ns to 20us delay a slope of 0.91 ± 0.01 was found. This result confirms a monomolecular process typical of the thermally-assisted mechanism (as opposed to TTA, which is by definition a bimolecular process).

[4] The onset of the DF at RT (TD=1us) was used to find the energy of S_1, and the onset of the phosphorescence at 77K (TD=70ms) corresponds to the energy of T_1, both allow to calculate the $\Delta E_{S\text{-}T}$.

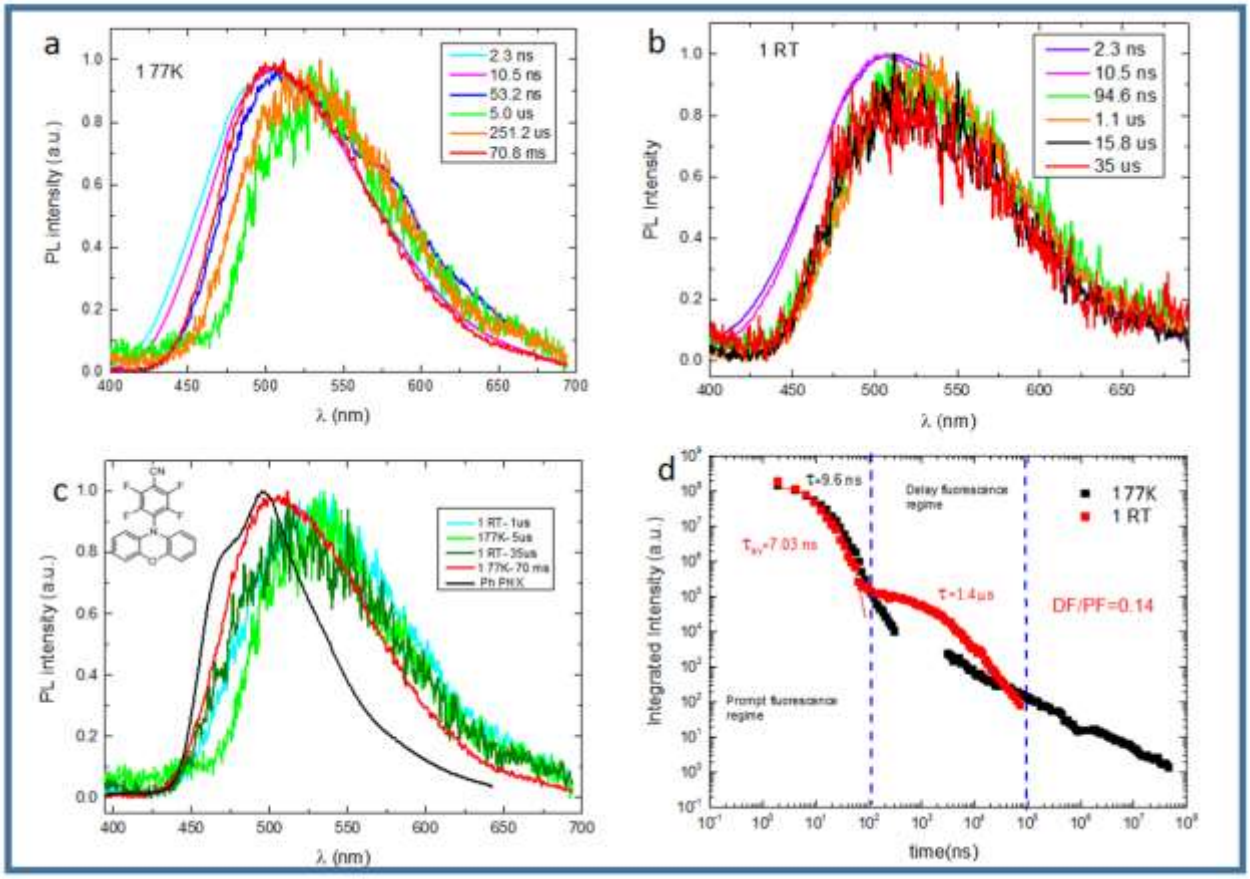

Figure 2.22: ***a)*** *and* ***b)*** *show the time-resolved emission spectra of* ***1*** *in PMMA at room temperature (RT) and 77K respectively;* ***c)*** *delayed emission at the longest TD and delayed emission in TADF regime of* ***1****, for RT and 77 K compared with phosphorescence of phenoxazine;* ***d****) decay curve of* ***1*** *in PMMA at RT and 77K. All experiments were carried out at* λ_{ex}*= 355 nm.*

The early emission of molecule **4** also presents a blue shift, however, in this case, a shoulder is visible especially at 77K. Beyond the initial LE contribution of the donors, we can attribute this shoulder to the CT state emission relative to the BzN-Cz moiety. Increasing the delay time, the shoulder at higher energy progressively disappears in both 77K and RT spectra, and the emission redshifts. At RT, after 100 ns the DF emission arises exclusively from the ^{1}CT state involving the phenoxazine. At 77K the $\Delta E_{S\text{-}T}$ (0.1 eV) is too high to ensure an efficient RISC, and thus the DF (after 100 ns) is attributed to a TTA process. Increasing the delay time we can see that the emission progressively blue shifts for both RT and 77K. In particular, at RT, for a delay time of 35 µs, the blue shift to the initial PF is attributed to the DF contribution that arises from the CT involving the carbazole[5]. When the delay time increases, and up to 1ms (RT), the emission associated to the CT of the Cz-BzN moiety becomes dominant (**Figure 2.23c**). At 77K the late

[5] In **Figures 23-26** is reported, as a reference, the time-resolved emission relative to Cz-BzN molecule in PMMA, after a time delay of 10us. This emission represents the delayed emission arising exclusively from the CT state between Cz and BzN. The photophysical properties of Cz-BzN will be presented in Chapter 5.

emission (70ms) presents the onset close to the phosphorescence of phenoxazine, and therefore is assigned to the localized phosphorescence of the phenoxazine moiety. At RT, from the decay shown in **Figure 2.23d**, two decay times are obtained of PF and two of DF (**Table 12**). The two PF decay are associated with the ^{1}LE emission of phenoxazine and the ^{1}CT emission involving the phenoxazine. On the other hand, the two decays in the microsecond regime are attributed to the DF arising from the ^{1}CT involving the phenoxazine and from the ^{1}CT involving the carbazole. Also in this case the intensity dependence of the DF emission as a function of the laser excitation dose (**Figure A2.31**) confirms that the emission arises from a TADF mechanism (a not strictly linear slope of 0.99 ± 0.01 was found).

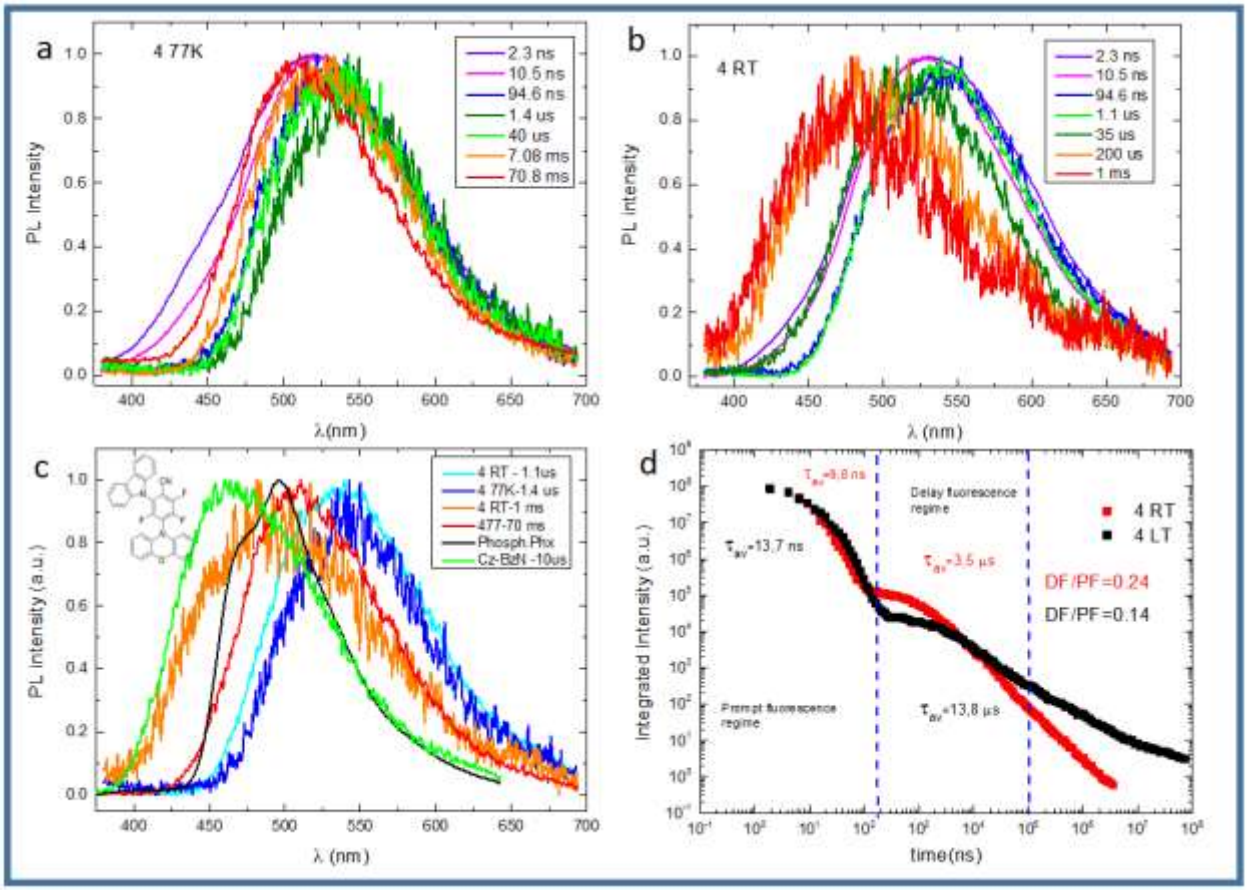

***Figure 2.23**: **a)** and **b)** show the time-resolved emission spectra of **4** in PMMA at room temperature (RT) and 77K respectively; **c)** delayed emission at the longest TD and delayed emission in TADF regime of **4**, for RT and 77 K compared with phosphorescence of phenoxazine and with the CT DF emission of Cz-BzN; **d)** decay curve of **4** in PMMA at RT and 77K. All experiments were carried out at λ_{ex}= 355 nm.*

Molecule **5** presents an additional carbazole donor, which allows to observe in the early time PF, an enhanced contribution of the CT emission involving the carbazole. The shoulder at higher energy is clearly visible in the PF of both RT and 77K. At lower energy, the PF presents an intense band assigned to the ^{1}CT relative to the Phx-BzN moiety. Increasing the delay time, the emission progressively redshifts, and for TD=100 ns the shoulder at 450 nm disappears for both 77K and RT measurements. Between 100 ns and 1µs, the DF emission arises exclusively from the ^{1}CT state involving the phenoxazine. Increasing the delay time we can observe that the emission progressively blue shifts again in both RT and 77K. In particular, at RT, after 20 µs the shoulder at higher energy appears again. Thus indicating a delayed fluorescence contribution from the ^{1}CT state involving the carbazole. When the delay time increases and up to 141 µs (RT), the emission associated with the CT of the Cz-BzN moiety becomes dominant (**Figure 2.24b**). On the other hand, at 77K the late emission (70ms) is similar to the phosphorescence of the phenoxazine (**Figure 2.24c**), and therefore we assign it to the localized phosphorescence (^{3}LE) relative to the phenoxazine moiety. At RT the PF part of the decay (**Figure 2.24d**), was fitted with a biexponential function. The two PF decay components are associated to ^{1}LE emission of phenoxazine and the other to the ^{1}CT emission involving the phenoxazine. The longer part of the decay was also fitted with a biexponential function, and the two decays components are attributed to the DF arising from the ^{1}CT involving the phenoxazine and the other to the DF arising from the ^{1}CT involving the carbazole. The not strictly linear exponent of 0.99 ± 0.01 for power dependence of DF emission, confirms a monomolecular process typical of the thermally-assisted mechanism (**Figure A2.31**).

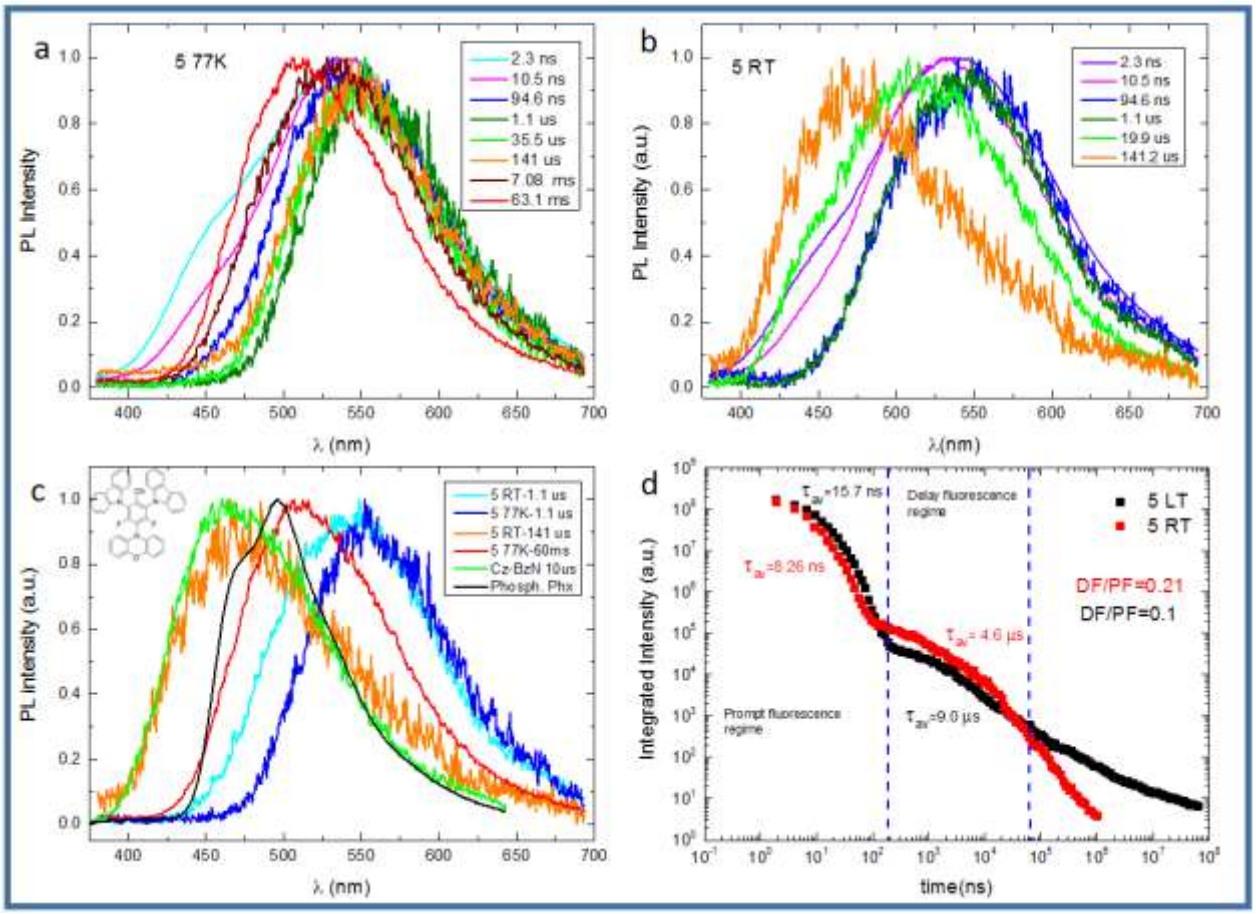

***Figure 2.24**: **a)** and **b)** show the time-resolved emission spectra of **5** in PMMA at room temperature (RT) and 77K respectively; **c)** delayed emission at the longest TD and delayed emission in TADF regime of **5**, for RT and 77 K compared with phosphorescence of phenoxazine and with the CT DF emission of Cz-BzN; **d)** decay curve of **5** in PMMA at RT and 77K. All experiments were carried out at λ_{ex}= 355 nm.*

The time-resolved measurements of molecules **6** (**Figure 2.25**) and **7** (**Figure 2.26**) present a behaviour similar to molecules **4** and **5**. Both present in the early PF (77K and RT) a shoulder at the higher energy that is assigned to both contributions of ^{1}LE emission of Phx and the ^{1}CT of Cz-BzN. Increasing the time delay, the shoulder at higher energy disappears, and all the emissions arise exclusively from the ^{1}CT excited state involving the phenoxazine. At longer delay time, also molecules **6** and **7** present blue shifts for both RT and 77K emissions. At RT, for a time delay of 35 µs, a shoulder reappears again for both **6** and **7** and this is associated with the DF contribution arising from the of the ^{1}CT state involving the Cz. Upon increase of delay time, for both **6** and **7**, the emission associated with the CT of the Cz-BzN moiety becomes dominant. On the other hand, at 77K the late emission for both **6** and **7** can be assigned to the ^{3}LE phosphorescence of phenoxazine. At RT the PF part of the decay of both **6** (**Figure 2.26d**) and **7** (**Figure 2.26d**), are fitted with a biexponential function. The two PF decays are associated, one to the ^{1}LE emission of

phenoxazine and the other to the ^{1}CT emission involving the phenoxazine. The longer part of the decay was also fitted for both **6** and **7** with a biexponential function, and the two decays are attributed, one to the DF arising from the ^{1}CT involving the phenoxazine and the other to the DF arising from the ^{1}CT involving the carbazole.

The not strictly linear gradient of 1.01 ± 0.01 found from the variation of the DF intensity upon rising the laser dose, confirms a monomolecular process typical of the thermally-assisted mechanism for both **6** and **7** (**Figure A2.31**).

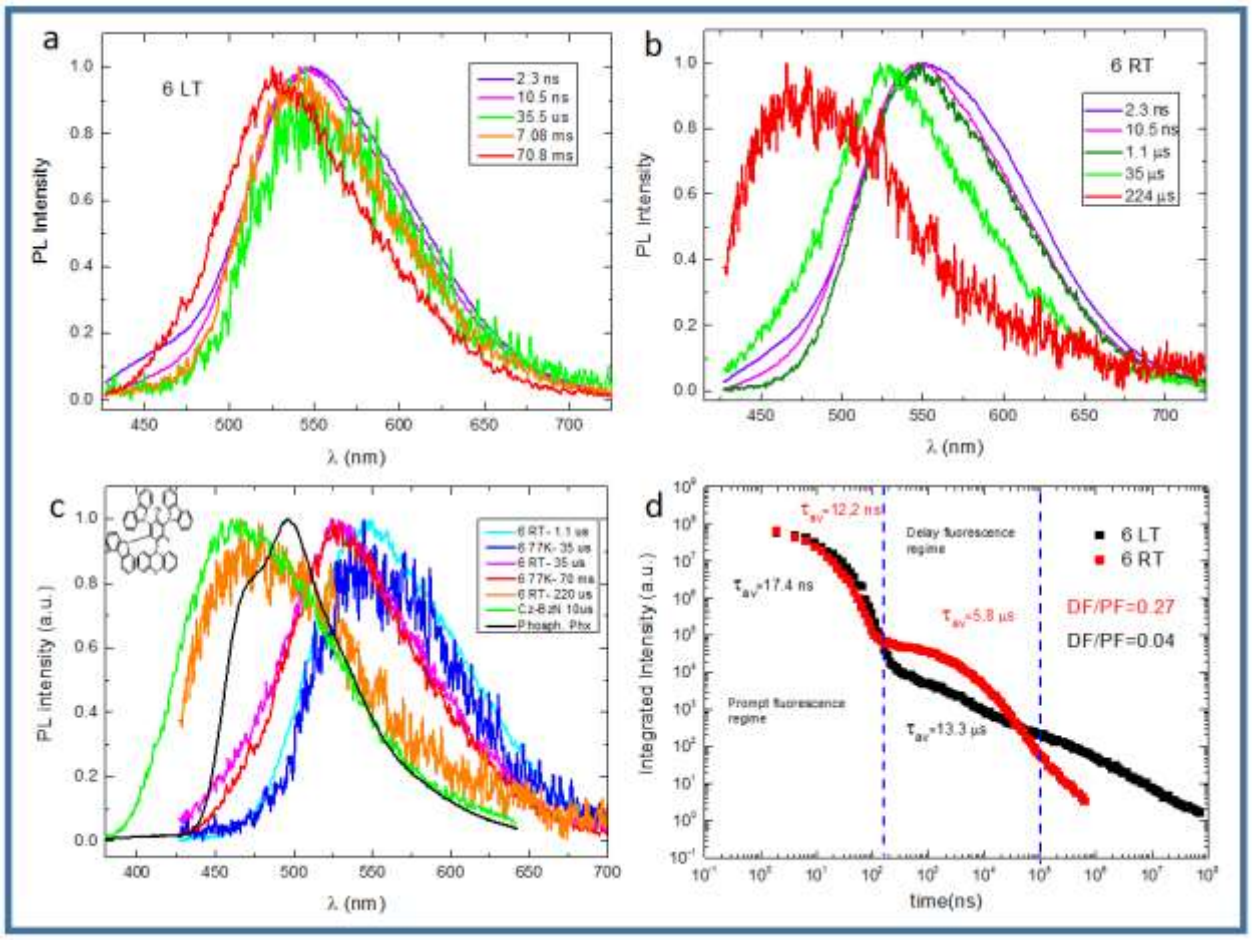

Figure 2.25**: **a)** and **b)** show the time-resolved emission spectra of **6** in PMMA at room temperature (RT) and 77K respectively; **c) delayed emission at the longest TD and delayed emission in TADF regime of **6**, for RT and 77 K compared with phosphorescence of the donors phenoxazine and with the CT DF emission of Cz-BzN; ***d**) decay curve of **6** in PMMA at RT and 77K. All experiments were carried out at λ_{ex}= 355 nm*.

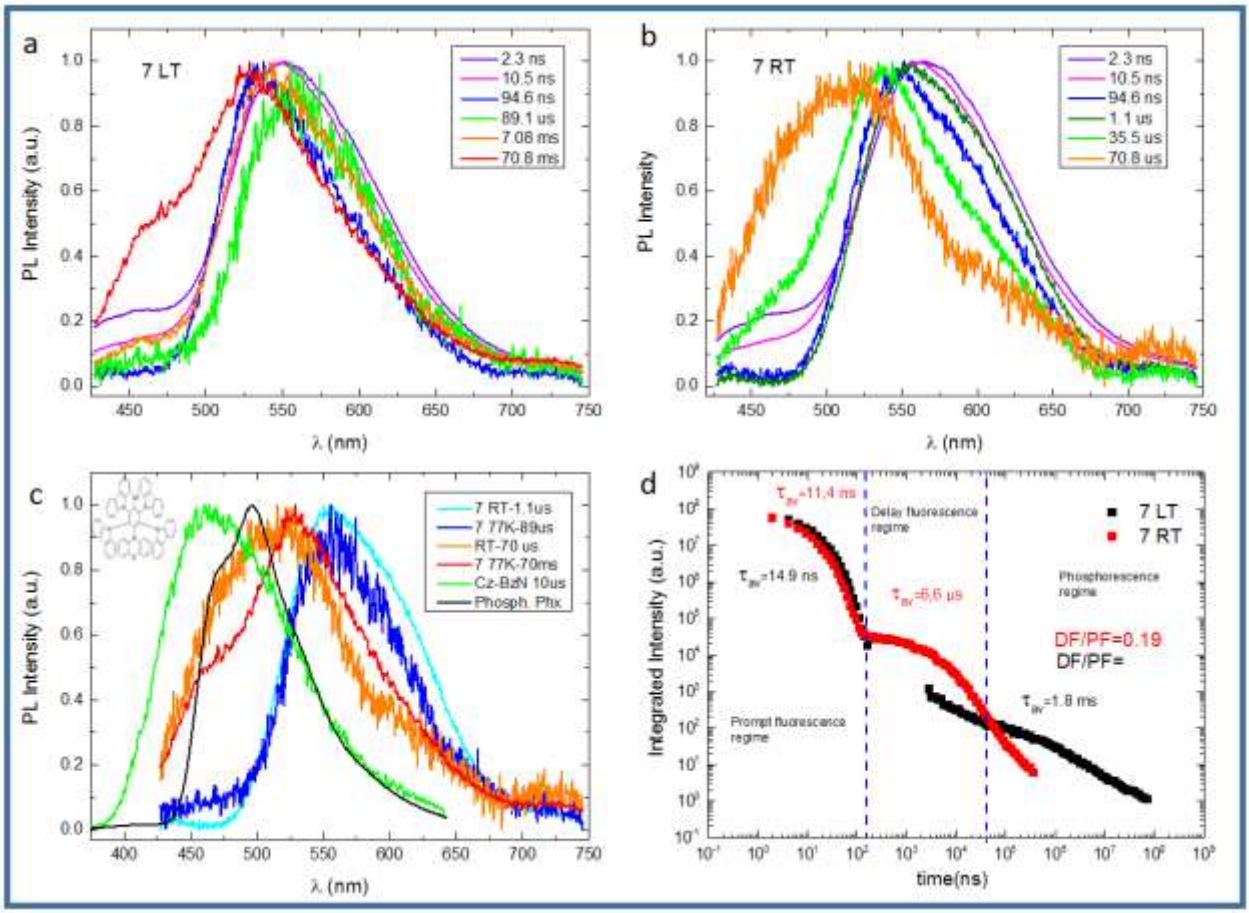

***Figure 2.26**: **a)** and **b)** show the time-resolved emission spectra of **7** in PMMA at room temperature (RT) and 77K respectively; **c)** delayed emission at the longest TD and delayed emission in TADF regime of **7**, for RT and 77 K compared with phosphorescence of phenoxazine and with the CT DF emission of Cz-BzN; **d)** decay curve of **7** in PMMA at RT and 77K. All experiments were carried out at λ_{ex}= 355 nm.*

7.3 Time-resolved study in PMMA for the 2nd and 3rd series.

The time-resolved measurements involving molecules of the 2nd series (**2**, **8**-**10**) are reported in the appendix at the end of this chapter (**Figure A2.17**, **A2.18**, **A2.19**, **A2.20**). In the early PF emission, all the molecules present the emission around 550 nm, assigned to the ^{1}CT excited state involving the phenoxazine. The shoulder at higher energy in the PF emission is visible for **2** (RT and 77K) and it is assigned exclusively to ^{1}LE of phenoxazine, and for **8** (77K) assigned to both contributions from ^{1}LE of phenoxazine and ^{1}CT involving the carbazole, but is not visible in **10**. Upon increasing the delay time, the emission slightly blue shifts for all molecules both at RT and 77K, however, the emission maintains the typical shape of the CT involving the phenoxazine. For **10** a shoulder at higher energy appears at the late time (40µs) and can be assigned to the weak contribution of the CT state involving the Cz. It is worth to note that the DF of **2**, **9a**, and **8** all live shorter than 10 µs, contrarily to **10** that presents a longer DF that extends up to 70 µs. The shorter

DF lifetime can be assigned to TADF originating from the phenoxazine-related CT, while the longer DF lifetime is linked to carbazole CT. At 77 K, all the molecules emit in the millisecond time regime. The emission is blue-shifted in respect to that in the microsecond regime, especially for molecule **2** in which the onset remains close to the phosphorescence of phenoxazine. On the other hand, the emission in the millisecond regime of **8**, **9a,** and **10** remain close to the ^{1}CT state involving the phenoxazine and therefore it probably presents a more delocalized character.

Regarding the 3rd series (**3**,**11** and **12**), the time resolved measurements are reported in the appendix (**Figure A2.27**, **A2.28**, **A2.29**). In all molecules, the early PF emission arises mainly from the ^{1}CT excited state involving phenoxazine. It is possible to observe ^{1}LE emission of phenoxazine in **3** at early times at RT and 77K. The same emission is also visible in **11** at 77K, but in this case, it can be assigned also to the initial contribution of the CT involving the Cz. Upon increasing the delay time the emission blue shifts in all the three molecules, both at RT and 77K. However, in **3**, the blue shift at RT is very weak. In contrary a more remarkable blue shift can be observed in **11** and **12**. In fact, up to 1 μs both molecules present the delayed emission typical of the ^{1}CT involving the phenoxazine, but at the longer delay (after 20μs) the emissions blue shifts indicating that the contribution of the CT state involving the Cz becomes dominant. At 77K, in the millisecond delay time, all molecules present the onset close to the phosphorescence of the phenoxazine, and therefore we can assign it to the localized phosphorescence (^{3}LE) relative to the phenoxazine moiety.

All decays at RT of all molecules of the 2nd and 3rd series (**Table 12**) are fitted in the PF region with a biexponential function. The two PF decays are associated with the ^{1}LE emission of phenoxazine and the other to the ^{1}CT emission involving the phenoxazine. The longer-lived components in molecules **2** and **3** that contain only phenoxazine units as donors are fitted with a monoexponential function, **8** and **9a** where the contribution of the ^{1}CT involving the carbazole is not visible, are fitted with a monoexponential decay. Monoexponential decay is in all cases attributed to the DF arising from the ^{1}CT involving phenoxazine. For **10**, **11**, and **15**, where a weak contribution of the DF arising from the ^{1}CT involving the carbazole is visible, the decay is fitted with a biexponential function. Hence, one decay is attributed to the DF arising from the ^{1}CT involving carbazole, and the other to ^{1}CT emission involving phenoxazine. For all molecules of the 2nd and 3rd series, a nearly linear exponent of ~1 was found in the variation of the DF intensity with the increase of laser excitation dose and thus TADF was confirmed (**Figures A2.32** and **A2.33**).

7.4 Simplified excited state energy diagram for the 1-12 molecules.

The 77K and RT time-resolved measurements allow to calculate the energy of the electronic states involved in the TADF process. In particular, the energy of the ^{1}CT state involving the phenoxazine is calculated from the onset energy of the RT emission with a time delay ≈1us, corresponding to the DF emission. The ^{1}CT state involving the carbazole is calculated from the onset energy of the RT emission of the **Cz-BzN**[6] molecule (TD=10us). On the other hand, from the onset of the late millisecond emission at 77K, it is possible to calculate for all molecules the energy relative to the ^{3}LE state involved in the TADF process. Both the ^{1}CT and ^{3}LE energy values calculated using this method are reported in **Table 12**. Furthermore in **Table 12** are also reported the triplet energy of carbazole (3.20 eV) and phenoxazine (2.81 eV). The triplet of phenoxazine is very close in energy to the ^{3}LE energy in molecules **1**-**12**. Using these data the simplified energy diagram shown in **Figure 2.27** was obtained. It is important to underline that for all **1**-**12** molecules the ^{3}LE state (Phx) is slightly above the ^{1}CT state (Phx) and this is in line with the calculations. The gap between ^{1}CT (Phx) and ^{3}LE (molecules) for **1**-**12** is between 0.02 and 0.35 eV. Regarding the ^{1}CT state related to the Cz moiety (3.1 eV), is 0.1 eV higher in energy than phosphorescence of Cz (3.2 eV).

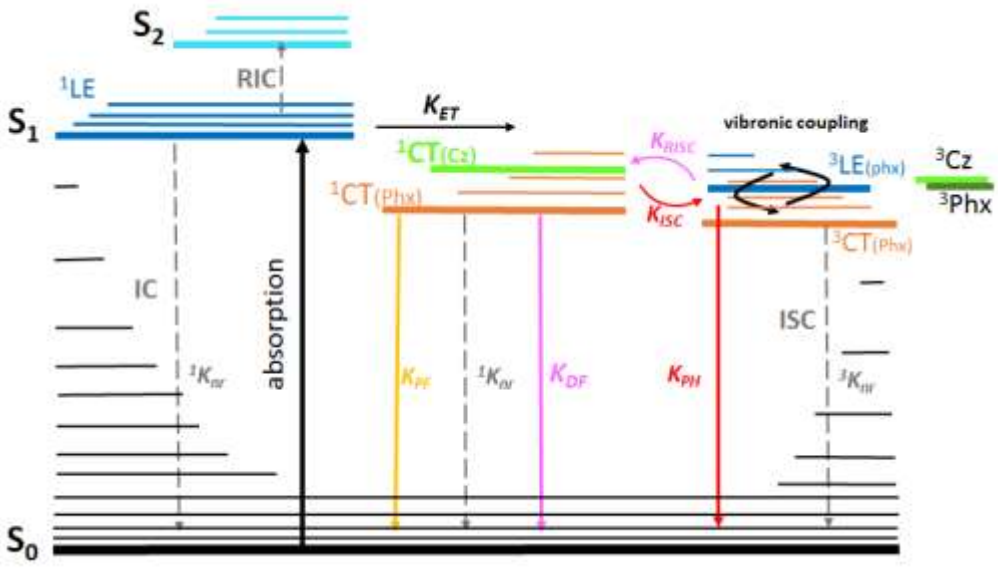

Figure 2.27: *Simplified general energy diagram for **1-12** molecules in PMMA 0.1 wt%, showing the electronic energy levels involved in TADF according to the vibronic coupling model. The relative energy of the phosphorescence of the donors, phenoxazine and carbazole are also reported in the scheme.*

[6] The photophysical study of Cz-BzN is presented in the Chapter 4

As shown in the energy diagram reported in **Figure 2.27,** the vibronic-coupling (VOC) is the main mechanism for TADF. In particular, we can see the TADF from the Phz-BzN moiety, as a process that starts with the populations of the ^{1}CT state. After that part of the energy is lost through PF (K_{PF}) or non-radiative paths (K_{nr}), the other part moves from ^{1}CT state to the mixed ^{3}LE and ^{3}CT (accordingly with the second-order vibronic-coupling model proposed by Gibbs *et al.*[26]). Then, from the mixed ^{3}LE-^{3}CT, the excitation goes back to the ^{1}CT state (RISC) and thus can decay as TADF emission. In regard to the TADF mechanism of the Cz-BzN moiety, it also should occur through a second-order vibronic-coupling mechanism: ISC/RISC between the ^{1}CT (Cz-BzN) state and the mixed ^{3}LE (Cz)-^{3}CT(Cz-BzN), however, the ^{3}LE of Cz was identified only in **7** (shoulder at higher energy in the 77K with TD=70ms) (**Figure 2.27a**). From the energy diagram in **Figure 2.27** it is possible to understand that to reduce the ΔE_{S-T} energy gap, it is possible to increase the ^{3}CT and ^{1}CT energy of these materials by using a host with a lower polarity than PMMA. However, as the ΔE_{S-T} (**Table 12**) are in general not too large, and as the DF/PF ratio are low (0.6 at the best) it means that the non-radiative paths affecting the triplet state, certainly have to play an important role in these kinds of systems.

Table 12: Photophysical properties of all the molecules **1**-**12** in PMMA.

	τ_1 (ns) RT	τ_2 (ns) RT	τ_{av}(ns) RT	τ_3(us) RT	τ_4(us) RT	τ_{av} (us) RT	ϕPL %	ϕPL^{deg} %	DF/PF	^{1}CT(eV) Onset	^{3}LE (eV) onset	ΔE_{S-T} (eV) $_{1CT-3LE}$
Cz	-	-	-	-	-	-	-	-	-	3.10	3.20	-
Phx	-	-	-	-	-	-	-	-	-	-	2.81	-
1	4.23	12.12	7.0	1.36	-	1.4	4.5	5.0	0.14	2.79	2.81	0.02
4	6.57	26.05	9.8	0.86	6.30	3.5	4.3	5.2	0.24	2.72	2.82	0.1
5	4.25	14.34	8.3	0.50	6.08	4.6	4.0	4.9	0.21	2.74	2.84	0.1
6	5.56	18.05	12.2	1.16	7.64	5.8	13.6	15.9	0.27	2.61	2.70	0.09
7	4.91	15.36	11.4	1.62	8.95	6.6	15.1	18.1	0.19	2.52	2.87/3.06	0.35/-0.54
2	7.02	28.71	16.1	0.89	-	0.9	3.3	4.3	0.60	2.64	2.71	0.07
8	6.89	30.19	13.1	1.23	-	1.2	3.7	4.9	0.41	2.57	2.74	0.17
9a	7.45	26.51	13.3	1.47	-	1.5	6.5	7.7	0.41	2.53	2.59	0.06
10	5.76	20.23	9.4	0.61	2.69	1.7	8.5	11.4	0.39	2.46	2.49	0.03
3	3.11	15.68	9.0	1.07	-	1.1	1.5	1.8	0.37	2.63	2.79	0.16
11	6.85	28.53	11.4	0.37	1.76	1.4	3.8	4.3	0.31	2.48	2.53	0.05
12	6.94	-	6.9	0.58	2.03	1.4	6.4	7.9	0.60	2.43	2.58/2.79	0.15/-0.36

*(for **7** and **12** is reported a second onset value, which is estimated from the second band at lower energy)*

7.5 General remarks.

Regarding the TADF properties with the increasing number of carbazole, considering the DF/PF (**Table 12**) and the decays in **Figure A2.34** it is possible to see that upon increasing the number of carbazoles within one series, no particular trend in the TADF characteristics of the molecules can be found. However, it is worth to note that the DF/PF ratio increases when the molecules contain two or three phenoxazines and this is in line with the fact that the phenoxazine being a stronger donor than carbazole allows to enhance the TADF properties.

Moreover, as in the solution steady-state measurements, also in the time-resolved study is confirmed that the emission arising from the CT-Cz is much more intense in the first series of molecules. In the 2nd and 3rd series only a weak CT-Cz contribution can be detected in **10**, **11** and **12,** where a higher number of Cz substituents is present. As in solution also in the solid state we can attribute the short DF decay to the CT relative to the phenoxazine moiety and the longer one to the CT involving the carbazole (**Table 12**). Interestingly, thanks to the time-resolved study we demonstrated that TADF emission arising from the CT state involving the carbazole, is also present in PMMA. However, according to what is observed in the steady-state measurements the emission relative to the CT-Cz in PMMA is weak respect to that relative to CT-Phx. To the best of our knowledge this is the first time that a TADF emission is demonstrated to occurs from 2 different CT formed from different donors on the same molecule.

8. CONCLUSION.

In this is chapter a series of twelve new asymmetric molecules are presented. All the new molecules are characterized by Donor^1-Acceptor-Donor^2 (D^1-A-D^2) systems featuring a central pentafluorobenzonitrile core with one to five fluorine atoms being substituted with various sets of donor units, e.g. carbazole and phenoxazine. The designing idea of these molecules finds its purpose in the tuning of the optical properties (in particular TADF) by increasing the number of substituents on the central core and using also different classes of substituents in different proportions. Beyond the photophysical properties, DFT calculations, XRD analysis, and the cyclic voltammetry measures are also presented. The different numbers of substituents and their nature allow obtaining a systematic fine-tuning of the band gap and emission colors. All compounds are deeply colored and their photoluminescence covers the visible range between 450 and 700 nm. Both the steady-state and time-resolved measurements show that these molecules are characterized by formation of different electronic excited states of localized (LE) and charge transfer (CT) nature. The DFT calculations shows that different CT electronic states

can be formed in addition to the localized electronic states typical of donors and acceptor moieties. Such results are confirmed in the absorption, emission, and decay experiments. Temperature-dependent decay time measurements and laser fluence experiments were also carried out to study and to confirm the TADF properties, which however cannot be considered very good. The most important result of this chapter is the dual emission developed by using both carbazole and phenoxazine donors. Such dual emission is considered a novel strategy for tuning luminescence by properly selecting parent molecules and to achieve a double TADF emission for lighting applications. In fact, single white-light-emitting DF molecules exhibit considerable significance for future display and lighting applications and this design strategy provides a novel direction for producing white-luminescente organic compounds. However further studies are necessary in order to achieve a more balanced and efficient dual TADF emission also in solid-state.

APPENDIX.

TD-DFT calculations

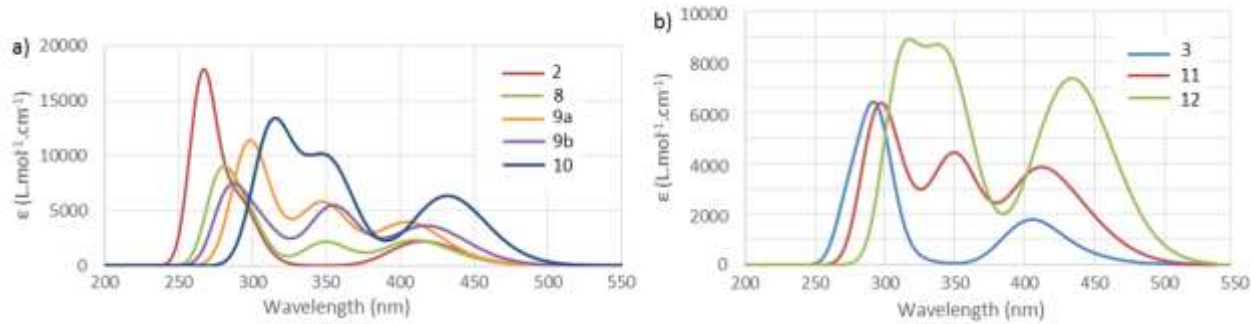

Figure A2.1: *calculated absorption spectra in vacuo for* ***a)*** *the compounds of the 2nd series and* ***b)*** *the compounds of the 3rd series.*

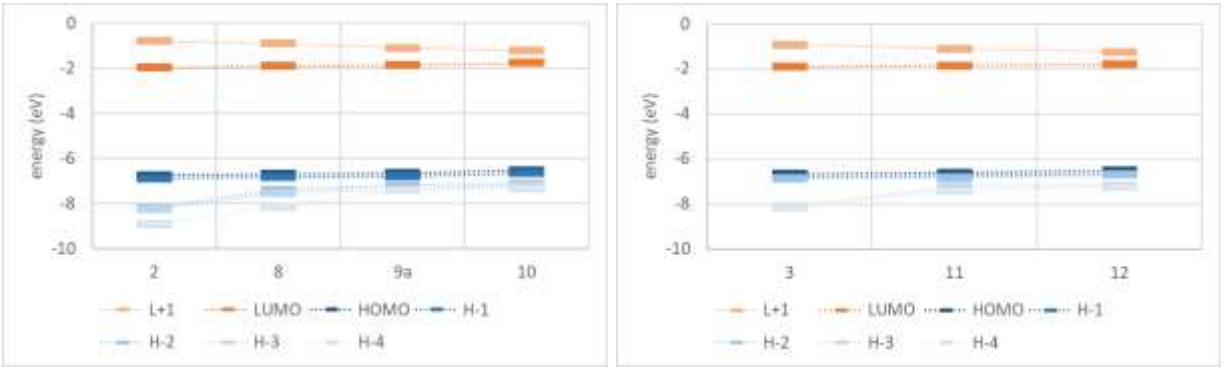

Figure A2.2: a) *Representation of the energy levels of the molecular frontier orbitals of the molecules of the 2nd and 3rd series.*

Table A1: calculated transitions, associated oscillator strength and electronic configuration for the compounds of the 2nd series (**2** and **8-10**).

	λ_{calc} (nm)	State	Osc. Strenght	Major contribution (H=HOMO, L=LUMO)
2	442	CT (Phx-BzN)	0.0044	H→L
	413	CT (Phx-BzN)	0.0284	H-1→L
	315	CT (Phx-BzN)	0.0007	H→L+1
	302	CT (Phx-BzN)	0.0025	H-1→L+1(52%)
	296	LE (Phx)	0.0141	H→L+4
8	434	CT (Phx-BzN)	0.0052	H→L
	408	CT (Phx-BzN)	0.0292	H-1→L
	349	CT (Cz-BzN)	0.0298	H-2→L
	298	LE (Phx)	0.0183	H→L+6
	295	LE (Phx)	0.0389	H-1→L+5
	279	LE (Cz)	0.0788	H-2→L+2
9a	432	CT (Phx-BzN)	0.023	H→L
	409	CT (Phx-BzN)	0.0332	H-1→L
	357	CT (Phx-BzN)	0.0248	H→L+1
	354	CT (Cz-BzN)	0.0488	H-2→L
	§5 CTs	-	-	-
	292	LE (Phx)	0.0186	H→L+7
	288	LE (Phx)	0.0257	H→L+6
	281	LE (Cz)	0.0582	H-2→L+3
10	436	CT (Phx-BzN)	0.0672	H→L
	419	CT (Phx-BzN)	0.0254	H-1→L
	363	CT (Phx-BzN)	0.0066	H→L+1
	358	CT (Cz-BzN)	0.0307	H-2→L

§(number) of other CT transition at lower energy

Table A2: calculated transitions, associated oscillator strength and electronic configuration for the compounds of the 3rd series (**3**, **11** -**12**).

	λ_{calc} (nm)	State	Osc. Strenght	Major contribution (H=HOMO, L=LUMO)
3	443	CT (Phx-BzN)	0.003	H→L
	419	CT (Phx-BzN)	0.0001	H-1→L
	404	CT (Phx-BzN)	0.0239	H-2→L
	332	CT (Phx-BzN)	0.0009	H→L+1
	319	CT (Phx-BzN)	0.001	H-1→L+1
	309	CT (Phx-BzN)	0.0009	H-2→L+1
	297	LE (Phx)	0.00175	H-1→L+5
11	441	CT (Phx-BzN)	0.0052	H→L
	418	CT (Phx-BzN)	0.0292	H-1→L
	406	CT (Phx-BzN)	0.0298	H-2→L
	358	CT (Phx-BzN)	0.0191	H→L+1
	348	CT (Cz-BzN)	0.039	H-3→L
	§4CTs	-	-	-
	298	LE (Phx)	0.0238	H-1→L+5
12	445	CT (Phx-BzN)	0.0633	H→L (91%)
	422	CT (Phx-BzN)	0.0134	H-1→L (87%)
	418	CT (Phx-BzN)	0.0414	H-2→L (83%)
	§3CTs (Phx-BzN)	-	-	-
	343	CT (Cz-BzN)	0.0006	H-3->LUMO
	340	CT (Cz-BzN)	0.0765	H-4->LUMO
	316	CT (Cz-BzN)	0.0584	H-3->L+1
	309	CT (Cz-BzN)	0.0403	H-4->L+1
	304	LE (Phx)	0.0153	H->L+6

§(number) of other CT transition at lower energy

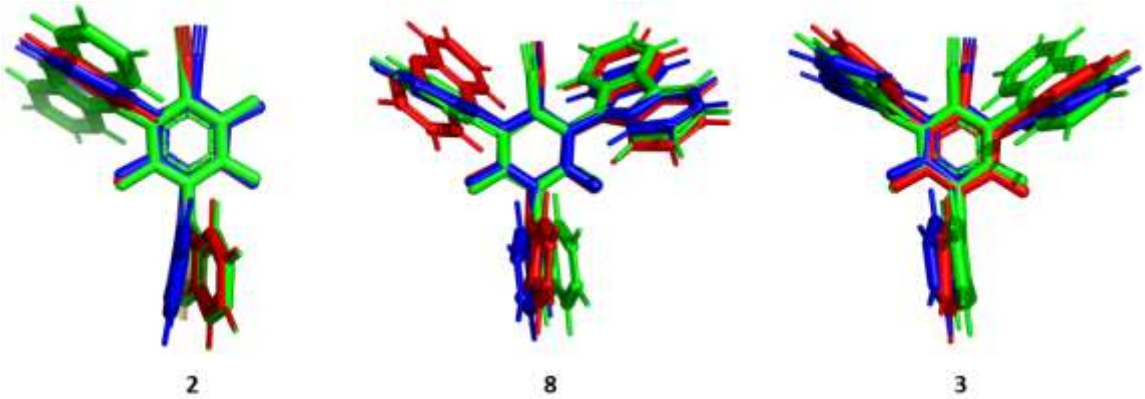

Figure A2.3*: overlap of the calculated structures of molecules **2**, **8** and **3** in their ground (blue), **S_1** (green) and **T_1** (red) states.*

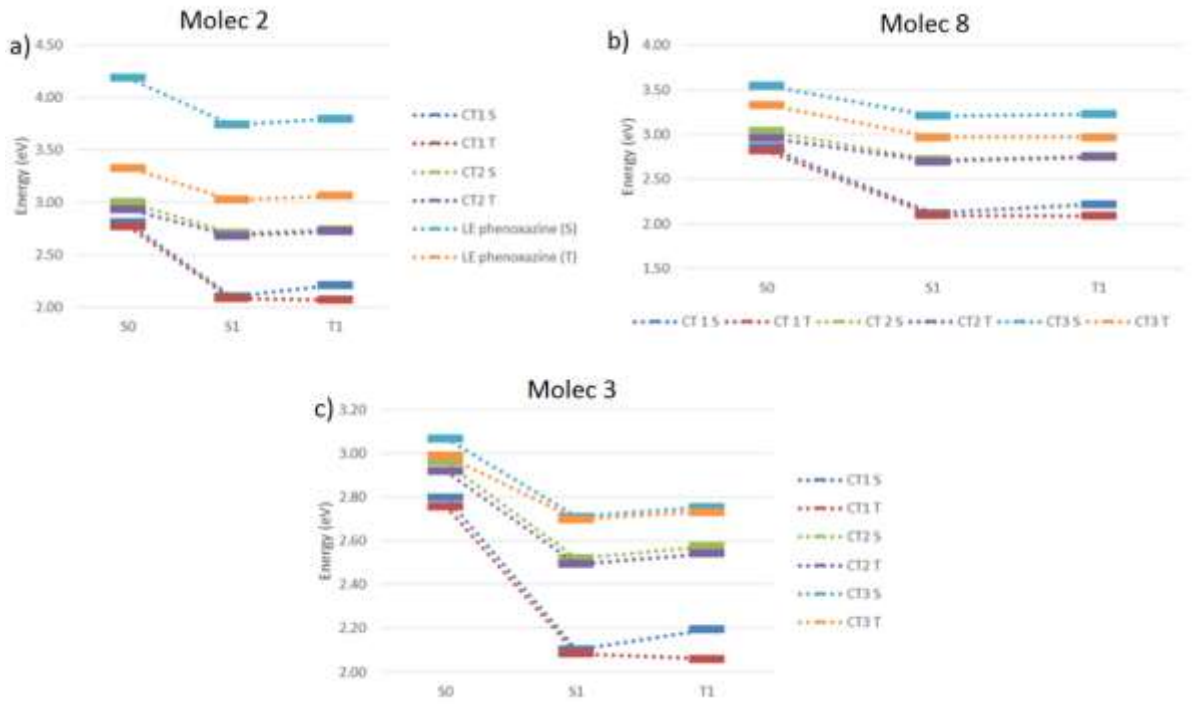

Figure A2.4: *Energy diagram of the triplet and singlet LE and CT states, for molecules **2**(a), **8** (b) and **3** (c) in the S_0, S_1 and T_1 geometry configuration, obtained with DTF calculations.*

Table A3: Calculated photophysical data for the 2nd and 3rd series

Compound	Abs (nm)	Fluo (nm)	S_1 (eV)*	T_1 (eV)*	Δ(S-T) eV S_0 geom.	Δ(S-T) eV S_1 geom.	Δ(S-T) eV T_1 geom.
2	416	595	2.10	2.08	0.04	0.02	0.14
8	410	584	2.12	2.10	0.04	0.02	0.14
9a	404	nc	nc	nc	0.07	nc	nc
10	431	nc	nc	nc	0.17	nc	nc
3	404	595	2.10	2.08	0.04	0.02	0.13
11	413	nc	nc	nc	0.05	nc	nc
12	435	nc	nc	nc	0.16	nc	nc

*n.c.=not calculated, * Calculated at the optimized S_1 geometry*

Cyclic Voltammetry

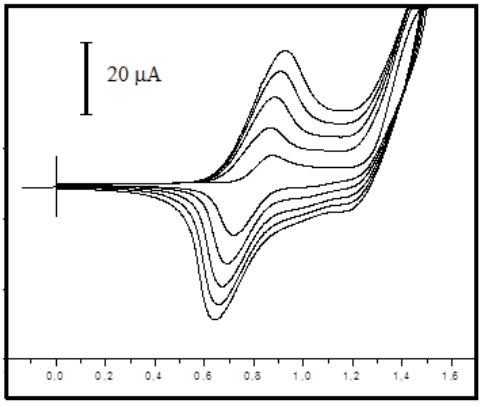

Figure A2.5: *CV trace showing the polymerization of **5** (1 mM in DCM/TBAFP, 100 mVs^{-1}), featuring both the electrooxidation of the carbazoles, and the increasing deposit of an electroactive poly(**5**) film at each successive scan.*

Photophysical properties

1st Series

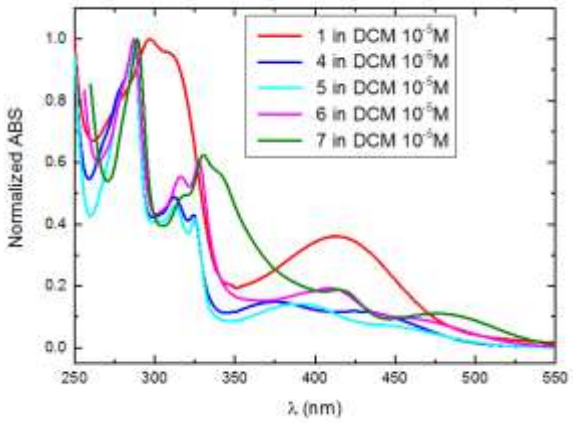

Figure A2.6*: normalized optical absorption spectra of molecules **1** and **4**-**7** in DCM (c=10^{-5} M).*

Table A4: absorption and emission maxima of compounds **1** and **4**-**7** in PMMA (c=0.05wt%)

In PMMA	Abs λ_{max} (CT),nm (λ_{ex} = 300-330 nm)	Abs, λ_{max} (LE), nm (λ_{ex} = 300-330 nm)	PL, λ_{max} nm (CT-Cz or LE), (λ_{ex} = 300-330 nm)	PL, λ_{max} nm (CT-Phx), (λ_{ex} = 300-330 nm)	PL, λ_{max} (CT-Phx), nm (λ_{ex} = 390-440 nm)
1	407	310, 297	411	519	524
4	416,369	325,312,287	413	533	531
5	440,387	325,313,287	423	548	548
6	453,406	327,316,287	440	553	559
7	471,411	330,320,289	440	568	567

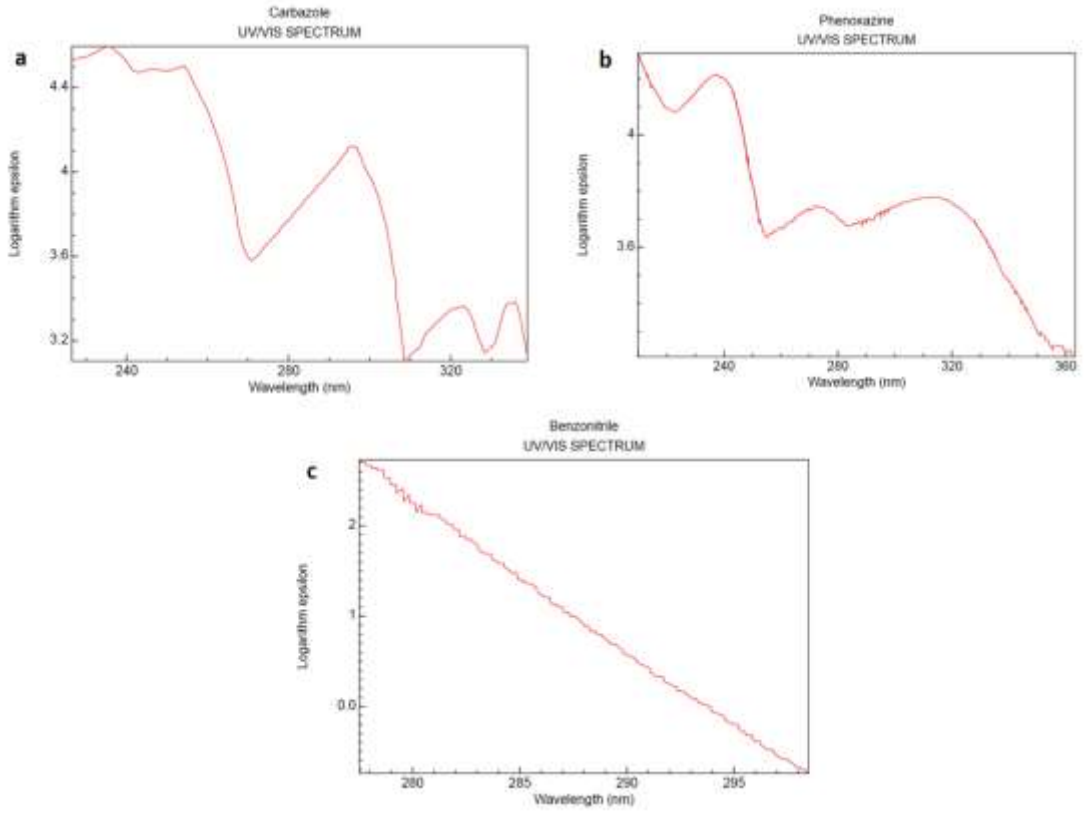

***Figure A2.7**: absorption spectra of the ligands: **a**) Carbazole **b**) Phenoxazine **c**) Benzonitrile. from National Institute of standards and technology (https://webbook.nist.gov/chemistry/#)*

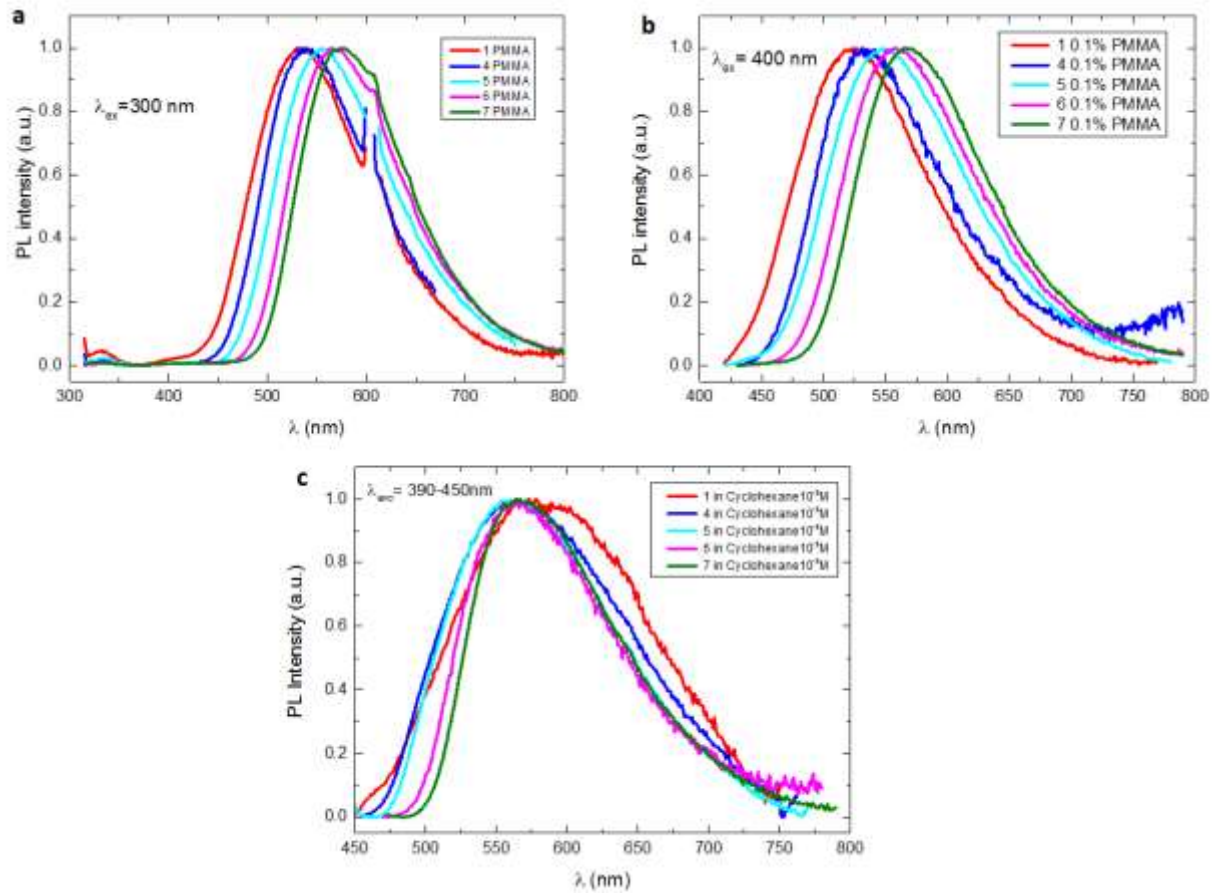

Figure A2.8: *Normalized photoluminescence (PL) spectra of molecules **1** and **4**-**7 a)** in PMMA (0.1wt%), λ_{exc}= 300 nm. **b)** in PMMA (0.1wt%), λ_{exc}= 400 nm. **c)** in cyclohexane (c=10^{-5} M), λ_{exc}= 390-450 nm.*

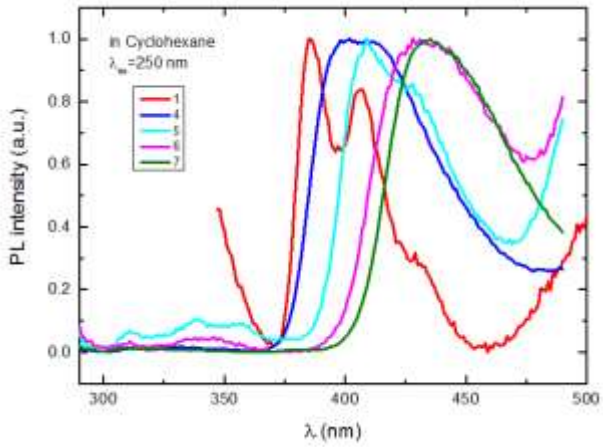

Figure A2.9: *Normalized photoluminescence (PL) spectra of molecules **1** and **4**-**7 a)** in cyclohexane (c=10^{-5} M), λ_{exc}= 250 nm in the range between 300 to 500 nm.*

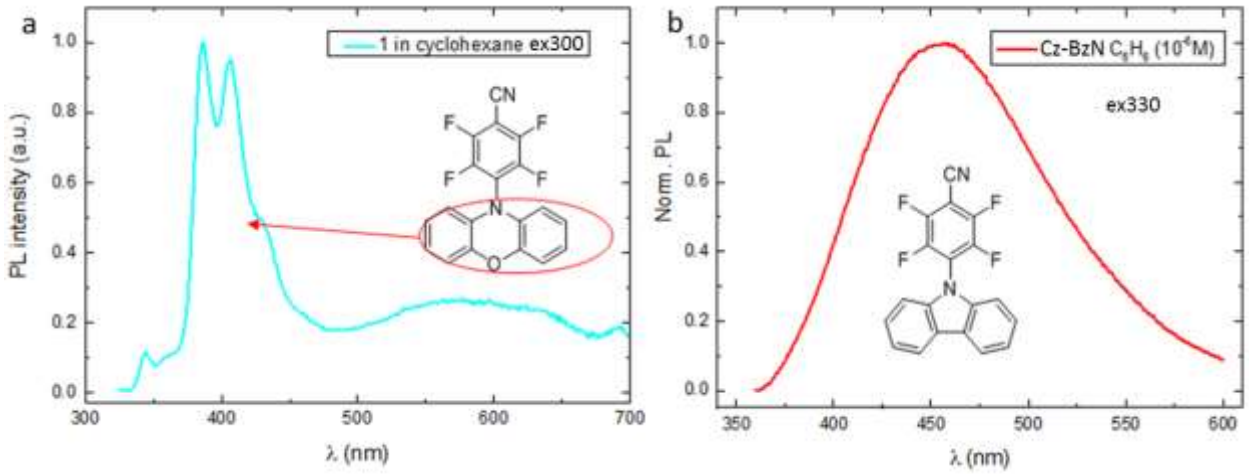

Figure A2.10: a) *normalized photoluminescence of PhX-BzN (the high energy peak emission corresponds to the ^{1}LE of phenoxazine and the low energy one to the ^{1}CT of the phenoxazine-benzonitrile)* ***b)*** *fluorescence emission of Cz-BzN showing the CT emission involving the Carbazole (CT-Cz).*

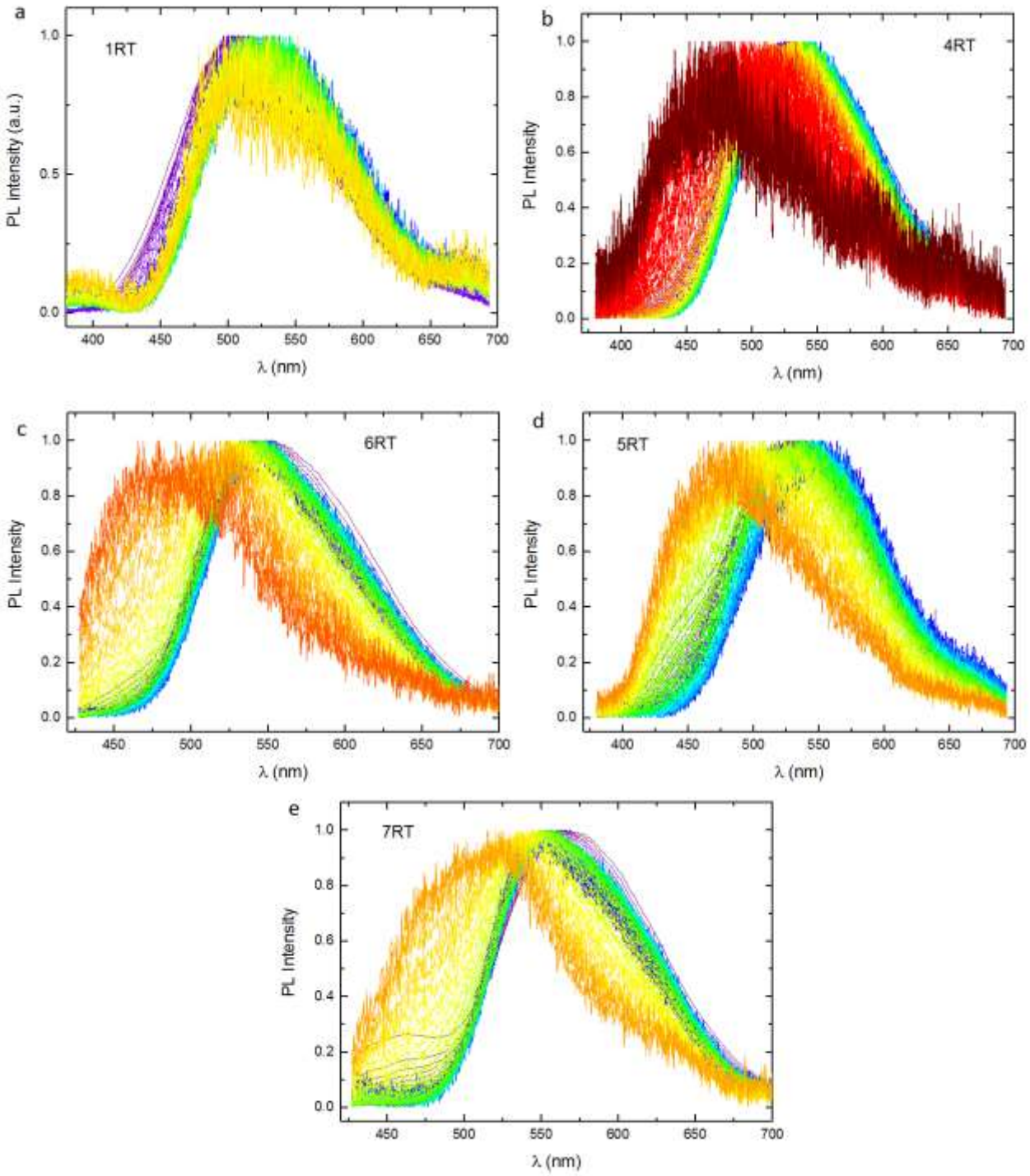

Figure A2.11: *time-resolved emission spectra (RT) of* ***a) 1****,* ***b) 4****,* ***c) 5****,* ***d) 6*** *and* ***d) 7*** *in PMMA (0.1wt %) from initial time delay (violet) to intermediate time delay (green) and then to final time delay (orange/red). All experiments were carried out at* λ_{ex}*= 355 nm.*

2nd Series

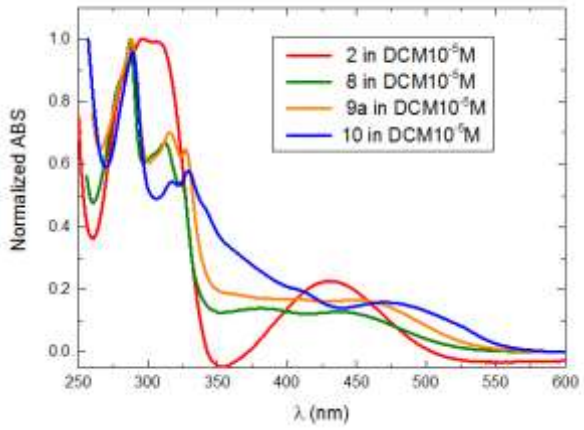

***Figure A2.12**: normalized optical absorption spectra of molecules **2** and **8**-**10** in DCM (c=10^{-5} M)*

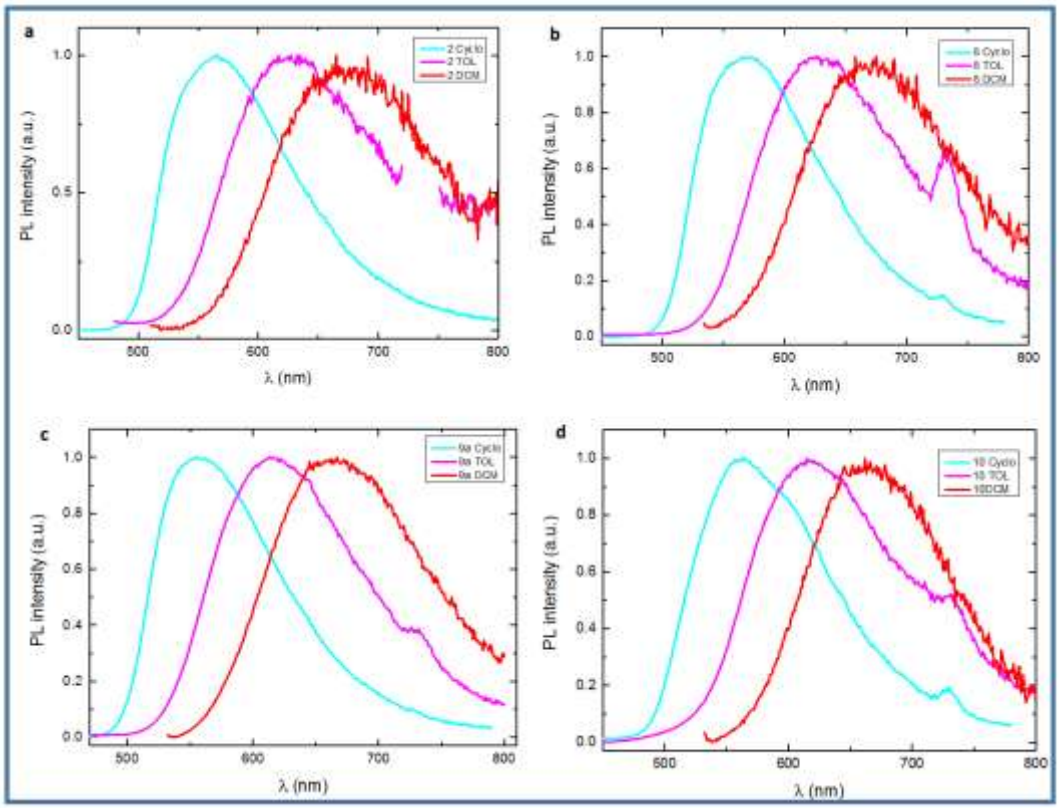

***Figure A2.13**: Normalized photoluminescence (PL) spectra of **2** and **8**-**10** in in cyclohexane, toluene, DCM. All experiments were carried out at λ_{ex}= 355 nm.*

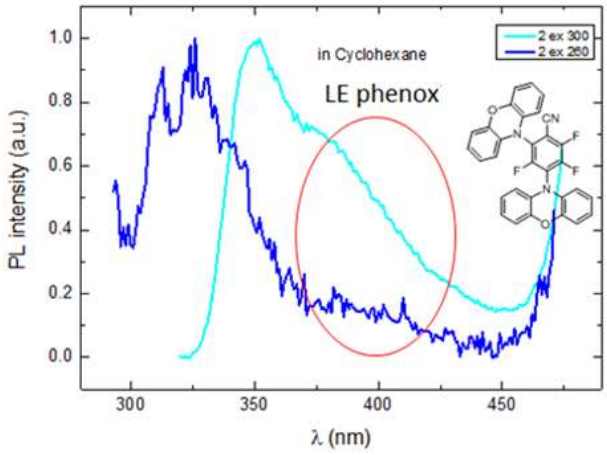

Figure A2.14: *Normalized photoluminescence (PL) spectra of molecule **2** in cyclohexane (c=10^{-5} M), λ_{exc}= 250 nm.*

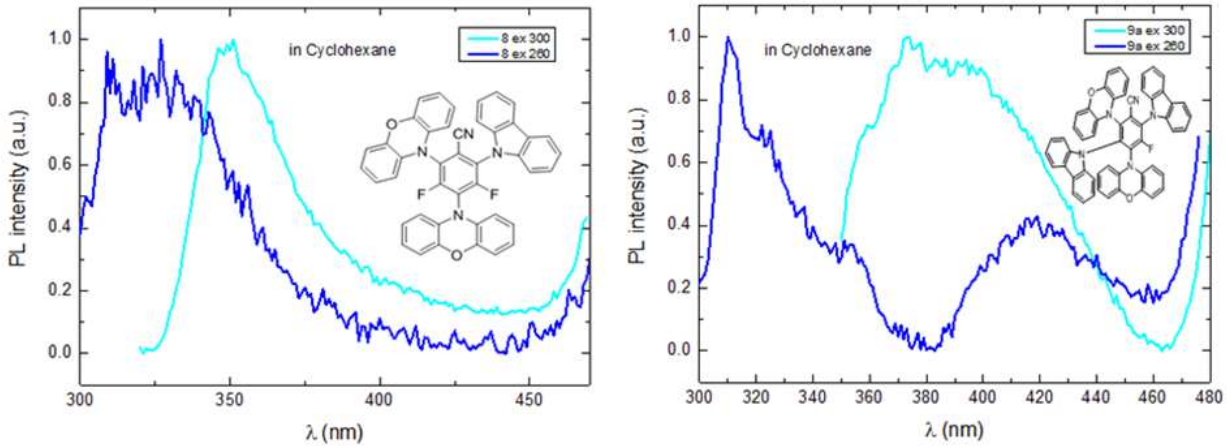

Figure A2.15: *Normalized photoluminescence (PL) spectra of molecules **8** and **9a** in cyclohexane (c=10^{-5} M), λ_{exc}= 260 nm, λ_{ex}= 300 nm.*

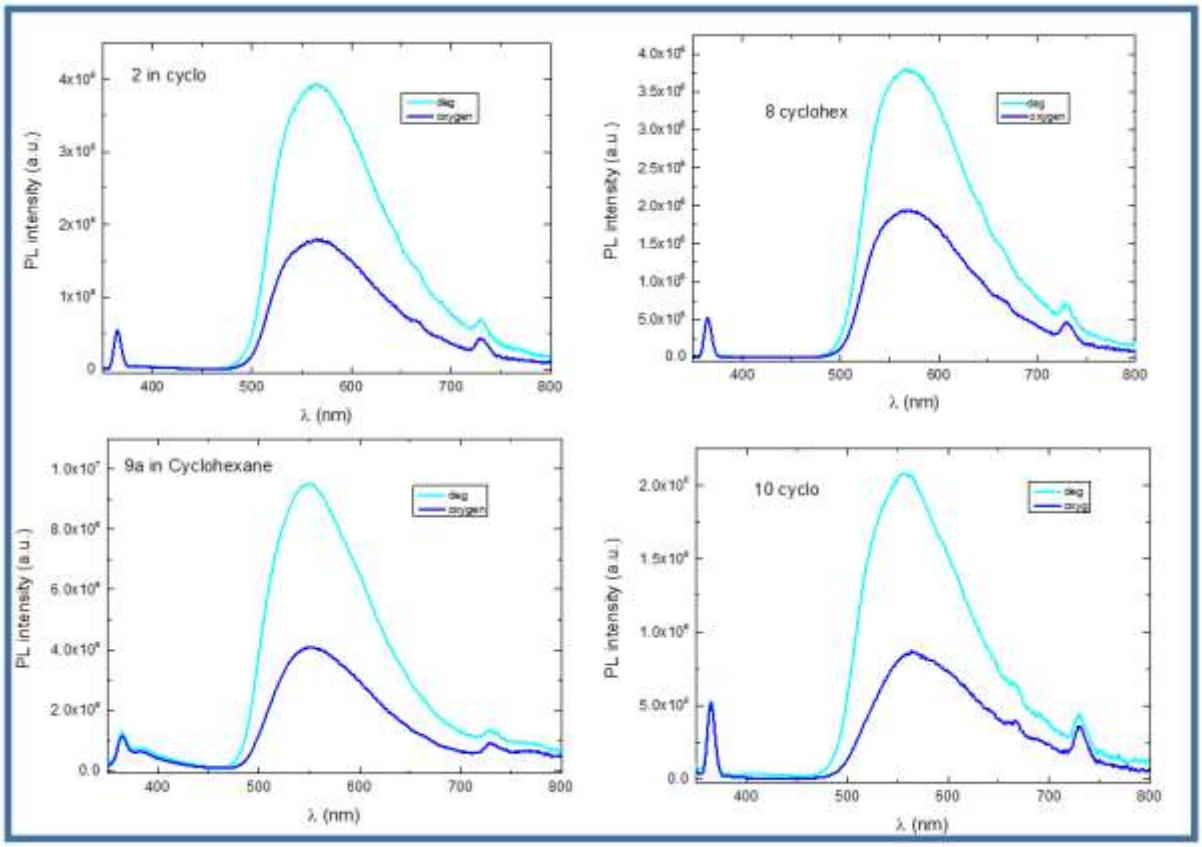

***Figure A2.16**: Photoluminescence of molecules **2** and **8, 9a, 10** in aerated cyclohexane and after degassing the solution. All experiments were carried out at λ_{ex}= 330 nm.*

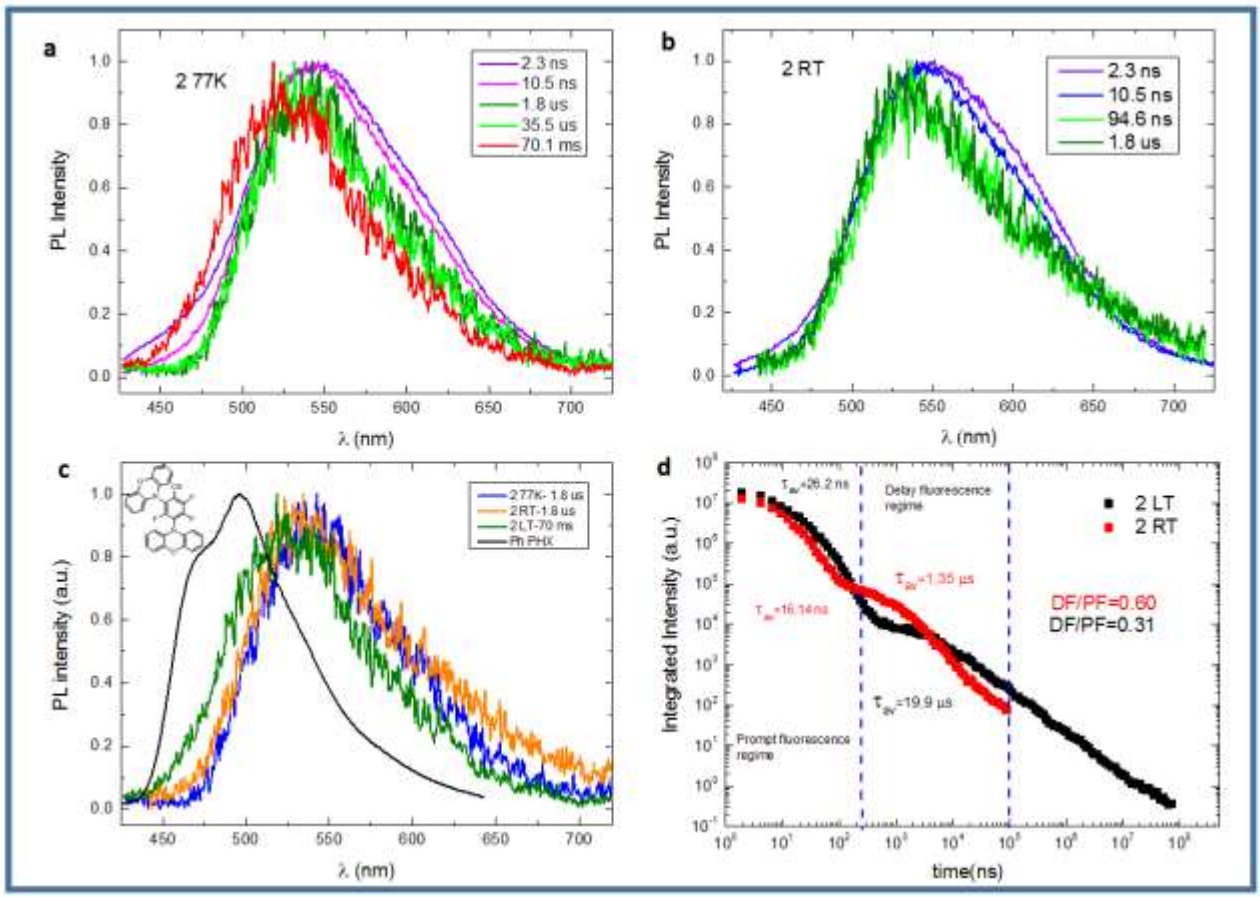

***Figure A2.17**: **a)** and **b):** time-resolved emission spectra of **2** in PMMA (0.1wt %), at room temperature (RT) and 77K respectively; **c)** delayed emission at the longest TD and delayed emission in TADF regime of **2**, for RT and 77 K compared with phosphorescence of the phenoxazine; **d**) decay curve of **2** in PMMA at RT and 77K. All experiments were carried out at λ_{ex}= 355 nm.*

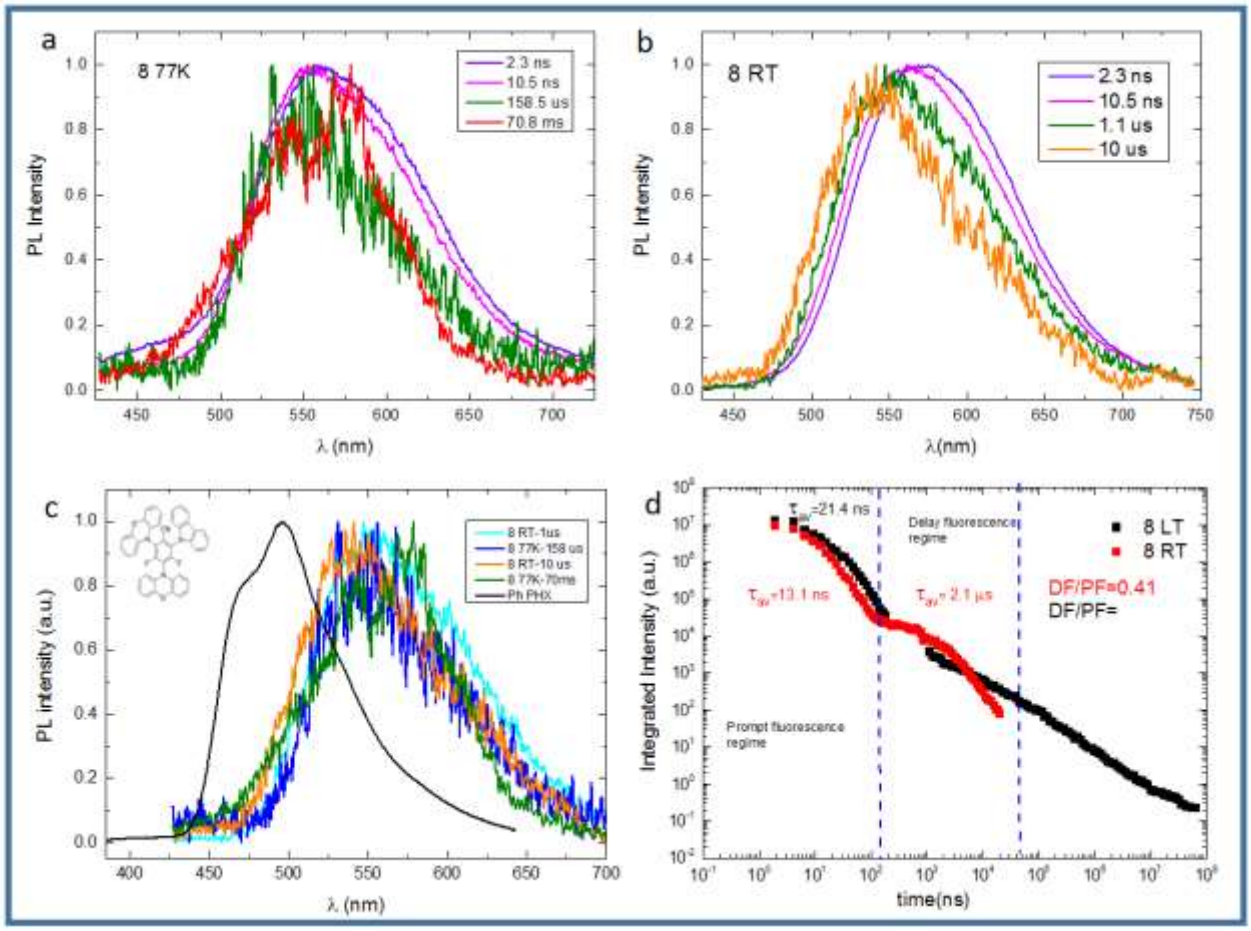

***Figure A2.18**: **a)** and **b):** the time-resolved emission spectra of **8** in PMMA (0.1wt %), at room temperature (RT) and 77K respectively; **c)** delayed emission at the longest TD and delayed emission in TADF regime of **8**, for RT and 77 K compared with phosphorescence of phenoxazine; **d**) decay curve of **8** in PMMA at RT and 77K. All experiments were carried out at λ_{ex}= 355 nm.*

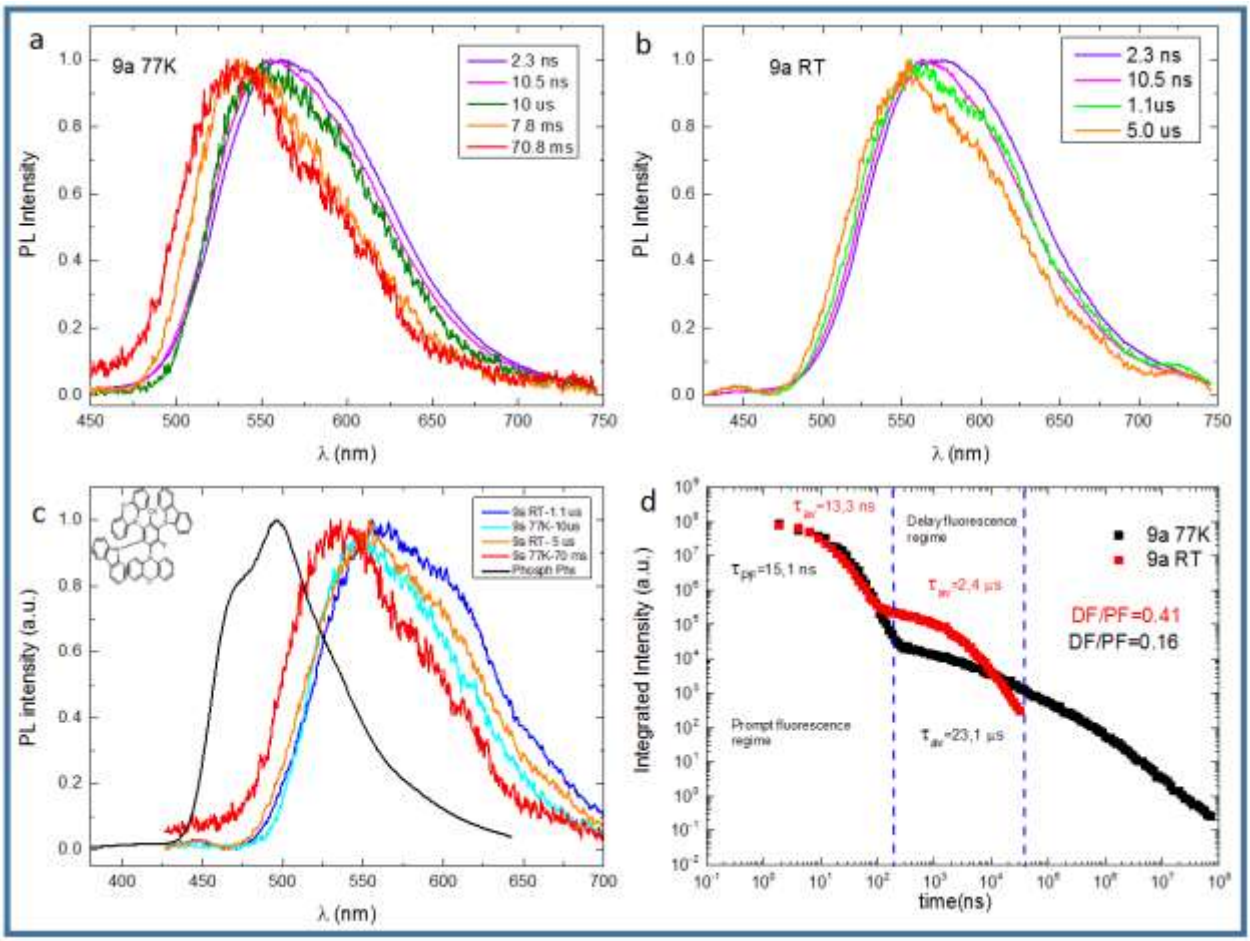

Figure A2.19 a) *and* ***b):*** *time-resolved emission spectra of* ***9a*** *in PMMA (0.1wt %), at room temperature (RT) and 77K respectively;* ***c)*** delayed emission at the longest TD and delayed emission in TADF regime of **9a**, for RT and 77 K compared with phosphorescence of phenoxazine*;* ***d****) decay curve of* ***9a*** *in PMMA at RT and 77K. All experiments were carried out at* λ_{ex}*= 355 nm.*

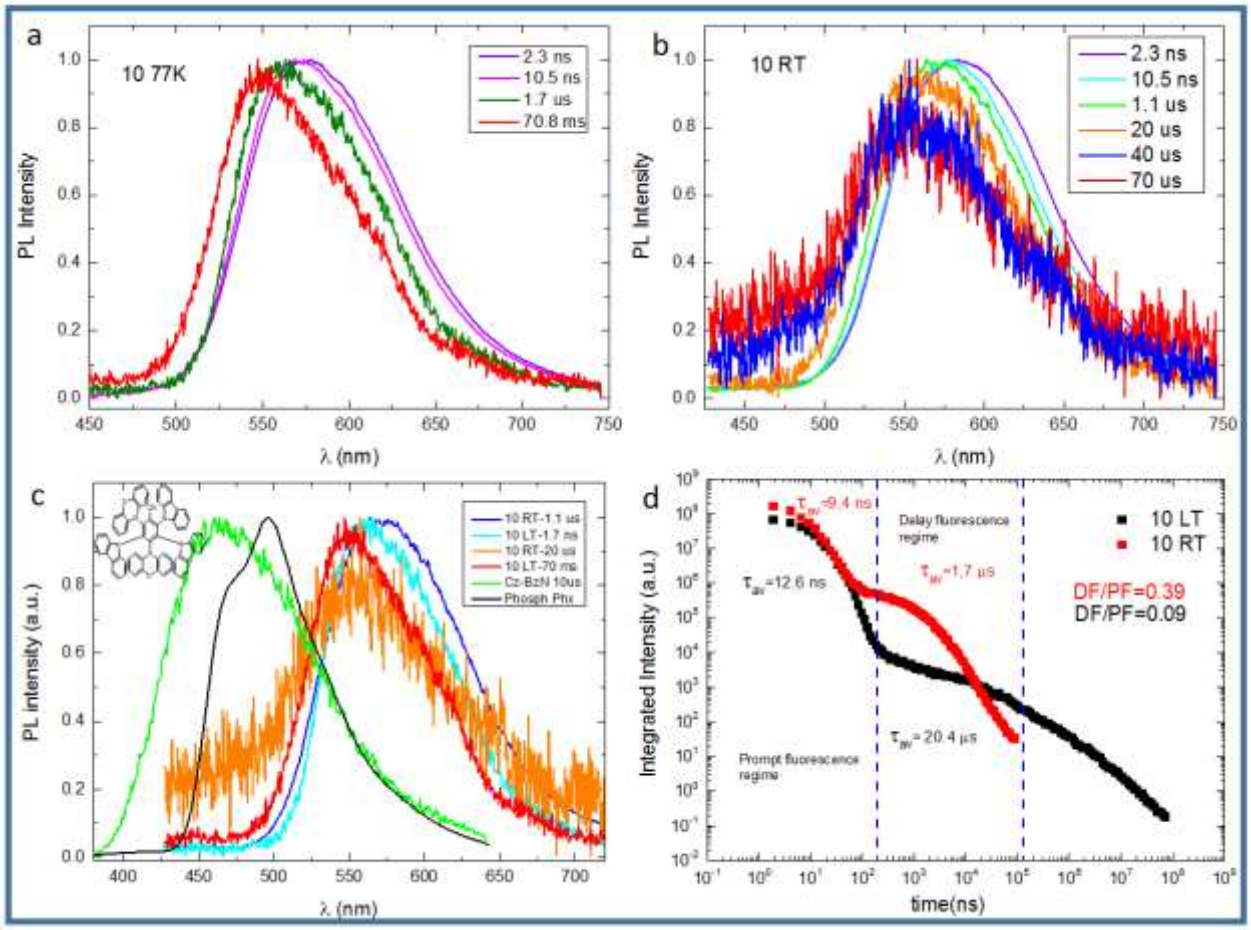

Figure A2.20**: **a)** and **b)**: time-resolved emission spectra of **10** in PMMA (0.1wt %), at room temperature (RT) and 77K respectively; **c) delayed emission at the longest TD and delayed emission in TADF regime of **10**, for RT and 77 K compared with phosphorescence of phenoxazine and with the CT DF emission of Cz-BzN*; **d)** decay curve of **10** in PMMA at RT and 77K. All experiments were carried out at λ_{ex}= 355 nm.*

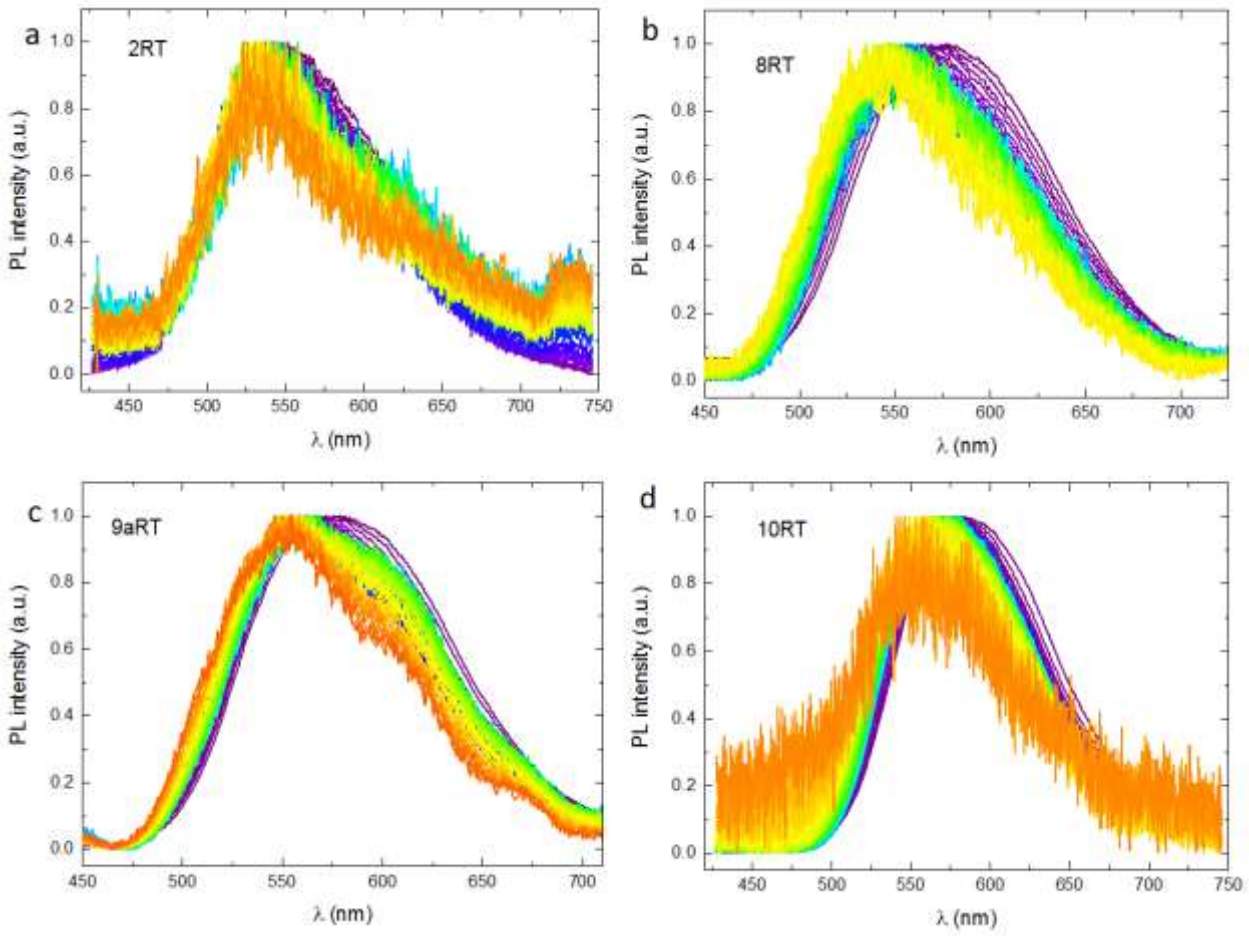

Figure A2.21: *time-resolved emission spectra (RT) of* ***a) 2, b) 8, c) 9a*** *and* ***d) 10*** *in PMMA (0.1wt %) from initial time delay (violet) to intermediate time delay (green) and then to final time delay (orange/red). All experiments were carried out at* λ_{ex} *= 355 nm.*

3RD SERIES

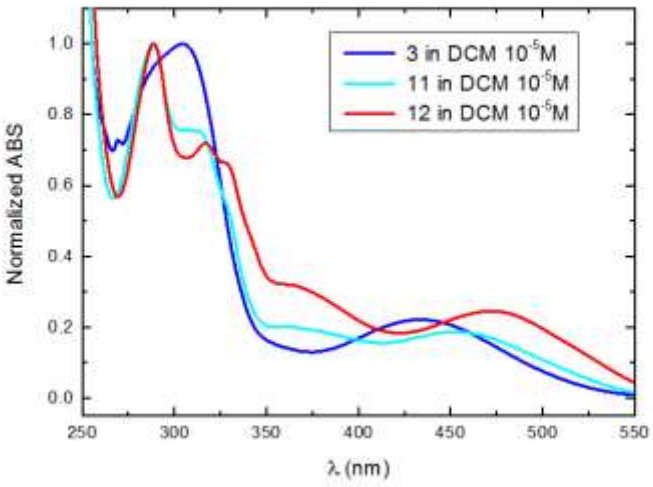

Figure A2.22*: normalized optical absorption spectra of molecules* ***3, 11*** *and* ***12*** *in DCM (c=10^{-5} M).*

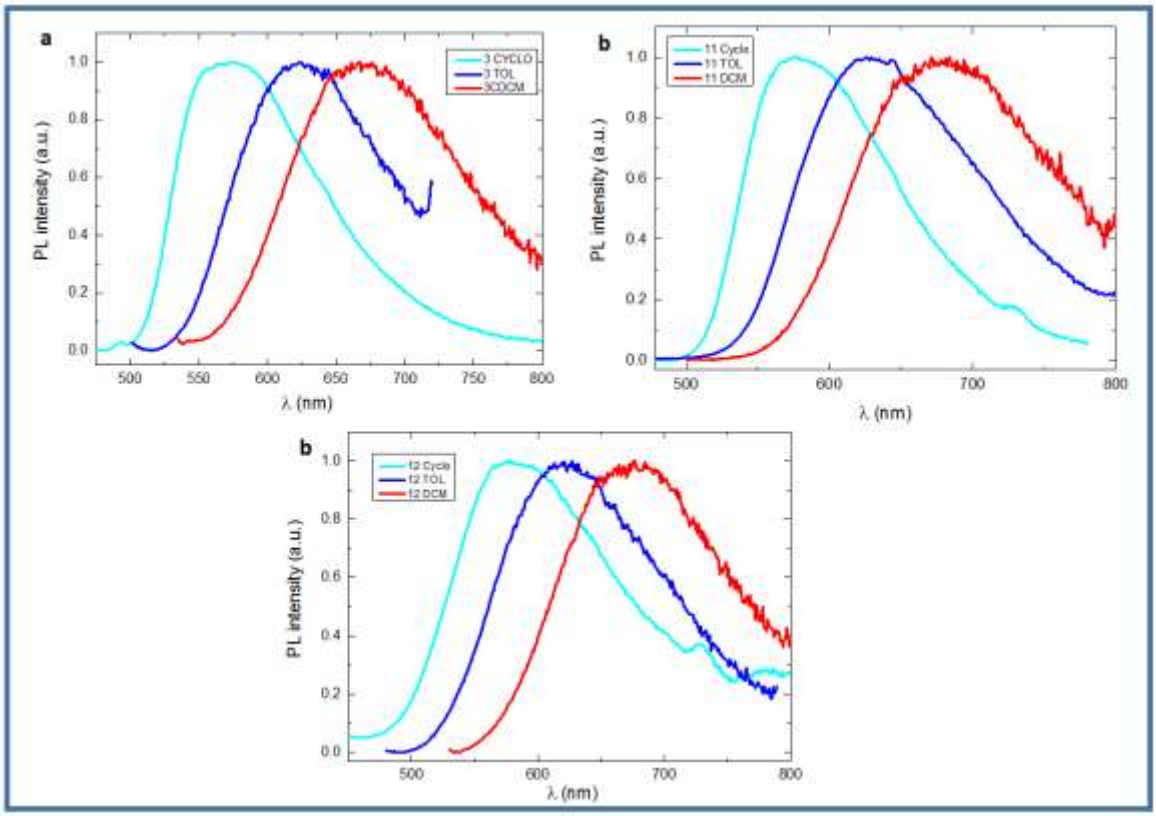

Figure A2.23*: Normalized photoluminescence (PL) spectra of* ***3*** *and* ***11****-****12*** *in in cyclohexane, toluene, and DCM. All experiments were carried out at* λ_{ex}*= 330 nm.*

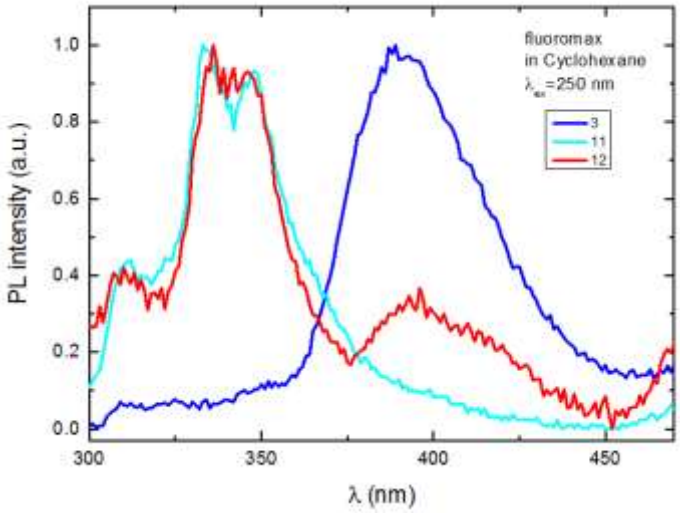

Figure A2.24: *Normalized photoluminescence (PL) spectra of molecules **3**, **11** and **12** in cyclohexane (c=10^{-5} M), λ_{exc}= 250 nm. Range between 300 to 450 nm.*

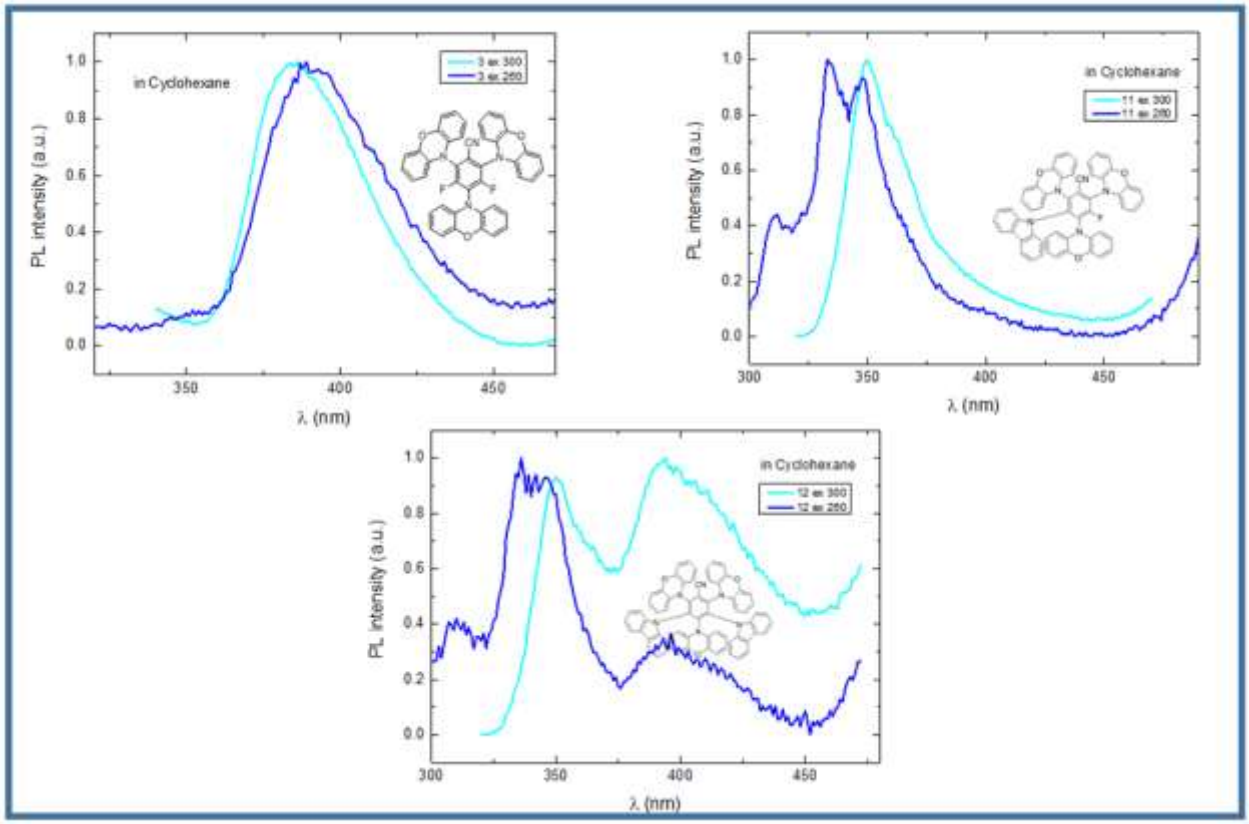

Figure A2.25: *Normalized photoluminescence (PL) spectra of molecules **3**, **11** and **12** in cyclohexane (c=10^{-5} M), λ_{exc}= 260 nm, λ_{exc}= 300 nm.*

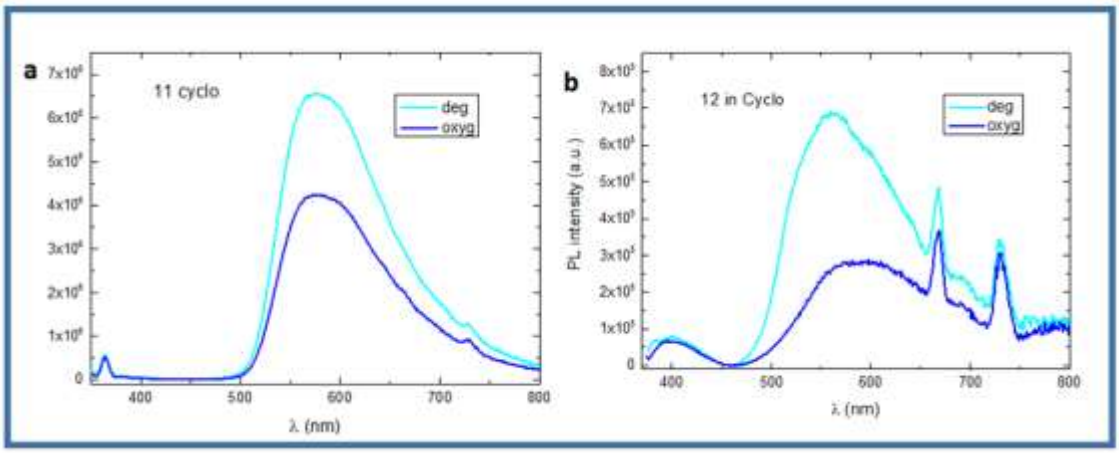

***Figure A2.26**: Photoluminescence of molecules **11** and **12** in aerated cyclohexane and after degassing the solution. λ_{ex}= 330 nm.*

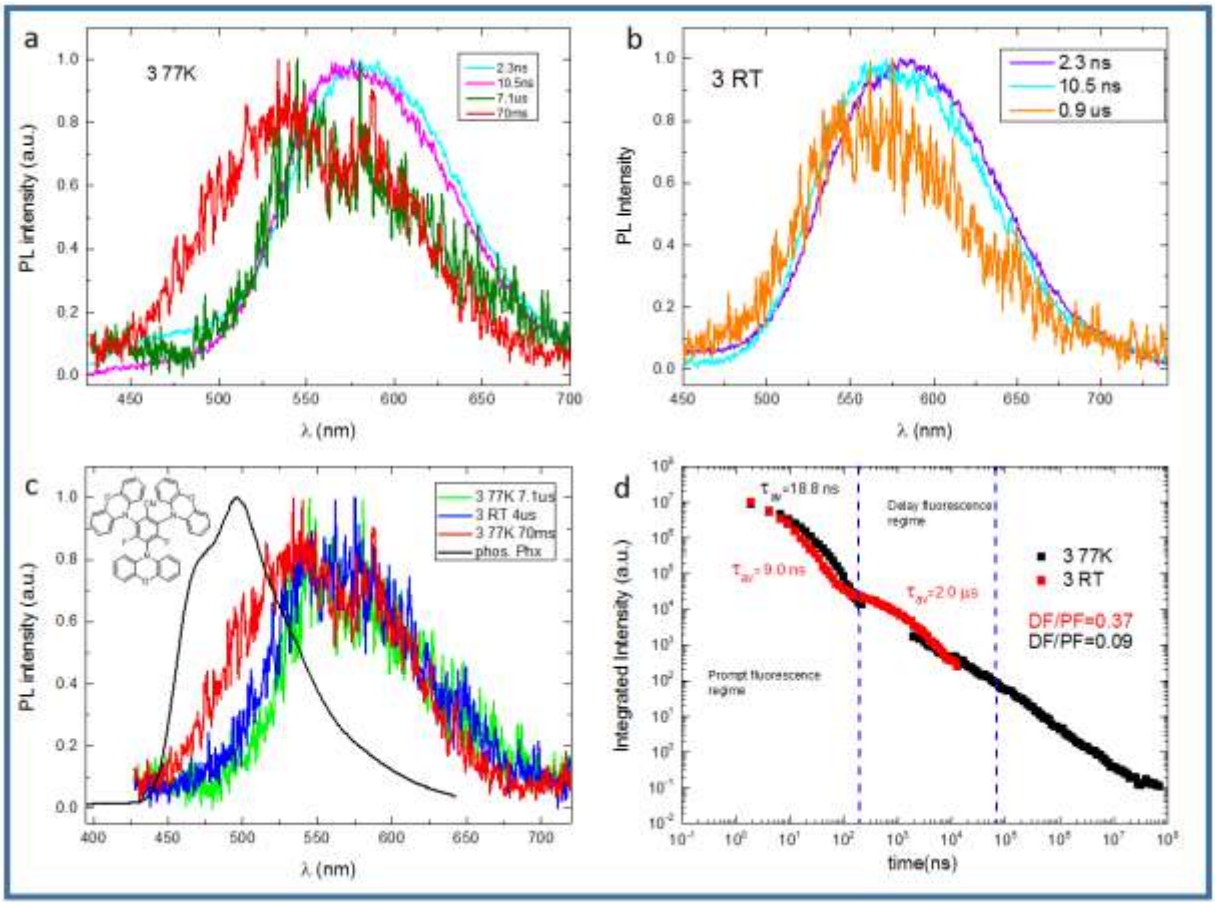

***Figure A2.27**: **a)** and **b):** time-resolved emission spectra of **3** in PMMA (0.1wt %), at room temperature (RT) and 77K respectively; **c)** delayed emission at the longest TD and delayed emission in TADF regime of **3**, for RT and 77 K compared with phosphorescence of the phenoxazine; **d**) decay curve of **3** in PMMA at RT and 77K. All experiments were carried out at λ_{ex}= 355 nm.*

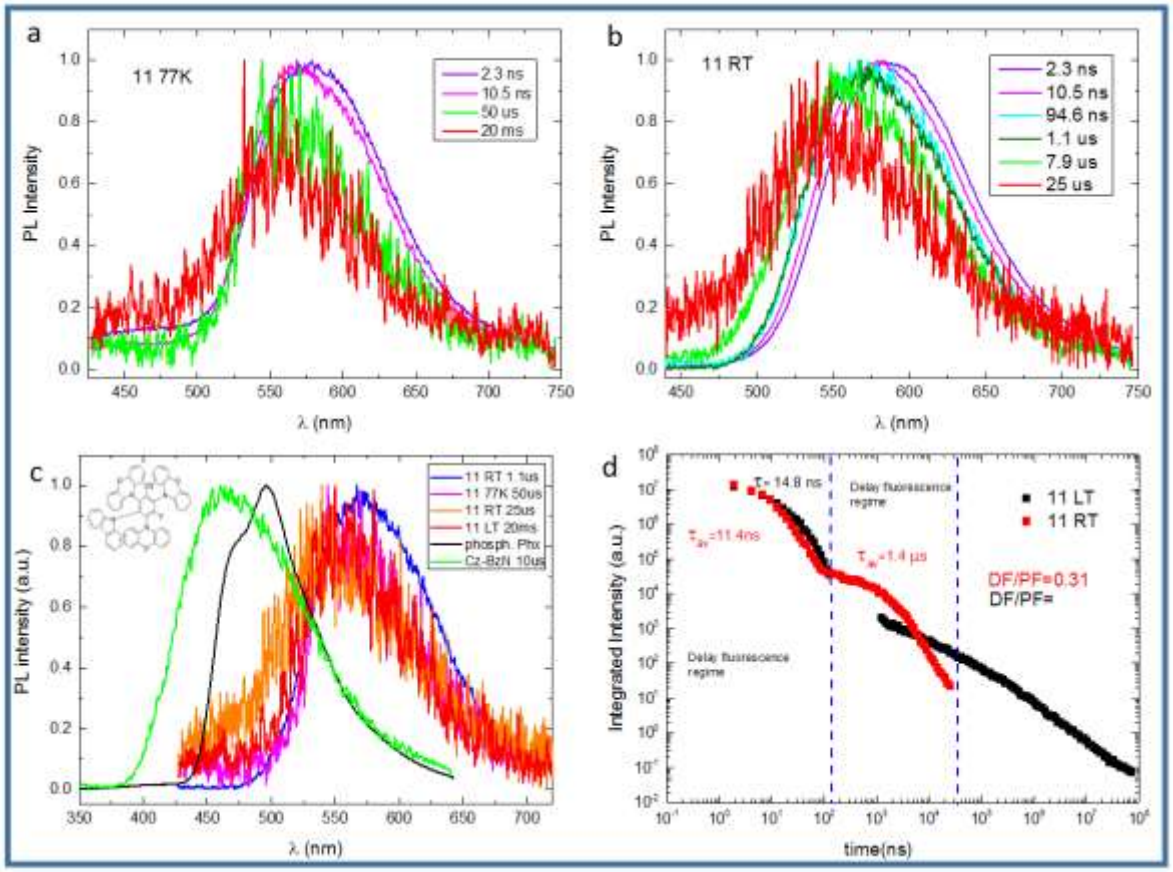

***Figure A2.28**: **a)** and **b):** time-resolved emission spectra of **11** in PMMA (0.1wt %) at room temperature (RT) and 77K respectively; **c)** delayed emission at the longest TD and delayed emission in TADF regime of **11**, for RT and 77 K compared with phosphorescence of the phenoxazine, and with the CT DF emission of Cz-BzN; **d**) decay curve of **11** in PMMA at RT and 77K. All experiments were carried out at λ_{ex}= 355 nm.*

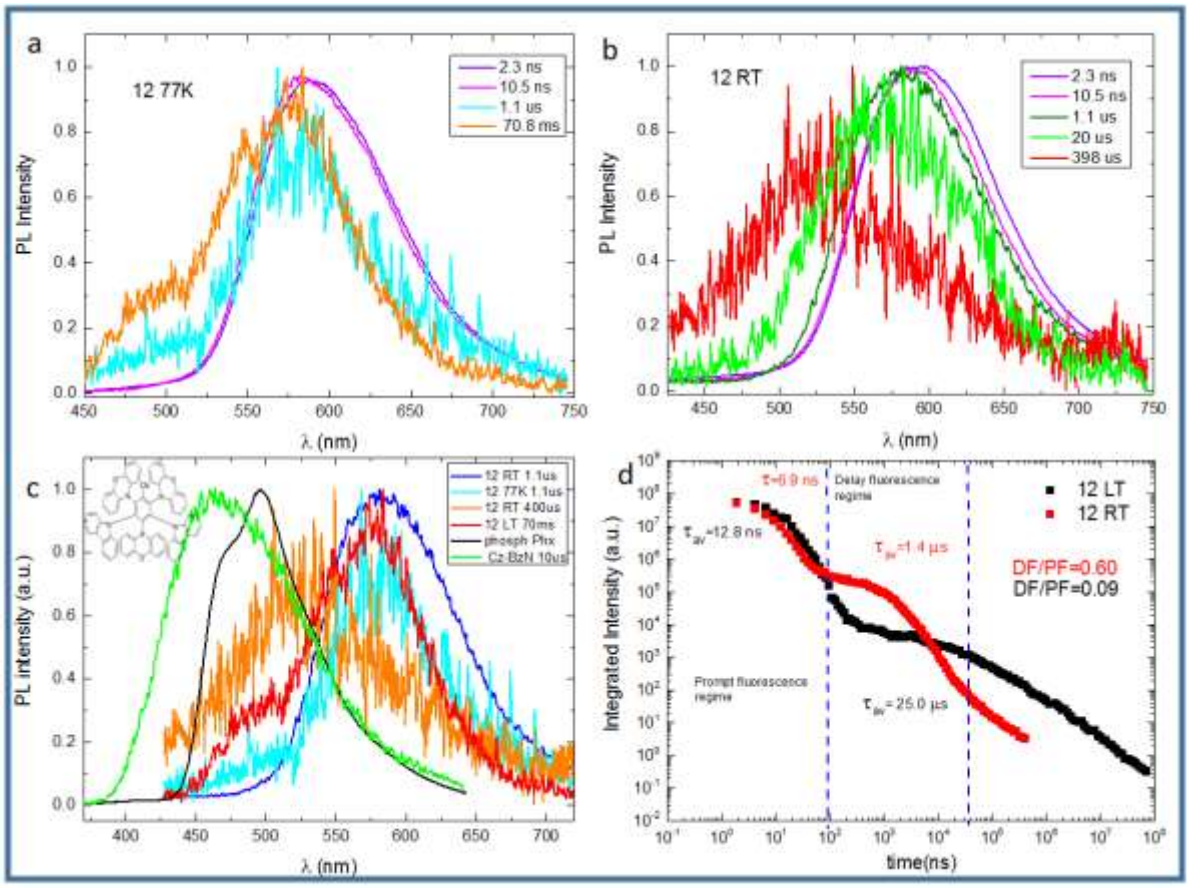

***Figure A2.29**: **a)** and **b)**: time-resolved emission spectra of **12** in PMMA (0.1wt %) at room temperature (RT) and 77K respectively; **c)** delayed emission at the longest TD and delayed emission in TADF regime of **12**, for RT and 77 K compared with phosphorescence of phenoxazine, and with the CT DF emission of Cz-BzN; **d**) decay curve of **12** in PMMA at RT and 77K. All experiments were carried out at λ_{ex}= 355 nm.*

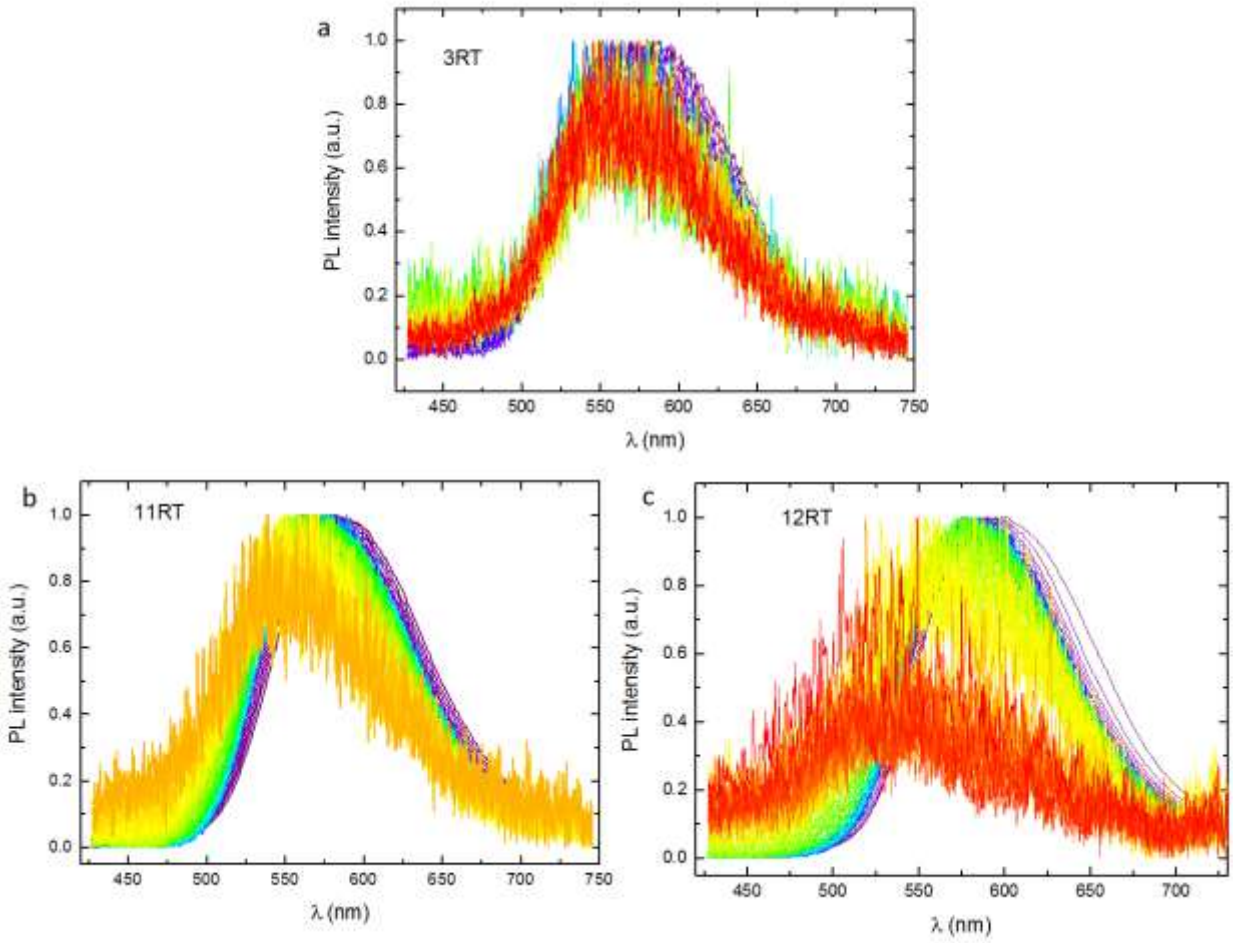

Figure A2.30*: time-resolved emission spectra of* ***a) 3, b) 11, c) 12*** *in PMMA (0.1wt %) from initial time delay (violet) to intermediate time delay (green) and then to final time delay (orange/red). All experiments were carried out at* λ_{ex}*= 355 nm.*

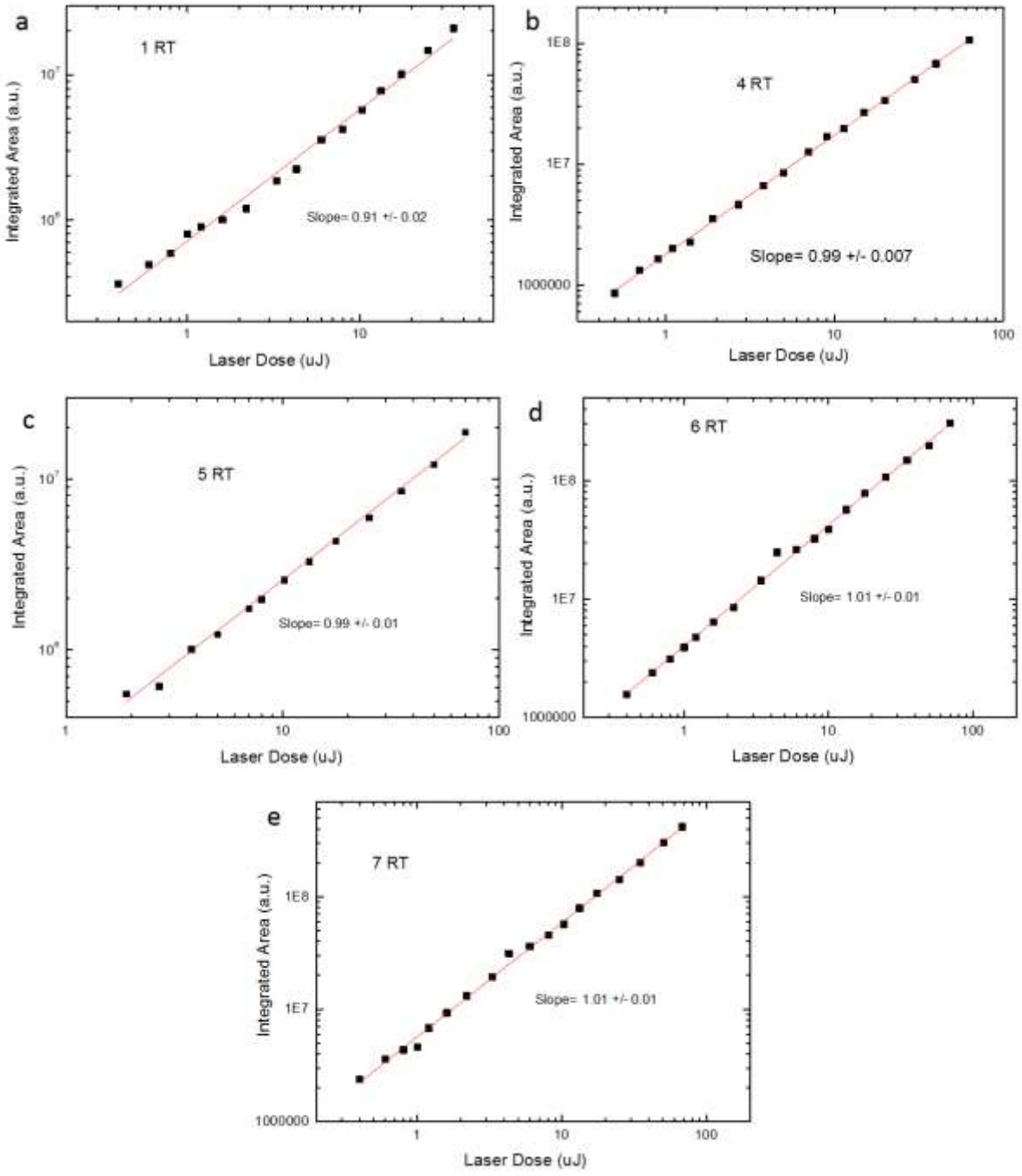

Figure A2.31 *- Power dependence of the integrated delayed fluorescence in PMMA thin films of molecule* ***1****, and* ***4****-****7****. All experiments were carried out at* λ_{ex}*= 337 nm.*

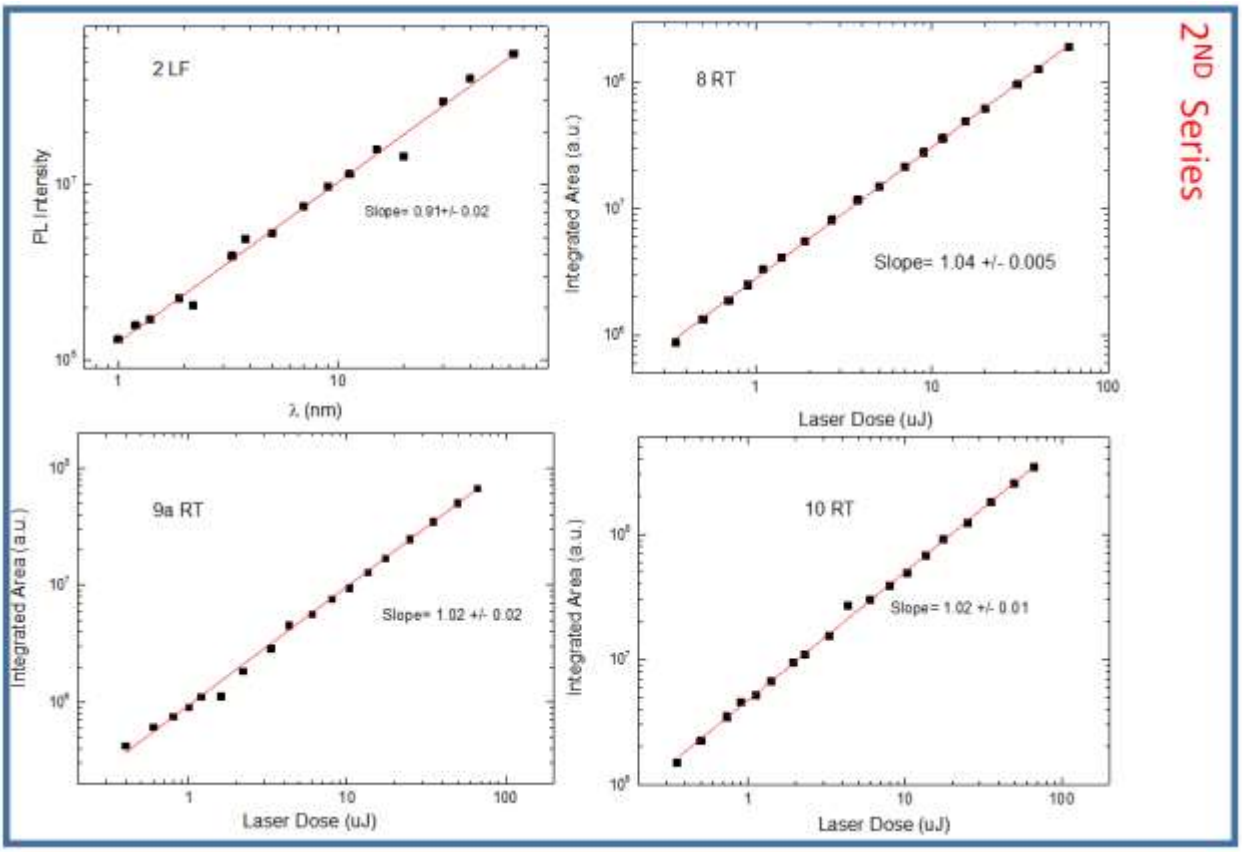

Figure A2.32 *- Power dependence of the integrated delayed fluorescence in PMMA thin films of molecule* ***2, 8, 9a*** *and* ***10****. All experiments were carried out at* λ_{ex}*= 337 nm.*

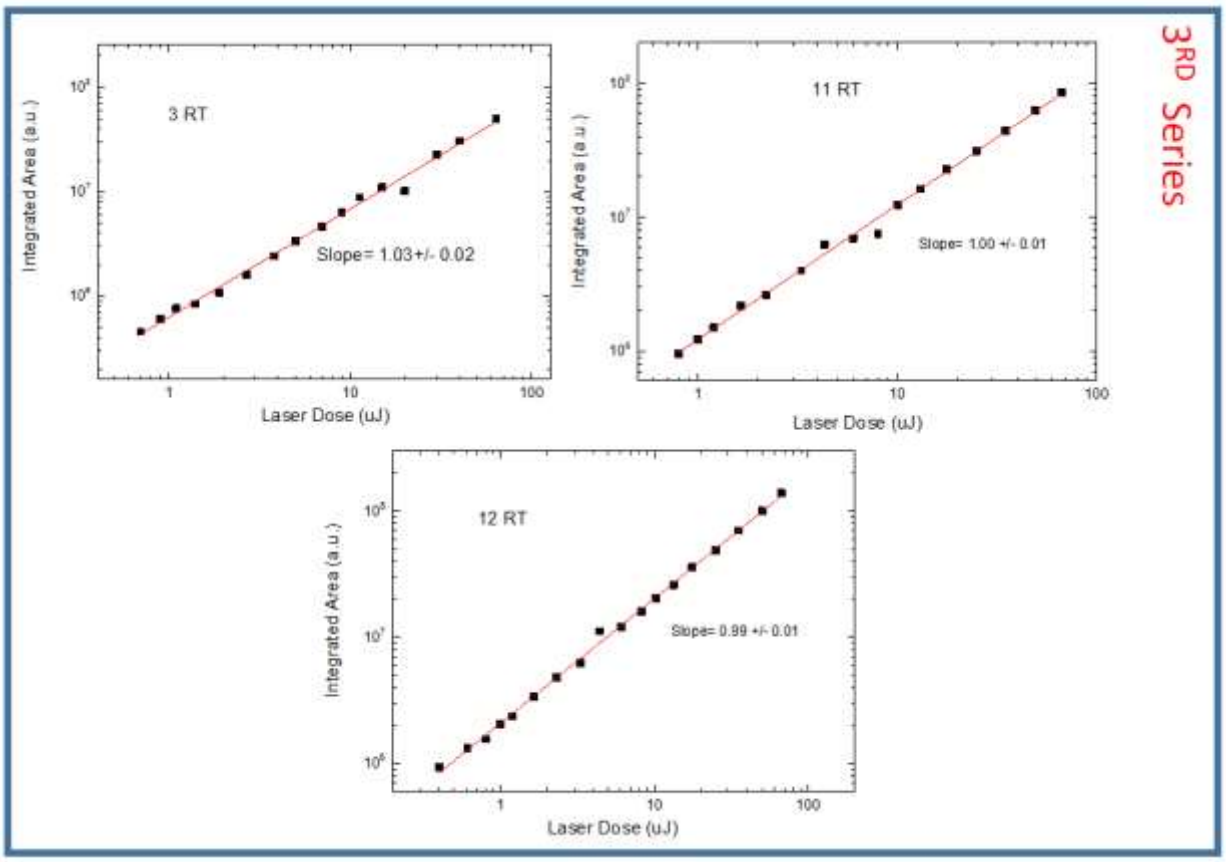

Figure A2.33 *- Power dependence of the integrated delayed fluorescence in PMMA thin films of molecule* ***3****,* ***11*** *and* ***12****. All experiments were carried out at* λ_{ex}*= 337 nm.*

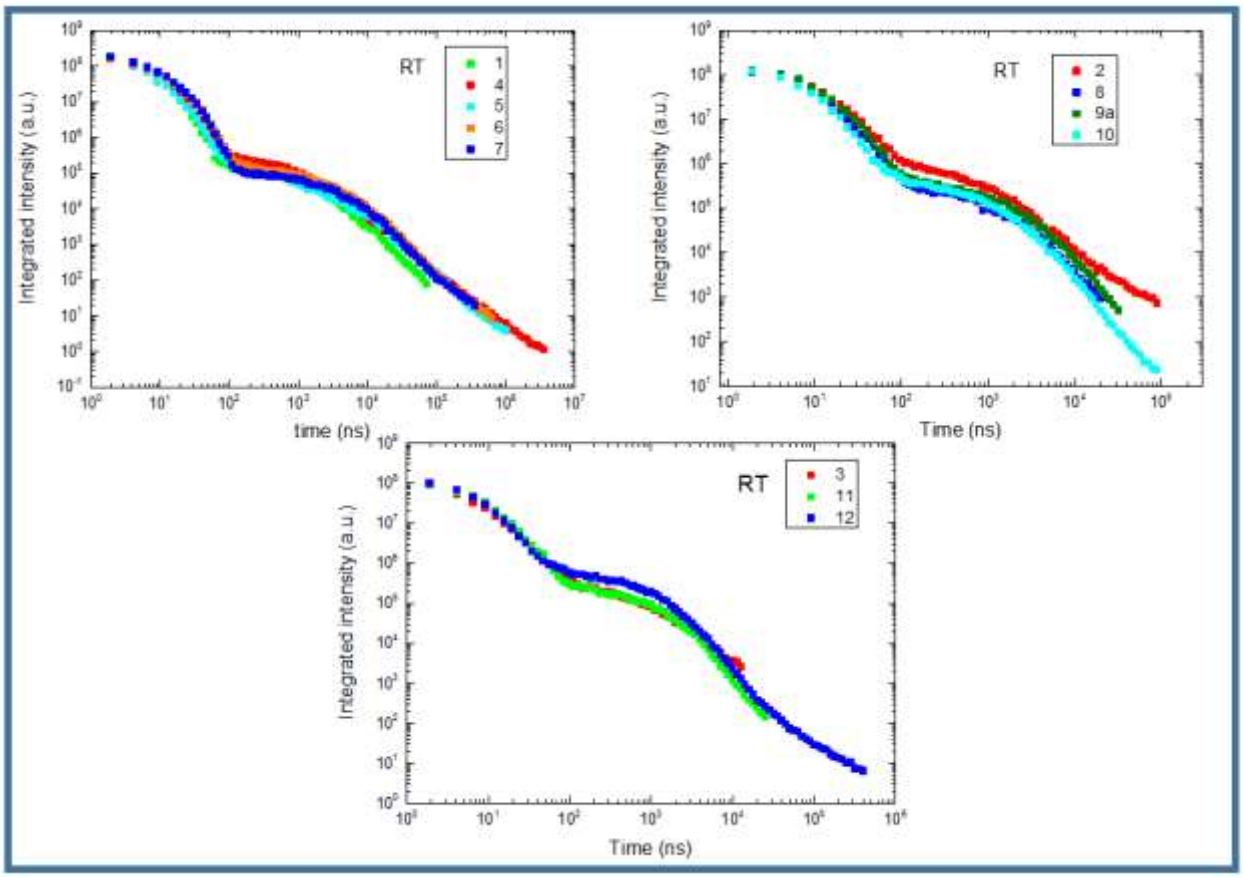

***Fig A2.34**: Comparison of the decay curve in the same series for the three series in PMMA at room temperature (RT). All experiments were carried out at λ_{ex}= 355 nm.*

CHAPTER 3.

STIMULUS RESPONSIVE BENZONITRILE DERIVATIVE EXIBITHING TADF, POLYMORPHISM, AND MECHANOCROMIC LUMINESCENCE.

1. INTRODUCTION.

Weak intermolecular interactions that exist between molecules are of great importance in many branches of science. They depend on the distance, and according to the Van der Waals equation, they generally decrease as R^3, where R represents the distance between two molecules. From the quantum mechanical point of view, the interactions between molecules are described as the overlap between the electron wave functions of all the single molecules, hence it results that intermolecular interactions can strongly affect the optical properties of the materials.

One of the main contribution to understanding how molecular packing impacts on photophysical properties were made by Michael Kasha[88] who demonstrated that the electrostatic interaction, as determined by the alignment of the transition dipoles, induces energetic shifts in the main absorption spectral peak and changes the radiative decay rate when compared to uncoupled molecules[88-91]. Besides aggregates reported by Kasha, it is important to reports the Aggregation Induced emission (AIE) phenomena studied for the first time by Tang, B. Z. in 2001[92]. Tang and co-workers demonstrated that in some molecules the emission is enhanced when aggregated because of restriction of the intramolecular rotations. This behaviour is in contrast with the aggregation caused quenching (ACQ) effect, very common in organic dyes. In particular, AIE materials present twisted conformations that afford loose packing patterns and prevent any detrimental strong interaction. It results that instead of activating new non-emissive deactivation paths, the non-radiative roto-vibration decay channels are blocked, and hence it changes the dyes into strong emitters[93-94]. This effect is enhanced in the crystalline state where the rigid and well-organized packing locks the molecular conformations more tightly than those in amorphous, and the regular weak interactions further reduce the roto-vibration degree of freedom of the molecules. The high level of molecular organization in the crystal allows also to obtain accurate information both on the relative molecules orientation and the nature of intermolecular interactions of neighbouring molecules through crystallography[95]. The supramolecular properties of the crystal also depend on the intermolecular interactions between the molecules that in general are electrostatic in nature, and their strength depends on the electronegativity of the donor and acceptor atoms[96]. As the crystal packing depends on a subtle balance of intermolecular

interactions, using different techniques it is possible to achieve different polymorphic crystal forms characterized by different molecular interactions. Interesting the search for polymorphic crystal forms allow obtaining favourable properties in various field and especially in the optical one. Especially in D-A compounds, different polymorphs can present molecules with different conformation that leads to different photophysical properties. In particular, the D-A torsional angle (dihedral angle) has demonstrated to have a strong impact on the TADF properties, and near orthogonal dihedral angle is considered a key factor to minimize the singlet-triplet energy gap[86]

However, in literature are reported only few studies[97-98] that demonstrate how the change in D-A dihedral angle can be observed as a consequence of different packing and therefore we consider the research on this kind of system very interesting. Another phenomena connected with the molecular interactions is mechanochromic luminescence (MCL), which consists in the change of the emission colour of organic molecules, when external stimuli, such as grinding, heating, fuming, melting or pressing, is applied. The change of the photophysical properties of the material is induced either by conformational changes that alter dipole-dipole interactions or changes in the intermolecular interactions between adjacent molecules[99-102]. The mechanochromism starts from an aggregated phase that passes to another crystalline or amorphous phase, after mechanical stress.

This chapter is focused on the photophysical and structural study of intermolecular interactions in crystalline solids and in the aggregates phases of a series of four new multifunctional CT luminogens (**Figure 3.1**). All four compounds present a Donor1-acceptor-donor2$_n$ (D_1-A-D_{2n}) design featuring in the central core a benzonitrile attractor substituted with a phenoxazine and an increasing number of carbazoles. The increasing number of electron-rich carbazoles can influences the change of the molecular geometry along with the dipolar moment and the torsion D-A angle, thus resulting in a tuning of the solid-state photophysical properties. Both, torsion D-A angle and dipolar moment can also change in the same molecule due to different molecular packing. Empirical models that correlate the dipole moment with the structure of organic molecules and their electronic distributions have been reviewed by O. Exner[103]. Another factor that influences the emission of D-A materials is the variation of the dielectric environment between the different phases. Recently in literature are reported few studies that investigate the role of dielectric constant in the TADF properties of the materials[104-105]. In the chapter will be illustrated how the different properties between crystal polymorphs or between crystal and amorphous phases are connected with MCL. In both phenomena, the change of intermolecular interactions is crucial to determine the molecular geometry of the D1-A-D2n molecules and therefore they play a fundamental role in the variation of the photophysical response. The different methods and conditions used to prepare the samples lead to different aggregated forms. This allows obtaining different supramolecular organizations along with an amorphous phase, which corresponds also to a variation of the TADF properties.

It is worth noting that, although combining MCL and TADF functions into a single molecule would offer the opportunity to develop new interesting multifunctional emissive materials, the research into such organic materials is still at the beginning. For this reason, we think that designing and studying new materials presenting these features constitute original and interesting work beyond the present literature.

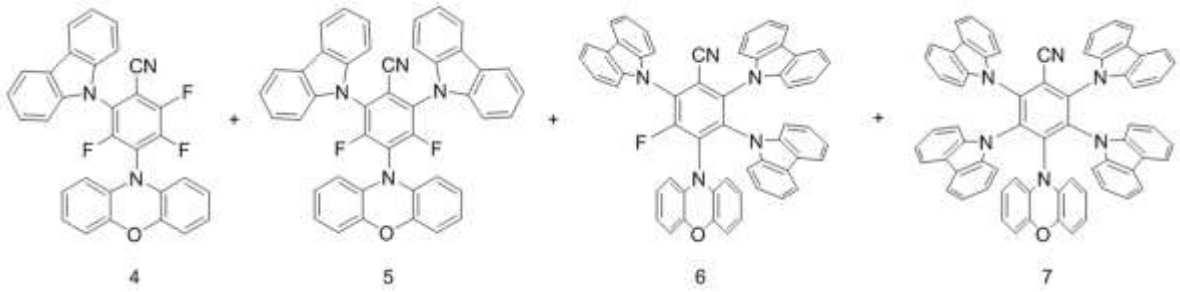

***Figure 3.1**: molecular structure of the molecules studied in this chapter.*

2. XRD ANALYSIS.

The geometrical structures of the **4**-**7** crystals emitters were identified by X-ray scattering analysis, to investigate the relationship between luminescent behavior and molecular packing (**Table 1** in **Chapter 2**). The crystals were grown from slow evaporation of different mixtures of two solvents [**4**: petroleum ether/dichloromethane (3:1) mixture, **5**: methanol/dichloromethane (1:1) mixture, **6**: ethyl acetate/dichloromethane (1:1), **7**: ethyl acetate/dichloromethane (1:1)].

Notably, the **5** crystalline unit cell contains two different molecules along with a molecule of solvent. These two molecules present a slightly different D-A angle (**Table 1** in **Chapter 2**). This configuration theoretically opens the possibility to CT states with different energies and therefore different emission colors. A molecule of solvent is also contained in the unit cell of **7**. On the other hand, two different polymorphs were isolated for molecule **6**. One of them containing only the molecule **6** and the other one containing also a molecule of solvent (ethyl acetate) in the unit cell. Also in this case we expect to observe different emission properties.

In general, the structural properties of the molecules are largely dependent on both the steric and electronic properties of the substituents. Based on this general principle the molecules adopt in their geometry a configuration that minimizes the electronic repulsion between their different moieties. In particular, these molecules present the possibility to rotate, twist, or bend their D-A angles. The molecules of this study present only one phenoxazine and they differ by their increasing number of carbazoles. Hence we expect to observe different angles that minimize the total energy. When we look at single molecules in crystals it is possible to define two different D-A angles. One is the D-A torsional angle (dihedral angle), and the other is the angle between the donors and acceptor mean planes. However here we only consider the D-A dihedral angle (**Table 1** in **Chapter 2**). Comparing the Phx-BzN dihedral angle in **4**-**7** crystals (**Table 1** in **Chapter 2**), we can see that it increases from crystal **4** (69.37°) to crystal **5** (89.36, 77.09) but after that, it decreases in crystal **6** (70.55°), crystal **6+solv**. (74.98°) and crystal **7** (65.24°). Regarding the Cz-BzN dihedral angle, we can see that in crystal **4** the carbazole in position 2 presents the largest dihedral angle (82.33°). In crystal **5** the Cz-BzN dihedral angle of the carbazole in position 6 decreases for both molecules present in the unit cell (58.43°, 70.29°). However, the carbazole in position 2 presents in both cases a larger torsional angle (73.82°, 72.36°). In crystal **6** the Cz-BzN dihedral increases in both positions 2 (76.46°) and 6 (76.20°), but in the additional carbazole in position 3, the dihedral angle is smaller (71.65°). In crystal **6+solv** both Cz-BzN dihedral angle in positions 2 and 6 are smaller (75.43°, 66.50°) than in crystal **6**. Contrarily the one in position 3 is slightly larger (72.98°). Finally, crystal **7** presents the smallest Cz-BzN dihedral angles (68.54, 70.21, 70.21, and 68.54°) compared to the other crystals. This is due to the higher steric hindrance caused by the full substitution of the BzN.

Besides the intramolecular geometrical features, the luminescent properties of solid-state materials depend also on the packing mode and intermolecular interactions. Therefore from their packing, it is possible to obtain information about the interactions and thus understand better the photophysical behavior of the materials. In **Figure 3.2** are reported the various molecular packing of the single crystals obtained for molecules **4**-**7**, from which it is possible to see the molecular orientations, measure their distance, and hence obtain the main intermolecular interactions.

In molecule **4** single crystal packing (**Figure 3.2a**, **Figure A3.9**) we can see that the molecules present a herringbone packing, where the main intermolecular contacts are C-H···N (2.611 Å), C-F···H (3.095 Å), C-F···C (3.064 Å), C-H···π (2.786 Å) and C-H···O (2.976 Å). No π-π stacking is observed for this molecule. On the other hand crystal **5** shows in the molecular alignment an offset π-π stacking between two carbazoles, by one ring (3.677, 3.705 and 3.702 Å) and no π-π stacking by the other (**Figure 3.2b** and **Figure A3.10**). The other main intermolecular interactions in crystal **5** are: C-H···N (2.688 and 2.770 Å), C-F···H (3.369 Å), C-H···π (2.957 and 2.987 Å) and C-H···O (2.533 Å). Regarding the crystal **6** (**Figure 3.2c**, **Figure A3.11**) in the packing it is possible to see that two phenoxazines are arranged face to face in a head to tail configuration, with a variable distance along the main axis (4.104, 3,875, 3.901 and 4.152 Å). Nevertheless, no π-π stacking interactions were found between the two phenoxazines. The other main intermolecular interactions in crystal **6** are: C-H···N (2.791 Å), C-F···H (2.992 Å), C-F···C (2.916 Å) and C-H···π (2.651, 2.854 and 2.935 Å). Contrarily in **6+solv** (**Figure 3.2d**, **Figure A3.12**) a closer π-π stacking interaction is present between two carbazoles, which are stacked in an offset head to tail configuration (3.867, 3.912 and 4.041 Å). The two phenoxazines are arranged in an offset head to tail configuration (3.381, 3.429 and 3.600 Å) and, also in this case they not present π-π stacking. Other intermolecular interactions in **6+solv** that hold molecules together are C-H···N (3.343 and 3.315Å), C-F···H (2.786 Å), C-H···π (2.844, 2.866 and 2.778 Å) and C-H···O (3.868 Å). Finally, due to the steric hindrance in the molecule, π-π stacking is prevented in crystal **7** (**Figure 3.2e**, **Figure A3.13**). The main intermolecular interactions are: C-H···π (2.635, 2.874 and 3.012 Å) and C-H···N (3.171, 3.313, and 3.537 Å and they plays a key factor in the formation of all crystals. The presence of multiple donor's moieties, along with not very strong molecular interactions, make these molecules to easily adopt a structural reassembly, which may induce the crystals to change morphology and to show MCL under pressure.

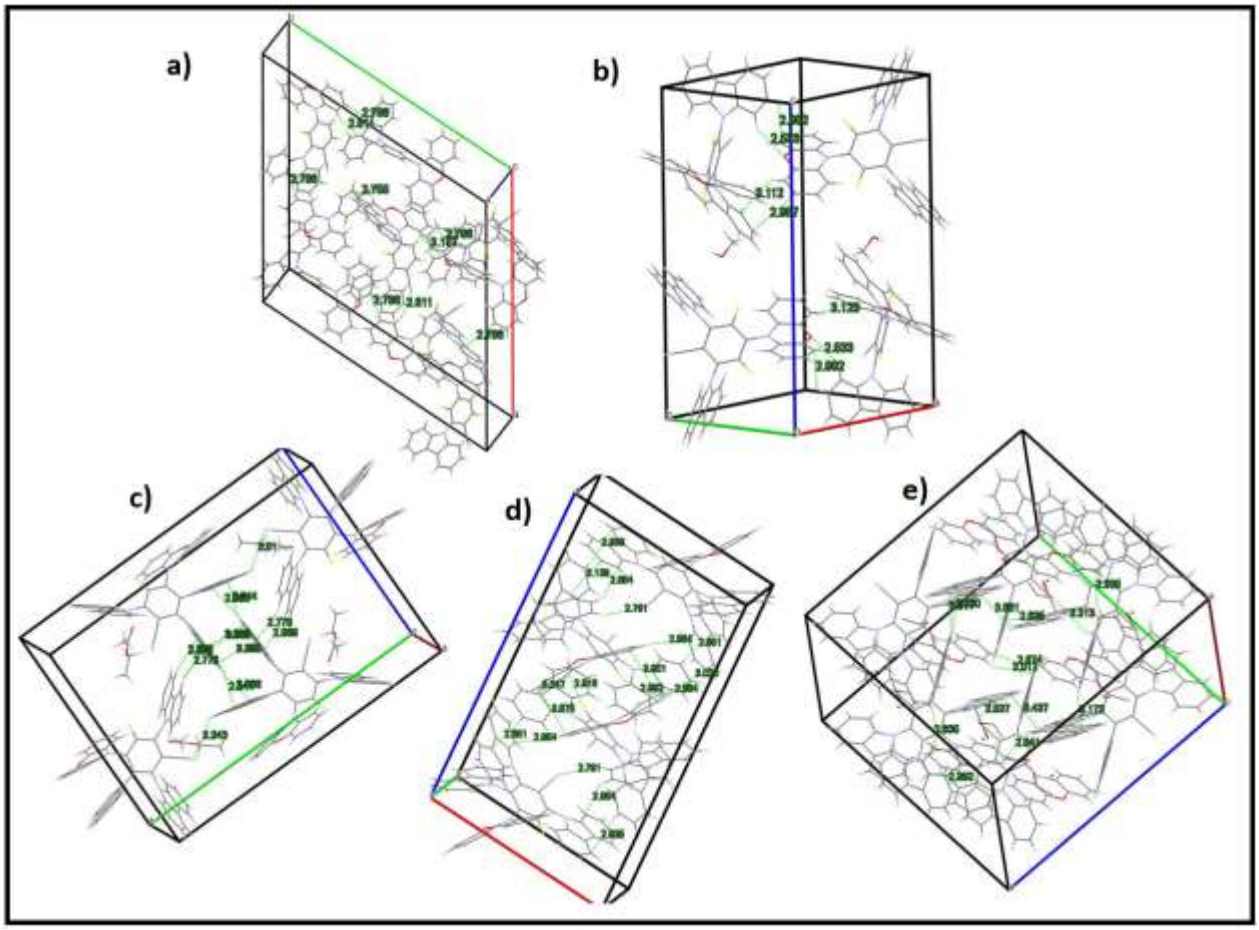

Figure 3.2**:** *molecular packing of* ***4 (a)****,* ***5(b)****,* ***6+solv.(c)****,* ***6(d)*** *and* ***7(e)*** *obtained from X-ray crystallographic structures.*

3. PREPARATION METHODS OF QUARTZ SUBSTRATES.

In order to explore the photophysical properties of the molecules in different aggregated forms, have been used different sample preparation methods. Depending on the processing conditions the films might be crystalline or amorphous. In principle, each method could lead to a different molecular assembly, arising from the change in the chemical and physical variables, e.g. the solvent polarity (different solvents have been used), temperature, and evaporation rate.

According to literature, employing faster processing conditions (fast solvent evaporation in our case), we assume to achieve an amorphous phase. On the other hand, slowing down and controlling the solvent evaporation generally is considered a good method to achieve a crystalline phase. Pictures of all the obtained samples are shown in the Appendix in **Figure A3.1-A3.4.** In particular, solvent vapour annealing (SVA) is an excellent method that allows to change and to control the environmental parameters for crystal growth processes (see Experimental section

§2.2.3). Hence it was used to form supramolecular structures featuring a higher degree of order[106]. All the samples obtained with this method will be indicated as from SVA (fSVA).

A second method used is the drop-casting (see Experimental section §2.2.2). Two different solvents, with different boiling point and viscosity, were used. In particular, DCM thanks to its low boiling point and fast evaporation at RT, prevents ordered self-organization and thus to obtain an amorphous organization. The random intermolecular interactions lead the material to present different molecular configurations. On the other hand, drop-casting a toluene solution may favour a high order molecular self-assembly, due to the high boiling point and viscosity that gives more time to the molecules to self-organize. All the samples obtained with this method will be indicated as from DCM (fDCM) or from toluene (fTOL).

Finally, another common approach used to obtain crystals is thermal annealing. In fact, higher temperatures favour molecular diffusion thus facilitating nucleation. Therefore, the molecules lying on the substrate may steadily assemble in an ordered fashion to form more emissive aggregates or pack into a crystalline phase. The thermal annealing treatment was realized (at 150°C or 200°C for 10/15 min) on the amorphous samples fDCM. All the samples obtained using this method are indicated as fSVA150 or fSVA200.

4. STEADY-STATE PHOTOPHYSICAL PROPERTIES OF THE SAMPLE DEPOSITED ON THE QUARTZ SUBSTRATES.

In this section, we show how the photophysical study allow to verify if the preparations methods described above lead to obtaining amorphous or crystalline phases as it was speculated. In particular, herein are reported both steady-state emission and excitation spectra of 17 different solid samples obtained from the compounds **4**, **5**, **6** and **7** (**Figure 3.3**). From the excitation spectra, it is possible to see which transitions populate the final emissive state. Comparing the absorption with excitation it is possible to understand if there are transitions in absorption that do not populate the final emissive state. This is verified when a particular transition is visible only in the absorption spectrum but not in the excitation one. On the other hand, from the emission, it is possible to obtain information about all the emissive states. The main photophysical properties of all the 17 solid samples are summarized in **Table 1** and **Table 2**. Further details are also presented in Appendix (end of the chapter). All four emitters present a different emission in the different solid samples. By comparing the excitation spectra with the emission ones, it is possible to obtain more information about the states involved in the photophysical process of the different solid forms.

4.1 Steady-state emission.

The emission of the more blue-shifted solid phase obtained from **4**-**7** molecules (crystalline phase) is firstly compared with the emission of the corresponding single molecules dispersed in PMMA (**Figure A3.14**). In all cases, the isolated molecule shows hypochromic shift respect to the different condensed samples. At first glance, this leads to thinking about the possible formation of a new aggregate emissive state. However, in XRD analysis long-distance π-π interactions were found (only between carbazoles) only in **5** and **6+solv** crystals (**Figure A3.10**, **A3.12**). Therefore we exclude the formation of aggregate species in our samples. Hence, the red-shifted emission respect to PMMA can be originated by the different polarities and different dielectric constant between the PMMA and solid phases, but also because of different molecular interactions that produce different molecular conformations. All these factors produce a redistribution of the electronic density on the molecule that downshift the energy of the CT state. The considerable lower FWHM observed in polycrystalline samples respect to PMMA (**Table 1**, **Table A3.2**), depends on the fact that the highly ordered packing typical of the crystal is characterized by the presence of one or maxima two discrete molecular configurations.. In contrast, different molecular configurations are allowed in PMMA.

In order to verify which phase (crystalline or an amorphous) is formed using the different preparation methods, four main parameters will be analysed. The emission maximum (λ_{max}^{em}) and the full width at half maxima (FWHM) will be considered to evaluate the level of organization. In particular, a bathochromic shift and a large FWHM mean an amorphous phase (distribution of configurations that gives a large emission band), while hypochromic shift and narrowed FWHM are assigned to a crystalline phase, characterized by the presence of one or maxima two discrete configurations. However, if the molecules crystallize with a configuration that redshift the CT state, can be also observed a narrowed emission but bathochromic shift respect to the amorphous phase. Another indication about the formation of a crystalline phase could be also obtained from the PLQY. In fact, the blue shift associated with an increase of PLQY means a more ordered phase and rigid environment (suppression of vibration and rotation) and therefore indicates that the material presents the crystallization induced enhancement emission (CIEE) phenomenon[94]. However, if the molecule in the crystal assumes a configuration that redshift the CT state, can also be observed a decrease of the PLQY. It is worth noting that the CIEE or AIE effects are particularly favoured in the systems presenting a large D-A angle (as in **1**-**7** molecules) that helps to prevent close interactions. Finally, the emission onset is connected with the energy of the excited state of a particular molecular configuration. This is particularly useful to evaluate the presence of different polymorphs.

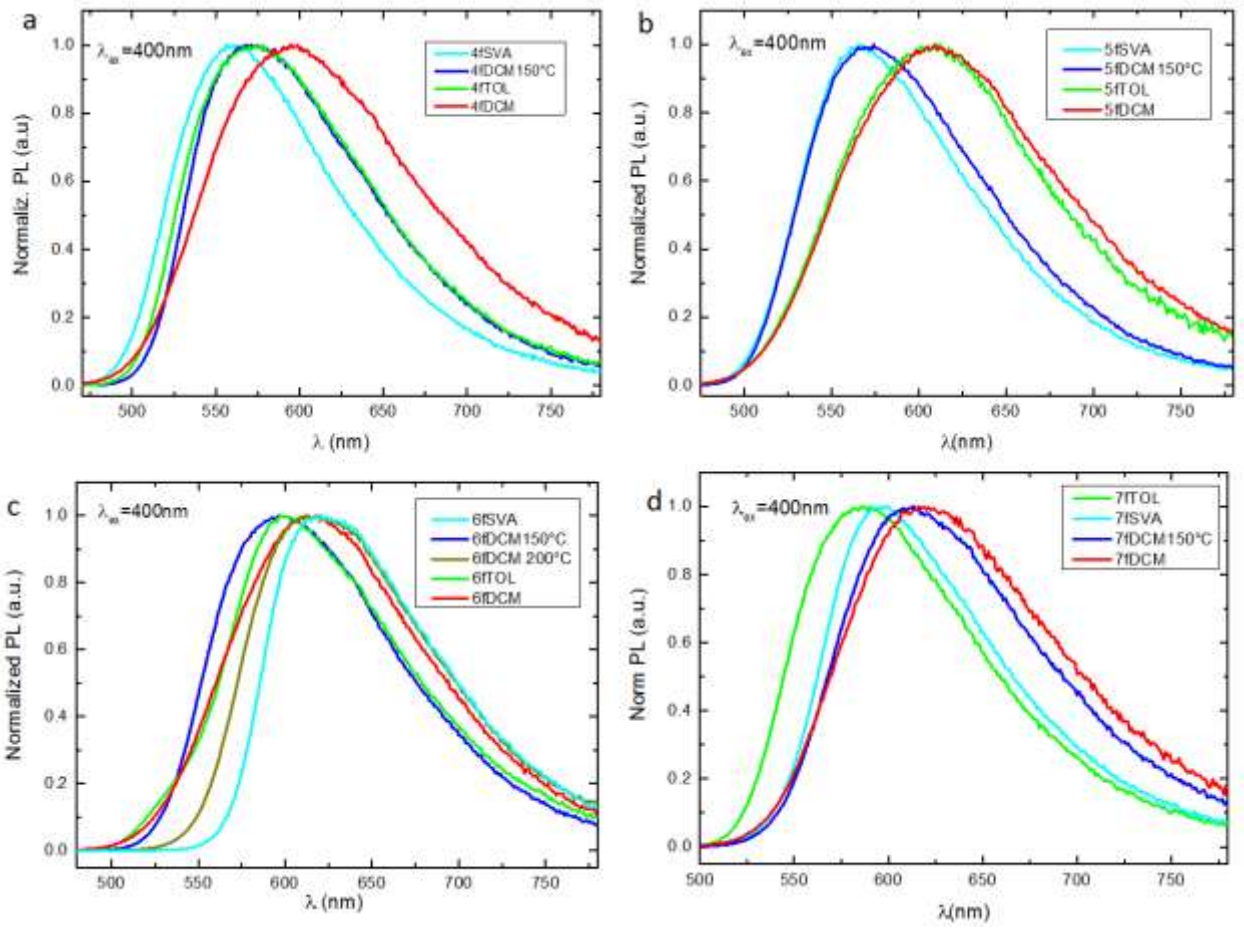

Figure 3.3: *Normalized fluorescence spectra (λ_{exc}=400 nm) of the different solid forms obtained for* ***a)*** *Molecule* ***4, b)*** *Molecule* ***5, c)*** *Molecule* ***6, d)*** *Molecule* ***7****.*

Considering the emission of **4** in their different condensed phases (**Figure 3.3a**) we can notice that **4**fSVA, **4**fDCM150, and **4**fTOL present both a strong hypochromic shift (between 21 and 33nm) and higher PLQY respect to **4**fDCM (**Table 1**). Moreover, **4**fDCM presents a considerably larger FWHM especially respect to **4**fSVA, but also respect to **4**fDCM150 and **4**fTOL. All these observations indicate that **4**fDCM presents an amorphous phase and that in **4**fSVA, **4**fDCM150, and **4**fTOL is formed a crystalline phase. Therefore the initial hypotheses are verified for all the samples. The CIEE effect is particularly intense in **4**fSVA (**Table 1**). In **4**fDCM150 and **4**fTOL both the λ_{max}^{em} and onset are slightly red-shifted respect to **4**fSVA (**Table 1**). This indicates a slightly different molecular configuration in the two crystalline samples.

From the emissions of the different phases obtained from **5** (**Figure 3.3b**), we can see that also in this case both **5**fDCM150 and **5**fSVA present strong hypochromic shift respect **5**fDCM along with a more narrowed emission (FWHM). Moreover, both samples present the CIEE effect which is stronger for **5**fSVA (**Table 1**). However, in this case, **5**fDCM150 and **5**fSVA present a very similar

emission which indicates that only a single crystalline form is obtained for molecule **5**. The lower QY and the slightly more broadened emission in **5**fDCM150, indicate that some molecules remain in a more amorphous phase (less emissive). Regarding **5**fTOL in this case it shows the same emission of the amorphous **5**fDCM. Hence, we can see that for **5** the initial hypothesis is verified only in **5**fDCM150, **5**fSVA, and **5**fDCM but not in **5**fTOL.

The emissions of the samples obtained with **6** are reported in **Figure 3.3c**. We can see that in this case, the crystalline **6**fSVA film presents bathochromic shift respect to **6**fDCM (14nm), which is also stronger respect to both **6**fDCM150 (28 nm) and **6**fTOL (28 nm) (**Table 1**). However, the FWHM of **6**fSVA is the narrowest between all the samples obtained from **6**, thus confirming the formation of the crystalline phase. On the other hand, the broadest emission of **6**fDCM confirms its amorphous phase (**Table 1**). In the crystalline **6**fSVA, the molecules are packed in a configuration that strongly redshift the CT state energy. It results that the QY of **6**fSVA is practically the same as the amorphous **6**fDCM. This depends on the fact that when the CT state is stabilized too much the non-radiative decays are favoured. With a second annealing on **6**fDCM150 (200°C, 15 min), an important bathochromic shift is observed in the obtained **6**fDCM200. In particular, the λ_{max}^{em} of **6**fDCM200 is close to that of **6**fSVA, however, its emission onset blue shifts respect to **6**fSVA. This indicates that part of the molecules remains in a different configuration. From the above considerations, we can understand that we are dealing with two main different polymorphs: one present in both **6**fSVA and **6**fDCM200 (red polymorph) and the other, present in both **6**fDCM150 and **6**fTOL (orange polymorph). The CIEE effect is strong only in **6**fDCM150 (**Table 1**) but is less intense in **6**fTOL. The latter in fact, presents a redshift in the edge part of the spectra (at high energy), thus indicating that some molecules present a configuration with a different CT state. Overall, we can say that also in **6** the initial hypotheses are verified. In fact with **6**SVA, **6**fDCM150, **6**fDCM200, and **6**fTOL preparation methods we obtained a crystalline phase, on the other hand, an amorphous phase is obtained in **6**fDCM.

Finally, with molecule **7**, we can observe that both **7**SVA and **7**fTOL present hypochromic shift respect to **7**fDCM and **7**fDCM150 (**Figure 3.3d**). However, in this case, **7**fDCM150 presents similar FWHM and emission onset of **7**fDCM (**Table 1**). This indicates that the effect of the temperature is not enough to increase the mobility of the molecule **7**. This could depend on the hindered geometry of **7** arising from the presence of five donor moieties. Therefore, despite a slight hypochromic shift (7 nm), **7**fDCM150 remains in a more amorphous configuration. A strong CIEE effect is obtained in both **7**SVA and **7**fTOL. Worth of note, **7**fTOL presents a hypochromic shift in both emission maxima (15 nm) and onset (0.09) along with a higher PLQY (**Table 1**). This indicates that **7** forms two different polymorphs: one in **7**fSVA (polymorph 1) and the other in **7**fTOL (polymorph 2).

From these analyses we can notice that only one crystalline form is obtained for **4** and **5** molecules, contrarily two polymorphs are obtained for **6** and **7** molecules. This behaviour could

depend on the fact that with the increasing number of carbazoles the molecules can increase their possibility to arrange in different crystalline configurations. This is interesting, because it allows to understand that it is possible to tune the solid-state emission of a single molecule by the use of different crystal polymorphs, and probably this can be achieved especially when the molecules present a high number of substituents. Moreover, considering the PLQY of the different solid samples obtained from the same molecule, it is possible to notice that more the sample is blue-shifted in both λ_{max}^{em} and onset, higher is the QY. This behaviour is respected, also between the different polymorphs present in **7**fTOL and **7**fSVA or between **6**fDCM150 and **6**fSVA. Therefore between the different solid phases of our compounds, when the molecules present a configuration that increases the energy of the CT state, the QY is always enhanced. This can be achieved through a higher D-A conjugation that can be obtained if the molecule, blocked in the crystalline structure, presents a lower D-A angle. Contrarily if the molecule in the crystal presents a more relaxed D-A angle that redshifts the emission, the non-radiative emission becomes predominant.

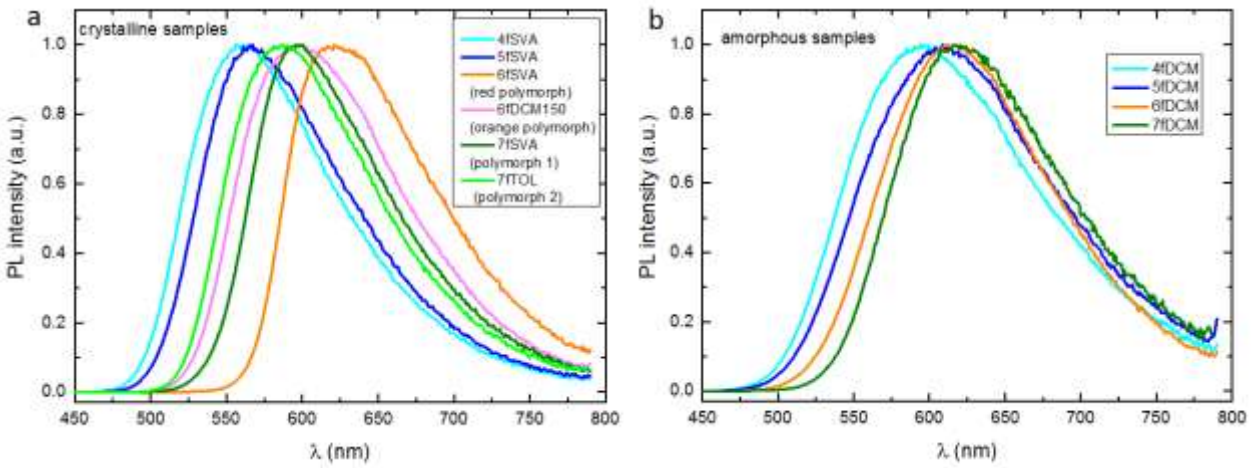

Figure 3.4: *Normalized fluorescence spectra (λ_{exc}=400 nm) of **a)** different crystalline phases obtained for for molecule **4**-**7**, **b)** amorphous phases obtained for molecule **4**-**7**.*

In **Figure 3.4a** are reported the emission of all the different crystalline forms. Interestingly, it is possible to notice that a progressive bathochromic shift in both maxima and onset, occurs from **4**fSVA, **5**fSVA, **6**fDCM150 to **7**fSVA. The bathochromic shift with the increasing number of Cz substituent was also observed in **Chapter 2**, for the same molecules dispersed in PMMA. This is in line with the more stabilized ICT state that can be obtained either by the use of donors with an increased donor's strength, but also by increasing the number of donor units. In particular, the presence of multiple donors induces the delocalization of the ICT state over the multiple D−A structures. However, the second polymorph obtained in **6** and **7** doesn't follow the same trend.

In particular **6**fSVA (red polymorph) is strongly red-shifted respect to both the polymorph crystal of **7**, on the other hand, the polymorph 2 obtained in **7**fTOL present slight hypochromic shift respect to **6**fDCM150. This depends on the fact that in one of the two polymorphs the molecular interactions alter the molecular configuration, and the polymorph is in a metastable state. Contrarily, the crystals that follow the trend should present a configuration more similar to the gas phase[7]. Interestingly, the same trend is also respected in the amorphous samples (**Figure 3.4b**). In fact, a progressive bathochromic shift of both emission maxima and onset is clearly visible from **4**fDCM, **5**fDCM, **6**fDCM to **7**fDCM.

Table 1: Summary of steady state photophysical properties of the different solid samples.

Comp.	Φ_{PL} (%) air	λ_{PL},nm Std. State	FWHM (nm)	Emiss. onset (eV)	Excitat. onset (eV)
4CrystSVA	9.0	561	112	2.51	2.36
4fDCM150°C	3.3	573	124	2.43	2.32
4fTOL	2.7	573	128	2.47	2.38
4fDCM	1.0	594	141	2.46	2.31
5CrystSVA	7.8	567	112	2.47	2.36
5fDCM150°C	4.1	574	121	2.47	2.37
5fTOL	1.1	610	140	2.44	2.35
5fDCM	1.0	612	149	2.44	2.34
6CrystSVA	2.4	626	113	2.19	2.07
6fDCM150°C	7.3	598	123	2.35	2.31
6fDCM200°C	2.9	621	125	2.25	2.16
6fTOL	2.6	598	116	2.33	2.15
6fDCM	2.3	612	132	2.36	2.35
7CrystSVA	8.5	600	104	2.29	2.16
7fDCM150°C	2.8	613	124	2.29	2.13
7fTOL	9.1	585	115	2.38	2.25
7fDCM	1.8	620	131	2.31	2.21

(for all Φ_{PL} the experimental error is ±20% of the value)

4.2 Steady-state excitation.

The excitation spectra allow to have information about the origin of the emission in the different **4**-**7** solid forms. In particular, it is possible to have information about which states, among the ones populated in absorption, contribute to the emission. Comparing the excitation spectra with the absorption spectra allows to understand if the emission takes place from the same states populated in absorption. Through the absorption, it is possible to obtain information also about eventually populated excited states that don't emit. Therefore, for a complete

[7] However we cannot exclude that in both polymorphs that don't follow the trend is present a molecule of solvent that alter the properties of the crystals.

comprehension of the states involved in the photophysics of our solid sample, in addition to the absorption spectra in PMMA, it would be also desirable to have the absorption for every solid samples. Unfortunately, the high scattering in the sample makes it difficult to record them.

In **Figure 3.5** are reported the excitation spectra of the different solid forms obtained from compounds **4**-**7**, compared with the corresponding excitation spectra of the isolated **4**-**7** molecules in PMMA. The maxima (λ_{max}^{exc}) and the onset of the different bands present in the excitation spectra of all **4**-**7** solid samples are reported in **Table 1**. The comparison between the excitation and the absorption spectra of **4**-**7** molecules in PMMA are reported in the Appendix (**Figure A3.14**).

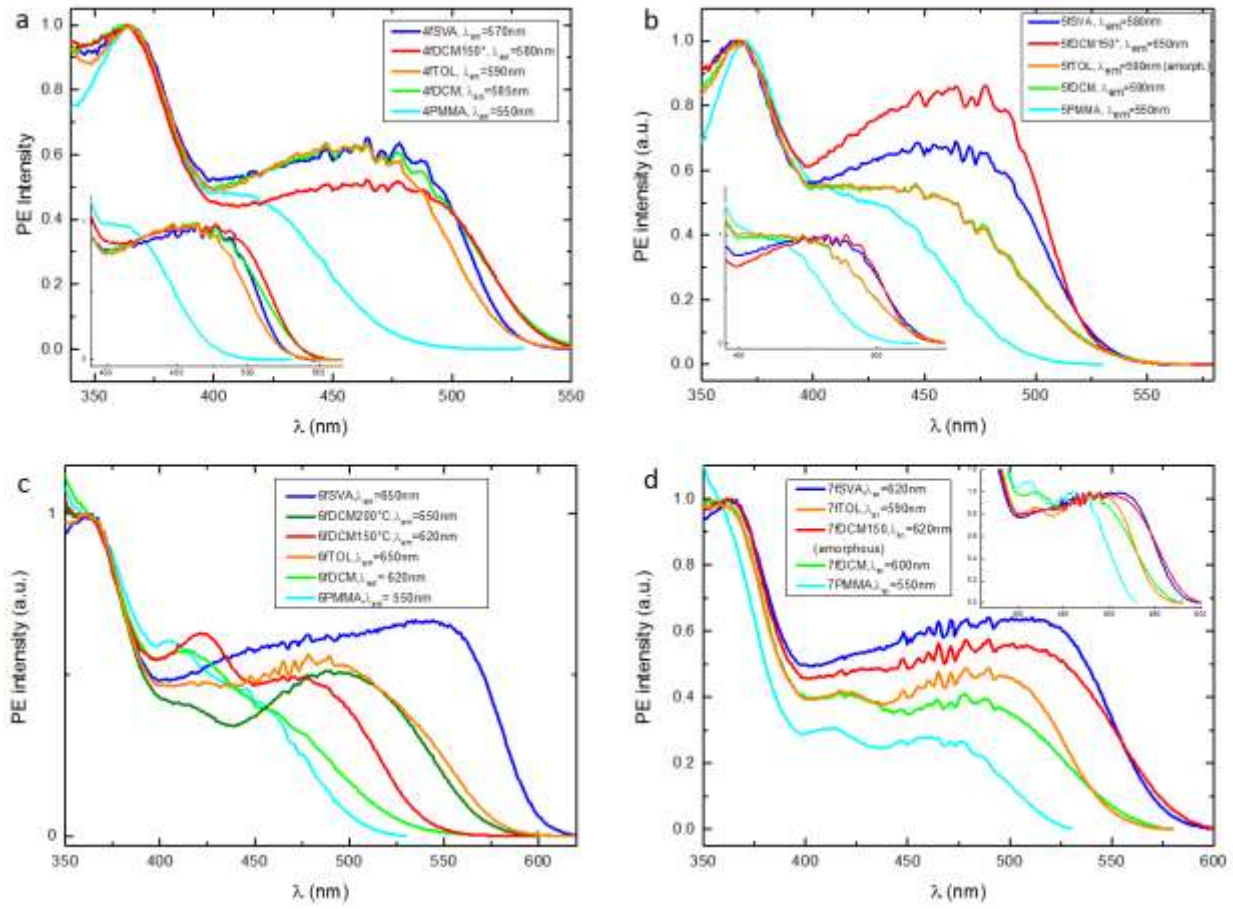

Figure 3.5: *Excitation spectra of the **4**-**7** solid samples compared with the corresponding excitation spectra of the isolated **4**-**7** molecules in PMMA. All spectra are normalized on the LE transition of the donors. **inset**) Excitation spectra normalized on the CT absorption band.*

Comparing the excitation spectra of **4**-**7** in PMMA with that of the corresponding different solid phases (**Figure 3.5**) we can see that all 17 samples (neat and PMMA) present in the bluest region

an intense peak between 363 and 367nm (**Table 2**) (all the spectra are normalized on this band). We assign this band to the population of the localized excited state of the donors. However, this band results in some case red-shifted respect to LE absorption visible in PMMA (**Figure A3.14**). On the other hand, at lower energy, the excitation spectra of **4**-**7** in PMMA present a better overlap with the CT bands observed in the absorption spectra (**Figure A3.14**). Therefore these bands are assigned to the CT state directly populated upon absorption. Contrarily, comparing the excitation spectra of **4**-**7** in PMMA with the corresponding solid forms (**Figure 3.5**, **Table 2**) we can see that both crystalline and amorphous samples present their CT bands always strongly red-shifted respect to PMMA. This depends on the fact that contrarily to the localized transition (blue region) that remain more and less the same, the CT transition is very sensitive to both the environment and packing effect. In particular, we can see that both solid samples obtained from **4** and **5** present only one CT band that we assign to the CT involving the phenoxazine. On the other hand, two different bands are clearly visible in the excitation spectra of the solid samples obtained from **6** and **7**. We assign these two bands to the two different CT transitions, involving carbazole (higher energy) and phenoxazine (red region) (reported in **Table 2** as CT1 and CT2 respectively). Moreover, if we consider in the excitation spectra (**Figure 3.5**) the CT bands relatively to LE transition, we can notice that the CT bands of all solid samples are always more intense respect to the corresponding CT bands of the molecule dispersed in PMMA. On the other hand, the CT bands of the different solid samples obtained from molecule **4** present similar intensity relative to LE transition. Contrarily, as regarding the **5**-**7** solid samples**,** we can see that the crystalline samples present the CT bands always more intense than that of the amorphous ones. This evidence that the CT transition is more favoured in the more crystalline samples obtained from these compounds. A possible explanation could arise from the fact that the alignment of molecules dipoles in the crystal, leads to an enhanced CT transition. In fact, as the CT transition mostly depends on the dipole moment between donor and acceptor moieties, to a higher dipolar moment in the ground state, corresponds a stronger CT transition between donors and acceptor.

Overall, the excitation spectra allow to confirm that that the bathochromic shift observed in the emission of the crystalline and amorphous phases respect the corresponding molecules dispersed in PMMA, depends on the variation of the CT state energy which, as already explained before, could be caused by different factors, i.e. change of polarity, change in dielectric constant and change of the molecular conformation. However, contrarily to the emission study, any particular trend can be observed between the excitation spectra of the crystalline phase or between the amorphous ones. The comparison between the excitation spectra of the crystalline samples and that between the different amorphous samples are reported in **Figure A3.15**.

Table 2: Summary of excitation photophysical properties of the different solid samples.

	PMMA, λ_{max}			fSVA, λ_{max}			fDCM150°, λ_{max}			fTOL, λ_{max}			fDCM200°, λ_{max}			fDCM, λ_{max}		
	CT1 CT2	LE	Ons. (eV)	CT1 CT2	LE	Ons (eV)	CT1 CT2	LE	Ons. (eV)	CT1 CT2	LE	Ons. (eV)	CT1 CT2	LE	Ons. (eV)	CT1 CT2	LE	Ons. (eV)
4	415 366	366	2.60	478	363	2.36	477	364	2.32	464	365	2.38	-	-	-	465	362	2.31
5	424, 400 (s)	368	2.54	464	368	2.33	477	367	2.36	454	367	2.36	-	-	-	454	367	2.36
6	446 406	361	2.44	544 460	364	2.07	476 421	361	2.31	490 418	362	2.15	498 416	363	2.16	460 (s) 415	365	2.35
7	465, 414	360 (s)	2.37	511 424	362	2.16	508 426	364	2.13	490 423	361	2.25	-	-	-	478 422	362	2.21

5. TIME-RESOLVED STUDY AND TADF PROPERTIES.

The time-resolved photoluminescence study of the different solid forms allow to have more information about the different phases present in our samples along with to understand if they also present TADF emission. In particular, in this work, thanks to the time-resolved study it is possible to understand if one sample contains only one molecular configuration or more than one.

The samples studied by time-resolved spectroscopy were prepared using the same techniques as the steady-state study, however, the substrates were different (Sapphire instead of Quartz). Nevertheless, the emission of the samples obtained in the time-resolved study follows the same trend as the steady-state one. This is particularly visible from the emission at the initial delay time (very close to that at longer delay time) for all the **4**-**7** solid samples, reported in **Figure 3.6**. In fact, except in **4**fTOL (that looks more amorphous), all the other solid samples obtained from **4**-**7** molecules respect the same trend as the steady-state emission, e.g. the more crystalline samples present a hypochromic shift and a narrowed emission respect to the amorphous ones. Furthermore, as it was observed in the steady-state study, **6**fSVA (red polymorph) presents redshift respect to all the other samples (**6**fDCM200, **6**fDCM, **6**fDCM150). Finally for **7** the two different polymorphs **7**fSVA and **7**fTOL (different onset and maxima) are also clearly visible.

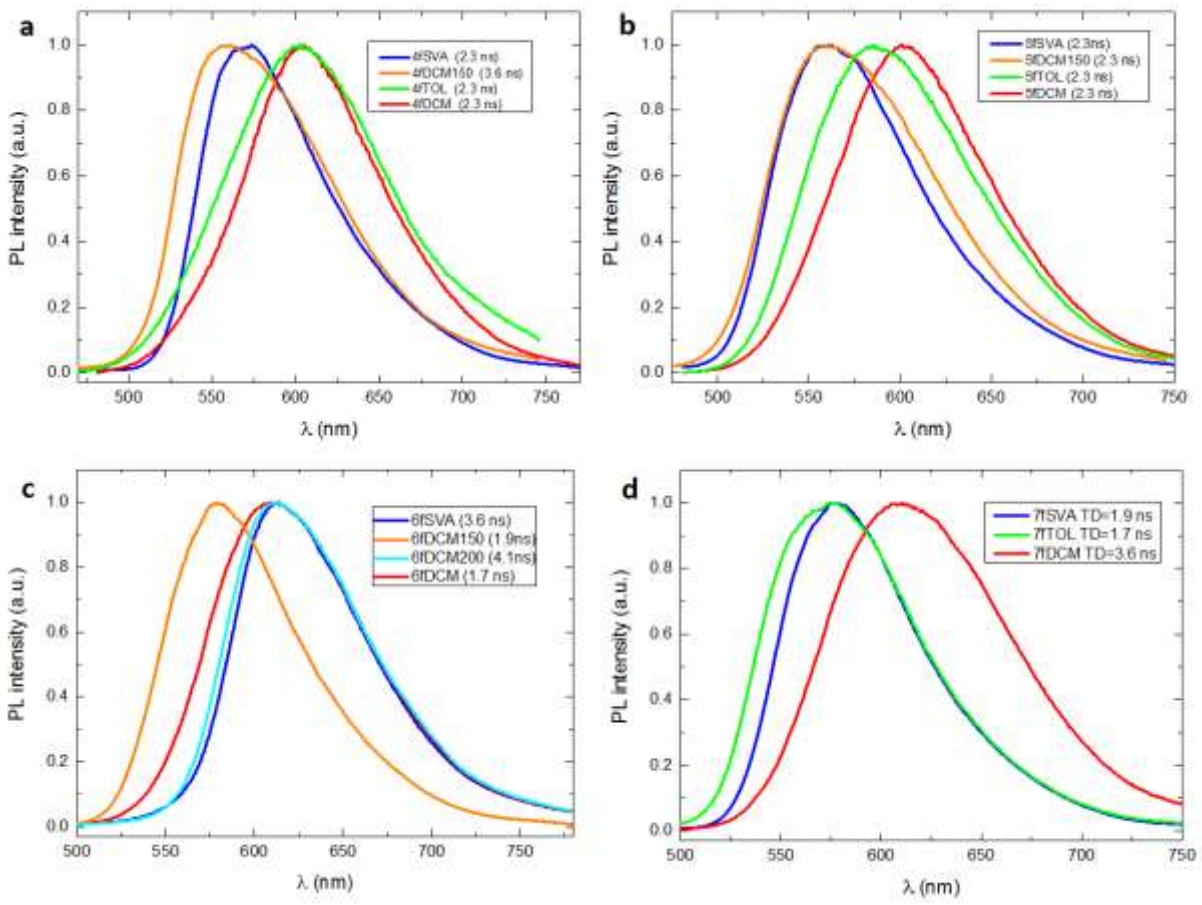

***Figure 3.6**: time-resolved PL spectra at initial time of the various solid forms obtained from molecules: **a) 4**, **b) 5**, **c) 6** and **d) 7**.*

The complete time-resolved study (short and long delay times) with the delayed fluorescence intensity dependence on power lasing are reported in **Appendix** (**Figures A3.15**-**A3.31**). The steady-state and time-resolved photophysical properties of the different solid forms are summarized In **Table 3**. In all cases, the decays present a typical behaviour of TADF materials. Furthermore, the strictly linear dependence of the DF intensity with laser power confirms the presence of TADF in all samples. From the emission at different delay times, it is possible to evaluate the number of molecular configurations present in our samples. In particular, when the emissions at different times remain the same it means that the emission arises from the same excited state and therefore is present only one molecular configuration. These systems are fitted with a mono-exponential decay. On the other hand, if the emission is slightly different for the

different time delays and present a bi- or multi-exponential decay, it means that the emission arises from different excited states of molecules that present different configurations[8].

In particular, a different emission for different delay times is visible in the more amorphous samples: **4**fDCM (**Figure A3.15a**), **5**fDCM (**Figure A3.20a**), **5**fTOL (**Figure A3.21a**), **6**fDCM (**Figure A3.25a**) and **7**fDCM (**Figure A3.30a**). All of them are fitted also with a bi- or multi-exponential curve, which furtherly indicates their inhomogeneity and the presence of molecules with different configurations. On the other hand, in the crystalline samples, the emission doesn't change for the different delay times. In particular, the PF and DF of **4**fSVA (**Figure A3.18**) and **4**fDCM150 (**Figure A3.17**) are perfectly overlapped and both present a mono-exponential fitting in both PF and DF region which confirms their good homogeneity and the presence of a singular molecular configuration. Also, **4**fTOL (**Figure A3.16**) presents a mono-exponential decay in both DF and PF but the very weak DF makes the emission at longer delay time very noisy. In **5**fSVA (**Figure A3.23**) the PF and DF are the same and both PF and DF present a mono-exponential decay. In **5**fDCM150 (**Figure A3.22**) the PF and DF are also the same but in this case, the DF is fitted with a bi-exponential decay, thus indicating that a small number of molecules remain in a more amorphous phase. For **6**fSVA (**Figure A3.28**), **6**fDCM200 (**Figure A3.27**), and **6**fDCM150 (**Figure A3.26**) the emission remains the same for all different delay times, and all decays are fitted with a mono-exponential function, which confirms the presence of only one molecular configuration. Finally, in **7**fSVA (**Figure A3.32**) and **7**fTOL (**Figure A3.31**) the PF and DF are very close but the decay in the DF region is bi-exponential. This is probably due to the presence of a small number of the second polymorphs in one sample and vice versa in the other.

In order to analyse the TADF properties, the best parameter to consider is the DF/PF ratio (**Table 3**) which indicates the amount of TADF produced respect to the prompt fluorescence. Comparing the DF/PF values of the different samples with their QYs, it is possible to understand when the TADF works better. In particular, if both DF/PF and the PLQY increases, it means that the triplets harvesting due to the TADF mechanism works better. Contrarily, if the PLQY increases but the DF/PF decreases, it means that the improvement depends on the more efficient PF. First of all, we compare the DF/PF of the molecules dispersed in PMMA (**Table A3**) with that corresponding to solid phases (**Table 3**). After, we compare the DF/PF of the different solid phases. For molecule **4**, the DF/PF ratio decreases from PMMA to the crystalline samples (**4**DCM150 and **4**fSVA), but a higher QY is obtained in the crystalline samples. Therefore the enhanced emission in the crystal is caused by the reducing of the non-radiative paths affecting the PF thanks to the rigid crystal effect. On the other hand, the crystalline samples present a DF/PF 2-3 times higher than the amorphous ones (**4**fDCM and **4**fTOL). In **5**PMMA the DF/PF is

[8] As the rigid environment (especially the crystalline one) prevents all possible molecular relaxation upon excitation we can exclude that the different emission (in the red region) arise from a geometry relaxation.

similar to **5**fSVA but the QY of **5**fSVA is 1.6 times higher respect to **5** in PMMA. Therefore, in this case the crystallinity has a good effect on both PF and DF. The amorphous phases (**5**fDCM and **5**fTOL) present the lower QY but the DF/PF of **5**fDCM doesn't decrease as much as in the other cases, remaining even higher than **5**fDCM150. As regarding **5**fTOL (amorphous), it presents the lower DF/PF which is comparable with the other amorphous phases obtained for the other molecules. From these considerations, it would seem that in this case we obtained a more ordered phase in **5**fDCM. In fact, in **Figure 3.6c** we can notice that **5**fDCM present a more narrowed emission than **5**fTOL (114 Vs 97 nm). For molecule **6** the DF/PF strongly decreases from **6** in PMMA to all the other solid samples. In this case **6**fDCM150 presents the best values among the others. However, as all DF/PF are very similar, molecule **6** doesn't show any particular TADF improvement in the crystalline phases. Finally, in **7**fTOL the DF/PF is higher respect to **7**PMMA. Moreover, the DF/PF of the polymorph present in **7**fTOL is higher than that in **7**fSVA. Contrarily, both DF/PF and QY strongly decrease in the amorphous **7**fDCM. The highest DF/PF in **7**fTOL respect to both PMMA and **7**fSVA indicates that the TADF is enhanced in this crystalline sample. However, the higher QY of **7**PMMA (15.1) respect to **7**fTOL (9.1) suggests that part of the molecules remain in a less emissive configuration

Besides the alterations of the steady-state photophysical properties in the different solid forms demonstrated in the previous section, from the time-resolved study we also obtained further indications, and we observed that the crystal phase can also improve the TADF properties, especially respect to the amorphous ones. This depends on the fact that the ordered packing in the crystal, allows to select and to block the molecule in only one molecular configuration that can lead to a decrease in the triplet singlet energy gap. This is particularly valid, especially when a higher PLQY in the crystalline phase corresponds also to an increase of TADF (DF/PF). On the other hand, in the more amorphous samples different molecular configurations are allowed, and every configuration is characterized by a CT state with different energy. It results that the different CT states formed in the different solid forms, can either promote or break down the TADF, because of the tuning or detuning between ^{1}CT and ^{3}LE energy. On the other hand, the localized states are not affected by the variation of the molecular configuration.

Table 3: Summary of Time resolved Photophysical Properties.

	$\lambda_{st.st.}$ (nm)	λ_{PF} (nm)	$S_{1,ons}$ (eV)	τ_1 (ns)	τ_2 (μs)	τ_3 (μs)	τ_4 (μs)	$\tau_{DF,av}$	QY, %	DF/PF
4fDCM	594	605	2.41	2.2	0.3	0.9	4.0	1.3	1.0	0.03
4fTOL	573	602	2.43	2.6	0.1	1.2	-	0.9	2.7	0.05
4fDCM150	573	560	2.43	4.0	1.4	-	-	1.4*	3.3	0.09
4fSVA	561	573	2.38	4.0	1.2	-	-	1.2*	9.0	0.08
5fDCM	612	600	2.36	2.2	0.2	0.8	3.7	1.4	1.0	0.17
5fTOL	610	585	2.40	2.0	0.1	0.6	2.6	1.2	1.1	0.07
5fDCM150	574	562	2.46	4.6	0.4	2.8	-	2.2	4.1	0.15
5fSVA	567	562	2.44	8.7	0.7	-	-	0.7*	7.8	0.22
6fDCM	612	609	2.28	3.1	0.2	1.3	4.4	1.3	2.3	0.05
6fDCM150	598	579	2.37	4.3	2.5	-	-	2.5*	7.3	0.06
6fDCM200	621	612	2.21	3.3	1.0	-	-	1.0*	2.9	0.04
6fSVA	626	614	2.19	3.1	1.1	-	-	1.1*	2.4	0.04
7fDCM	620	611	2.30	2.2	0.03	0.3	2.0	1.6	1.8	0.05
7fSVA	600	577	2.35	4.6	0.3	4.9	-	4.2	8.5	0.16
7fTOL	585	574	2.39	5.2	0.3	5.6	-	4.7	9.1	0.26

λ_{PF}= emission maximum of prompt fluorescence, $S_{1,onset}$= onset energy of singlet, $\tau_{PF,av}$= average decay time of PF, $\tau_{DF,av}$= average decay time of DF, *: monoexponential, DF/PF= ratio between DF to PF emission.

6. MECHANOCHROMIC LUMINESCENCE.

In order to study the effect of the mechanical stress (or the stress due to the solvent) on the photoluminescence properties of our materials, in this section is reported the MCL study. Several cases of MC luminogens are reported in the literature whose emission is altered by changing their aggregated morphology[100]. The most common transformations in the MCL materials are from a crystalline to an amorphous phase, from a stable to metastable liquid crystalline phase, or between two different crystalline phases. During this process, a variation of intermolecular interactions, such as π−π interaction, dipole−dipole interaction, or hydrogen bond occurs and alter the states involved in the photophysical process.

In the MCL study, we didn't use the samples obtained in the previous study, as it was difficult applying a mechanical stress on the quartz substrates. However, we studied the MCL properties of the **4**-**7** initial materials received directly as a synthesis purified product[9], which showed a similar emission to that of the materials deposited on the quartz substrates. In particular, the initial materials visually looked as multi-crystalline powders, or single crystals, or amorphous

[9] Notably, different phases were obtained from the purified compound of synthesis. For the XRD analysis were selected only the single crystals obtained upon recrystallization. In some cases a visually amorphous powder or multi-crystalline powder was also obtained after purification.

powders (**Figure A3.5-A3.8**). Hence, on all initial phases, we applied mechanical stress through grinding the materials with a pestle in a mortar. The obtained grinded materials were also directly exposed to the effect of solvents with different polarities (a drop of solvent), which follows a successive grinding. It is important to underline that the spectra obtained in this study were obtained using the setup described in the experimental section (**§3.5**). However, the emission detected by the CCD is not corrected with the emission of a standard lamp, and therefore in MLC measurements, we can observe a slight shift respect to the steady-state spectra. The emissions of the of **4**fSVA, **6**fSVA, **6**fDCM200, **6**fDCM150, **6**fDCM, **7**fSVA, **7**fTOL and, **7**fDCM150 were also measured with MCL setup and their λ_{max} are reported in **Table 5** in comparison to that obtained with the fluorimeter. In **Table 4** are reported the emission maxima for all the different phases obtained in the MCL study.

6.1 Molecule 4.

The initial crystalline powder of compound **4** presents a bright yellow emission similar to **4**fSVA (**Figure 3.7**). When the material was grinded (grinding #1), an initially bathochromic shift to orange was observed (**Table 4**). Continuing to grind more vigorously (grinding#2) the emission further shifts to red with a visible brightness decrease. This emission matches with **4**fDCM (steady-state study), thus indicating the formation of the amorphous phase. On the other hand, the orange emission in grinding #1, indicates the presence of a mixture between crystalline and amorphous phases. When the obtained grinded powder of **4** was exposed to DCM, the emission furtherly red-shifts, thus indicating that even after the second grinding, not all crystalline domains were completely destroyed. The obtained grinded powders were then exposed to toluene, which blue-shifted the emission back to 582 nm, indicating the reformation of the crystalline form, according to what was observed in the previous study in **4**fTOL. Finally, the material was grinded again, and the bathochromic shift to 601 nm indicates the formation of the amorphous phase.

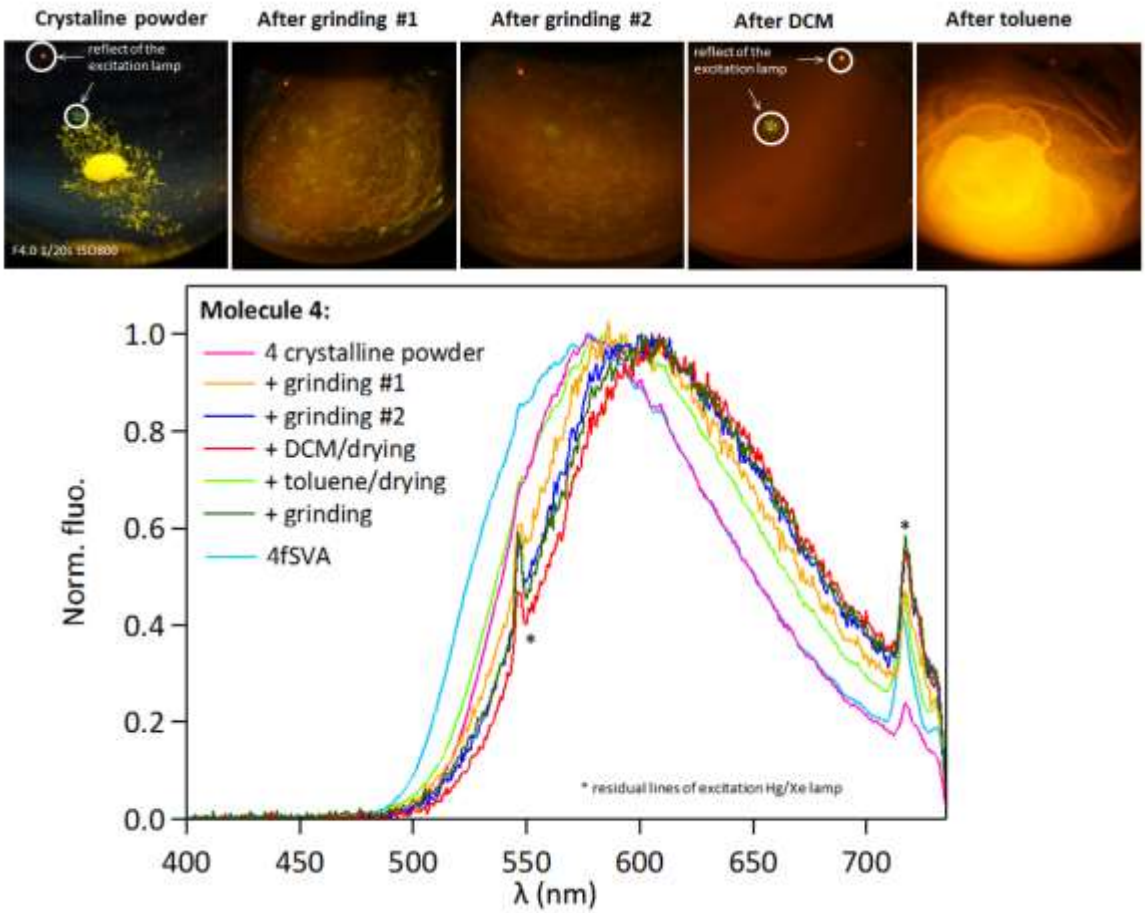

Figure 3.7*: MLC study for molecule* ***4****: **top)** photographs of various forms obtained during the MCL study (the photographs were taken at 365 nm excitation); **bottom)** PL spectra of the various forms studied in MCL, and PL spectra of* ***4****fSVA obtained with the MCL setup.*

6.2 Molecule 5.

The initial crystalline powder of **5** presents also a yellow emission (**Figure 3.8**), similar to **5**fSVA (steady-state study) which upon grinding red shifts (**Table 4**), thus indicating the formation of the amorphous phase. When the obtained grinded powder is exposed to DCM, the emission slightly redshifts of only 5nm, indicating that after grinding few molecules remained in a more crystalline configuration. Finally, when the powder was exposed to toluene, the emission didn't evolve much, and only a slight hypochromic shift was observed (**Figure 3.8**). In this case, the effect of toluene didn't change the amorphous phase, and this is in line with what was observed in **5**fTOL (steady-state study).

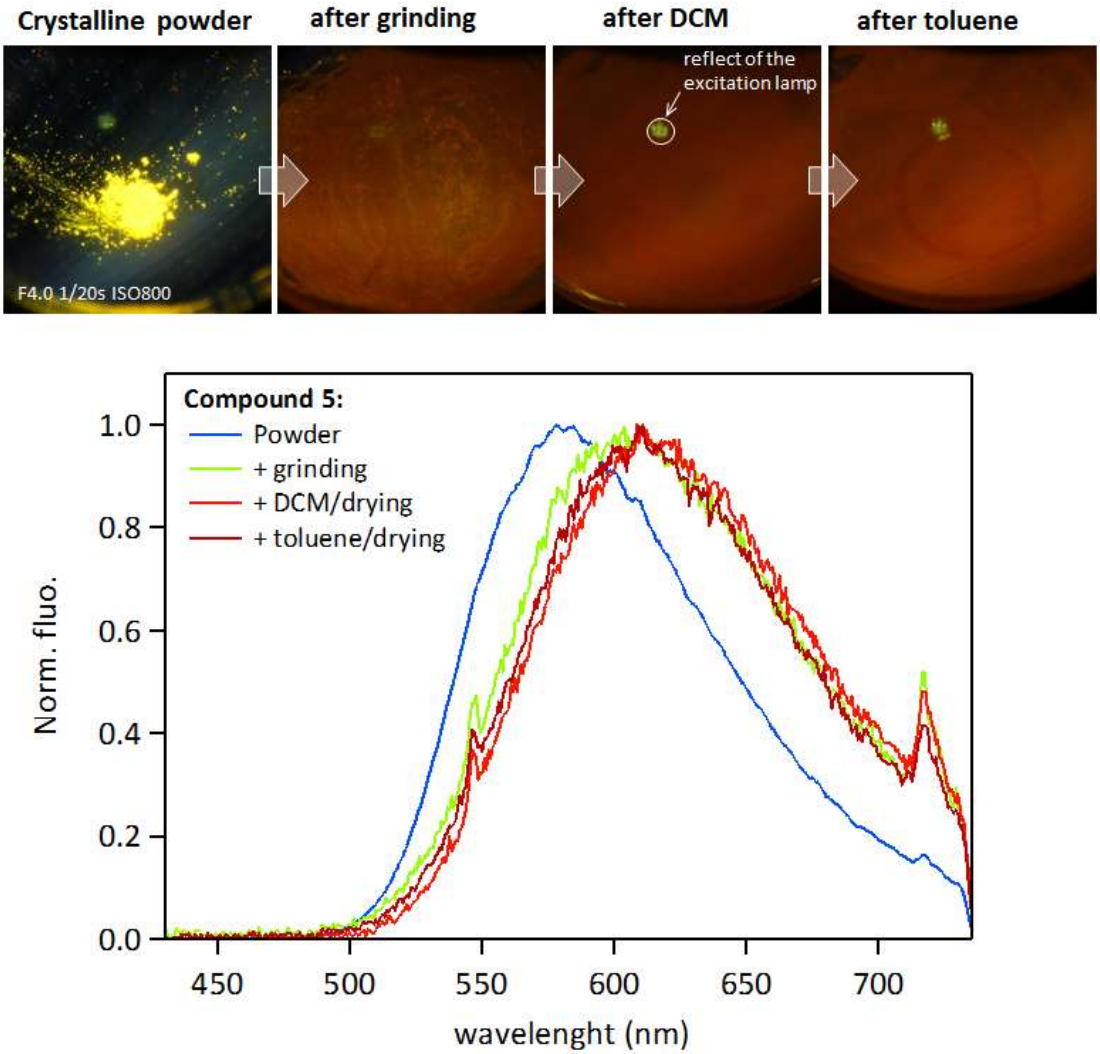

***Figure 3.8**: MLC study for molecule **5**: **top)** photographs of various forms obtained during the MCL study (the photographs were taken at 365 nm excitation); **bottom)** PL spectra of the various forms studied in MCL study.*

6.3 Molecule 6.

Regarding compound **6**, we have two different initial solid powders. The first one reported in **Figure 3.9** and **Figure A3.7** looks like a polycrystalline red powder and present a narrowed emission with maxima at 629 nm, similar to **6**fSVA (steady state). In **Figure 3.9** are also reported the spectra of **6**SVA and **6**fDCM200 collected with the MCL setup. However, although they appear not well resolved we can notice that they follow a similar profile of the polycrystalline red powder. Grinding the polycrystalline red powder, interestingly we observed a remarkable hypochromic shift of 18 nm along with a more broadened emission. This presents a similar emission of **6**fDCM indicating that we obtained the amorphous phase. The blue shift after grinding is an unusual MCL

behaviour as in general the amorphous phase is red-shifted respect to the crystalline one. However, what we observed here is in line with what we observed in the red polymorph present in **6**fSVA, which presents bathochromic shift respect to the amorphous **6**fDCM.

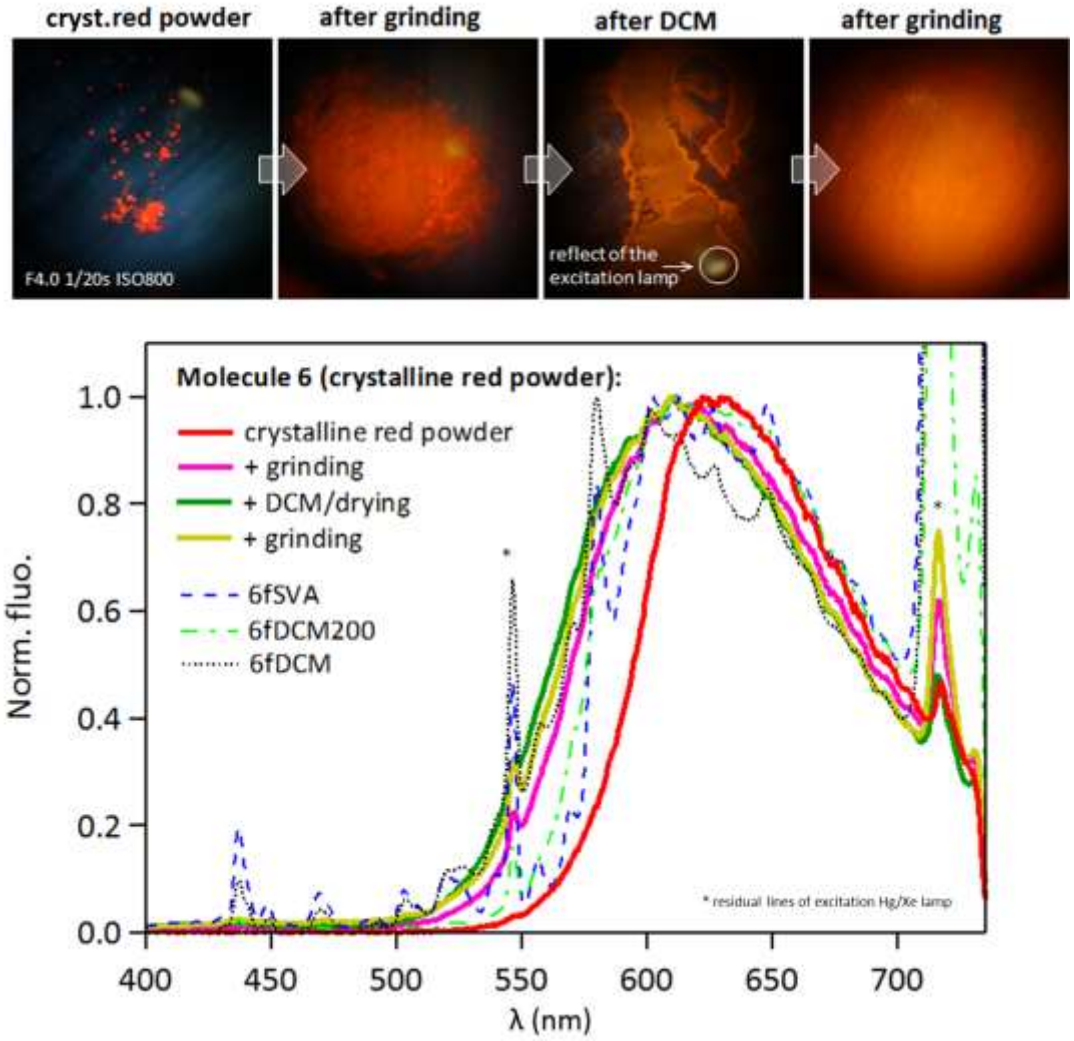

Figure 3.9*: MLC study for molecule **6** (crystalline red powder): **top)** photographs of various forms obtained during the MCL study (the photographs were taken at 365 nm excitation); **bottom)** PL spectra of the various forms studied in MCL, and PL spectra of **6**fSVA, **6**fDCM200 and **6**fDCM, obtained with the MCL setup.*

The second initial form of **6** is reported in **Figure A3.7** (**circle**) and **Figure 3.10,** and visually appears as an orange crystal (610 nm). Grinding the crystal, the emission becomes broadened but blue shifts of 9nm. We can see that this emission of the grinded crystal is practically the same as **6**fDCM150 collected with the MCL setup (**Figure 3.10**). However, the blue shift of the grinded orange crystal is in contrast with what we expected, in fact, in this case, it seems that the

mechanical stress switches the material to another crystalline phase. When the material is exposed to toluene a further strong hypochromic shift of 23 nm is observed. The yellow and narrowed emission, along with the blue shifted onset, indicate the formation of a new polymorph. Grinding the yellow material, in this case, it is observed that the emission becomes more similar to the amorphous **6**fDCM, therefore, in this case, we can attribute this behaviour to the formation of the amorphous phase. Notably, the amorphous phase presents the same maxima as the orange crystal, however, it presents a larger FWHM (121 nm) respect to that of the orange crystal (FWHM=97nm). Furthermore, the amorphous phase emission starts before (in the blue region) and dies after (red region). These observations indicates that in the crystal there is only one of the molecular configurations present in the amorphous phase.

By comparing the steady-state of the materials deposited on quartz with the phases obtained in the MCL study, we can make some interesting observations. Firstly, we can notice that in the steady-state study on quartz we observed two polymorphs, one (red polymorph) present in both **6**fSVA (626nm) and in **6**fDCM200 (621nm), and the other (orange polymorph), present in both **6**fDCM150 (598nm) and **6**fTOL (598 nm). The amorphous phase was obtained in **6**fDCM (612nm). On the other hand, in the MCL study we started from two different polymorphs, both present in the initial material: one as red crystalline powder (629nm) and one as orange crystal (611nm). When the orange crystal was grinded we obtained the same spectra of the polymorph present in **6**fDCM150. After exposing the grinded powder to toluene we obtained a more yellowish emission (578 nm). These considerations demonstrate that in the MCL study appears two new polymorphs respect the quartz samples. The one at 578 nm (after toluene) and the other at 610 nm, present in the initial orange crystal.

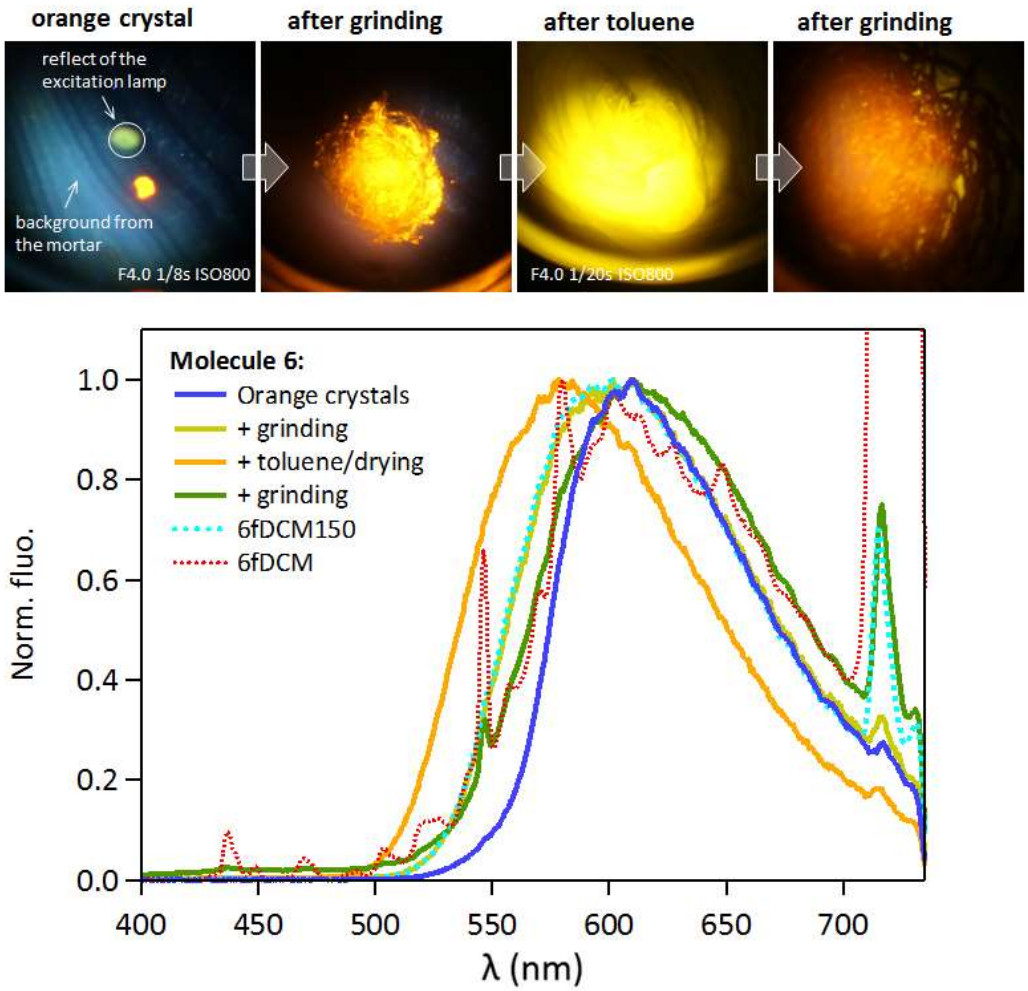

***Figure 3.10**: MLC study for molecule **6** (orange crystal): **top)** photographs of various forms obtained during the MCL study (the photographs were taken at 365 nm excitation); **bottom)** PL spectra of the various forms studied in MCL, and PL spectra of **6**fDCM150 and **6**fDCM obtained with the MCL setup.*

6.4 Molecule 7.

Compound **7** also present two different forms in the initial powder: one that visually looks as a multi-crystalline orange powder (601 nm) reported in **Figure 3.11**, and the other that looks like an amorphous red powder (621 nm) reported in **Figure 3.12**.

The multi-crystalline orange powder has similar emission as **7**fSVA (**Figure 3.11**). After grinding the crystalline powder, the emission redshifts and becomes broadened and very similar to **7**fDCM, thus indicating the formation of the amorphous phase.

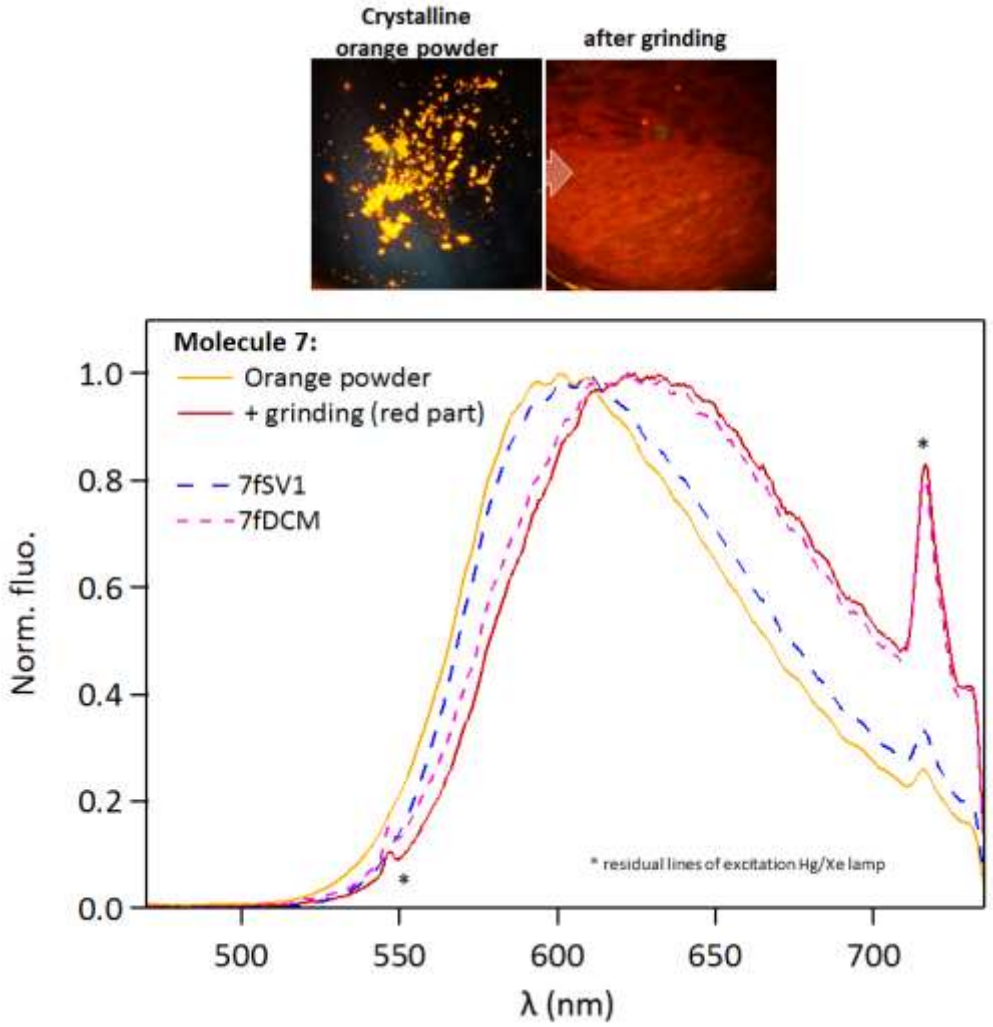

Figure 3.11*: MLC study for molecule* ***7*** *(orange crystalline powder):* ***top)*** *photographs of various forms obtained during the MCL study (the photographs were taken at 365 nm excitation);* ***bottom)*** *PL spectra of the various forms studied in MCL study, and PL spectra of* ***7****fSVA and* ***7****fDCM obtained with the MCL setup.*

In **Figure 3.12** is reported the MCL study of the red powder. We can observe that after grinding the powder, the emission maxima remain the same, but the spectra become broadened and the onset blue shifts. This indicates that the initial red powder contains a more ordered phase. However, we consider both as amorphous. Notably, the grinded powder presents the same emission as **7**fDCM. After exposing the grinded powder to DCM, we observed a negligible blue shift only on the edge part of the sample (emission not reported), and therefore we consider that under DCM the material remains amorphous. After exposing the grinded material to toluene we observed a strongly blue shift to 592 nm, whit the emission profile that becomes very similar to **7**fTOL. This confirms that the exposure to toluene favours the crystallization. A second grinding, redshifts again the emission back to the amorphous phase.

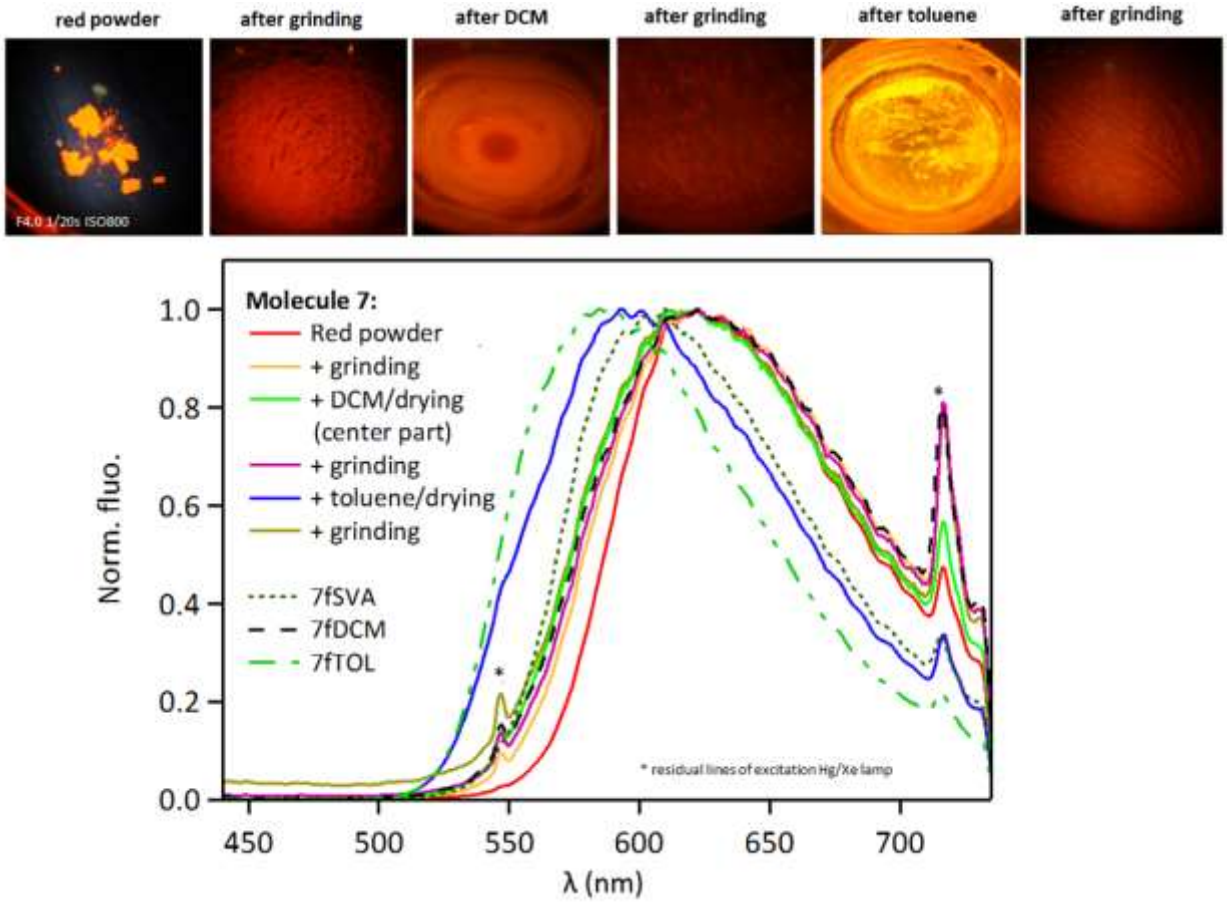

***Figure 3.12**: MLC study for molecule **7** (red powder): **top)** photographs of various forms obtained during the MCL study (the photographs were taken at 365 nm excitation); **bottom)** PL spectra of the various forms studied in MCL study, and PL spectra of **7**fSVA and **7**fDCM obtained with the MCL setup.*

Table 4: emission maxima of the different phases obtained in the MCL study.

	λ_{PL},nm (initial)	**+grinding λ_{PL},nm**	**+DCM/dryng λ_{PL},nm**	**+grinding λ_{PL},nm**	**+TOL/dryng λ_{PL},nm**	**+grinding λ_{PL},nm**
4 cryst. powd.	577	#1, 586 #2, 599	608	-	582	601
5 cryst. powd.	578	603	608		608	-
6 cryst-red powd.	629	611	610	-	609	-
6 orange cryst	610	601	-	-	578	610
7 crystal	602	624	-	-	-	-
7 red powder	621	621	621	621	592	621

Table 5: emission maxima of the samples deposited on Quartz (MCL setup and fluorimeter).

	MCL setup λ_{PL},nm	**Fluorimeter λ_{PL},nm**
4fSVA	577	561
6fSVA	626*	626
6fDCM150	600	598
6fDCM200	618	621
6fDCM	608*	612
7fSVA	607	600
7fTOL	585	585
7fDCM	622	620

* noisy spectra (extimated λ_{PL})

6.5 General remarks.

In the steady-state study (on quartz substrates), we demonstrated that for each **4**-**7** compound it is possible to obtain different morphologies presenting different photophysical properties by using different preparation methods. Interestingly, from the MCL study, we can see that similar results can be obtained by using external stimuli (mechanical and solvent) directly on the initial materials. For all **4**-**7** compounds, the mechanical stress produces a change of the supramolecular organization in the material that results in a different colour emission. In particular, all the crystalline initial forms studied in the MCL study present a similar emission of the crystalline samples obtained on the quartz substrates, using SVA, thermal annealing or in some case drop-casting (toluene). On the other hand, the grinded material present in general the spectra similar to the amorphous fDCM samples. Interestingly, in one case (**6** orange crystal) upon grinding the crystal, it was obtained a second blue-shifted polymorph. This is an uncommon behaviour. On the other hand, grinding the **6** red crystal a blue-shifted amorphous phase was obtained, which is also uncommon. All these considerations allow to understand the emission colour change, obtained in MCL study, originates from the alterations in the solid samples that produce the different molecular configurations under mechanical stress. This directly affects the energy of the CT states, characteristic of these molecules. Finally, the two new polymorphs obtained in MCL study for molecule **6**, beyond to confirm that a higher number of carbazoles favours the formations of more polymorphs, opens also the possibility to obtain a higher number of polymorphs also for the other molecules. This could be achieved by changing the crystallization parameters.

7. CONCLUSION.

In summary, the solid-state photophysical properties of four new D_1-A-D_{2n} compounds featuring a central benzonitrile acceptor moiety substituted with a phenoxazine and an increasing number of carbazole donors, are presented in this chapter. All compounds present emission properties tuned by the morphology of the solid i.e. crystalline polymorphs or amorphous phase. All the solid samples studied by steady-state and time-resolved measures were obtained using different preparation techniques. On the other hand, the MCL study was performed directly on the initial materials obtained after purifications and recrystallization. The XRD analysis allows to exclude the formation of strong π-π interaction that leads to observe the formation of aggregates emissive states. The emission of the initial crystalline powders detected with the MCL setup showed the same emission as the crystalline samples obtained from the same molecules on the quartz substrates. Interestingly, were obtained different polymorphs for molecules **6** and **7**. This seems to be correlated with the increasing number of carbazole donors that increases the possible molecular interactions giving the possibility to form different packing motifs in crystal structures. All different solid forms obtained from **4**-**7** present a red-shifted emission respect to the isolated molecules in PMMA, thus indicating that the aggregation downshifts the optical gap due to the different properties of the solid phase (polarity and dielectric constant). On the other hand, photophysical investigations reveal that the crystalline states show in general a blue-shifted emission relative to the amorphous forms, due to the presence of only one molecular configuration in which the CT state is at higher energy. In contrast, several molecular configurations are formed in the amorphous phase. Compound **6** is an exception since it presents two different polymorphs, one of which has a red-shifted emission respect to the amorphous form. All these compounds present good CIEE properties, as highlighted from a strong increase in the emission intensity from solution to crystalline solid state. Moreover, for each molecule, it is shown that the molecular configuration that presents the CT state higher in energy presents a higher PLQY. Remarkably all the solid samples show TADF properties, confirmed by the linearity of the emission intensity with the laser fluency. The TADF properties change for each compound between the different phases thus demonstrating that it is possible to tune the TADF in a material by changing the molecular geometry/conformation through the different supramolecular organizations present in the different phases. However, the TADF properties decrease for the most of solid samples respect to the isolated molecule in PMMA, though in some case there is also a weak improvement. In particular in **4**fSVA, **6**fDCM150 and **7**fSVA the CIEE effect arises only from the increased PF due to the restriction of intramolecular rotations in the crystalline form. On the other hand, in **5**fSVA and especially in **7**fTOL the CIEE effect enhances also the TADF properties of the materials. We also demonstrated that all the materials present multicolour changing MCL characteristics with good mechanoluminescent properties under external stimuli.

In particular, we demonstrated that the MCL is strictly correlated with the change between the different phases obtained with the different deposition techniques.

In conclusion, in this study, we demonstrated how molecular assembly and external stimuli, are parameters that play an important role in the control of the CT state energy, which influences both the colour emission and the TADF behaviour. However, further experiments are necessary, e.g. especially XRD analysis on the quartz samples and experiments in order to calculate the different polarity and dielectric constant of the different samples respect to PMMA. This will allow to go deeper into the parameters governing the changes of the photophysical properties of these materials. We think that based on the results obtained in this study, it would be worth to furtherly explore the supramolecular properties of multiple donors (D) attached to a single acceptor (A) moieties systems, in order to better understand the key factors that allow improving the solid-state photophysical properties in term of TADF, MCL and PLQY.

APPENDIX

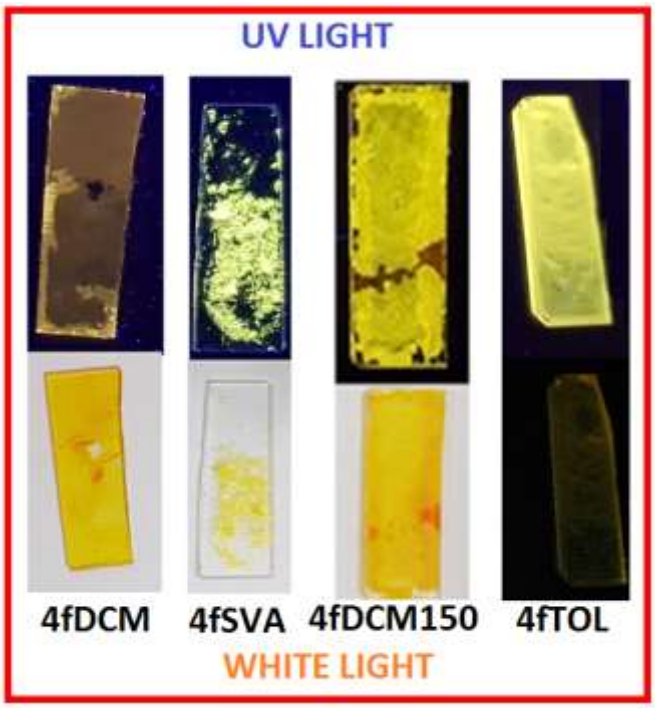

Figure A3.1: *Photographs of the various samples prepared with the different methods, taken under ordinary visible light and under UV lamp (360 nm) for molecule* ***4****.*

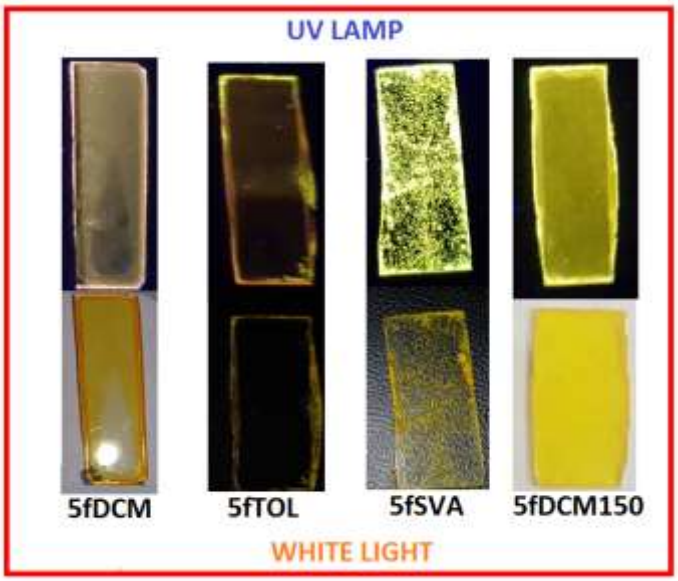

Figure A3.2: *Photographs of the various samples prepared with the different methods, taken under ordinary visible light and under UV lamp (360 nm) for molecule* ***5.***

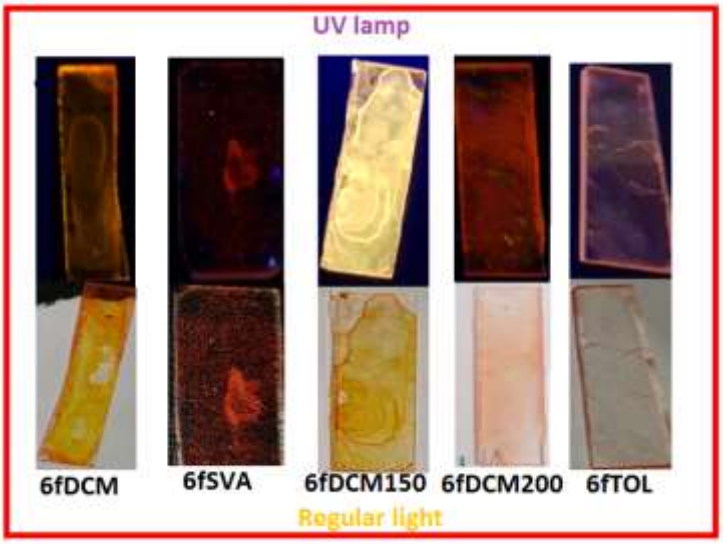

Figure A3.3: *Photographs of the various samples prepared with the different methods, taken under ordinary visible light and under UV lamp (360 nm) for molecule* ***6.***

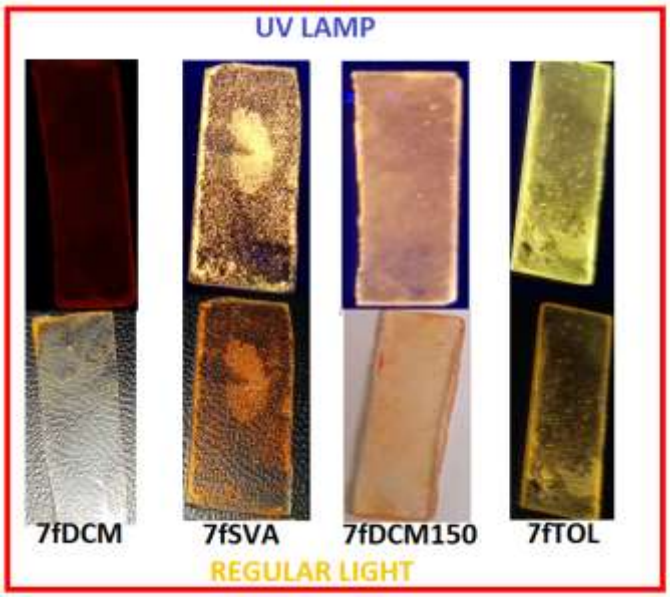

Figure A3.4: *Photographs of the various samples prepared with the different methods, taken under ordinary visible light and under UV lamp (360 nm) for molecule* ***7****.*

Figure A3.5 a) *Photographs of* ***4*** *initial crystalline powder under natural lamp* ***b)*** *Photographs of* ***4*** *initial crystalline powder under UV lamp.*

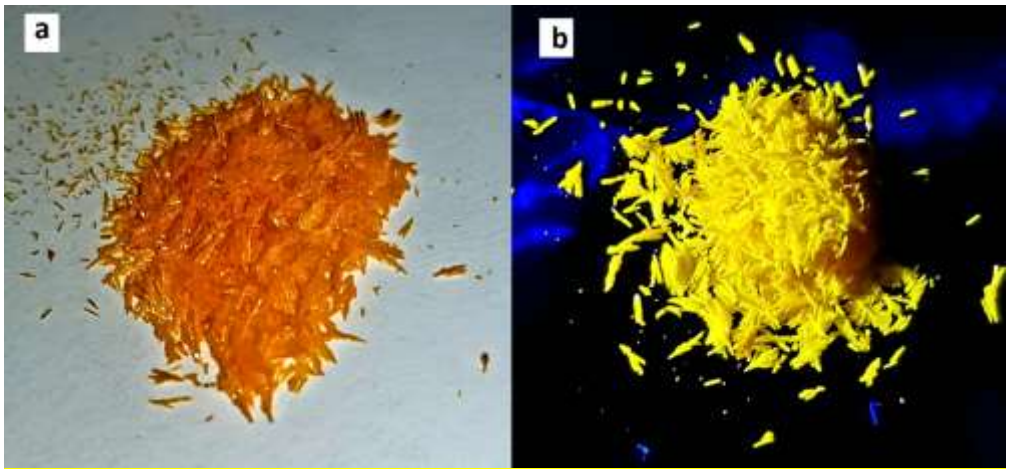

Figure A3.6 a) *Photographs of* ***5*** *initial crystalline powder under natural lamp* ***b)*** *Photographs of* ***5*** *initial crystalline powder under UV lamp.*

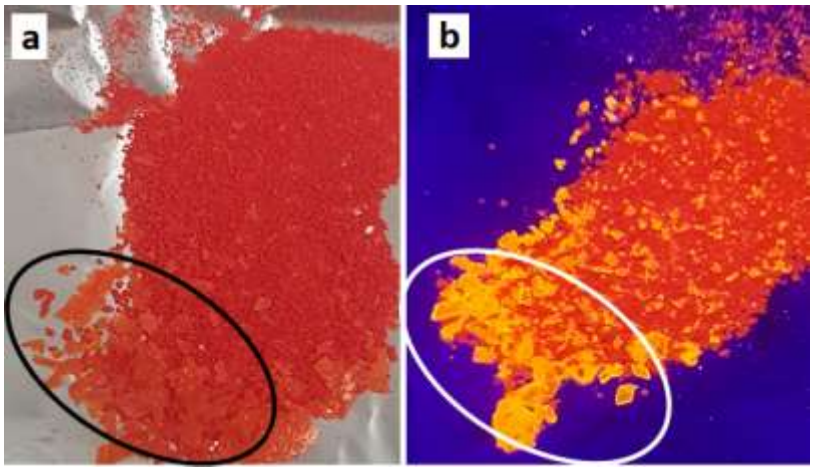

Figure A3.7 a) *Photographs of **6** initial red crystalline powder and **6** initial orange crystals (circle) under natural lamp **b)** Photographs of **6** initial red crystalline powder and **6** initial orange crystals (circle) under UV lamp.*

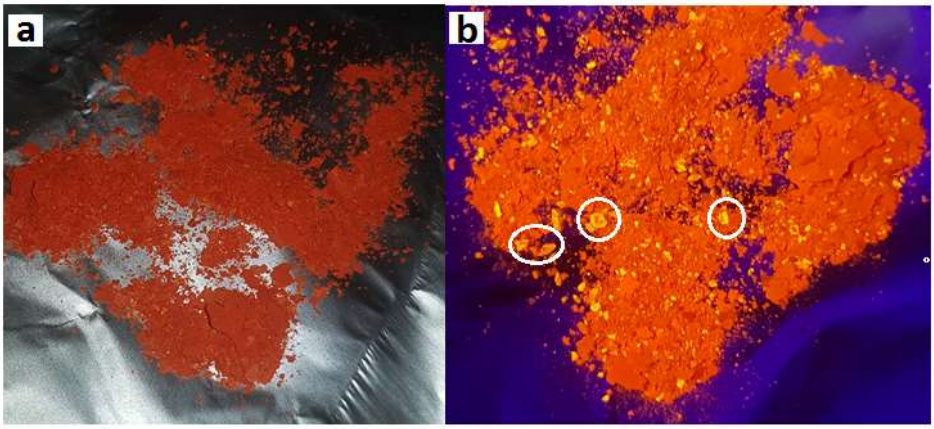

Figure A3.8 a) *Photographs of **7** initial red powder and **7** initial orange crystalline powder under natural lamp **b)** Photographs of **7** initial red powder and orange **7** initial crystalline powder (circle) under UV lamp.*

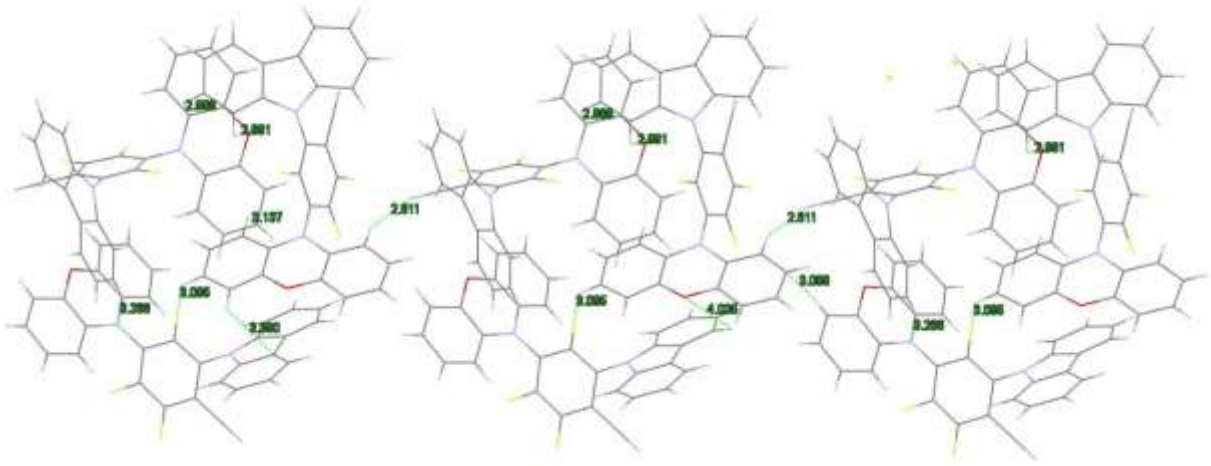

Figure A3.9**: molecular packing and intermolecular distances in crystal **4.

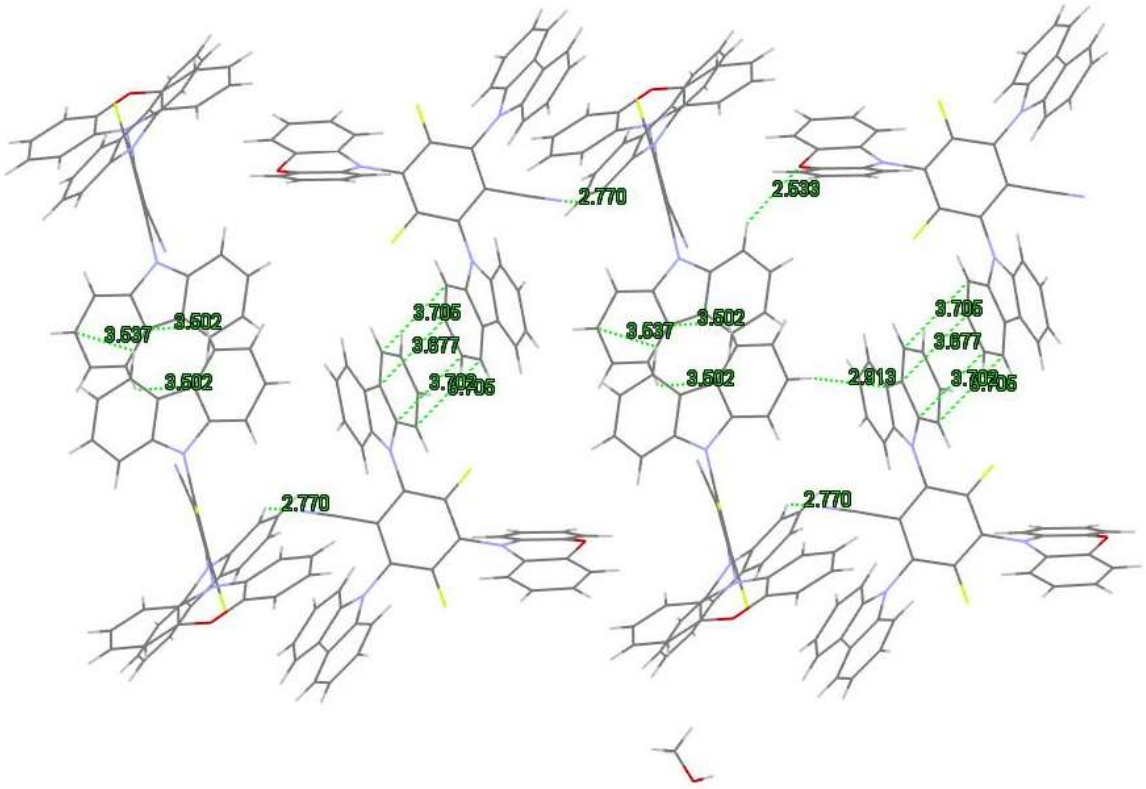

Figure A3.10**: molecular packing and intermolecular distances in crystal **5.

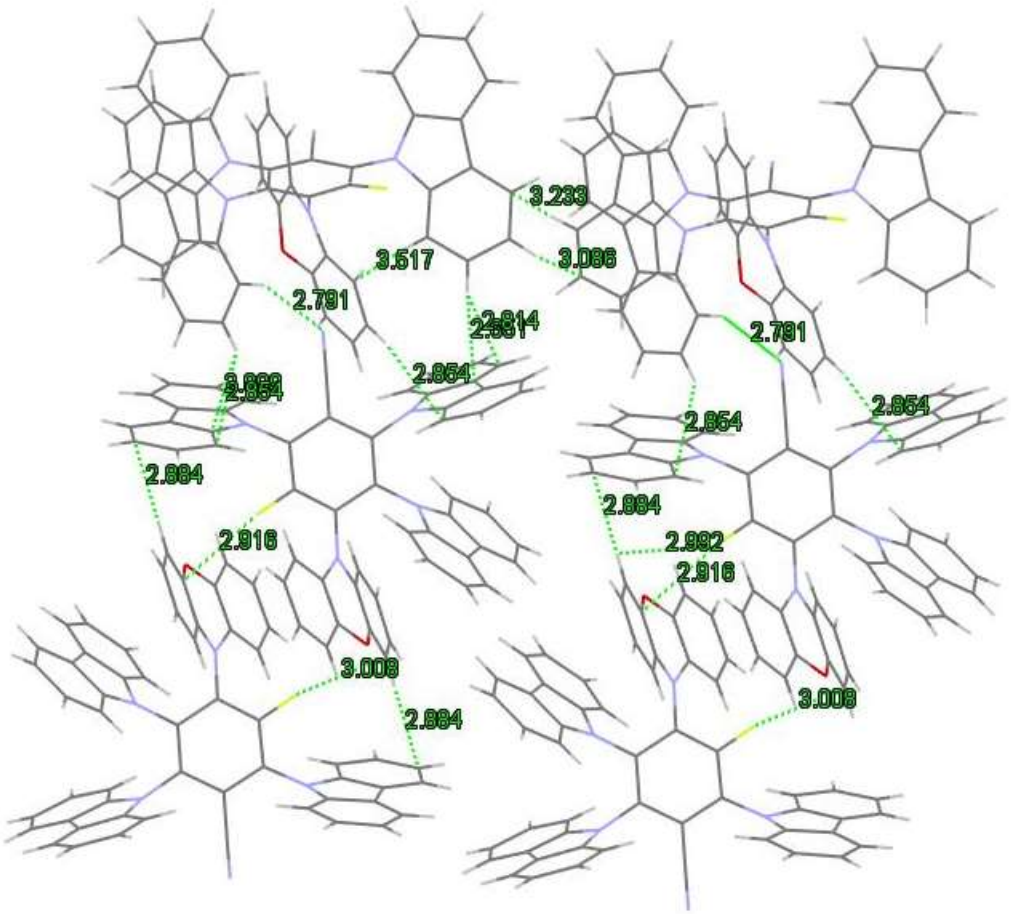

Figure A3.11*: molecular packing and intermolecular distances in crystal* ***6.***

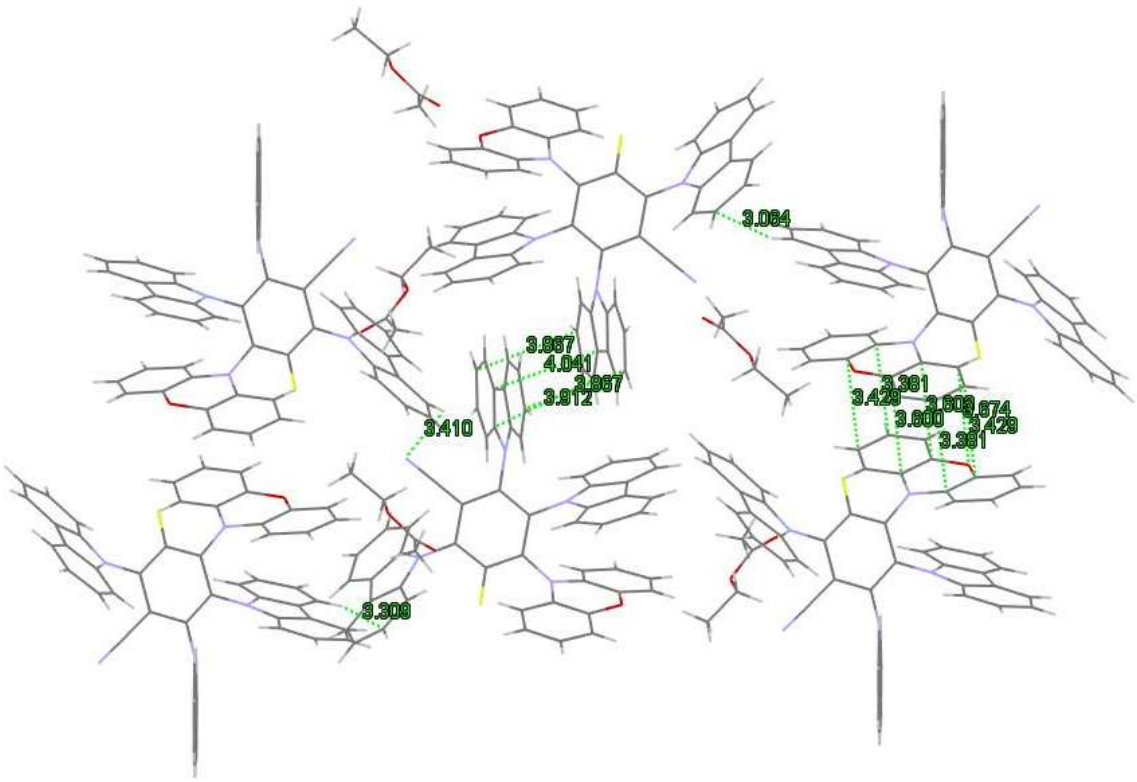

Figure A3.12**: molecular packing and intermolecular distances in crystal **6+solv.

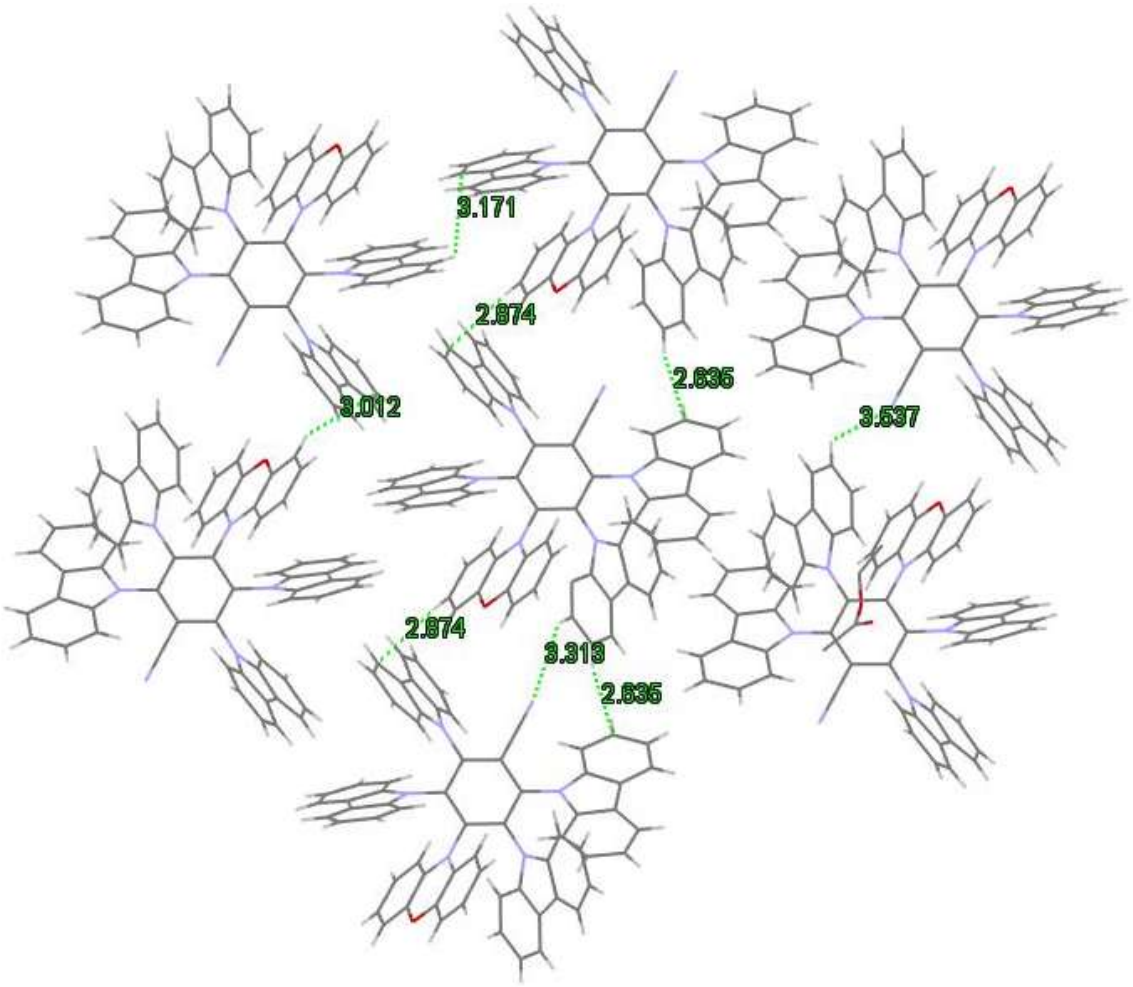

Figure A3.13: *molecular packing and intermolecular distances in crystal* **7**.

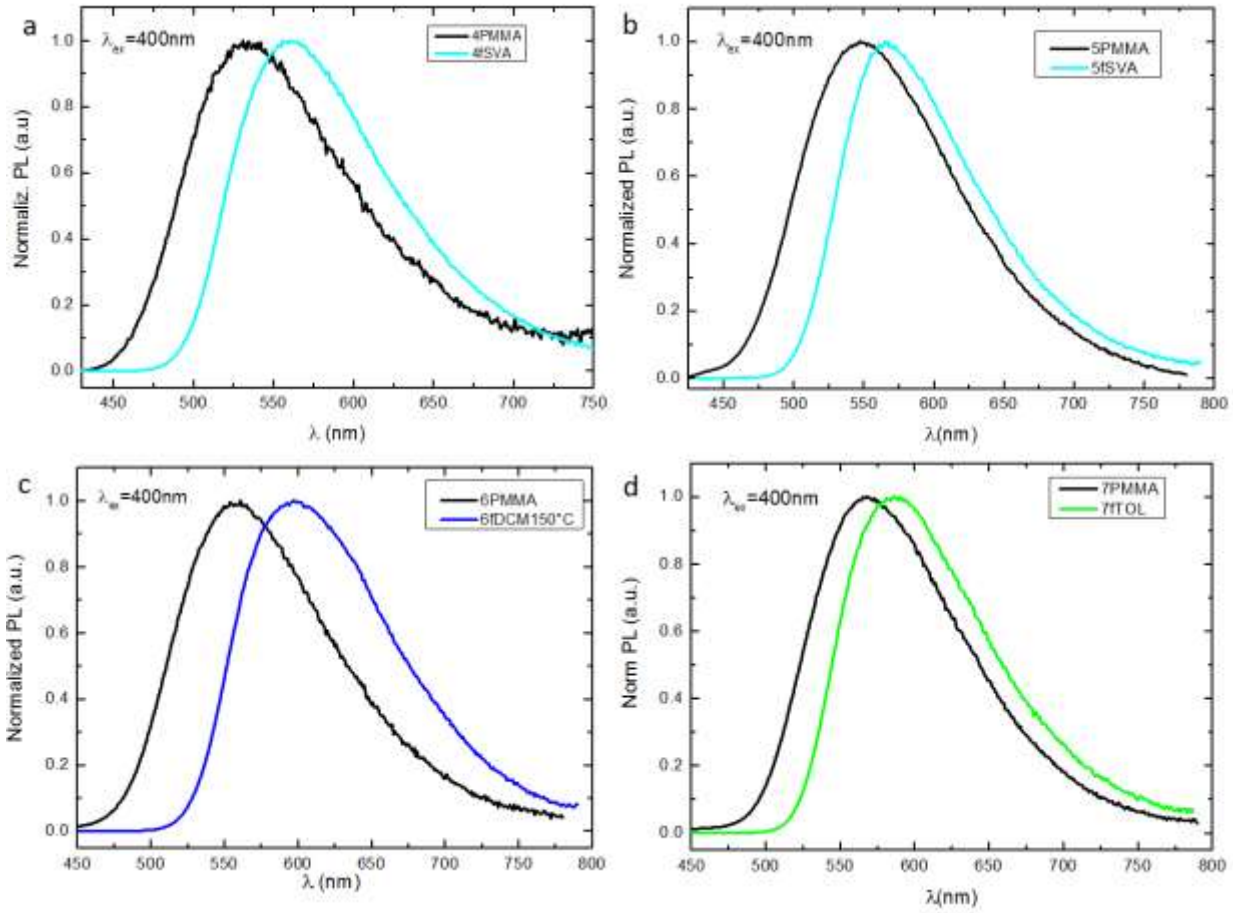

Figure A3.14*: Normalized fluorescence spectra (λ_{exc}=400 nm) of the more blue shifted crystalline form obtained for molecule* ***4****-****7*** *compared with the corresponding isolated molecule in PMMA.*

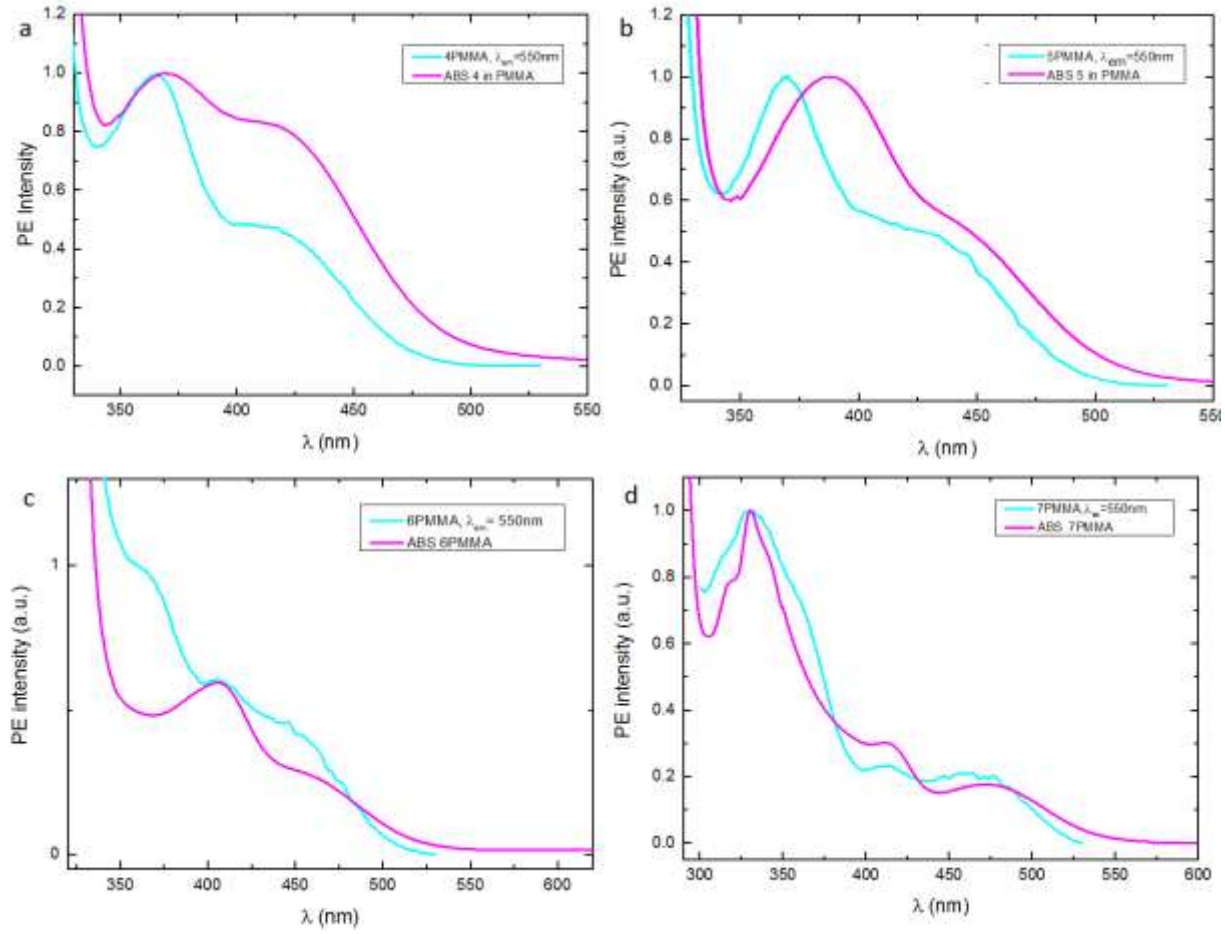

Figure A3.14*: comparison between the excitation and the absorption spectra of* ***4****-****7*** *molecules in PMMA.*

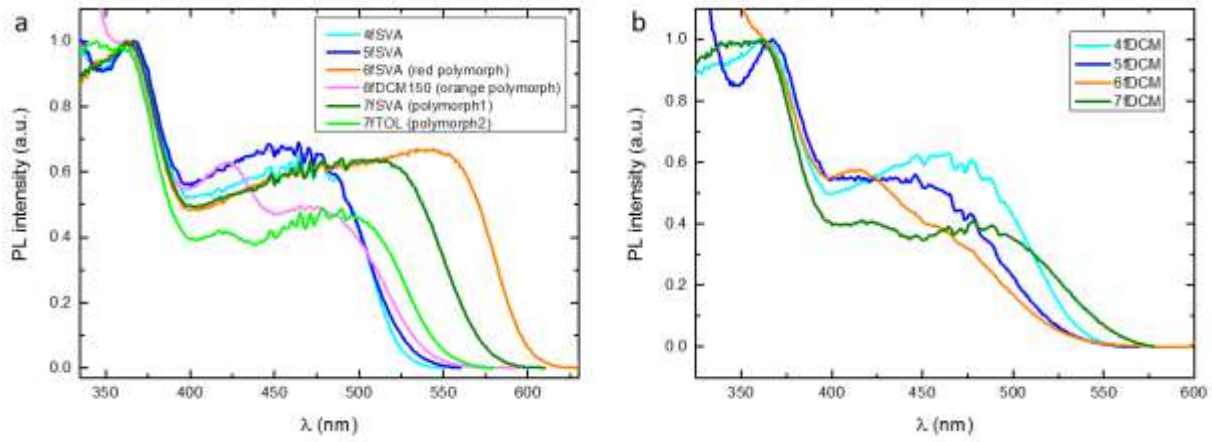

Figure A3.14*: **a)** comparison between the excitation spectra of the* ***4****-****7*** *molecules crystalline samples, and* ***b)*** *comparison between the excitation spectra of the different amorphous samples obtained from* ***4****-****7*** *molecules.*

Table A1: Summary of absorption photophysical properties in PMMA

Abs	PMMA, λ_{max} ,nm (CT1, CT2)	PMMA, λ_{max}, (LE), nm	PMMA, onset (eV)	Cyclohex, λ_{max} (CT1, CT2, LE), nm
4	416, 369	325, 312 ,287	2.56	426, 385, 368
5	440, 387	325, 313, 287	2.48	432, 391, 378(s)
6	453, 406	327, 316, 287	2.40	440, 404, 388(s)
7	471, 411	330, 320, 289	2.31	467, 411, 373(s)

Table A2: Summary of absorption photophysical properties in PMMA

Comp.	$\lambda_{PL, st.state}$	FWHM (nm)	Emiss. onset (eV)	Excitat. onset (eV)
4 in PMMA	535	116	2.70	2.60
5 in PMMA	548	129	2.66	2.54
6 in PMMA	560	122	2.58	2.44
7 in PMMA	567	123	2.51	2.37

Table A3: Summary of photophysical properties in PMMA

	QY,%[a]	$\lambda_{st.st.}$ (nm)	λ_{PF} (nm)	$S_{1,ons}$ (eV)	τ_1 (ns)	τ_2 (ns)	$\tau_{PF,av}$ (ns)	τ_3 (µs)	τ_4 (µs)	$\tau_{DF,av}$ (µs)	DF/PF
4PMMA	4.3 (5.2)	535	531	2.73	6.6	26.0	9.8	0.9	6.2	3.5	0.24
5PMMA	4.0 (4.9)	548	537	3.10	4.2	14.3	8.3	0.5	6.1	4.6	0.21
6PMMA	13.6 (15.9)	560	552	2.60	5.6	18.0	12.2	1.2	7.6	5.8	0.27
7PMMA	15.1 (18.1)	567	564	2.48	4.9	15.4	11.4	1.6	9.0	6.6	0.19

a: values in parenthesis measured in degassed conditions, λ_{PF}= emission maximum of prompt fluorescence, $S_{1,onset}$= onset energy of singlet, $\tau_{PF,av}$= average decay time of PF, $\tau_{DF,av}$= average decay time of DF,
*: monoexponential, DF/PF= ratio between DF to PF emission

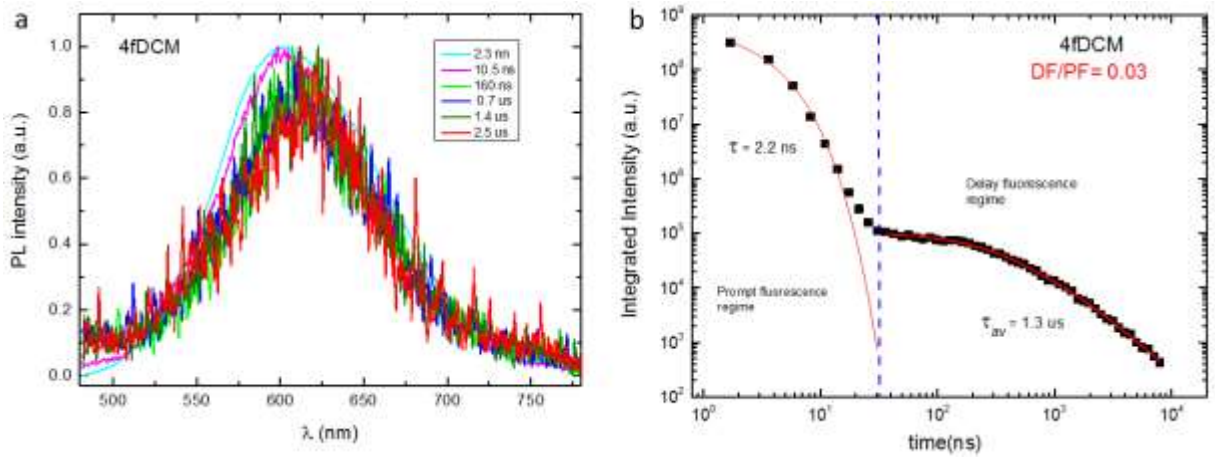

***Figure A3.15**: **a)** time-resolved emission spectra of **4**fDCM at room temperature (RT); **b)** decay curve of **4**fDCM at RT. λ_{ex}= 355 nm.*

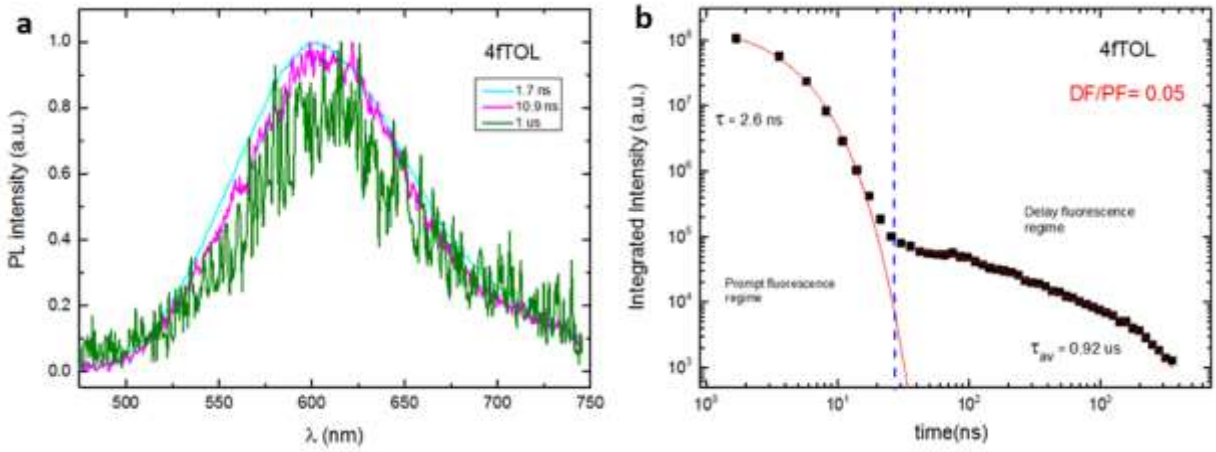

***Figure A3.16**: **a)** time-resolved emission spectra of **4**fTOL at room temperature (RT); **b)** decay curve of **4**fTOL at RT. λ_{ex}= 355 nm*

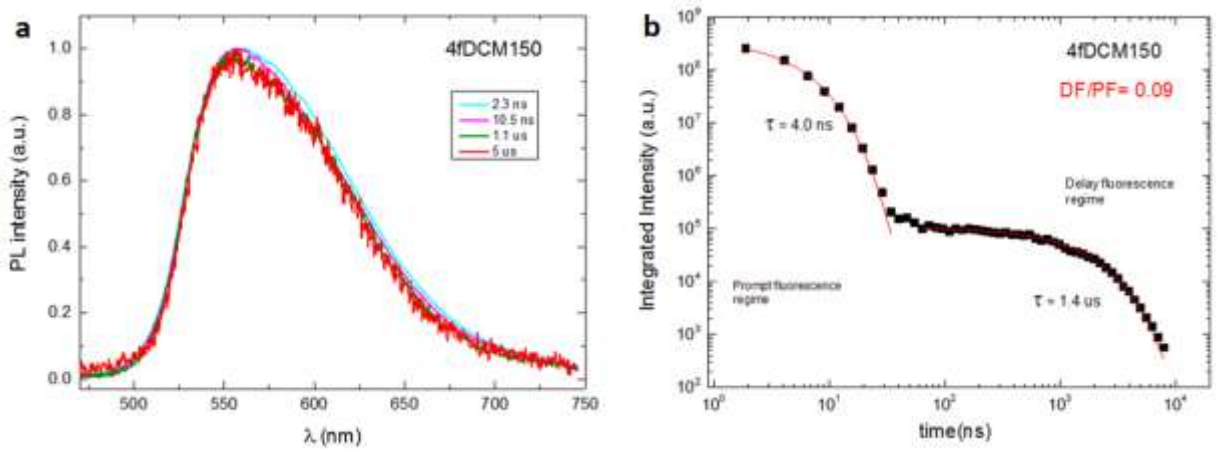

***Figure A3.17**: **a)** time-resolved emission spectra of **4**fDCM150 at room temperature (RT); **b)** decay curve of **4**fDCM150 at RT. λ_{ex}= 355 nm.*

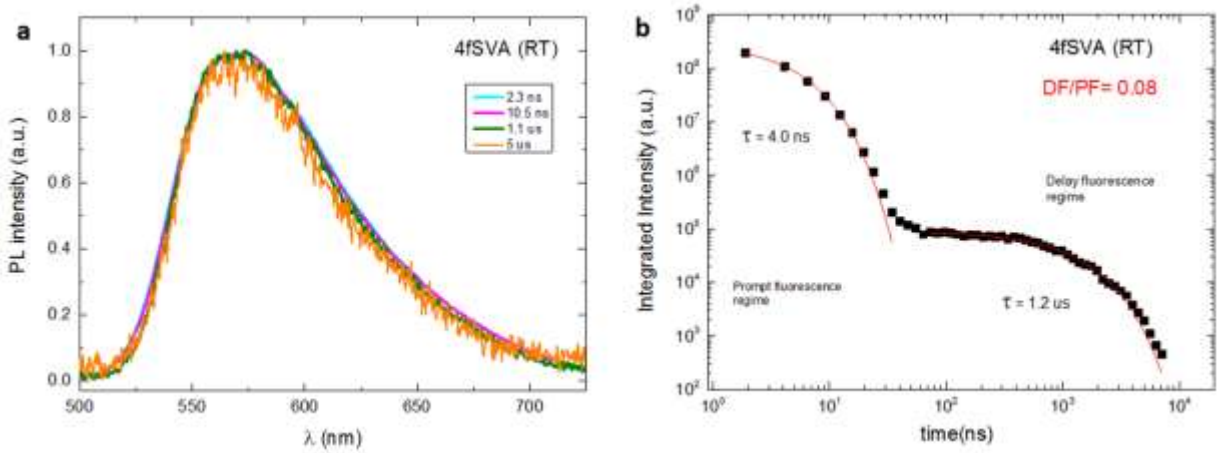

***Figure A3.18**: **a)** time-resolved emission spectra of **4**fSVA at room temperature (RT); **b)** decay curve of **4**fSVA at RT. λ_{ex}= 355 nm.*

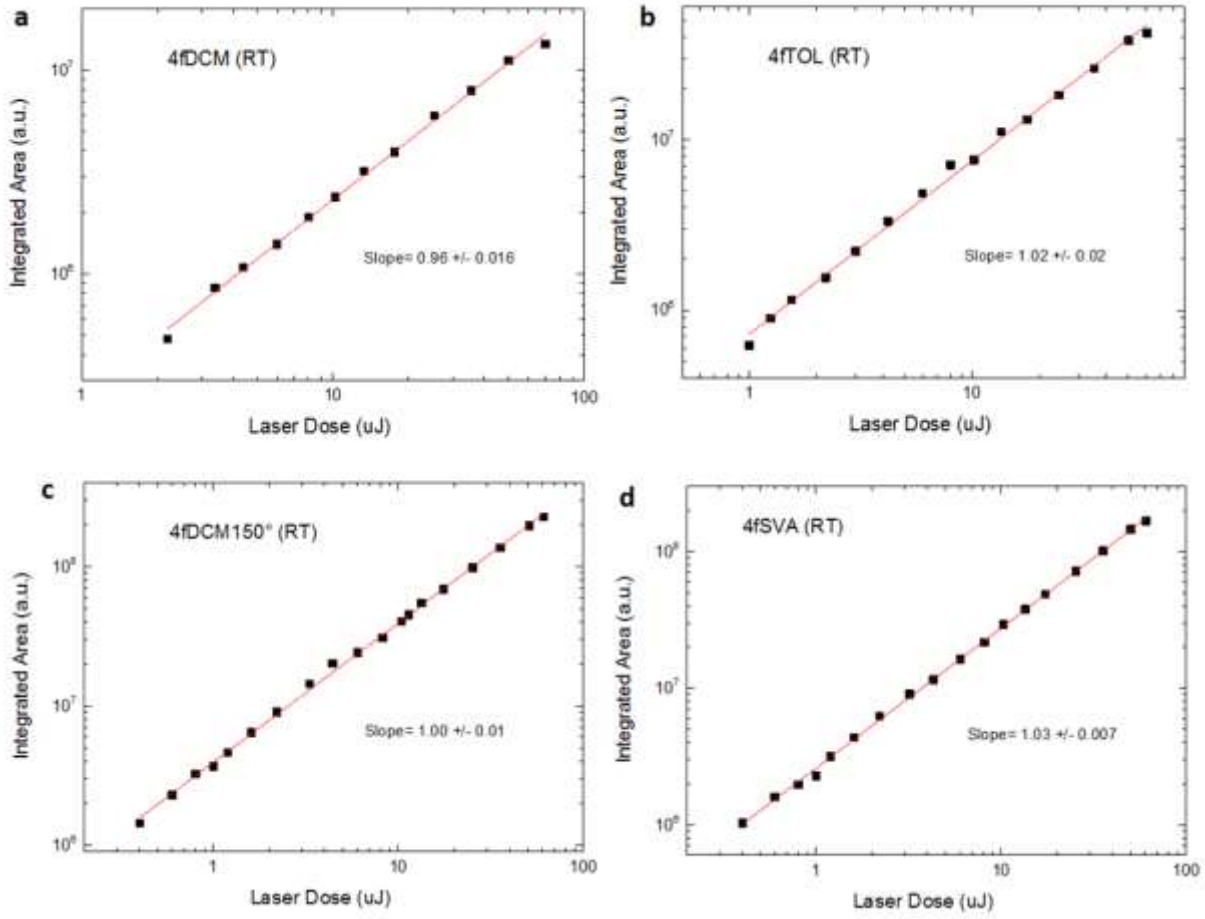

Figure A3.19*: Power dependence of the integrated delayed fluorescence at room temperature for the different samples:* ***a) 4****fDCM,* ***b) 4****fTOL,* ***c) 4****fDCM150,* ***d) 4****fSVA.* λ_{ex}*= 337 nm.*

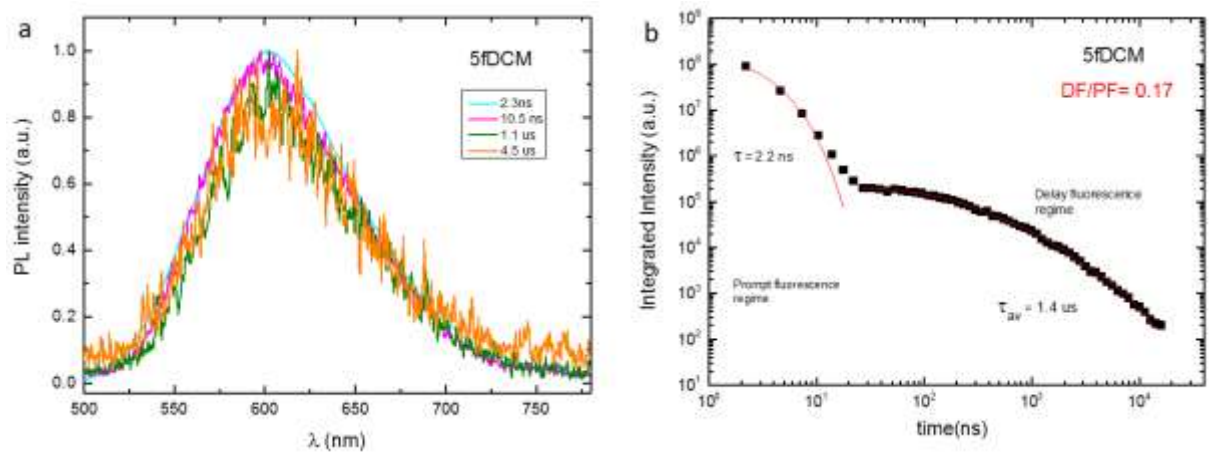

***Figure A3.20**: **a)** time-resolved emission spectra of **5**fDCM at room temperature (RT); **b)** decay curve of **5**fDCM at RT. λ_{ex}= 355 nm.*

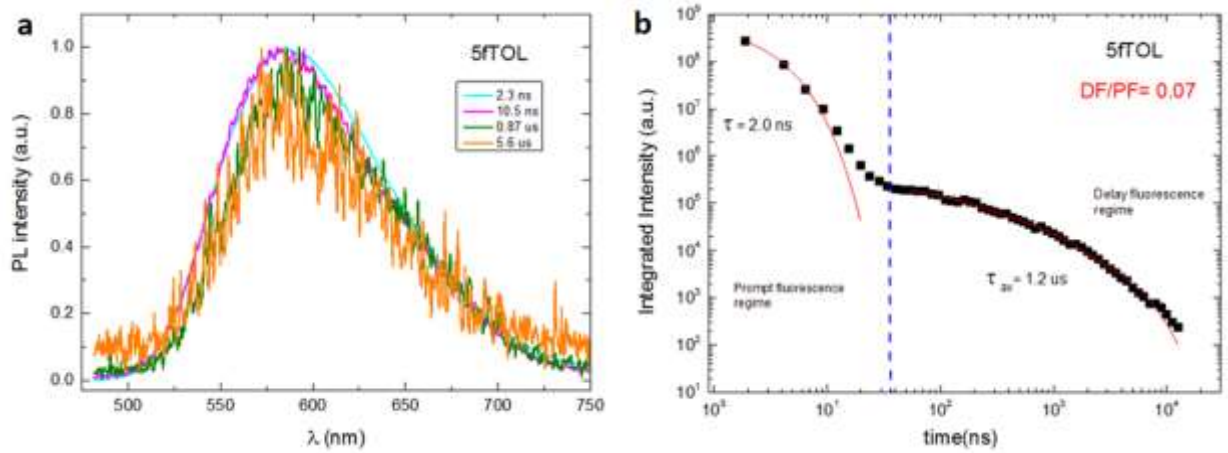

***Figure A3.21**: **a)** time-resolved emission spectra of **5**fTOL at room temperature (RT); **b)** decay curve of **5**fTOL at RT. λ_{ex}= 355 nm.*

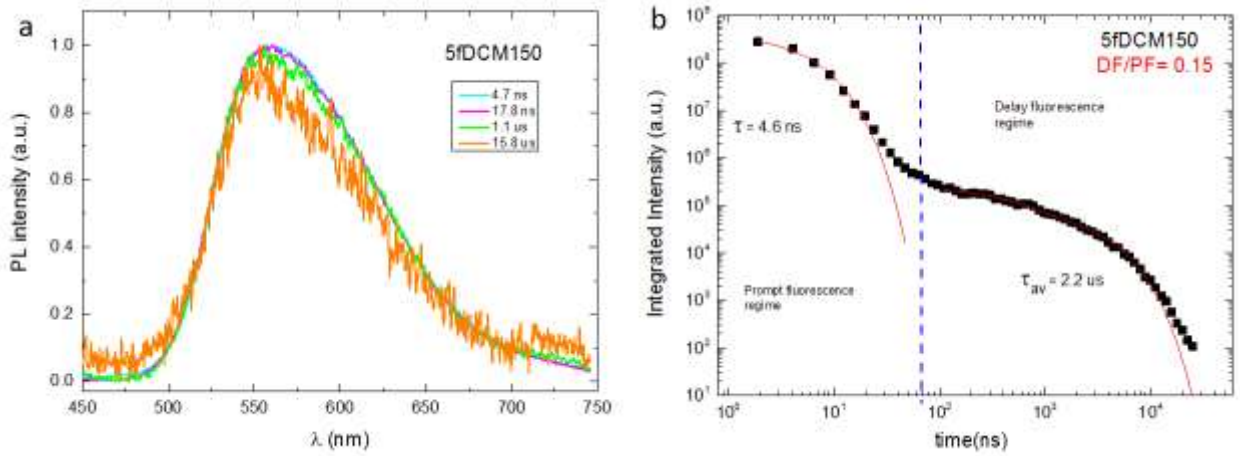

***Figure A3.22**: **a)** time-resolved emission spectra of **5**fDCM150 at room temperature (RT); **b)** decay curve of **5**fDCM150 at RT. λ_{ex}= 355 nm.*

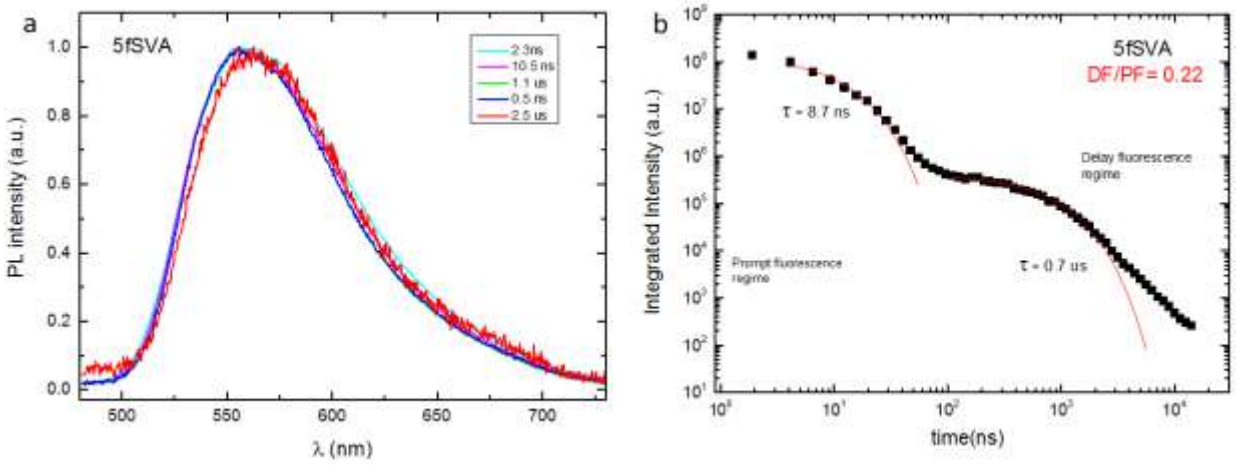

***Figure A3.23**: **a)** time-resolved emission spectra of **5**fSVA at room temperature (RT); **b)** decay curve of **5**fSVA at RT. λ_{ex}= 355 nm.*

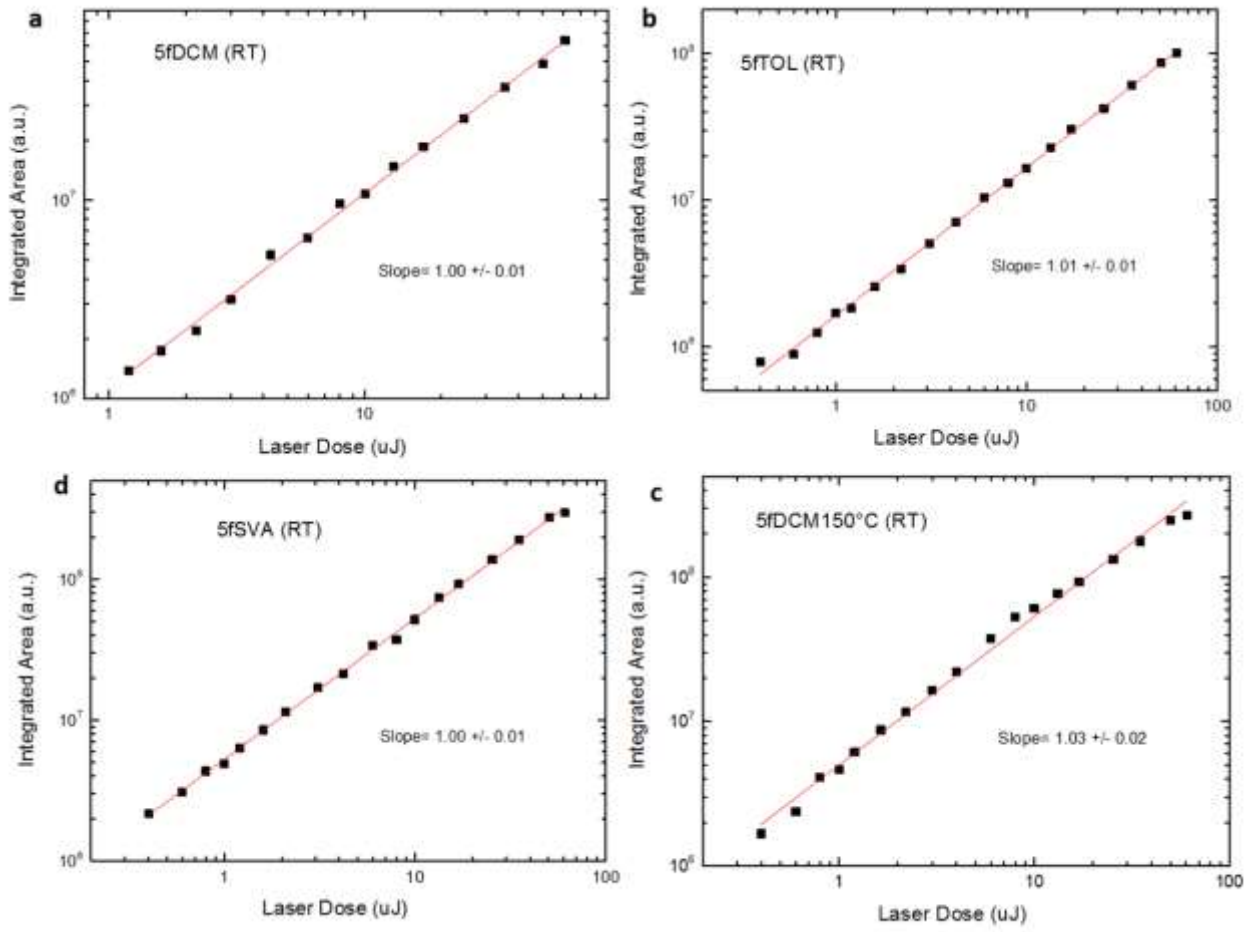

Figure A3.24*: Power dependence of the integrated delayed fluorescence at room temperature for the different samples:* ***a) 5****fDCM,* ***b) 5****fTOL,* ***c) 5****fDCM150,* ***d) 5****fSVA.* λ_{ex}*= 337 nm.*

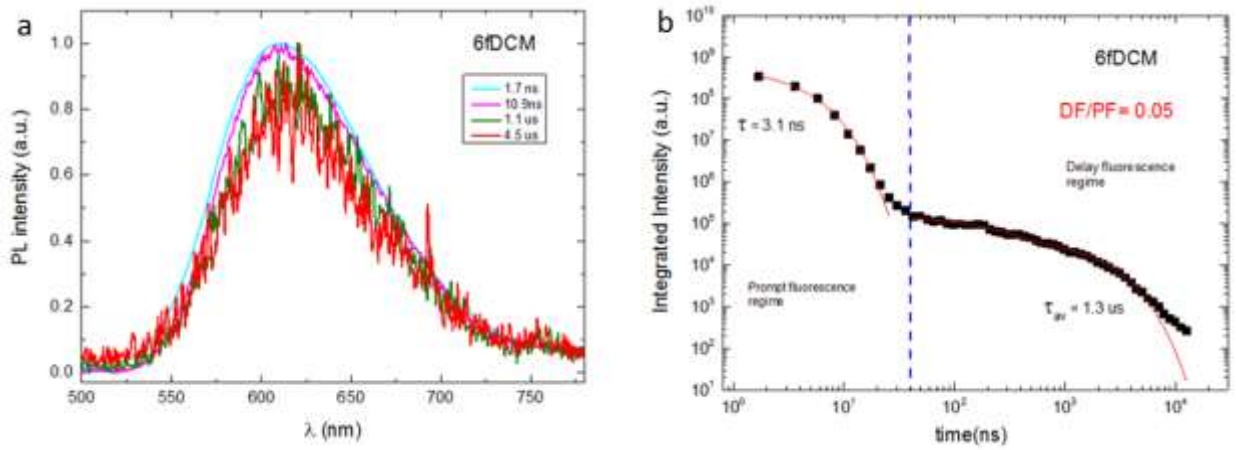

***Figure A3.25**: **a)** time-resolved emission spectra of **6**fDCM at room temperature (RT); **b)** decay curve of **6**fDCM at RT. λ_{ex}= 355 nm.*

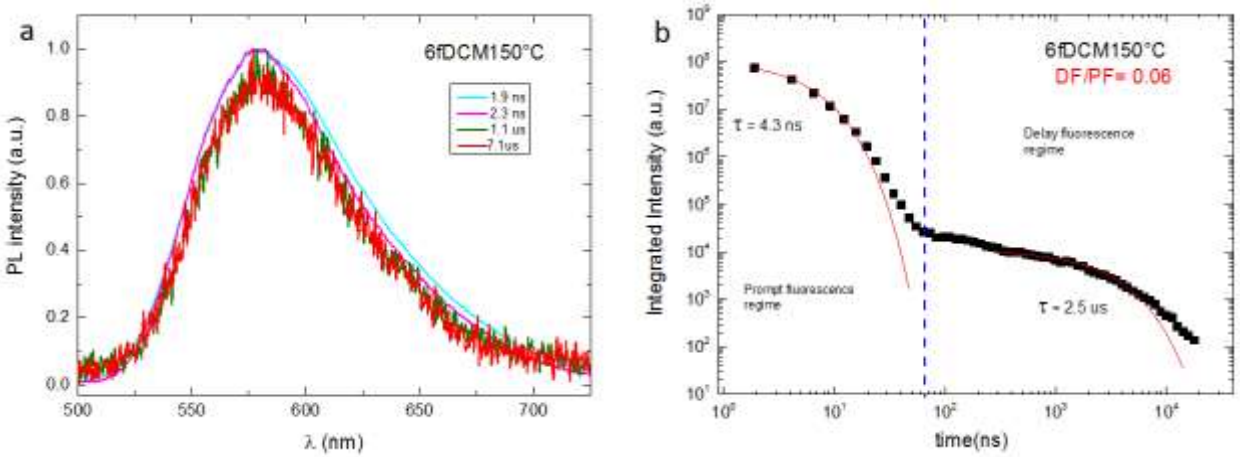

***Figure A3.26**: **a)** time-resolved emission spectra of **6**fDCM150° at room temperature (RT); **b)** decay curve of **6**fDCM150° at RT. λ_{ex}= 355 nm.*

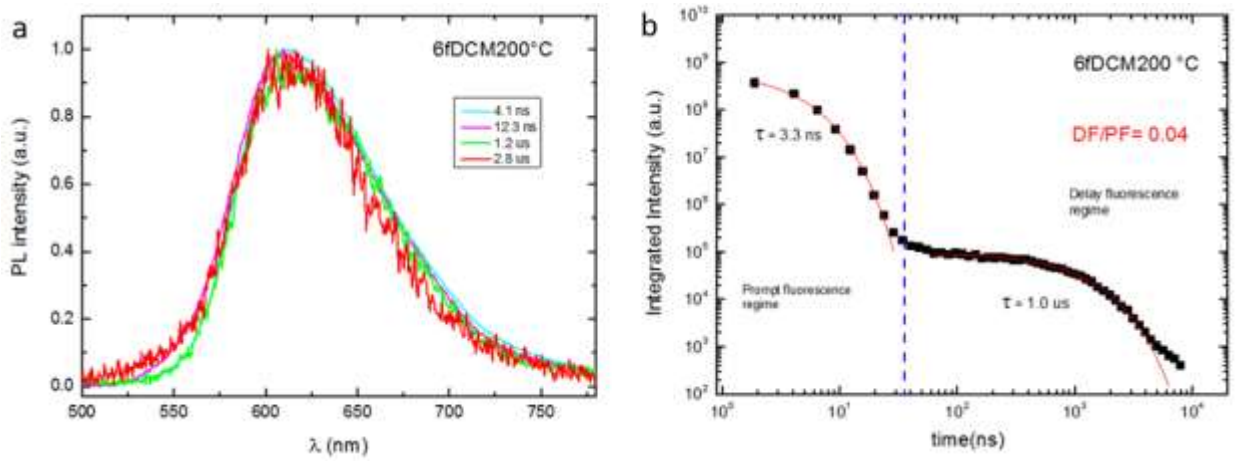

***Figure A3.27**: **a)** time-resolved emission spectra of **6**fDCM200 at room temperature (RT); **b)** decay curve of **6**fDCM200 at RT. λ_{ex}= 355 nm.*

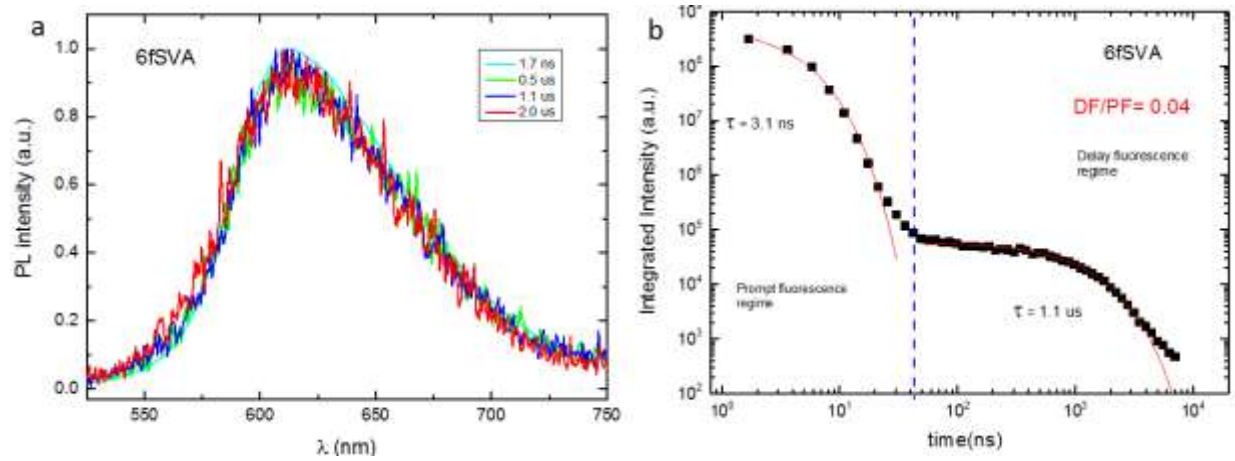

***Figure A3.28**: **a)** time-resolved emission spectra of **6**fSVA at room temperature (RT); **b)** decay curve of **6**fSVA at RT. λ_{ex}= 355 nm.*

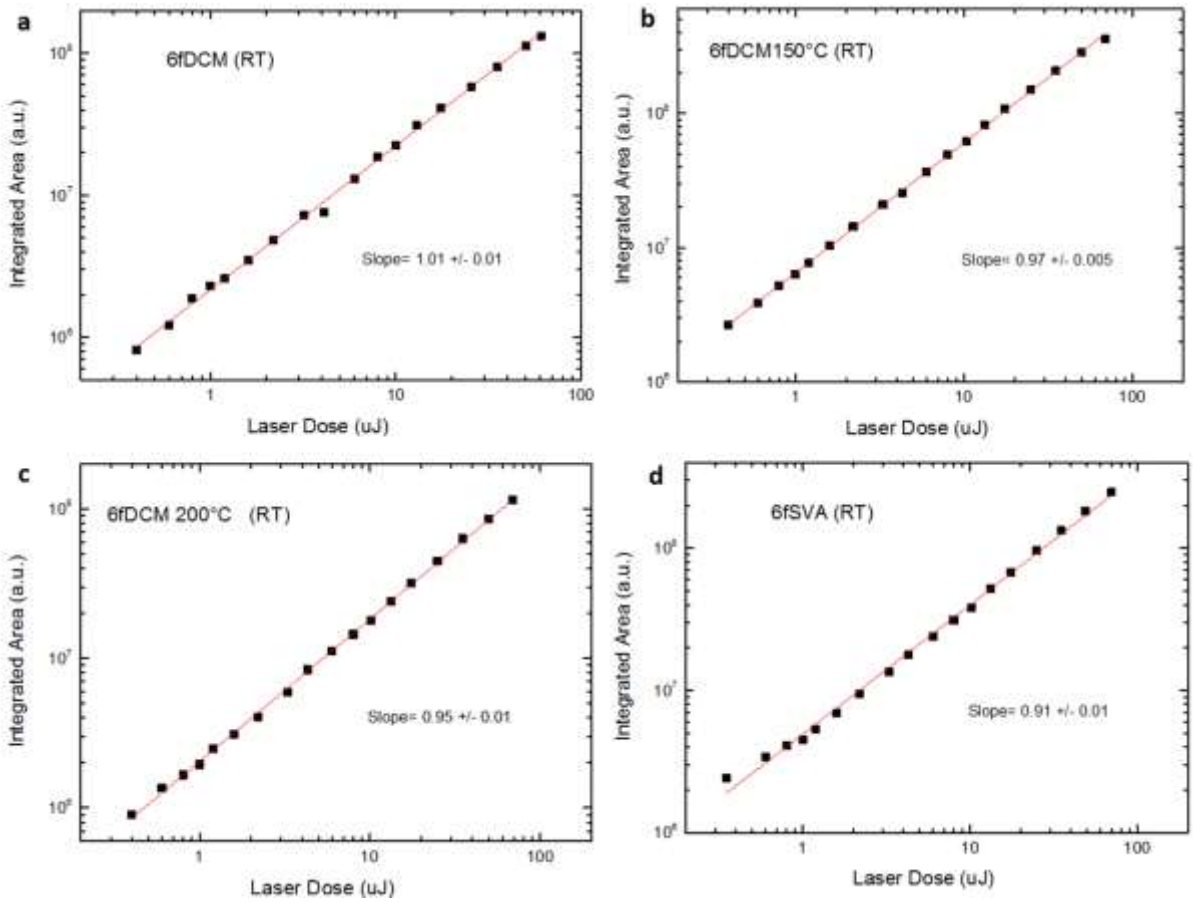

***Figure A3.29**: Power dependence of the integrated delayed fluorescence at room temperature for the different samples: **a) 6**fDCM, **b) 6**fDCM150, **c) 6**fDCM200, **d) 6**fSVA. λ_{ex}= 337 nm.*

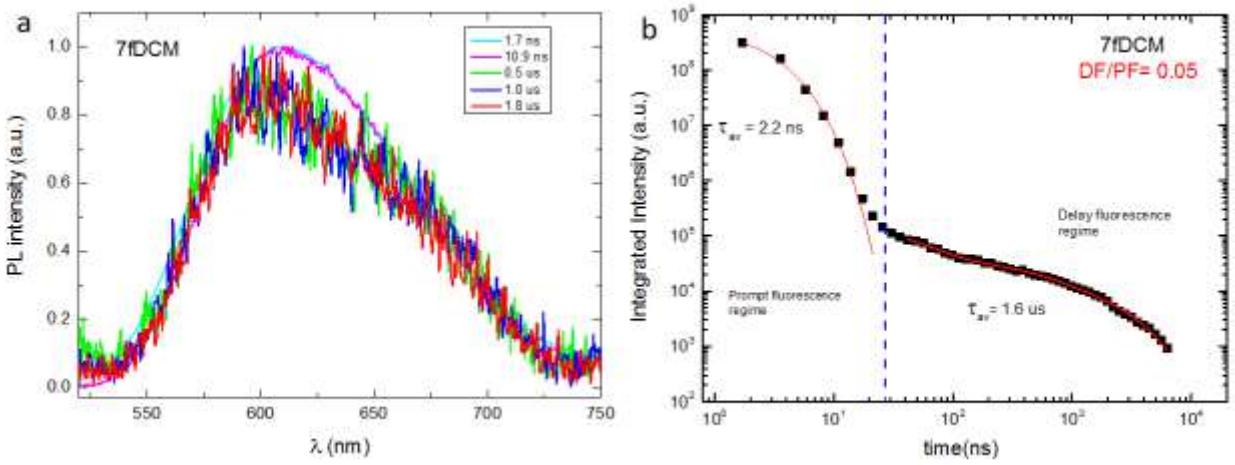

***Figure A3.30**: **a)** time-resolved emission spectra of **7**fDCM at room temperature (RT); **b)** decay curve of **7**fDCM at RT. λ_{ex}= 355 nm.*

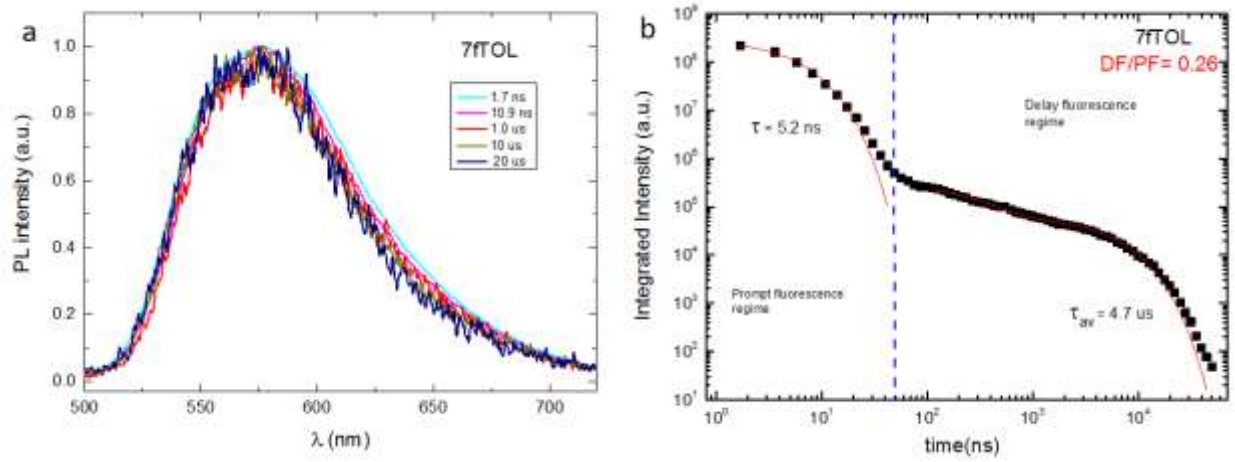

***Figure A3.31**: **a)** time-resolved emission spectra of **7**fTOL at room temperature (RT); **b)** decay curve of **7**fTOL at RT. λ_{ex}= 355 nm.*

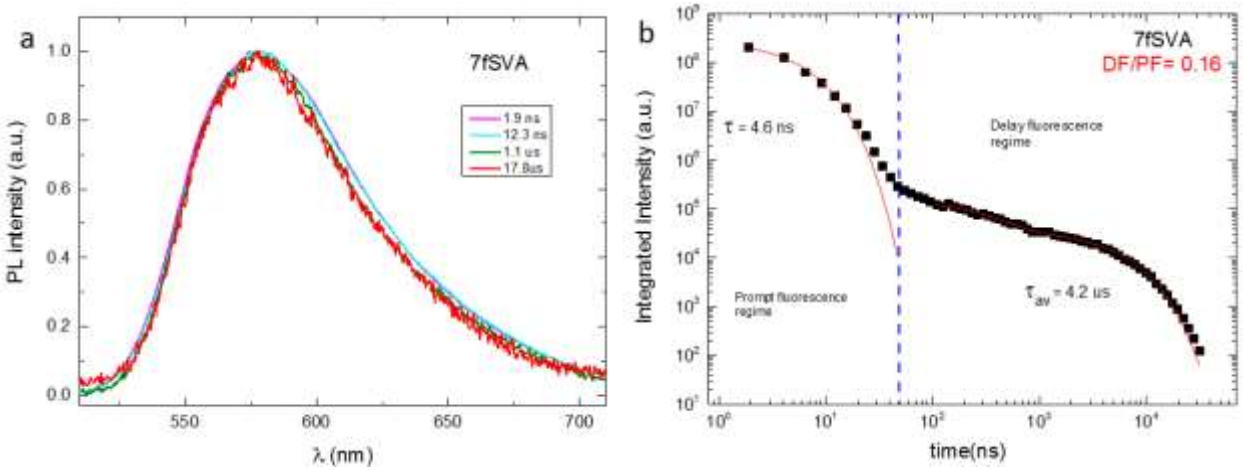

***Figure A3.32**: **a)** time-resolved emission spectra of **7**fSVA at room temperature (RT); **b)** decay curve of **7**fSVA at RT. λ_{ex}= 355 nm.*

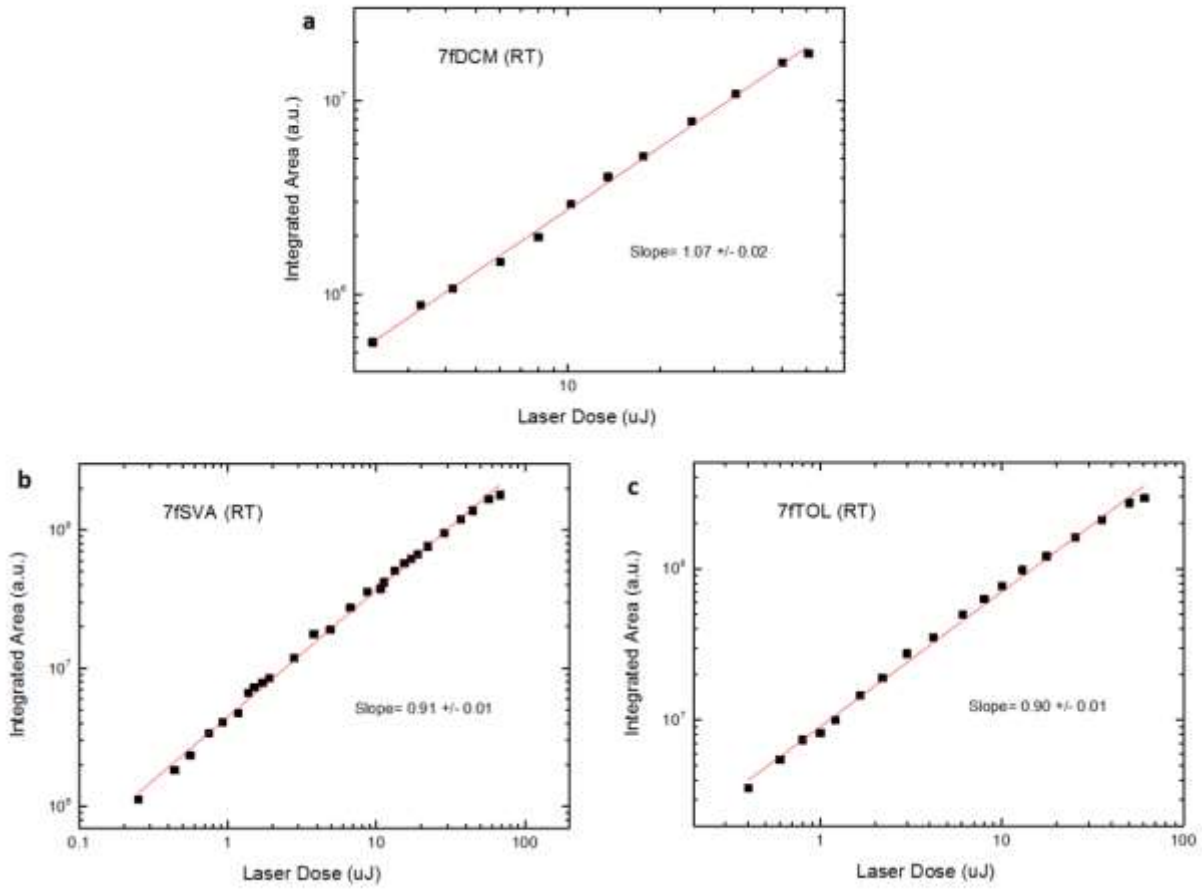

Figure A3.33*: Power dependence of the integrated delayed fluorescence at room temperature for the different samples:* ***a) 7****fSVA,* ***b) 7****fDCM,* ***c) 7****fTOL.* λ_{ex}*= 337 nm.*

CHAPTER 4.

SWITCHING ON THE TADF TROUGH THE DISTORTION OF THE MOLECULAR CONFIGURATION IN THE CRYSTAL, AND SONOCRYSTALLIZATION INDUCED TADF.

1. INTRODUCTION

The most of TADF materials need to be dispersed into an opportune matrix to suppress emission quenching and exciton annihilation[19, 107]. Recently, it was demonstrated that organic emitters showing both TADF and aggregation-induced emission (AIE), known as aggregation-induced delayed fluorescence (AIDF), provide an advisable strategy to solve the problem[108]. In fact, such compounds offer a great solution to avoid the use of a matrix in the active layer of OLED devices, which constitutes an important critical step in OLED technology. AIDF materials do not suffer from concentration quenching and can exhibit strong delayed fluorescence upon aggregation. It results that in AIDF materials the exciton quenching (S-T and T-T annihilation) is strongly suppressed. The first AIDF donor-acceptor compound was developed by Wang et al. in 2014[109] which showed that weak intermolecular non-covalent interactions in solid-state, such as π··π and C-H··π, are fundamental to turn on the emission thanks to the suppression of molecular roto-vibration. They reported an increase in the PLQY from < 0.05 in solution to 0.93 in neat film. After that, several groups have developed AIDF-active emitters for non-doped emitting layers in OLEDs[63, 110-114]. Lee's group demonstrates by using theoretical calculations that in AIDF molecules ACQ is prevented thanks to the almost-orthogonal conformation of the D-A molecule in the condensed state[110]. The near orthogonality between the D and A moieties, besides preventing π-π electronic interaction, is very important in TADF materials design, as leads to achieve small ΔE_{S-T}, a fundamental requirement for an efficient RISC.

The photophysical properties of two novels D-A emitters (**Figure 4.1**) are presented in this chapter along with the solid state study in crystal and neat film of **BzN-Phx**[10]. The nature of donor and acceptor moieties used in TADF emitters has a profound impact on their photophysical properties [61, 115]. The molecules presented in this chapter were carefully designed and selected with the aim to study the effect of three different donors on the solid-state TADF properties. All the materials present a benzonitrile core as an electron acceptor unit substituted with three

[10] The photophysical properties of BzN-Phx (N4) in solution and PMMA are already reported in Chapter 2.

different donors with increasing donating properties: one carbazole (**Cz-BzN**), one phenoxazine (**Phx-BzN**) and one phenothiazine (**Pht-BzN**). As it is common in TADF materials, these molecules are also characterized by the formation of an internal charge transfer (ICT) state, and consequently, the emission can occur from both the locally excited (LE) and (ICT) states[116-117]. In particular, this study allows exploring how the effect of the donor strength changes the geometry and affects the TADF properties of the materials especially upon different aggregation forms in solid-state. Although in the literature, there are several examples of TADF molecules that also present the AIE phenomenon, in this chapter will be presented a completely new mechanism to activate both the luminescence and TADF properties upon the arrangement in a crystal lattice. Furthermore, in this chapter it is presented the proof of concept of a singular method to create luminescent nano-crystals (~250 nm) thanks to the use of ultrasound. To our knowledge, this is the first time that sono-crystallization is used to obtain luminescent nanocrystals.

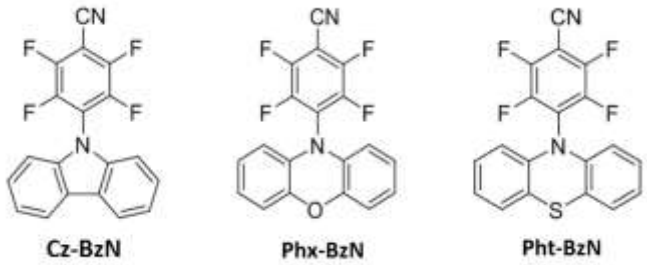

***Figure 4.1**: molecular structures of the molecules studied in this chapter.*

2. STRUCTURAL PROPERTIES.

The structural properties play a crucial role to understand the photophysical properties of the materials reported in this chapter. In **Figure 4.2** are reported the geometrical structures obtained by X-ray scattering, and we can notice that in the unit cell of **Pht-BzN** crystal are present two molecules with a slightly different configuration. In **Table 1** are reported the three different angles, identified in the single crystals: 1) the angle between the mean planes of the two phenyl rings of the Donors, 2) the torsional angle (dihedral angle) relative to the donor-acceptor bond and 3) the angle between the mean planes of the donor and acceptor. Interestingly we can see that in **Cz-BzN** both D-A dihedral angle and the angle between mean planes are respectively 50.70° and 50.14°. Since this D-A angle is far from orthogonality we can expect that TADF is not favored for **Cz-BzN**. Contrarily this relatively small angle should favor PF because the higher conjugation leads to a larger oscillator strength for the S_0-S_1 transition. In **Phx-BzN**, both D-A dihedral angle and the angle between mean planes become closer to perpendicularity (respectively 83.31°, 78.17°) thanks to the better donor properties of phenoxazine. Therefore, we can expect to observe TADF for this molecule. Interestingly in **Pht-BzN** unit cell, both molecules

present a near-orthogonal dihedral angle: 89.22° (***molecule 1***) and 86.11° (***molecule 2***) but the angles between the mean planes is smaller: 79.58°(***molecule 1***) and 81.19°(***molecule 2***). The pronounced difference between torsion angles and mean planes is due to the fact that the phenothiazine present a bent configuration (see angle D in **Table 1**) contrarily to the carbazole and phenoxazine that are more or less flat. It results that the mean plane of phenothiazine does not interpolate all the atoms but only their average position.

The molecular packing of the three crystals is reported in **Figure 4.3** and **Figure A4.1-A4.4** and allows to investigate the interactions between the molecules. In **Cz-BzN** single crystal (**Figure 4.3a**, **Figure A4.1a**) the molecules present a herringbone packing and the main intermolecular interactions are: C-H···π (3.238 Å-3.480 Å), C-N···π (3.516 Å) C-N ···H (2.552 Å) and C-F···H (2.553 Å) (**Figure A4.2**). Also in **Phx-BzN** crystal (**Figure 4.3b**, **Figure A4.1b**) the molecules are stacked in a head to tail herringbone packing and the main intermolecular interactions are: C-H···π (2.847 Å), C-F··π (3.166Å), C-F···H (2.634Å, 2.499Å) and 0···H (2.563Å) (**Figure A4.3**). Finally, in **Pht-BzN** crystal (**Figure 4.3c**, **Figure A4.1c**) the molecules are stacked in a herringbone packing with a head to tail configuration and the main intermolecular interactions in are: C-F···π (3.072Å), C-F···H (3.025Å), C-H···π (3.004Å) and C-N···H (2.656Å) (**Figure A4.4**). From these analysis, we can see that the weak intermolecular interactions plays a key role in the formation of all crystals. Furthermore, as no π-π stacking were found we assumes that all possible emissive aggregates, e.g. dimer, excimer, J- and H-aggregates are prevented.

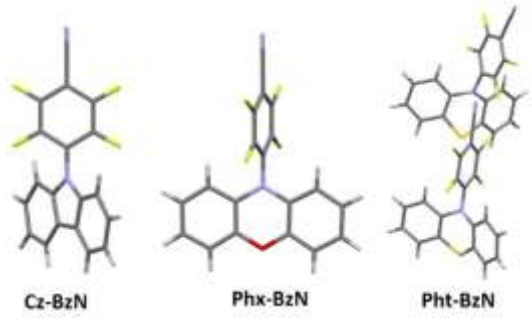

Figure 4.2: *X-ray crystallographic structures of, from left to right,* ***Cz-BzN***, ***Phx-BzN***, ***Pht-BzN***.

Table 1: Main angles for the XRD structures of Cz-BzN, Phx-BzN, Pht-BzN.

	D(°)[a]	**D-A(°)[b]**	**D-A° dihedral angle**
Cz-BzN	2.71°	50.14°	50.70°
Phz-BzN	4.90°	78.17°	83.31°
Pht-BzN	42.68° (mol1), 33.75° (mol2)	79.58°(mol1), 81.19°(mol2)	89.22°(mol1), 86.11°(mol2)

a) D angle refers to the angle between the mean planes of the two phenyl rings of the Donor; b) A-D angle refers to the angle between the mean planes of the Donor and the Acceptor.

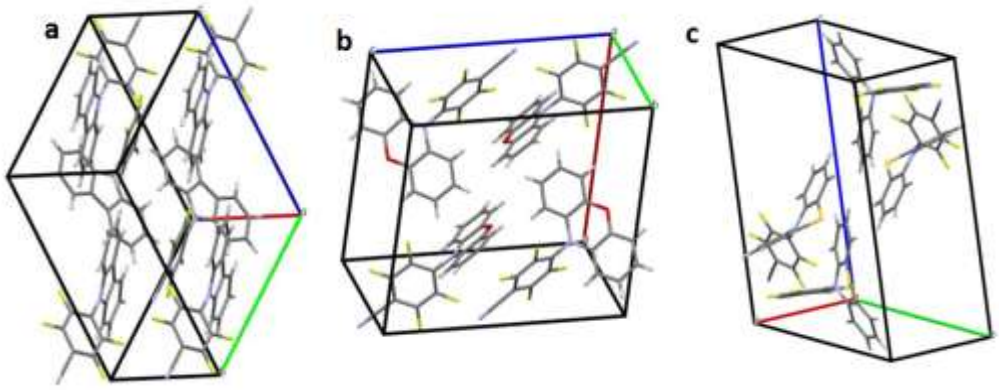

Figure 4.3: *molecular packing of **Cz-BzN** (a), **Phx-BzN** (b), **Pht-BzN** (c) obtained from X-ray crystallographic structures.*

3. QUANTUMECHANICAL CALCULATIONS.

All compounds have been studied by (TD)DFT calculation in their ground and first excited state geometries to facilitate the interpretation of experimental photophysical data. First, the ground state geometries of the compounds were obtained and the calculated structures match quite well with the XRD structures (**Figure 4.4** and **Table 1** vs **Table 4.3**). This allows understanding that calculations reproduce quite well the real system. In particular, like in XRD, DFT calculations show that the carbazole and phenoxazine donors are flat (**Fig. 4.4**, angle D° in **Tables 1** and **3**) but phenothiazine is bent with a calculated angle between the mean planes of the two phenyl rings of 31.6°.

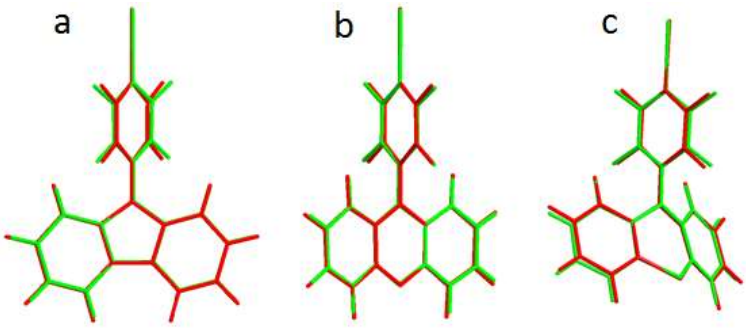

Figure 4.4*: Overlap between the calculated and XRD structures* of (a) ***Cz-BzN,*** *(b)* ***Phx-BzN,*** *(c)* ***Pht-BzN,*** *colors: red = calculated, green = X-Ray.*

According to the calculated HOMO level (strong donors have high energy HOMO) (**Figure 4.5**, **Table 2**), the donor strength goes in the order carbazole<phenothiazine<phenoxazine. This in agreement with the position of the CT band in absorption (in CH Cz-BzN ≈360nm, Pht-BzN≈395nm; Phx-BzN≈425nm). These results are in agreement with the oxidation potentials of the *N*-methyl derivatives of the three donors reported in literature[118-120]. However, the electrochemistry in the next paragraph gives a slightly different result (Pht easier to oxidize than Phx).

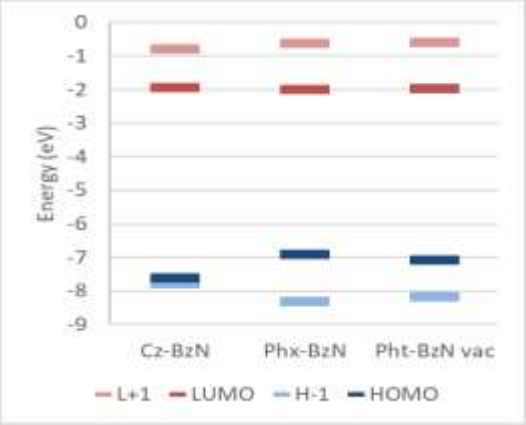

***Figure 4.5**: Representation of the energy levels of the frontier molecular orbitals of* **Cz-BzN, Phx-BzN,** and **Pht-BzN**.

Table 2: Energies in eV of the MOs calculated

	Cz-BzN	**Phx-BzN**	**Pht-BzN**
L+1	-0.79	-0.63	-0.6
LUMO	-1.95	-2.01	-1.98
HOMO	-7.62	-6.92	-7.09
H-1	-7.77	-8.31	-8.17

3.1 Ground state geometry.

The electron density distributions in the S_0 molecular geometry, for the HOMO-LUMO calculated transition, are reported in **Figure 4.6**. We can see that in **Cz-BzN** the HOMO is localized mostly on the carbazole while the LUMO is localized mainly on benzonitrile, however, there is also partial participation of benzonitrile in the HOMO, and of the carbazole in the LUMO. In **Phx-BzN** the HOMO localization on the carbazole moiety increases as well as the LUMO on

benzonitrile. However, also in this case a small contribution of benzonitrile in the HOMO, and of the phenoxazine in the LUMO is present. In **Pht-BzN** is observed an exclusive localization of the HOMO on the phenothiazine donor, and of the LUMO on the benzonitrile acceptor. From these observations, we can expect that the CT absorption is more intense in **Cz-BzN**, less in **Phx-BzN**, and mostly negligible in **Pht-BzN**. In **Figures A4.5-A4.7**, are reported the calculated spectra that show how the lowest energy transition corresponding to a D-A charge transfer CT transition (**Table A1**) is in fact more intense for **Cz-BzN** but becomes very weak for **Pht-BzN** (**Figure A4.7**). The oscillator strength relative to these transition are in fact: **Cz-BzN** (0.2155)>**Phx-BzN** (0.052)> **Pht-BzN** (0.0006). The second-lowest calculates transition corresponds to a π-π* localized transition centred on the Donor (**Table A1**). Higher energy transitions are either π-π* ones, centred on the D or A moiety, but also other CTs.

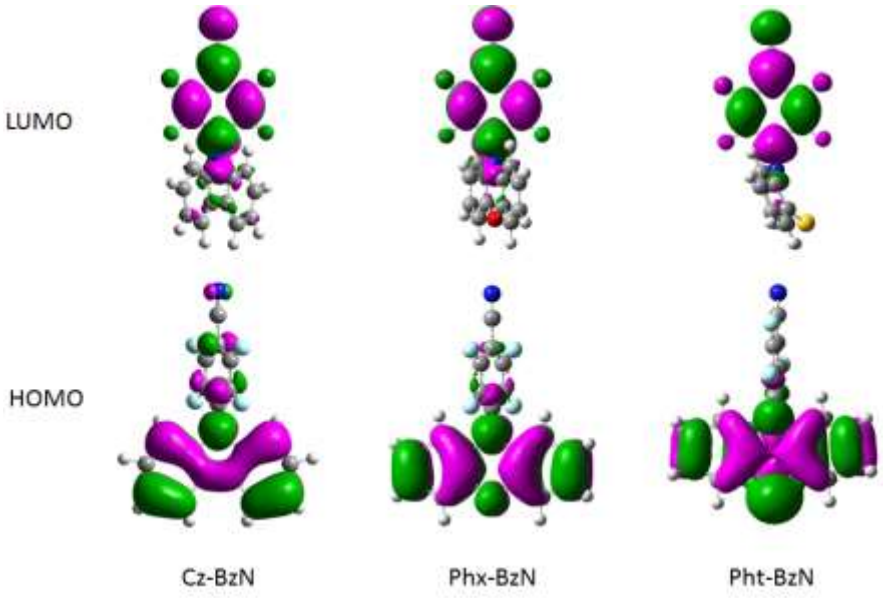

Figure 4.6: *Electron density distributions in molecular orbital energy levels involved in the HOMO-LUMO calculated transition in the S_0 molecular geometry, of (from left to right) Cz-BzN, Phx-BzN, Pht-BzN.*

3.2 Excited state geometries (S_1 and T_1).

The geometries of the first singlet excited state were then optimised (**Figure 4.7**). For **Cz-BzN** the D-A angle increases from (59.36°=dihedral, 59.91°=mean planes) in the ground state to (71.23°=dihedral, 90.00°=mean plane) in the S_1 excited state (**Table 3**); thus the larger angle could increase the possibility to have TADF. Moreover, **Cz-BzN** when passing from S_0 to S_1 configuration undergoes also a rather large reorganization mainly through the twisting of the benzonitrile relatively to the carbazole (**Figure 4.7**). In **Phx-BzN** the D-A angle goes from (73.45°=dihedral,

73.61°=mean planes) in the ground state to (73.29°=dihedral, 90.00°=mean plane) in the S_1 state, while the angle between the two phenyl rings of phenoxazine changes very little: from 1.21° in S_0 configuration to perfectly flat (0°) in S_1 (**Table 3**). Nevertheless, in **Phx-BzN**, from the ground state to the excited states, a large reorganization occurs mainly through the twisting of the benzonitrile relative to the phenoxazine (**Figure 4.7**). In **Pht-BzN** the D-A angle goes from (dihedral= 85.55°, mean plane=89.77°) in the ground state to (dihedral=89.98°, mean plane= 89.98°) in S_1. However, the twisting of the benzonitrile is smaller but there is a higher reorganization in the angle between the two phenyl rings of phenothiazine, which goes from 31.59° in the ground state to 0.03° in S_1.

The electron density distributions for the S_1 and T_1 molecular geometry, in the HOMO-LUMO, calculated transition are reported in **Figure 4.8** and **Figure 4.9** respectively. We can see that in the S_1 geometry in **Cz-BzN** and **Phx-BzN** the HOMO is localized mostly on the donor moiety with small participation of benzonitrile, while the LUMO is localized mainly on benzonitrile with small participation of the donor. On the other hand, in the T_1 geometry, the electron density in the HOMO and LUMO, is more delocalized on the full molecule. This is especially valid in **Cz-BzN**, where the HOMO is fully delocalized on both D and A moiety. The higher delocalization of the electron density on the whole molecule should result in a phosphorescence with a more delocalized nature. In **Pht-BzN** both S_1 and T_1 configurations show the HOMO and LUMO exclusively localized on the donor and acceptor respectively.

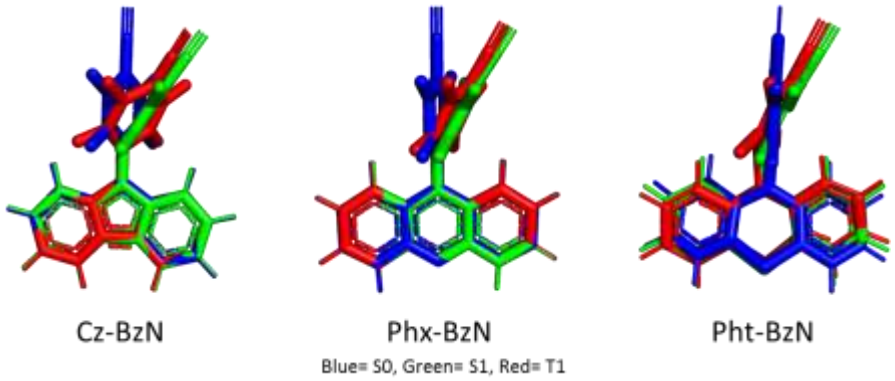

Figure 4.7: *Optimized structures in the ground and excited states of, from left to right* ***Cz-BzN*** *(blue=S_0, green=S_1, red=T_1) ,* ***Phx-BzN*** *(blue=S_0, green=S_1, red=T_1) and* ***Pht-BzN*** *(blue=S_0, green=S_1).*

Table 2: Calculated main angles for the ground state and excited structures of Cz-BzN, Phx-BzN, Pht-BzN.

	D(°)[a] (S_0)	D-A° (S_0) dihedral-angle	D-A (°)[b] (S_0)	D(°)[a] (S_1)	D-A° (S_1) dihedral-angle	D-A (°)[b] (S_1)
Cz-BzN	0.40	59.36	59.91	0.00	71.23	90.00
Phz-BzN	1.21	73.45	73.61	0.00	73.29	90.00
Pht-BzN	31.59	85.55	89.77	0.03	75.35	89.98

a) D angle refers to the calculated angle between the mean planes of the two phenyl rings of the Donor; b) A-D angle refers to the calculated angle between the mean planes of the Donor and the Acceptor.

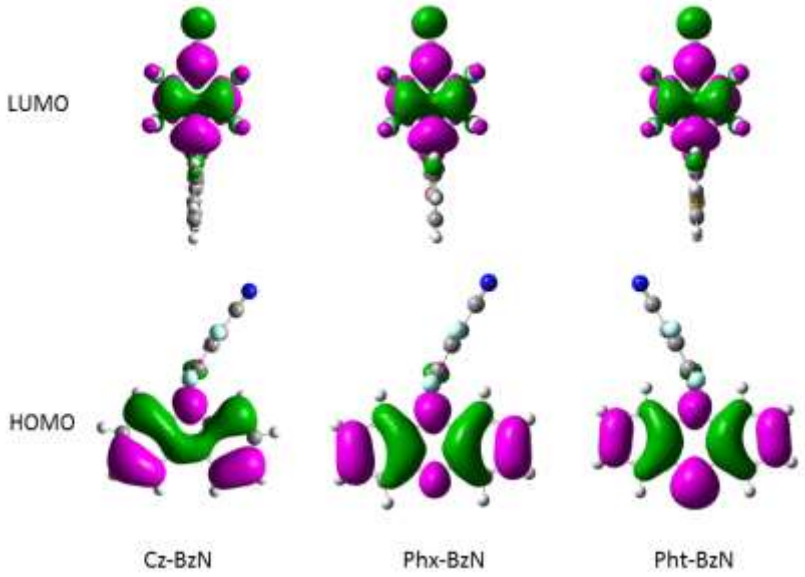

Figure 4.8: *Electron density distributions in molecular orbital energy levels involved in the HOMO-LUMO calculated transition in the S_1 molecular geometry, of (from left to right) Cz-BzN, Phx-BzN, Pht-BzN.*

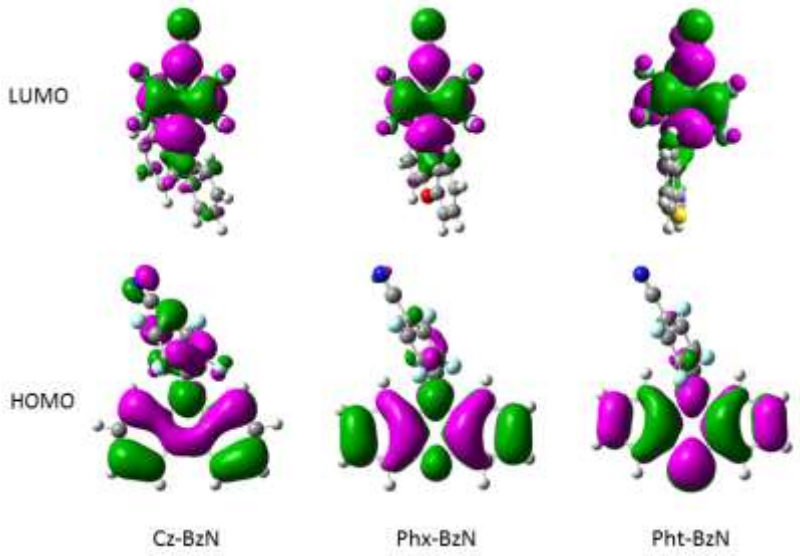

Figure 4.9: *Electron density distributions in molecular orbital energy levels involved in the HOMO-LUMO calculated transition in the T_1 molecular geometry, of (from left to right) Cz-BzN, Phx-BzN, Pht-BzN.*

3.3 Remarks.

In conclusion, from DFT calculation we can expect that these molecules are less emissive in solution. In particular, in **Cz-BzN** and **Phx-BzN** the non-radiative relaxation caused by the pronounced twisting of benzonitrile should reduce the emission. When D is a phenoxazine or phenothiazine the compound in S_1 configuration should be non-emissive because there is no HOMO-LUMO overlap and the oscillator strength in S_1 configuration is equal to zero (**Table A1**). When D is Carbazole the oscillator strength of the CT transition in S_1 configuration is ≠0 (**Table A1**), and therefore we expect to observe emission in solution.

However, we can expect to observe a different behaviour if the molecules are blocked in the S0 configuration in the rigid crystal packing. In particular, in **Cz-BzN** crystal the emission should increase because the twisting of benzonitrile is prevented. However, the small D-A angle should leads to increase the singlet-triplet energy gap and to reduce the TADF contribution. In **Phx-BzN** and **Pht-BzN** crystals, we expect to see an activation of the emission with good TADF properties because the molecules in the S_0 configuration present a near orthogonal D-A angle but in this case, the oscillator strength of the CT transition in the S_1 geometry is ≠0 (**Table A1**). Moreover, the benzonitrile twisting is also prevented and this should consume less excitation energy and then contribute to increasing the overall emission in the crystal. From DFT analysis results that the more important limiting factor of the **Phx-BzN** and **Pht-BzN** emission in solution is not the excitation energy that is consumed trough the benzonitrile twisting but the fact that the relaxation of the molecule occurring after excitation results in a CT transition that becomes forbidden by geometry.

4. ELECTROCHEMISTRY (CYCLIC VOLTAMMETRY).

Cyclic voltammetry (CV) experiments have been performed on all three donor-acceptor benzonitrile derivatives (**Figure 4.10**). In particular, they feature an irreversible reduction peak, which can be assigned to the benzonitrile core reduction. Furthermore, they present an oxidation peak, which can be assigned to the peripheral donor moieties (carbazole, phenoxazine or phenothiazine). It is important to note that the phenoxazine and phenothiazine are reversibly oxidized, while the oxidation of the carbazole moieties is irreversible. Therefore, only **Phx-BzN** and **Pht-BzN** present solely reversible waves in oxidation (**Figure 4.10b**, **4.10c**). Contrarily in **Cz-BzN**, the oxidation process is non-reversible (**Figure 4.10a**). The peak ratio between the first oxidation and first reduction is about 0.93 for **Phx**-**BzN** and 0.83 for **Pht**-**BzN**. Both correspond to the one-electron oxidation of phenoxazine and phenothiazine therefore the reduction of benzonitrile involves also one electron for both. The redox potentials are given in **Table 4** for all the compounds, along with the 1st oxidation peak vs. 1st reduction peak ratios, and the HOMO and LUMO values obtained from 1st oxidation peak potential (HOMO) and 1st reduction peak potential (LUMO). However from the obtained HOMO and LUMO, the donor's strength results slightly higher for phenothiazine than phenoxazine. This not in agreement either with the HOMO and LUMO energies obtained on the MOs DFT calculations and also with the oxidation potentials of the *N*-methyl derivatives of the three donors reported in literature[118-119, 121].

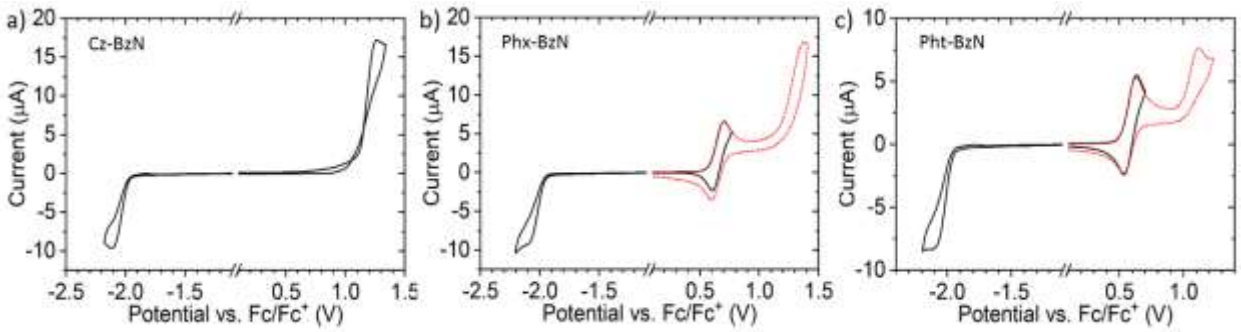

Figure 4.10: *CV traces of* (a) ***Cz-BzN,*** *(b)* ***Phx-BzN,*** *(c)* ***Pht-BzN.***

Table 4: Electrochemical data of all benzonitrile derivatives.

	E_{ox} vs Fc/Fc+ (V)[(a)]	E_{red} vs Fc/Fc+ (V)[(a)]	Anodic vs. cathodic peak current ratio	N° of electron	HOMO (eV)[(b)]	LUMO (eV)[(c)]	HOMO-LUMO (eV)
Cz-BzN	1.12	-1.98	/	irreversible	-6.23	-3.13	3.10
Phx-BzN	0.58	-1.96	1.73	1	-5.66	-3.15	2.51
Pht-BzN	0.51	-1.96	2.2	1	-5.59	-3.17	2.42

(a)Measured in DCM at room temperature by cyclic voltammetry.
(b)Estimated from the oxidation potential in DCM, HOMO = E_{ox} + 5.1
(c)Estimated from the reduction potential in DCM, LUMO = E_{red} + 5.

5. PHOTOPHYSICAL PROPERTIES.

The photophysical properties of the molecules were studied either in solution but especially in solid-state. The study in solution was carried out mainly in absorption by using three different solvents with increasing polarity (cyclohexane, toluene, and DCM). Nevertheless, the emission properties were also tested especially for **Cz-BzN**. On the other hand, a complete study was performed in solid-state. In particular, the single-molecule photophysical properties were obtained by dispersing the compound in a PMMA or Zeonex rigid matrix (0.05-0.1wt %). Different aggregated forms were also studied. In particular, more amorphous samples were obtained after a fast DCM evaporation of a droop casted concentrated solution directly deposited on quartz substrates. As regarding the crystalline forms, the solvent vapour annealing (SVA) method was used for growth the crystals directly on the quartz substrates, and the samples obtained using this method were studied in steady-state experiments. On the other hand, in the time-resolved experiment were used the initial crystalline powders obtained for all the three compounds trough slow evaporation of petroleum ether and DCM (3:1) mixture.

5.1 Photophysical Properties of Cz-BzN.

5.1.1 Steady-state study of Cz-BzN.

The UV-Vis absorption spectra of **Cz-BzN** (**Figure 4.11a**) show that, between 400 and 360 nm, where carbazole no longer absorbs, a weak CT absorption band appears. Such transition derives from the electron transfer from the HOMO of the D (carbazole) to the LUMO of the A (benzonitrile). This is a transition forbidden by geometry and this is the reason why it appears very weak. At higher energy, are present two main absorption bands typical for carbazole derivatives [79, 122]: The first peak is at λ_{max}= 325-330 nm, and the more intense peak is at λ_{max}= 286 nm. Both are associated with two LE states centred on the carbazole.

The **Cz-BzN** present intense emission in solution (**Figure 4.11b** and **Table 5**), and this is in agreement with the stronger oscillator strength between the three molecules. Moreover, the moderately strong QY indicates that the twisting of benzonitrile occurring upon excitation, in this case, does not consume all the excitation energy. The effect of solvatochromism on the emission was also tested using three different solvents with increasing polarity (**Figure 4.11b**). The presence of a strong positive solvatochromism with increasing polarity confirms the charge-transfer character in the excited state[123]. In order to magnify the TADF the higher PLQY is obtained in toluene (**Table 5**) which, among the three solvent tested, presents the appropriate polarity to reduce the distance between the ^{3}LE and ^{1}CT, and thus to minimize the ΔE_{ST}. In the highly polar DCM, the emission redshifts and the intensity decreases. It results that the CT state of **Cz-BzN** is

stabilized too much and the ^{1}CT emission is outcompeted by non-radiative processes[26, 60, 84, 86]. Such redshift of ^{1}CT energy can result also in the detuning of the singlet and triplet energy with a consequence to increase of ΔE_{ST}.

The steady-state photophysical properties of different solid samples were also studied (**Figure 4.11c**, **Table 5**). They consist in: 1) isolated molecule dispersed in PMMA rigid matrix, 2) neat film obtained after fast evaporation of a drop casted DCM solution, 3) crystalline film obtained through solvent vapour annealing (SVA) process. Comparing the emission in PMMA with that in solution (**Figure 4.11b**) we can notice that the emission in PMMA is blue shifted compared to the three solvents. This is due to the rigidocromic effect that limits both rotational motions and the stabilization of the CT excited state by geometry relaxation. The rigidochromic effect leads also to a strong reduction of FWHM and increase of PLQY in PMMA (**Table 5**) thanks to the suppression of roto-vibrational motion that leads to energy loss. The rigidochromic effect becomes even much more intense in the crystalline SVA sample (**Figure 4.11c** and **Table 5**) where the molecules are certainly more blocked. In fact, beyond a 25 nm blue-shift respect to PMMA, the crystalline SVA sample presents also a higher QY (41.4%) along with a strong decrease of the FWHM (**Table 5**). All these elements indicate that this material presents a moderate CIEE [94, 124] which consists in the enhancement of the light emission upon the formation of highly ordered crystalline structures. This phenomenon is due to the restriction of molecular motions inside the crystal lattice, which also causes the blue shift of the emission. The CIEE effect is in contrast with the common ACQ effect present in the crystals, which normally redshifts the luminescence spectra of the dyes and decreases their emission quantum yields because of the formation of detrimental aggregated species such as dimer, excimers and H-aggregates via strong intermolecular π-π interactions[94, 125]. The neat film presents a photophysical behaviour between PMMA and SVA crystal (**Figure 4.11c** and **Table 5**). This demonstrates that the neat film is partially amorphous with some molecules presenting a certain degree of freedom for vibration and geometry relaxation in the excited state. This leads both to consume part of the excitation energy and to stabilize the CT excited state and a red-shifted emission respect to the pure crystalline form.

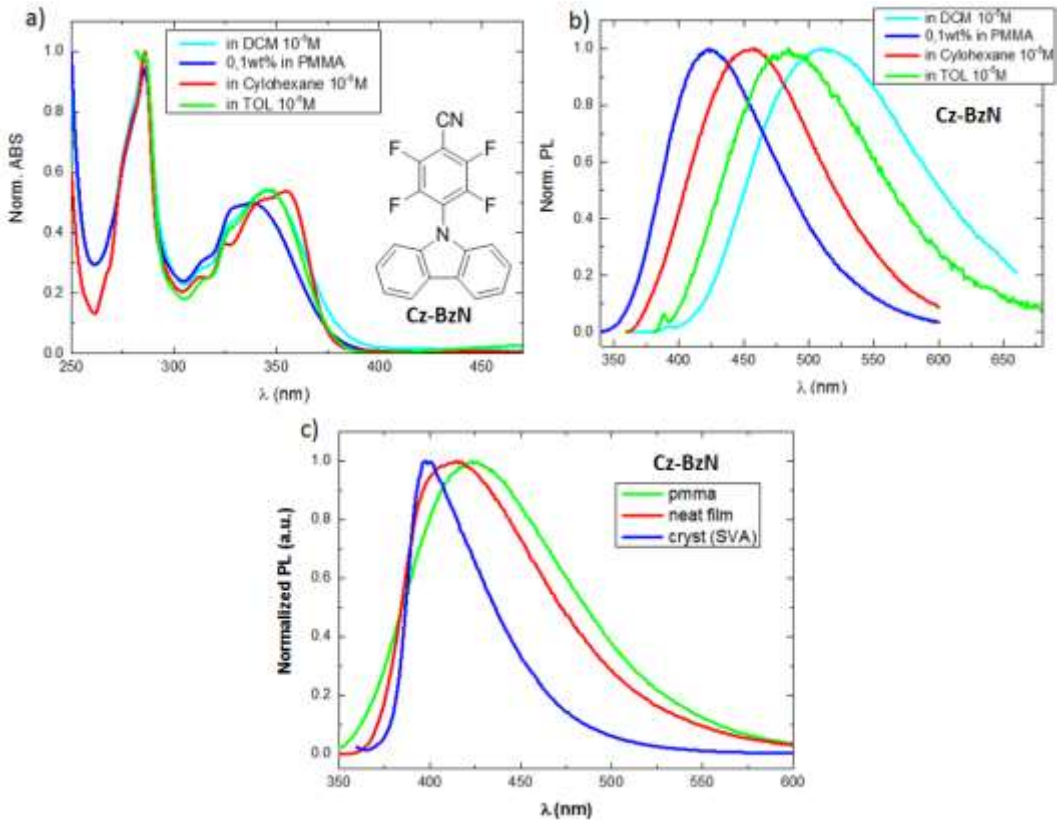

***Figure 4.11**: **a)** Absorption spectra of **Cz-BzN** in cyclohexane (10^{-5} M), toluene (10^{-5} M), dichloromethane (10^{-5} M) and PMMA. **b)** Normalized photoluminescence (PL) spectra of **Cz-BzN** in solvent with increasing polarity: cyclohexane, toluene, DCM, and in PMMA, λ_{ex}= 330 nm **c)** Normalized photoluminescence (PL) spectra of **Cz-BzN** in various solid forms: isolated molecule in PMMA, amorphous neat film, and crystal from SVA, λ_{ex}= 330 nm.*

Table 5: summary of steady state photophysical properties of **Cz-BzN**.

	λ_{PL} (nm)	Φ_{PL}^{air}- Φ_{PL}^{degas} (λ_{exc}=330nm)	FWHM (nm)
cyclohexane	457	13.6 – 16.2%	115
Toluene	485	14.6% – 18.2%	134
DCM	511	6.2% – 7.6%	149
PMMA	423	29.9% – 39.0%	101
Crystal (SVA)	398	41.4% – n.c.	49
Neat film (DCM)	415	32.8% – n.c	87

(for all Φ_{PL} the experimental error is ±20% of the value) n.c.=not calculated

5.1.2 Time-resolved study of Cz-BzN.

The time-resolved photophysical properties of **Cz-BzN** molecule were studied in the three different solid forms (PMMA, neat film, crystalline initial powder) to gain insight into the nature of the emission. All the experiments in solid-state where realized at RT and 77K, using the iCCD camera equipment. The decays in solution were obtained using a time-correlated single-photon counting (TCSPC) set-up for the PF decays (ns regime), while the DF decay curves (µs regime) were obtained using the Edinburgh instrument LP920 laser flash photolysis spectrometer.

5.1.3 Decay time of Cz-BzN in solution

The decay time in solution are reported in **Table A4.4**. Two typical decay time were obtained for all the three solvent. The shorter one, presenting a decay in the nanosecond domain is assigned to the prompt fluorescence and was fitted with a mono-exponential function. The longer one in the in µs regime is also fitted with a monoexponential and demonstrates the presence of TADF in a diluted solution. The monoexponential decay obtained in the three different solvents indicates that both PF and DF emission arise only from the CT state and no LE emission contribution is present.

5.1.4 Time-resolved properties of Cz-BzN in PMMA

Two different measurements were performed for the degassed sample: one at room temperature (RT) and another at 77K. In particular, at RT it is possible to investigate the TADF properties of the material and to explore the states (e.g. nature and energy) involved in the TADF mechanism. On the other hand, the 77K experiments allow to investigate the phosphorescence of the material to find the triplet energy level obtained from the onset of the last emission spectra collected after a milliseconds delay time.

The analysis of the spectra at RT, acquired after different delay times shows that it is possible to distinguish between different situations (**Figure 4.12a**). At early times (2.3-10 ns) the emission is more blue-shifted and this is generally due to the ^{1}LE contribution of the D and A moiety to the PF. Increasing the delay time, only the CT emission remains, becoming very weak after 70 ns, but strongly increasing after 2 µs (**Figure 4.12d**). The CT band shows a temporal spectral shift over time (**Figure 4.12a**), with the emission that after an initial red shift progressively blue shifts again. This could depend on the presence of a distribution of CT states as a result of conformation heterogeneity[126] of the molecules in PMMA. It results that the molecules that relax their geometry to a larger D-A angle emits more in the red. This produces a distribution of ΔE_{ST} with a consequent distribution of ISC rates that leads to different emissions with different decay times.

Interestingly, the RT emission remains quite intense up to 70 ms with a slight blue shift. We attribute this emission to a very long TADF, although a weak RTP contribution cannot be excluded. The PF decay was fitted with a mono-exponential function obtaining a decay time of 8.4 ns. On the other hand, the very long delayed emission was fitted with two different decay times (20.5 μs and 2.7 ms). The intensity dependence of the DF emission as a function of the laser excitation dose for **Cz-BzN** at RT (**Figure A4.11**) confirms a monomolecular process typical of the thermally-assisted mechanism.

The time-resolved emission of **Cz-BzN** at 77K (**Figure 4.12b**) show that only a PF (early time) and a very long and weak phosphorescence (ms regime) are present. As we can also see from the decay profile (**figure 4.12d**) no delayed fluorescence is detected between 80ns and 0.3ms. As the phosphorescence of carbazole is strongly blue shifted respect to the millisecond 77K emission of **Cz-BzN** in PMMA (**Figure 4.12c**) we can exclude that the origin of phosphorescence in our sample arise from a LE phosphorescence. Therefore its origin can be attributed either to a ^{3}CT or from a triplet that is delocalized on the whole molecule. The last hypothesis is corroborated from the electron density distributions in the triplet excited state geometry showed in DFT calculation (**Figure 4.9**).

The triplet energy of **Cz-BzN** is calculated from the onset of the late emission at 77K and it is found to be equal to E_T= 3.04 eV. On the other hand, the energy of the ^{1}CT state is calculated from the onset of the TADF[11] emission (TD=10μs) and it corresponds to E_s= 3.16 eV. It results an energy gap involved in the ISC/RISC equal to ΔE_{S-T}=0.12 eV which should be enough to ensure an efficient RISC. However, the very low PF/DF (0.09) indicates that after the ISC most of the energy decay non-radiatively and therefore only a low amount of triplet can be up converted back to the singlet by RISC.

[11] After 1 us the initial contribution of the LE emission is not present anymore, and therefore the emission relative to a TD of 1-10us is the most suitable to find the energy relative to the 1CT state involved in the TADF process.

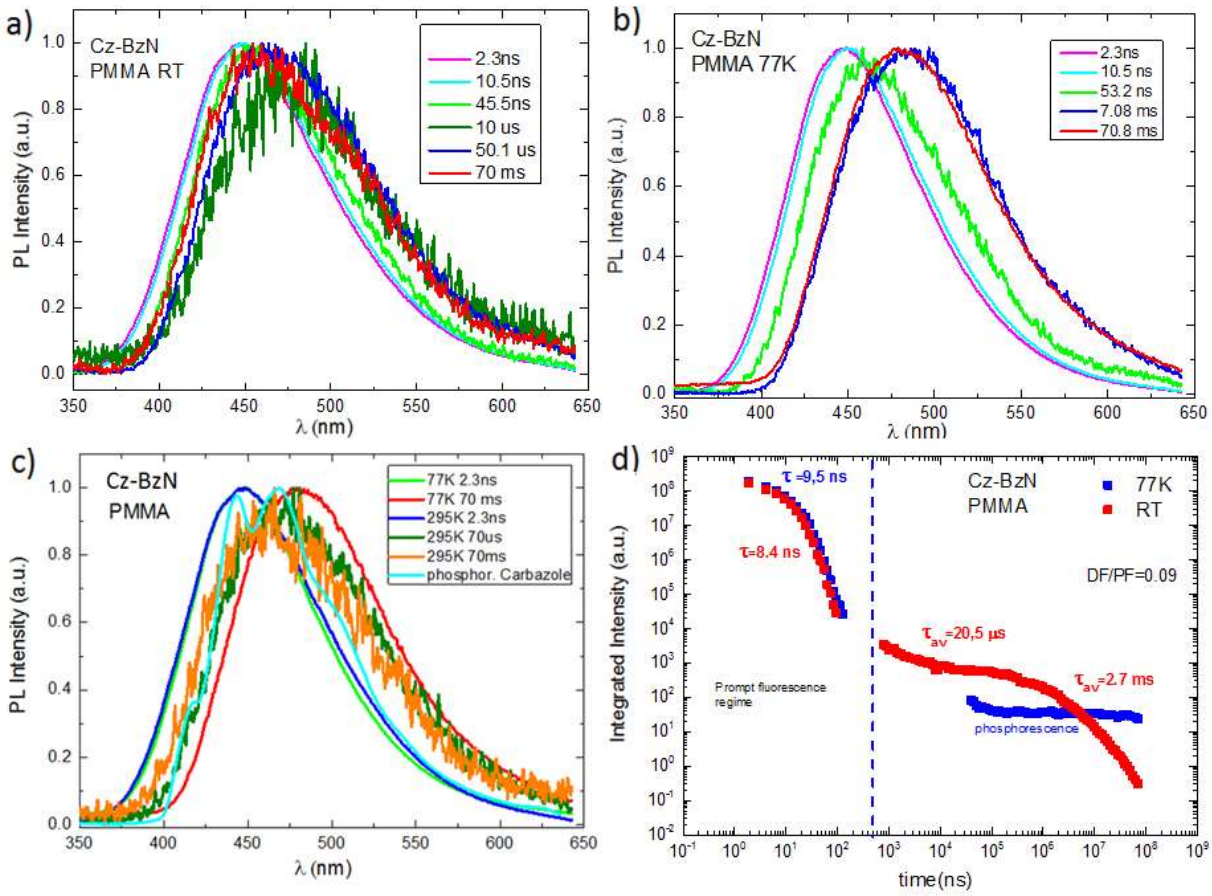

Figure 4.12: a) *time-resolved emission spectra of* ***Cz-BzN*** *in PMMA at room temperature (RT)* ***b)*** *time-resolved emission spectra of* ***Cz-BzN*** *in PMMA at 77K* ***c)*** *PF, DF and phosphorescence of* ***Cz-BzN*** *in PMMA with phosphorescence of Carbazole.* ***d)*** *Decay curve of N1 in PMMA for RT and 77K. All experiments were carried out at* λ_{ex}*= 355 nm.*

5.1.5 Time-resolved properties of Cz-BzN initial crystalline powder and neat film.

The time-dependent photoluminescence of the **Cz-BzN** initial crystalline powder was also studied and allows understanding the photophysical processes that occur in the rigid crystal packing. In particular, we can see that at RT, the PF emission slightly red shift after 10 ns thus indicating a weak ^{1}LE contribution in the initial 1-3 ns (**Figure 4.13a**). However, no DF is detected at RT. A PF a decay time of 2.8 ns was obtained by fitting the decay curve (**Figure 4.13d** and **Table 6**). When the system was cooled down to 80K, at intermediate time appears a DF emission and a longer time a well-resolved phosphorescence (**Figure 4.13b**). This phosphorescence is strongly red-shifted respect to the phosphorescence of carbazole (**Figure 4.13c**) and therefore we exclude that it arises from a ^{3}LE state. On the other hand, we can also exclude its ^{3}CT character because the band is also strongly red-shifted respect to the ^{1}CT DF of **Cz-BzN**. This long-lived

phosphorescence could originates from a delocalized state on the whole D-A molecule. In fact in DFT calculations we can see that in the ground state geometry, Cz-BzN present the electron density delocalized on the whole molecule (**Figures 4.7**). Comparing the time-resolved emission at RT of the crystalline powder (**Figure 4.13a**) with the steady-state of SVA crystalline film we can see that the latter present 41 nm of blue shift along with a more broadened emission (**Figure 4.11c**). This indicates that the crystalline powder may also contain amorphous phase. From the phosphorescence and prompt fluorescence onsets (no DF available) of **Cz-BzN** crystalline powder (**Figure 4.13c**), it is possible to find a ΔE_{S-T}= 0.47eV, which being too high for allow an efficient RISC, explains why it no TADF emission is observed in **Cz-BzN** crystalline powder. On the other hand, such high ΔE_{S-T} allows understanding that the DF observed at 80K (**Figure 4.13b** and **4.13d**) should be the result of a TTA process rather than of TADF. The DFT calculations demonstrate that the D-A angle is small in the ground state configuration and so ΔE_{S-T} is large in that conformation. Therefore, such a high singlet-triple energy gap might depend on the fact that upon excitation the molecule in the crystal, cannot relax its configuration to increase the D-A dihedral angle, but remain blocked in the configuration of the ground state. Contrarily in the softer PMMA, the D-A angle can relax to a larger angle (S_1 configuration) to which corresponds a smaller ΔE_{S-T}

The time-resolved emission for **Cz-BzN** neat film is reported in **Figure 4.13e**. We can see that after a PF emission at early delay time (TD=1.5ns) no emission (or very weak) is present between a delay time of 100 ns up to 0.5 µs. However between 1 and 6 µs, a very weak and strongly red-shifted delayed emission appears. Interestingly this redshifted emission matches well with the phosphorescence measured on the powder at 77K (**Figure 4.13f**). Therefore, we cannot exclude the presence of a weak RTP contribution.

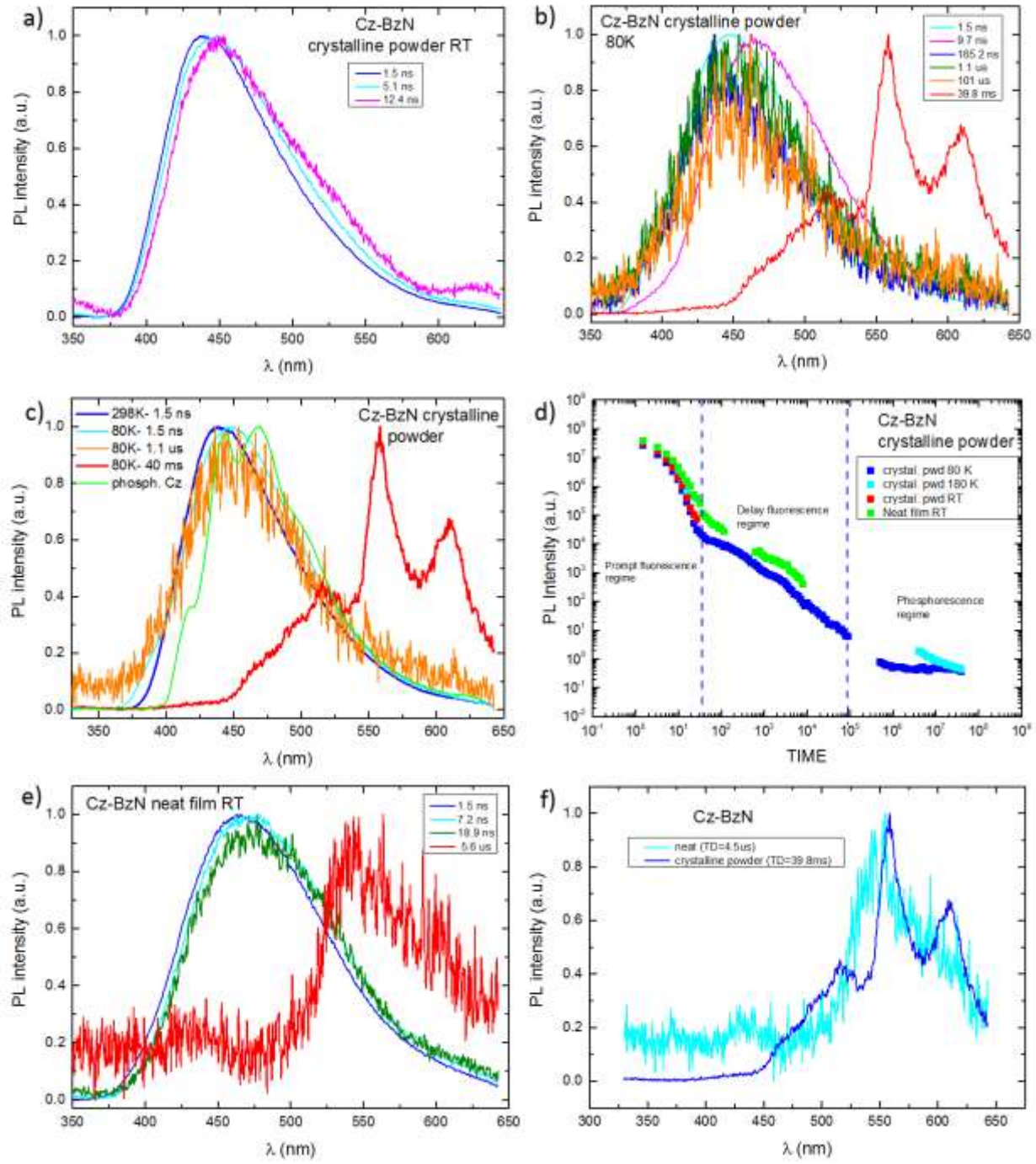

Figure 4.13: a) *time-resolved emission of* ***Cz-BzN*** *crystalline powder at room temperature (RT)* ***b)*** *time-resolved emission of* ***Cz-BzN*** *crystalline powder at 80K* ***c)*** *time-resolved emission spectra of* ***Cz-BzN*** *at RT and 80K with phosphorescence of Carbazole* ***d)*** *decay curve profile of* ***Cz-BzN*** *crystalline powder at RT, 180K, and 80K, and for neat film at RT* ***e)*** *time-resolved emission of* ***Cz-BzN*** *neat film at room temperature* ***f)*** *phosphorescence of* ***Cz-BzN*** *crystalline powder in comparison with the long-time emission (TD=4.5us) of* ***Cz-BzN*** *neat film at RT. All experiments were carried out at* λ_{ex}*= 355 nm.*

Table 6: Photophysical properties of **Cz-BzN.**

Cz-BzN	λ_{PL} (nm)	$\Phi_{PL}{}^{air}/\Phi_{PL}{}^{degas}$	τ_{PF} (ns)	τ_{DF} (µs)	$\tau_{phos.}$ (ms)	DF/PF
Crystal pwd. RT	439	45.6%	2.8	/	/	/
Crystal pwd. 180K	445	§67.5%	3.3	/	46.8*	/
Crystal pwd. 80K	446	§100%	3.0	1.6*	#	0.05[µ]
Neat film	465	32.8%	4.1	2.7*	/	/
PMMA	448	29.9%/39%	8.4	20.5*/2700*		0.09
PMMA 77K	450	§58%	9.5	/	#	/

(deg) degas, §estimated PLQY *biexponential average decay #not fitted, µ from TTA. (for all Φ_{PL} the experimental error is ±20% of the value)

5.2 Photophysical Properties of Phx-BzN.

5.2.1 Steady-State study of Phx-BzN.

The photophysical properties of **Phx-BzN** molecule in solution (Cyclohexane and DCM) and in PMMA are reported in Chapter 2, where was demonstrated the presence of a CT absorption, *i.e.* electron transfer from the HOMO of the D (phenoxazine) to the LUMO of the A (benzonitrile) and the negligible emission in cyclohexane (mainly through LE of phenoxazine).

On the other hand, in **Figure 4.14** it is shown that intense emission is present in neat film, crystalline film and PMMA (PLQY in aerated conditions of 2.8%, 5.4%, and 3.8% respectively). After degassing the PMMA sample, PLQY increases to 4.4%. The activation of the emission in solid-state indicates that **Phx-BzN** presents both AIE [93, 127] and CIE properties. As seen from the DFT calculations (**Figure 4.6**), the molecule presents an important relaxation of its geometry (especially by the twisting of the benzonitrile moiety) when going from the ground to the excited state configuration but also a relaxation of the dihedral angle to an orthogonal configuration. Both the non-radiative relaxation, but especially the zero oscillator strength of the CT transition in S_1 configuration (**Table A1**) caused by the 90° D-A angle explain the negligible emission observed in solution. Contrarily, the geometry relaxation is prevented in the crystal and the emission can be activated as the oscillator strength of the CT transition in the S_0 configuration is ≠0 (**Table A1**). Emission in neat and crystalline (SVA) films present a bathochromic shift respect to the isolated molecule in PMMA (**Figure 14.4**). In general, this indicates the formation of aggregates. However, the **Phx-BzN** crystal packing did not show any π-π stacking and therefore we think that the redshift is probably due to a different polarity and dielectric constant of the material that shifts the CT state at lower energy. In the more randomly organized neat film, the emission further redshifts and becomes considerably broadened (FWHM= 122 nm) respect to the crystal (FWHM= 83nm). Moreover, the decrease of the emission quantum yield (QY_{neat} = 2.8% vs $QY_{SVA\ cryst}$ = 5.4%) indicates that in the more amorphous neat film are allowed different molecular

configurations that produces CT states at lower energy where the non-radiative deactivation paths are more favoured.

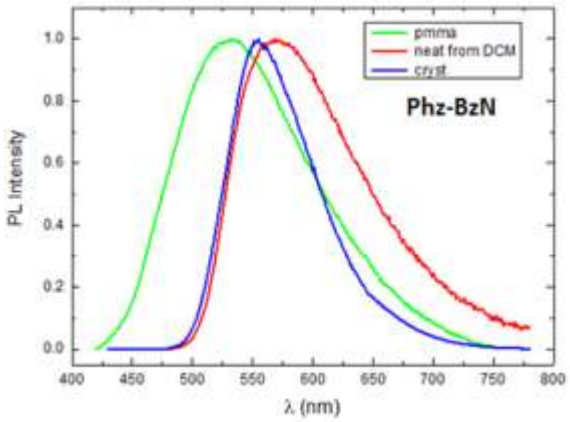

***Figure 4.14**: Normalized photoluminescence (PL) spectra of **Phx-BzN** in various solid forms: isolated molecule in PMMA, amorphous neat film, and crystal from SVA. λ_{ex}= 330 nm.*

5.2.2 Aggregation Induced Emission (AIE).

To prove the AIE properties of **Phx-BzN**, a common test consists of verifying if the emission spectrum intensifies when a large amount of water is added into a THF solution of **Phx-BzN**. In fact, since water is a non-solvent for the most of organic dyes, the molecules must aggregate in the mixture when the water content increases. **Figure 4.15** shows that the emission is very weak for dispersion of **Phx-BzN** in a mixture of THF/water for a water fraction up to f_w= 90%. When additional water is added, up to a water fraction of f_w= 99% an intensified emission arises upon precipitation (**Figure 4.15**). The AIE effect is in general due to the restriction of rotations and vibrations. In our particular case, as already explained above, it comes from both the preventing of the geometry relaxation of the molecule to an orthogonal D-A angle and to a the twisting of the benzonitrile moiety relative to the phenoxazine one.

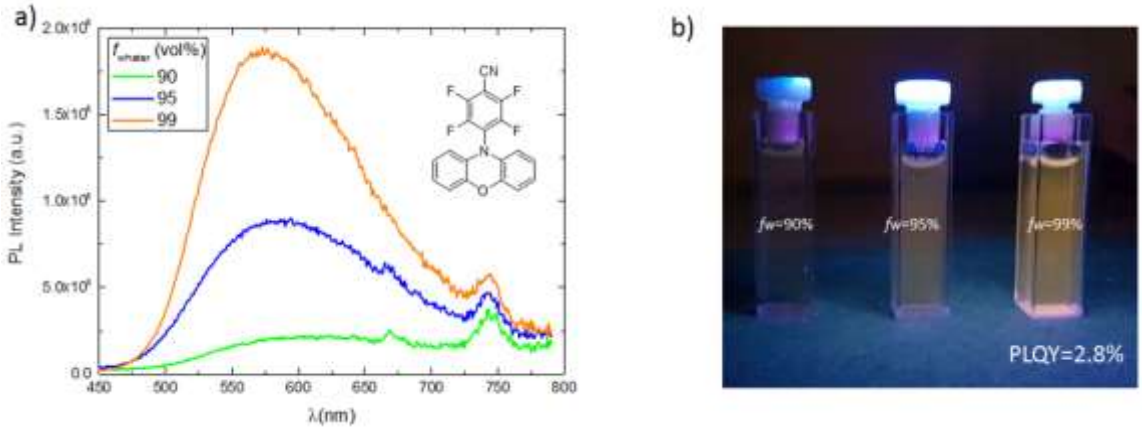

Figure 4.15: a) *PL spectra of* ***Phx-BzN*** *in THF/water mixtures with different water fractions (f_w).* ***b)*** *Pictures of* ***Phx-BzN*** *in different THF/water mixtures (f_w=90, 95 and 99% from left to right) under UV light (365nm) irradiation. λ_{ex}= 370 nm.*

5.2.3 Time-resolved study of Phx-BzN.

In this section are discussed the time-resolved photophysical properties of the different solid forms of **Phx-BzN.** The isolated molecule in PMMA and the initial crystalline powder are studied at room temperature and 77K. The neat film was studied only at RT (**Figure A4.15e** and **Figure A4.15f**). However, as the neat film looks partially crystalline the photophysical properties remain similar to that of crystalline initial powder with a more broadened emission.

5.2.3.1 Time-resolved properties of Phx-BzN in PMMA.

The time-resolved properties of **Phx-BzN** molecule in PMMA are already reported in **Chapter 2** and are summarized herein in **Figure 4.16.** The onset of the early emission is blue-shifted indicating an initial contribution of the ^{1}LE of phenoxazine. At RT after 100ns, only the CT state clearly remains (**Figure 4.16a**), and as we can see in the decay profile, the DF emission lives up to ~100 μs (**Figure 4.16b**). A PF/DF ratio of 0.15 was calculated from the PL decay of **Phx-BzN** in PMMA at RT (**Table 7**) indicating poor TADF properties. At 77K there is a weak DF contribution. It is possible that thanks to the very low $\Delta E_{S\text{-}T}$ =0.04eV we observe TADF, but we cannot exclude a TTA process. The onset of the (77K) late emission spectrum, in the millisecond regime, is blue-shifted (2.81 eV) and it matches with the phosphorescence of phenoxazine (2.81eV). Therefore the phosphorescence of **Phx-BzN** in PMMA (70.8ms, 77K) can be assigned to the ^{3}LE emission arising from the phenoxazine moiety.

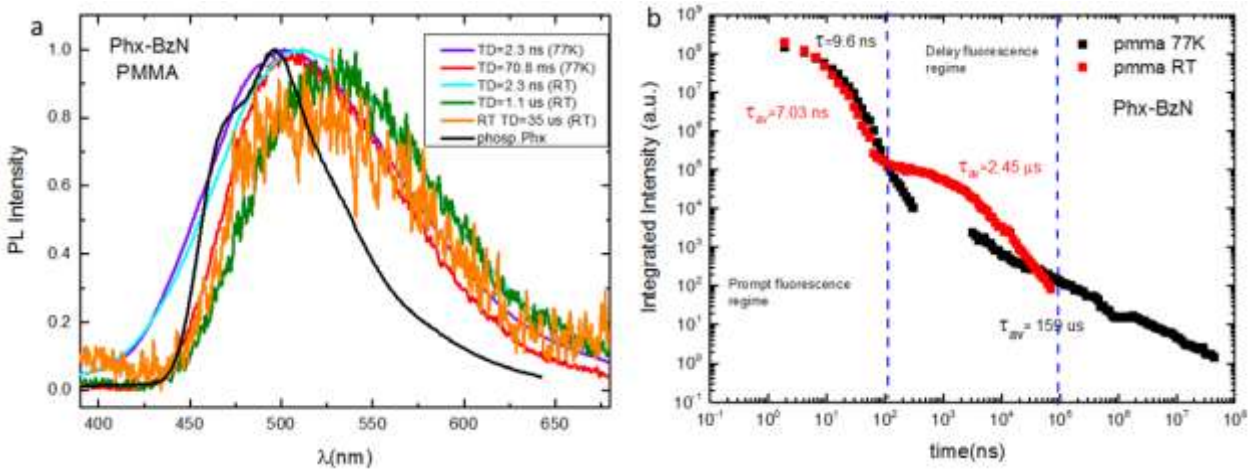

Figure 4.16: a) *time-resolved emission spectra of* ***Phx-BzN*** *in PMMA at RT, 77k and phosphorescence of Phenoxazine.* ***b)*** *decay curve of* ***Phx-BzN*** *in PMMA for RT and 77K. All experiments were carried out at* λ_{ex}*= 355 nm.*

5.2.3.2 Time-resolved properties of Phx-BzN crystalline initial powder.

The time-dependent emission properties of **Phx-BzN** initial crystalline powder were also studied to understand the photophysical processes in the rigid crystal packing. The experiments were done at four different temperatures (RT in **Figure A4.14a**, 80K in **Figure A4.15a**, 200K in **Figure A4.14c**, and 140K in **Figure A4.14e**). The spectra don't evolve for each temperature (as seen in the appendix) but they change from one temperature to another. The non-evolution of the emission with increasing time delays indicates that only one molecular conformation is present in the crystalline packing, but also that the molecule cannot relax its conformation upon excitation. Since the emission does not shift with the increase of TD, only the PF emission spectra are reported for each temperature in **Figure 4.17a**. In particular, we can see that from RT down to 140K, the emission moderately blue shifts but the FWHM increases. This is in contrast with the rigidochromic effect expected at low temperature, where a spectral narrowing occurs because of the suppression of the rotovibrations. This behaviour becomes even more pronounced when the system is further cooled down to 80K. Beyond the strong blue shift, the spectrum becomes very broadened and two different peaks appear (λ_1= 506, $\lambda_{2,max}$ = 532nm).

The non-normalized decays for the different temperatures are reported in **Figure 4.17b**. We can notice a strong increase in the total emission especially passing from 200K to 80K. The surface below the decays is proportional to the total photons emitted upon the acquisition. If we assume that the absorption does not change with temperature, it results that the ratio between the integral of the different decays has to be equal to the ratio between the PLQYs at the different temperatures. Therefore from the PLQY calculated at RT, it is possible to estimate the PLQY for

the other temperatures. According to this procedure, the PLQY increased ~140 times from RT to 80K giving a PLQY of 714% at 80K. This is not physically possible and necessarily it means that at 80K the absorption is more efficient than at RT. We think that we are dealing with the formation of a new polymorph (**polymorph II**), which explains the drastic change of the photophysical properties. Once the system is heated back to RT we can observe that the emission redshifts again (λ_{max}= 571nm, onset= 2.33 eV) becoming close to the initial one at RT (λ_{max}= 580nm onset= 2.43 eV). This indicates partial reversibility of the process from the **polymorph II** to the initial **polymorph I**. The blue shift of only 20 nm in the emission from RT to 140K indicates that the transition between **Polymorph I** to **Polymorph II** occurs mainly between 140K and 80K.

The decays for the different temperatures are reported in **Figure 4.17b**. We can notice that the decay at 80K assumes a typical long-living TADF profile that is also moderately intense. This seems to be in contrast with the TADF phenomena that need thermal energy to be activated. However, since the emission in **polymorph II** does not evolve with increasing delay times (**Figure A4.15a)** we can assume that the triplet state lies very close in energy to the singlet ($\Delta E_{S\text{-}T}$~0). With such a singlet-triplet energy gap close to zero, the triplet needs much less energy to go back to the singlet. However, the onset of the phosphorescence of phenoxazine (2.80 eV) is considerably higher in energy respect to the late ms emission of **polymorph II** (2.62eV) (**Figure 17a**). Therefore, as the ^{3}LE is far from the ^{3}CT, it results that the vibronic coupling[7, 26] (VOC) between ^{3}LE and ^{3}CT of **polymorph II** is weak. Nevertheless, as we think that the triplet involved in the RISC should have mainly ^{3}CT character, it results that for $\Delta E_{S\text{-}T}$ approaching zero, the hyperfine coupling[27, 31-32] (HFC) could play a role in the RISC between ^{3}CT and ^{1}CT. We think that both VOC and HFC mechanisms are involved in the ISC and RISC processes of **polymorph II**[12]. Thanks to the fact that at low temperatures the non-radiative decay is also suppressed it is possible to observe a very long decay time of 513µs (**Table 7**) which is orders of magnitude longer respect to that at RT (0.2 µs).

The intensity dependence of the DF emission as a function of the laser excitation dose for **Phx-BzN** initial crystal powder at RT (**Figure A4.16a**) confirms a monomolecular process typical of the thermally-assisted mechanism. The PF/DF ratio calculated from the decay profile at RT (**Table 7**) shows that TADF works almost five times better in crystal and in neat films than in PMMA matrix. However, the QY increases only from 3.8% in PMMA to 5.1% in crystal and decreases in neat film (2.8%). Therefore, it is possible to assume that the molecular configuration in both neat film and crystalline powder favours an increase of the TADF respect to PF. However, certainly in neat film part of the molecules are present in an amorphous phase where the non-radiative deactivation

[12] However we cannot exclude the formation of a completely new triplet state in **polymorph II** arising from an aggregated state. In such situation, the triplet could present a delocalized character, with the HOMO and LUMO density function delocalized on the whole molecule.

pathways remain dominant. The DF/PF ratio for crystal at different temperature (**Table 7**) decreases when the system is cooled down to 200K because the thermal energy effect decreases. Nevertheless, the DF/PF of **polymorph II** (80K) cannot be compared with that of **polymorph I** (RT to 140K).

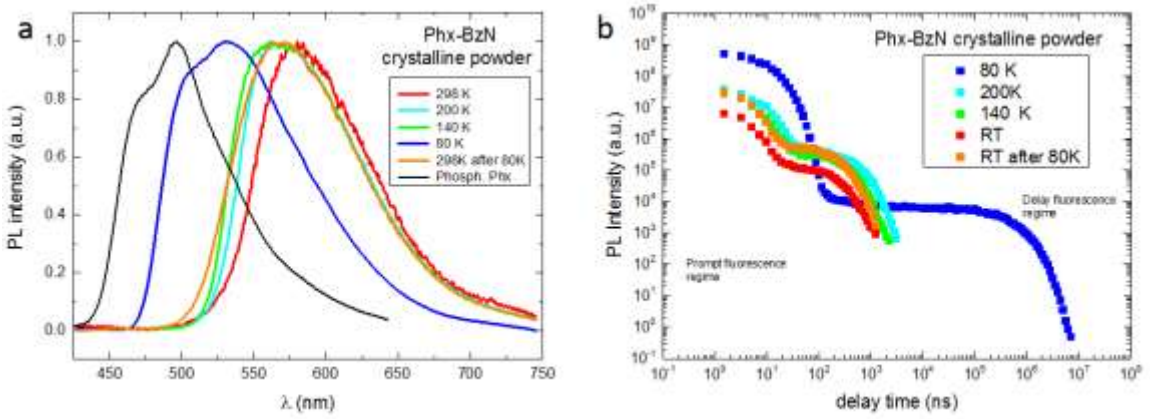

Figure 4.17: ***a)*** *Time-resolved emission spectra of* ***Phx-BzN*** *crystalline powder for RT, 200K, 140K, 80K and RT after 80K, from the early prompt emission (same for longer TD) 80K in comparison with phosphorescence of Phenoxazine.* ***b)*** *Decay curve profile of* ***Phx-BzN*** *crystalline powder for RT, 200K, 140K, 80K and RT after 80K. All experiments were carried out at* λ_{ex}*= 355 nm.*

Table 7 Summary of the time resolved photophysical properties of **Phx-BzN**.

Phx-BzN	λ_{PL} (nm)	$\Phi_{PL}{}^{air}$-$\Phi_{PL}{}^{deg}$	τ_{PF} (ns)	τ_{DF} (µs)	$\tau_{phos.}$ (ms)	$\Delta E_{S\text{-}T}$(eV)	DF/PF
Crystal pwd. RT	580	5.1%	3.9	0.20	-	-	0.86
Crystal pwd. RT after 80K	570	n.c.	3.8	0.20	-	-	0.76
Crystal pwd. 200K	563	§21.9%	4.7	0.29	-	-	0.68
Crystal pwd. 140K	560	§38.3%	6.7	0.45	-	-	0.73
Crystal pwd. 80K	506/532	-	10.3	513*	-	0.00	0.56
Neat film RT	575	2.8%	3.0	0.20	-	-	0.84
PMMA RT	506	3.8-4.4%	7.03*	3.78*	-	-0.04	0.15
PMMA 77K	506	n.c.	9.58	-	#		/

(deg) degas, §estimated, *biexponential, #not fitted, n.c. not calculated. (for all Φ_{PL}, the experimental error is ±20% of the value)

5.3 Photophysical Properties of Pht-BzN.

5.3.1 Steady-State study of Pht-BzN.

The UV-Vis absorption spectra of **Pht-BzN** in three different solvents and in PMMA are reported in **Figure 4.18a**. Between 500 and 360 nm, where phenothiazine no longer absorbs, the CT absorption band appears. At higher energy, the peak at λ_{max}= 290 and the shoulder at 315 nm are typical of phenothiazine derivatives[78] and therefore are associated to the LE state associate

to phenotiazine. Similarly to **Phx-BzN,** also **Pht-BzN** presents a negligible emission in cyclohexane (CH) solution (**Figure 4.18b**) with a very low quantum efficiency of 0.2% (**Table 8**), but is completely non-emissive in any other solvent[13]. Therefore, can be considered this material practically not emissive in solution. Moreover, the emission intensity does not change in aerated or degassed CH solutions (**Figure A4.17**), thus indicating that no remarkable TADF properties. As demonstrated by DFT calculations, **Pht-BzN** is non-emissive in solution because upon excitation the molecule relaxes to the S_1 excited state configuration where the perfectly isolated HOMO and LUMO results in an integral overlap (J) equal to zero that leads to a zero oscillator strength of the transition (**Table A1**).

The molecule emits moderately in PMMA and Zeonex with a PLQY respectively of 1.4% and 1.7% in aerated conditions and 1.7% and 2.1% after degassing. The lower QY in aerated conditions is due to the triple quenching of the **Pht-BzN** by the oxygen triplet ground state. This is a first sign of TADF characteristics. Nevertheless, in PMMA and Zeonex the oxygen permeability is low and thus the partial quenching allow to detect TADF even in not degassed conditions. The bathochromic shift of the emission in PMMA respect to Zeonex relies on the higher polarity of the former that shifts the CT state to lower energy. As regarding the neat film, the QY increase from 0.2% in CH to 0.5% in amorphous neat film. At first sight, this indicates poor AIE properties, which probably depends on the free space in the amorphous film that allow a partial geometry relaxation to a quasi-orthogonal configuration. However, the red shift respect the two polymers along with the decrease of the QY from 1.7 to 0.5% could be also a sign that in the amorphous phase emission quenching also occurs.

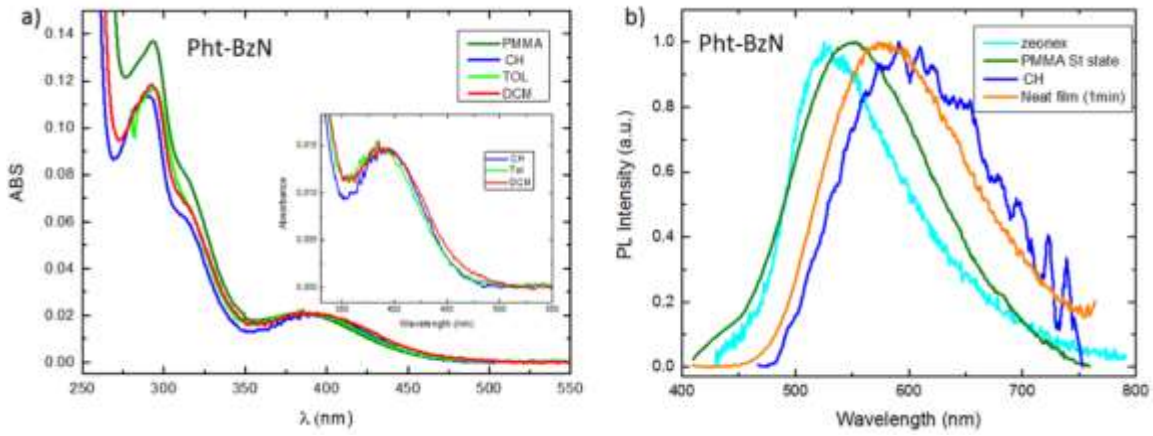

Figure 4.18 a) *UV-Vis absorption spectra of* **Pht-BzN** *in cyclohexane (10^{-5} M), Dichloromethane (10^{-5} M), Toluene (10^{-5} M), and PMMA,* ***inset)*** *absorption in the solvent with different polarity normalized on the CT band* ***b)*** *Normalized photoluminescence (PL) of* **Pht-BzN** *in Zeonex 0.1wt%, PMMA 0.1wt%, diluted cyclohexane and neat film, λ_{ex}= 330 nm. .*

[13] The completely no emission in toluene depends on the fact that being the phenotiazine a stronger donor than carbazole, it results that the higher polarity of toluene stabilizes too much the Pht-BzN CT state, that already present a negligible emission in CH.

5.3.2 Crystallisation Induced Emission (CIE) and Sonication Induced Crystallization (SIC).

Surprisingly it was observed that after 30 min the emission of neat film spontaneously start to changes from dim yellow to bright blue. After one hour, the process is complete. The blue emission it is narrower (Δ_{FWHM}= 59 nm), strongly blue-shifted (82 nm) and with a PLQY of 8.2%. This behaviour indicates a strong tendency of this material to self-organize in a more stable configuration which dramatically increases the emission. In order to explore the nature of this self-assembled configuration a crystalline film was obtained through the SVA method. The SVA crystalline sample presents the emission profiles identical to both the initial crystalline powder and the neat film after 1h (**Figure 4.19a**), thus indicating a crystallization induced emission (CIE) process. The high quality crystals obtained through the slow evaporation of petroleum ether/dichloromethane (3:1) allow to obtaining a spectacular PLQY of 39%. The excitation spectra (**Figure 4.19b**) shows that in the neat film (1min) there is a slight batochromic shift in the CT absorption band that becomes dramatically less intense and seems to disappear once the crystal is formed (neat 60min). Similarly, the excitation spectrum in PMMA shows a low contribution of the CT transition to the emission. The drastic reduction of the absorption of the CT band in the crystalline form should depend on the different conformation that the molecule assumes in the crystal. This is in agreement with what was already observed for different conformers of phenothiazine derivatives[121]. The TDDFT calculation show in fact, that when the molecule is in the S_0 geometry (the same as that in crystal) the CT band presents a very weak oscillator strength (0.0006) (**Figure A4.7**, **Table A1**), that further decreases in the S_1 configuration (0) but increase orders of magnitude in the T_1 configuration (0.0297).

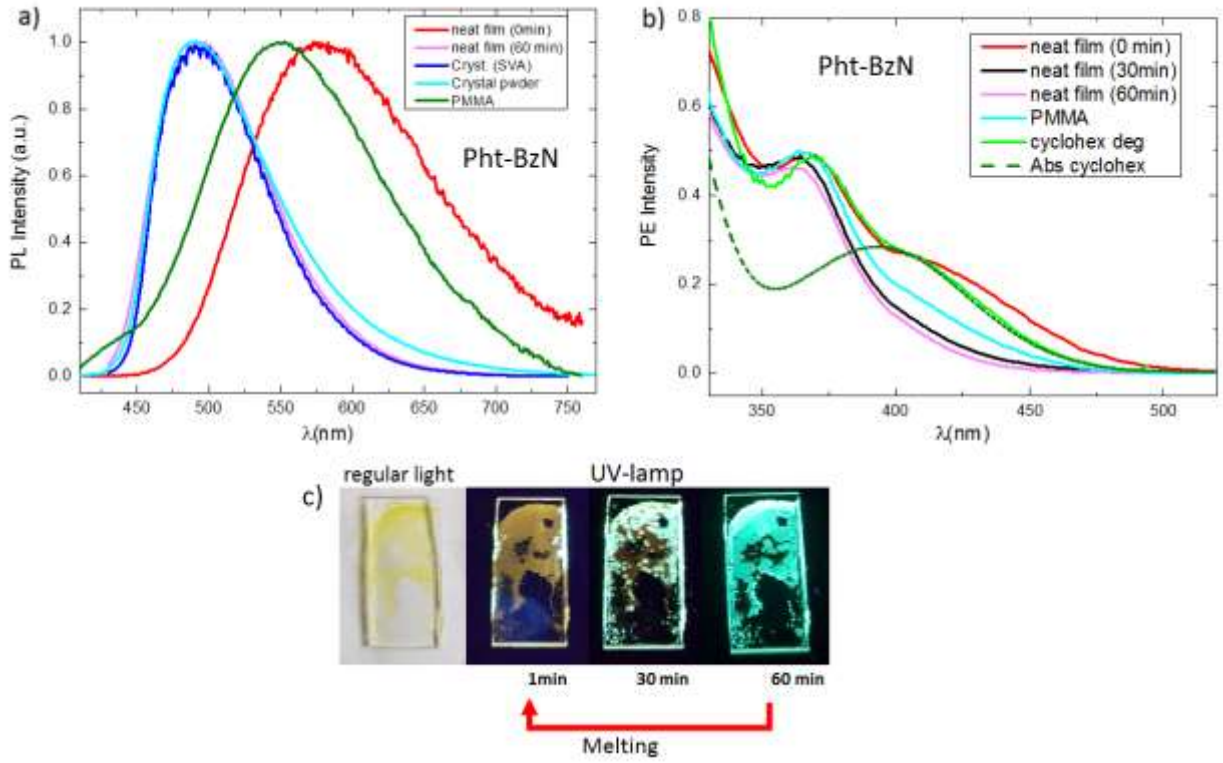

Figure 4.19 a) *Normalized photoluminescence (PL) spectra of* ***Pht-BzN*** *in various solid forms: neat film obtained from DCM solution fresh(0-3min), neat film crystallized (60 min), crystalline film from SVA, crystal in cuvette and isolated molecule in PMMA,* λ_{ex}*= 370 nm.* ***b)*** *Excitation Spectra of* ***Pht-BzN*** *of the various solid forms compared with the Excitation and Absorption in Cyclohexane* ***c)*** *fluorescence images of* ***Pht-BzN*** *neat film after 1min, after 30min, and after 60 min. Melting the* ***Pht-BzN*** *neat film after crystallization is obtained the initial (neat 1min) amorphous emission.*

AIE and CIE properties were also studied through the THF/water test described above for **Phx-BzN** molecule. In **Figure 4.20a** it is shown that when the water fraction f_w increases from 90 up to 99%, the emission progressively appears and becomes more and more intense upon aggregates formation. However, the PLQY does not exceed 1%. The yellowish emission with λ_{max}= 575 nm corresponds to that of the fresh neat film (1min) thus indicating the formation of amorphous aggregates during the THF/water test. To induce a reorganization in the dispersion we applied ultrasound to the obtained solution, and satisfactorily after 10 min of sonication, the amorphous yellowish dispersion (QY =1%) blue shifts to cyan (λ_{max}= 500nm) and becomes intensely bright (QY=22%). The emission colour corresponds to that of the crystalline form (**Figure 4.20b**). The dimensions of the obtained nanocrystals were measured by using the DLS techniques (See Experimental section **§ 4.8**) obtaining particle sizes of 271 and 653 nm (**Figure A4.22**). As demonstrated both from the blue shift and the strong increase of the emission we think that sonication induces the formation of crystals. It has already been reported in the literature that

ultrasounds are often used to induce the crystallization of a solution. This is valid especially in the pharmacology field, where sonication is used to yield crystals of very small dimensions with a narrow size distribution. Ultrasonic irradiation decreases the induction time and metastable zone and increases the nucleation rate, thanks to the improved micro-scale mixing and turbulence caused by acoustic cavitation[128-131]. However, although the PLQY of the sonicated dispersion is more than doubled compared to that of the neat film (1h) and SVA crystalline film, it remains lower than that of the crystal prepared by slow evaporation of petroleum ether/DCM. We think that it depends on the quality of the crystals as probably not all the molecules are able to form microcrystals upon sonication.

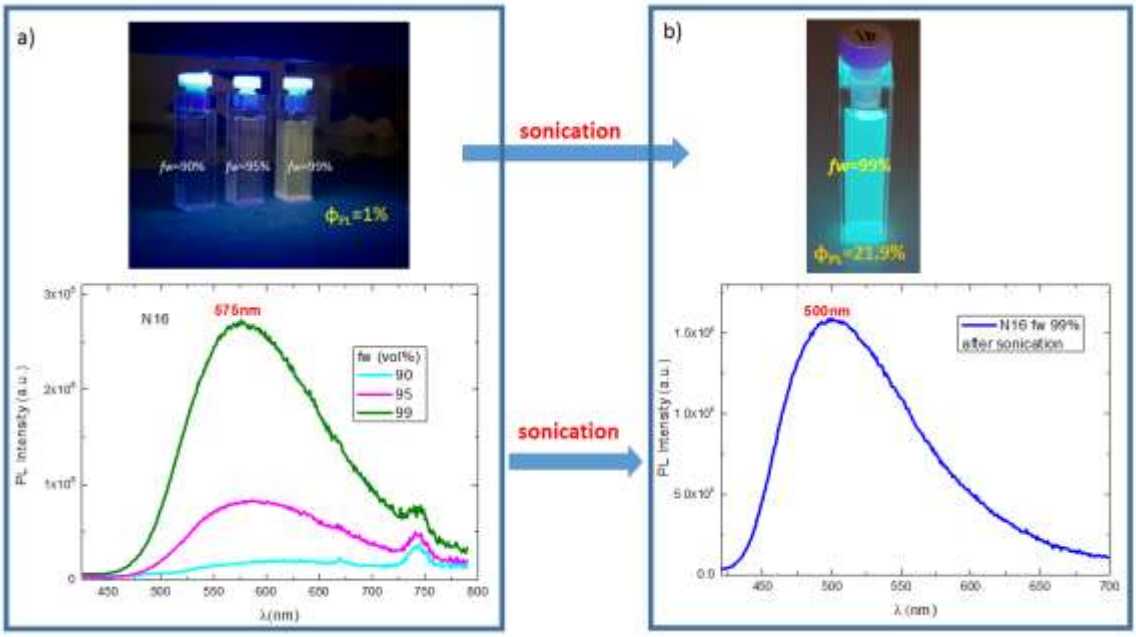

Figure 4.20 a) down*) PL spectra of* ***Pht-BzN*** *in THF/water mixtures with different water fractions (f_w =90, 95 and 99%), λ_{ex}= 370 nm.* ***Up****) fluorescence images of* ***Pht-BzN*** *in different THF/water mixtures (f_w =90, 95 and 99%) under UV light irradiation.* ***b) down****) PL spectra of sonicated* ***Pht-BzN*** *in THF/water mixtures with different water fractions (f_w=90, 95 and 99%), λ_{ex}= 370nm.* ***Up****) fluorescence images of* ***Pht-BzN*** *in different THF/water mixtures (f_w =90, 95 and 99%) under UV light irradiation.*

5.3.3 Time-resolved photophysical properties of Pht-BzN in Zeonex.

The time-resolved photophysical properties of **Pht-BzN** in Zeonex at RT are depicted in **Figure 4.21**. We can see a slight red shift between the early PF (TD=0.7ns) and the DF emission (1.1µs) (**Figure 4.21a**) indicating both geometry relaxation and a partial initial contribution of ^{1}LE from phenothiazine. After 1 µs, the DF emission does not evolve anymore living up to 230 microseconds. The RT decay profile (**Figure 4.21d**) is fitted with a shorter decay time of 4.1ns (**Table 8**) typical of PF emission and an average decay time of 1.4 µs typical of DF. The PF emission

at 80K is slightly blue-shifted respect to the PF emission at RT (**Figure 4.21c**). This is due to rigidochromism. However, the DF at 80K (1.1 μs) is similar to the one at RT (**Figure 4.21c**, $onset_{RT}$=2.61eV, $onset_{80K}$=2.58 eV). After 50μs, at 80K, the DF progressively blue shifts up to 100ms (onset=2.69 eV), where the structured emission clearly indicates its phosphorescence nature. The onset of the phenothiazine triplet (2.57eV) (**Figure 4.21c**), lay at lower energy respect to the phosphorescence of **Pht-BzN** in Zeonex. Besides the ^{3}LE contribution of phenothiazine, likely a small ^{3}LE contribution of the Benzonitrile of **Pht-BzN** in Zeonex. We can notice that between 2 and 100ms the emission progressively blue shifts (onset from 2.65 to 2.69 eV). Therefore the ΔE_{S-T} is estimated between 0.08 to 0.04eV. The very low ΔE_{S-T} in addition to the fact that the decay curve (**Figure 4.21d**) doesn't show any change of profile in the μs-ms region might indicates a a coexistence of phosphorescence and DF. The 80K decay profile (**Figure 4.21d**), was fitted with a short decay time of 6.9ns (**Table 8**) typical of PF emission, an intermediate average decay time of 50.5 μs typical of DF and a long decay time of 6.7 ms in the phosphorescence region. The intensity dependence of the DF emission as a function of the laser excitation dose for **Pht-BzN** in Zeonex (**Figure A4.21a**) confirms a monomolecular process typical of the thermally-assisted mechanism. The relative small PLQY of 2.1% and the small DF/PF ratio value of 0.61 (**Table 8**) indicate a weak TADF contribution in Zeonex. The poor photophysical properties in zeonex probably depends on the fact that the molecules dispersed in polymer have some space to relax its geometry. Therefore part of the excitation energy is lost non radiatively. Furthermore, the relaxation to a quasi-orthogonal configuration reduces the oscillator strength and thus the emission is diminished.

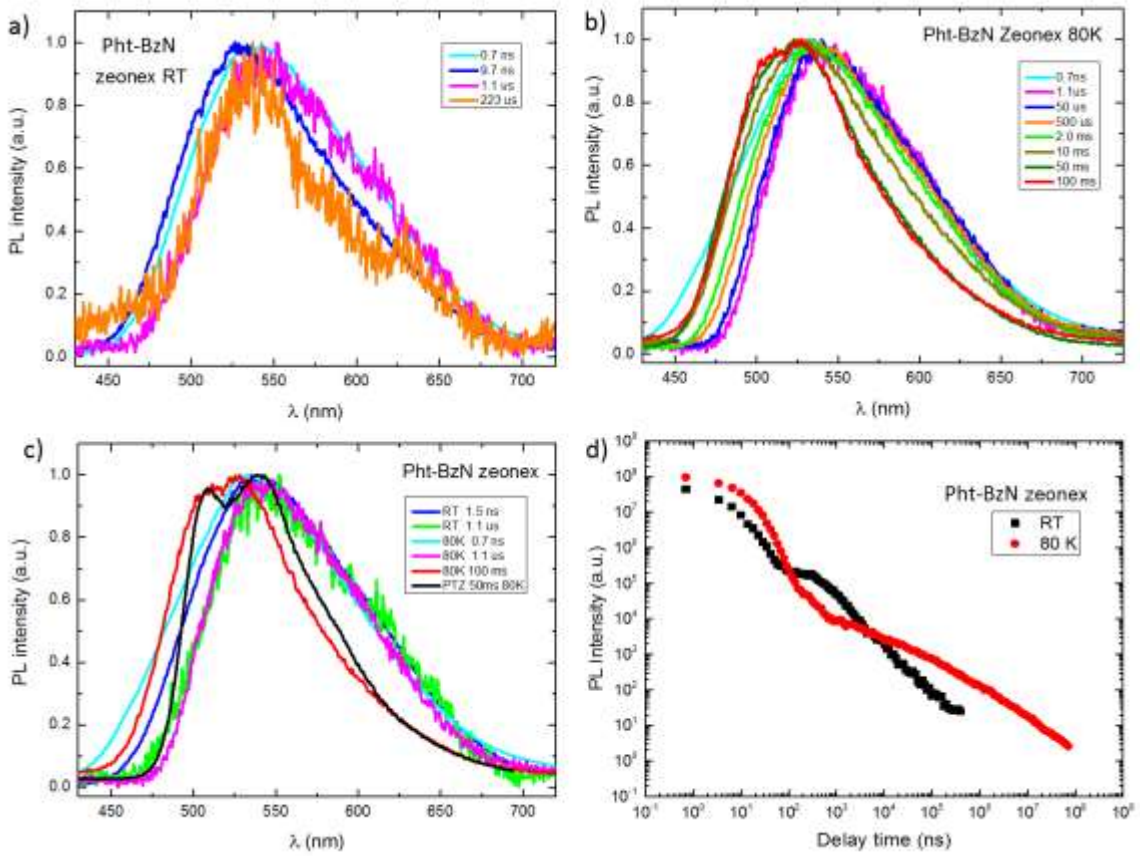

Figure 4.21 a) *time-resolved emission spectra of* ***Pht-BzN*** *in Zeonex at room temperature (RT)* ***b)*** *time-resolved emission spectra of* ***Pht-BzN*** *in Zeonex at 80k* ***c)*** *time-resolved emission spectra of* ***Pht-BzN*** *in Zeonex at 80K and RT in comparison with the phosphorescence of Phenothiazine.* ***d)*** *Decay curve of* ***Pht-BzN*** *in Zeonex for RT and 80K. All experiments were carried out at* λ_{ex}*= 355 nm.*

5.3.4 Time-resolved photophysical properties of Pht-BzN neat film.

The time-resolved emission of neat film at RT doesn't change between the PF and DF emission, thyus indicating that the molecule is tightly blocked and cannot relax its configuration after photon absorption. However, at 80K, the slightly blue-shift of the early PF emission might depends on the initial local contribution of phenothiazine (^{1}LE). From the decay profile (**Figure 4.22d**) we can see that at RT the DF emission starts to appear around 100ns. We consider that TADF is clearly formed after 1µs (**Figure 4.22b**) to which corresponds an onset of 2.79 eV. At 80K the DF emission appears later (1µs) (**Figure 4.22d**) but lives much longer (up to 1 ms). On the other hand, the phosphorescence is clearly detected after 4ms (**Figure 4.22a**) and becomes more structured at 50ms. Also in this case the phosphorescence of **Pht-BzN** (onset=2.66 eV) appears blue shifted respect to the phosphorescence of phenothiazine (onset= 2.57 eV) (**Figure 4.22c**). Therefore, we think that the **Pht-BzN** triplet state carry both local contributions from

phenothiazine and benzonitrile. The RT decay profile (**Figure 4.22d**) was fitted in the PF regime, with a short decay time of 6.6 ns (**Table 8**), and in the DF regime with a longer decay time of 0.6 µs. At 80K the PF decay time moderately increases (τ_{PF}= 12.2ns) but the DF becomes ~500 times longer (τ_{DF}= 295 µs). The decay reported in **Figure 4.22d** shows that for both RT and 80K the profile presents the typical trend of TADF. In fact, a moderately good DF/PF ratio was obtained at both RT and 80K. A PF/DF value of 2.6 was found at RT and of 2.45 at 80K (**Table 8**), thus obtaining a relative increase of TADF of more than four times respect to Zeonex.

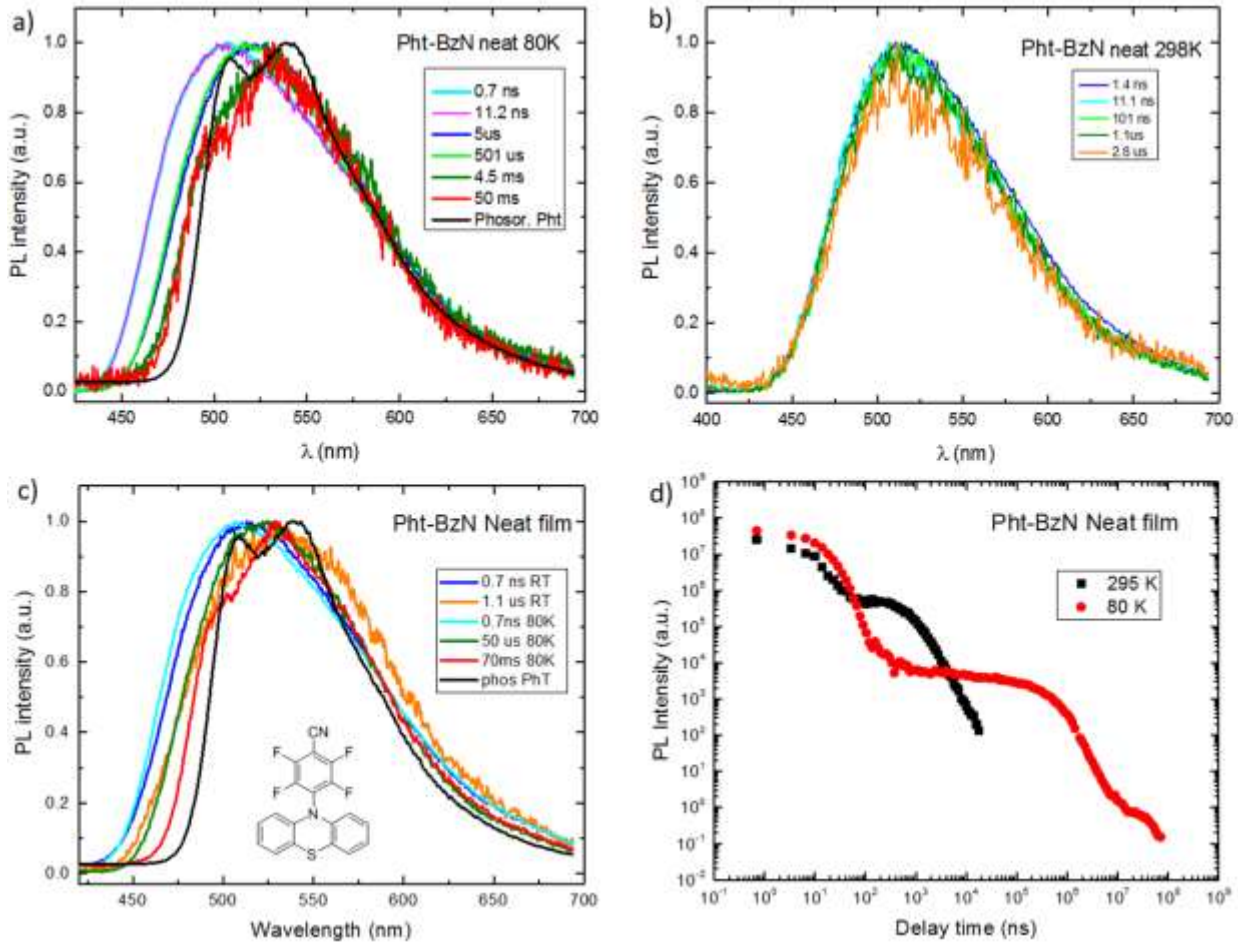

Figure 4.22 a) *time-resolved emission spectra of* ***Pht-BzN*** *in neat film at 80K,* ***b)*** *time-resolved emission spectra of* ***Pht-BzN*** *in neat film at room temperature (RT)* ***c)*** *time-resolved emission spectra of* ***Pht-BzN*** *in neat film at 80K and RT in comparison with the phosphorescence of the Phenothiazine.* ***d)*** *Decay curve of* ***Pht-BzN*** *neat film for RT and 77K. All experiments were carried out at* λ_{ex}*= 355 nm.*

5.3.5 Time-resolved photophysical properties of Pht-BzN nanocrystals dispersion.

The time-resolved photophysical properties of the water sonicated dispersion of **Pht-BzN** (nanocrystals) were also studied at RT (**Figure 4.23**). The early emission spectra do not evolve at a longer time thus indicating that in the nanocrystal the molecule cannot relax. Moreover, the **Pht-BzN** presents quite good TADF characteristics with a DF/PF ratio of 3.46 (**Table 8**). However, similarly to the values of QY (21%), the PF/DF ratio remains smaller respect to the crystal (*vide infra*). As already explained, this probably comes from the fact that during the sonication process, some molecules remain in an amorphous state that weakens the TADF characteristic.

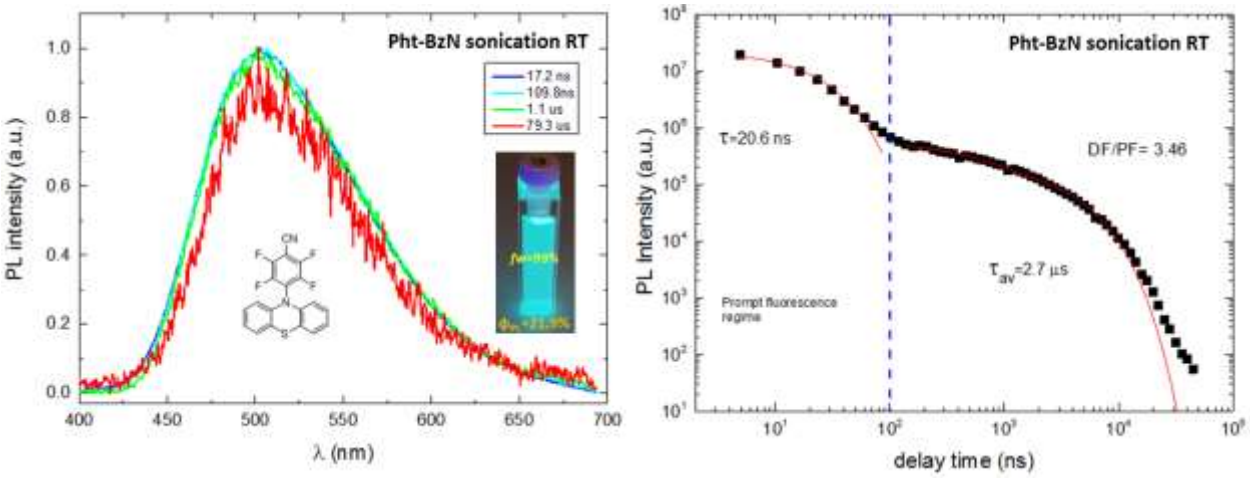

Figure 4.23 a) *time-resolved emission spectra of* ***Pht-BzN*** *sonicated dispersion at room temperature (RT) ,* λ_{ex}*= 355 nm.* ***b)*** *Decay curve of* ***Pht-BzN*** *sonicated dispersion at RT.*

5.3.6 Time-resolved photophysical properties of Pht-BzN Crystal.

Finally, the time-resolved characteristics of the **Pht-BzN** crystal were studied at four different temperatures (RT, 200, 140, and 80 K). At RT and 200K the early emission doesn't evolve over time (**Figure 4.24b** and **Figure A4.19a**). However, there is a slight red shift at 140K between the PF and DF emission (**Figure A4.19b**), which becomes even more pronounced at 80K (**Figure 4.24a**). The slight blue shift in the early PF emission is attributed to a local contribution from phenothiazine (^{1}LE).

As already mentioned above, the PLQY of **Pht-BzN** shows a 200-times increase from CH solution (PLQY = 0.2%) to crystal (PLQY = 39 %). The PLQY progressively increases decreasing the temperature, and a very high value of 92 % is obtained at 80K (estimated comparing the decay at RT with that at 80K, **Table 8**).From both decay profile (**Figure 4.24d**) and time-resolved emission (**Table 8**), we can see that also the TADF properties dramatically improve in the crystal, reaching very high PF/DF= 5 at RT (**Table 8**). Surprisingly, the TADF characteristic of **Pht-BzN** crystal

furtherly improves when the temperature decrease (**Figure 4.24d**), achieving at 80K a spectacular DF/PF ratio of 7.3 (**Table 8**). The high TADF at 80K clearly indicates that ΔE_{S-T} is approaching zero, which also explains the fact that no clear phosphorescence is detected. By using the equations reported in Chapter 1 (**§7.3**), valid only for DF/PF ≥ 4, for **Pht-BzN** crystal was possible to calculate the k_{RISC} and k_{ISC} (**Table 8**). At 80K the k_{RISC} results in three orders of magnitude lower than that at RT (**Table 8**) and this is in line with the strong reduction of vibration that is necessary for have an efficient RISC. However, at low temperatures, the non-radiative deactivation channels are strongly suppressed and the k_{RISC} can efficiently compete with k_{nr}, and thus both PLQY and TADF can increase. It results that the excitation can live longer in the triplet state before to repopulate the singlet, with an increase of the TADF decay time up to 1.1 ms (**Table 8**). Moreover, we expect that in **Pht-BzN** crystal, beyond the ^{1}CT and ^{3}CT states, the LE triplet state involved in the TADF process is rather the one of benzonitrile than that of phenothiazine. This because both the onsets[14] of the initial and late emission of **Pht-BzN** crystal (RT and 77K) are considerably higher in energy respect to the triplet of phenothiazine molecule[15] (**Figure 4.24c**).

For the first time, we demonstrate that it is possible to activate TADF in a crystal through a new phenomenon that we define as crystallization induce TADF (CITADF). Contrarily to the well-known CIE phenomenon, where the emission is activated in the crystal because of the suppression of rotovibrational motion, in CITADF both PF emission and, even more, TADF properties are activated because the molecules in the crystal lattice are forced to maintain the ground state configuration (near orthogonal D-A angle that result in a HOMO-LUMO≠0). Therefore upon excitation, the molecules cannot relax to their excited state configuration as it is typical in solution (S_1), where the perfectly isolated HOMO and LUMO deactivate the emission as the zero exchange energy result in a zero oscillator strength of the transition. On the other hand, when the D and A units are forced to stay in a near-orthogonal orientation, the transition becomes allowed and the low singlet-triplet energy gap maximizes the RISC, thus obtaining very good TADF properties.

Finally, it is noteworthy that the decay profiles of **Pht-BzN** crystal in degassed and aerated conditions have almost no difference (**Figure A4.18**). This indicate that oxygen does not affect the TADF property of the crystal. This behaviour is due to the crystal molecular packing that preventing the oxygen permeability, prevents the triplet exciton quenching. This effect is highly desirable, as it allows to obtain excellent TADF characteristics in the air without the necessity of employing any encapsulation system.

[14] From the onset of the late emission (ms) at 77K it is possible to estimate the energy of the triplet involved in the TADF mechanism. On the other hand, from the onset of the DF emission (~1us), for all temperatures, it is possible to find the energy of the ^{1}CT.

[15] The triplet of phenotiazine is obtained from the onset of the phosphorescence of the phenotiazine (phosph. Pht)

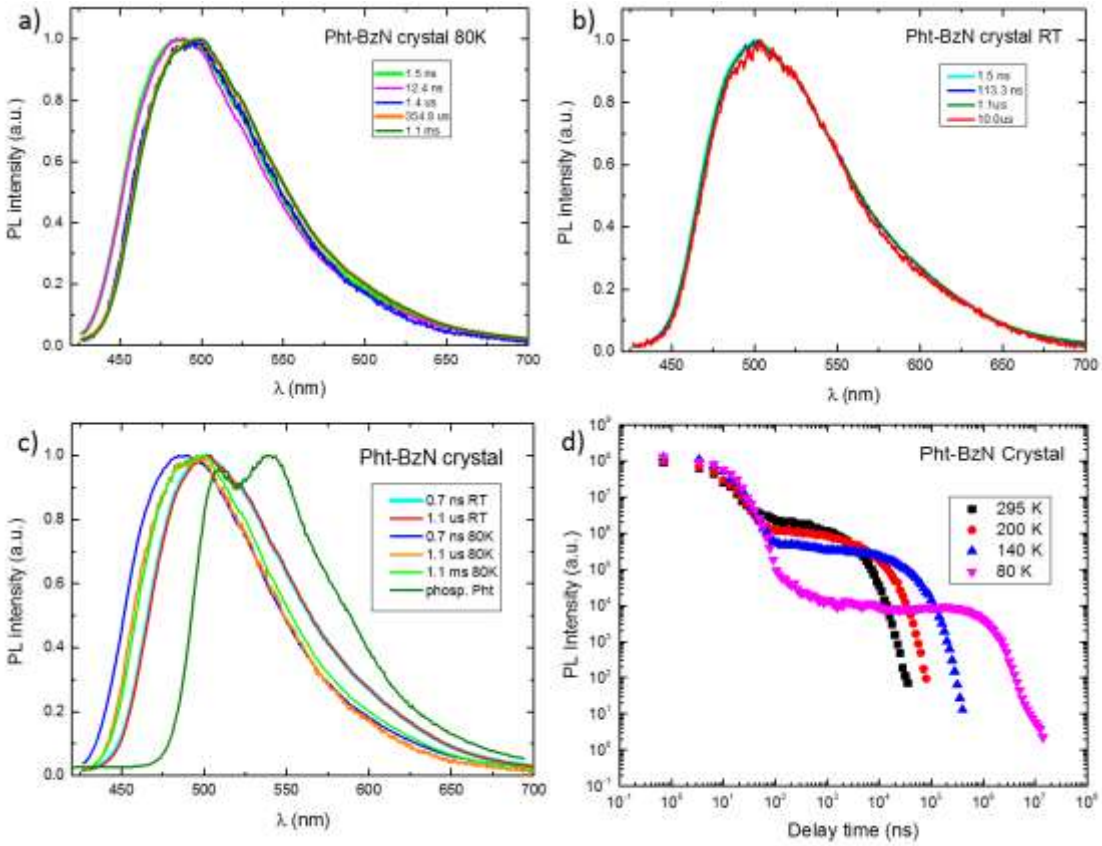

Figure 4.24 a) *time-resolved emission spectra of* ***Pht-BzN*** *crystal at 80K* ***b)*** *time-resolved emission spectra of* ***Pht-BzN*** *crystal at RT* ***c)*** *time-resolved emission spectra of* ***Pht-BzN*** *crystal at room temperature and 80k in comparison with the phosphorescence of Phenothiazine.* ***d)*** *Decay curve of* ***Pht-BzN*** *crystal for different temperatures (RT, 200K, 140K and 80K). All experiments were carried out at* λ_{ex}*= 355 nm.*

Table 8: photophysical properties of **Pht-BzN**

Pht-BzN	λ_{PL} **(nm)**	$\Phi_{PL}{}^{air}/\Phi_{PL}{}^{deg}$	τ_{PF} **(ns)**	τ_{DF} **(μs)**	$\tau_{phos.}$ **(ms)**	ΔE_{S-T} **(eV)**	**DF/PF**	K_{ISC} **(s^{-1})**	K_{RISC} **(s^{-1})**
Crystal RT	500	39.0% [deg]	8.5	2.3	-	0.02	5.0	$9.7x10^7$	$2.6x10^6$
Crystal 200 K	498	[§]51.6% [deg]	10	5.1	-	0.01	5.6	$8.5x10^7$	$1.3x10^6$
Crystal 140 K	494	[§]86.4% [deg]	10.6	23.6	-	0.01	6.3	$8.1x10^7$	$3.1x10^5$
Crystal 80 K	488	[§]92% [deg]	12	1187	-	0.01	7.3	$7.3x10^7$	$7.0 x10^3$
Neat film RT (1 min)	573	0.5%	-	-	-	-	-	-	-
Neat film RT(60 min)	510	8.2%	6.6*	0.46*	-	0.10	2.6	-	-
Neat film 80 K	506	[§]28.3%	12.2	295	33.2	0.08	2.45	-	-
sonication	502	22%	20.6*	2.7*	-	-	3.46	-	-
Zeonex RT	540	1.7%/2.1%	4.1	1.4*	-	0.09	0.61		
Zeonex 80 K	532	[§]10.5 [deg]	6.9	50.5*	6.70	-	0.31	-	-
cyclohexane	602	0.2%	-	-		-	-	-	-

[(deg)] degas, [§]estimated, *average decay (biexponential) (for all Φ_{PL} the experimental error is ±20% of the value)

6. CONCLUSION AND PERSPECTIVES.

The compounds studied in this work are characterized by the same electron-accepting core (benzonitrile) but differs for the three different donors with different donating ability.

Thanks to DFT calculations and XRD analysis, it was demonstrated that when the donor is weak (**Cz-BzN**), the ground state configuration presents a small D-A angle which upon excitation relaxes, and becomes larger. This effect allows observing TADF properties in solution, with a moderate PLQY in toluene. Contrarily, in the rigid crystalline environment, the molecule cannot relax its configuration and a small D-A angle is retained also in the excited state. It results that the $\Delta E_{S\text{-}T}$ is too high to have TADF and therefore only CIEE-PF can be observed. In PMMA being softer than crystal, the more free space allows the **Cz-BzN** to relax to a larger D-A angle and thus TADF can be activated.

The better-donating properties of phenoxazine, lead the **Phx-BzN** to present a larger D-A angle also in the ground state configuration. However, in this case, both the large reorganization of the molecule in the excited state, and the zero oscillator strength arising from the D-A angle of 90°, lead the material to become practically not emissive in solution. Contrarily, in crystal initial powder the molecule is blocked in the ground state configuration, and hence the emission becomes moderately intense with good CIE-TADF properties. At 77K the strong blue shift of the emission, along with the drastic change of the photophysical properties (e.g. absorption) indicates the formation of a new polymorph (**polymorph II**).

The **Pht-BzN** compound is also practically not emissive in solution. The quenching of the emission in solution is due to the reorganization that occurs when the molecule upon excitation relaxes in a perfectly orthogonal D-A configuration that totally isolates HOMO and LUMO. This leads to an extreme decrease in the oscillator strength with a very low probability of radiative decay. In solid-state the emission becomes intense and especially in the crystal, a strong TADF is activated. The strong activation of TADF emission depends on the fact that in the crystal lattice the molecule cannot relax to a perfect D-A orthogonal configuration as in solution, and therefore is forced to maintain a near orthogonal configuration with a oscillator strength higher than zero. This ensures a very small singlet-triplet energy gap that favouring the RISC. Surprisingly the TADF of crystal furtherly increases with decreasing of temperature reaching at 80K a very high PLQY near to unit with a DF/PF ratio of 7.3. Moreover, in this work it is also demonstrated that applying ultrasound to a water dispersion of **Pht-BzN** amorphous nano/microparticles, it is possible to induce distortion of the molecular conformation trough crystallization, blue shifting the emission, and strongly increasing both QY and TADF properties.

In summary, to the best of our knowledge, we demonstrate for the first time, that it is possible to activate TADF in crystal through a new phenomenon that we called crystallization induced

TADF (CITADF). Furthermore, for the first time, we also introduce the sono-crystallization as a method to obtain luminescent nanocrystal. We consider these results as a new strategy to develop new TADF materials using the crystals, especially for high performance organic molecule-based optoelectronic devices application. In fact, because of long-range order, high chemical purity, optical emission enhancement, waveguiding phenomenon, and higher stability than metastable amorphous, organic crystals have exhibit unique properties and attracted a lot of interest for application in solid-state to various devices[132-135]. Thus, we think that further development of TADF nanocrystals thanks to sono-crystallization, could play an important role in the field of optoelectronic organic luminescent materials.

APPENDIX.

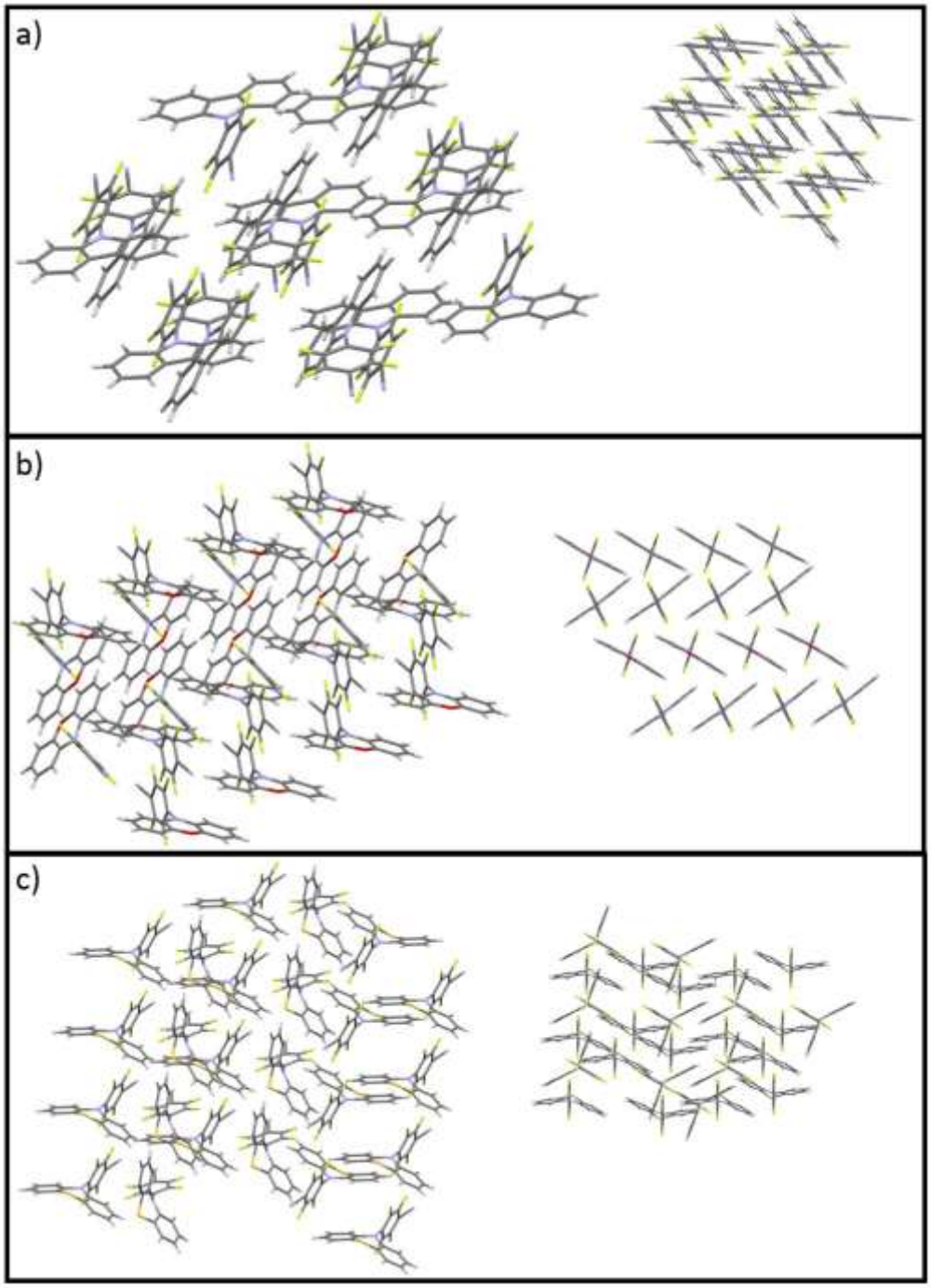

***Figure A4.1**: **a)** molecular packing in **Cz-BzN** crystal;* **b)** *molecular packing in **Phx-BzN** crystal; **c)** molecular packing in **Pht-BzN** crystal.*

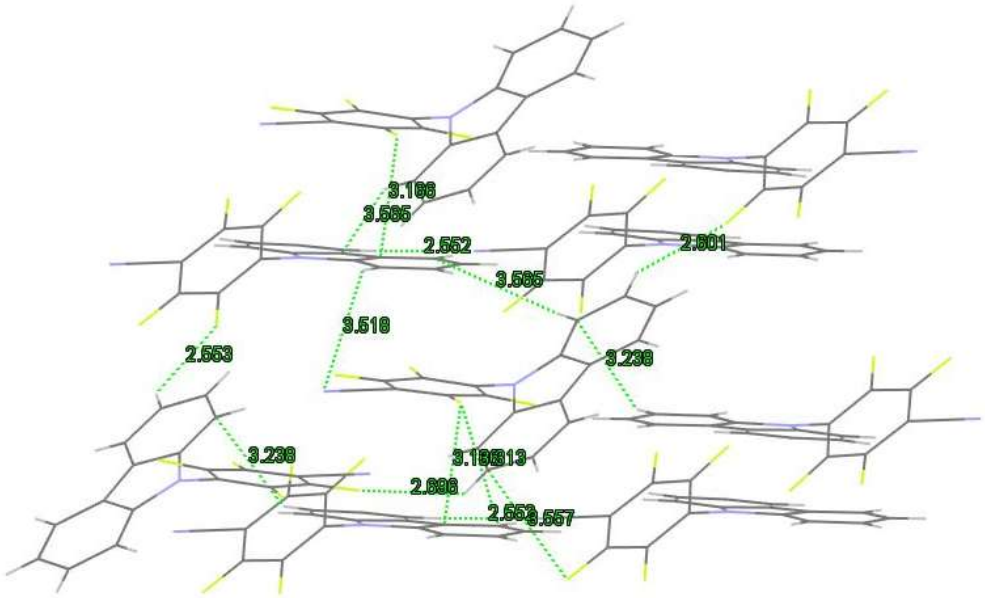

Figure A4.2**: molecular packing with intermolecular interactions in crystal **Cz-BzN.

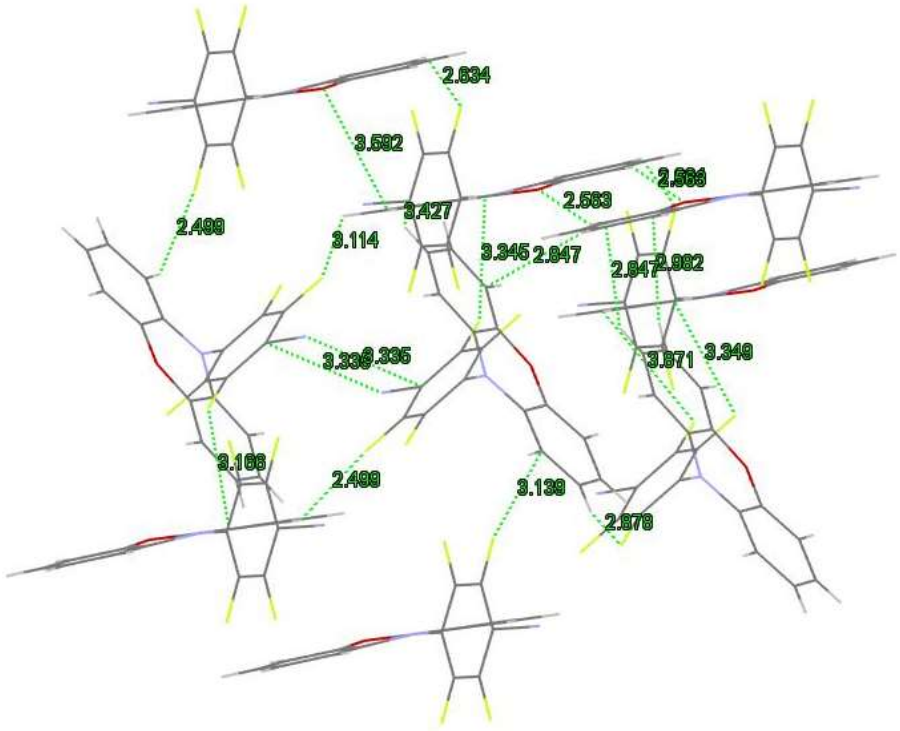

Figure A4.3**: molecular packing with intermolecular interactions in crystal **Phx-BzN.

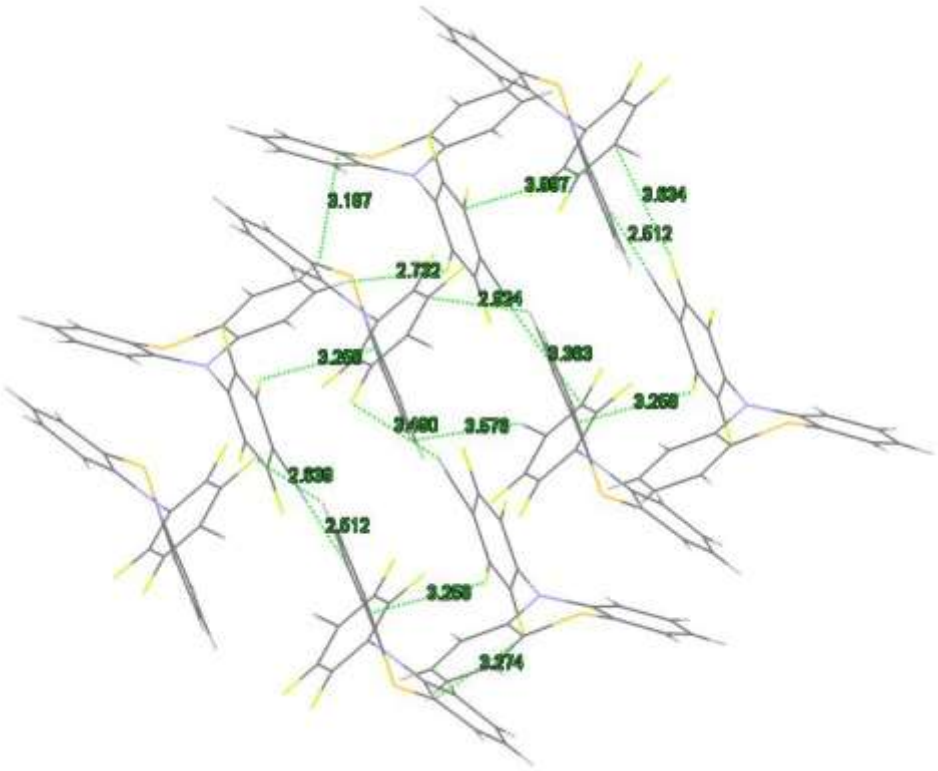

Figure A4.4**: molecular packing with intermolecular interactions in crystal **Phx-BzN.

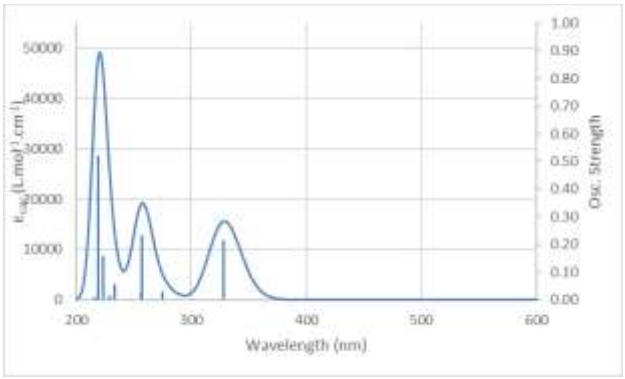

***Figure A4.5**: Calculated spectra and transitions of **Cz-BzN**.*

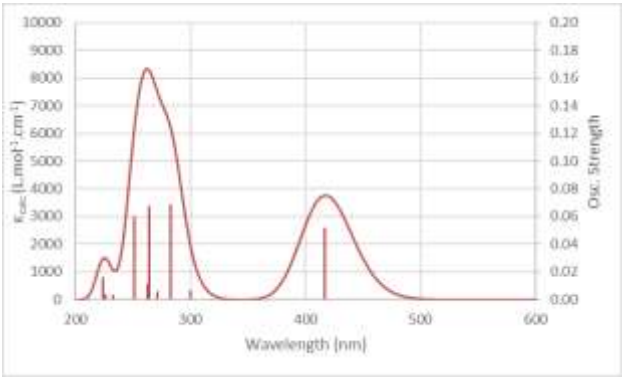

***Figure A4.6**: Calculated spectra and transitions of **Phx-BzN**.*

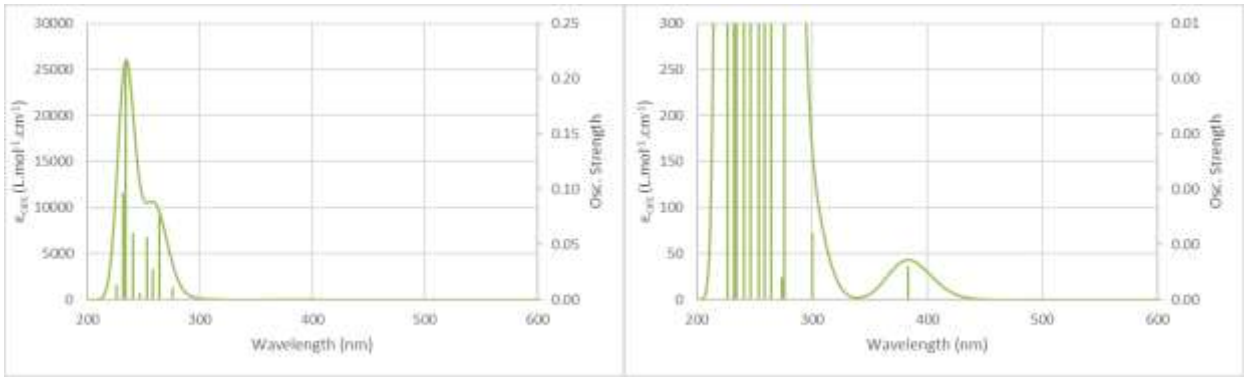

***Figure A4.7**: Calculated spectra and transitions of **Pht-BzN**. The calculated oscillator strength of the first CT of **Pht-BzN** is very small so the band is weak (zoom on the left).*

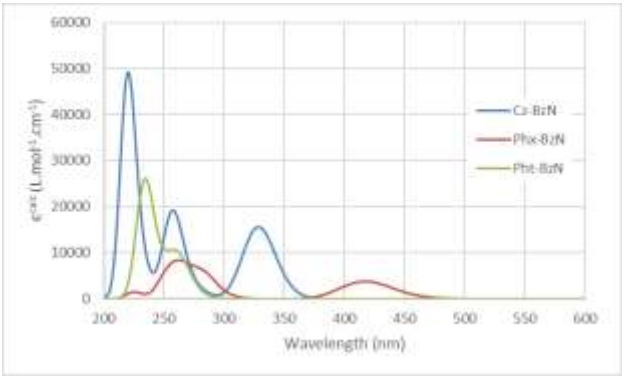

***Figure A4.8**: Overlay of calculated spectra of **Cz-BzN** (blue), **Phx-BzN** (red) and **Pht-BzN** (green).*

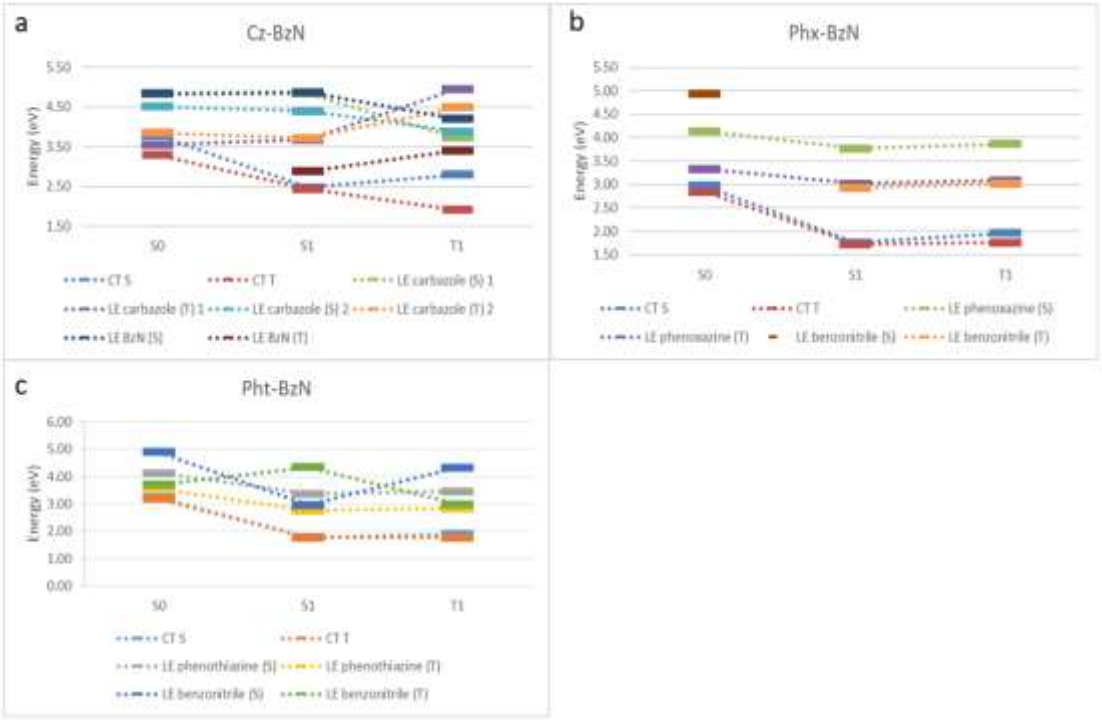

***Figure A4.9**: Energy diagram of the triplet and singlet LE and CT states, for **a) Cz-BzN** and **b) Phx-BzN c) Pht-BzN** molecules in the S_0, S_1 and T_1 geometry configuration, obtained with DTF calculations.*

Table A1 Calculated energy values of the first energy transitions at the ground state (S_0), first singlet excited (S_1) and first triplet (T_1) geometries for **Cz-BzN, Phx-BzN**, and **Pht-BzN** in vacuum.

	S (S_0)	T (S_0)	Osc. St (S_0)	Transition	S (S_1)	T (S_1)	Osc. S(S_1)	Transition	S (T_1)	T (T_1)	Osc. S(T_1)	Transition	
Cz-BzN	3.78	3.29	0.2155	H->L	2.47	2.44	0.0002	H->L	2.80	1.91	0.2682	H->L	CT
Cz-BzN	4.82	3.55	0.2328	H-1->L+1	4.84	3.67	0.1162	H-4->L	-	3.72	0	H-1->L+1	LE Cz
Cz-BzN	4.51	3.85	0.0308	H->L+1	4.39	3.71	0	H->L+1	-	3.88	0	H->L+1	LE Cz
Cz-BzN	4.84	-	0.0281	H-3->L	4.87	2.88	0.4314	H-4->L	4.20	3.40	0.0352	H-3->L	LE BzN
Phx-BzN	2.97	2.84	0.052	H->L	1.76	1.73	0	H->L	1.96	1.76	-	H->L	CT
Phx-BzN	4.13	3.33	0.0064	H->L+3	3.77	3.01	0.0111	H->L+1	3.86	3.09	-	H-1->L+3	LE Phx
Phx-BzN	4.93	3.77	0.0604	H-4->L	-	2.93	0	H-4->L		3.02	-	H-4->L	LE BzN
Pht-BzN	3.24	3.18	0.0006	H->L	1.79	1.77	0	H->L	1.90	1.77	0.0297	H->L	CT
Pht-BzN	4.13	3.56	0.0012	H->L+3	3.37	2.76	0	H->L+1	3.46	2.85	0.0005	H->L+3	LE Pht
Pht-BzN	4.89	3.70	0.0565	H-4 ->L	4.34	3.42	0.0454	H-5 ->L	-	3.42	0	H-4->L	LE BzN

Table A2 Calculated Photophysical data (TDDFT) compared with experimental

	TDDFT	Cyclohexane	DCM	PMMA
Cz-BzN (abs)	329	354	344	350
Phx-BzN (abs)	419	421	414	407
Pht-BzN (abs)	385	395	385	385

Table A3 Energy difference between S_1 and T_1 ($\Delta E_{S\text{-}T}$) obtained from the calculations of the molecules in S_0, S_1 and T_1 geometry configuration.

	$\Delta(_{S\text{-}T})$ (S_0)	$\Delta(_{S\text{-}T})$ (S_1)	$\Delta(_{S\text{-}T})$ (T_1)
Cz-BzN	0.49	0.03	0.89
Phx-BzN	0.13	0.03	0.20
Pht-BzN	0.06	0.02	0.13

Table A4 Decay time in solution for Cz-BzN

Cz-BzN	τ_{PF} [ns]	τ_{DF} [µs]
Cyclohexane[(d)]	9.0	26.8
Toluene[(d)]	11.6	35.2
DCM[(d)]	4.8	43.6

[(d)] degas

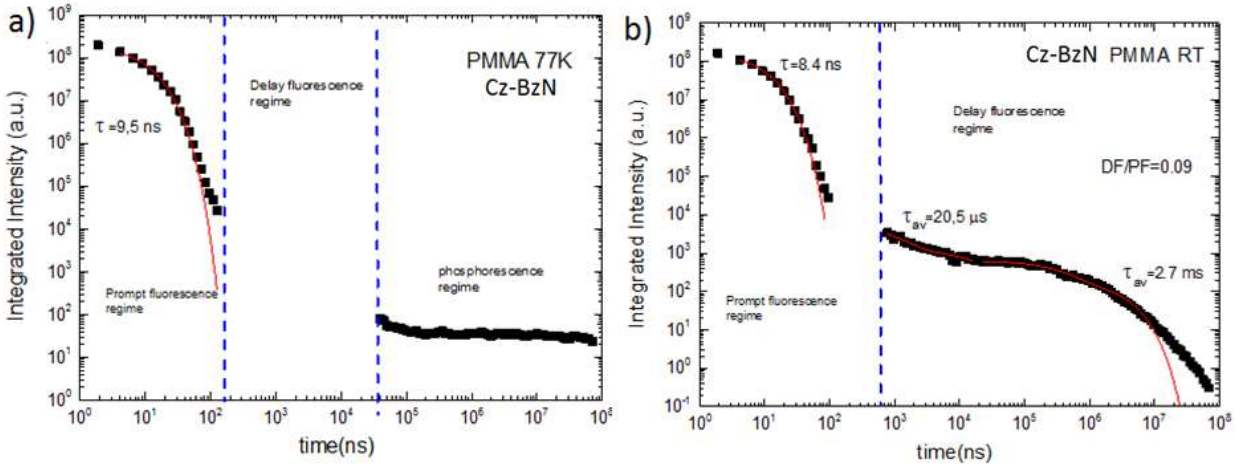

Figure A4.10: *Decay curve and fitting of* ***Cz-BzN*** *in PMMA at* ***a)*** *77K and* ***b)*** *RT.* λ_{ex}*= 355 nm.*

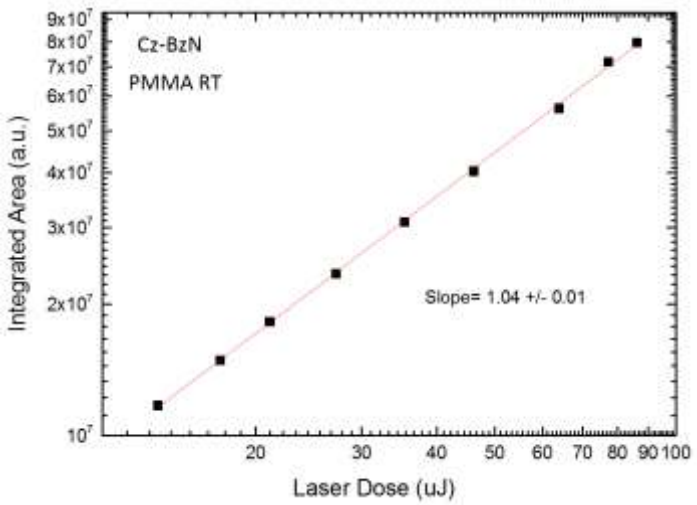

Figure A4.11: *intensity dependence of the DF emission as a function of the laser excitation dose for* ***Cz-BzN*** *in PMMA at RT.* λ_{ex}*= 337 nm*

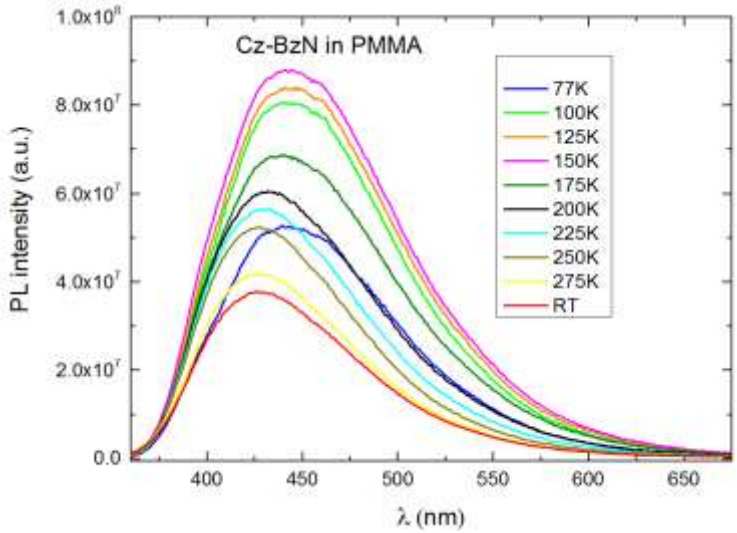

Figure A4.12: *Steady state emission of* ***Cz-BzN*** *in PMMA at different temperatures (from 77k to RT).* λ_{ex}*= 330nm*

Table A5 Estimated PLQY at different temperatures (from 77k to 275).
(PLQY at RT calculated with integration sphere)

	77K	100K	125K	150K	175K	200K	225K	250K	275K	RT
PLQY(%)	58.0	88.9	97.2	100	78.1	65.6	57.4	51.2	40.9	37.4

(for all Φ_{PL}, the experimental error is ±20% of the value)

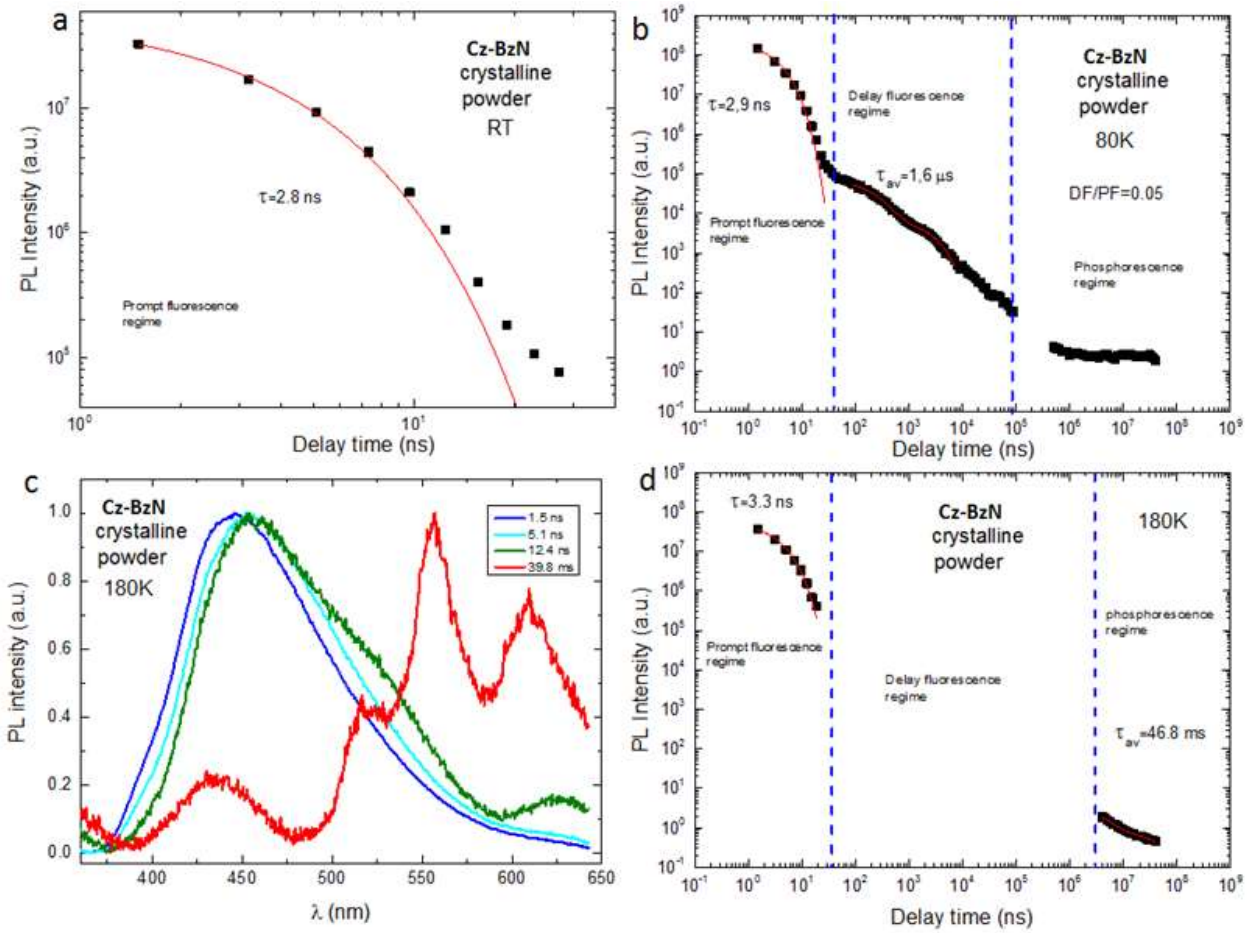

Figure A4.13: a) *Decay curve and fitting of* ***Cz-BzN*** *crystal at room temperature.* ***b)*** *Decay curve and fitting of* ***Cz-BzN*** *crystal at 80K.* ***c)*** *time-resolved emission spectra of* ***Cz-BzN*** *crystal at 180K.* ***d)*** *Decay curve and fitting of* ***Cz-BzN*** *crystal at 180K.*

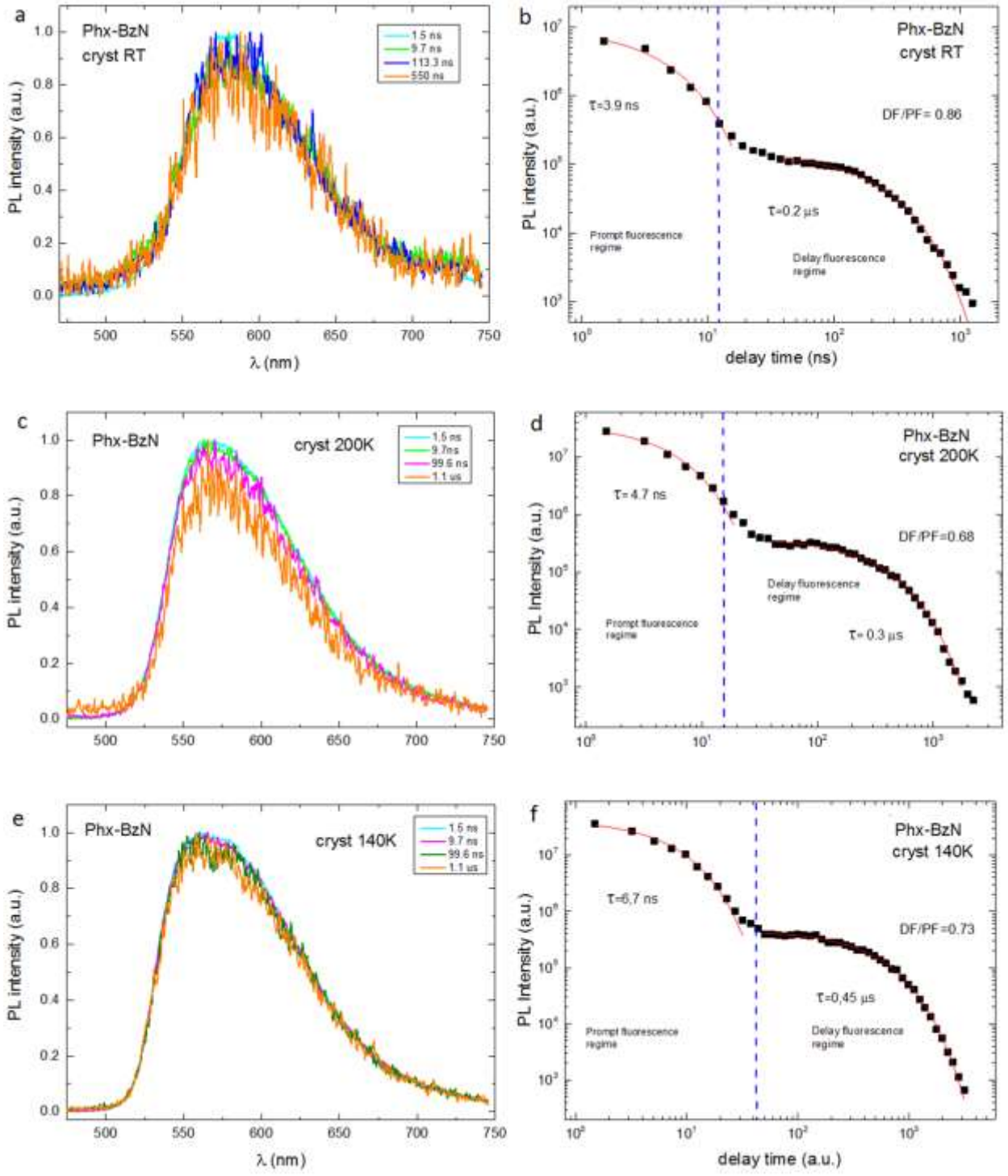

Figure A4.14: *time-resolved emission spectra of* ***Phx-BzN*** *crystal powder at* ***a)*** *RT* ***c)*** *200K and* ***e)*** *140K. Decay curve and fitting of* ***Phx-BzN*** *crystal powder for* ***b)*** *RT and* ***d)*** *200 K and* ***f)*** *140K. All experiments were carried out at* λ_{ex}*= 355 nm.*

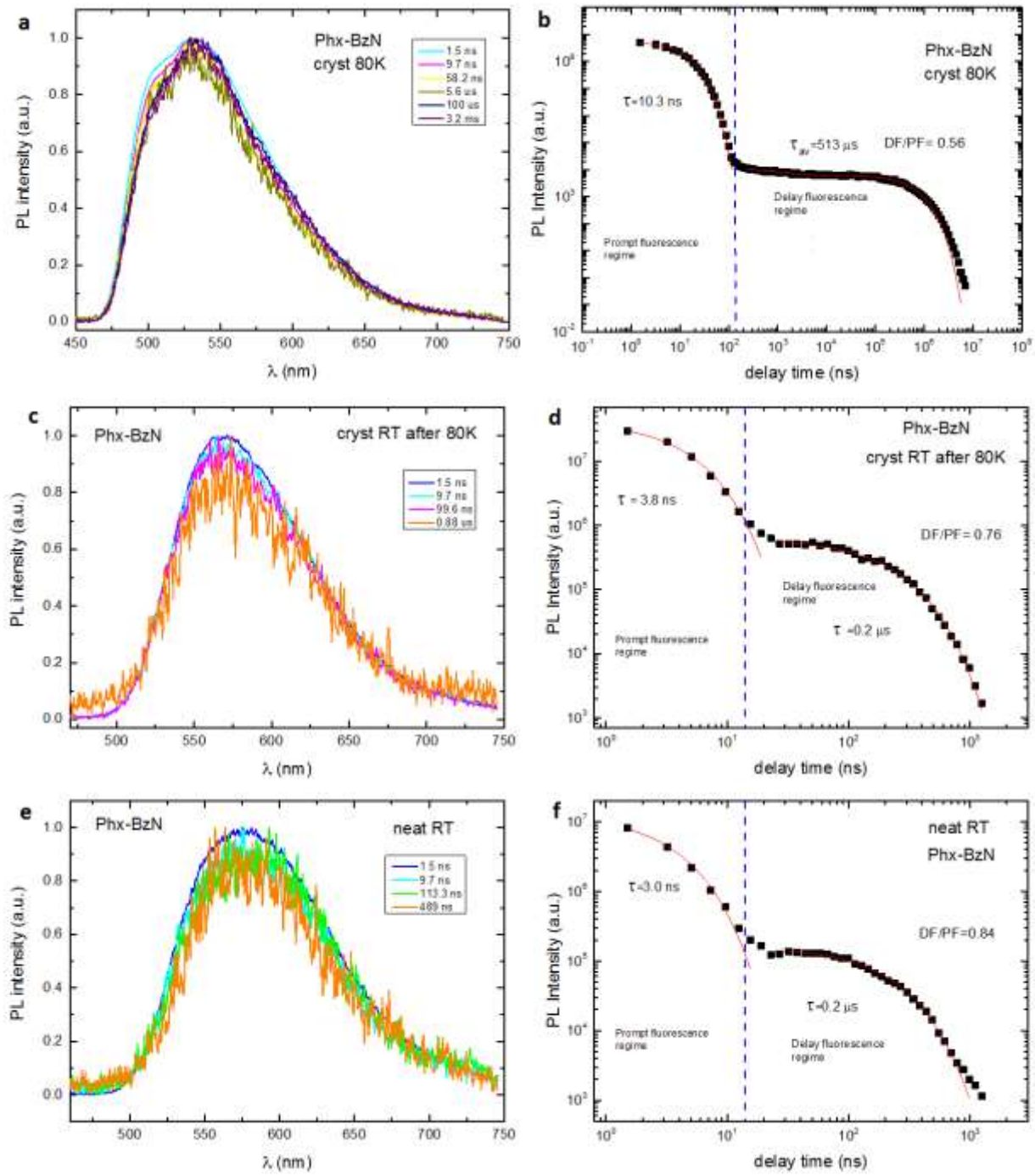

Figure A4.15: *time-resolved emission spectra of* ***Phx-BzN*** *crystal powder at* ***a)*** *80K* ***c)*** *RT after cooling at 80K, and decay curve and fitting of* ***Phx-BzN*** *crystal powder for* ***b)*** *80K and* ***c)*** *RT after cooling at 80K.* ***e)*** *Time-resolved emission spectra of* ***Phx-BzN*** *neat film at RT* ***f)*** *and decay curve and fitting of* ***Phx-BzN*** *neat film at RT. All experiments were carried out at* λ_{ex}*= 355 nm.*

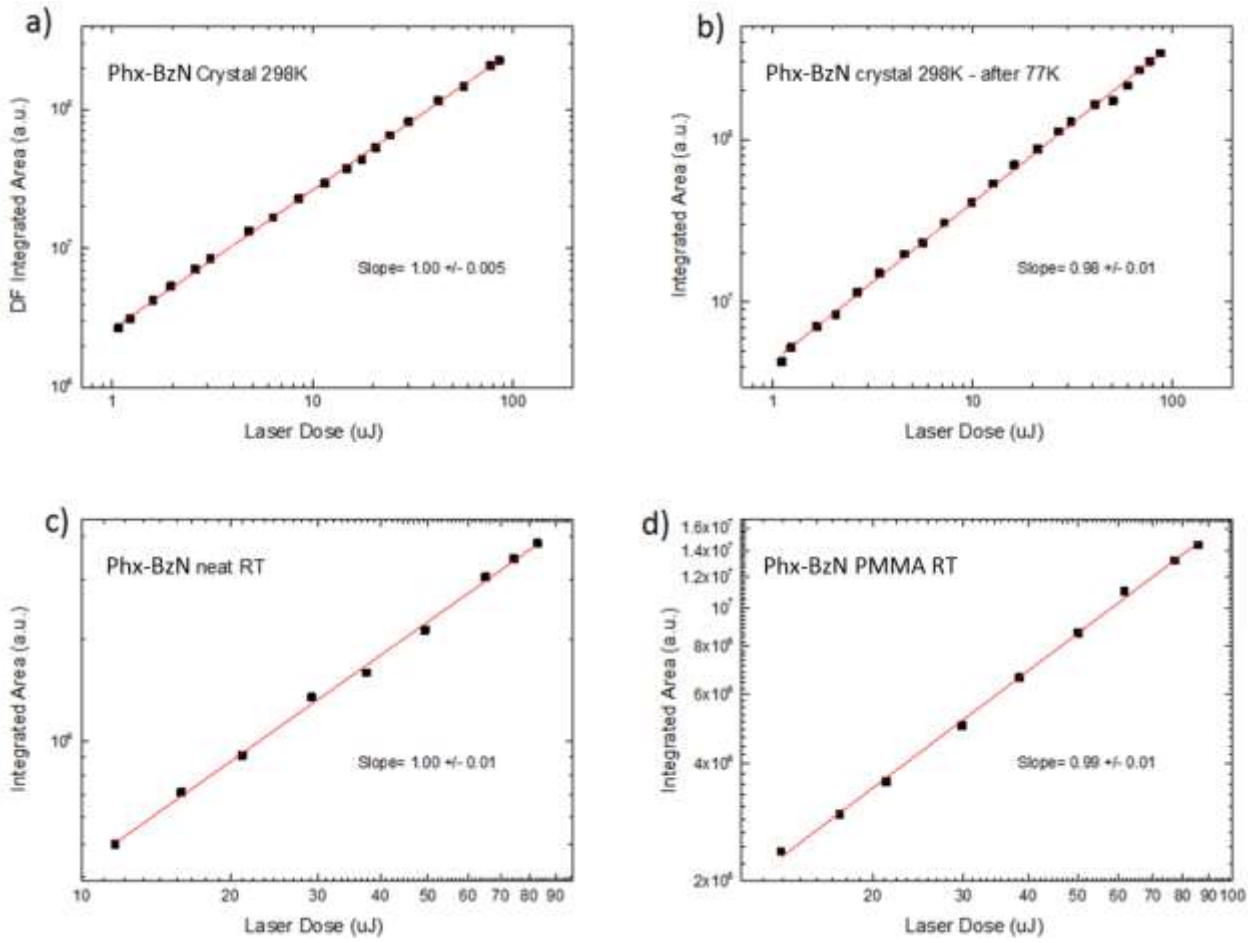

Figure A4.16: *intensity dependence of the DF emission as a function of the laser excitation dose for* ***a) Phx-BzN*** *crystal RT,* ***b) Phx-BzN*** *crystal RT after 77K,* ***c) Phx-BzN*** *neat film at RT, and* ***d) Phx-BzN*** *in* ***PMMA*** *at RT.* λ_{ex}*= 337 nm.*

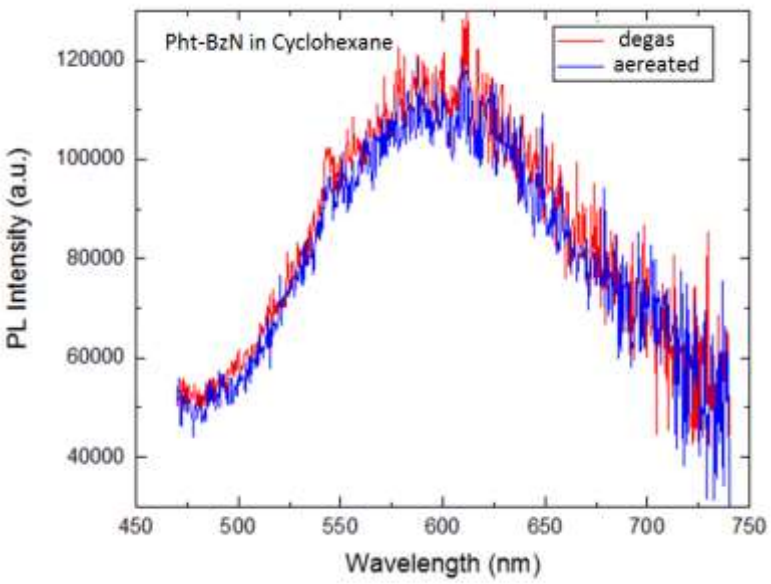

Figure A4.17: *PL spectra of* ***Pht-BzN*** *in degassed and air-equilibrated CH at room temperature,* λ_{ex}*= 330nm.*

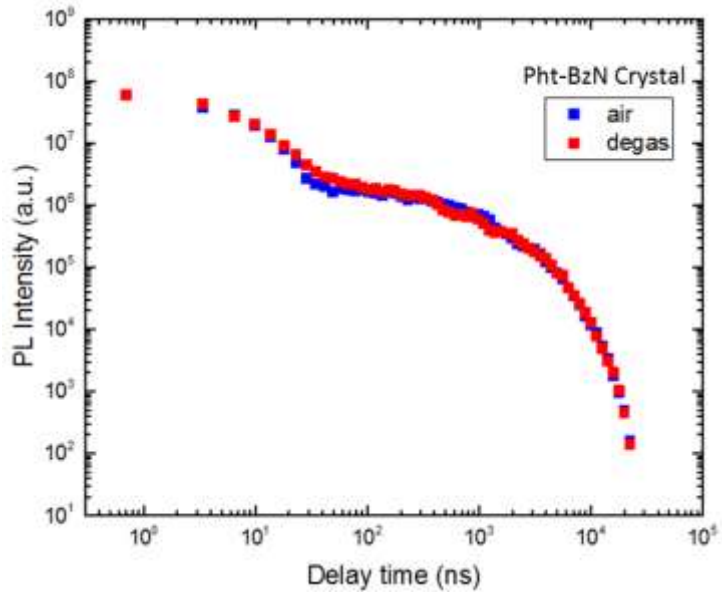

Figure A4.18: *PL decays of* ***Pht-BzN*** *crystal in degassed and air-equilibrated atmosphere at room temperature,* λ_{ex}*= 355 nm.*

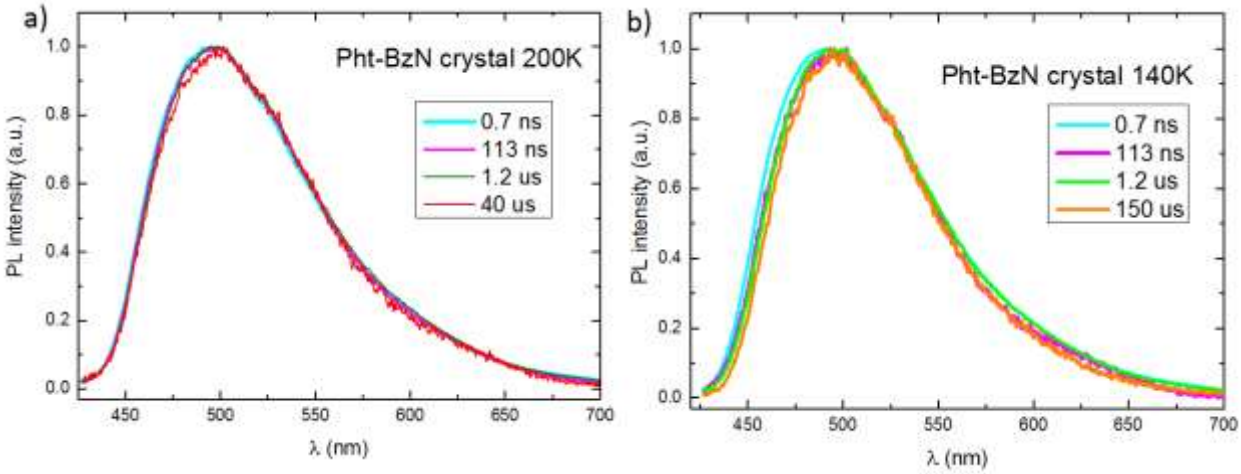

Figure A4.19: a) *time-resolved emission spectra of* ***Pht-BzN*** *crystal at 200K* ***c)*** *time-resolved emission spectra of* ***Pht-BzN*** *crystal at 140K, λ_{ex}= 355 nm.*

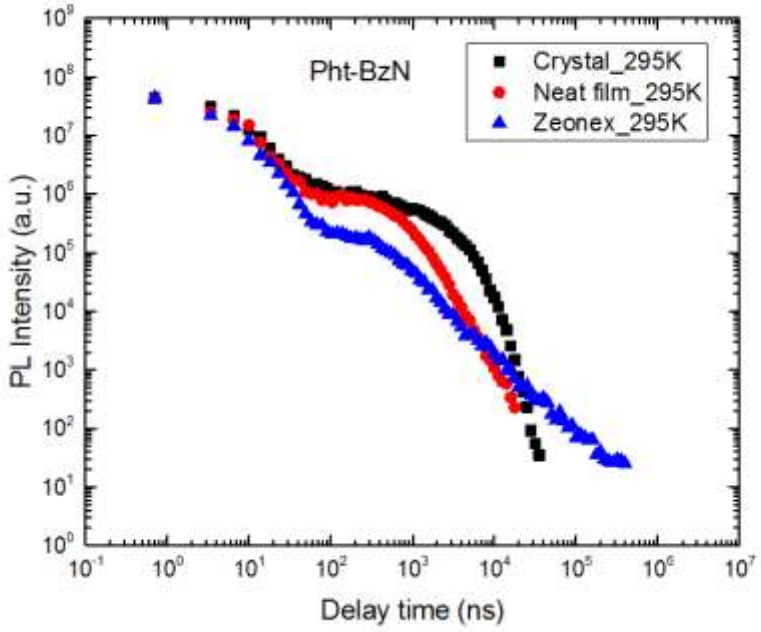

Figure A4.20: *Decay curve of* ***Pht-BzN*** *crystal, neat film and, in zeonex for RT, λ_{ex}= 355 nm.*

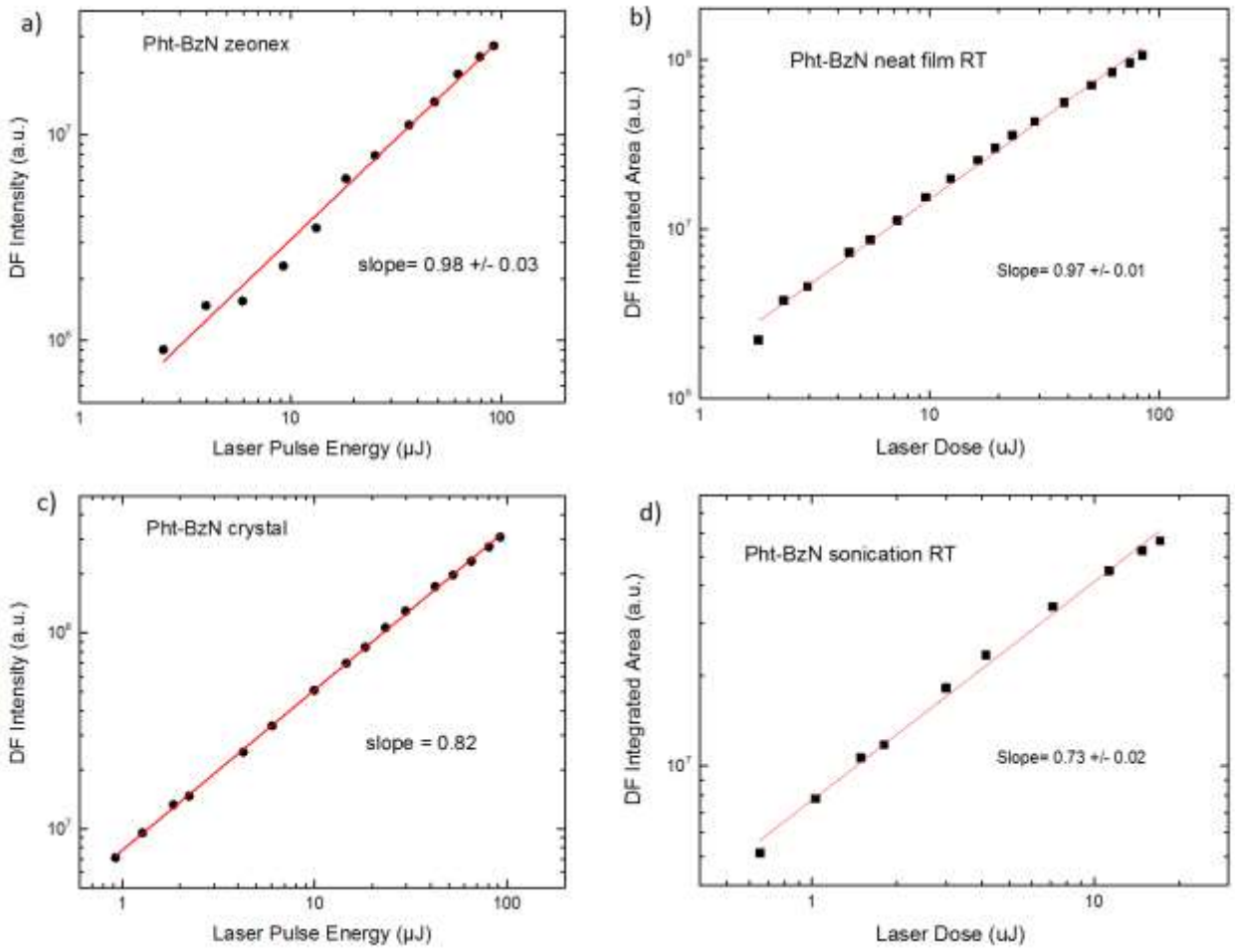

Figure A4.21: *intensity dependence of the DF emission as a function of the laser excitation dose for* ***Pht-BzN,*** λ_{ex}*= 337 nm* ***a)*** *Zeonex at RT* ***b)*** *neat film (1h) at RT,* ***c)*** *crystal RT and* ***d)*** *crystalline dispersion obtained trough sonication.*

Pade Laplace | *Acquisition: Continuous (Number) 01:00:18 24.99 °C*

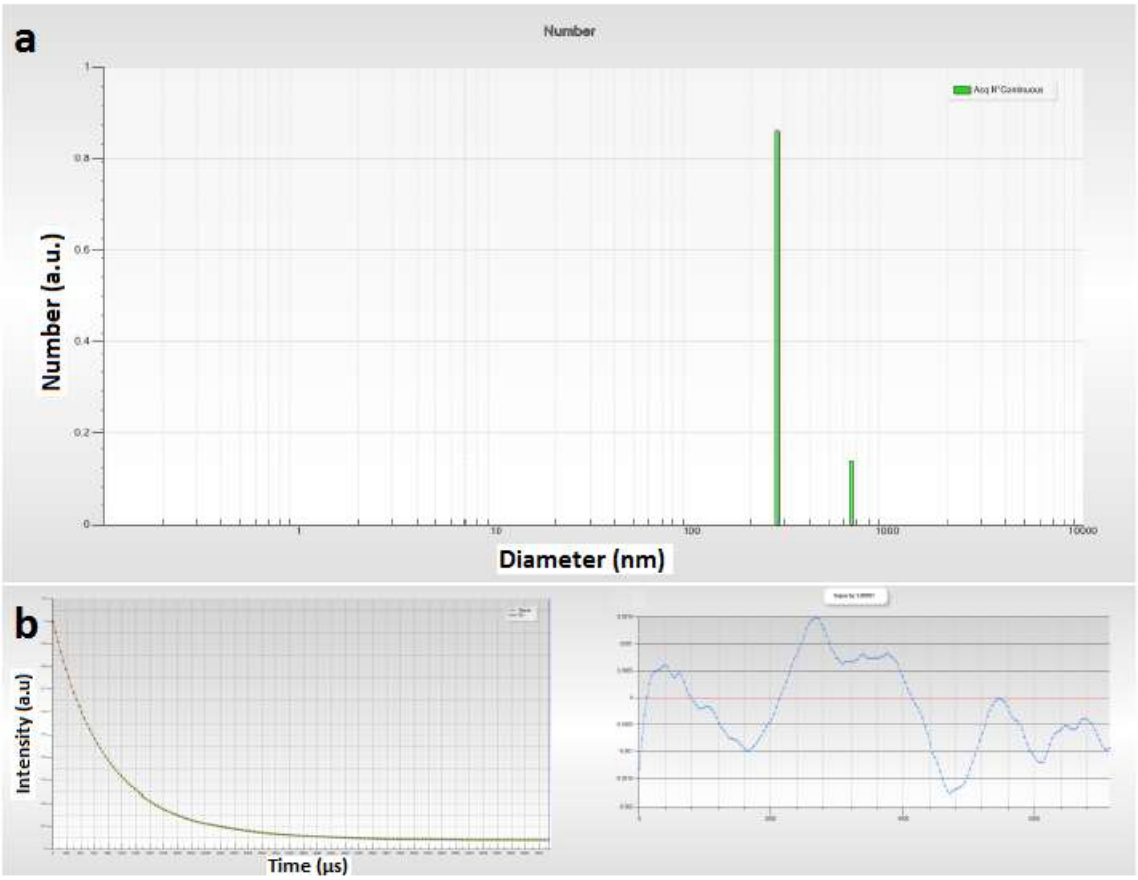

Dispersion statistics

Dn 10%: *271.48 nm* ***Dn 50%:*** *271.48 nm* ***Dn 90%:*** *653.52 nm*
Mean Number: *324.44 nm*

Detected size(s)

Size (nm)	Number	Decay Rate	Diffusion Coeff. (m²/s)
267.7	0.86	970.45	18.35936E-013
653.71	0.14	397.4	75.18168E-014

Dispersion datas

Size (nm)	Number	Size (nm)	Number
271.48	0.86	653.52	0.14

Figure A4.22: a*) Size histogram of the* ***Pht-BzN*** *nanocrystal dispersion obtained with Padé-Laplace algorithm and the statistical acquisition mode. The horizontal axe shows the hydrodynamic diameter in nm and the vertical axe the amplitude in intensity (a.u.).* ***b****) Correlogram obtained from the* ***Pht-BzN*** *nanocrystal dispersion, (green spots) and fit of the Padé-Laplace algorithm (red curve). In the Table are reported the dimension of the 2 particle obtained from the acquisition.*

CHAPTER 5.

NOVEL CHROMOPHORES WITH CONDENSED 1,2,4-TRIAZINE SYSTEM SYMULTANEOUSLY ACHIEVE THERMALLY ACTIVATED DELAYED FLUORESCENCE AND CRYSTALLIZATION-INDUCED PHOSPHORESCENCE.

1. INTRODUCTION.

Besides the TADF phenomena, another strategy to harvest triplet excited states using pure organic small molecules is to take advantage from the room temperature phosphorescence (RTP) which has also been a centre of great recent interest, especially in the last years. RTP it has been observed when small molecules were dispersed in solvents or materials in which the molecular motion is hindered. In particular, the most relevant methods to obtain efficient RTP are aggregation-induced or crystallization-induced enhanced emission.[136] The crystallization-induced RTP emission results from the formation of highly ordered crystalline structures, which restrict the molecular motion inside the crystal lattice and prevent oxygen quenching of the phosphorescence. Among all the acceptors used in TADF, triazine has attracted great attention because it can undergo various functionalization and ring transformations.[137-138] There are three possible triazine isomers but 1,3,5-triazine (*s*-triazine, *s*-TAZ) received the greatest attention because of the availability of starting building blocks, its strong electron deficiency and rigid structure. It has thus been widely used to synthesize excellent electron transporting materials, host materials, emitters and ligands for organometallic phosphorescent complexes used in OLEDs.[57, 139-140] Consequently, there are numerous research papers dealing with 1,3,5-triazines based luminescent TADF materials[141]. In particular, Adachi *et al.* prepared a state-of-the-art green TADF-based OLED with a maximum EQE of 29.6% by utilizing a symmetric triazine as the electron acceptor.[139]

The asymmetric 1,2,4-triazine (*as*-triazine, *as*-TAZ) unit has rarely been used as a building block for organic active materials, especially as an OLED emissive layer. Recently Xiang *et al.*[142] reported TADF emitters featuring a 1,2,4-triazine core as the electron acceptor and 2 or 3 phenoxazines (Phx) as donors. The tris-Phx-*as*-TAZ based OLED displayed yellow emission and achieved a high EQE of 13.0% which is comparable to similar devices based on 1,3,5-triazine. Xiang's work demonstrated that 1,2,4-triazine-based luminescent materials could have great potential. 1,2,4-triazine can also be condensed with other aromatic rings to form new delocalized aromatic

structures.[92, 143] Investigation of such condensed 1,2,4-triazine systems as luminescent materials is still unknown.

In this work we studied new fused 1,2,4-triazines: benzofuro[3,2-*e*]-1,2,4-triazine and benzothieno[3,2-*e*]-1,2,4-triazine substituted with various common donors (carbazole, phenoxazine, phenothiazine and 3,6-di-*tert*-butylcarbazole, **Figure 5.1**). Interestingly, we will show that it is possible to switch the emission of some of these derivatives from TADF to RTP by changing their aggregation state and restricting their intramolecular motion. Indeed, these derivatives show only TADF when dispersed in PMMA matrix at RT and RTP in crystalline form. We think that RTP is the result of an aggregation enhanced emission process.

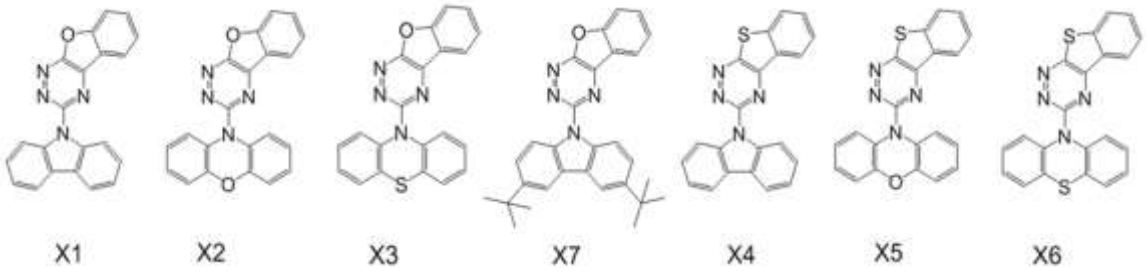

***Figure 5.1**: Molecular structures of the new fused 1,2,4-triazines studied in this work.*

The compounds were synthesized by Xiaofeng Tan (Department of Organic Technology, Kaunas University of Technology, Lithuania) PhD student of the EXCILIGHT project while visiting our laboratory. The synthetic pathway was adapted from the work of Seitz et *al.*[144] The benzofuro[3,2-*e*]-1,2,4-triazine and benzothieno[3,2-*e*]-1,2,4-triazine were prepared starting from the 3,6-dichloro-*s*-tetrazine, a common building block in our team, in two steps: a Nucleophilic Aromatic Substitution (SN_{Ar}) followed by an intramolecular cycloaddition. The intermediates bear a chlorine atom that can undergo another SN_{Ar} with heterocyclic donors to yield the final products (**Scheme 1**).

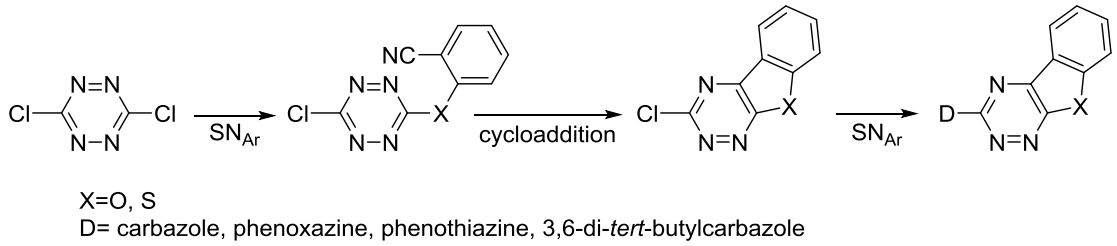

***Scheme 1**: synthetic pathway used to prepare the new donor substituted benzofuro[3,2-e]-1,2,4-triazines and benzothieno[3,2-e]-1,2,4-triazines.*

All compounds have been characterized by ^{1}H and ^{13}C NMR and mass spectrometry. Their thermal stabilities have also been evaluated by thermal gravimetric analysis (TGA). The compounds show good thermal stability with a thermal decomposition temperature (T_d, corresponding to 5% weight loss) ranging from 285 to 320°C (**Table 1**).

Table 1: thermal decomposition temperature (T_d) and melting points (mp) of the fused 1,2,4-triazines.

	T_d (°C)	mp (°C)
X1	306	228
X2	285	205
X3	298	257
X4	310	256
X5	288	223
X6	319	256
X7	321	307

2. QUANTUM MECHANICHAL CALCULATION

All compounds **X1**-**X7** have been studied by (TD)DFT calculation in their ground and first excited state geometries to facilitate the interpretation of experimental photophysical data.

2.1 Ground state structures.

The calculated structure of the benzofuro[3,2-*e*]-1,2,4-triazines and benzothieno[3,2-*e*]-1,2,4-triazines acceptors are flat in all cases (**Table 2** angle A). In the case of **X1**, **X4** and **X7** the carbazole donor is flat as well (**Table 2** angle D) and the D and A subunits are almost conjugated (angles <20°, **Figure 5.2** and **Table 2** angle A-D). However when D is a phenoxazine (**X2** and **X5**) or a phenothiazine (**X3** and **X6**) the donor is bent (angle 35° or 47°, **Figure 5.3** and **Table 2** angle D) and D and A are quasi axial (**Table 2** angle A-D) as previously noticed for similar compounds.[62, 145]

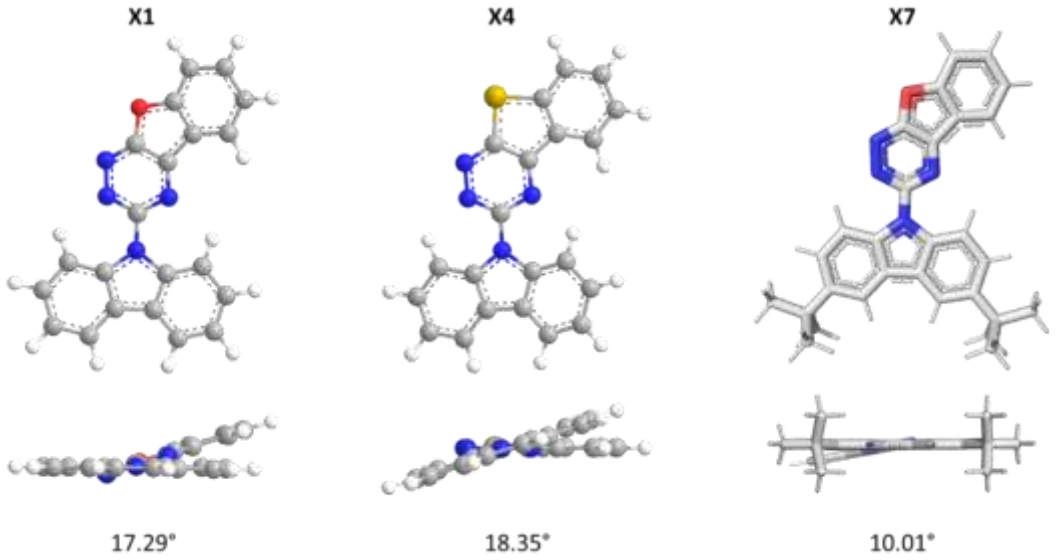

***Figure 5.2**: Optimized molecular structures of **X1** (left), **X4** (center) and **X7** (right). The D-A angle refers to the calculated angle between the mean planes of the Donor and the Acceptor.*

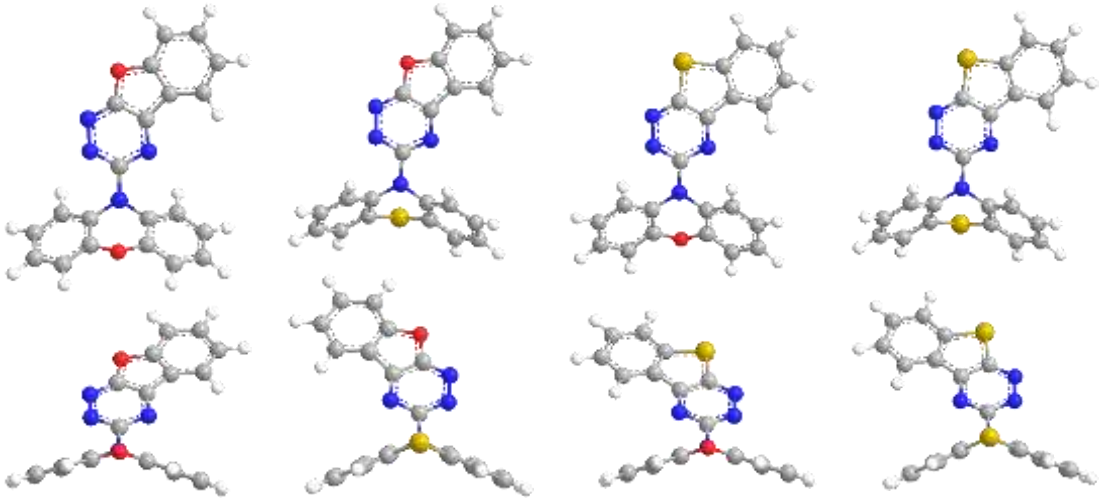

D Angle:	35.44°	47.02°	35.47°	47.03°
D-A Angle:	46.86°	58.16°	46.41°	57.69°

***Figure 5.3**: Optimized molecular structures of, from left to right, **X2**, **X3**, **X5** and **X6**. D angle refers to the calculated angle between the mean planes of the two phenyl rings of the Donor; D-A angle refers to the calculated angle between the mean planes of the Donor and the Acceptor.*

Table 2: calculated main angles of the fused 1,2,4-triazines.

	A (°)[a]	D (°)[b]	A-D (°)[c]	A-D dihedral angle (°)
X1	0.05	1.15	17.29	16.66
X2	0.21	35.44	46.86	10.20
X3	0.12	47.02	58.16	6.74
X4	0.39	1.22	18.35	16.93
X5	0.06	35.83	46.41	54.56
X6	0.10	47.22	57.69	6.52
X7	0.04	0.71	10.01	9.60

a) A angle refers to the calculated angle between the mean planes of the two rings of the fused 1,2,4-triazine acceptors; b) D angle refers to the calculated angle between the mean planes of the two phenyl rings of the Donor; c) A-D angle refers to the calculated angle between the mean planes of the Donor and the Acceptor.

2.2 Ground state molecular orbitals

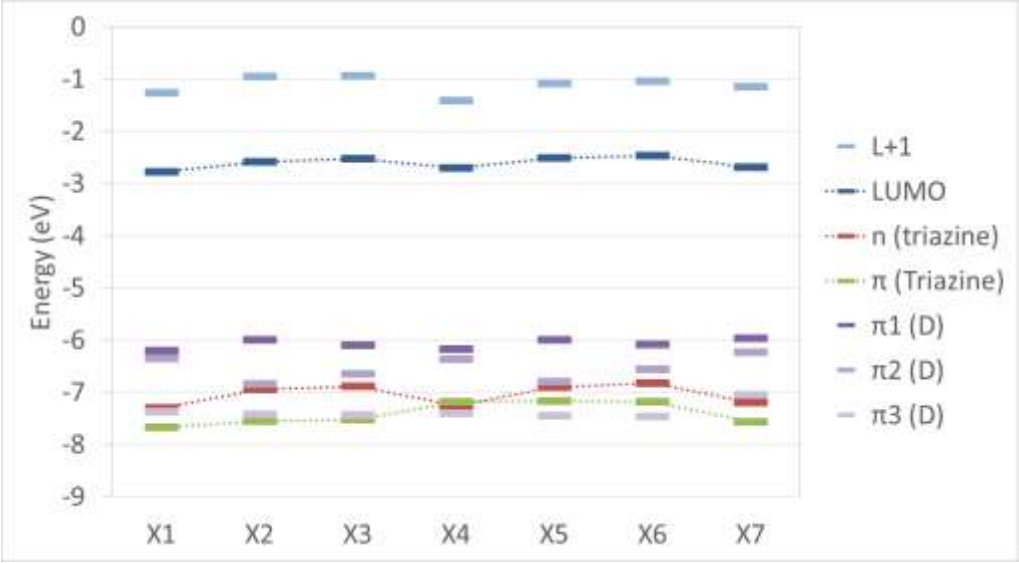

***Figure 5.4**: Representation of the energy levels of the frontier molecular orbitals of the fused 1,2,4-triazines.*

The benzofuro[3,2-*e*]-1,2,4-triazines is a slightly stronger acceptor than the benzothieno[3,2-*e*]-1,2,4-triazines because the LUMO of the former is approximately 0.08 eV lower in energy than the latter (**Figure 5.4**).

The HOMO is mainly located on the donor moiety with a small participation from the *as*-triazine and LUMO exclusively on the fused *as*-triazine moiety. The HOMO-2 is the first non-bonding n orbital of the *as*-triazine (**Figure 5.5**).

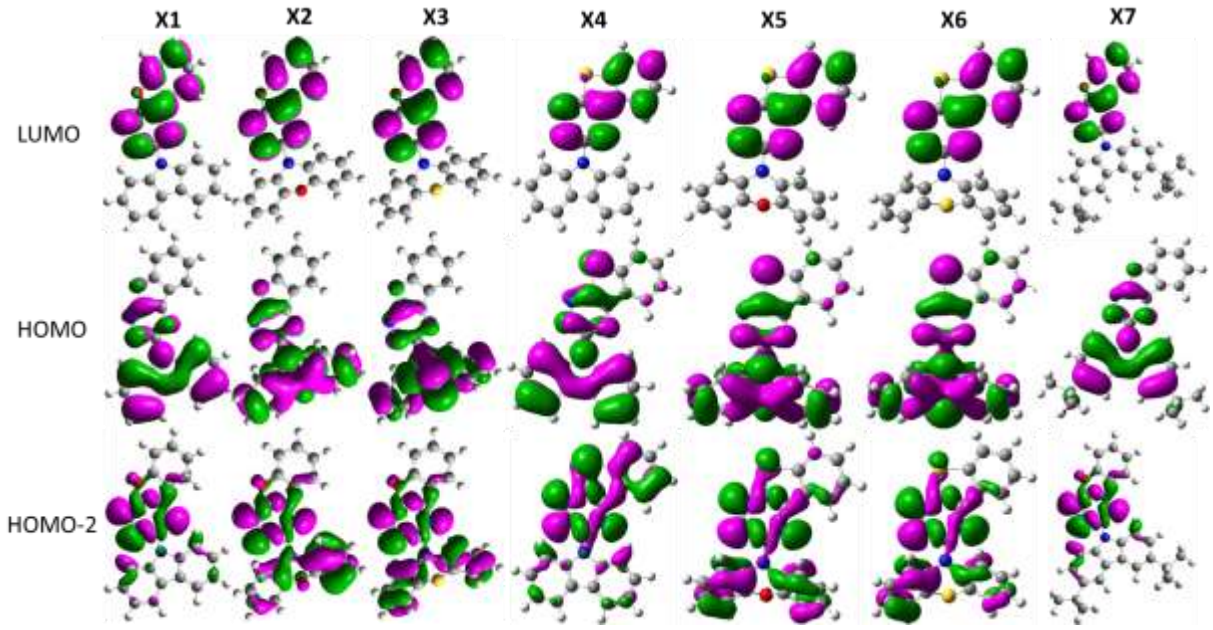

Figure 5.5*: Electron density distributions in molecular orbital energy levels involved in the first two calculated transitions of D-A as-triazines.*

2.3 TDDFT at the ground state S_0 geometry.

The lowest energy transition is a D-A charge transfer (CT) involving the HOMO and LUMO orbitals. The second lowest transition is an *as*-triazine centered n-π* one (**Table 3**) from the HOMO-2 to the LUMO. Higher energy transitions are π-π* centered on the D or A.

Table 3: Two lowest energy calculated transitions and singlet – triplet energy difference

	vacuo		toluene	
	λ_{calc} (nm)	ΔE(s-t) (eV)	λ_{calc} (nm)	ΔE(s-t) (eV)
X1	462 (CT) 411 (n-π*)	0.45	449 (CT) 402 (n-π*)	0.47
X2	467 (CT) 424 (n-π*)	0.50	462 (CT) 415 (n-π*)	0.50
X3	438 (CT) 423 (n-π*)	0.54	435 (CT) 415 (n-π*)	0.57
X4	454 (CT) 413 (n-π*)	0.50	445 (CT) 406 (n-π*)	0.50
X5	458 (CT) 424 (n-π*)	0.51	457 (CT) 418 (n-π*)	0.51
X6	434 (CT) 421 (n-π*)	0.55	433 (CT) 416 (n-π*)	0.60
X7	481 (CT) 426 (n-π*)	0.42	470 (CT) 406 (n-π*)	0.43

2.4 First singlet excited state geometry.

For **X1**, **X4** and **X7**, A-D angle increases from less than 20° in S_0 to ≈52° in S_1. MOs are less delocalized so the S_1 state has a more pronounced CT character than the first excited state at S_0 geometry and $\Delta E_{(S-T)}$ is ≈ 0.1eV.

For the other derivatives, D becomes flat and A-D angle is close to 90° (quasi-equatorial according to what previously observed for similar compounds.[62, 145]. D and A are orthogonal and S_1 is a pure CT state with strong stabilization and very small ΔE(s-t) (0.02eV).

When D is a carbazole derivative it should be more favorable for fluorescence and TADF. When D is phenoxazine or phenothiazine the compound should be non-emissive because the pure CT is a symmetry forbidden transition.

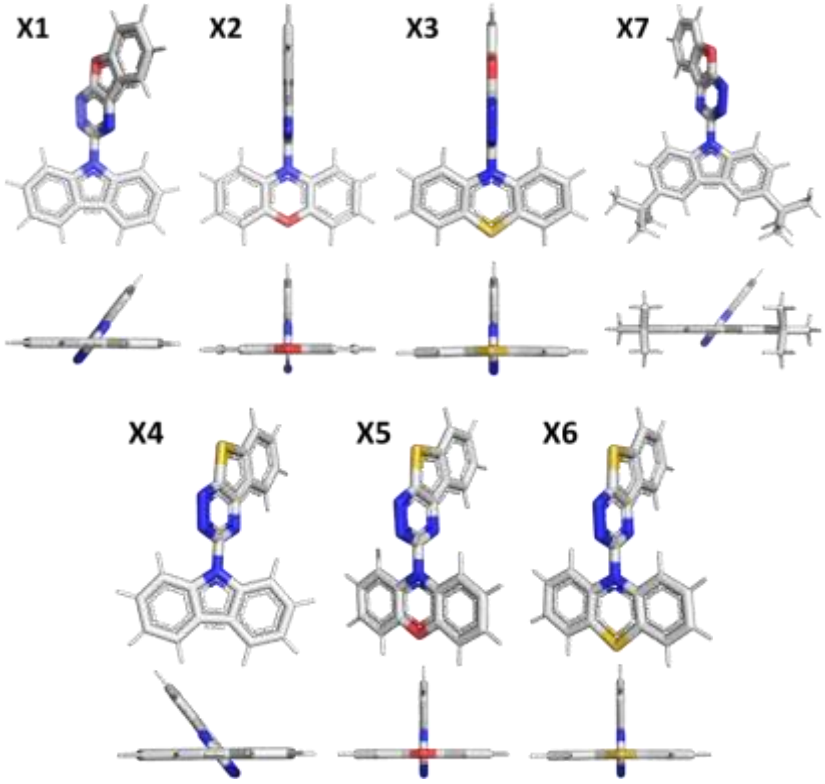

Figure 5.6: *Optimized molecular structures of the first excited state of the as-triazines.*

Table 4: Calculated $\Delta E_{(S-T)}$ in eV at the S_1 geometry and values of A-D angle.

	$\Delta E_{(S-T)}$ in vacuo	$\Delta E_{(S-T)}$ in toluene	A-D (°)
X1	0.09	0.10	52.23
X2	0.02	0.02	89.99
X3	0.02	0.02	89.99
X4	0.10	0.11	52.03
X5	0.02	0.02	90.00
X6	0.02	0.02	89.98
X7	0.09	0.09	51.75

A-D angle refers to the calculated angle between the mean planes of the Acceptor and the Donor.

3. PHOTOPHYSICAL STUDY OF X2, X3, X5, AND X6.

Before discussing deeply the photophysical results and properties of the compounds, it is important to note that a complete study has been carried out only on compounds **X1**, **X4** and **X7**, which display the most interesting properties. For the other four molecules, **X2**, **X3**, **X5**, and **X6** only the steady-state properties have been fully studied and only partial time-resolved experiments have been carried out. In fact, these derivatives do not emit in solution and the emission in solid-state reaches a QY value of 0.5% only with **X2** and **X6** crystals. **X2**, **X3**, **X5**, and **X6** will thus be presented first and the properties of **X1**, **X4**, and **X7** in the last part of this chapter.

3.1 Absorption.

In **Figure 7** are reported the UV-Vis absorption spectra of **X2** and **X5** molecules at the top and of **X3** and **X6** molecules at the bottom. **X2** and **X5** compounds exhibit two absorption bands peaking at λ_{max} *ca.* 280 nm and 310 nm typical of phenoxazine derivatives[78]. All absorption spectra exhibit two weak bands in the region between 350nm and 500 nm: they are assigned to the CT transition derived from electron transfer from the HOMO of the D (phenoxazine) to LUMO of the A (asymmetric triazine) and to n-π* transition respectively. Regarding **X3** and **X6** compounds, they also present two absorption bands between 350 nm and 500 nm assigned to CT and n-π* transitions. On the other hand, the two more intense peaks at higher energy (**X3**: λ_{max} = 290 and the shoulder at 310 nm, **X6**: λ_{max} = 290 and the shoulder at 308 nm) are typical of phenoxazine derivatives.[78]

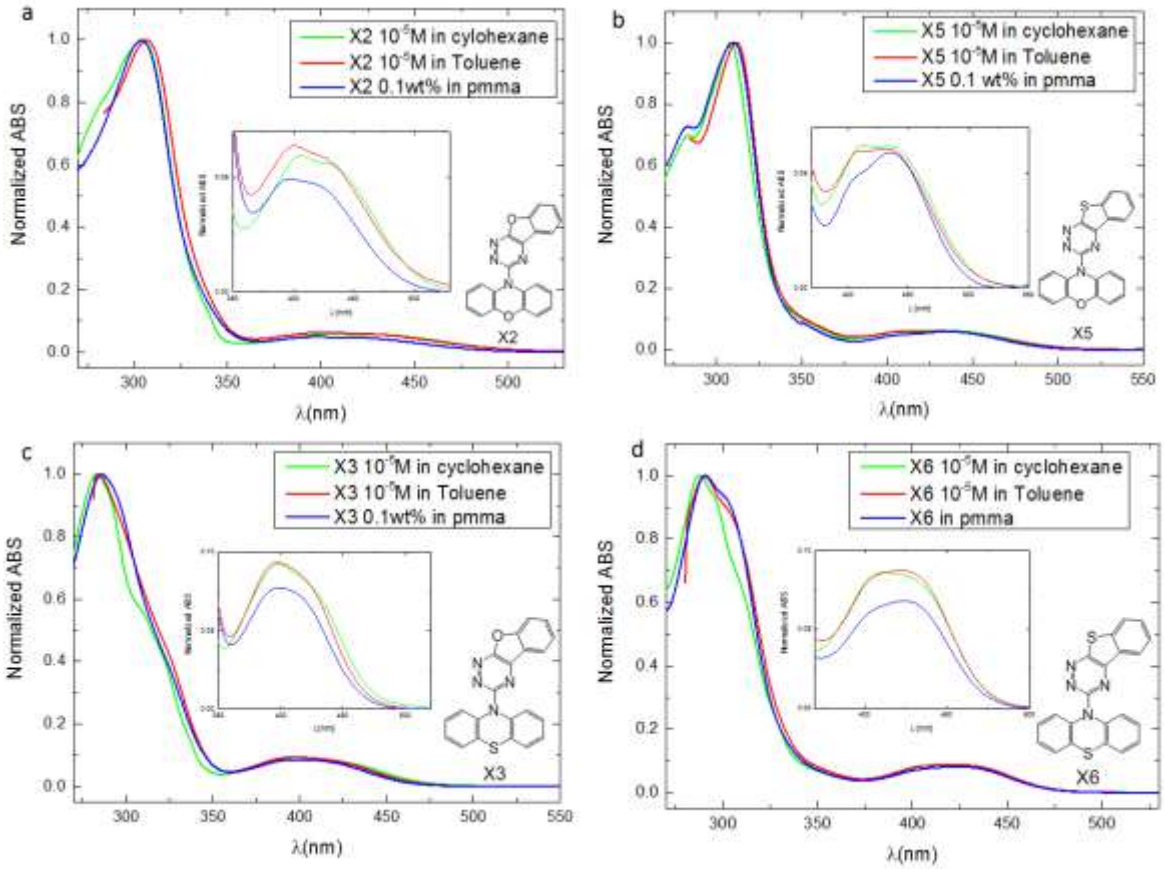

***Figure 5.7**: Absorption spectra of **X2** (a), **X3** (c), **X5** (b) and **X6** (d) in cyclohexane (10^{-5} M, green), Toluene (10^{-5} M, red), and PMMA (0.1wt%, blue). Inset in graphs: zoom of the low energy bands between 350 nm and 500 nm.*

Table 5: maximum absorption and emission wavelengths for **X1**-**X7** in cyclohexane, toluene, and DCM.

MOLECULE	Absorption (nm)			Emission (nm)		
	Cyclohexane	Toluene	DCM	Cyclohexane	Toluene	DCM
X1	454(s), 432, 412, 393, 323, 309, 297(s), 288	416(s), 388, 325, 312, 298(s), 289	414(s), 381, 324, 311, 299(s), 289	548(s), 510, 477	556	609
X2	433(s), 405, 304, 283(s)	429(s), 401, 306	/	388	385	no
X3	397,310(s),283	398, 284	/	566, 416	no	no
X4	454, 433,413(s), 397, 325, 311, 296, 287	419, 399, 327, 315, 296, 288	423, 392, 327, 314, 296, 289	547(s), 504,474	543	601
X5	432, 413, 308, 284	431, 412, 312, 284	/	394	398	no
X6	413, 308(s), 296(s), 288	422, 301(s), 290	/	no	no	no
X7	479(s), 450, 430, 400	427, 395, 383, 331, 317	426, 389, 330, 316, 301, 294	589(s), 544, 508	599	648

3.2 Steady-state emission and decay time.

The steady-state emission spectra of **X2**, **X3**, **X5**, and **X6** in solution (cyclohexane and toluene) and in solid-state (PMMA, neat film, and crystal powder) are shown in **Figure 5.8**. The neat films for these four compounds seem not crystalline and they look amorphous and glassy. All the molecules can be considered as non-emissive in solution even if a Locally Excited (LE) emission typical of the phenoxazine[34] peak around 395 nm is detectable for **X2** which becomes much more intense for **X5** in both solvents.

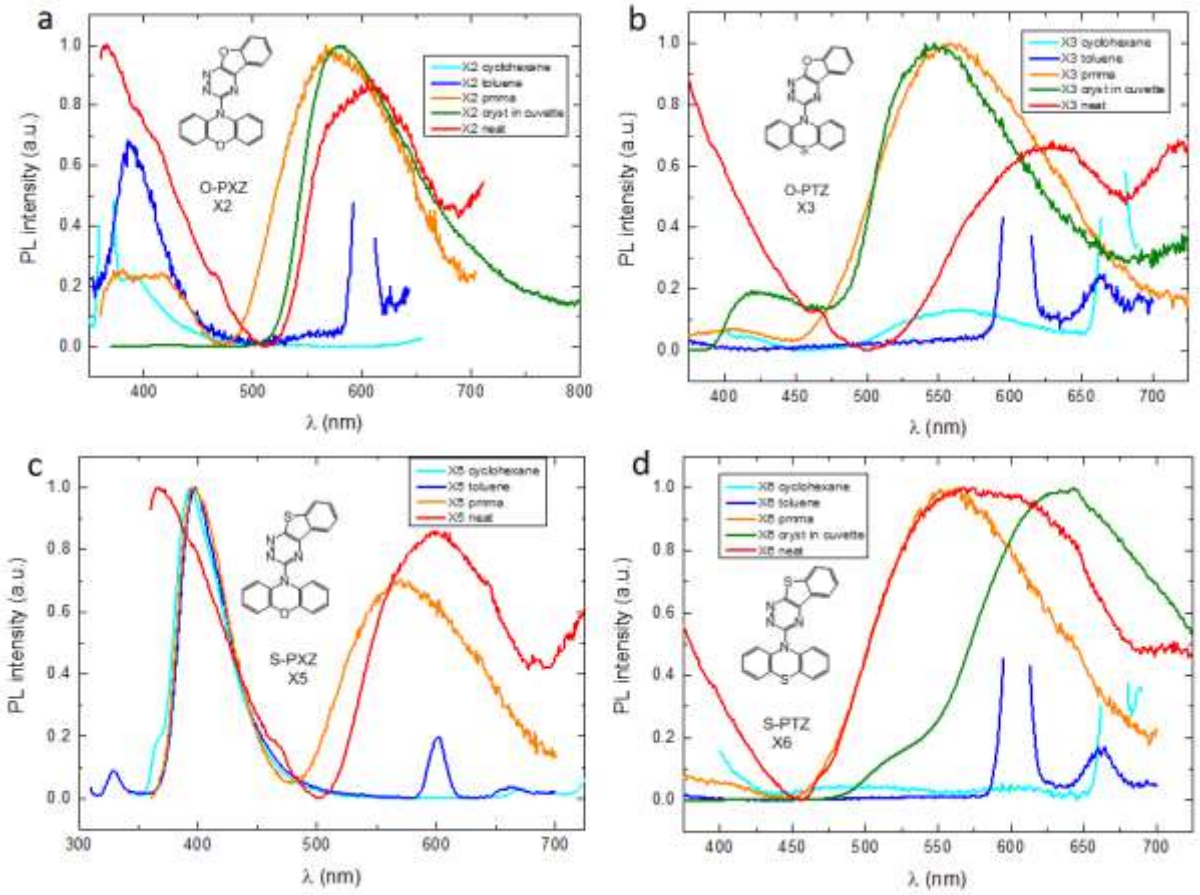

***Figure 5.8**: Emission spectra of **X2** (a), **X3** (b), **X5** (c) and **X6** (d) in cyclohexane (10^{-5} M, cyan), Toluene (10^{-5} M, blue), PMMA (0.1wt%, orange), crystalline powder in cuvette (green, except c, no emission) and neat film (red). λ_{exc} = between 300-350 nm.*

When dispersed in PMMA, all compounds display a CT emission but its intensity is very low that spectra acquisition was difficult. At best **X3** and **X6** present a measurable QY of 0.2% (table 3). In addition, the LE fluorescence band of phenoxazine is also present, especially for **X5**. Two different average decay times values were obtained for **X2**, **X3**, **X5**, and **X6** in PMMA (**Table 6**). The short decay in the **ns** regime is assigned to the PF. A second decay time value was obtained

in the **µs** regime and it is assigned to the DF emission. Nevertheless, without the time-resolved emission study (at RT and 77K) and without experiment at different laser power, it is not possible to understand if the origin of DF arises from TTA or from the recursive population of the ^{1}CT state through a RISC (TADF process).

The neat films that are mostly glassy can be considered as practically non-emissive. This is caused by a strong self-quenching effect typical of neat films. Interestingly the crystalline powders of these compounds show the best properties in terms of efficiency. In particular, the **X2** crystal reaches a QY of 0.5% (**Table 6**) while maintaining the CT emission characteristic of the single-molecule and therefore we can say that we are dealing with Crystallization Induced Enhanced Emission (CIEE) phenomena. **X6** crystal also reaches a QY of 0.5%, which is 2.5 times higher than the molecule in PMMA and therefore presents CIEE. However, in this case, the important red shifting of the emission maximum (~100 nm) respect to the PMMA would lead to thinking either to the presence of aggregate emission or, as observed for **X1** and **X4**, to the presence of RTP favored in crystalline rigid environment. We think that the increased emission in solid medium originated probably to the retained of the ground state configuration of the molecules in the rigid environment. Contrarily in solution, the molecules are free to relax its configuration to a completely orthogonal A-D torsional angle which results in a pure CT is a symmetry-forbidden transition.

Table 6: QY and decay time of **X2**, **X3, X5** and **X6** in solid state.

	Φ_{PL} PMMA	Φ_{PL} cryst. powd.	$\tau_{1,av.}$ (ns) PMMA	$\tau_{2,av.}$ (µs) PMMA	$\tau_{1,av.}$ (ns) cryst. powd.	$\tau_{2,av.}$ (µs) cryst. powd.
X2	§	0.5%	1.29	9.29	2.34	0.2
X3	0.2%	§	1.20	21.10	n.c.	n.c.
X5	§	n.e.	1.07	11.16	n.e.	n.e.
X6	0.2%	0.5%	0.62	14.45	2.44	0.84

§ = less than 0.05%, n.e= not emissive, n.c. = not calculated (for all Φ_{PL} the experimental error is ±20% of the value)

4. PHOTOPHYSICAL STUDY OF X1, X4 AND X7 IN SOLUTION.

4.1 Absorption spectra.

Figure 5.9 displays the UV-Vis absorption spectra of molecules **X1**, **X4**, and **X7**. All molecules exhibit a first broad absorption band at lower energy attributed to a charge transfer (CT) coming from the HOMO of the donor (carbazole) to the LUMO of the acceptor (*as*-TAZ)[57]. The second band is probably the n-π* transition located on the triazine core as noticed before in simple *as*-triazines[146]. Both CT and n-π* transitions are forbidden by the total spatial separation of orbitals[120]. In fact, the two orbitals involved in a transition must possess large amplitudes in the same region, otherwise, the transitions are "overlap forbidden". It results that if the HOMO and LUMO are orthogonal to each other the overlap integral is close to zero ($\langle D|A\rangle = 0$ and $\langle n|\pi^*\rangle = 0$). This is consistent with the DFT calculation. The three higher energy absorption bands are associated with π-π* transitions due to their larger relative intensity. These absorption bands peaking at λ_{max}= 325-330 nm and λ_{max}≈292 nm are typical of carbazole derivatives[79, 122].

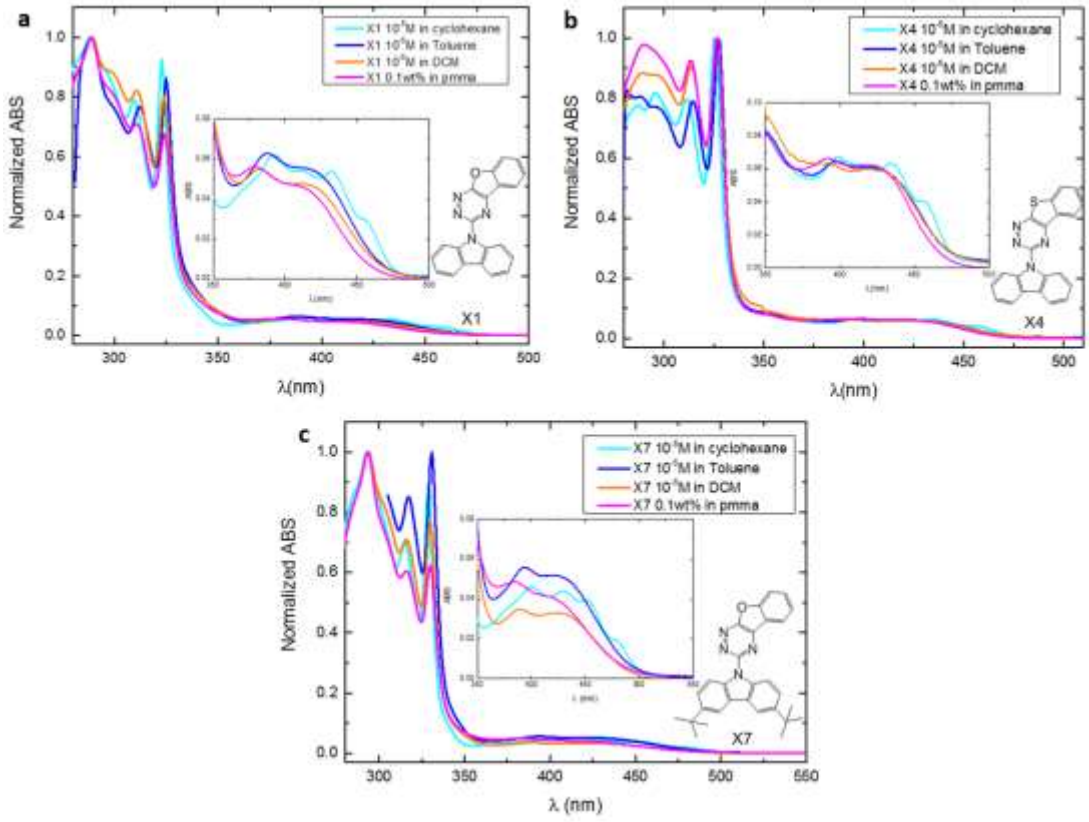

***Figure 5.9**: Absorption spectra of: **a**) **X1**, **b**) **X4** and **c**) **X7** in cyclohexane (10^{-5} M, cyan), toluene (10^{-5} M, blue), dichloromethane (10^{-5} M, orange) and PMMA (0.1wt%, pink). Inset in all four graphs: zoom of the low energy bands between 350 nm and 500 nm.*

4.2 Emission spectra.

To investigate the effect of the different donors and acceptors moieties on the maximum emission wavelength, we only consider in this section the photoluminescence (PL) spectra of the compounds in toluene solution (**Figure 5.10**) since this solvent has been shown to have the best polarity, among the others tested, to magnify the TADF properties for these compounds. In fact, the higher QY were obtained in toluene while maintaining a CT emission. It is therefore expected that toluene allows aligning the energy of the singlet and triplet excited states and to reduce the ΔE_{S-T}, increasing the TADF properties of these materials[7, 22, 24]. First, we compare **X1** and **X7** which differ by the nature of their donor: carbazole (Cz) and 3,6-di-*tert*-butylcarbazole (dtbuCz) respectively. As we can see in the previous section the position of the CT absorption band red-shift in **X7** ($\lambda_{abs(\mathbf{X7})}$=427; $\lambda_{abs(\mathbf{X4})}$=419) and this is due to the inductive effect of the tBu substituent in tBuCz which increases the donor effect of Cz leading to a lower energy ICT state. The emission maxima and color for **X1** and **X7** are 543 nm (green) and 598 nm (orange) respectively. In particular, the half-width at half maximum (FWHM) of the emission spectrum increases from 128 nm for **X1** to 146 nm for **X7**. The onset of the emission spectra of these two compounds also shifts from 2.60 eV for **X1** to 2.46 eV for **X7**. Similarly, the bathochromic shift and the broadening of the **X7** emission respect to **X4** is due to the inductive effect of the tBu. Finally, the broadening of the emission in toluene indicates a fast intramolecular charge transfer (CT) from Cz/tBuCz to the electron-deficient triazine moiety. In fact, the CT state is stabilized by the solvent polarity which produces a structural reorganization of the new electronic density distribution of the molecule in the excited state[29].

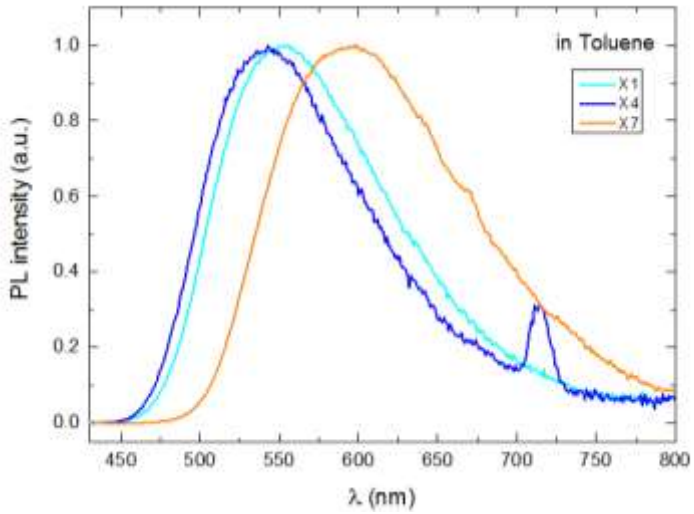

***Figure 5.*10:** *Photoluminescence spectra of **X1** (cyan), **X4** (blue) and **X7** (orange) in toluene (c=10^{-5} M). λ_{exc} =330-360 nm*

Secondly, we compare **X1** and **X4**, which differ by their acceptor units: benzofuro-*as*-triazine and benzothieno-*as*-triazine respectively. As it can be seen in **Figure 5.10** the replacement of the Oxygen (**X1**) by the Sulphur (**X4**) in the Acceptor unit weakly affects their emission maxima that blue-shift only of 13 nm (**X4** = 543nm, **X1**= 556 nm). Such a blue shift is due to the slightly better acceptor properties of benzofuro-*as*-triazine respect to benzothieno-*as*-triazine, as indicated by the DTF calculations, which show that the benzofurotriazine is a slightly better acceptor than the benzothienotriazine. Furthermore, the FWHM changes only slightly, from 128 nm for **X1** to 120 nm for **X4**. Nevertheless, it is interesting to note how the replacement of sulphur by oxygen in the triazine strongly affects their QY that is double for **X1** respect to **X4** (**Table 7**). This is probably due to the heavy atom effect induced by the sulphur, which increases the ISC from singlet S_1 to the triplet T_1 state, however, once the energy is in the triplet state, it decays by non-radiative channels.

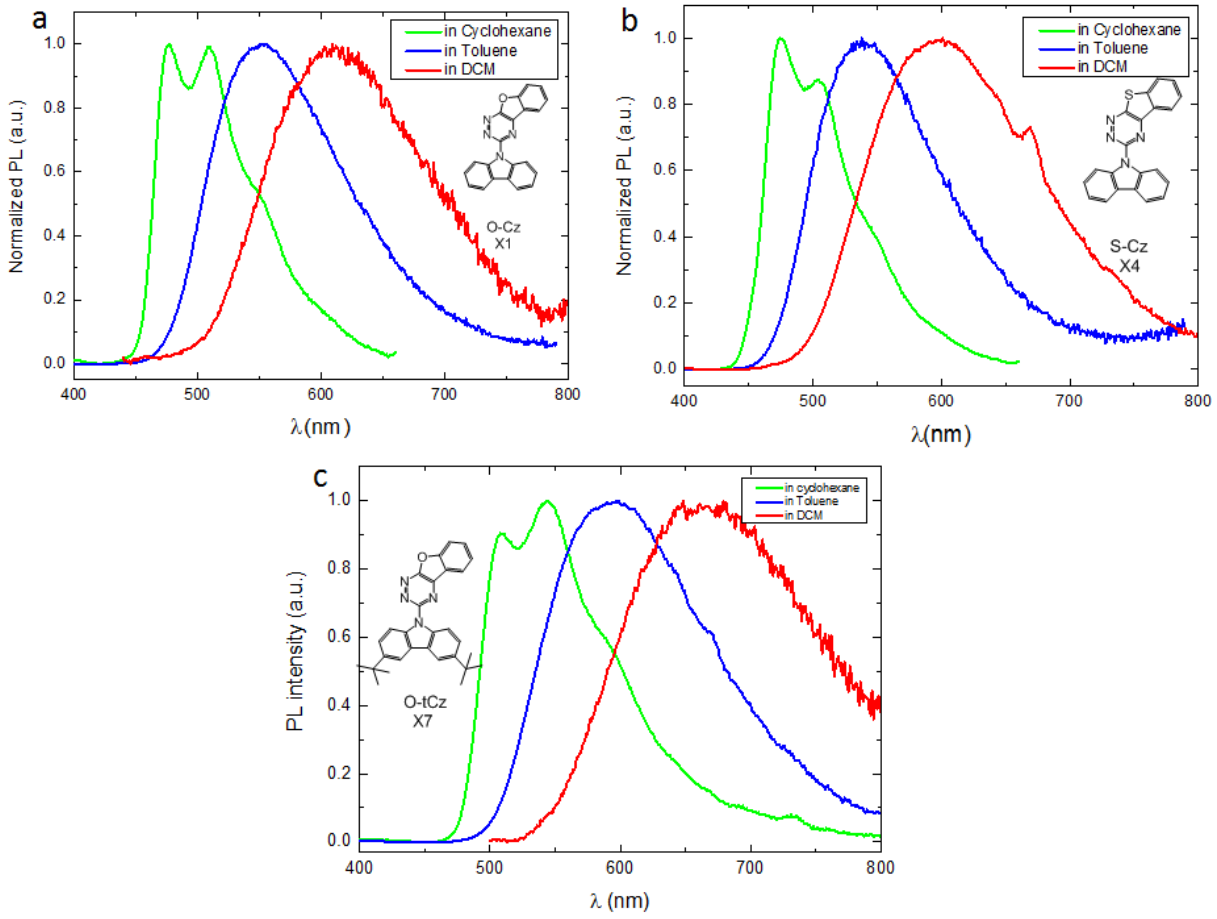

***Figure 5.11**: Photoluminescence spectra in cyclohexane (10^{-5} M, green), toluene (10^{-5} M, blue) and dichloromethane (10^{-5} M, red) of: **a) X1**, **b) X4**, and **c) X7**. λ_{exc} = 330-360 nm*

Figure 5.11 displays the normalized photoluminescence (PL) spectra of molecules **X1**, **X4**, and **X7** in three different solvents with increasing polarity in order to investigate their solvatochromism. In fact, the emission wavelength of a molecular system with an ICT state generally undergoes a large redshift as the polarity of the solvent increases.[123] For all three molecules the emission maximum exhibits a strong redshift as the polarity of the solvent increases (the values are reported in **Table 5**). The dependence on solvent polarity is more or less the same for all three compounds. The FWHM increases with the solvent polarity but is larger for **X7**. This result indicates that the ICT state of **X7** is the most stable among the three compounds and the enhancement of donor properties by the *t*-Bu-Cz stabilizes the ICT state. The emission of all three compounds in non-polar cyclohexane is narrow and clearly well-structured and resolved. This indicates that in non-polar solvent the emission mainly derives from the lowest localized excited state ^{1}LE through a π-π* transition. This is because the weak interaction between the excited state dipole moment of the compound and the weak dipole moment of the solvent molecules causes only a slightly structural change on the molecule excited state and thus the vibronic structure is visible. This is in accordance with the Frank-Condon principle, as there is a good overlap between the vibrational wave function of the ground and excited state. In the more polar toluene and dichloromethane solvents, a typical broad CT emission is observed for all three compounds. In those solvents, the interactions between the excited state dipole moment of the compounds and the dipole moment of the solvent are stronger and they promote higher charge separation and larger structural changes resulting in a large Stokes shift and broadened emission.

4.3 PLQY and Decay.

To study the TADF photophysical properties in solution of **X1**, **X4**, and **X7**, PLQY were measured in aerated and degassed cyclohexane and toluene solution (**Table 7**). The PLQY of all three compounds in cyclohexane solution are low and even very low for **X4**. Furthermore, they do not undergo any quenching effect with oxygen. Therefore we can assume that for these compounds the emission in cyclohexane arises mostly from a ^{1}LE state that does not promote efficiently the population of a triplet state, as the ^{1}CT electronic state is only barely formed. This is in agreement with the structured PL emission observed in this solvent (**Figure 5.11**). However, although the PLQY doesn't change after degassing, the microsecond-order decay time obtained in cyclohexane indicates that a negligible contribution of TADF is present. On the other hand, the PLQYs in toluene for the three compounds increase more than 3 times respect to cyclohexane and the presence of Oxygen quenching in addition to their broad emission confirms the presence of a TADF process in toluene for this compounds.

The decay times of the three compounds (**Table 7**) in the toluene degassed solution further confirms the presence of the TADF phenomenon. In fact, in the decay, there are two different

components. The first component has an average lifetime (τ_1) in the nanosecond-order and is assigned to the prompt fluorescence, derived from the direct S_1 (^{1}CT) → S_0 transition. The second component is assigned to the delayed component resulting from the recursive S_1 → S_0 transition via successive ISC and up-conversion of the excitons from the T_1 state, which exhibits a microsecond-order lifetime (τ_2).

The different QY behavior follows the trend of the $\Delta E_{S\text{-}T}$ obtained by quantum mechanical calculations with the higher value (1.6%) obtained for **X7** corresponding to the smallest singlet-triplet energy gap (0.09). This is due to the inductive effect of *t*-But substituent, which increases the donor properties of carbazole thus stabilizing the ICT state.

Table 7: Photophysical *properties of* **X1***,* **X4** *and* **X7** *in cyclohexane and toluene.*

Comp	QY Cycloh. (air)	QY Cycloh. (degas)	QY Tol. (air)	QY Tol. (deg)	λ_{PL}, TOL (nm)	FWHM (nm)	($\Delta E_{S\text{-}T}$, eV)*	$\tau_{1,av.}$ (ns), Cycloh.	$\tau_{2,av.}$ (µs) Cycloh.	$\tau_{1,av.}$(ns), TOL	$\tau_{2,av.}$ (µs) TOL
X1	0.20%	0.20%	0.98%	1.40%	556	127	0.47	0.40	1.85	3.10	4.70
X4	0.08%	0.09%	0.46%	0.55%	543	119	0.50	0.26	1.64	1.00	2.01
X7	0.60%	0.60%	1.00%	1.60%	599	146	0.43	1.70	6.97	3.15	11.08

**DFT quantomechanichal calculation* (for all Φ_{PL} the experimental error is ±20% of the value)

5. PHOTOLUMINESCENCE OF X1, X4, X7 IN THE SOLID STATE (PMMA, NEAT FILM AND CRYSTAL).

5.1 Steady-state.

In this section is reported the steady-state emission of **X1**, **X4**, and **X7** in three different solid-state forms:

- molecules dispersed in PMMA at 0.1-0.05 % in weight to study the isolated molecules emission in a rigid matrix.;
- neat films prepared from a DCM solution of the molecules and deposited on a quartz substrate. The neat films for all three compounds are visually crystalline;
- polycrystalline powders collected from the as-synthesized compounds studied in a 1mm quartz cuvette.

In this section, we will only discuss the main differences in terms of steady-state emission spectra (band positions and energy of the onset of the spectra). A detailed discussion to assign the nature of the emission is included in the next paragraphs.

Interestingly, the photoluminescence of all three compounds is significantly different for the three different forms (**Figure 5.12**). The emission in PMMA appears as a broad featureless band for all three compounds. It is fair to suppose that it arises from a low energy CT state and therefore could have TADF properties. The emission in PMMA result blue-shifted respect that in Toluene and this is due to the rigido-chromic effect that suppresses roto-vibrational motion. The maximum emission wavelength for **X1** and **X4** in PMMA presents a hypochromic shift with respect to **X1** and **X4** crystalline samples. Conversely, the emission of **X7** in PMMA presents bathochromic shift respect the crystalline film, although both the emission onset are mostly the same. (**Table 8**). The hypochromic shift observed in the crystal is due to the rigid effect that reduces the roto-vibrational degrees of freedom. The same emission onset for all the three different solid forms of **X7** is a sign that the emission originates from the same state. Furthermore, the *t*-Bu substituents in **X7** give more free space to the molecule in PMMA, which can relax its conformation in upon excitation leading to a stabilization of the CT excited state and in a red-shifted emission (**Table 8**).

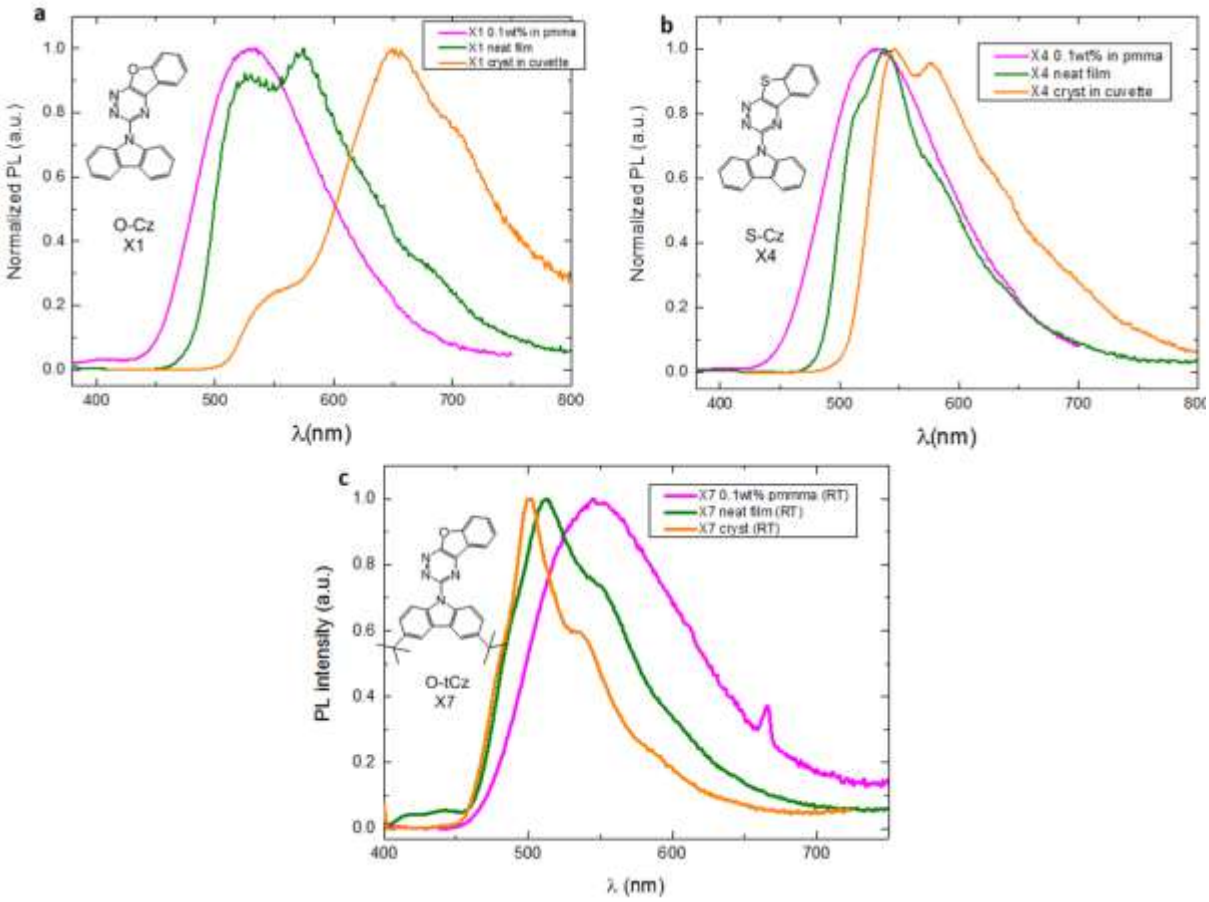

***Figure 12**: Steady state Photoluminescence of **a) X1, b) X4** and **c) X7** in PMMA, neat film and powder.*
λ_{exc} = 360nm

Conversely, **X1** and **X4** neat crystal and crystalline powder show a clearly different emission respect PMMA. They present multiple bands with the emission onset that clearly blueshift in PMMA. This effect is particularly apparent for **X1** compound where the emission maximum of the crystalline powder shifts by more than 150 nm respect to PMMA (**Table 8**).

The different behaviour for **X1** and **X4** compared to **X7** is probably due to the fact that without the hindrance effect of *t*-Bu it is easier to form aggregates (e.g. dimers, excimers) through the π-π interaction of the carbazole phenyl-ring. The different emission between the neat polycrystalline film of **X1** and **X4** and the corresponding crystal powder is due to the presence of a strong RTP contribution (also in air), in the crystal powder. This is clearly visible from the correspondence between the low energy band (steady-state emission) of **X1** and **X4** crystalline powder (**Figure 12**) and the phosphorescence observed booth at RT and 80K in **X1** and **X4** neat films (**Figure 16** and **17**). In the steady-state emission, the RTP is visible especially in the crystals powder because the higher dimension of the crystals can shield more efficiently the molecules from the effect of oxygen quenching, but also because the higher size of crystal can block more efficiently the molecules.

Table 8: maximum emission wavelengths and band onset for **X1**, **X4** and **X7** in PMMA, neat film and powder.

	PMMA		neat film		powder	
	λ_{max}(nm)	E_{ons}(eV)	λ_{max}(nm)	E_{ons}(eV)	λ_{max}(nm)	E_{ons}(eV)
X1	530	2.74	530, 575, 640s, 685s	2.57	545,650, 705s	2.43, 2.35
X4	532	2.72	518s, 538, 575s, 639s	2.56	546, 576, 640, 700s	2.46
X7	545	2.64	512, 545s, 590s	2.67	500, 535, 583s	2.70

(s denotes a shoulder instead of a maximum)

5.2 Time-resolved photophysical properties in PMMA.

The time-resolved photophysical properties of **X1**, **X4**, and **X7** dispersed in a PMMA matrix (0.1%in weight) are discussed in this section. They allow a better understanding of the nature of the emission introduced in the previous paragraph. For each sample, experiments were performed at room temperature (RT) and 77K (LT) after degassing the sample with a high vacuum pump.

The 77K measurements allow to investigate the phosphorescence of the material and determine the triplet state energy level. It is generally obtained from the onset of the most delayed time-resolved emission spectrum.

The RT measurements allow investigating the TADF properties of the samples. In particular, if after long delay times the emission remains the same without no particular shift, it means that it arises from the same singlet state and the longer decay time is due to the population of the triplet state that up-convert to the singlet one through a RISC process. Furthermore, for each measurement, it is important to compare the time-resolved emission with the decay time profile. This allows a better understanding of the states involved in each process. In addition to the time-resolved emission spectra in each graph, the steady-state emission of the sample is also reported.

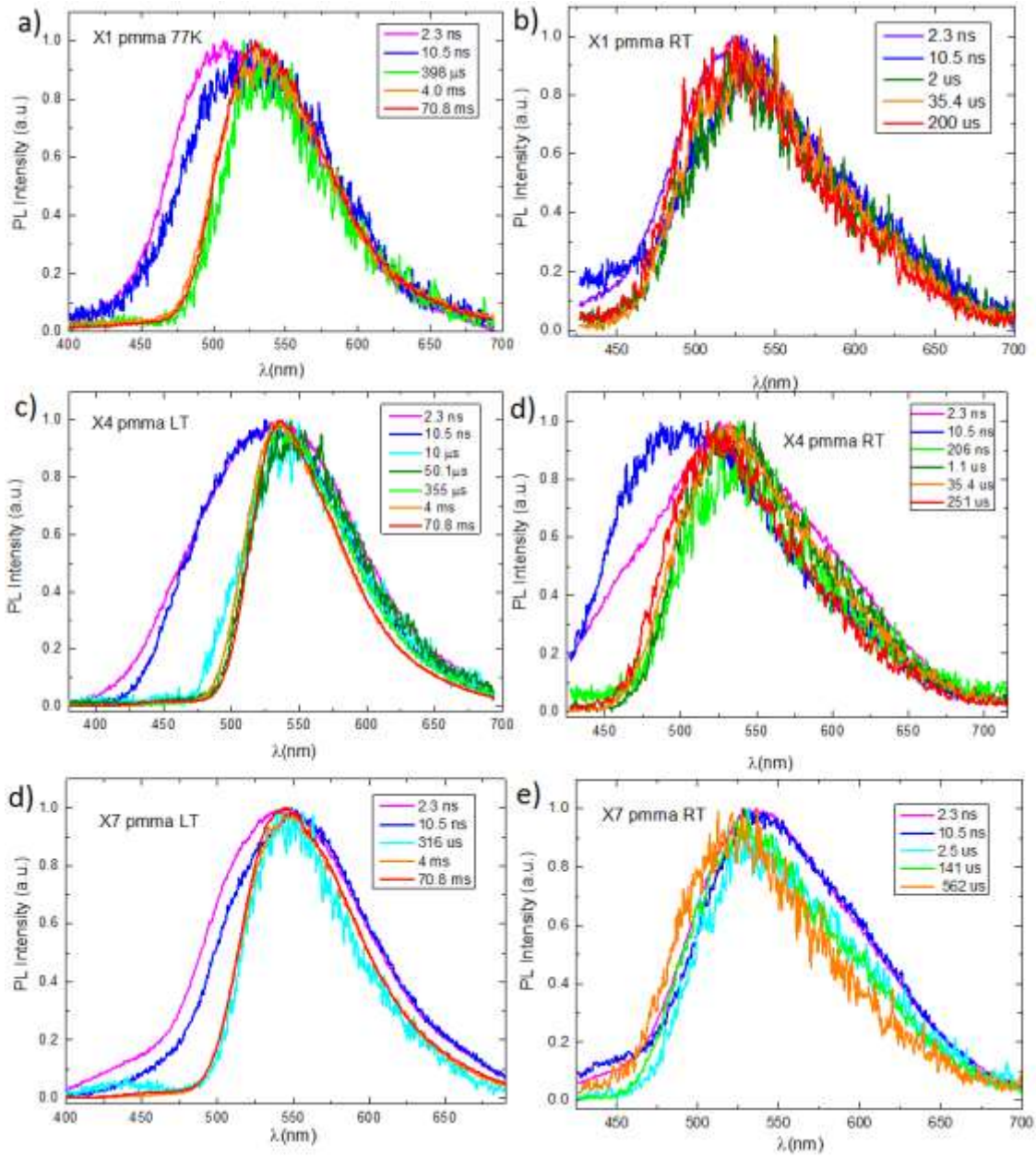

***Figure 5.13**: time-resolved emission spectra at increasing delay times of **X1** (top), **X4** (middle) and **X7** (bottom) 0.1%wt PMMA films at 77K (left) and room temperature (right). λ_{exc} =355nm.*

The analysis of the spectra acquired after different delay times (**Figure 5.13**) shows that it is possible to distinguish between different situations. For **X1** and **X7** at RT (**Figure 5.13b** and **g**) at early times (2.3-10ns), there is a weak emission at higher energy that is more intense for **X4** (**Figure 5.13d**). This emission is attributed to a locally excited state ^{1}LE from D or A moieties. When increasing the delay time, the emission spectra progressively red shift, and the initial weak ^{1}LE emission disappear. After TD= 0.5µs, and up to 2µs remain only the CT emission which shows a slight temporal spectral shift. In particular after a first slight red shift of the CT band follow a little more pronounced blue shift. This could depend on the presence of a distribution of CT states as

a result of conformation heterogeneity[126] of the molecules in PMMA. It results that the most relaxed geometry with a near orthogonal orientation emit more in the red. This produce a distribution of ΔE_{ST} and therefore a distribution of ISC rate which lead to emit with different decay time emission spectra progressively red shifts. After the CT state is formed (TD=0.5µs to 2µs) the emission onset remains the same even when the delay time increases more than an order of magnitude (TD_{X1}= 200µs, TD_{X4}= 250µs, TD_{X7}= 500µs). This is a first proof of a TADF emission for these materials in PMMA at RT. This is also confirmed by the decay time profile (**Figure 5.14b**, **d** and **f**) that extends to 1 ms with an average lifetime of 59.5 µs for **X1**, 53.0 µs for **X4** and 56.8 µs for **X7**.

The 77K decays show for all compounds a shorter decay in the nanosecond regime typical of PF emission and very long decay time in the millisecond regime typical of phosphorescence. However **X1** and **X7** (**Figure 5.14b** and **f** respectively) clearly show only prompt fluorescence and phosphorescence but no TADF. In fact in the figures are not reported experimental point in the intermediate region of the decay (between 10 ns and ~300 µs) as the signal is very noisy. This is typical of the measures at 77K and it is consistent with the fact that TADF needs thermal activation to allow the triplet state convert back to the singlet one. Contrarily in the decay of **X4** (**Figure 5.14d**), it is possible to see a clear DF contribution in the intermediate region. However, since the thermal energy effect at 77K is very low, the relative high ΔEST (0.14 eV) gap doesn't allow the triplet to go back to the singlet trough RISC. Moreover, this is also indicated by the 10 times shorter decay time (4.4µs) at 77K. If the origin of the 77K DF cames from a RISC process it would results in a longer TADF lifetime, in line with the fact that without the thermal energy, the RISC process is in general strongly reduced. This leads to observe TADF in particular cases, e.g. ΔEST≈0, but with a much longer lifetime. Therefore we assigned this emission to triplet-triplet annihilation (TTA) which probably depends on the fact that a low amount of molecules could not be well dispersed in PMMA.

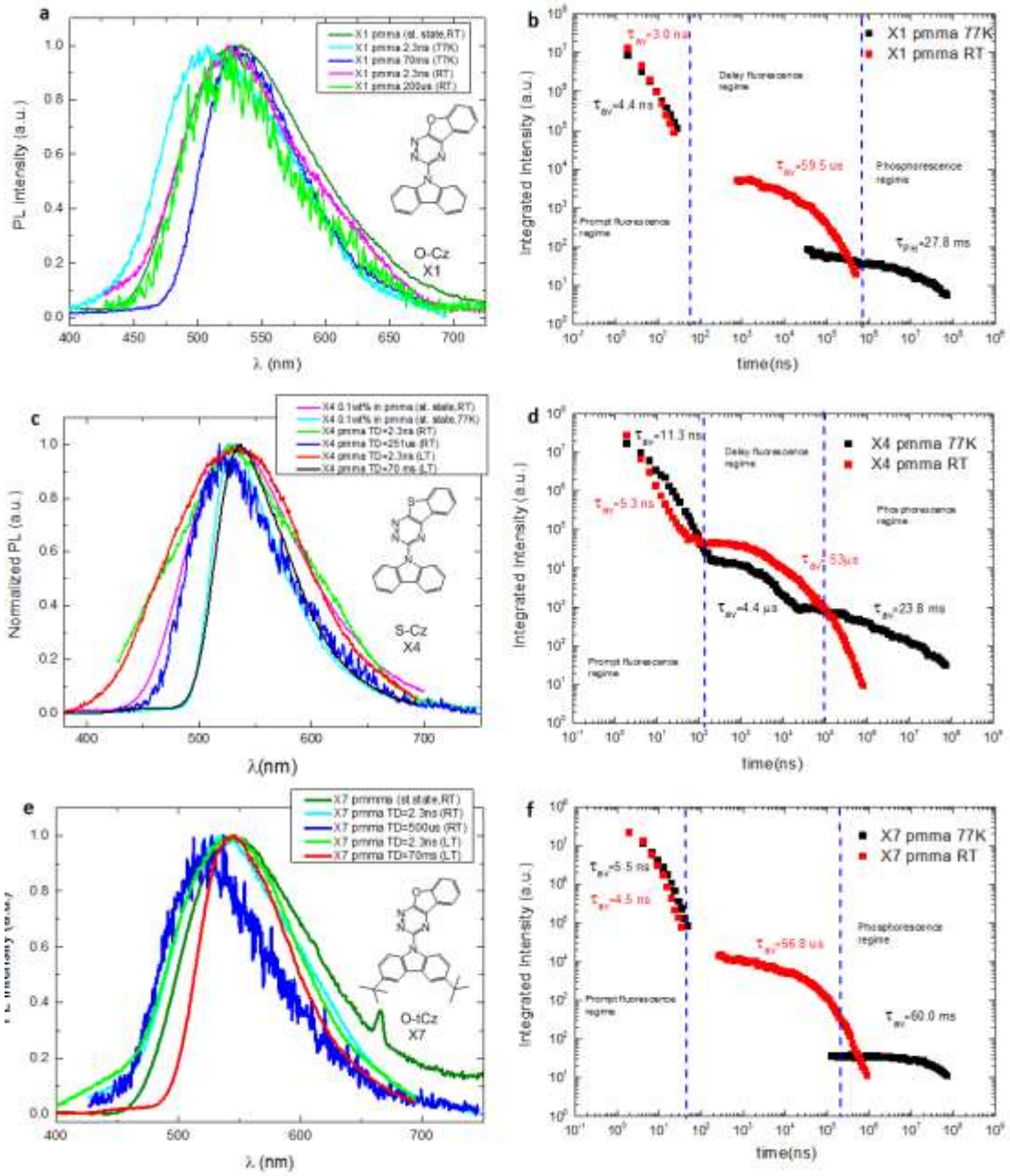

***Figure 5.14**: Left: steady state (st) and time-resolved emission spectra in PMMA at room temperature and 77K and at various delayed time after excitation of molecules a) **X1**, c) **X4** and e) **X7**. Right: decay curves in PMMA at room temperature and 77K of molecules b) **X1**, d) **X4** and f) **X7**. λ_{exc} =355nm*

The energy of the first triplet state was obtained from the onset of the 77K spectra with the longest delay (**Figure 5.13 a**, **c** and **f**, TD=70 ms). They can be estimated at E_T(**X1**)= 2.58 eV, E_T(**X4**)= 2.50 eV and E_T(**X7**)= 2.52eV. On the other hand, the energy of the CT singlet state was obtained from the onset of the CT emission at RT (TD=0.5-2μs) and it can be estimated at E_S(**X1**)= 2.70 eV ,E_S(**X4**)= 2.64 eV and E_S(**X7**)= 2.63 eV. Subtracting the E_T from E_S it is possible to obtain the very

important parameter $\Delta E_{S\text{-}T}$(**X1**)= 0.12 eV ,$\Delta E_{S\text{-}T}$(**X4**)= 0.14 eV and $\Delta E_{S\text{-}T}$(**X7**)= 0.11 eV. These relatively small singlet-triplet energy gap (ideally less than 150 meV) allow to observer at RT at long decay time typical of TADF emission. In fact the thermal energy allow the triplet to win the energy gap, and to up convert back on the singlet. The best parameter describing the amount of TADF produced is the delayed to prompt fluorescence ratio (DF/PF) and as indicated by the values obtained (**Table 9**) it is possible to assume that TADF works moderately well for these compounds. This gives an indication that the RISC rate should be faster than both phosphorescence and triplet non-radiative deactivation rates (*i.e.* $k_{risc}>(k_{ph}+k_{nr}(T))$, thus indicating that the main loss arises from the non-radiative S_1 deactivation rather than from crossing to T_1. Therefore, since the luminescence QY are low (**Table 9**), it results that only a small part of the excitation decays radiatively while most is lost through non-radiative pathways from singlet state (S_1).

Finally, **Figure 5.15** shows the intensity dependence of the DF emission as a function of the laser excitation dose. The 100 ns to 30 µs time span was analysed and a linear dependence with a directing coefficient of 0.99 ± 0.01 was found. This result confirms a monomolecular process typical of the thermally assisted mechanism as opposed to TTA which is characterized by a bimolecular process (see §1.4.2 in chapter 1).

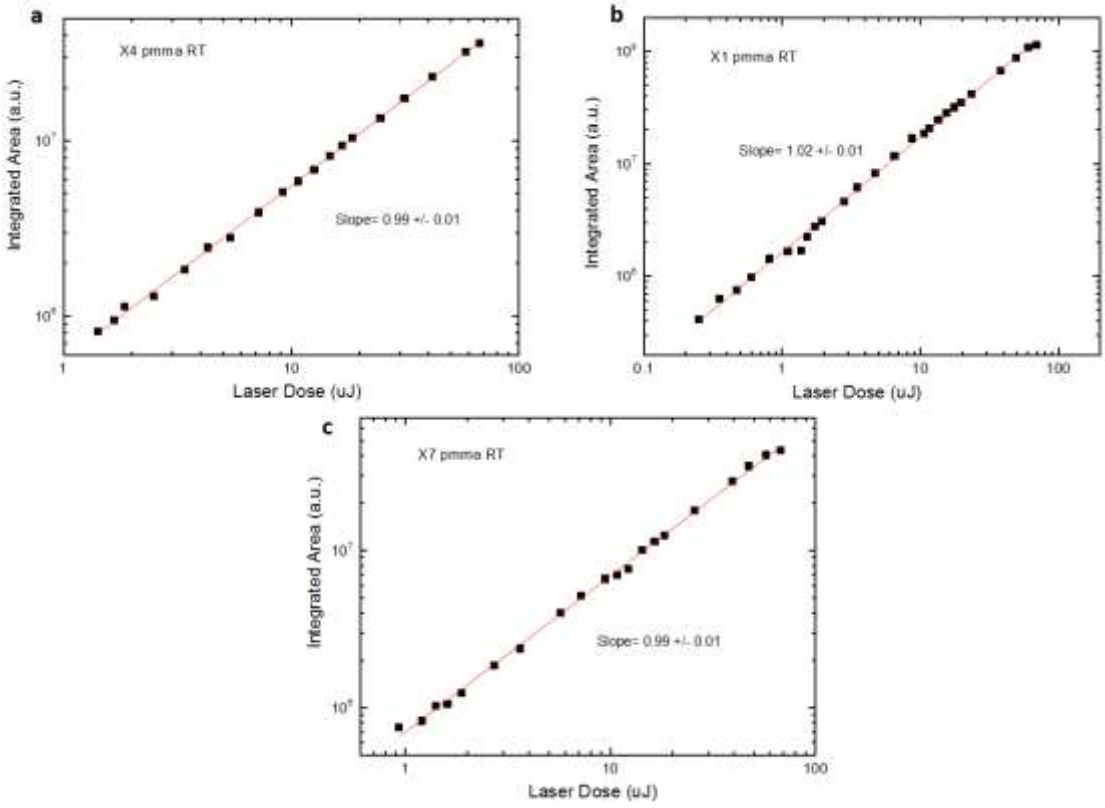

***Figure 5.15**: Power dependence of the integrated delayed fluorescence in PMMA thin films of (a) **X1**, (b) **X4** and (c) **X7**. λ_{exc} =337nm.*

5.3 Time-resolved photophysical properties in neat films.

Like the steady-state photoluminescence, the time-dependent photoluminescence of polycrystalline films is significantly different from the one of PMMA films, or toluene solution for **X1**, **X4** and **X7**. We have seen in §5.1 that the steady-state fluorescence spectra of those neat films are composed of several bands. Time-resolved fluorescence spectra and decays were collected to evaluate the origin of each peak. In particular, we can see from the spectra recorded at different delay times that it is possible to distinguish different regimes (**Figure 5.16, 5.17, 5.18**).

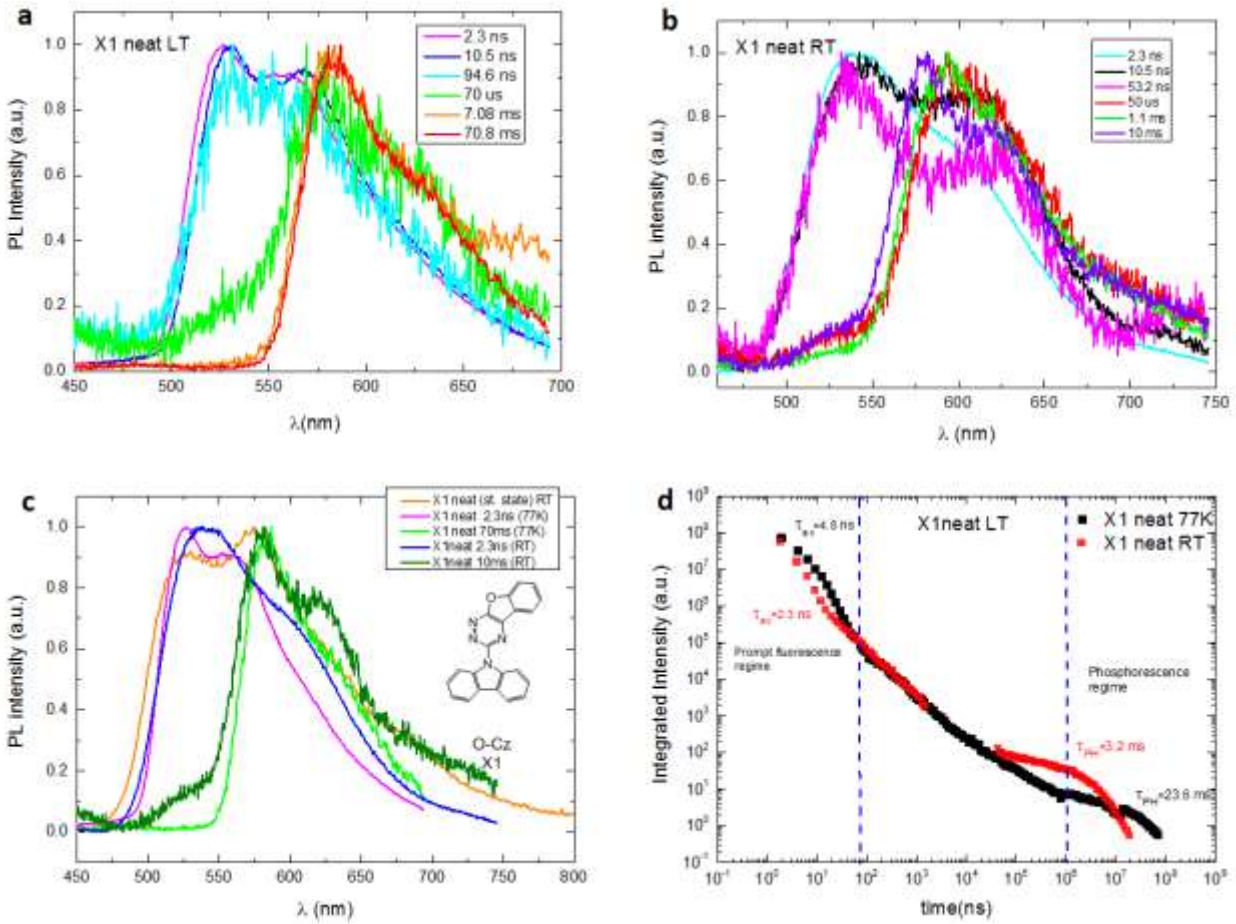

***Figure 5.16**: time-resolved emission spectra and decays of **X1** in neat films: a) time-resolved spectra at 77K, b) time-resolved spectra at room temperature, c) comparison of steady state (st) with representative time-resolved emission spectra at 77K and room temperature and d) decay curves at room temperature and 77K. λ_{exc} =355nm.*

For **X1** the short time (2.3 ns) emission at RT is broad with a maximum at 538 nm and a shoulder at 580 nm (**Figure 5.16b**). However, at 77K, two resolved bands are observed at 526 nm and 560 nm (**Figure 5.16a**). Nevertheless the onset is quite similar ($E_{onset\ RT}$ = 2.53 eV; $E_{onset\ 77K}$ =2.50 eV). At 77K, the blue-shifted and more resolved emission is due to the rigidochromic effect, which reduces the degrees of freedom for molecular relaxation.

At intermediate times, a red-shifted band appears in the spectra at RT and 77K located at 594 nm and 583 nm respectively. The blue band becomes a shoulder at ~525 – 530 nm after 50 µs at RT and 70 µs at 77K. This shoulder that remains up to the microsecond regime indicates the presence of a very weak DF contribution that probably arises from a triplet-triplet annihilation (TTA) process that is common in aggregates. Finally, at long delays, the RT spectra up to 10 ms do not evolve with the coexistence of the weak blue shoulder and the red band. However, at 77K the blue shoulder disappears and only the red band remains. Two characteristic average times have been extracted from the decay curves at RT and 77K (**Figure 5.16d**): a short one at 2.3 and 4.8 ns respectively and a long one at 3.2 and 23.6 ms respectively. The blue band at ≈525-530 nm is attributed to the prompt fluorescence of **X1**, which is predominant at short times at both temperatures. More interestingly, the red band at 580-600 nm is attributed to a long-lived phosphorescence emission that could be observed at 77K and RT. The comparison of the steady-state emission and time-resolved spectra (**Figure 5.16c**) shows that the structure observed in the former comes from the two bands resolved in the latter, thus demonstrating that RTP is present also in aerated condition.

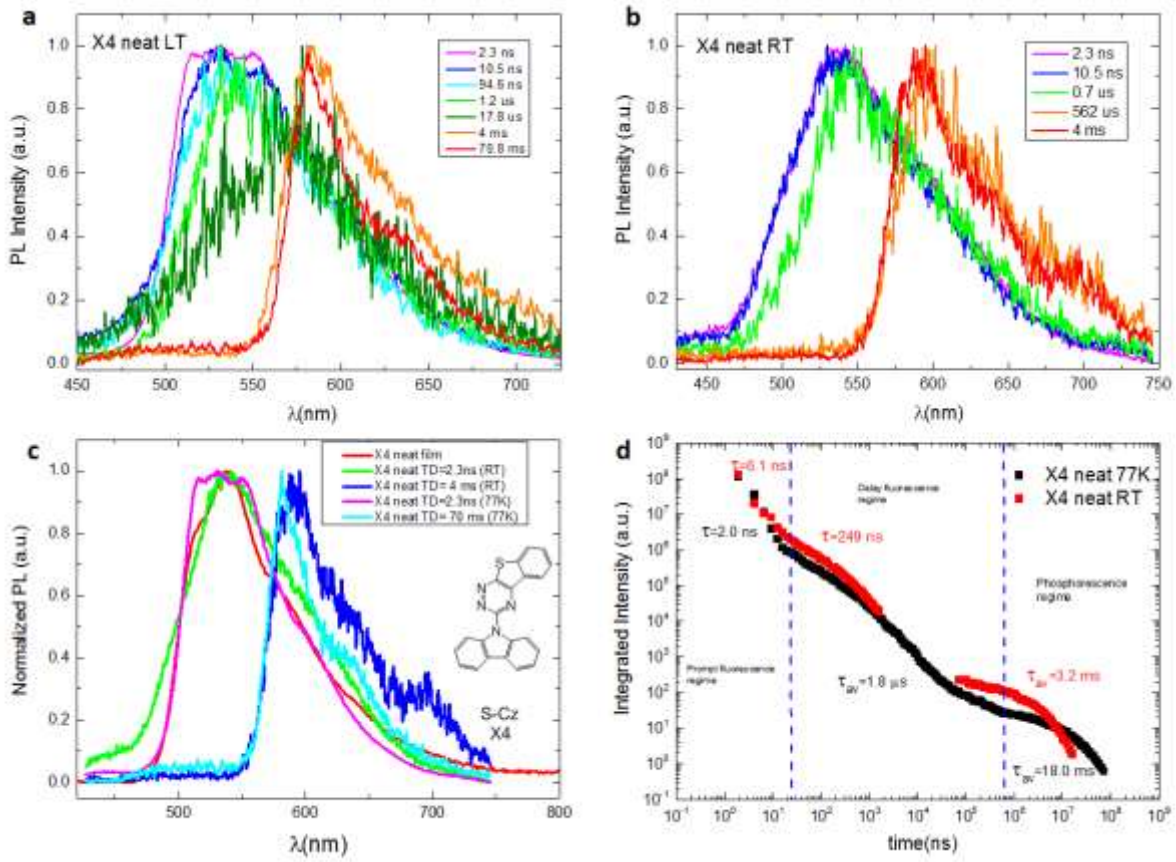

***Figure 5.17**: time-resolved emission spectra and decays of **X4** in neat films: a) time-resolved spectra at 77K, b) time-resolved spectra at room temperature, c) comparison of steady state (st) with representative time-resolved emission spectra at 77K and room temperature and d) decay curves at room temperature and 77K. λ_{exc} =355nm.*

X4 behaves almost similarly to **X1**. In particular, at a short time (2.3 ns) the emission at 77K is blue-shifted with three resolved bands at 515 nm, 532 nm and 549 nm, and a shoulder at 595 nm (**Figure 5.17a**). The short time (2.3 ns) RT emission is broader with a maximum at 542 nm (**Figure 5.17b**). The onset of the RT early time emission is blue-shifted by 0.1 eV compared to the 77K emission ($E_{onset\ RT}$ = 2.64 eV; $E_{onset\ 77K}$ =2.55 eVAt intermediate times, up to 1 microsecond, the emission slightly redshifts for both RT and 77K measurements. Between 1 and 17 μs, at 77K is detected a very weak red-shifted emission, whereas no emission between 1 and 550 μs is present at RT thus indicating that TADF emission decay fast. At a longer time for RT and 77K, after 550 μs and after 4ms respectively, both the emission maxima and the emission onset are strongly red-shifted and the early emission band completely disappears. These characteristic indicate also in this case the presence of phosphorescence emission both at RT and 77K. Three characteristic times have been extracted from the decay curve in the nanosecond and microsecond and millisecond regime, at RT and 77K (**Figure 5.17d**): a short one at 6.1 and 2.0 ns respectively an intermediate one at 0.25 μs and 1.8 μs respectively, and a long one at 3.2 and 18.0 ms respectively. The short time of 6.1 and 2.0 ns is typical of the PF emission. Conversely, the long one at 3.2 and 18.0 ms is attributed to the phosphorescence emission. However, the intermediate one at 0.25 and 1.8 μs is attributed to delayed fluorescence. But because of the large singlet-triplet energy gap (ΔE_{ST}= 0.35 eV), we think that the origin of the DF emission at 77K arises from a TTA process. On the other hand, such a high ΔE_{ST} gap is typical of room temperature phosphorescence (RTP) emitters[22, 46, 147]. The clearly red-shifted emission at 77K after a delay time of 17 μs is probably due to a mix between TTA-DF and phosphorescence. Finally, at long delay times, after 550 μs and after 4ms for 77K and RT respectively, a red-shifted band appears in the spectra at RT and 77K located at 594 nm and 581 nm respectively. As for **X1**, the red band at 580-600 nm is attributed to a long-lived phosphorescence emission that could be observed at 77K and RT.

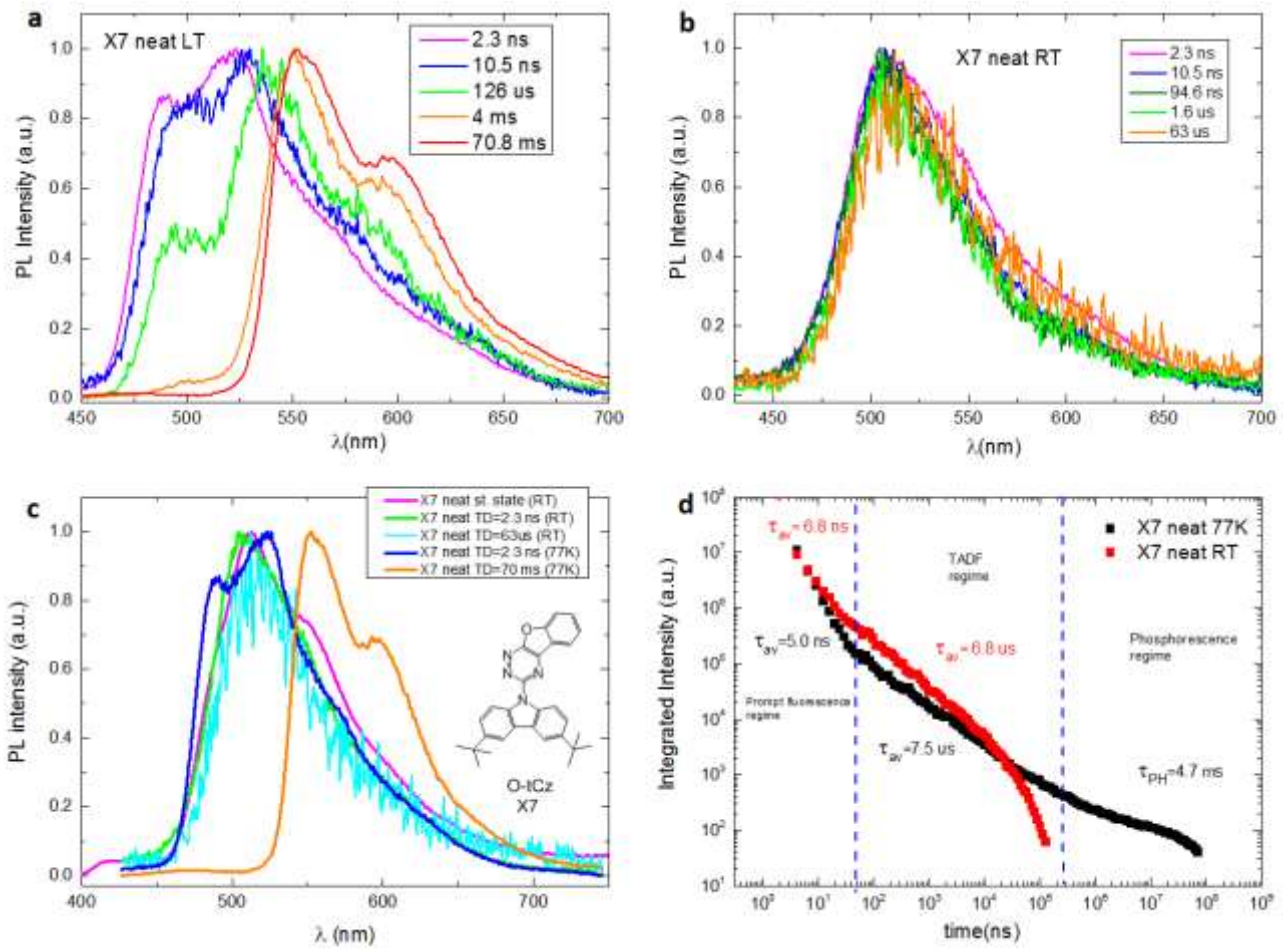

Figure 5.18*: time-resolved emission spectra and decay of* ***X7*** *in neat films: a) time-resolved spectra at 77K, b) time-resolved spectra at room temperature, c) comparison of steady state (st) with representative time-resolved emission spectra at 77K and room temperature and d) decay curves at room temperature and 77K.* λ_{exc} *=355nm.*

For **X7** the short time (2.3 ns) emission at RT is narrower than for **X1** and **X4** with a maximum at 504 nm (**Figure 5.18b**). However, at 77K two resolved bands are observed at 491 nm and 523 nm and a shoulder at 570 nm (**Figure 5.18a**). The onset for both early time measurements is quite similar ($E_{onset\ RT}$ = 2.66 eV and $E_{onset\ 77K}$ =2.67 eV). At long delay times, comparing the time-resolved emission at RT and 77K (**Figure 5.18c**), it becomes clear that **X7** neat films do not show RTP. In fact, while at 77K with a millisecond delay time clear phosphorescence of the material is observed, the same does not happen at RT where the emission ends before reaching 100 µs. Furthermore, the RT emission spectra do not change after 60 µs delay time respect to the prompt emission and the onset of the emission is the same as for the molecule dispersed in PMMA (**Figure 5.13d**). These two evidences demonstrate that **X7** polycrystalline neat film emits from the same state as the single molecule without forming emissive aggregates while maintaining TADF properties.

We think that the lack of RTP for this material is due to a different packing of the **X7** crystal compared to **X1** or **X4**. Indeed, the *t*-But-Cz is more hindered with respect to the unsubstituted carbazole **X1** or **X4**. This makes the molecules more distant from each other and they are less likely to form new aggregate states while packed in the crystal. Several examples are reported in literature [148-150] where it is demonstrated that bulky substituents are used to avoid aggregation quenching phenomena. This leads the **X7** molecule to maintain in the crystal the photophysical characteristics of the single molecule with only TADF emission.

5.4 Comparison between phosphorescence in PMMA and neat films.

The shape, onset, and phosphorescence maxima of **X1**, **X4** and **X7** in neat films are very different from those in PMMA (**Figure 5.19a**, **b**, and **c**). For all compounds, the emission band in PMMA has a Gaussian shape, while the emission in the neat film is structured with vibronic resolution typical of phosphorescence. In PMMA, both the phosphorescence maxima ($\lambda_{Ph\ \mathbf{X1}}$= 529 nm, $\lambda_{Ph\ \mathbf{X4}}$= 535 nm and $\lambda_{Ph\ \mathbf{X7}}$= 546 nm) and especially the phosphorescence onset ($E_{onset\ Ph\ \mathbf{X1}}$= 2.58 eV, $E_{onset\ Ph\ \mathbf{X4}}$= 2.50 eV and $E_{onset\ Ph\ \mathbf{X7}}$= 2.52 eV) are similar for all three compounds, thus indicating that the emission probably arises from the same triplet state. Since carbazole has the triplet energy at 3.20 eV, we can exclude that it is responsible for the phosphorescence of **X1**, **X4**, and **X7**. Therefore we hypothesize that it may arise either from the ^{3}LE of the TAZ Acceptor or from a mixed ^{3}LE and ^{3}CT state. It is indeed reported that for some TADF derivatives, the phosphorescence spectrum also shows some ^{3}CT character[151]. On the other hand, there is no data available for the phosphorescence of the benzofuro[3,2-*e*]-1,2,4-triazine or benzothieno[3,2-*e*]-1,2,4-triazine. Further experiments would thus be needed to conclude definitively.

On the other hand the phosphorescence emission spectra of neat films of **X1** ($\lambda_{Ph\ \mathbf{X1}}$=580, 628(s) nm; $E_{onset\ Ph\ \mathbf{X1}}$= 2.24eV) and **X4** ($\lambda_{Ph\ \mathbf{X4}}$=581, 630(s) nm; $E_{onset\ Ph\ \mathbf{X4}}$ = 2.21eV) look similar and strongly red-shifted compared to PMMA films. This indicates that the origin of the phosphorescence emission in **X1** and **X4** neat films is different from the one in PMMA. We think that it probably arises from the formation of a low lying triplet aggregated states, which is favored by the close proximity of the molecules in the solid-state. This interpretation is also corroborated by the work of Zhongfu An *et al*[141, 152]. They reported three different carbazolyl-1,3,5-triazine derivatives (**Figure 5.19d**) which present strong phosphorescence very close to that of our compounds. They conclude that the origin of the phosphorescence arises from the formation of H-aggregates. As already explained above, for **X7** we exclude the formation of aggregates and this is clearly indicated by the same onset of the PF in PMMA and neat film. Moreover, the onsets are similar also in the steady-state emission of **X7** in PMMA and **X7** neat film.

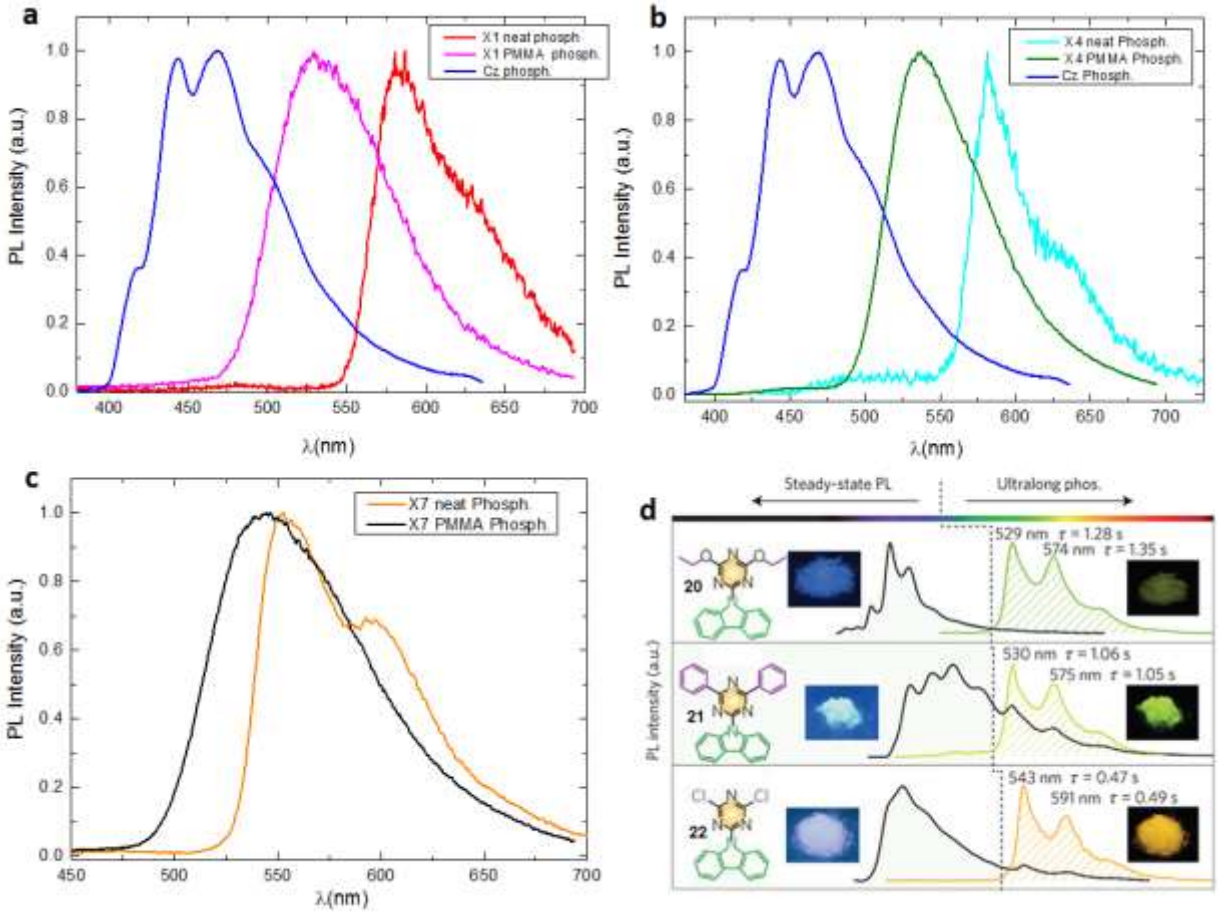

***Figure 5.19**: **a**) phosphorescence (77K) spectra of **X1** in neat film and PMMA in compared to the phosphorescence of carbazole; **b**) phosphorescence spectra (77K) of **X4** in neat film and PMMA compared to the phosphorescence of carbazole; **c**) phosphorescence spectra (77K) of **X7** in neat film and PMMA and **d**) photoluminescence and phosphorescence spectra of different carbazolyl-1,3,5-triazine derivatives.[141] λ_{exc} =355nm.*

5.5 Comparison between the photophysical properties of X1, X4, and X7 compounds in PMMA and neat films.

The properties that have been presented so far demonstrate that **X1** and **X4** clearly show aggregation-induced phosphorescence emission at room temperature. (AIE) is generally due to the blocking of intramolecular motions (mainly rotation) thanks to the restrained environment of the molecules blocked in the crystal[153] It has already been reported that aggregation-induced emission (AIE) could also be at the origin of room temperature phosphorescence (RTP) in crystals or amorphous films[46, 136]. In fact, since the transition between a triplet state and the singlet ground state is spin-forbidden the decay rate of the triplet state's radiative decay rate ($k_r(T)$)is

considerably longer than the singlet state radiative ($k_r(S)$) and all non-radiative (k_{nr}) ones. In the solid rigid medium and especially in crystals, large-amplitude motions, collision with solvent molecules and oxygen molecules, that occur in a solution and that constitute efficient paths for non-radiative deactivation, are strongly suppressed. Therefore, the radiative decay rate from the triplet state is able to compete with non-radiative decay processes that are slowed down even at room temperature, enabling RTP to be observed. Moreover, since the triplet state is located at lower energy than the singlet state, luminescence quenching is enhanced according to the energy gap law, which states that the non-radiative decay rates of electronic excited states increase as the energy gap decreases. It comes from the higher probability of coupling between the low energy excited state, with higher vibrational levels of the ground state, associated with large-amplitude molecular motions. Phosphorescence is also favored in aromatic compounds by the presence of O, N and S heteroatoms. These atoms are known to favor n-π* electronic transitions and hence to facilitate the intersystem crossing processes that populate triplet excited states.[154]

In addition to the AIE properties, the compounds show rigidochromic effect since there is a blue shift of the emission and enhanced quantum yields in PMMA (**Table 8**) with respect to toluene solutions (**Table 5**). In fact, if the QYs reported in (**Table 7**) for degassed toluene solution are compared with the ones reported in **Table 8** for PMMA films at RT, where the compounds also demonstrate TADF properties, we can see that the latter are the same or higher than the former. Finally, as discussed in the previous paragraph, **X1** and **X4** both exhibit RTP in neat films, contrarily to PMMA where they only present TADF at RT and phosphorescence at 77K.

X7 has a different behavior since it presents TADF both in neat film and PMMA at RT with phosphorescence only at 77K. DFT calculations show that at the optimized S_0 geometry (**Figure 5.2**) the $\Delta E_{(S-T)}$ is large (**Table 3**) because all three compounds have a rather flat structure with a partially delocalized HOMO (**Figure 5.5**). On the other hand, at the relaxed S_1 (CT) geometry (**Figure 5.6**, the compounds are more twisted and the $\Delta E_{(S-T)}$ is small (**Table 4**). Therefore, we think that in PMMA, which is a soft polymer, it is possible that the compounds undergo partial reorganization in the excited state so that $\Delta E_{(S-T)}$ is reduced leading to TADF at RT and phosphorescence at 77K. However, in **X1** and **X4** neat films, in addition to the formation of aggregates, the molecules are more constrained so the reorganization is not possible and a large $\Delta E_{(S-T)}$ is probably maintained, even in the excited state that cannot relax anymore to the optimal S_1 geometry. This means that phosphorescence is favored. In the case of **X7** the bulky *t*-Bu substituents do not allow tight packing in the polycrystalline film so the molecules can as well undergo some reorganization at RT and lead to TADF, while at 77K the more frozen environment allows observing phosphorescence.

Table 9: Photophysical properties of **X1**, **X4** and **X7** in solid state.

Sample	QY[b] (%)	λ_{PF}, nm	$\lambda_{Phos.}$, nm	DF/PF	S_1/T_1, eV	ΔE_{S1-T1} eV	$\tau_{1,av.}$ RT/77K (ns)	$\tau_{2,av}$ RT/77K (µs)	$\tau_{3,av.}$ RT/77K (ms)
X1 neat film Cryst	1.2%	538, 580 (s)	580, 628(s)	-	2.53/2.24	0.29	2.3/4.8	n.m	3.2/23.6
X1 Cryst powder	0.4%	n.m.	n.m.	-	2.43/n.m	n.m	n.m	n.m	n.m
X1 PMMA	1.2%	523	529	2.0	2.70/2.58	0.12	3.0/4.4	59.5/-	-/27.8
X4 neat film Cryst	0.4%	542	581, 630 (s)	-	2.56/2.21	0.35	6.1/2.0	0.25/1.8	3.2/18.0
X4 Cryst powder	0.6%	n.m.	n.m.	-	2.45/ n.m	n.m	n.m	n.m	n.m
X4 PMMA	0.8%	525	535	2.0	2.64/2.50	0.14	5.3/11.3	53.0/4.4	-/23.8
X7 neat film Cryst	0.4%	504	552, 592(s)	2.8	2.66/2.33	0.33	6.8/5.0	6.8/7.5	-/4.7
X7 Cryst powder	0.2%	n.m.	n.m.	-	2.68/ n.m	n.m	n.m	n.m	n.m
X7 PMMA	2.0%	531	546	2.7	2.63/2.52	0.11	4.5/5.5	56.8/-	-/60.0

[a]: n.m= not measured; [b]: measured in air

6. CONCLUSION.

A series of seven new asymmetric triazine-cored D-A compounds featuring a fused benzofuro[3,2-*e*]-1,2,4-triazine and benzothieno[3,2-*e*]-1,2,4-triazine moiety as the electron acceptor are presented in this chapter. The DFT calculations show that when the donor is phenoxazine (**X2** and **X5**) or phenothiazine (**X3** and **X6**), upon excitation the molecules relax their geometry and the A-D angle in the excited state becomes ~90°. The photophysical study confirms what observed in the calculations. These compounds do not emit in solution because the pure CT is a symmetry forbidden transition. However, they present emission in solid-state with AIE and CIE properties. The presence of emission only in the solid-state, and especially in the crystal, is probably due to the fact that the molecules cannot relax their ground state configuration in the excited state and thus the D-A angle deviates from 90°. The photophysical experiments of these molecules were limited to steady-state properties and the time-resolved properties have been only coarsely studied. Therefore more experiments are needed also to understand the states from where the emission is originated.

For the other molecules (**X1**, **X4** and **X7**), containing as a donor one carbazole derivative, the DFT calculation shows that MOs are less delocalized. In particular, for **X1** and **X4**, good TADF properties are observed only in toluene and in PMMA, where the molecules having the possibility to relax their configuration, can increase the spatial orbital localization and reduce the ΔE_{ST}. On the other hand, when **X1** and **X4** are in a crystalline form, their possibility to relax their configuration upon excitation is strongly suppressed and the ground state configuration results in a higher ΔE_{ST} that leads to a $K_{ISC} >> K_{RISC}$. This allows to strongly decrease the TADF and to observe crystallization induced RTP, which has been demonstrated arising from an aggregated state. The observation of RTP in the **X1** and **X4** crystals is favoured either from the presence of heteroatoms which plays a role in both $n \rightarrow \pi^*$ transition and “heavy atom effect”, but also from the strong suppression of non-radiative roto-vibration channels in the rigid crystal.

Contrarily, **X7** crystalline film displays only TADF properties without the formation of a new aggregate emissive state. This is due to the lower packing that arises from the bulky t-but-Cz which beyond to avoid the formation of aggregates, gives more free space to the molecule to relax its conformation even in the crystalline packing and thus to reduce the ΔE_{ST}.

To conclude, it is worthy of note that the occurrence of fluorophores deriving from an asymmetric triazine attractor is a completely new finding in the area of organic fluorophores and might open the way for the elaboration of new efficient TADF organic fluorophores.

GENERAL CONCLUSIONS AND PERSPECTIVES.

This thesis is mainly focused on the solid-state photophysical investigation of pure new organic materials, presenting intramolecular charge transfer states. Two different sets of compounds are presented, which are characterized by a donor-acceptor (D-A) or $Donor_1$-Acceptor-$Donor_2$ (D_1-A-D_2) systems molecule. Thanks to DFT calculations and XRD analysis we were able to finely analyse the molecular mechanisms leading to observe the interesting photophysical properties presented in this thesis. The novel donor-acceptor derivatives proved to exhibit TADF, crystallization induced emission (CIE), mechanochromc luminescence, and RTP. Interestingly, further understandings of TADF and RTP mechanisms, beyond the present literature were obtained. Firstly we focused on the development of a single white light TADF dual emission molecule. This is particularly advantageous both in the improvement of device stability and reproducibility but also because allows simplification of the device fabrication process.

In particular, we have studied the photophysical properties of a new class of TADF materials, which thanks to the D_1-A-D_2 design, present a double CT emission. Beyond the benzonitrile acceptor core, phenoxazine was chosen for its strong electron donor character that allows to achieve a yellow-emission, on the other hand, thanks to the weak donor properties of carbazole was possible to obtain a blue-emission. These kinds of systems have been only few a studied in the literature. Therefore we consider very interesting the results obtained in our study, where we demonstrate that our systems can efficiently cover the emission in the entire visible range. Hence, the presented design strategy provides a novel direction for producing white-light organic compounds.

Successively, we demonstrated how some selected materials, could change their color emission upon different supramolecular organizations. The different methods and conditions used to prepare the samples lead to different intermolecular interactions in the different aggregated forms. The presence of multiple D-A moieties facilitates the possibility to obtain different polymorphs, characterized by different molecular configurations that show different emission colours and TADF properties. Moreover, in this study, we showed how polymorphism is connected with mechanochromic luminescence (MCL), demonstrating that both phenomena bring the same photophysical properties. The research into organic multifunctional materials, combining into a single molecule both MCL and TADF functions, is still at the beginning, and therefore we think that the solid-state study of the photophysical properties of these materials could be interesting.

Successively, beyond the carbazole and phenoxazine donors, was introduced a new donor, e.g. phenothiazine, connected on the same benzonitrile acceptor core. Comparing the photophysical properties, it was demonstrated that if a relative weak donor, as carbazole is used, then it leads

to a small D-A angle in the ground state configuration. In solution, the free environment allows the D-A relaxation in the excited state, which allows activating the TADF properties. In the rigid crystal environment, the molecule cannot relax its configuration and the ground state configuration is maintained also in the excited. This results in good prompt fluorescence CIEE properties, but, the too-high ΔE_{S-T} prevents the TADF to be observed. When a strong phenothiazine donor replaces the carbazole, the ground state D-A angle becomes close to 90°. Upon excitation, the molecule relaxes in a perfectly orthogonal D-A configuration that totally isolating the HOMO and LUMO leads to a zero oscillator strength. It results that the compounds become practically not emissive in solution. In solid-state, the molecules blocked in the crystal lattice, cannot relax to a perfect D-A orthogonal configuration as in solution, and therefore are forced to maintain a near orthogonal configuration. This ensures a very small singlet-triplet energy gap that favours the RISC. It results that the emission becomes intense, and especially in the crystal a strong TADF is activated. We called this new phenomenon crystallization induces TADF (CITADF). Thanks to the very small singlet-triplet energy gap, the TADF is maintained, and even increases also at 80K, although the thermal activation is dramatically reduced. Moreover, in this work we demonstrated for the first time, that applying ultrasound to a water dispersion of amorphous nano/microparticles, it is possible to induce crystallization and thus to strongly increase both QY and TADF properties. We consider these results as a new strategy to develop new TADF materials using the unique properties of crystals, especially for optoelectronic devices application.

Finally, asymmetric 1,2,4-triazines (*as*-triazine) units, have been used as acceptor building blocks, substituted with various common donors, e.g. carbazole, phenoxazine, and phenothiazine. The strong donor properties of phenoxazine and phenothiazine lead also in this case to a completely orthogonal D-A angle in the excited state configuration that allows to observe emission only in solid-state and to suppress any possibility of emission in solution. On the other hand, the weaker donor ability of carbazole results in a flat D-A angle in the ground state configuration that becomes more orthogonal in the excited state. This allows to observe TADF emission both in solution and PMMA where the molecules can increase the D-A angle upon excitation, and thus reduce the singlet-triplet energy gap. On the other hand, in the crystalline film the molecules, upon excitation remain more blocked in the ground state configuration. This results that the higher singlet-triplet energy gap favourite the ISC but strongly reduces the RISC, and thus only crystallization induce RTP is observed. The presence of heteroatoms in these kind of systems also favour the RTP because of both $n \rightarrow \pi^*$ transition and the “heavy atom effect”. When the carbazole is functionalized with a bulky terbutyl group the lower crystalline packing gives more free space to the molecule, which can relax its conformation, and thus the reduced ΔE_{ST} allowed to observe TADF also in crystal, and the phosphorescence becomes visible only at 77K. Worthily of note, the occurrence of fluorophores deriving from an asymmetric triazine

attractor is a completely new finding in the area of organic fluorophores and might open the way for the elaboration of new efficient TADF and RTP organic fluorophores.

In conclusion, the remarkable photophysical properties of the molecules studied in this thesis have a strong potential in organic electronics and especially in OLED devices. Nevertheless, certainly further improvement can be obtained, especially in terms of quantum efficiency. In particular to achieve this goal it will be worthy functionalizing both the acceptor and the donor moieties, with bulky, electron-rich, or electron-poor substituents. This would allow, either to make the systems more rigid, and thus to reduce the non-radiative deactivation paths, but also to change the electronic properties of the materials, e.g. the donor and acceptor strengths.

In particular as regarding the optimization of the single white light molecule presented in Chapter 2, we think that it would be worth making the carbazole even more hindered. This because, the blue emissive peak relative to carbazole, was much more visible in solution respect to solid-state, and we think this could depend on the fact that in the more rigid environment the carbazole cannot relax its configuration. This effect was demonstrated in Chapter 5, where we have shown that if the carbazole is hindered, e.g. with terbutyl substituents, then the molecule has more possibility to relax its configuration even upon aggregation. Therefore the use of a more bulky substituent on the weaker (blue emissive) donors could be the key strategy to obtain an intense double emission even in solid-state.

Furthermore, it would be also worth trying to change the family of one, or the two donors connected on the central benzonitrile acceptor core. Moreover, it would be also interesting to explore and investigate the photophysical effect that could result, if the benzonitrile would be substituted with three different donors instead of two. As different donors, one may suggest investigating the family of dihydroacridine and diphenylamine, but especially the less common phenazasiline, phenazagermine, and tetramethylcarbazole. The design strategy proposed above could also lead to interesting improvements in mechanochromic luminescence and TADF properties. In addition, it would be also interesting to explore the mechanochromic luminescence properties of the other molecules, along with to try to synthesize different polymorphs using different techniques, e.g. physical vapor transport (PVT), flow-type PVT (f-PVT) and liquid–liquid interface precipitation (LLIP).

The results obtained in chapter 4 are certainly to be considered the most interesting of the whole thesis, as they are particularly original in the literature of TADF compounds. The crystal obtained with the **BzN-Pht** compound definitely needs particular attention and more investigations. In fact, due to its interesting properties, it could represent a promising active material in optoelectronic applications, especially in OLED and organic light-emitting field-effect transistor (OLEFET). In addition, the interesting switch on properties of the crystal could be used as in new mechanic sensors that may need the activation or suppression of the TADF emission. Moreover, further investigations of a new class of materials presenting the same CITADF

phenomena would be also interesting and could introduce in literature a completely new class of materials. Finally, we think that the ultrasound synthetic methodologies that lead to luminescent nanocrystals could represent a new interesting strategy, which may increase the possibility of using crystalline states in optoelectronic nano-devices. Hence, beyond the work of this thesis, more investigations are surely needed, either to better control the dimensions of the obtained nanocrystals, but also to develop a good technique that can integrate the obtained nanocrystal in devices. Additionally, are certainly expected to investigate how to scale-up the sonocrystallization process to other materials.

Finally, as regarding a-triazine compounds studied in Chapter 5, we think that also in this case it is worth optimizing the molecular structures by functionalizing the phenoxazine and phenothiazine donors, in order to try to reduce the D-A angle and thus to make the compounds emissive also in solution. Furthermore, it would be also interesting to investigate the effect of multiple donors on the same a-triazine core. Finally, as the a-triazine acceptors are considered definitely quite new in literature, it would be also interesting to design and study new molecules using the same class of acceptors.

EXPERIMENTAL SECTION.

1. QUANTUM MECHANICAL CALCULATIONS.

Ground state geometries were optimized at the B3LYP/6-31+g(d) level of calculation and the true nature of the minima verified by a subsequent frequency calculation. TDDFT on these geometries were done at the M06-2X/6-311+g(d,p) level of theory looking for both singlets and triplets levels in vacuo. Then first singlet excited state geometries were optimized at the M06-2X/6-31+g(d,p) level followed by a frequency calculation at the same level. Finally, a TDDFT calculation was done on these S_1 optimized geometries at the M06-2X/6-311+g(d,p) level of theory looking for both singlets and triplets levels in vacuo. The same approach was applied for the evaluation of the structure and properties of the first triplet excited state in some cases. All calculations were done with Gaussian 16 (Revision B.01) software. Data were analyzed with GaussView 6.0, PyMOL (The PyMOL Molecular Graphics System, Version 2.1.1 Schrödinger, LLC), Mercury 4.1.0 and GaussSum3.0 softwares.

2. CYCLIC VOLTAMMETRY.

The electrochemical cell comprised a platinum electrode with a 1 mm diameter of working area as a working electrode, an Ag electrode as a reference electrode and a platinum coil as an auxiliary electrode. Cyclic voltammetry measurements were conducted at room temperature at a potential scan rate of 50 mV/s and were calibrated against the ferrocene/ferrocenium redox couple. All voltammograms were recorded on a CH Instruments Electrochemical Analyzer model 660 potentiostat. Electrochemical measurements were conducted at 1.0 mM in electroactive molecules, in 0.1 M solutions of Bu_4NPF_6 (99%) in DCM at room temperature.

3. SAMPLE PREPARATION.

3.1 Solution.

In order to prepare the samples solution an opportune amount of material was first weighed and then it was dissolved in the solvent by sonicating the solution for half an hour to ensure fully dissolved solutions and avoid aggregation. The final concentrations were typically in the range between 10^{-6} and 10^{-5} M. All measurements were taken in a quartz cuvette both in air and degassed conditions. Degassing of the solution was obtained by a nitrogen flux bubbled into the

cuvette for 15 min, in order to remove all the oxygen dissolved. All the measurements in solutions were performed at room temperature.

3.2 Solid-State.

3.2.1 Dye dispersed in PMMA matrix.

PMMA is the most commercially important acrylic polymer that is also known as an organic glass thanks to its high transparency. This property makes it perfect to be used as a rigid matrix in the photophysical study. The drop-casting method at room temperature, assisted by solvent, was employed to prepare the sample with a final concentration of 0.1-0.05% in weight of the dye (0.1wt%PMMA). For preparing the sample, PMMA grains and the fluorescent TADF dyes were dissolved separately in dichloromethane (DCM) with the proper concentration and sonicated for half an hour at 40 °C, and then cast on a highly cleaned quartz slide. Fluorescent PMMA films were left to dry in solvent saturated conditions (i.e. to control the evaporation, fresh samples were confined into a chamber saturated with DCM) which ensures a slow (1 night) evaporation. All blends formed clear, glassy, transparent solid films.

3.2.2 Neat films casting.

All films were obtained by drop-casting DCM solutions at room temperature. This consists on solubilize the material in a suitable solvent and to cast by dropping on a target substrate. Follow the solvent evaporation which could be either fast if an amorphous film is desired, or slow (1 night in solvent saturated conditions) if a polycrystalline film is desired.

3.2.3 SVA crystalline film.

Another method used to obtain crystalline film consists in the SVA method (solvent vapour annealing), which is used to obtain macroscopic molecular assembly on the substrate surface and to form supramolecular structures featuring a higher degree of order. The SVA method consists to deposit the sample on a substrate (in general in quartz) contained in a chamber saturated with the vapours of an opportunely selected solvent (**Figure 6.1**). It results that the material is reorganized at the surfaces thanks to a partial re-solubilisation of the deposited layers. This allows the molecules to rearrange into structures characterized by a higher degree of order which in general may results in steadily assembled crystalline clusters.

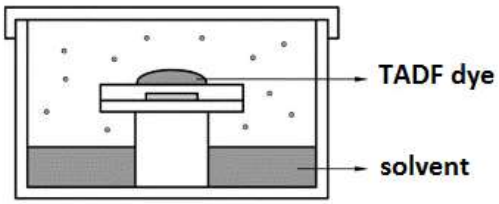

***Figure 6.1**: equipment set-up for the solvent vapour annealing method.*

3.2.4 Polycrystalline powders.

The crystals were grown from slow evaporation of different mixtures of two solvents and studied in a 1mm quartz cuvette or NMR tube.

4. PHOTOPHYSICAL EXPERIMENTS.

4.1 Optical Absorption.

UV−visible spectra were collected using a Cary 4000 double-beam spectrometer (Agilent) which has a reference beam and a sampling beam that passes through the sample. For solution studies, we used a 10 mm path quartz cuvette containing the solution with the sample and another cuvette of the same dimension containing only the solvent as a blank. For solid-state measures were used 2.5x2.5 cm quartz substrates on which was drop-casted a film of sample 0.1 wt% in PMMA matrix. In this case, the blank used was a clean substrate of quartz.

4.2 Steady-state spectrofluorimetry.

Emission spectra were measured on a Fluorolog-3 (Horiba) spectrofluorimeter equipped with a Peltier-cooled photomultiplier tube. A right-angle configuration was used for solutions, as well as a front-face configuration for efficient collection of light from films. The optical density of the samples was checked to be less than 0.1 to avoid reabsorption artifacts. A Xenon arc lamp was used as the excitation source. All the reported spectra are corrected from the instrumental response using a calibration curve supplied with the instrument.

4.3 Photoluminescence quantum yield (PLQY).

PLQY of a material is defined as the number of photons emitted divided by the number of photons absorbed. The relative fluorescence quantum yields in solution were determined from corrected spectra using the approach reported by Demas and Crosby[155] and using two different standards: quinine dication (Φ_F = 0.59 in HCl 0.1M) and $Ru(bpy)_3$ (Φ_F = 0.04 in H_2O) as references.

To obtain the absolute quantum yield of the films it was used a barium sulphate-coated Integrating Sphere F-3018(Horiba) inserted into the spectrofluorimeter sample compartment, following the method described by de Mello et al.[156]

4.4 Decay in Solution.

The fluorescence decay curves in the **ns** regime were obtained by the time-correlated single-photon counting (TCSPC) method with a femtosecond laser excitation composed of a Titanium Sapphire laser (Tsunami, Spectra-Physics) pumped by a doubled Nd:YVO_4 laser (Millennia Xs, Spectra-Physics). Light pulses at 990 nm from the oscillator were selected by an acousto-optic crystal at a repetition rate of 4 MHz, and then tripled at 330nm by non-linear crystals. Fluorescence photons were detected at 90° through a monochromator and a polarizer at magic angle by means of a Hamamatsu MCP R3809U photomultiplier, connected to a SPC-630 TCSPC module from Becker & Hickl. The instrumental response function was recorded before each decay measurement with a FWHM (full width at half-maximum) of ~25 ps. The fluorescence data were analysed using the Globals software package developed at the Laboratory for Fluorescence Dynamics at the University of Illinois at Urbana-Champaign, which includes reconvolution analysis and global non-linear least-squares minimization method.

The **µs** fluorescence decay curves were obtained using an Edinburgh instrument LP920 laser flash photolysis spectrometer combined with an Nd:YAG laser (Continuum) tripled at 355 nm via non-linear crystals. This third harmonic is optimized to pump an OPO that can generate 660nm signal and 330nm after a doubler stage. The Fluorescence photons were detected at 90° through a long pass filter and a monochromator by means of a Hamamatsu R928 photomultiplier. The Levenberg-Marquardt algorithm was used for non-linear least square fit (tail fit) as implemented in the L900 software (Edinburgh instrument). In order to estimate the quality of the fit, the weighted residuals were calculated.

4.5 Mechanochromic luminescence study.

The study of mechanochromism was performed using the simple setup shown in **Figure 6.2**. The sample was placed inside a ceramic mortar and the emission was collected before and after grinding the sample with a pestle. As excitation source was used a led Lamp coupled to an optic fiber. Another fiber was used to detect the emission and sent to a CCD camera which reconstructs the emission spectrum (not corrected).

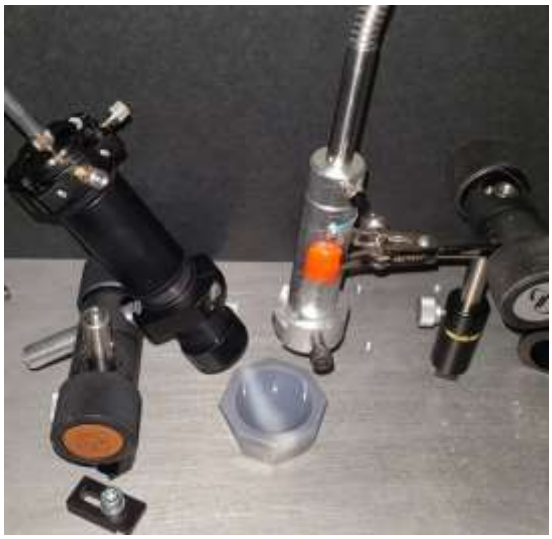

***Figure 6.2**: Setup used for the mechanochromic luminescence study.*

4.6 Time-resolved Emission.

All the time-resolved experiments were realized using an iCCD camera equipment that allows to measure individual spectra at a specific time delay (TD) with a given integration time (IT) after pulsed laser excitation. TD is the time at which the collection of photons emitted by the sample starts while IT is how long the photons are collected. Moreover, this technique allows to build decay curves by collecting several spectra with logarithmically increasing TD and IT. The data were collected at RT and 77K.

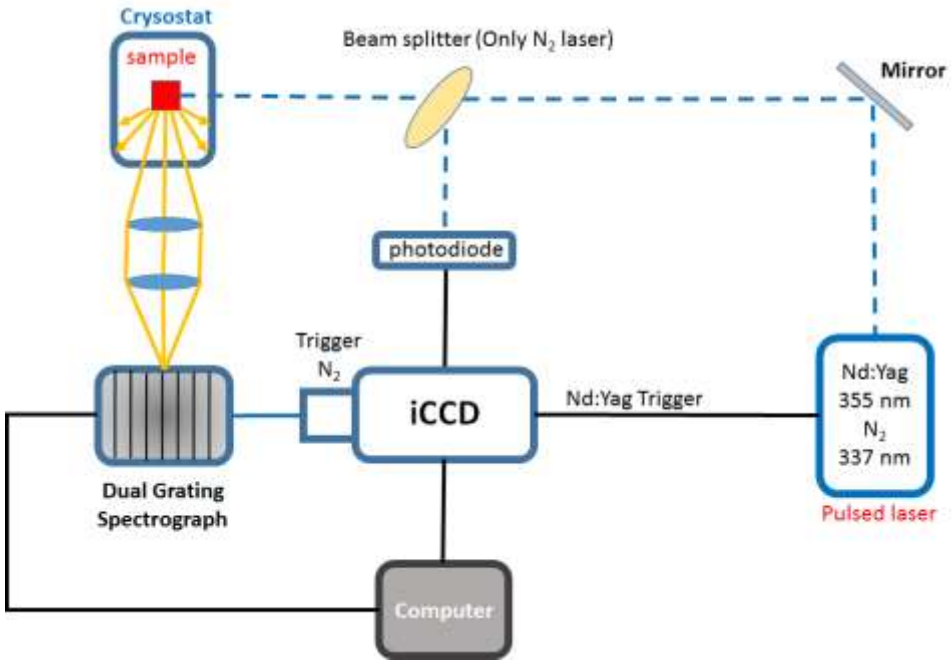

***Figure 6.3**: Time Gated Acquisition system setup. The Pulsed laser can be trigged to the iCCD by an electronic trigger (Nd:Yag) or through a fast photodiode (N_2 Laser).*

The system used to collect the time-resolved emission is schematized in **Figure 6.3**. The excitation source used was either the 3rd harmonic of a pulsed Nd:YAG laser emitting at 355/266 nm (150 ps FWHM) or nitrogen laser emitting at 337 nm (3 ns FWHM). The shorter pulsed Nd:YAG was used to collect the PL decays since it allowed better temporal resolution in the prompt region of the decay, while the N_2 laser allowed better control of the excitation power and therefore was used for the laser fluence acquisition. The 10Hz pulsed laser hits the sample inserted inside a cryostat oriented at 45°. The photons emitted by the sample are collimated and focused using two lenses into a spectrograph equipped with a 300 lines/mm grating that passes a variable spectral window to a sensitive gated intensified charge-coupled device (iCCD) camera (Stanford Computer Optics) with 200 ps resolution. The iCCD camera and Nd:YAG laser is synchronized by

an electrical trigger in two different ways according to the laser used. The Nd:YAG laser uses an electrical pulse to trigger the iCCD camera while for the nitrogen laser, part of the excitation beam is sent into a fast photodiode which sends electrical pulses to the iCCD. After the camera receives the trigger signal coming from the Nd:YAG laser, the zero time has to be determined. The zero time is the time taken by the laser pulse to excite the sample in the cryostat, this delay time arises mostly from the internal optical processes inside laser itself such as the flashlamp/Qswitch timing. Therefore many spectra of the laser were collected with short integration times and delay times. This delay time is constant and it has been measured at 975.5 ns, which added to the FWHM of the Nd:YAG laser (150 ps) constitutes also the zero time Spectra are obtained with the camera control software (4 Picos software) where TD and IT can be controlled with an accuracy of 0.1 ns. The intensity of the spectra collected with the iCCD at each delay time is integrated and normalised over the specific integration time. The integrated time normalised spectra are then plotted versus the delay time to build the PL decay curve. The sample temperature is controlled (from 80 to 320 K) using liquid nitrogen as a cooling system. As the laser fluence measurements are collected after a long TD (µs regime, where TADF works) can be used the N2 laser triggered optically by a fast photodiode which doesn't need to introduce any delay constant to set the zero time of the system.

4.7 Average life time.

To calculate average lifetimes (τ_{av}) for multi-exponential fits, were used the fitting parameters such as A_i and τ_i, where A_i is amplitude of i^{th} lifetime component and τ_i is the respective lifetime value. In the decay profiles acquired using time-resolved emission measurements, the y-axis is actually the number of photons and the x-axis is arrival time. So, Ai itself is not the number of photons with lifetime τ_i, but it is equal to Ai* τ_i.

So the average lifetime is equal to:

$$\tau_{av} = \frac{\sum A_i * \tau_i^2}{\sum A_i * \tau_i}$$

4.8 DLS Analysis

The nanocrystal dimensions obtained through sonication, was measured trough the DLS analysis techniques, by using the instrument NanoQ Vasco 2.5.9.0 - Cordouan Technologies (**Figure 6.4**). Dynamic Light Scattering (DLS) is a technique to characterize dilute and transparent dispersions of particles. Based on the analysis of scattered light fluctuations caused by the Brownian motion of particles, it provides sizes measurements from the nanometer up to a few microns.

***Figure 6.4**: NanoQ Vasco Dynamic Light Scattering system.*

In order to obtain the water nanocrystals dispersion was firstly prepared a solution of 1mg/ml of **Pht-BzN** in THF. Then, with a micropipette, 30 µl of the solution was taken and added to 30 ml of water and after 25 min of sonication, the nanocrystal dispersion was clearly obtained as indicated from the emission passing from dark yellow to bright sky-blue. A dilution of the sample in water was performed at 1/10 prior to DLS analysis. A few microliters of diluted solution were dropped off in the centre of the cell with a pipette and analysed by DLS.

REFERENCE

1. Perrin, R. D. e. F., Durées de fluorescence des sels d'uranyle solides et de leurs solutions,. *J. Phys. Radium* **1929,** *10* (5), 177-186.
2. Gilbert N. Lewis, D. L., T. Magel, Reversible Photochemical Processes in Rigid Media. A Study of the Phosphorescent State. *J. Am. Chem. Soc.* **1941,** *63* (11), 3005-3018.
3. Parker, C. A.; Hatchard, C. G., TRIPLET-SINGLET EMISSION IN FLUID SOLUTIONS - PHOSPHORESCENCE OF EOSIN. *Transactions of the Faraday Society* **1961,** *57* (11), 1894-&.
4. Parker, C. A.; Joyce, T. A., ACTIVATION-CONTROLLED DELAYED FLUORESCENCE OF BENZIL. *Chemical Communications* **1968,** (22), 1421-&.
5. R, W. F. a. H. A., *Phosphorescence and delayed fluorescence of organic substances Luminescence in Chemistry*

1968 p116–53.
6. Hirata, S.; Sakai, Y.; Masui, K.; Tanaka, H.; Lee, S. Y.; Nomura, H.; Nakamura, N.; Yasumatsu, M.; Nakanotani, H.; Zhang, Q. S.; Shizu, K.; Miyazaki, H.; Adachi, C., Highly efficient blue electroluminescence based on thermally activated delayed fluorescence. *Nature Materials* **2015,** *14* (3), 330-336.
7. Dias, F. B.; Santos, J.; Graves, D. R.; Data, P.; Nobuyasu, R. S.; Fox, M. A.; Batsanov, A. S.; Palmeira, T.; Berberan-Santos, M. N.; Bryce, M. R.; Monkman, A. P., The Role of Local Triplet Excited States and D-A Relative Orientation in Thermally Activated Delayed Fluorescence: Photophysics and Devices. *Adv Sci (Weinh)* **2016,** *3* (12), 1600080.
8. Zhang, Y.; Lai, S. L.; Tong, Q. X.; Lo, M. F.; Ng, T. W.; Chan, M. Y.; Wen, Z. C.; He, J.; Jeff, K. S.; Tang, X. L.; Liu, W. M.; Ko, C. C.; Wang, P. F.; Lee, C. S., High Efficiency Nondoped Deep-Blue Organic Light Emitting Devices Based on Imidazole-pi-triphenylamine Derivatives. *Chemistry of Materials* **2012,** *24* (1), 61-70.
9. Park, H.; Lee, J.; Kang, I.; Chu, H. Y.; Lee, J. I.; Kwon, S. K.; Kim, Y. H., Highly rigid and twisted anthracene derivatives: a strategy for deep blue OLED materials with theoretical limit efficiency. *Journal of Materials Chemistry* **2012,** *22* (6), 2695-2700.
10. Zou, Y.; Zou, J. H.; Ye, T. L.; Li, H.; Yang, C. L.; Wu, H. B.; Ma, D. G.; Qin, J. G.; Cao, Y., Unexpected Propeller-Like Hexakis(fluoren-2-yl)benzene Cores for Six-Arm Star-Shaped Oligofluorenes: Highly Efficient Deep-Blue Fluorescent Emitters and Good Hole-Transporting Materials. *Advanced Functional Materials* **2013,** *23* (14), 1781-1788.
11. Baldo, M. A.; O'Brien, D. F.; You, Y.; Shoustikov, A.; Sibley, S.; Thompson, M. E.; Forrest, S. R., Highly efficient phosphorescent emission from organic electroluminescent devices. *Nature* **1998,** *395* (6698), 151-154.
12. Lamansky, S.; Djurovich, P.; Murphy, D.; Abdel-Razzaq, F.; Lee, H. E.; Adachi, C.; Burrows, P. E.; Forrest, S. R.; Thompson, M. E., Highly phosphorescent bis-cyclometalated iridium complexes: Synthesis, photophysical characterization, and use in organic light emitting diodes. *Journal of the American Chemical Society* **2001,** *123* (18), 4304-4312.
13. Sun, Y.; Forrest, S. R., High-efficiency white organic light emitting devices with three separate phosphorescent emission layers. *Applied Physics Letters* **2007,** *91* (26).
14. Yersin, H., *Highly Efficient OLEDs with Phosphorescent Materials*. Wiley-VCH ed.; Wiley-VCH: 2008; p 458.
15. Sivasubramaniam, V.; Brodkorb, F.; Hanning, S.; Loebl, H. P.; van Elsbergen, V.; Boerner, H.; Scherf, U.; Kreyenschmidt, M., Fluorine cleavage of the light blue heteroleptic triplet emitter FIrpic. *Journal of Fluorine Chemistry* **2009,** *130* (7), 640-649.

16. Deaton, J. C.; Switalski, S. C.; Kondakov, D. Y.; Young, R. H.; Pawlik, T. D.; Giesen, D. J.; Harkins, S. B.; Miller, A. J. M.; Mickenberg, S. F.; Peters, J. C., E-Type Delayed Fluorescence of a Phosphine-Supported Cu-2(mu-NAr2)(2) Diamond Core: Harvesting Singlet and Triplet Excitons in OLEDs. *Journal of the American Chemical Society* **2010,** *132* (27), 9499-9508.
17. Czerwieniec, R.; Yersin, H., Diversity of Copper(I) Complexes Showing Thermally Activated Delayed Fluorescence: Basic Photophysical Analysis. *Inorganic Chemistry* **2015,** *54* (9), 4322-4327.
18. Kondakov, D. Y., Characterization of triplet-triplet annihilation in organic light-emitting diodes based on anthracene derivatives. *Journal of Applied Physics* **2007,** *102* (11).
19. Kondakov, D. Y., Role of triplet-triplet annihilation in highly efficient fluorescent devices. *Journal of the Society for Information Display* **2009,** *17* (2), 137-144.
20. Zhang, D. D.; Cai, M. H.; Zhang, Y. G.; Zhang, D. Q.; Duan, L., Sterically shielded blue thermally activated delayed fluorescence emitters with improved efficiency and stability. *Materials Horizons* **2016,** *3* (2), 145-151.
21. Kim, H. M.; Choi, J. M.; Lee, J. Y., Blue thermally activated delayed fluorescent emitters having a bicarbazole donor moiety. *Rsc Advances* **2016,** *6* (68), 64133-64139.
22. Dias, F. B.; Bourdakos, K. N.; Jankus, V.; Moss, K. C.; Kamtekar, K. T.; Bhalla, V.; Santos, J.; Bryce, M. R.; Monkman, A. P., Triplet Harvesting with 100% Efficiency by Way of Thermally Activated Delayed Fluorescence in Charge Transfer OLED Emitters. *Advanced Materials* **2013,** *25* (27), 3707-3714.
23. Penfold, T. J., On Predicting the Excited-State Properties of Thermally Activated Delayed Fluorescence Emitters. *Journal of Physical Chemistry C* **2015,** *119* (24), 13535-13544.
24. Nobuyasu, R. S.; Ren, Z. J.; Griffiths, G. C.; Batsanov, A. S.; Data, P.; Yan, S. K.; Monkman, A. P.; Bryce, M. R.; Dias, F. B., Rational Design of TADF Polymers Using a Donor-Acceptor Monomer with Enhanced TADF Efficiency Induced by the Energy Alignment of Charge Transfer and Local Triplet Excited States. *Advanced Optical Materials* **2016,** *4* (4), 597-607.
25. Luo, Y. J.; Lu, Z. Y.; Huang, Y., Triplet fusion delayed fluorescence materials for OLEDs. *Chinese Chemical Letters* **2016,** *27* (8), 1223-1230.
26. Gibson, J.; Monkman, A. P.; Penfold, T. J., The Importance of Vibronic Coupling for Efficient Reverse Intersystem Crossing in Thermally Activated Delayed Fluorescence Molecules. *Chemphyschem* **2016,** *17* (19), 2956-2961.
27. Ogiwara, T.; Wakikawa, Y.; Ikoma, T., Mechanism of Intersystem Crossing of Thermally Activated Delayed Fluorescence Molecules. *Journal of Physical Chemistry A* **2015,** *119* (14), 3415-3418.
28. Milian-Medina, B.; Gierschner, J., Computational design of low singlet-triplet gap all-organic molecules for OLED application. *Organic Electronics* **2012,** *13* (6), 985-991.
29. Dias, F. B.; Pollock, S.; Hedley, G.; Palsson, L. O.; Monkman, A.; Perepichka, II; Perepichka, I. F.; Tavasli, M.; Bryce, M. R., Intramolecular charge transfer assisted by conformational changes in the excited state of fluorene-dibenzothiophene-S,S-dioxide co-oligomers. *Journal of Physical Chemistry B* **2006,** *110* (39), 19329-19339.
30. Lim, B. T.; Okajima, S.; Chandra, A. K.; Lim, E. C., RADIATIONLESS TRANSITIONS IN ELECTRON DONOR-ACCEPTOR COMPLEXES - SELECTION-RULES FOR S1- T INTERSYSTEM CROSSING AND EFFICIENCY OF S1- S0 INTERNAL-CONVERSION. *Chemical Physics Letters* **1981,** *79* (1), 22-27.
31. Bunce, N. J., INTRODUCTION TO THE INTERPRETATION OF ELECTRON-SPIN RESONANCE-SPECTRA OF ORGANIC RADICALS. *Journal of Chemical Education* **1987,** *64* (11), 907-914.
32. Griffiths, D. J., HYPERFINE SPLITTING IN THE GROUND-STATE OF HYDROGEN. *American Journal of Physics* **1982,** *50* (8), 698-703.
33. Ward, J. S.; Nobuyasu, R. S.; Batsanov, A. S.; Data, P.; Monkman, A. P.; Dias, F. B.; Bryce, M. R., The interplay of thermally activated delayed fluorescence (TADF) and room temperature organic phosphorescence in sterically-constrained donor-acceptor charge-transfer molecules. *Chemical Communications* **2016,** *52* (12), 2612-2615.

34. Santos, P. L.; Ward, J. S.; Data, P.; Batsanov, A. S.; Bryce, M. R.; Dias, F. B.; Monkman, A. P., Engineering the singlet–triplet energy splitting in a TADF molecule. *Journal of Materials Chemistry C* **2016,** *4* (17), 3815-3824.
35. Chen, X. K.; Zhang, S. F.; Fan, J. X.; Ren, A. M., Nature of Highly Efficient Thermally Activated Delayed Fluorescence in Organic Light-Emitting Diode Emitters: Nonadiabatic Effect between Excited States. *Journal of Physical Chemistry C* **2015,** *119* (18), 9728-9733.
36. Marian, C. M., Mechanism of the Triplet-to-Singlet Upconversion in the Assistant Dopant ACRXTN. *Journal of Physical Chemistry C* **2016,** *120* (7), 3715-3721.
37. Gibson, J.; Penfold, T. J., Nonadiabatic coupling reduces the activation energy in thermally activated delayed fluorescence. *Physical Chemistry Chemical Physics* **2017,** *19* (12), 8428-8434.
38. Turro, N. J.; Ramamurthy, V.; Scaiano, J. C., *Principles of molecular photochemistry : an introduction*. University Science Books: Sausalito, Calif., 2009.
39. Goushi, K.; Yoshida, K.; Sato, K.; Adachi, C., Organic light-emitting diodes employing efficient reverse intersystem crossing for triplet-to-singlet state conversion. *Nature Photonics* **2012,** *6* (4), 253-258.
40. Foresman, J. B. F., *Æ., Exploring Chemistry with Electronic Structure Methods* 3rd ed ed.; Gaussian, Inc.: Wallingford, CT, , 2015.
41. Li, W. J.; Pan, Y. Y.; Yao, L.; Liu, H. C.; Zhang, S. T.; Wang, C.; Shen, F. Z.; Lu, P.; Yang, B.; Ma, Y. G., A Hybridized Local and Charge-Transfer Excited State for Highly Efficient Fluorescent OLEDs: Molecular Design, Spectral Character, and Full Exciton Utilization. *Advanced Optical Materials* **2014,** *2* (9), 892-901.
42. Haseyama, S.; Niwa, A.; Kobayashi, T.; Nagase, T.; Goushi, K.; Adachi, C.; Naito, H., Control of the Singlet–Triplet Energy Gap in a Thermally Activated Delayed Fluorescence Emitter by Using a Polar Host Matrix. *Nanoscale Research Letters* **2017,** *12* (1), 268.
43. Zhang, Q. S.; Kuwabara, H.; Potscavage, W. J.; Huang, S. P.; Hatae, Y.; Shibata, T.; Adachi, C., Anthraquinone-Based Intramolecular Charge-Transfer Compounds: Computational Molecular Design, Thermally Activated Delayed Fluorescence, and Highly Efficient Red Electroluminescence. *Journal of the American Chemical Society* **2014,** *136* (52), 18070-18081.
44. Nobuyasu, R. S.; Ward, J. S.; Gibson, J.; Laidlaw, B. A.; Ren, Z. J.; Data, P.; Batsanov, A. S.; Penfold, T. J.; Bryce, M. R.; Dias, F. B., The influence of molecular geometry on the efficiency of thermally activated delayed fluorescence. *Journal of Materials Chemistry C* **2019,** *7* (22), 6672-6684.
45. Chan, C. Y.; Cui, L. S.; Kim, J. U.; Nakanotani, H.; Adachi, C., Rational Molecular Design for Deep-Blue Thermally Activated Delayed Fluorescence Emitters. *Advanced Functional Materials* **2018,** *28* (11).
46. Pander, P.; Swist, A.; Turczyn, R.; Pouget, S.; Djurado, D.; Lazauskas, A.; Pashazadeh, R.; Grazulevicius, J. V.; Motyka, R.; Klimash, A.; Skabara, P. J.; Data, P.; Soloducho, J.; Dias, F. B., Observation of Dual Room Temperature Fluorescence–Phosphorescence in Air, in the Crystal Form of a Thianthrene Derivative. *The Journal of Physical Chemistry C* **2018,** *122* (43), 24958-24966.
47. dos Santos, P. L.; Ward, J. S.; Bryce, M. R.; Monkman, A. P., Using Guest-Host Interactions To Optimize the Efficiency of TADF OLEDs. *Journal of Physical Chemistry Letters* **2016,** *7* (17), 3341-3346.
48. Stachelek, P.; Ward, J. S.; dos Santos, P. L.; Danos, A.; Colella, M.; Haase, N.; Raynes, S. J.; Batsanov, A. S.; Bryce, M. R.; Monkman, A. P., Molecular Design Strategies for Color Tuning of Blue TADF Emitters. *Acs Applied Materials & Interfaces* **2019,** *11* (30), 27125-27133.
49. Zeng, W. X.; Lai, H. Y.; Lee, W. K.; Jiao, M.; Shiu, Y. J.; Zhong, C.; Gong, S. L.; Zhou, T.; Xie, G.; Sarma, M.; Wong, K. T.; Wu, C. C.; Yang, C., Achieving Nearly 30% External Quantum Efficiency for Orange-Red Organic Light Emitting Diodes by Employing Thermally Activated Delayed Fluorescence Emitters Composed of 1,8-Naphthalimide-Acridine Hybrids. *Advanced Materials* **2018,** *30* (5).
50. Chen, J. X.; Wang, K.; Zheng, C. J.; Zhang, M.; Shi, Y. Z.; Tao, S. L.; Lin, H.; Liu, W.; Tao, W. W.; Ou, X. M.; Zhang, X. H., Red Organic Light-Emitting Diode with External Quantum Efficiency beyond 20% Based on a Novel Thermally Activated Delayed Fluorescence Emitter. *Advanced Science* **2018,** *5* (9).

51. Chen, J. X.; Tao, W. W.; Chen, W. C.; Xiao, Y. F.; Wang, K.; Cao, C.; Yu, J.; Li, S. L.; Geng, F. X.; Adachi, C.; Lee, C. S.; Zhang, X. H., Red/Near-Infrared Thermally Activated Delayed Fluorescence OLEDs with Near 100 % Internal Quantum Efficiency. *Angewandte Chemie-International Edition* **2019,** *58* (41), 14660-14665.
52. Englman, R.; Jortner, J., The energy gap law for radiationless transitions in large molecules. *Molecular Physics* **1970,** *18* (2), 145-164.
53. Duan, L. A.; Qiao, J. A.; Sun, Y. D.; Qiu, Y., Strategies to Design Bipolar Small Molecules for OLEDs: Donor-Acceptor Structure and Non-Donor-Acceptor Structure. *Advanced Materials* **2011,** *23* (9), 1137-1144.
54. Lee, S. Y.; Yasuda, T.; Nomura, H.; Adachi, C., High-efficiency organic light-emitting diodes utilizing thermally activated delayed fluorescence from triazine-based donor-acceptor hybrid molecules. *Applied Physics Letters* **2012,** *101* (9).
55. Jenekhe, S. A.; Lu, L. D.; Alam, M. M., New conjugated polymers with donor-acceptor architectures: Synthesis and photophysics of carbazole-quinoline and phenothiazine-quinoline copolymers and oligomers exhibiting large intramolecular charge transfer. *Macromolecules* **2001,** *34* (21), 7315-7324.
56. Jankus, V.; Chiang, C. J.; Dias, F.; Monkman, A. P., Deep Blue Exciplex Organic Light-Emitting Diodes with Enhanced Efficiency; P-type or E-type Triplet Conversion to Singlet Excitons? *Advanced Materials* **2013,** *25* (10), 1455-1459.
57. Tanaka, H.; Shizu, K.; Nakanotani, H.; Adachi, C., Twisted Intramolecular Charge Transfer State for Long-Wavelength Thermally Activated Delayed Fluorescence. *Chemistry of Materials* **2013,** *25* (18), 3766-3771.
58. Daub, J.; Engl, R.; Kurzawa, J.; Miller, S. E.; Schneider, S.; Stockmann, A.; Wasielewski, M. R., Competition between conformational relaxation and intramolecular electron transfer within phenothiazine-pyrene dyads. *Journal of Physical Chemistry A* **2001,** *105* (23), 5655-5665.
59. Etherington, M. K.; Franchello, F.; Gibson, J.; Northey, T.; Santos, J.; Ward, J. S.; Higginbotham, H. F.; Data, P.; Kurowska, A.; Dos Santos, P. L.; Graves, D. R.; Batsanov, A. S.; Dias, F. B.; Bryce, M. R.; Penfold, T. J.; Monkman, A. P., Regio- and conformational isomerization critical to design of efficient thermally-activated delayed fluorescence emitters. *Nature Communications* **2017,** *8*.
60. Etherington, M. K.; Gibson, J.; Higginbotham, H. F.; Penfold, T. J.; Monkman, A. P., Revealing the spin-vibronic coupling mechanism of thermally activated delayed fluorescence. *Nature Communications* **2016,** *7*.
61. Dias, F. B.; Penfold, T. J.; Monkman, A. P., Photophysics of thermally activated delayed fluorescence molecules. *Methods and Applications in Fluorescence* **2017,** *5* (1).
62. Aydemir, M.; Xu, S. D.; Chen, C. J.; Bryce, M. R.; Chi, Z. G.; Monkman, A. P., Photophysics of an Asymmetric Donor-Acceptor-Donor' TADF Molecule and Reinterpretation of Aggregation-Induced TADF Emission in These Materials. *Journal of Physical Chemistry C* **2017,** *121* (33), 17764-17772.
63. Xu, S. D.; Liu, T. T.; Mu, Y. X.; Wang, Y. F.; Chi, Z. G.; Lo, C. C.; Liu, S. W.; Zhang, Y.; Lien, A.; Xu, J. R., An Organic Molecule with Asymmetric Structure Exhibiting Aggregation-Induced Emission, Delayed Fluorescence, and Mechanoluminescence. *Angewandte Chemie-International Edition* **2015,** *54* (3), 874-878.
64. Xie, Z. L.; Chen, C. J.; Xu, S. D.; Li, J.; Zhang, Y.; Liu, S. W.; Xu, J. R.; Chi, Z. G., White-Light Emission Strategy of a Single Organic Compound with Aggregation-Induced Emission and Delayed Fluorescence Properties. *Angewandte Chemie-International Edition* **2015,** *54* (24), 7181-7184.
65. Zhao, J.; Chen, X. J.; Yang, Z.; Liu, T. T.; Yang, Z. Y.; Zhang, Y.; Xu, J. R.; Chi, Z. G., Highly-Efficient Doped and Nondoped Organic Light-Emitting Diodes with External Quantum Efficiencies over 20% from a Multifunctional Green Thermally Activated Delayed Fluorescence Emitter. *Journal of Physical Chemistry C* **2019,** *123* (2), 1015-1020.

66. Huang, L. L.; Wen, X.; Liu, J. W.; Chen, M. X.; Ma, Z. Y.; Jia, X. R., An AIE molecule featuring changeable triplet emission between phosphorescence and delayed fluorescence by an external force. *Materials Chemistry Frontiers* **2019,** *3* (10), 2151-2156.
67. Yang, Z.; Mao, Z.; Xu, C.; Chen, X. J.; Zhao, J.; Yang, Z. Y.; Zhang, Y.; Wu, W.; Jiao, S. B.; Liu, Y.; Aldred, M. P.; Chi, Z. G., A sterically hindered asymmetric D-A-D ' thermally activated delayed fluorescence emitter for highly efficient non-doped organic light-emitting diodes. *Chemical Science* **2019,** *10* (35), 8129-8134.
68. Huang, J.; Nie, H.; Zeng, J. J.; Zhuang, Z. Y.; Gan, S. F.; Cai, Y. J.; Guo, J. J.; Su, S. J.; Zhao, Z. J.; Tang, B. Z., Highly Efficient Nondoped OLEDs with Negligible Efficiency Roll-Off Fabricated from Aggregation-Induced Delayed Fluorescence Luminogens. *Angewandte Chemie-International Edition* **2017,** *56* (42), 12971-12976.
69. Uoyama, H.; Goushi, K.; Shizu, K.; Nomura, H.; Adachi, C., Highly efficient organic light-emitting diodes from delayed fluorescence. *Nature* **2012,** *492* (7428), 234-+.
70. Cho, Y. J.; Yook, K. S.; Lee, J. Y., High Efficiency in a Solution-Processed Thermally Activated Delayed-Fluorescence Device Using a Delayed-Fluorescence Emitting Material with Improved Solubility. *Advanced Materials* **2014,** *26* (38), 6642-6646.
71. Cho, Y. J.; Chin, B. D.; Jeon, S. K.; Lee, J. Y., 20% External Quantum Efficiency in Solution-Processed Blue Thermally Activated Delayed Fluorescent Devices. *Advanced Functional Materials* **2015,** *25* (43), 6786-6792.
72. Cho, Y. J.; Jeon, S. K.; Chin, B. D.; Yu, E.; Lee, J. Y., The Design of Dual Emitting Cores for Green Thermally Activated Delayed Fluorescent Materials. *Angewandte Chemie-International Edition* **2015,** *54* (17), 5201-5204.
73. Cho, Y. J.; Jeon, S. K.; Lee, J. Y., Molecular Engineering of High Efficiency and Long Lifetime Blue Thermally Activated Delayed Fluorescent Emitters for Vacuum and Solution Processed Organic Light-Emitting Diodes. *Advanced Optical Materials* **2016,** *4* (5), 688-693.
74. Park, I. S.; Lee, S. Y.; Adachi, C.; Yasuda, T., Full-Color Delayed Fluorescence Materials Based on Wedge-Shaped Phthalonitriles and Dicyanopyrazines: Systematic Design, Tunable Photophysical Properties, and OLED Performance. *Advanced Functional Materials* **2016,** *26* (11), 1813-1821.
75. Tanimoto, S.; Suzuki, T.; Nakanotani, H.; Adachi, C., Thermally Activated Delayed Fluorescence from Pentacarbazorylbenzonitrile. *Chemistry Letters* **2016,** *45* (7), 770-772.
76. Matsuo, K.; Yasuda, T., Blue thermally activated delayed fluorescence emitters incorporating acridan analogues with heavy group 14 elements for high-efficiency doped and non-doped OLEDs. *Chemical Science* **2019,** *10* (46), 10687-10697.
77. Karon, K.; Lapkowski, M., Carbazole electrochemistry: a short review. *Journal of Solid State Electrochemistry* **2015,** *19* (9), 2601-2610.
78. Vanallan, J. A.; Adel, R. E.; Reynolds, G. A., POLYNUCLEAR HETEROCYCLES .1. 1H-BENZO B PYRIDOL 1,2,3-MN PHENOXAZIN-1-1 AND RELATED SUBSTANCES. *Journal of Organic Chemistry* **1962,** *27* (5), 1659-&.
79. Sergio MBonesi, R.-B., Electronic spectroscopy of carbazole and N- and C-substituted carbazoles in homogeneous media and in solid matrix. *Journal of Luminescence*

Volume , Issue 1, May 2001, Pages 51-74 **2001,** *93* (1), 51-74.
80. Hirt, R. C.; King, F. T., SEARCH FOR WEAK ABSORPTION BANDS OF BENZONITRILE IN THE NEAR ULTRAVIOLET. *Journal of Chemical Physics* **1952,** *20* (11), 1821-1822.
81. Grabowski, Z. R.; Rotkiewicz, K.; Rettig, W., Structural changes accompanying intramolecular electron transfer: Focus on twisted intramolecular charge-transfer states and structures. *Chemical Reviews* **2003,** *103* (10), 3899-4031.

82. Zachariasse, K. A.; Grobys, M.; Tauer, E., Absence of dual fluorescence with 4-(dimethylamino)phenylacetylene. A comparison between experimental results and theoretical predictions. *Chemical Physics Letters* **1997,** *274* (4), 372-382.
83. Techert, S.; Zachariasse, K. A., Structure determination of the intramolecular charge transfer state in crystalline 4-(diisopropylamino)benzonitrile from picosecond X-ray diffraction. *Journal of the American Chemical Society* **2004,** *126* (17), 5593-5600.
84. Santos, P. L.; Ward, J. S.; Data, P.; Batsanov, A. S.; Bryce, M. R.; Dias, F. B.; Monkman, A. P., Engineering the singlet-triplet energy splitting in a TADF molecule. *Journal of Materials Chemistry C* **2016,** *4* (17), 3815-3824.
85. Luo, J. D.; Xie, Z. L.; Lam, J. W. Y.; Cheng, L.; Chen, H. Y.; Qiu, C. F.; Kwok, H. S.; Zhan, X. W.; Liu, Y. Q.; Zhu, D. B.; Tang, B. Z., Aggregation-induced emission of 1-methyl-1,2,3,4,5-pentaphenylsilole. *Chemical Communications* **2001,** (18), 1740-1741.
86. Dias, F. B.; Santos, J.; Graves, D. R.; Data, P.; Nobuyasu, R. S.; Fox, M. A.; Batsanov, A. S.; Palmeira, T.; Berberan-Santos, M. N.; Bryce, M. R.; Monkman, A. P., The Role of Local Triplet Excited States and D-A Relative Orientation in Thermally Activated Delayed Fluorescence: Photophysics and Devices. *Advanced Science* **2016,** *3* (12).
87. Feng-Ming Xie, J.-X. Z., Yan-Qing Li, Jian-Xin Tang Effects of the relative position and number of donors and acceptors on the properties of TADF materials. *Journal of Materials Chemistry C* **25 Jun 2020**.
88. Kasha, M., ENERGY TRANSFER MECHANISMS AND MOLECULAR EXCITON MODEL FOR MOLECULAR AGGREGATES. *Radiation Research* **1963,** *20* (1), 55-&.
89. Kasha, M. R., H. R.; El-Bayoumi, M. A., The Exciton Model in Molecular Spectroscopy. *Butterworths: London* **1965,** *11*, 371-392.
90. Hochstrasser, R. M.; Kasha, M., APPLICATION OF THE EXCITON MODEL TO MONOMOLECULAR LAMELLAR SYSTEMS. *Photochemistry and Photobiology* **1964,** *3* (4), 317-331.
91. Hestand, N. J.; Spano, F. C., Molecular Aggregate Photophysics beyond the Kasha Model: Novel Design Principles for Organic Materials. *Accounts of Chemical Research* **2017,** *50* (2), 341-350.
92. H., N., *1,2,4-Triazines and their Benzo-Derivatives. Comprehensive Heterocyclic Chemistry II(6), 507-574*.
93. Hong, Y. N.; Lam, J. W. Y.; Tang, B. Z., Aggregation-induced emission: phenomenon, mechanism and applications. *Chemical Communications* **2009,** (29), 4332-4353.
94. Dong, Y. Q.; Lam, J. W. Y.; Qin, A. J.; Li, Z.; Sun, J. Z.; Sung, H. H. Y.; Williams, I. D.; Tang, B. Z., Switching the light emission of (4-biphenylyl)phenyldibenzofulvene by morphological modulation: crystallization-induced emission enhancement. *Chemical Communications* **2007,** (1), 40-42.
95. Desiraju, G. R., Designer crystals: intermolecular interactions, network structures and supramolecular synthons. *Chemical Communications* **1997,** (16), 1475-1482.
96. Merz, K.; Vasylyeva, V., Development and boundaries in the field of supramolecular synthons. *Crystengcomm* **2010,** *12* (12), 3989-4002.
97. Data, P.; Takeda, Y., Recent Advancements in and the Future of Organic Emitters: TADF- and RTP-Active Multifunctional Organic Materials. *Chemistry-an Asian Journal* **2019,** *14* (10), 1613-1636.
98. Pashazadeh, R.; Pander, P.; Lazauskas, A.; Dias, F. B.; Grazulevicius, J. V., Multicolor Luminescence Switching and Controllable Thermally Activated Delayed Fluorescence Turn on/Turn off in Carbazole-Quinoxaline-Carbazole Triads. *Journal of Physical Chemistry Letters* **2018,** *9* (5), 1172-1177.
99. Sagara, Y.; Kato, T., Mechanically induced luminescence changes in molecular assemblies. *Nature Chemistry* **2009,** *1*, 605.
100. Chi, Z. G.; Zhang, X. Q.; Xu, B. J.; Zhou, X.; Ma, C. P.; Zhang, Y.; Liu, S. W.; Xu, J. R., Recent advances in organic mechanofluorochromic materials. *Chemical Society Reviews* **2012,** *41* (10), 3878-3896.

101. Ma, Z. Y.; Wang, Z. J.; Teng, M. J.; Xu, Z. J.; Jia, X. R., Mechanically Induced Multicolor Change of Luminescent Materials. *Chemphyschem* **2015,** *16* (9), 1811-1828.
102. Sagara, Y.; Yamane, S.; Mitani, M.; Weder, C.; Kato, T., Mechanoresponsive Luminescent Molecular Assemblies: An Emerging Class of Materials. *Advanced Materials* **2016,** *28* (6), 1073-1095.
103. Exner, O., *Dipole Moments in Organic Chemistry*. 1975.
104. Sun, H. T.; Hu, Z. B.; Zhong, C.; Chen, X. K.; Sun, Z. R.; Bredas, J. L., Impact of Dielectric Constant on the Singlet-Triplet Gap in Thermally Activated Delayed Fluorescence Materials. *Journal of Physical Chemistry Letters* **2017,** *8* (11), 2393-2398.
105. Ye, J. T.; Wang, L.; Wang, H. Q.; Pan, X. M.; Xie, H. M.; Qiu, Y. Q., Effective Impact of Dielectric Constant on Thermally Activated Delayed Fluorescence and Nonlinear Optical Properties: Through-Bond/-Space Charge Transfer Architectures. *Journal of Physical Chemistry C* **2018,** *122* (33), 18850-18859.
106. De Luca, G.; Treossi, E.; Liscio, A.; Mativetsky, J. M.; Scolaro, L. M.; Palermo, V.; Samori, P., Solvent vapour annealing of organic thin films: controlling the self-assembly of functional systems across multiple length scales. *Journal of Materials Chemistry* **2010,** *20* (13), 2493-2498.
107. Tao, Y.; Yuan, K.; Chen, T.; Xu, P.; Li, H. H.; Chen, R. F.; Zheng, C.; Zhang, L.; Huang, W., Thermally Activated Delayed Fluorescence Materials Towards the Breakthrough of Organoelectronics. *Advanced Materials* **2014,** *26* (47), 7931-7958.
108. Li, Y. F.; Xie, G. H.; Gong, S. L.; Wu, K. L.; Yang, C. L., Dendronized delayed fluorescence emitters for non-doped, solution-processed organic light-emitting diodes with high efficiency and low efficiency roll-off simultaneously: two parallel emissive channels. *Chemical Science* **2016,** *7* (8), 5441-5447.
109. Wang, H.; Xie, L. S.; Peng, Q.; Meng, L. Q.; Wang, Y.; Yi, Y. P.; Wang, P. F., Novel Thermally Activated Delayed Fluorescence Materials-Thioxanthone Derivatives and Their Applications for Highly Efficient OLEDs. *Advanced Materials* **2014,** *26* (30), 5198-5204.
110. Lee, I. H.; Song, W.; Lee, J. Y., Aggregation-induced emission type thermally activated delayed fluorescent materials for high efficiency in non-doped organic light-emitting diodes. *Organic Electronics* **2016,** *29*, 22-26.
111. Gan, S. F.; Luo, W. W.; He, B. R.; Chen, L.; Nie, H.; Hu, R. R.; Qin, A. J.; Zhao, Z. J.; Tang, B. Z., Integration of aggregation-induced emission and delayed fluorescence into electronic donor-acceptor conjugates. *Journal of Materials Chemistry C* **2016,** *4* (17), 3705-3708.
112. Furue, R.; Nishimoto, T.; Park, I. S.; Lee, J.; Yasuda, T., Aggregation-Induced Delayed Fluorescence Based on Donor/Acceptor-Tethered Janus Carborane Triads: Unique Photophysical Properties of Nondoped OLEDs. *Angewandte Chemie-International Edition* **2016,** *55* (25), 7171-7175.
113. Aizawa, N.; Tsou, C.-J.; Park, I. S.; Yasuda, T., Aggregation-induced delayed fluorescence from phenothiazine-containing donor–acceptor molecules for high-efficiency non-doped organic light-emitting diodes. *Polymer Journal* **2017,** *49* (1), 197-202.
114. Xiang, S. P.; Huang, Z.; Sun, S. Q.; Lv, X. L.; Fan, L. W.; Ye, S. F.; Chen, H. T.; Guo, R. D.; Wang, L., Highly efficient non-doped OLEDs using aggregation-induced delayed fluorescence materials based on 10-phenyl-10H-phenothiazine 5,5-dioxide derivatives. *Journal of Materials Chemistry C* **2018,** *6* (42), 11436-11443.
115. Im, Y.; Kim, M.; Cho, Y. J.; Seo, J.-A.; Yook, K. S.; Lee, J. Y., Molecular Design Strategy of Organic Thermally Activated Delayed Fluorescence Emitters. *Chemistry of Materials* **2017,** *29* (5), 1946-1963.
116. W., R., Photoinduced charge separation via twisted intramolecular charge transfer states. *Electron Transfer I. Topics in Current Chemistry* **1994,** *169*.
117. Bernard Valeur, M. N. B.-S., Molecular Fluorescence: Principles and Applications, 2nd ed. *Wiley-VCH, Weinheim,* **2012**, 592.
118. Speck, F.; Rombach, D.; Wagenknecht, H. A., N-Arylphenothiazines as strong donors for photoredox catalysis - pushing the frontiers of nucleophilic addition of alcohols to alkenes. *Beilstein Journal of Organic Chemistry* **2019,** *15*, 52-59.

119. McCarthy, B. G.; Pearson, R. M.; Lim, C. H.; Sartor, S. M.; Damrauer, N. H.; Miyake, G. M., Structure-Property Relationships for Tailoring Phenoxazines as Reducing Photoredox Catalysts. *Journal of the American Chemical Society* **2018,** *140* (15), 5088-5101.
120. Gorse, A. D.; Pesquer, M., INTRAMOLECULAR CHARGE-TRANSFER EXCITED-STATE RELAXATION PROCESSES IN PARASUBSTITUTED N,N-DIMETHYLANILINE - A THEORETICAL-STUDY INCLUDING SOLVENT EFFECTS. *Journal of Physical Chemistry* **1995,** *99* (12), 4039-4049.
121. Tanaka, H.; Shizu, K.; Nakanotani, H.; Adachi, C., Dual Intramolecular Charge-Transfer Fluorescence Derived from a Phenothiazine-Triphenyltriazine Derivative. *Journal of Physical Chemistry C* **2014,** *118* (29), 15985-15994.
122. Siraj, N.; Das, S.; Hasan, F.; Lu, C. F.; Kiruri, L. W.; Gall, K. E. S.; Warner, I. M., Enhanced S-2 emission in carbazole-based ionic liquids. *Rsc Advances* **2015,** *5* (13), 9939-9945.
123. Reichardt, C., SOLVATOCHROMIC DYES AS SOLVENT POLARITY INDICATORS. *Chemical Reviews* **1994,** *94* (8), 2319-2358.
124. Dong, Y. Q.; Lam, J. W. Y.; Li, Z.; Qin, A. J.; Tong, H.; Dong, Y. P.; Feng, X. D.; Tang, B. Z., Vapochromism of hexaphenylsilole. *Journal of Inorganic and Organometallic Polymers and Materials* **2005,** *15* (2), 287-291.
125. Tong, J. Q.; Wang, Y. J.; Wang, Z. Y.; Sun, J. Z.; Tang, B. Z., Crystallization-Induced Emission Enhancement of a Simple Tolane-Based Mesogenic Luminogen. *Journal of Physical Chemistry C* **2015,** *119* (38), 21875-21881.
126. Cotts, B. L.; McCarthy, D. G.; Noriega, R.; Penwell, S. B.; Delor, M.; Devore, D. D.; Mukhopadhyay, S.; De Vries, T. S.; Ginsberg, N. S., Tuning Thermally Activated Delayed Fluorescence Emitter Photophysics through Solvation in the Solid State. *Acs Energy Letters* **2017,** *2* (7), 1526-1533.
127. Hong, Y. N.; Lam, J. W. Y.; Tang, B. Z., Aggregation-induced emission. *Chemical Society Reviews* **2011,** *40* (11), 5361-5388.
128. Kenneth S. Suslick, E. V., Ultrasound. Its Chemical, Physical, and Biological Effects. *Science* **17 Mar 1989,** *243* (4897).
129. Leighton, T., The Acoustic Bubble

1st Edition. *Academic Press* **15th May 1997**, 613.
130. Sander, J. R. G.; Zeiger, B. W.; Suslick, K. S., Sonocrystallization and sonofragmentation. *Ultrasonics Sonochemistry* **2014,** *21* (6), 1908-1915.
131. Kim, H. N.; Suslick, K. S., The Effects of Ultrasound on Crystals: Sonocrystallization and Sonofragmentation. *Crystals* **2018,** *8* (7).
132. Park, C.; Park, J. E.; Choi, H. C., Crystallization-Induced Properties from Morphology-Controlled Organic Crystals. *Accounts of Chemical Research* **2014,** *47* (8), 2353-2364.
133. Diplom-Physiker; Effertz, C., Organic molecular crystals: from thin-films to devices : investigation of thin-film formation and electronic transport properties of polycrystalline perylene films. *Publikationsserver der RWTH Aachen University (2011) [Dissertation / PhD Thesis]* **2011**.
134. Dong, Y. Q.; Lam, J. W. Y.; Qin, A. J.; Liu, J. Z.; Li, Z.; Tang, B. Z., Aggregation-induced emissions of tetraphenylethene derivatives and their utilities as chemical vapor sensors and in organic light-emitting diodes. *Applied Physics Letters* **2007,** *91* (1).
135. Maggiore, A.; Pugliese, M.; Di Maria, F.; Accorsi, G.; Gazzano, M.; Fabiano, E.; Tasco, V.; Esposito, M.; Cuscuna, M.; Blasi, L.; Capodilupo, A.; Ciccarella, G.; Gigli, G.; Maiorano, V., Exploiting Photo- and Electroluminescence Properties of FIrpic Organic Crystals. *Inorganic Chemistry* **2016,** *55* (13), 6532-6538.
136. Hayduk, M.; Riebe, S.; Voskuhl, J., Phosphorescence Through Hindered Motion of Pure Organic Emitters. *Chemistry-a European Journal* **2018,** *24* (47), 12221-12230.
137. Prokhorov, A. M.; Kozhevnikov, D. N., Triazines, Tetrazines, and Fused Ring Polyaza Systems. In *Progress in Heterocyclic Chemistry, Vol 23*, Gribble, G. W.; Joule, J. A., Eds. 2011; Vol. 23, pp 403-425.

138. DeRosa, T. F., *Advances in Synthetic Organic Chemistry and Methods Reported in US Patents*. 2006; p 1-686.
139. Kaji, H.; Suzuki, H.; Fukushima, T.; Shizu, K.; Suzuki, K.; Kubo, S.; Komino, T.; Oiwa, H.; Suzuki, F.; Wakamiya, A.; Murata, Y.; Adachi, C., Purely organic electroluminescent material realizing 100% conversion from electricity to light. *Nature Communications* **2015,** *6*, 8476.
140. Nikolaenko, A. E.; Cass, M.; Bourcet, F.; Mohamad, D.; Roberts, M., Thermally Activated Delayed Fluorescence in Polymers: A New Route toward Highly Efficient Solution Processable OLEDs. *Advanced Materials* **2015,** *27* (44), 7236-+.
141. An, Z.; Zheng, C.; Tao, Y.; Chen, R.; Shi, H.; Chen, T.; Wang, Z.; Li, H.; Deng, R.; Liu, X.; Huang, W., Stabilizing triplet excited states for ultralong organic phosphorescence. *Nature Materials* **2015,** *14* (7), 685-690.
142. Xiang, Y. P.; Gong, S. L.; Zhao, Y. B.; Yin, X. J.; Luo, J. J.; Wu, K. L.; Lu, Z. H.; Yang, C. L., Asymmetric-triazine-cored triads as thermally activated delayed fluorescence emitters for high-efficiency yellow OLEDs with slow efficiency roll-off. *Journal of Materials Chemistry C* **2016,** *4* (42), 9998-10004.
143. Diana, P.; Martorana, A.; Barraja, P.; Lauria, A.; Montalbano, A.; Almerico, A. M.; Dattolo, G.; Cirrincione, G., Isoindolo 2,1-c benzo 1,2,4 triazines: A new ring system with antiproliferative activity. *Bioorganic & Medicinal Chemistry* **2007,** *15* (1), 343-349.
144. Seitz, G., & Richter, J. , Donorsubstituierte Benzonitrile als Seitenkettendienophile bei der intramolekularen [4+ 2]-Cycloaddition mit inversem Elektronenbedarf. Chemische Berichte, . **1989,** *122* (11), 2177-2181.
145. Stockmann, A.; Kurzawa, J.; Fritz, N.; Acar, N.; Schneider, S.; Daub, J.; Engl, R.; Clark, T., Conformational control of photoinduced charge separation within phenothiazine-pyrene dyads. *Journal of Physical Chemistry A* **2002,** *106* (34), 7958-7970.
146. Courcot, B.; Tran, D. N.; Fraisse, B.; Bonhomme, F.; Marsura, A.; Ghermani, N. E., Electronic properties of 3,3 '-dimethyl-5,5 '-bis(1,2,4-triazine): Towards design of supramolecular arrangements of N-heterocyclic Cu-I complexes. *Chemistry-a European Journal* **2007,** *13* (12), 3414-3423.
147. Huang, R. J.; Avo, J.; Northey, T.; Chaning-Pearce, E.; dos Santos, P. L.; Ward, J. S.; Data, P.; Etherington, M. K.; Fox, M. A.; Penfold, T. J.; Berberan-Santos, M. N.; Lima, J. C.; Bryce, M. R.; Dias, F. B., The contributions of molecular vibrations and higher triplet levels to the intersystem crossing mechanism in metal-free organic emitters. *Journal of Materials Chemistry C* **2017,** *5* (25), 6269-6280.
148. Langhals, H.; Ismael, R.; Yuruk, O., Persistent fluorescence of perylene dyes by steric inhibition of aggregation. *Tetrahedron* **2000,** *56* (30), 5435-5441.
149. Anthony, S. P., Organic Solid-State Fluorescence: Strategies for Generating Switchable and Tunable Fluorescent Materials. *Chempluschem* **2012,** *77* (7), 518-531.
150. Kubota, Y.; Uehara, J.; Funabiki, K.; Ebihara, M.; Matsui, M., Strategy for the increasing the solid-state fluorescence intensity of pyrromethene-BF2 complexes. *Tetrahedron Letters* **2010,** *51* (47), 6195-6198.
151. Huang, R. J.; Kukhta, N.; Ward, J. S.; Danos, A.; Batsanov, A. S.; Bryce, M. R.; Dias, F. B., Balancing charge-transfer strength and triplet states for deep-blue thermally activated delayed fluorescence with an unconventional electron rich dibenzothiophene acceptor. *Journal of Materials Chemistry C* **2019,** *7* (42), 13224-13234.
152. Baroncini, M.; Bergamini, G.; Ceroni, P., Rigidification or interaction-induced phosphorescence of organic molecules. *Chemical Communications* **2017,** *53* (13), 2081-2093.
153. He, Z. K.; Ke, C. Q.; Tang, B. Z., Journey of Aggregation-Induced Emission Research. *Acs Omega* **2018,** *3* (3), 3267-3277.
154. Zhao, J. Z.; Wu, W. H.; Sun, J. F.; Guo, S., Triplet photosensitizers: from molecular design to applications. *Chemical Society Reviews* **2013,** *42* (12), 5323-5351.

155. Demas, G. A. C. a. J. N., Measurement of photoluminescence quantum yields. Review. *J. Phys. Chem. 75* (8), 991–1024.
156. deMello, J. C.; Wittmann, H. F.; Friend, R. H., An improved experimental determination of external photoluminescence quantum efficiency. *Advanced Materials* **1997,** *9* (3), 230-&.

université PARIS-SACLAY
ÉCOLE DOCTORALE
Sciences Chimiques: Molécules, Matériaux, Instrumentation et Biosystèmes (2MIB)

Titre : Études photophysiques de nouveaux matériaux moléculaires hétérocycliques présentant du TADF et de la luminescence à l'état solide.

Mots clés : photochimie**,** photophysique, fluorescence retardée, dérivés de benzonitrile, dérivés de triazine, cristal.

Résumé : Dans cette thèse sont présentées les propriétés photophysiques de nouveaux émetteurs donneurs-accepteurs (D-A) caractérisés par des états de transfert de charge (CT). Les systèmes étudiés comprennent deux classes principales de molécules, caractérisées par des unités accepteurs de benzonitrile et de triazine. En ce qui concerne les unités donneuses, les deux systèmes présentent du carbazole, de la phénoxazine et de la phénothiazine. Les matériaux présentent une large gamme de propriétés optiques, telles que TADF, RTP, ainsi que des propriétés supramoléculaires telles que la luminescence mécanochromique (MCL) et l'émission induite par cristallisation (CIE). En résumé, dans le deuxième chapitre sont présentées trois séries de nouvelles molécules de systèmes Donor-Acceptor (D-A) et Donor1-Acceptor-Donor2 (D1-A-D2), comprenant un attracteur benzonitrile et divers ensembles de substituants carbazole et phénoxazine. En particulier, il est montré soit la possibilité d'accorder l'émission de couleur avec le nombre de substituants, mais aussi d'obtenir une double émission de TADF. Ensuite, au chapitre 3, l'étude des propriétés supramoléculaires des composés les plus efficaces est explorée. L'utilisation de différentes méthodes de préparation des échantillons a permis d'obtenir différents emballages moléculaires qui présentent différentes propriétés photophysiques.

Le comportement des MCL a également été constaté lorsque des contraintes externes (comme la pression ou l'effet du solvant) ont changé leur couleur et leurs propriétés photophysiques en réponse à un changement de leur environnement et de leur garnissage. Dans le chapitre 4, à notre connaissance, il est présenté pour la première fois qu'une molécule de TADF peut être activée par un mécanisme CIE lorsqu'elle est disposée dans un réseau cristallin. La distorsion de la géométrie moléculaire est à la base de ce phénomène, plutôt que la restriction du mouvement intramoléculaire comme cela se produit généralement pour les matériaux AIE courants. Ce chapitre montrera également comment l'application ultrasonore à un système de nanoparticules non solvant / AIE-TADF, peut affecter de manière significative l'auto-organisation de la nanoparticule et changer radicalement leur morphologie, d'une forme amorphe désordonnée à une forme cristalline. Enfin, dans le dernier chapitre, une série de nouvelles molécules donneur-accepteur (D-A) à base de noyau A-triazine sont également étudiées. Au-delà des propriétés du TADF, ils montrent une phosphorescence à température ambiante (RTP) dans les films cristallins purs. En particulier, il est démontré comment la conception moléculaire et la rigidité du milieu sont cruciales pour déterminer si la molécule émet par le biais du TADF ou du RTP.

Title: Photophysical studies of new heterocyclic molecular materials exhibiting TADF and solid-state luminescence.

Keywords : photochemistry**,** photophysic, delayed fluorescence, benzonitrile derivatives, triazine derivatives, crystal.

Abstract : In this thesis are presented the photophysical properties of new Donor-Acceptor (D-A) emitters characterized by charge transfer (CT) states. The systems studied comprise two main classes of molecules, characterized by benzonitrile and triazine acceptor units. Regarding donor units, both systems present carbazole, phenoxazine, and phenothiazine. The materials show a wide range of optical properties, such as TADF, RTP, along with supramolecular properties such as Mechanochromic luminescence (MCL) and crystallization induced emission (CIE). In summary, in the second chapter are presented three series of new Donor-Acceptor (D-A) and Donor1-Acceptor-Donor2 (D1-A-D2) systems molecules, featuring a benzonitrile attractor and various sets of carbazole and phenoxazine substituents. In particular, it is shown either the possibility to tune the color emission with the number of substituents, and also to obtain a double TADF emission. Then, in Chapter 3 the study of the supramolecular properties of the most efficient compounds is explored. Using different sample preparation methods was possible obtaining different molecular packings that present different photophysical properties.

MCL behavior was also found when external stress (like pressure or the effect of solvent) changed their colour and photophysical properties in response to a change in their environment and packing. In Chapter 4 to the best of our knowledge, for the first time is presented that a TADF molecule can be activated through a CIE mechanism when arranged in a crystal lattice. Distortion of the molecular geometry lies at the base of this phenomenon, rather than the restriction of intramolecular motion as generally happens for common AIE materials. This chapter will also demonstrate how the ultrasound application to a system of non-solvent/AIE-TADF nanoparticles, can significantly affect the self-organization of the nanoparticle and dramatically change their morphology, from a disordered amorphous form to a crystalline one. Finally, in the last Chapter, a series of new A-triazine core-based Donor-Acceptor (D-A) molecules are also studied. Beyond the TADF properties, they show room temperature phosphorescence (RTP) in the crystalline neat films. In particular, it is demonstrated how the molecular design and rigidity of the medium, are crucial to determining whether the molecule emits through TADF or RTP.

Université Paris-Saclay
Espace Technologique / Immeuble Discovery
Route de l'Orme aux Merisiers RD 128 / 91190 Saint-Aubin, France